

# **THESE**

présentée en vue d'obtenir le grade de

## **DOCTEUR**

en Sciences de la Terre et de l'Univers

par

**Roger ROIG RODELAS**

Doctorat de l'Université de Lille délivré par IMT LILLE DOUAI

Titre de la thèse:

### **Chemical characterization, sources and origins of secondary inorganic aerosols measured at a suburban site in Northern France**

Soutenue publiquement le 29 juin 2018 devant le jury d'examen:

<b>Rapportrice</b>	Magda CLAEYS	Professeure émérite, University of Antwerp
<b>Rapporteur</b>	Jean-Luc JAFFREZO	Directeur de Recherche, CNRS IGE Grenoble
<b>Examineur</b>	Laurent POULAIN	Chercheur, TROPOS Leipzig
<b>Examineur</b>	Olivier FAVEZ	Ingénieur docteur, INERIS
<b>Encadrante</b>	Esperanza PERDRIX	Maître-Assistante, IMT Lille Douai
<b>Directrice de Thèse</b>	Véronique RIFFAULT	Professeure, IMT Lille Douai

Laboratoire d'accueil:

Département Sciences de l'Atmosphère et Génie de l'Environnement, IMT Lille Douai

Ecole Doctorale SMRE 104 (Lille, Artois, ULCO, UVHC, Centrale Lille, Chimie Lille, IMT Lille Douai)



## Résumé

Les particules fines troposphériques de diamètre aérodynamique inférieur à  $2,5\ \mu\text{m}$  ( $\text{PM}_{2.5}$ ) peuvent impacter la santé et les écosystèmes. Les aérosols inorganiques secondaires (AIS) et organiques (AO) contribuent fortement aux  $\text{PM}_{2.5}$ . Pour comprendre leur formation et leur origine, une campagne d'1 an (août 2015 - juillet 2016) de mesures horaires de gaz précurseurs inorganiques et d'ions hydrosolubles particuliers a été menée sur un site suburbain du nord de la France avec un MARGA 1S, complétées par les concentrations massiques en  $\text{PM}_{2.5}$ , carbone suie, oxydes d'azote et éléments traces. Des niveaux élevés de nitrate d'ammonium (NA) ont été observés la nuit au printemps et de sulfate d'ammonium la journée en été. L'étude de la contribution des sources par le modèle PMF (Positive Matrix Factorization) a permis d'identifier 8 facteurs sources: 3 régionaux (riche en sulfates, riche en nitrates et marin) pour 73 à 78%, et 5 locaux (trafic, combustion de biomasse, fond industriel métallurgique, industrie locale et poussières minérales) (22-27%). De plus, un HR-ToF-AMS (spectromètre de masse à aérosols) et un SMPS (granulomètre) ont été utilisés lors d'une campagne intensive en hiver, afin de mieux documenter l'AO et la formation de nouvelles particules, respectivement. L'application du PMF aux spectres de masses d'AO a permis d'identifier 5 facteurs liés au trafic (15%), à la cuisson (11%), à la combustion de biomasse (25%), et à une oxydation plus ou moins forte de la matière organique (33% et 16%). Plusieurs événements nocturnes de formation de nouvelles particules impliquant les AIS, notamment du NA, ont été observés.

**Mots clés:** particules fines, aérosol inorganique secondaire, aérosol organique, gaz précurseur, nitrate d'ammonium, spectrométrie de masse à aérosols, identification de sources, Positive Matrix Factorization

## Abstract

Tropospheric fine particles with aerodynamic diameters less than 2.5  $\mu\text{m}$  ( $\text{PM}_{2.5}$ ) may impact health, climate and ecosystems. Secondary inorganic (SIA) and organic aerosols (OA) contribute largely to  $\text{PM}_{2.5}$ . To understand their formation and origin, a 1-year campaign (August 2015 to July 2016) of inorganic precursor gases and  $\text{PM}_{2.5}$  water-soluble ions was performed at an hourly resolution at a suburban site in northern France using a MARGA 1S, complemented by mass concentrations of  $\text{PM}_{2.5}$ , Black Carbon, nitrogen oxides and trace elements. The highest levels of ammonium nitrate (AN) and sulfate were observed at night in spring and during daytime in summer, respectively. A source apportionment study performed by positive matrix factorization (PMF) determined 8 source factors, 3 having a regional origin (sulfate-rich, nitrate-rich, marine) contributing to  $\text{PM}_{2.5}$  mass for 73-78%; and 5 a local one (road traffic, biomass combustion, metal industry background, local industry and dust) (22-27%). In addition, a HR-ToF-AMS (aerosol mass spectrometer) and a SMPS (particle sizer) were deployed during an intensive winter campaign, to gain further insight on OA composition and new particle formation, respectively. The application of PMF to the AMS OA mass spectra allowed identifying 5 source factors: hydrocarbon-like (15%), cooking-like (11%), oxidized biomass burning (25%), less- and more-oxidized oxygenated factors (16% and 33%, respectively). Combining the SMPS size distribution with the chemical speciation of the aerosols and precursor gases allowed the identification of nocturnal new particle formation (NPF) events associated to the formation of SIA, in particular AN.

**Keywords:** fine particles, secondary inorganic aerosols, organic aerosols, precursor gases, ammonium nitrate, aerosol mass spectrometry, sources apportionment, Positive Matrix Factorization



## Table of contents

List of Figures .....	10
List of tables .....	14
List of Abbreviations.....	15
GENERAL INTRODUCTION .....	21
CHAPTER 1. Atmospheric Context .....	29
1.1 General introduction to atmospheric aerosols .....	29
1.1.1 Definition of atmospheric particulate matter (PM) .....	29
1.1.2 Size of aerosols .....	29
1.1.3 Sources.....	31
1.1.4 Aerosol life cycle .....	39
1.1.5 Chemical composition of aerosols .....	41
1.1.6 Effects .....	44
1.1.7 Legal framework.....	47
1.2 Secondary inorganic aerosols (SIA) .....	48
1.2.1 Sulfur species.....	48
1.2.2 Nitrogen species.....	52
1.2.3 Neutralization reactions for SIA formation .....	55
1.2.4 Ammonium nitrate formation .....	56
1.3 Techniques for the measurement of aerosols and gaseous precursors in the ambient air.....	60
1.3.1 Offline measurements .....	60
1.3.2 Online measurements.....	62
1.4 Source apportionment.....	62
1.4.1 Source receptor models.....	62
1.4.2 Positive matrix factorization (PMF) .....	64
1.4.3 PM <sub>2.5</sub> source apportionment with PMF in North-Western Europe.....	65
1.5 Work motivation.....	66
1.5.1 Pollution in Northern France .....	66
1.5.2 Previous studies in the region of Northern France .....	69
1.5.3 Issues in air quality modelling .....	71
1.6 Objectives and scientific strategy .....	75

1.7	References .....	78
CHAPTER 2. Materials and methods .....		89
2.1	Location of the campaign and summary of the instrumentation used .....	89
2.1.1	Site description .....	89
2.1.2	Air quality in Douai .....	90
2.1.3	Instrumentation .....	93
2.2	MARGA .....	96
2.2.1	Description.....	96
2.2.2	Literature review .....	101
2.2.3	Data validation.....	112
2.2.4	Detection limit calculations .....	113
2.3	Aethalometer .....	114
2.4	Partisol 2300 – filter sampling and ICP-MS analysis of trace and major elements	116
2.5	BAM-1020.....	117
2.6	Gas monitors.....	118
2.6.1	NO <sub>x</sub> .....	118
2.6.2	SO <sub>2</sub> .....	118
2.7	HR-ToF-AMS.....	119
2.7.1	Description and operating principle.....	119
2.7.2	Data collection .....	120
2.7.3	Data analysis .....	121
2.7.4	Calibrations of the AMS .....	124
2.8	Scanning Mobility Particle Sizer (SMPS) .....	127
2.9	Calculation of uncertainties .....	129
2.9.1	MARGA .....	129
2.9.2	Filter sampling and ICP-MS analysis of trace and major elements.....	130
2.10	Ratios for the analysis of the aerosol acidity and the oxidation of nitrogen and sulfur .....	132
2.11	Source apportionment.....	134
2.11.1	Application of PMF to hourly to daily-resolved data of inorganic compounds.....	134
2.11.2	Application of PMF to mass spectrometry data of organic compounds .....	136
2.12	Geographical determination of sources .....	137
2.12.1	Local sources.....	137

2.12.2 Distant sources .....	138
2.13 Thermodynamic partitioning analysis: ISORROPIA II .....	140
2.14 References .....	142
CHAPTER 3. Characterization and variability of inorganic aerosols and their gaseous precursors at a suburban site in northern France over one year (2015-2016) (ARTICLE 1)	149
1. Introduction.....	152
2. Materials and methods .....	154
2.1. Campaign description .....	154
2.2. Instrumentation.....	155
2.3. Ratios (NR and GR) .....	156
2.4. Weather and trajectory models .....	156
2.4.1.Non-parametric wind regression.....	156
2.4.2.Back-trajectory calculations .....	157
2.4.3.Potential source contribution function.....	157
2.5. Thermodynamic module.....	158
3. Results.....	158
3.1. PM <sub>2.5</sub> chemical composition and correlations between species .....	158
3.2. Seasonal daily variability of precursor gases and inorganic aerosol species .....	162
3.2.1.Precursor gases .....	162
3.2.2.Aerosols .....	167
3.3. Study of ratios and SIA partitioning.....	172
3.3.1.Ammonium neutralization ratio (NR) and gas ratio (GR).....	172
3.3.2.Hourly gas-aerosol partitioning of SIA .....	175
3.4. Source identification.....	177
3.4.1.Local sources .....	177
3.4.2.Distant sources.....	179
3.5. Characteristics of high daily PM <sub>2.5</sub> concentrations.....	181
4. Conclusions.....	184
5. Data availability .....	185
6. Acknowledgements.....	185
7. References.....	185
CHAPTER 4. Real-time assessment of wintertime organic aerosol characteristics and sources at a suburban site in northern France .....	193
1. Introduction.....	196

2. Materials and methods .....	198
2.1. Measurement site.....	198
2.2. Instrumentation.....	198
2.3. Source apportionment of OA.....	200
2.4. Geographical determination of sources .....	200
2.5. Ventilation coefficient .....	202
3. Results and discussion .....	202
3.1. Overview of NR-PM <sub>1</sub> .....	202
3.2. OA characteristics.....	204
3.3. Source apportionment of OA.....	206
3.3.1. HOA.....	207
3.3.2. COA .....	209
3.3.3. oBBOA .....	211
3.3.4. LO-OOA and MO-OOA .....	212
3.4. Impact of meteorological parameters and long range transport on NR-PM <sub>1</sub> characteristics .....	213
4. Conclusions.....	216
5. Acknowledgements.....	217
6. References.....	218
CHAPTER 5. Effect of high temporal resolution and database composition on source apportionment of PM <sub>2.5</sub> using positive matrix factorization .....	227
1. Introduction .....	230
2. Materials and methods .....	232
2.1. Site description .....	232
2.2. Instrumentation.....	233
2.3. Source apportionment.....	234
2.4. Geographical determination of sources .....	236
2.4.1. Non-parametric wind regression (NWR).....	236
2.4.2. Potential source contribution function (PSCF) .....	236
3. Results and discussion.....	238
3.1. Dataset presentation.....	238
3.2. Hourly PMF results .....	239
3.3. Daily PMF results.....	247
3.4. Geographical determination of source factors.....	254

3.5. Comparison with other SA studies .....	258
4. Conclusions .....	260
5. Acknowledgements .....	262
6. References .....	262
CONCLUSIONS AND PERSPECTIVES .....	271
ANNEX 0: Scientific Valorization .....	281
ANNEX 1: Detection limits for major and trace elements .....	282
ANNEX 2: Supplementary material for Article 1 .....	284
ANNEX 3: Supplementary material for Article 2.....	318
ANNEX 4: Supplementary material for Article 3.....	331

## List of Figures

Figure 1.1 Representation of aerosol size distribution and main processes of the aerosol life cycle (Buseck and Adachi, 2008).....	31
Figure 1.2 (a) Emission shares of NO <sub>x</sub> for EEA member countries for 2011 and (b) atmospheric emissions of NO <sub>x</sub> (in Kt per year) in the metropolitan France; *2016= Estimation (CITEPA, 2017) .....	35
Figure 1.3 (a) Emission shares of SO <sub>2</sub> for EEA member countries for 2011 and (b) atmospheric emissions of SO <sub>2</sub> (in Kt per year) in the metropolitan France; *2016= Estimation (CITEPA, 2017) .....	37
Figure 1.4 (a) Emission shares of NH <sub>3</sub> for EEA member countries for 2011 and (b) atmospheric emissions of NH <sub>3</sub> (in Kt per year) in the metropolitan France; *2016= Estimation (CITEPA, 2017) .....	38
Figure 1.5 Representation of the nucleation process from H <sub>2</sub> SO <sub>4</sub> , NH <sub>3</sub> , organics and other ions (Pierce, 2011) .....	40
Figure 1.6 Average size distribution of main aerosol ions (Seinfeld and Pandis, 2006) .....	42
Figure 1.7 PM <sub>2.5</sub> relative average composition at different European sites (Putaud et al., 2010) .....	44
Figure 1.8 Deposition potential of PM depending on the size (Kim et al., 2015) .....	45
Figure 1.9 Predicted average gain in life expectancy (in months) for 30-year old aged people in 25 European cities for a decrease in the annual average PM <sub>2.5</sub> level to the WHO recommendation of 10 µg m <sup>-3</sup> (Aphekom report) .....	45
Figure 1.10 Scattering of a radiation beam by (A) reflection, (B) refraction, (C) refraction and internal reflection and (D) diffraction (Jacob, 1999) .....	46
Figure 1.11 Comparison of aqueous-phase main oxidation pathways at 298 K (Seinfeld and Pandis, 2006).....	52
Figure 1.12 NH <sub>4</sub> NO <sub>3</sub> concentration dependence on temperature for a system with 7 and 26.5 µg m <sup>-3</sup> of NH <sub>3</sub> and HNO <sub>3</sub> , respectively, and RH 30% (from Seinfeld and Pandis, 2006).....	56
Figure 1.13 Deliquescence and efflorescence curves for some hygroscopic salts in relation to RH at 20 °C (Hidy, 1984).....	59
Figure 1.14 Schematic of a denuder-filter pack (Limón-Sánchez et al., 2002) .....	61
Figure 1.15 Synthesis of the different receptor models used for estimating pollution source contributions (from Viana et al., 2008) .....	63
Figure 1.16 Maps of France (left, in red the Hauts-de-France) and of the Hauts-de-France region (right). .....	67
Figure 1.17 Monthly averaged meteorological trends from 1981 to 2010 (blue and red curves: minimum and maximum temperatures; blue bars: cumulative precipitations; shaded yellow area: solar radiation).....	68
Figure 1.18 PM <sub>2.5</sub> seasonal averages (Wi: winter, Sp: spring; Su: Summer; Au: Autumn) measured in the station of Douai Theuriet between 2010 and 2016 .....	68
Figure 1.19 Measured and modelled monthly concentrations for NO <sub>3</sub> <sup>-</sup> (a), NH <sub>4</sub> <sup>+</sup> (b), SO <sub>4</sub> <sup>2-</sup> (c), HNO <sub>3</sub> (d) and NH <sub>3</sub> (e) (Schaap et al., 2011) .....	73
Figure 1.20 Measured and modelled daily concentrations for NO <sub>3</sub> <sup>-</sup> (a), SO <sub>4</sub> <sup>2-</sup> (b) and NH <sub>4</sub> <sup>+</sup> (c) (Schaap et al., 2011).....	74

Figure 1.21 Measured and modelled hourly concentrations for $\text{NO}_3^-$ (a), $\text{NH}_4^+$ (b), $\text{SO}_4^{2-}$ (c), $\text{HNO}_3$ (d) and $\text{NH}_3$ (e) (Schaap et al., 2011) .....	75
Figure 2.1 Maps of France (left) and “Hauts-de-France” (right) .....	90
Figure 2.2 Map of Douai showing the urban area (shaded grey area), main roads (orange lines), rivers (blue lines), railroad track (black line), industrial activities (blue symbols) and sampling site (red symbol). .....	91
Figure 2.3 View of the Portakabin where the permanent instrumentation was located (left) and MARGA 1S setup (right) .....	95
Figure 2.4 OMEGA trailer (left) where the HR-ToF-AMS (right) was installed .....	95
Figure 2.5 MARGA front view (left) and flow diagram (right).....	96
Figure 2.6 (a) Sample box front view; (b) WRD and (c) SJAC schematics .....	98
Figure 2.7 (a) Detector box front view; (b) syringe pumps; (c) sampling valves; (d) ion chromatographs .....	99
Figure 2.8 Example of calculated retention times for the anions.....	100
Figure 2.9 Air flow control box .....	101
Figure 2.10 HR-ToF-AMS diagram (DeCarlo et al., 2006).....	120
Figure 2.11 Data collection configuration for the campaign carried out in Douai .....	121
Figure 2.12 Flow calibration curve for the campaign carried out in Douai .....	125
Figure 2.13 Velocity of the particle relative to the aerodynamic diameter.....	127
Figure 2.14 Schematics of the DMA (left) and the CPC (right) .....	128
Figure 2.15 Fishbone diagram of the main sources of uncertainty in the analysis of aerosols and gases by the MARGA.....	129
Figure 2.16 Fishbone diagram of sources of uncertainty for metals.....	131
Figure 2.17 Scheme of the deconvolution of the organic matrix X into two different factors and a residual matrix (Zhang et al., 2011).....	136
Figure P1.1 Maps of France (left) and Douai (right) with the sampling site (yellow cross), the main roads (red lines), railroad (black line), city center (grey area), non-ferrous metal industry (brown area), slaughterhouse (green cross) and waste water treatment plant (WWTP, blue cross). .....	154
Figure P1.2 $\text{PM}_{2.5}$ average monthly (a) mass concentration and (b) relative contribution for the major chemical species, ND: not determined, BC: Black carbon. ....	161
Figure P1.3 Average daily profiles of (a) $\text{NO}$ , (b) $\text{NO}_2$ , (c) $\text{O}_3$ , (d) $\text{HONO}$ , (e) $\text{NH}_3$ , (f) $\text{SO}_2$ for each season (winter: blue; spring: green, summer: red, autumn: brown). * $\text{O}_3$ was obtained from the Atmo-HdF station in Douai Theuriet.....	163
Figure P1.4 $\text{HONO}$ vs. $\text{NO}_x$ concentrations for (a) all daytime-averaged points and (b) data averaged over rush hours (6:00-10:00 am). ....	164
Figure P1.5 Daily profiles of (a) $\text{PM}_{2.5}$ , (b) $\text{NO}_3^-$ , (c) $\text{NH}_4^+$ , (d) $\text{SO}_4^{2-}$ , (e) $\text{C}_2\text{O}_4^{2-}$ , (f) $\text{Na}^+$ , (g) $\text{Cl}^-$ , (h) $\text{Mg}^{2+}$ , (i) $\text{Ca}^{2+}$ , (j) $\text{K}^+$ , and (k) BC for each season (winter: blue; spring: green, summer: red, autumn: brown). ....	169
Figure P1.6 Neutralization ratio (NR) daily profiles for each season, with the corresponding seasonal averages. ....	173
Figure P1.7 (a) Observed vs. predicted $\text{NH}_4^+$ colored by $\text{Na}^+$ concentration; and (b) NWR annual plot for the neutralization ratio (NR). ....	174

Figure P1.8 Comparison between ISORROPIA II predicted values and MARGA measurements for (a) $\text{NH}_3$ , (b) $\text{HNO}_3$ , (c) $\text{NH}_4^+$ , and (d) $\text{NO}_3^-$ .....	176
Figure P1.9 NWR plots for the main precursor gases and particulate ions (concentrations in $\mu\text{g m}^{-3}$ ) over the whole field campaign. The radial and tangential axes represent the wind direction and speed in $\text{km h}^{-1}$ , respectively. ....	178
Figure P1.10 PSCF analysis for the three main particulate ions. The selected threshold is set at the 75 <sup>th</sup> percentile. All used back-trajectories were weighted using a sigmoidal function. ...	180
Figure P1.11 (a) Number of hours when hourly $\text{PM}_{2.5}$ is above $25 \mu\text{g m}^{-3}$ . (b) Average chemical composition for $\text{PM}_{2.5}$ hourly mass concentrations above $25 \mu\text{g m}^{-3}$ and (c) below $25 \mu\text{g m}^{-3}$ .....	182
Figure P2.1 Time series of NR- $\text{PM}_{10}$ , elemental ratios (OM:OC, H:C and O:C) and of the main meteorological parameters (T: temperature, RH: relative humidity, P: atmospheric pressure, WD: wind direction and WS: wind speed) .....	203
Figure P2.2 Median daily profiles for OM:OC, O:C, H:C and N:C .....	206
Figure P2.3 Van Krevelen diagram for all the data colored by time, with identified PMF factors (HOA: Hydrogen-like OA, COA: cooking-like OA; oBBOA: oxidized biomass burning OA, MO-OOA: more oxidized – oxygenated OA, LO-OOA: less oxidized – oxygenated OA). ....	206
Figure P2.4 (a) Factor profiles with fragments colored by chemical families, and (b) time series of the concentrations and mass fractions of the PMF factors (HOA: Hydrogen-like OA, COA: cooking-like OA; oBBOA: oxidized biomass burning OA, MO-OOA: more oxidized – oxygenated OA, LO-OOA: less oxidized – oxygenated OA). ....	208
Figure P2.5 Daily profiles of PMF factors by (a) concentration and (b) contribution to OA (HOA: Hydrogen-like OA, COA: cooking-like OA; oBBOA: oxidized biomass burning OA, MO-OOA: more oxidized – oxygenated OA, LO-OOA: less oxidized – oxygenated OA). .	209
Figure P2.6 NWR plots for AMS PMF factors, colored by mass concentration (radius: wind speed in $\text{km h}^{-1}$ ). HOA: Hydrogen-like OA, COA: cooking-like OA; oBBOA: oxidized biomass burning OA, MO-OOA: more oxidized – oxygenated OA, LO-OOA: less oxidized – oxygenated OA. ....	210
Figure P2.7 Averaged mass concentrations and relative contributions of PMF factors as a function of RH bins (the width of the bins, represented by the horizontal bars, was chosen to increase the representativeness of each interval, with $n \geq 40$ ). HOA: Hydrogen-like OA, COA: cooking-like OA; oBBOA: oxidized biomass burning OA, MO-OOA: more oxidized – oxygenated OA, LO-OOA: less oxidized – oxygenated OA. ....	212
Figure P2.8 Average chemical composition of NR- $\text{PM}_{10}$ for (a) period I and (b) period II. The OA fraction (highlighted in light green) is subdivided into its PMF factors. ....	215
Figure P3.1 (Left) $\text{PMF}_h$ factor profiles with concentrations (shaded grey bars) in $\mu\text{g m}^{-3}$ and contributions (red dots) in % for every species; (Right) Time series of $\text{PMF}_h$ factors together with the main tracer of each source. ....	241
Figure P3.2 (Left) annual and (right) seasonal average contributions (in %) of $\text{PMF}_h$ source factors to $\text{PM}_{2.5}$ (modeled concentrations) .....	242
Figure P3.3 Daytime and nighttime averaged contributions (in %) of $\text{PMF}_h$ source factors to $\text{PM}_{2.5}$ (modeled concentrations) .....	244



Figure P3.4 Daily variations of PMF <sub>h</sub> factor concentrations (in $\mu\text{g m}^{-3}$ ) for every season and for the whole year.....	245
Figure P3.5 Daily variations of (a) sulfate-rich, (b) nitrate-rich and (c) road traffic concentrations (in $\mu\text{g m}^{-3}$ ) together with the main trace gases for each source .....	246
Figure P3.6 PMF <sub>d</sub> source profiles with the concentrations (shaded grey bars) in $\mu\text{g m}^{-3}$ and contributions (red dots) in % for every species. MIB: Metal Industry Background. ....	248
Figure P3.7 Time series of PMF <sub>d</sub> factors together with the main tracer for each source (concentrations in $\mu\text{g m}^{-3}$ ). MIB: Metal Industry Background. ....	249
Figure P3. 8 Annual (left) and seasonal (right) average contributions (in %) of PMF <sub>d</sub> source factors to PM <sub>2.5</sub> (modeled concentrations). MIB: Metal Industry Background. ....	251
Figure P3.9 Comparison of the species concentrations (shaded bars, in $\mu\text{g m}^{-3}$ ) and contributions (filled circles, in %) for the common factors between PMF <sub>d</sub> (in blue) and PMF <sub>h</sub> (in red) approaches (only common species are shown). ....	254
Figure P3.10 Annual NWR plots of PMF <sub>h</sub> and PMF <sub>d</sub> factor concentrations (in $\mu\text{g m}^{-3}$ ) per wind direction. The radial axis represents the wind speed in $\text{km h}^{-1}$ .....	255
Figure P3.11 Annual PSCF probability maps for PMF <sub>h</sub> factors identified as regional. The selected threshold is set at the 75 <sup>th</sup> percentile. All used backtrajectories were weighted using a sigmoidal function.....	256
Figure P3.12 Comparison of the relative contributions of sources to PM <sub>2.5</sub> (in %) between various western European sites where the site typology and average PM mass concentration (in $\mu\text{g m}^{-3}$ ) are indicated below each bar.....	259

## List of tables

Table 1.1 Global emission estimates for major aerosol classes .....	32
Table 1.2 Inorganic tracers associated with industrial activities and traffic .....	36
Table 1.3 Settling velocities of aerosol particles at 1 atm (adapted from Hinds, 1999) .....	41
Table 1.4 Main characteristics of coarse and fine particles .....	42
Table 1.5 Dependence of the dissociation coefficient on temperature (T, in K) .....	57
Table 1.6 Thermodynamic cases for ammonium nitrate dissociation.....	57
Table 1.7 DRH and concentration for saturated solutions at 25°C (Hidy, 1984) .....	59
Table 1.8 Equilibrium state of ammonium nitrate and its precursor gases with relation to temperature and RH .....	60
Table 1.9 Distribution of estimated regional emissions in the Nord-Pas-de-Calais region for 2008 (emission inventory from Atmo Nord- Pas-de-Calais) .....	69
Table 2.1 Summary of main industrial activities in Douai and its surroundings by wind sector .....	92
Table 2.2 Summary of the used instrumentation in the field campaign.....	94
Table 2.3 Experimental detection limits of the MARGA .....	103
Table 2.4 Characteristics and results of the comparisons between MARGA and filter-based measurements published in recent studies .....	107
Table 2.5 Comparison results of the MARGA SO <sub>2</sub> against two SO <sub>2</sub> monitors .....	109
Table 2.6 Characteristics and results of the comparison between the MARGA and the AMS .....	109
Table 2.7 Summary of the performance of the MARGA based on the comparison between two MARGA units performed by Rumsey et al. (2014) .....	111
Table 2.8 This study and manufacturer DLs for every species analyzed by the MARGA (in µg m <sup>-3</sup> ) .....	114
Table 2.9 Fragments ( <i>m/z</i> ) used for the determination of major chemical species in low resolution mode (from Canagaratna et al., 2007).....	123
Table 2.10 Summary of the different calibrations and their frequency during the campaign in Douai .....	124
Table P1.1 Statistical summary (mean ± one standard deviation) of meteorological parameters for each season .....	159
Table P1.2 Statistical summary of all measured parameters at the site of Douai for each season: average, standard deviation (SD) and percentiles (P <sub>i</sub> ) are concentrations in µg m <sup>-3</sup> ; n <sub>v&gt;D</sub> : percentage of valid data, i.e. above the detection limit (DL) for each compound .....	160
Table P1.3 Summary of ambient HONO/NO <sub>x</sub> ratios reported in this work and other studies .....	166
Table P1.4 Summary of PM <sub>2.5</sub> chemical composition for each high concentration episode (concentrations in µg m <sup>-3</sup> ) .....	183
Table P3.1 Main statistics for the input data as used in PMF <sub>h</sub> (7862 points) and PMF <sub>d</sub> (298 points) (concentrations are in µg m <sup>-3</sup> except for elements analyzed by ICP-MS (from Ca to Zn) which are in ng m <sup>-3</sup> ).....	240

## List of Abbreviations

AE:	Aethalometer
AIM-IC:	Ambient Ion Monitor – Ion chromatography
AMS:	Aerosol Mass Spectrometer
BAM:	Beta Attenuation Monitor
BBOA:	Biomass burning-like aerosol
BC:	Black carbon
BVOC:	Biogenic volatile organic compound
CCN:	Cloud condensation nuclei
CDCE:	Composition-dependent collection efficiency
CE:	Collection efficiency
CMB:	Chemical mass balance
COA:	Cooking-like aerosol
CPC:	Condensation Particle Counter
CTM:	Chemistry Transport Model
C-ToF-AMS:	Compact Time-of-Flight Aerosol Mass Spectrometer
CV:	Coefficient of variation
DL:	Detection limit
DMA:	Differential Mobility Analyzer
DMPS:	Differential Mobility Particle Sizer
DMS:	Dimethyl sulfide
DRH:	Deliquescence relative humidity
EC:	Elemental carbon
EEA:	European Economic Area
EMEP:	European Monitoring and Evaluation Program
EPA:	United States Environmental Protection Agency
ERH:	Efflorescence relative humidity
FCB:	Flow control box
GAC:	Gas and Aerosol Collector
GPIC:	Gas Particle Ion Chromatography
GR:	Gas ratio
GV:	Guideline value
HEPA:	High Efficiency Particle Arrestance
HOA:	Hydrocarbon-like organic aerosol
HPLC:	High performance liquid chromatography
HR:	High resolution
HR-ToF-AMS:	High-Resolution Time-of-Flight Aerosol Mass Spectrometer
HYSPLIT:	HYbrid Single-Particle Lagrangian Integrated Trajectory
IB:	Ionic balance
IC:	Ion chromatography
ICP-MS:	Inductively Coupled Plasma – Mass Spectrometry
IE:	Ionization efficiency
LO-OOA:	Less oxidized - oxygenated organic aerosol

LOTOS-EUROS:	Long Term Ozone Simulation – European Operational Smog
LRT:	Long-range transport
LV:	Limit value
MARGA:	Monitor for Gases and AeRosols in ambient Air
MCP:	Multichannel Plate
MDRH:	Mutual deliquescence relative humidityx
ME:	Multilinear Engine
MEL:	European Metropolis of Lille
MFC:	Mass Flow Controller
MO-OOA:	More oxidized – oxygenated organic aerosol
MS:	Mass Spectrometry
MU:	Marga Unit
NOR:	Nitrogen oxidation ratio
NPF:	New particle formation event
NR:	Neutralization ratio
NR-PM1:	Non-refractory fine particles
NWR:	Non-parametric wind regression
OA:	Organic aerosol
oBBOA:	Oxidized biomass burning-like aerosol
OM:	Organic matter
OOA:	Oxygenated organic aerosol
PAH:	Polycyclic aromatic hydrocarbons
PBL:	Planetary Boundary Layer
PCA:	Principal Component Analysis
PE:	Polyethylene
PFA:	Perfluoroalkoxy
PIKA:	Peak Integration by Key Analysis
PILS:	Particle-Into-Liquid-Sampler
PM:	Particulate matter
PMF:	Positive matrix factorization
PNSD:	Particle number size distribution
POA:	Primary organic aerosol
POP:	Persistent organic pollutant
PSCF:	Potential source contribution function
PTFE:	Polytetrafluoroethylene
PToF:	Particle time of flight
QC:	Quality control
RIE:	Relative ionization efficiency
RH:	Relative humidity
RM:	Receptor model
SCOA:	Sulfur-containing organic aerosol
SCR:	Selective catalytic reduction system
SIA:	Secondary inorganic aerosols
SJAC:	Steam Jet Aerosol Collector

SMPS:	Scanning Mobility Particle Sizer
SNR:	Signal-to-noise ratio
SOA:	Secondary inorganic aerosols
SOR:	Sulfur oxidation ratio
SQUIRREL:	SeQUential Igor data RetRIEvaL
T:	Temperature
TEOM-FDMS:	Tapered Element Oscillation Monitor – Filter Dynamics Measurement System
UMR:	Unit mass resolution
UTC:	Universal Time Coordinated
VK:	Van Krevelen
VOC:	Volatile organic compound
WHO:	World Health Organization
WRD:	Wet Rotating Denuder
WSII:	Water soluble inorganic ions



---

# **GENERAL INTRODUCTION**

---





## GENERAL INTRODUCTION

The interest in atmospheric aerosols or particulate matter (PM) has grown large in the last decades due to their numerous effects towards the climate (Hallquist et al., 2009), environment (EEA, 2017) and most notably, human health (Kelly and Fussell, 2012). Only in the year 2016, ambient air pollution was responsible for 4.2 million deaths worldwide, mostly due to the inhalation of particulate matter (WHO, 2018). In Europe, the premature mortality associated to ambient air pollution is also alarmingly high, with estimations for the year 2012 ranging from 190,000 to 289,000 for low- to middle-income and high-income countries, respectively (WHO, 2016) . In France alone, a comprehensive study reported an annual average of 48,000 premature deaths related to PM<sub>2.5</sub> exposure (Santé publique France, 2016).

Particularly the region of northern France is frequently affected by high ambient levels of PM<sub>2.5</sub>. These recurring particulate pollution events are partly attributed to the presence of industrialized, agricultural or highly populated areas nearby despite of the flat topography which favors the dispersion of pollutants. While SIA is a great contributor to PM<sub>2.5</sub> in northwestern Europe (Putaud et al., 2010), it has previously been shown that in the north of France there is a particularly high contribution of biomass burning emissions during wintertime (Joaquin, 2015).

In order to reduce the PM<sub>2.5</sub> levels, it is necessary to apply effective pollution reduction strategies. A good knowledge on the sources of PM and its composition is therefore necessary both at the local and regional scales. A common and effective approach is the identification of PM sources by the use of statistical receptor models applied to a database of pollutants collected at a given location, also known as source apportionment. However, up to date most source apportionment studies have been carried out with low time resolution databases, which do not provide information about the (trans)formation processes of the aerosols or the change of pollution sources at a high time resolution, and are rather a reflection of the long-term equilibrium. This hampers the understanding of source patterns, which might be essential in the implementation of mitigation policies (Peng et al., 2016).

In this context, the main goal of this work is to improve the scientific knowledge on SIA and their precursor gases, as well as on their main drivers and their interaction with other particulate constituents. For this purpose, a MARGA 1S (Monitor for AeRosols and Gases in ambient Air), financed within the framework of the Laboratoire Central de Surveillance de la Qualité de l’Air funded by the French Ministry of Environment, has been implemented for the

first time in France over a year to measure the concentrations of SIA and their precursor gases at an hourly time resolution. The chosen site is an urban background one and the database obtained allows identifying the sources of PM<sub>2.5</sub> SIA, in order to help policymakers to devise effective mitigation strategies. This part of the work is inserted within the ISARD (*Identification des Sources d'AéRosols dans le Douaisis*) project, which is funded by ADEME (French Environment and Energy Management Agency), and aims at designing strategies to decrease particulate pollution in Douai and other similar cities of the northern Coal Basin. This long campaign was complemented by additional instruments, and more particularly, by an intensive wintertime campaign carried out using a High-Resolution Time-of-Flight Aerosol Mass Spectrometer (HR-ToF-AMS) in order to study the sources of organic aerosol (OA) and evaluate the importance of biomass burning emissions.

The first chapter of this manuscript presents an overview on the current knowledge about tropospheric aerosols, including their composition, sources and effects, with a specific focus towards SIA and their gaseous precursors. A summary on the main measurement techniques and a thorough description of the source apportionment approach and its application in North-Western Europe is also given. The chapter is completed by a presentation of the specific air pollution issues in northern France and of the main objectives of the thesis and work strategy.

The second chapter is centered on the description of the instrumentation used throughout the long-term and intensive campaigns. For the MARGA, the main instrument of work of this thesis, a special consideration is given, with a detailed description complemented by a review of its use in previous studies and its validation. While the HR-ToF-AMS, used in the intensive campaign, is also described thoroughly, the rest of the instrumentation is presented more briefly. In addition, we present the details of the methodologies used in this thesis, including the calculation of uncertainties, use of ratios, source apportionment, geographical determination of sources and study of the thermodynamic partitioning.

The core of the manuscript focuses on the presentation of the results, and is divided into three chapters in the form of scientific articles:

- The third chapter is based on the measurements obtained from the long-term measurement campaign and is presented under the form of an article entitled “Characterization and variability of inorganic aerosols and their gaseous precursors at a suburban site in northern France over one year (2015-2016)” submitted to

Atmospheric Environment. It describes the main characteristics and the variability of secondary inorganic aerosols and their gaseous precursors throughout one year, and presents a first approach on the possible sources of aerosol and their geographical origins. The study is complemented by the analysis of the characteristics of high pollution episodes.

- The fourth chapter is centered on the results of the intensive measurement campaign and focuses on the “Real-time assessment of wintertime organic aerosol characteristics and sources at a suburban site in northern France”, which is ready for submission. The article describes the main characteristics of the organic aerosol during winter and presents the results obtained from a typical source apportionment study applied to the organic fraction of the aerosol.
- The fifth chapter presents a thorough source apportionment study of  $PM_{2.5}$  based on the hourly database of MARGA and 2- $\lambda$  aethalometer measurements. This approach being not so common, a comparison with other source apportionment approaches performed with two more typical datasets (different input variables and/or temporal resolutions) is presented. The first one consists of a daily database where the hourly MARGA and aethalometer measurements have been averaged to daily values and major and trace elements have been included in order to take advantage of their tracing capabilities and eventually determine additional sources. The second one is based on the organic mass spectra presented in the fourth chapter. This chapter is also presented as a research article named “Effect on high temporal resolution and database composition on source apportionment of  $PM_{2.5}$  using positive matrix factorization” which is currently under preparation and needs to be sent to some co-authors.

Finally, the main conclusions drawn from the data analysis of these extended datasets are given together with some guidelines and perspectives for future work.

## References

- EEA: Air Quality in Europe 2017. [online] Available from: <https://www.eea.europa.eu/publications/air-quality-in-europe-2017>, 2017.
- Hallquist, M., Wenger, J. C., Baltensperger, U., Rudich, Y., Simpson, D., Claeys, M., Dommen, J., Donahue, N. M., George, C., Goldstein, A. H., Hamilton, J. F., Herrmann, H., Hoffmann, T., Iinuma, Y., Jang, M., Jenkin, M. E., Jimenez, J. L., Kiendler-Scharr, A., Maenhaut, W., McFiggans, G., Mentel, T. F., Monod, A., Prévôt, A. S. H., Seinfeld, J. H., Surratt, J. D., Szmigielski, R. and Wildt, J.: The formation, properties and impact of secondary organic aerosol: current and emerging issues, *Atmos Chem Phys*, 9(14), 5155–5236, doi:10.5194/acp-9-5155-2009, 2009.
- Joaquin: Composition and source apportionment of PM10. Joint Air Quality Initiative, Work Package 1 Action 2 and 3. Flanders Environment Agency, Aalst. [online] Available from: <http://joaquin.eu/>, 2015.
- Kelly, F. J. and Fussell, J. C.: Size, source and chemical composition as determinants of toxicity attributable to ambient particulate matter, *Atmos. Environ.*, 60(Supplement C), 504–526, doi:10.1016/j.atmosenv.2012.06.039, 2012.
- Peng, X., Shi, G.-L., Gao, J., Liu, J.-Y., HuangFu, Y.-Q., Ma, T., Wang, H.-T., Zhang, Y.-C., Wang, H., Li, H., Ivey, C. E. and Feng, Y.-C.: Characteristics and sensitivity analysis of multiple-time-resolved source patterns of PM2.5 with real time data using Multilinear Engine 2, *Atmos. Environ.*, 139(Supplement C), 113–121, doi:10.1016/j.atmosenv.2016.05.032, 2016.
- Putaud, J.-P., Van Dingenen, R., Alastuey, A., Bauer, H., Birmili, W., Cyrys, J., Flentje, H., Fuzzi, S., Gehrig, R., Hansson, H. C., Harrison, R. M., Herrmann, H., Hitzenberger, R., Hüglin, C., Jones, A. M., Kasper-Giebl, A., Kiss, G., Kousa, A., Kuhlbusch, T. A. J., Löschau, G., Maenhaut, W., Molnar, A., Moreno, T., Pekkanen, J., Perrino, C., Pitz, M., Puxbaum, H., Querol, X., Rodriguez, S., Salma, I., Schwarz, J., Smolik, J., Schneider, J., Spindler, G., ten Brink, H., Tursic, J., Viana, M., Wiedensohler, A. and Raes, F.: A European aerosol phenomenology – 3: Physical and chemical characteristics of particulate matter from 60 rural, urban, and kerbside sites across Europe, *Atmos. Environ.*, 44(10), 1308–1320, doi:10.1016/j.atmosenv.2009.12.011, 2010.
- Santé publique France: Impacts de l'exposition chronique aux particules fines sur la mortalité en France continentale et analyse des gains en santé de plusieurs scénarios de réduction de la pollution atmosphérique, [online] Available from: <http://invs.santepubliquefrance.fr/Publications-et-outils/Rapports-et-syntheses/Environnement-et-sante/2016/Impacts-de-l-exposition-chronique-aux-particules-fines-sur-la-mortalite-en-France-continentale-et-analyse-des-gains-en-sante-de-plusieurs-scenarios-de-reduction-de-la-pollution-atmospherique>, 2016.
- WHO: Mortality and burden of disease from ambient air pollution, WHO [online] Available from: [http://www.who.int/gho/phe/outdoor\\_air\\_pollution/burden\\_text/en/](http://www.who.int/gho/phe/outdoor_air_pollution/burden_text/en/), 2014.
- WHO: Ambient air pollution: A global assessment of exposure and burden of disease. [online] Available from: <http://www.who.int/phe/publications/air-pollution-global-assessment/en/>, 2016.

WHO: 9 out of 10 people worldwide breathe polluted air, but more countries are taking action, World Health Organ. [online] Available from: <http://www.who.int/news-room/detail/02-05-2018-9-out-of-10-people-worldwide-breathe-polluted-air-but-more-countries-are-taking-action>, 2018.



---

# **CHAPTER 1**

## **Atmospheric context**

---





## **CHAPTER 1. Atmospheric Context**

### **1.1 General introduction to atmospheric aerosols**

#### **1.1.1 Definition of atmospheric particulate matter (PM)**

In atmospheric sciences, aerosols, or particulate matter (PM), are defined as a collection of solid or liquid particles suspended in a gas, excluding hydrometeors such as cloud and rain droplets or ice crystals (Meszaros, 1999). The size of PM ranges from a few nanometers up to several micrometers (see section 1.1.2).

Aerosols may be directly emitted to the atmosphere from a variety of sources, resulting in primary aerosols, or formed in the atmosphere from precursor compounds, leading to secondary aerosols. The sources of primary aerosols are really diverse and a classification between natural and anthropogenic sources is typically made (and is further detailed in section 1.1.3). The type of source might determine the physical characteristics of the aerosols (e.g. size, density, and surface) and their chemical composition (Calvo *et al.*, 2013), which will be presented in section 1.1.5.

After being released into the atmosphere, PM or their precursor gases experience a number of physicochemical processes sometimes called ageing, including homogeneous and heterogeneous nucleation, coagulation, adsorption / desorption (Delmas *et al.*, 2005), affecting as well their physical and chemical properties. The removal of particles from the atmosphere occurs through dry and wet deposition, as well as heterogeneous chemistry. Overall, their lifetime will depend on their physical and chemical properties, their concentration, their altitude in the atmosphere, and may range from a few seconds to several years (Hinds, 1999). The aerosol life cycle will be described in section 1.1.4.

The interest in studying aerosols becomes evident when their adverse impacts are assessed, which include effects on health (Kim *et al.*, 2015), climate (Jacob, 1999), ecosystems (EEA, 2014), and economy (Calvo *et al.*, 2013). These issues will be presented in section 1.1.6, followed by a discussion on the legal framework concerning aerosols (section 1.1.7).

#### **1.1.2 Size of aerosols**

The size of airborne particles is one of the most important physical characteristics of aerosols, since many other parameters are dependent on it. Even though the vast majority of particles have irregular shapes, they are considered to be ideally spherical for modelling purposes. The size of a particle is then defined through the equivalent diameter of a non-

spherical (i.e. irregular) particle, which equals the diameter of a spherical (i.e. ideal) particle that exhibits identical properties to those of the non-spherical particle.

Different definitions of equivalent diameter are available; among which the aerodynamic diameter ( $d_a$ ) is commonly adopted and used to study the physical nature of particles and their deposition in the human respiratory systems. It is defined as the diameter of a unit density sphere ( $1 \text{ g cm}^{-3}$ ) that would have an identical settling velocity as the particle of interest (Renoux and Boulaud, 1998). The  $d_a$  of airborne particles ranges from  $0.002 \text{ }\mu\text{m}$  to  $100 \text{ }\mu\text{m}$ , even though the lower end is not clearly defined, as there is not a rigorous agreement on where a cluster of molecules becomes a particle (Finlayson-Pitts and Pitts Jr, 1999).

According to the  $d_a$ , a first classification between coarse ( $d_a > 2.5 \text{ }\mu\text{m}$ ) and fine ( $d_a < 2.5 \text{ }\mu\text{m}$ ) particles is made. The distinction between fine and coarse aerosols is essential in the study of aerosols since they proceed from different origins, are transformed separately, get removed from the atmosphere by different processes, have different chemical composition, and differ significantly regarding their deposition in the respiratory tract (Seinfeld and Pandis, 2006). In addition, according to this latter parameter, another classification is commonly made, distinguishing between  $\text{PM}_{10}$  (Particulate Matter with  $d_a < 10 \text{ }\mu\text{m}$ ),  $\text{PM}_{2.5}$  ( $d_a < 2.5 \text{ }\mu\text{m}$ ) and  $\text{PM}_1$  ( $d_a < 1 \text{ }\mu\text{m}$ ), where particles with smaller  $d_a$  might be deposited in deeper regions of the respiratory system.

**Coarse particles** are mainly formed by mechanical natural and anthropogenic processes. Natural processes include soil erosion, sea spray generation, volcano eruptions and dispersion of plant debris, while anthropogenic activities involve wearing (e.g. of pneumatics and brake pads), land changes, construction and mining. The size of coarse particles implies high sedimentation velocities and that these particles settle in a relatively short period of time.

**Fine particles** are generally formed due to condensation of gases and coagulation of smaller particles, although they can also be emitted directly by natural and anthropogenic sources. A more detailed classification into three size modes is usually made in order to study different processes and properties that do not affect all fine particles the same manner:

- The *nucleation or nuclei mode* accounts for particles from 1-2 to 10 nm (again, the lower end is not strictly defined). Although particles in this mode are the most numerous (see number distribution of Figure 1.1), they present a very small size and therefore constitute a small percentage of the aerosol mass. They are generally formed by nucleation (condensation) of hot vapors during combustion processes and from the condensation of gaseous species, and are lost due to coagulation with bigger particles or to condensational growth to give place to particles of the Aitken mode.

- The *Aitken mode* includes particles from 10 to 100 nm. It is often described together with the nucleation mode as one unique mode due to its similar characteristics. This mode also accounts for a very small percentage of the aerosol mass and the processes of formation and loss are very similar to those of the nucleation mode.
- The *accumulation mode* refers to particles from 100 nm up to 2.5  $\mu\text{m}$ . It accounts for a substantial part of the aerosol volume and mass (Figure 1.1). Particles in this mode originate from the coagulation of particles in the nuclei and Aitken modes and from condensation of hot vapors onto pre-existing particles. Particles tend to accumulate in this mode, since other methods of particle removal like condensation or coagulation (nuclei and Aitken modes) and sedimentation (coarse mode) are not efficient in this size region.

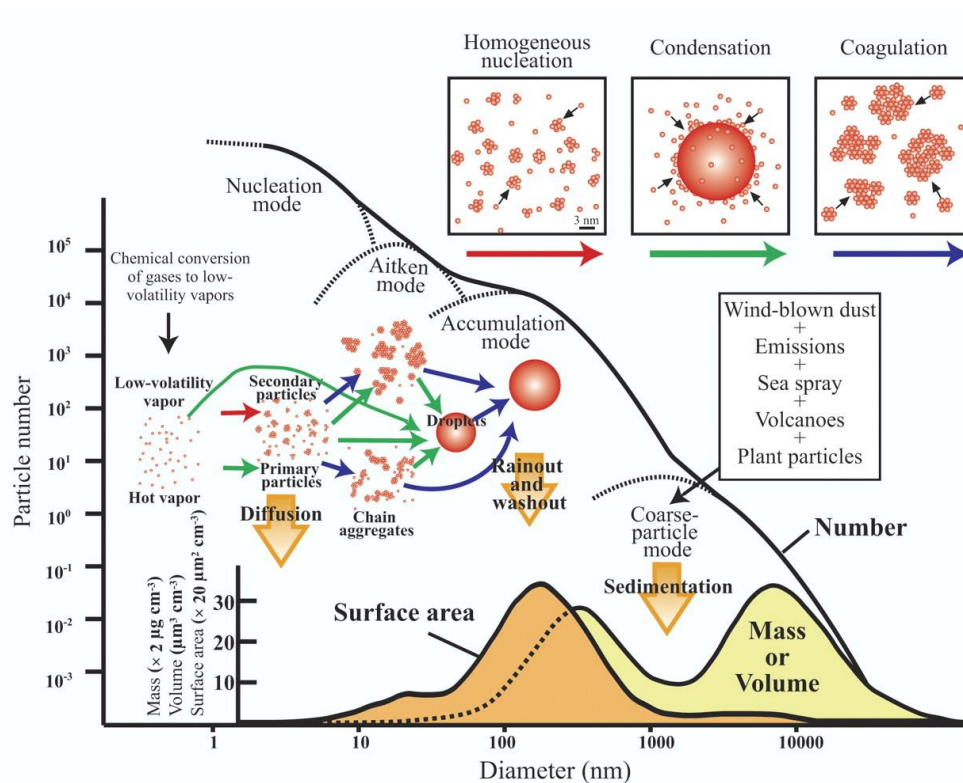


Figure 1.1 Representation of aerosol size distribution and main processes of the aerosol life cycle (Buseck and Adachi, 2008)

### 1.1.3 Sources

Particulate matter, as well as the precursor gases that might lead to its formation, can present natural or anthropogenic origins. Natural sources include emissions from seas and oceans, deserts, soils, volcanoes, vegetation, wildfires and lightning, and represent the vast majority of aerosol sources in the world, mainly due to sea salt and mineral dust. On the other hand, anthropogenic sources of aerosols and precursor gases involve a number of different

activities such as industry, construction, biomass burning, and farming (Calvo et al., 2013). The average aerosol emissions for major sources are summarized in Table 1.1.

Table 1.1 Global emission estimates for major aerosol classes  
(adapted from Seinfeld and Pandis, 2006)

Source	Estimated flux (Tg yr <sup>-1</sup> )
<i>Natural</i>	
Primary	
Mineral dust (0.1 – 2.5 µm)	308
Mineral dust (2.5 – 10 µm)	1,182
Sea salt	10,100
Volcanic dust	30
Biological debris	50
Secondary	
Sulfates from DMS	12.4
Sulfates from volcanic SO <sub>2</sub>	20
Organic aerosol from BVOC	11.2
<i>Anthropogenic</i>	
Primary	
Industrial dust (w/o BC)	100
BC	12*
Organic aerosol	81*
Secondary	
Sulfates from SO <sub>2</sub>	48.6**
Nitrates from NO <sub>x</sub>	21.3***

\*Tg C ; \*\*Tg S ; \*\*\*Tg NO<sub>3</sub><sup>-</sup>

#### 1.1.3.1 Natural sources

**Mineral dust**, also referred to as the crustal fraction of the aerosol, is generated by the action of the wind on the Earth surface. Even though any type of soil is a potential source of dust, deserts, dry lake beds and semi-arid surfaces are the main contributors. The chemical composition of mineral dust may vary greatly from one region to another, although it is generally composed of calcite, quartz, dolomite, clays, feldspar and small amounts of calcium sulfate and iron oxides. Most of mineral particles are found in the coarse mode, with only between 7% and 20% of the annual dust emissions (in mass) with a diameter lower than 1 µm (Cakmur et al., 2006). Some authors have estimated that dust concentrations in the atmosphere have doubled over the last century and have attributed this increase to anthropogenic activity (Calvo *et al.*, 2013).

**Sea spray** is the most important contributor to the total aerosol mass in the world. It consists mainly of primary marine salt, made of Na<sup>+</sup> and Cl<sup>-</sup>, and smaller amounts of SO<sub>4</sub><sup>2-</sup>, K<sup>+</sup>, Mg<sup>2+</sup> and Ca<sup>2+</sup>. Part of the Cl<sup>-</sup> might be depleted through chemical reactions with sulfuric

acid and nitric acid to give place to Na-based aerosols such as  $\text{NaNO}_3$  and  $\text{Na}_2\text{SO}_4$ . In addition, there is a significant emission at the surface of seas and oceans of organic compounds such as dimethyl-sulfide (DMS), which is the main precursor of sulfate over the oceans. Marine aerosols generally contribute to the coarse aerosol, although a significant fraction is also found in fine particles, and can be transported over long distances implying it is not restricted to coastal areas.

After mineral dust and sea spray, **biogenic aerosols** (primary and secondary), emitted by several types of vegetation and microorganisms, are the third most important contributors to natural PM. Primary biogenic aerosols include pollen, fern spores, fungal spores, and other particles with diameters up to  $100\text{ }\mu\text{m}$ , or small fragments and excretions from plants, animals, bacteria, viruses, carbohydrate, proteins, waxes, ions, etc. with diameters less than  $10\text{ }\mu\text{m}$ , which might be transported over long distances. Moreover, biogenic volatile organic compounds (BVOC) (mostly isoprene and monoterpenes) which are also emitted to the atmosphere may act as precursors of secondary organic aerosols (SOA).

**Volcanic eruptions** contribute to the increase of aerosol ambient concentrations in the atmosphere. These mainly consist of  $\text{H}_2\text{O}$  (v), followed by  $\text{CO}_2$ ,  $\text{SO}_2$ ,  $\text{HCl}$  and heavy metals. In addition, large amounts of secondary sulfate might be formed from the oxidation of  $\text{SO}_2$ . Volcanic ashes are generally found in the size range of  $1\text{-}10\text{ }\mu\text{m}$  and present an atmospheric lifetime of about 1 week.

Although a direct release of particles to the atmosphere is not associated to **lightning**, it is one of the most important natural sources of  $\text{NO}_x$  and, consequently, of secondary nitrogen aerosols.

#### 1.1.3.2 Anthropogenic sources

**Road traffic** (i.e. mainly cars, but also motorcycles, trucks and buses) is today one of the main sources of anthropogenic particulate matter, particularly in urban areas. A distinction between exhaust and non-exhaust traffic emissions is usually made.

Exhaust emissions are released through vehicle pipes and consist of precursor gases such as  $\text{NO}_x$  (precursors of secondary nitrogen compounds) and ultrafine primary carbon particles.  $\text{NO}$  is the dominant component of primary road traffic emissions, while  $\text{NO}_2$  is also directly emitted but only with a contribution of 5 to 10% to total  $\text{NO}_x$  emissions, and is mostly formed in the atmosphere. Diesel vehicles are an important exception, since their exhaust after-treatment systems causes  $\text{NO}_2$  emission rates to increase up to 70 % of their total  $\text{NO}_x$

emissions (Grice et al., 2009). In Europe, due to the increased use of diesel vehicles, the primary emissions of  $\text{NO}_2$  are increasing, particularly for newer vehicles (Euro 4 and 5). Despite this increase, the emissions of  $\text{NO}_x$  in the EU28 fell by 30% in the period 2003-2012. Transport is the sector that emits the most  $\text{NO}_x$ , accounting for 40% of the total European Economic Area (EEA) emissions in 2011, followed by the energy (22%), commercial and institutional households (13%) and industry (13%) sectors (Figure 1.2a). Similarly, the emissions of  $\text{NO}_x$  in France experienced a substantial decrease in the recent years, with road transport also being the main emitter, followed by the industry and residential/tertiary sectors (Figure 1.2b).

On the other hand, non-exhaust emissions comprise particles and trace metals emitted from brake wear, tire wear, road surface abrasion and resuspension. Table 1.2 illustrates the main elements released in different types of non-exhaust emissions. Both exhaust and non-exhaust emissions have been found to contribute equally to total traffic emissions (Querol et al., 2004).

Recently,  $\text{NH}_3$  emissions derived from traffic have raised concern in Europe, where new light duty vehicles have started implementing the De $\text{NO}_x$  selective catalytic reduction system (SCR) in order to meet the new Euro 6 standards (Suarez-Bertoa et al., 2014). SCR aims at reducing  $\text{NO}_x$  emissions by reacting NO and  $\text{NO}_2$  with  $\text{NH}_3$ , which is formed by reduction of urea injected into the system, on a catalyst surface. However, some process defaults such as over-doping of urea, low temperatures in the system or catalyst degradation may lead to  $\text{NH}_3$  emissions (Suarez-Bertoa et al., 2014).

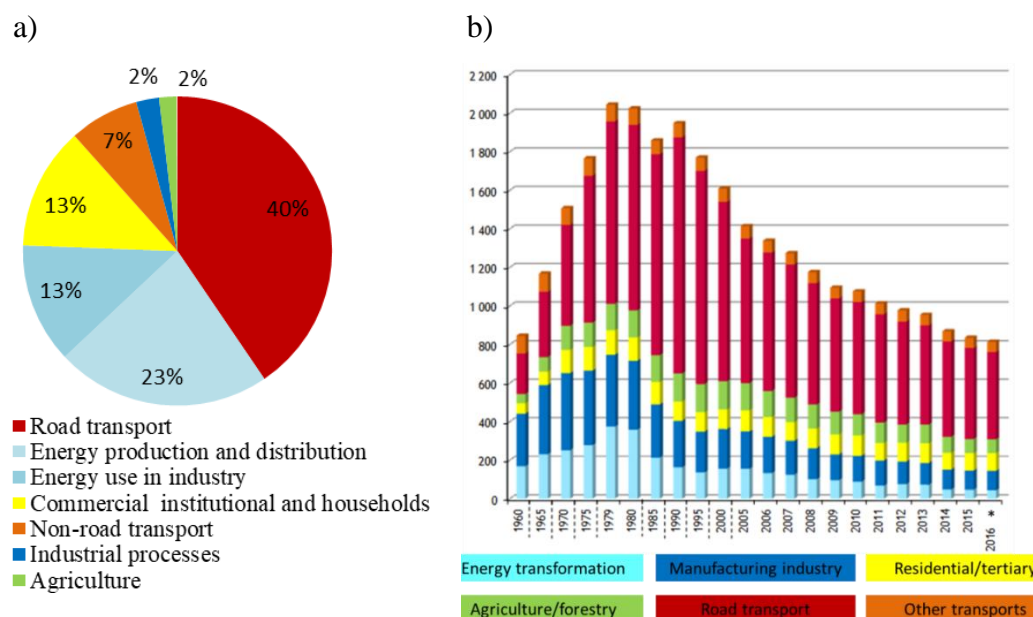


Figure 1.2 (a) Emission shares of NO<sub>x</sub> for EEA member countries for 2011 and (b) atmospheric emissions of NO<sub>x</sub> (in Kt per year) in the metropolitan France; \*2016= Estimation (CITEPA, 2017)

Other types of traffic might contribute to PM ambient concentrations in certain environments and have also been subject of study. For instance, **railway traffic** emissions of iron, aluminum and calcium particles might issue from the abrasion of the gravel bed and the resuspension of mineral dust (Lorenzo et al., 2006). **Maritime traffic** is also responsible for the emission of important quantities of SO<sub>2</sub> (16% of global sulfur emissions), but also NO<sub>x</sub> and carbonaceous aerosols (Corbett and Fischbeck, 1997).

**Industrial activities** are responsible for the emission of particulate matter and precursor gases. Due to the great diversity of industrial activities and processes, the span of emitted pollutants is also very large. The activities that generate more emissions of PM include industries involved in the production of ceramics, bricks and cement, foundries, mining and quarrying (Jang et al., 2007; Riffault et al., 2015). Table 1.2 summarizes the main inorganic tracers associated with a number of industrial activities.

**Coal burning** is mainly employed for the production of electricity and heat, even though coal might also be consumed in non-industrial sectors. For instance, residential coal combustion represents a serious problem in developing countries. Aside from the emitted carbonaceous aerosols, the added presence of polycyclic aromatic hydrocarbons (PAHs) and heavy metals contributes to a higher toxicity and more severe health effects to population exposed to this type of emissions (Linak et al., 2007). In addition, coal also contains varying quantities of sulfur, which might be emitted as SO<sub>2</sub> (precursor of sulfate aerosols) when it is

burned. However, the use of coal for energy production has substantially decreased in Europe over the last decades and hence the total emissions of SO<sub>2</sub> (Vestreng et al., 2007; EEA, 2016), with energy production still being the first source, as shown in the graph of the emissions share of SO<sub>2</sub> in Europe (Figure 1.3a). Similarly, SO<sub>2</sub> emissions have greatly decreased in France (CITEPA, 2017) (Figure 1.3b). However, it is observed that the manufacturing industry is now the major contributor to SO<sub>2</sub> emissions in France.

Table 1.2 Inorganic tracers associated with industrial activities and traffic  
(adapted from Calvo *et al.*, 2013)

Activity	Tracers	Activity	Tracers
Steel industry	Cr, Ni, and Mo	Cement industry	Ca
Copper metallurgy	Cu and As	Refuse incineration	K, Zn, Pb, and Sb
Ceramic industries	Ce, Zr, and Pb	Biomass burning	K and Br
Heavy industry (refinery, coal mine, power stations)	Ti, V, Cr, Co, Ni, Zn, As, and Sb	Firework combustion	K, Pb, Ba, Sb, and Sr
Petrochemical industry	V and Ni	Vehicle tailpipe	Pt, Ce, Mo, and Zn
Oil burning	V, Ni, Mn, Fe, Cr, As, S, and SO <sub>4</sub> <sup>2-</sup>	Automobile gasoline	Ce, La, Pt, SO <sub>4</sub> <sup>2-</sup> , and NO <sub>3</sub> <sup>-</sup>
Coal burning	Al, Sc, Se, Co, As, Ti, Th, S, Pb, and Sb	Automobile diesel	S, SO <sub>4</sub> <sup>2-</sup> , and NO <sub>3</sub> <sup>-</sup>
Iron and steel industries	Mn, Cr, Fe, Zn, W, Rb	Mechanical abrasion of tires	Zn
Non-ferrous metal industries	Zn, Cu, As, Sb, Pb, and Al	Mechanical abrasion of brakes	Ba, Cu, and Sb



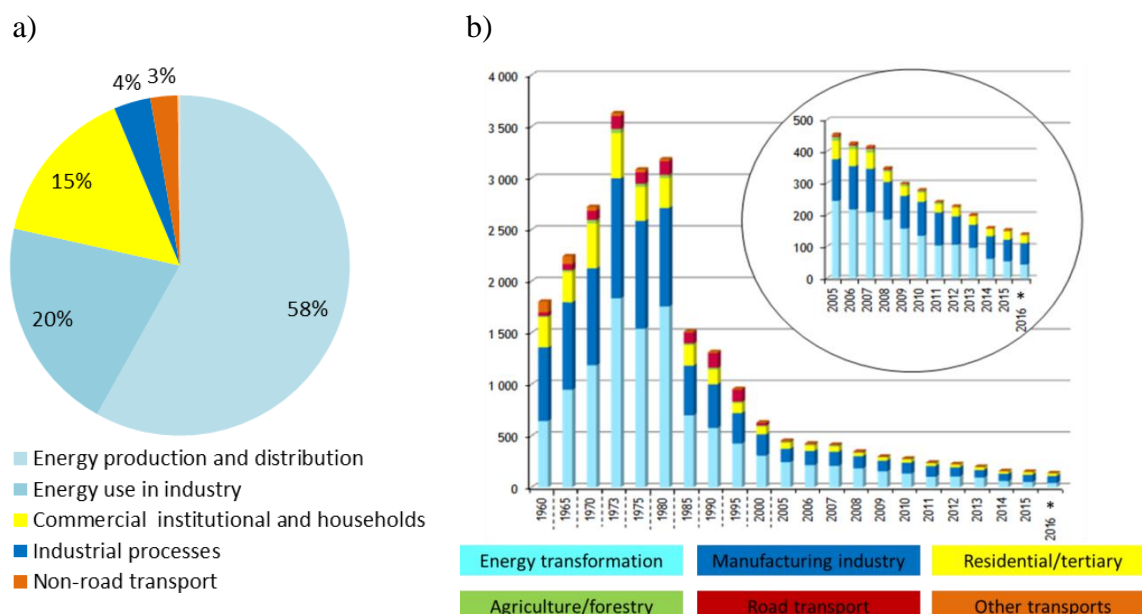
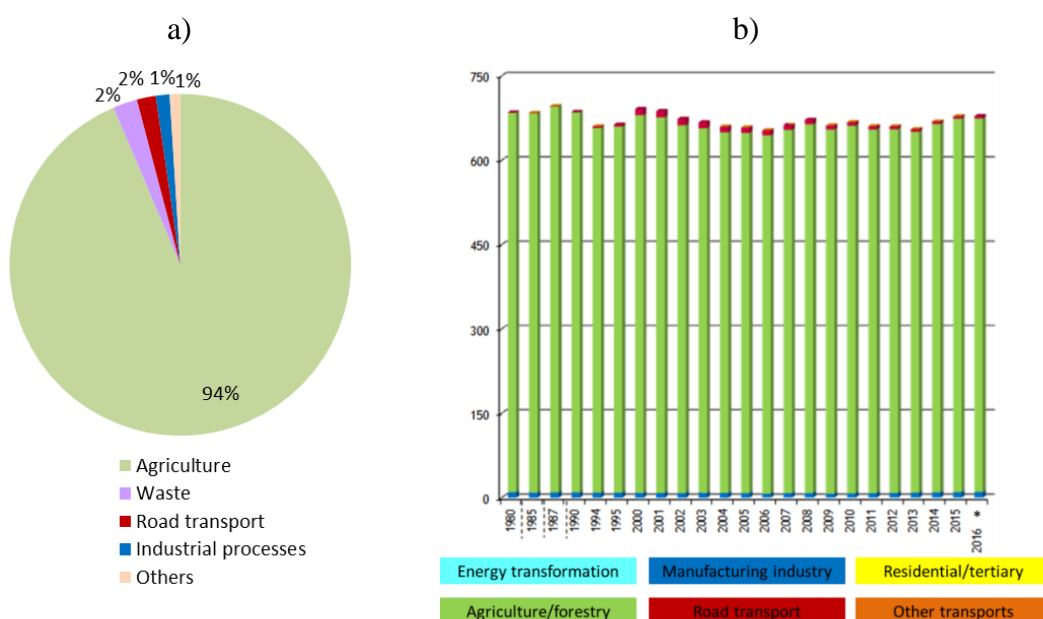


Figure 1.3 (a) Emission shares of SO<sub>2</sub> for EEA member countries for 2011 and (b) atmospheric emissions of SO<sub>2</sub> (in Kt per year) in the metropolitan France; \*2016= Estimation (CITEPA, 2017)

**Biomass burning** includes the burning of woods, grazing lands, and croplands after harvesting activities. The aerosols emitted by biomass burning mainly consist of carbonaceous compounds and minor amounts of inorganic compounds such as insoluble dust and ashes, and soluble salts like potassium, ammonium, sulfate and nitrate. In particular, levoglucosan is an organic compound formed from the pyrolysis of carbohydrates which is commonly used as a tracer of biomass combustion. **Domestic biomass burning** is another type of biomass burning activity which, even though being done at a small scale in fireplaces or wood stoves, might represent an important contribution to ambient PM during cold periods in certain countries, such as rural European sites. Particles emitted in biomass burning are mostly found in the fine mode, with a median diameter between 100-150 nm (Badarinath et al., 2009).

**Food cooking** represents an important source of fine particles in urban areas. As an example, a study in Los Angeles attributed 20% of fine PM organic matter to meat charbroiling and frying (McDonald *et al.*, 2003). The composition of the emitted aerosol will depend on parameters such as the cooking method, temperature, and used materials. For instance, higher concentrations of organic pollutants and metals were found when oil-based materials were used, compared to water-based cooking methods emitting more water soluble ions (See and Balasubramanian, 2008).

**Agricultural activities** include land fertilizing and livestock breeding. Despite non-significant particulate emissions, they are the main contributors to atmospheric ammonia (precursor of secondary ammonium). In Europe, agriculture was responsible for 94% of total  $\text{NH}_3$  emissions in the EEA in 2011 (Figure 1.4a). Although European policies have cut the emissions of precursor gases significantly over the last years,  $\text{NH}_3$  emissions have almost not decreased. The same tendency is observed in France, where the emissions of  $\text{NH}_3$  have been very similar during the last 40 years (CITEPA, 2017) (Figure 1.4b).



**Waste burning** is a significant emission source in both urban and rural areas. Several studies have shown that half of the garbage generated in the world ( $\sim 1000 \text{ Tg year}^{-1}$ ) might be incinerated or burnt in open fires (Christian *et al.*, 2010), suggesting an important amount of carbonaceous aerosols and other substances are emitted from this activity. The heterogeneity of garbage as a fuel also implies the emission of several hazardous compounds (Lemieux *et al.*, 2004). HCl is a specific compound found in garbage burning emissions, issued from large contents of polyvinyl chloride (PVC) and has been observed in a recent campaign carried out by our group in Senegal, West Africa (Rivellini *et al.*, 2017).

Finally, even though **fireworks** present only a transitory effect, they constitute an important source of gases and particles (mainly metals, organic compounds and to a lesser

extent inorganic compounds) in specific events, creating short-term air pollution and serious health hazards.

#### 1.1.4 Aerosol life cycle

The concentration of aerosols in the atmosphere is not constant, but continuously changing as a function of several production and removal processes, as illustrated in Figure 1.1 and developed in the next subsections.

##### 1.1.4.1 Production processes

**Mechanical production** processes are the most important in aerosol formation since they account for the majority of natural aerosol emissions (in mass). They are usually classified in mechanical suspension of mineral dust and production of sea spray.

Mechanical suspension of mineral dust is started by high velocity winds, causing phenomena such as dust suspension (particles of 70  $\mu\text{m}$  or less present a similar or lower weight than vertical drag forces and can be carried by the air) and saltation (particles bigger than 70  $\mu\text{m}$  are lifted from the ground but pulled down again by gravity, causing other particles to be ejected or suspended by the impact) (Shao, 2008). Experiments have shown that usually particle suspension starts above a critical velocity ranging from 0.2 to 1  $\text{m s}^{-1}$  and depends on the particle diameter (Marticorena et al., 1997). Particles smaller than 20  $\mu\text{m}$  tend to remain suspended for days and might therefore be transported over long distances (Qureshi et al., 2009).

Similarly to the mechanical suspension of dust, the production of sea spray aerosol is also initiated by the wind. Speeds beginning at around 10  $\text{m s}^{-1}$  might cause wave cleavage which leads to the production of spume drops. Alternatively, lower wind speeds might also produce smaller film drops and jet drops which are formed as a result of bubble bursting (Qureshi et al., 2009).

**Nucleation**, or **gas-to-particle conversion**, is the production and growth of particles in the presence of condensable vapors (Hidy, 1984). In order for nucleation to take place, the system has to overcome an energy threshold before nucleation clusters are formed (i.e. the ambient air requires a super-saturation). Once they are formed, nuclei tend to grow rapidly. Different types of nucleation are distinguished, depending if one or more species are present in the nucleation process and whether it occurs on another nuclei or surface.

In homogeneous nucleation particles are formed on molecular clusters in a supersaturated vapor in the absence of particles in the condensable vapor, while in heterogeneous nucleation the process takes place in a multicomponent system (more than one

phase) and particles may act as nuclei for condensation. Heterogeneous nucleation is also known as condensation Figure 1.1 and since it requires a much lower energy threshold compared to regular (homogeneous) nucleation, it is the preferential gas-to-particle conversion process in the atmosphere (Hinds, 1999).

In the troposphere, nucleation is observed in two main types of situations (Hinds, 1999): (1) in combustion processes, where hot exhaust gases form nuclei as they cool down; and (2) in ambient air under high concentrations of sulfuric acid, ammonia or low-volatile organic species. In Figure 1.5, the nucleation pathway between sulfuric acid, ammonia and organic molecules is represented. In addition, in urban environments, ion-induced nucleation has been found to contribute to new particle formation events (Iida et al., 2006).

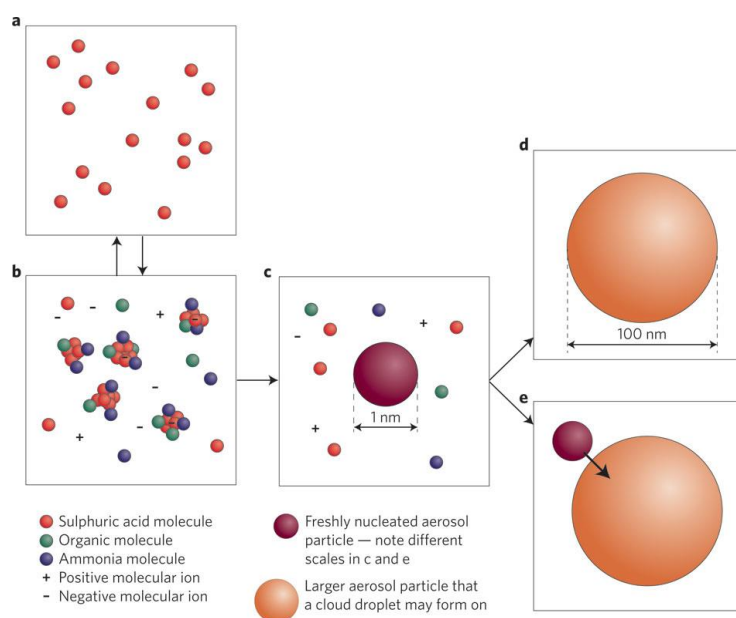


Figure 1.5 Representation of the nucleation process from  $\text{H}_2\text{SO}_4$ ,  $\text{NH}_3$ , organics and other ions (Pierce, 2011)

**Coagulation** represents the process in which two small clusters collide and join forming a new larger particle (Figure 1.1). Coagulation becomes more effective when the difference of sizes between the clusters is larger. This is due to the large diffusion coefficient of small particles or clusters which makes them to diffuse faster onto the large surface area of bigger particles.

**Evaporation** is the reverse process of condensation in which molecules abandon the particle surface. The absence of an energy barrier makes aerosol droplet particles to evaporate under sub-saturation conditions.

#### 1.1.4.2 Elimination processes

Aerosols are naturally eliminated from the atmosphere by two main processes known as dry and wet deposition.

**Dry deposition** is the means by which particles are removed onto surfaces in the absence of precipitation. The way in which dry deposition will affect any aerosol depends on several factors, including the atmospheric turbulence, the nature of the aerosol and its size, density and shape. The smallest particles behave similarly to gases; they are rather governed by a Brownian diffusion movement, and are rather advected by winds and removed by wet deposition. Therefore, only large aerosols ( $> 4\text{-}5\ \mu\text{m}$ ) have enough mass to be affected by gravitational forces and fall through the atmosphere (Maxey, 1987). In Table 1.3 the mean settling velocities depending on the particle diameter are shown.

**Wet deposition**, also called wet removal, washout or rainout, is the natural process in which particulate matter is scavenged by different atmospheric precipitation (e.g. rain, snow, and fog). The term is also used to describe nucleation scavenging, that is, when particles act as cloud condensation nuclei (CCN).

Table 1.3 Settling velocities of aerosol particles at 1 atm (adapted from Hinds, 1999)

Particle diameter ( $\mu\text{m}$ )	Settling velocity ( $\text{m s}^{-1}$ )
0.001	$6.9 \times 10^{-9}$
0.01	$7.0 \times 10^{-8}$
0.1	$8.8 \times 10^{-7}$
1	$3.5 \times 10^{-5}$
10	0.0031
100	0.25

#### 1.1.5 Chemical composition of aerosols

Aerosol in the troposphere may contain several chemical species: inorganic ions such as sulfate, ammonium, nitrate, sodium and chloride, trace metals, carbonaceous material, crustal elements, and water (Seinfeld and Pandis, 2006). This composition may vary dramatically depending on the location and time of the year.

Depending on the size, the chemical composition of aerosols may also greatly change. For instance, ultrafine particles are mostly composed of sulfates and organics (Jimenez et al., 2003). Fine particles are mostly made of elemental and organic carbon (EC and OC) and inorganic species such as nitrate, ammonium and sulfate (Colbeck, 2008). On the other hand, coarse particles are rich in Earth constituents, including Ca, Fe, Si, and in sea salt, but also in nitrate, OC, and trace metals. Figure 1.6 presents the size distribution of some of the main

aerosol chemical constituents. Most of the species present a bimodal distribution, with a maximum inferior to 1  $\mu\text{m}$  and another one around 2-3  $\mu\text{m}$ , suggesting most of the inorganic mass is found in the fine mode.

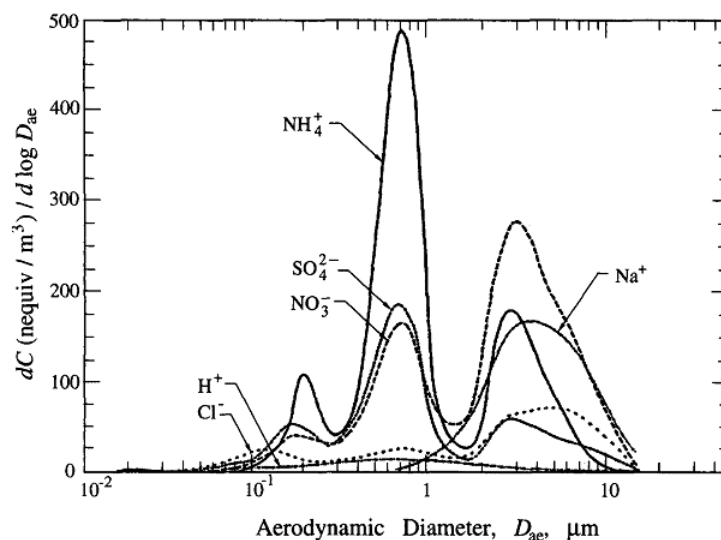


Figure 1.6 Average size distribution of main aerosol ions (Seinfeld and Pandis, 2006)

The chemical composition of fine and coarse particles together with their different sources and formation pathways, sinks and other characteristics are summarized in Table 1.4 and detailed below.

Table 1.4 Main characteristics of coarse and fine particles  
(adapted from Wilson and Suh, 1997)

	Fine particles	Coarse particles
<b>Formation pathways</b>	Chemical reactions, nucleation, condensation, coagulation, cloud/fog processing	Mechanical disruption, suspension of dust
<b>Composition</b>	$\text{SO}_4^{2-}$ , $\text{NO}_3^-$ , $\text{NH}_4^+$ , $\text{H}^+$ , EC, OM, $\text{H}_2\text{O}$ , metals	Dust, ashes, crustal elements (Ca, Fe, Si, Ti), NaCl, OM, $\text{NO}_3^-$
<b>Solubility</b>	Very soluble, hygroscopic	Insoluble, non-hygroscopic
<b>Sources</b>	Combustion, gas-to-particle conversion of precursor gases, chemical reactions	Suspension of dust, ocean spray, biological sources
<b>Sinks</b>	Growth into accumulation mode, wet deposition, dry deposition (Brownian diffusion, turbulence)	Wet deposition, dry deposition (sedimentation, turbulence)
<b>Atmospheric lifetime</b>	Minutes to hours (ultrafine particles) Days to weeks (fine particles)	Minutes to days
<b>Travel distance</b>	$10^2$ - $10^3$ km	< to $10^2$ km

**Elemental carbon (EC)**, often referred to as **black carbon (BC)** or soot, is the mixture of graphitic particles and light absorbing organic matter, and originates mainly from

anthropogenic combustion processes. In urban environments it is typically associated with vehicle exhaust emissions.

**Organic matter (OM) or organic aerosol (OA)** is a complex mixture of different organic compounds which can be emitted directly from several natural and anthropogenic sources giving rise to primary organic aerosols (POA) or be formed in the atmosphere mainly due to the oxidation of volatile organic compounds (VOCs) followed by gas-to-particle conversion, resulting in secondary organic aerosols (SOA). Natural sources of OM include emissions of pollen, microbes, leaf wax, and sea spray, whereas anthropogenic sources involve emissions from biomass burning, fossil fuel combustion (traffic, industry, domestic), paved road dust and cooking (Medeiros et al., 2006; O'Dowd et al., 2004; Schauer et al., 1996). A few hundreds of organic compounds have been identified in airborne particles, including alkanes, aromatic polycarboxylic acids, polycyclic aromatic compounds (PAHs), alcohols, and several other macromolecular compounds (Seinfeld and Pandis, 2006).

**The inorganic fraction** of the aerosol is mainly composed of major ions including nitrate ( $\text{NO}_3^-$ ), sulfate ( $\text{SO}_4^{2-}$ ) and ammonium ( $\text{NH}_4^+$ ). The nitrate found in fine particles is usually a result of the reaction of nitric acid and ammonia, whereas the one found in the coarse fraction is rather formed through the reaction of nitric acid with sea salt or crustal compounds such as calcium carbonate (Finlayson-Pitts and Pitts, 1999).

**Trace metals** are also present in airborne particles emitted from several processes such as fossil fuel combustion, biomass burning, waste incineration and a vast number of industrial activities (see Table 1.2).

**Crustal elements** such as Al, Ca, Fe, K, and Si are mainly related to soil emissions and are mainly found in the coarse fraction.

In addition, the average composition of  $\text{PM}_{2.5}$  at different sites of North-Western and Central Europe is illustrated in Figure 1.7. It is clearly observed that secondary inorganic ions ( $\text{NO}_3^-$ ,  $\text{SO}_4^{2-}$  and  $\text{NH}_4^+$ ) are dominating, sometimes contributing to more than 50% of the  $\text{PM}_{2.5}$  mass on average. Organic matter is also an important contributor to  $\text{PM}_{2.5}$ , whereas EC makes up a small fraction of the aerosol.

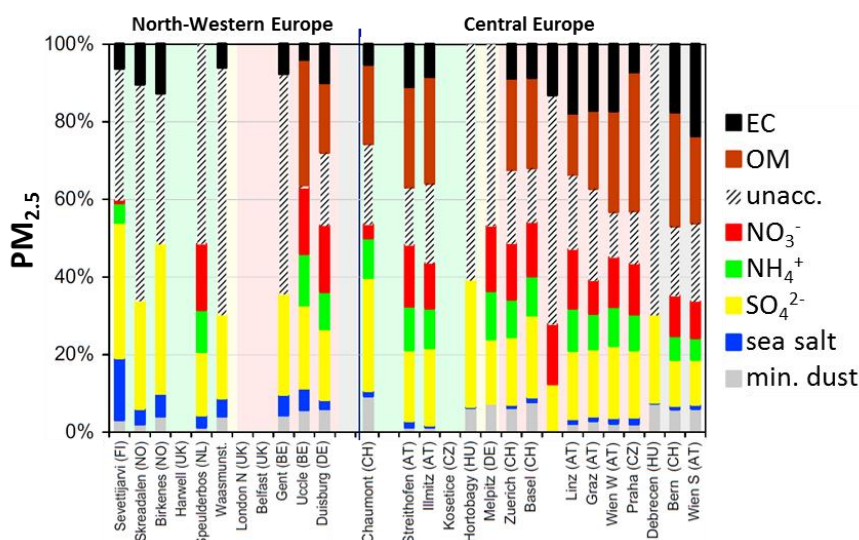


Figure 1.7 PM<sub>2.5</sub> relative average composition at different European sites (Putaud et al., 2010)

### 1.1.6 Effects

The variety of effects towards the human health, environment, climate and economy has instigated an exponential increase in the study of aerosols in the last decades. In this section the main effects of aerosols are described, with a particular emphasis to the health-related ones.

#### 1.1.6.1 Health effects

Particulate matter is one of the main responsible for an increased incidence of several respiratory and cardiovascular diseases, which lead to significant reductions in human life expectancy. Particle size has been directly linked to the potential of PM for causing health problems, with smaller particles likely to be deposited in deeper parts of the respiratory system (Kelly and Fussell, 2012; Kim et al., 2015). Figure 1.8 shows how deep PM of different sizes reaches the respiratory tract.

Health effects of PM result from either short-term (hours-days) or long-term (months-years) exposure, and include respiratory and cardiovascular morbidity and mortality from cardiovascular and respiratory diseases including lung cancer (WHO, 2018). Population with pre-existing lung or heart diseases, as well as elderly people and children, are particularly vulnerable. Long-term exposure to PM<sub>2.5</sub> is associated with an increase in the long term risk of cardiopulmonary mortality by 6-13% for every increase of 10 µg m<sup>-3</sup> of PM<sub>2.5</sub> (WHO, 2018). Only in the year 2016, ambient air pollution was responsible for 4.2 million deaths worldwide, most of which were due to the inhalation of fine particulate matter (WHO, 2018).



Another study carried out in France reported 48,000 premature deaths related to PM<sub>2.5</sub> exposure (Sant  publique France 2016).

More specifically, the European APHEKOM project estimated the average life expectancy gain in different European cities for a decrease in the PM<sub>2.5</sub> levels down to the recommended level set by the WHO (10 µg m<sup>-3</sup>). Among the different cities, the calculated increase in life expectancy in the city of Lille, located in northern France, is of 5.8 months (Figure 1.9).

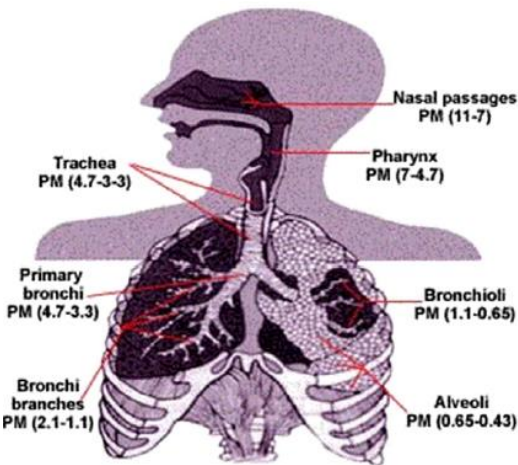


Figure 1.8 Deposition potential of PM depending on the size (Kim et al., 2015)

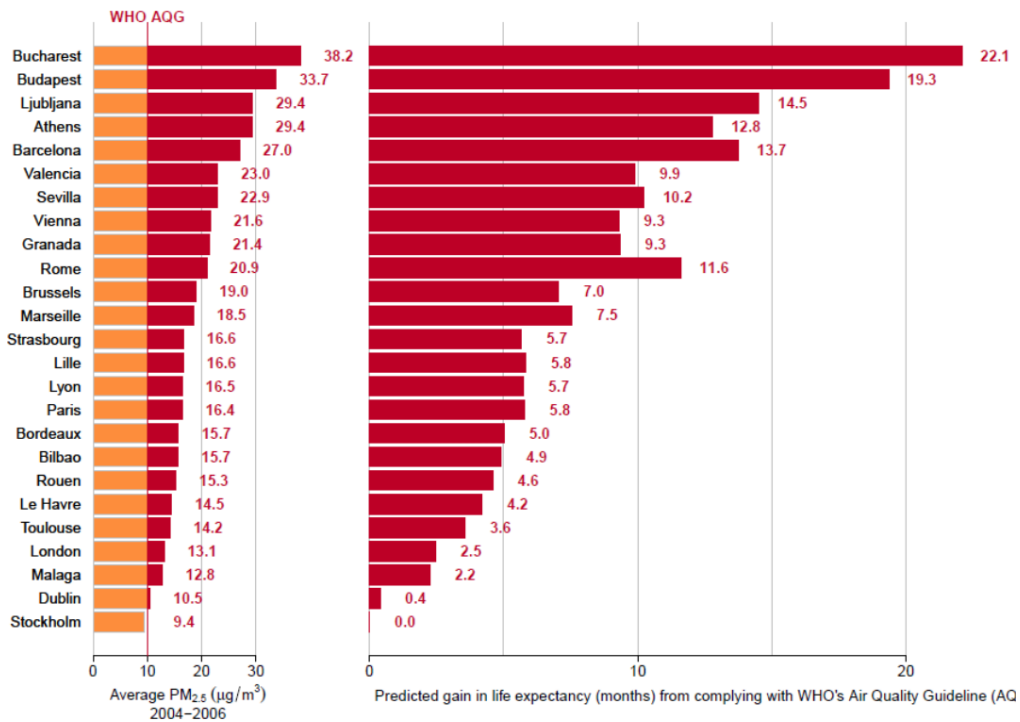


Figure 1.9 Predicted average gain in life expectancy (in months) for 30-year old aged people in 25 European cities for a decrease in the annual average PM<sub>2.5</sub> level to the WHO recommendation of 10 µg m<sup>-3</sup> (Aphekom report)

### 1.1.6.2 Environmental effects

**Eutrophication** is defined as an excess of nutrients in soils or water bodies (Hutchinson, 1973). It endangers biodiversity through the excessive growth of certain species which take advantage of the added nutrients ahead of other species which are adapted to live in lower-nutrient environments. Deposition of nitrate and ammonium-rich aerosols might contribute to eutrophication in certain regions (Mahowald et al., 2017).

**Acidification** is the phenomenon through which acidic species are removed from the atmosphere through dry or wet deposition, the latter being known as acid rain (EEA, 2014). When acidic species in the ambient air are deposited in the ground they create an accumulation of hydrogen ions in the soil. This leads to a reduction of the soil pH (soil acidification) and contributes to the leaching of cations such as  $\text{Ca}^{2+}$ ,  $\text{Mg}^{2+}$ ,  $\text{K}^{+}$  and  $\text{Na}^{+}$  (EEA, 2014). When the deposition takes place in water bodies the pH of water becomes lower and the ecosystem is altered. In general, acidification damages plant and animal life, both on land and in water.

### 1.1.6.3 Climate effects

Scattering of the radiation by aerosols is the underlying phenomenon under the alteration of climate by aerosols. A beam of radiation is scattered by a particle in its path when the direction of propagation is altered with no absorption (Jacob, 1999), and might take place through three main ways: reflection, refraction or diffraction (Figure 1.10). The scattering will reach a maximum for a particle radius corresponding to the wavelength of the radiation. Therefore, particles in the accumulation mode will scatter radiation very efficiently since their size is of the same order as the wavelength of radiation (around  $1\ \mu\text{m}$ ).

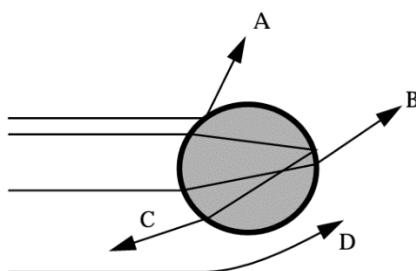


Figure 1.10 Scattering of a radiation beam by (A) reflection, (B) refraction, (C) refraction and internal reflection and (D) diffraction (Jacob, 1999)

The scattering of solar radiation by aerosols causes a fraction of the scattered light to be reflected back to space, increasing the Earth albedo. In this way, anthropogenic aerosols exert a significant cooling effect on the Earth climate, also known as negative forcing. It is

calculated that aerosols have compensated about a third of the greenhouse radiative forcing over the past century (Jacob, 1999).

However, not all aerosols exert a negative forcing. For example, whereas sulfate particles scatter radiation very efficiently and participate for most of the negative forcing, black carbon particles absorb the radiation, giving place to a positive forcing, which may counteract the cooling effect of sulfate aerosols (Schult et al., 1997).

In addition, there is an indirect effect associated with the role of aerosols as CCN for cloud droplet formation. When a cloud is formed in a polluted atmosphere, the water is distributed over a larger number of aerosol particles compared to when the same process occurs in a clean atmosphere, thus leading to a larger area of cloud droplets and therefore increasing the albedo.

On the other hand, although it does not contribute to altering the climate, another related effect to radiation scattering is visibility reduction. Scattering by aerosols is the main limitation to visibility in the troposphere. In the absence of aerosols, the human visual range would be about 300 km (Jacob, 1999). Anthropogenic aerosols may reduce visibility by one order of magnitude compared to unpolluted conditions. The reduction in visibility is more important at high relative humidities, when the aerosols grow due to the water uptake, giving place to a phenomenon known as haze.

#### **1.1.7 Legal framework**

In France, particulate matter pollution is regulated by the European Directive 2008/50/EC on ambient air quality and cleaner air for Europe, which concerns ambient air concentrations of SO<sub>2</sub>, NO<sub>x</sub>, PM<sub>10</sub> and PM<sub>2.5</sub>, Pb, benzene (C<sub>6</sub>H<sub>6</sub>), carbon monoxide (CO), and O<sub>3</sub>. This directive sets a limit value of 25 µg m<sup>-3</sup>, a target value of 20 µg m<sup>-3</sup>, and a quality goal of 10 µg m<sup>-3</sup>, all values for PM<sub>2.5</sub> in annual average. This has been transposed into the French law by the decree n°2010-1250. In addition, the WHO sets air quality guideline values for PM<sub>2.5</sub> of 10 and 25 µg m<sup>-3</sup> for annual mean and 24-hour mean, respectively.

The directive declares that measurements have to be performed at rural background locations (away from significant sources of pollution), for the purposes of providing information on the total mass concentration and chemical speciation concentrations of PM<sub>2.5</sub> on an annual average basis (Article 6, section 5). The knowledge of the concentrations at background sites is essential in order to evaluate the enhanced levels in more polluted areas (such as urban background, industrial and traffic sites), assess the possible contributions from

long-range transport of air pollutants, support source apportionment analysis and understand specific pollutants such as particulate matter. It is also essential for the increased use of modelling also in urban areas.

The measurement of PM<sub>2.5</sub> must include the total mass concentration and concentrations of appropriate compounds to characterize its chemical composition. At least, the list of following chemical species should be included: SO<sub>4</sub><sup>2-</sup>, NO<sub>3</sub><sup>-</sup>, Cl<sup>-</sup>, NH<sub>4</sub><sup>+</sup>, K<sup>+</sup>, Na<sup>+</sup>, Ca<sup>2+</sup>, Mg<sup>2+</sup>, EC, OC. The sum of the concentrations of these compounds may correspond to up to 80 % of the PM<sub>2.5</sub> fraction, while the rest is given as an unknown fraction of the aerosol (Putaud *et al.*, 2004).

## **1.2 Secondary inorganic aerosols (SIA)**

Inorganic aerosols present a very important contribution to the PM<sub>2.5</sub> mass. Secondary inorganic aerosols (SIA) are inorganic aerosols which are not emitted directly to the atmosphere, but instead formed through chemical reactions or gas-to-particle conversion of gaseous precursors, including nitric acid (HNO<sub>3</sub>), sulfuric acid (H<sub>2</sub>SO<sub>4</sub>) and ammonia (NH<sub>3</sub>). Although in some regions of the world their contribution to the mass of PM is not significant, in Europe SIA may account for more than half of the PM<sub>2.5</sub> mass (Putaud *et al.*, 2004). The main components of SIA are NO<sub>3</sub><sup>-</sup>, NH<sub>4</sub><sup>+</sup> and SO<sub>4</sub><sup>2-</sup>, which are found mainly as ammonium nitrate (NH<sub>4</sub>NO<sub>3</sub>) and ammonium sulfate ((NH<sub>4</sub>)<sub>2</sub>SO<sub>4</sub>). However, minor ions like Cl<sup>-</sup>, K<sup>+</sup>, Mg<sup>2+</sup>, and Ca<sup>2+</sup> might also contribute significantly. Specifically, in North-Western Europe, NH<sub>4</sub>NO<sub>3</sub> might reach up to 27% of the PM<sub>2.5</sub> mass (Putaud *et al.*, 2004). This high contribution highlights the importance of the study of SIA, which are the main subject of interest of this work, and are presented more in detail in the following sections.

### **1.2.1 Sulfur species**

Most particulate sulfur species consist of secondary sulfate aerosols formed by the oxidation of gaseous precursors, followed by particle formation through nucleation and condensation processes. The main contributors of sulfate aerosols are sulfur dioxide (SO<sub>2</sub>) and dimethyl sulfide (DMS).

#### **1.2.1.1 Sulfur aerosol precursors**

##### ***1.2.1.1.1 Sulfur dioxide***

SO<sub>2</sub> is emitted by both anthropogenic and natural sources, even though it has been estimated that more than 70% of SO<sub>2</sub> global emissions have an anthropogenic origin (Seinfeld and Pandis, 2006). Activities including stationary power generation and transport, and domestic heating, where sulfur-containing fuels are burned, are the main contributors to

anthropogenic SO<sub>2</sub>. Other anthropogenic sources of SO<sub>2</sub> are shipping, metal smelting, agricultural waste burning, pulp and paper processing (Calvo *et al.*, 2013).

Sulfur dioxide is soluble in water, giving other species such as HSO<sub>3</sub><sup>-</sup> and SO<sub>3</sub><sup>2-</sup> in aqueous solution, all compounds with an oxidation state +IV (S(IV)), the sum of which is expressed as follows:

$$[S(IV)] = [SO_2 \cdot H_2O] + [HSO_3^-] + [SO_3^{2-}] \quad \text{Eq. 1.1}$$

Although most of the SO<sub>2</sub> in the atmosphere is primarily emitted, the chemical reaction of other compounds might also lead to the formation of SO<sub>2</sub>. For instance, reduced sulfur-containing species such as hydrogen sulfide, methanethiol and DMS react with OH and NO<sub>3</sub> radicals to ultimately result in the formation of SO<sub>2</sub>. The main sources of hydrogen sulfide include volcanic eruptions, natural decomposition of sulfates, production by anaerobic bacteria, coal pits, landfills, livestock manure and thermal or polluted waters (Borrás *et al.*, 2016; Li *et al.*, 2014). Methanethiol might be found near marshes, surface seawater, natural gas and also pulp-mills, among others (Toda *et al.*, 2010). DMS is mainly produced by marine microorganisms via enzymatic cleavage of another marine compound (dimethyl sulfoniopropionate), and is of particular importance, since it is one of the most important contributors to the formation of SO<sub>2</sub> (Wang *et al.*, 2018). The oxidation of DMS will depend on the latitude where it is found, with the majority of the path occurring by OH at low latitudes and by NO<sub>3</sub> in colder, darker regions (higher latitudes) (Seinfeld and Pandis, 2006).

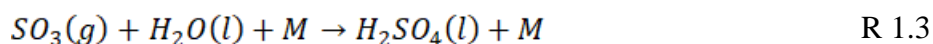
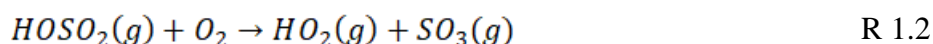
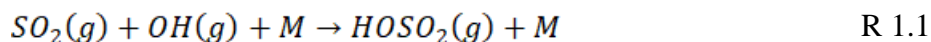
#### 1.2.1.1.2 Sulfuric acid

In general, sulfuric acid, which presents the oxidation state +VI, results from the atmospheric oxidation of SO<sub>2</sub>. H<sub>2</sub>SO<sub>4</sub> presents a very low vapor pressure ( $1.3 \cdot 10^{-3}$  Pa at 23°C) and therefore its anhydrous form is never seen in the atmosphere, and is instead diluted in water as aqueous sulfate particles (Ayers *et al.*, 1980). The conversion from S(IV) to S(VI) takes place through a variety of reaction paths, which are explained in the following section.

#### 1.2.1.2 Atmospheric chemistry of sulfur compounds

The conversion of the gas precursor SO<sub>2</sub> into sulfuric acid and then sulfate aerosols is mainly carried out in two ways: homogeneous (gas-phase) reactions and heterogeneous (liquid-phase) reactions.

In the **homogeneous** or **gas-phase** pathway, the reaction of SO<sub>2</sub> with the OH radical is the dominant path for the production of SO<sub>3</sub>, which in the presence of water is further converted to H<sub>2</sub>SO<sub>4</sub> (Stockwell and Calvert, 1983), following reactions R 1.1 to R 1.3. At typical ambient concentrations of OH·, the lifetime of SO<sub>2</sub> based on the gas-phase oxidation with OH· is about one week. The homogeneous path takes place mainly during daytime due to the higher concentration of OH in the ambient air.



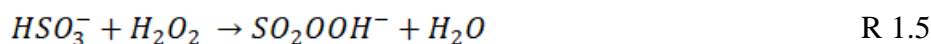
In the **heterogeneous** or **aqueous-phase** pathway, the oxidation of SO<sub>2</sub> can be accomplished through many reactions with different oxidant species. Aqueous-phase reactions mainly take place during nighttime or under cloudy and foggy conditions, and are the dominant path of SO<sub>2</sub> oxidation, given the relatively long lifetime of SO<sub>2</sub> according to its oxidation with OH radicals in the gas phase (Finlayson-Pitts and Pitts, 1999). Among the different aqueous-phase reaction pathways of SO<sub>2</sub> oxidation, the oxidation by dissolved (1) O<sub>3</sub>, (2) H<sub>2</sub>O<sub>2</sub>, (3) O<sub>2</sub> (catalyzed by metals), (4) OH·, and (5) NO<sub>2</sub>, are predominant:

(1) The oxidation of S(IV) (R 1.4) by dissolved O<sub>3</sub> has been proposed to occur by nucleophilic attack of O<sub>3</sub> by SO<sub>2</sub> · H<sub>2</sub>O, HSO<sub>3</sub><sup>-</sup> and SO<sub>3</sub><sup>2-</sup> (Hoffmann and Calvert, 1985). Ozone reacts more rapidly with SO<sub>3</sub><sup>2-</sup> than with HSO<sub>3</sub><sup>-</sup>, and with the latter than with SO<sub>2</sub> · H<sub>2</sub>O. Since the presence of SO<sub>3</sub><sup>2-</sup> and HSO<sub>3</sub><sup>-</sup> is favored at high pH values, an increase of the pH results in an increase of their concentrations and hence in an increase of the overall reaction rate. The ubiquitousness of atmospheric O<sub>3</sub> highlights the role of this path as a sink of SO<sub>2</sub>.



(2) Hydrogen peroxide is one of the most effective oxidants in clouds and fogs and as such promotes the oxidation of S(IV) (R 1.5 and R 1.6). It is highly soluble in water and under typical ambient conditions its aqueous-phase concentration is around six orders of

magnitude higher than that of dissolved ozone. This reaction is very fast and, as a result,  $H_2O_2(g)$  and  $SO_2(g)$  rarely coexist in clouds and fogs.

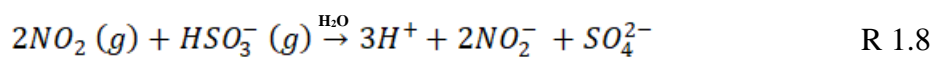


(3) In the presence of oxygen, iron in the ferric state (Fe(III)) and manganese (Mn(II)) catalyze the oxidation of S(IV) in aqueous solutions (R 1.7). When Fe and Mn are present in the atmosphere, a synergistic effect which enhances the reaction rate is triggered. Rates 3 to 10 times higher than expected from the sum of the independent rates have been reported (Martin, 1984).



(4) Free radicals such as  $OH\cdot$  and  $HO_2$  can be scavenged from the gas phase by cloud droplets or produced in the aqueous phase, and participate in the oxidation of S(IV). More than 30 aqueous-phase reactions involving both radicals have been described in the literature (Seinfeld and Pandis, 2006).

(5) The oxidation of S(IV) by  $NO_2$  is presented in R1.8. Nitrogen dioxide has limited water solubility and consequently a low concentration in the aqueous phase, suggesting this path is not significant in typical conditions. However, for fogs in urban areas where high  $NO_2$  concentrations are encountered, this reaction could be an important pathway for S(IV) oxidation (Seinfeld and Pandis, 2006):



All aqueous-phase reactions are dependent on pH and temperature.  $H_2O_2$ -oxidation is the dominant way when pH is under 5. At  $pH \geq 5$ , the oxidation by  $O_3$  and by  $O_2$  catalyzed by Fe and Mn becomes important.  $H_2O_2$  is the only identified oxidant that produces S(VI) with a reaction rate almost independent from the pH value (Figure 1.11).

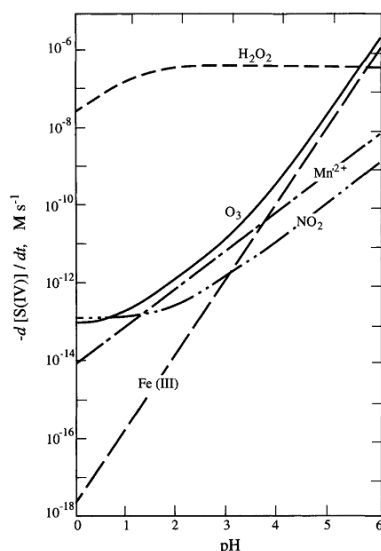


Figure 1.11 Comparison of aqueous-phase main oxidation pathways at 298 K (Seinfeld and Pandis, 2006)

### 1.2.2 Nitrogen species

Even though the most abundant gas in the atmosphere is  $N_2$ , it is very stable and practically inert, and therefore has very limited role in tropospheric chemistry, with the exception of  $NO_x$  production during lightning events. However, other nitrogen-containing species show higher reactivity and present a greater influence in atmospheric chemistry. The main nitrogen-based gaseous species are nitrous oxide ( $N_2O$ ), nitric oxide ( $NO$ ), nitrogen dioxide ( $NO_2$ ), nitric acid ( $HNO_3$ ) and ammonia ( $NH_3$ ), precursors of aerosols such as nitrate ( $NO_3^-$ ), nitrite ( $NO_2^-$ ) and ammonium ( $NH_4^+$ ). Additionally, organo-nitrogen species are also found in the atmosphere such as amines emitted by animal husbandry operations.

#### 1.2.2.1 Nitrogen aerosol precursors

##### 1.2.2.1.1 Ammonia

Ammonia is the major basic gas in the atmosphere and plays an important role in atmospheric chemistry as a precursor of fine inorganic secondary aerosol by the neutralization of acids (Sharma et al., 2007). It is known to also play a key role in the formation of new particles (Kulmala, Pirjola, and Mäkelä 2000). After  $N_2$  and  $N_2O$ , it is the most abundant N-containing compound in the atmosphere, and is principally emitted by agricultural activities.

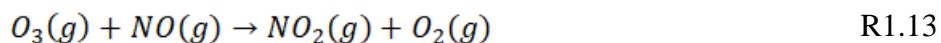
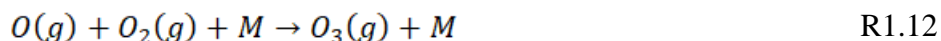
It is readily absorbed by surfaces such as water bodies and soil, and thus its residence time in the lower atmosphere is expected to be low (ca. < 10 days). Ammonia is very soluble in water and dissociates readily into  $NH_4^+$  ions (R 1.9 and R 1.10):





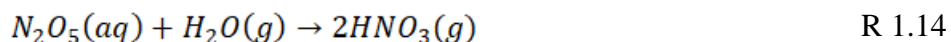
#### 1.2.2.1.2 Nitrogen oxides

Nitrogen oxides (NO<sub>x</sub>) are a family of gases which include NO and NO<sub>2</sub>. High temperature combustion processes (e.g. in car engines and power plants) are the main sources. While NO is only directly emitted, NO<sub>2</sub> is mainly formed by the oxidation of NO in the presence of sunlight and at wavelengths smaller than 424 nm as shown in reactions R 1.11 to R 1.13:



#### 1.2.2.1.3 Nitrogen radicals

The NO<sub>3</sub> radical, either as such or as dinitrogen pentoxide (N<sub>2</sub>O<sub>5</sub>), is the most reactive nitrogen species in the aqueous phase during nighttime, given its rapid photolysis during daytime. NO<sub>3</sub> and N<sub>2</sub>O<sub>5</sub> are very soluble in water and are a potential source of nitrate (R 1.14 and R 1.15). The NO<sub>3</sub> radical might also be converted into nitrate ions through its reaction with Cl<sup>-</sup>, or with HSO<sub>3</sub><sup>-</sup> when little chloride is available (R 1.16 and R 1.17).

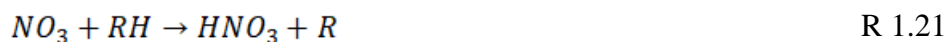


#### 1.2.2.1.4 Nitric acid

The formation of HNO<sub>3</sub> in the atmosphere is accomplished mainly through aqueous-phase reactions (R 1.18 or R 1.19):



However, it is also formed in gas-phase reactions by reaction of NO<sub>2</sub> with OH radicals (daytime) or hydrocarbons with NO<sub>3</sub> radicals (nighttime) (R 1.20 and R 1.21) (Finlayson-Pitts and Pitts, 1999):

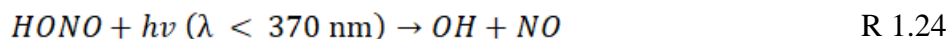


Nitric acid is a very sticky gas and adsorbs easily to surfaces, particularly if there is water on the surface, and therefore it undergoes fast dry and wet deposition. Dry deposition of HNO<sub>3</sub> may be responsible for the majority of the removal of inorganic nitrogen in the troposphere. Nitric acid is highly water-soluble and easily dissociates into nitrate ions (R 1.22 and R 1.23) (Seinfeld and Pandis, 2006):

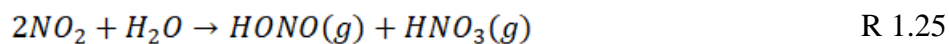


#### 1.2.2.1.5 Nitrous acid

HONO or HNO<sub>2</sub> presents a high importance in the day-time chemistry due to its decomposition into OH radicals (R 1.24):



Direct sources of HONO include primary emissions from light-duty motor vehicles having high levels of NO<sub>x</sub> in exhaust gases, but it is also naturally emitted from land-cover or vegetation (Su et al., 2011). Additionally, it is formed from precursor compounds, as in the heterogeneous reaction of NO<sub>2</sub> onto surfaces (R 1.25) and the daytime reaction of NO with the OH radical (R 1.26). However, since the photolysis of HONO is very fast during daytime, significant concentrations are not generated (Finlayson-Pitts and Pitts, 1999).

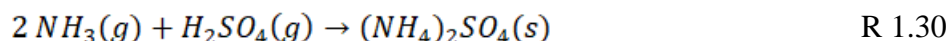
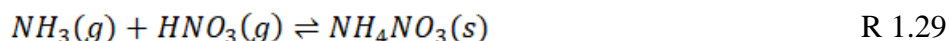


In addition, HONO might react with HCl in order to give place to ClNO (R 1.27) (Wingen et al., 2000), or be oxidized by O<sub>2</sub> in the aqueous phase, particularly at low temperatures (R 1.28) (Takenaka et al., 1996):



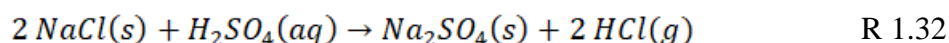
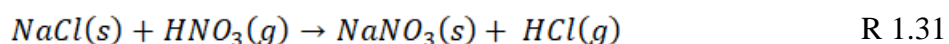
### 1.2.3 Neutralization reactions for SIA formation

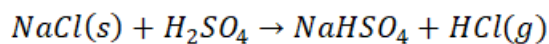
As previously presented, ammonia is the main basic gas in the atmosphere and as such plays a key role in the formation of SIA by neutralizing acid gases such as HNO<sub>3</sub> (R 1.29) and H<sub>2</sub>SO<sub>4</sub> (R 1.30), to mainly form NH<sub>4</sub>NO<sub>3</sub>, (NH<sub>4</sub>)<sub>2</sub>SO<sub>4</sub> and NH<sub>4</sub>HSO<sub>4</sub>:



The neutralization of sulfate by ammonia occurs preferentially to that of nitrate. Therefore, ammonium nitrate is usually formed in areas characterized by high concentrations of ammonia and nitric acid and low sulfate concentrations (Seinfeld and Pandis, 2006).

In addition, other species than those mentioned above might also play a significant role in the formation of SIA in specific environments. For instance, in coastal regions, Na<sup>+</sup> and Cl<sup>-</sup> contribute significantly to PM<sub>2.5</sub> concentrations and might interact with several aerosol components. The presence of NaCl in urban environment might lead to the formation of several aerosol compounds, including ammonium chloride (NH<sub>4</sub>Cl), sodium nitrate (NaNO<sub>3</sub>), sodium sulfate ((Na<sub>2</sub>)SO<sub>4</sub>), and sodium bisulfate (NaHSO<sub>4</sub>) (R 1.31 to R 1.33). Aerosols resulting from these reactions are typically associated with coarse particles.





R 1.33

#### 1.2.4 Ammonium nitrate formation

The equilibrium between ammonium nitrate and its gaseous precursors described by R1.29 is reversible, and depends on temperature and relative humidity (RH). Figure 1.12 shows the temperature dependence of ammonium nitrate equilibrium. The lower temperatures shift the equilibrium of the system towards the aerosol phase, increasing the aerosol mass of  $NH_4NO_3$ . In addition, depending on RH, ammonium nitrate may exist as a solid or as an aqueous solution of  $NH_4^+$  and  $NO_3^-$ .

The standard free energy of dissociation ( $\Delta G_d^\circ$ ) of ammonium nitrate is equal to  $\Delta G_d^\circ = 93.4 \pm 0.3 \text{ kJ mol}^{-1}$  at  $25^\circ\text{C}$  and 1 atm for its crystalline phase IV (stable between  $-17^\circ\text{C}$  and  $32^\circ\text{C}$ ) (Mozurkewich, 1993). The constant of dissociation  $K_d$  of ammonium nitrate is related to  $\Delta G_d^\circ$  through equation:

$$\Delta G^\circ = -RT \ln K_d \quad \text{Eq. 1.2}$$

and to R1.29 by taking into account the activity coefficients of the involved species ( $a_i$ ):

$$K_d = \frac{a_{NH_3} \cdot a_{HNO_3}}{a_{NH_4NO_3}} \quad \text{Eq. 1.3}$$

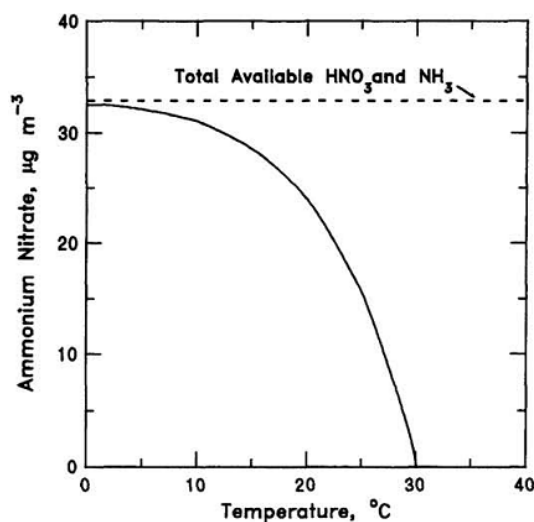


Figure 1.12  $NH_4NO_3$  concentration dependence on temperature for a system with 7 and  $26.5 \mu\text{g m}^{-3}$  of  $NH_3$  and  $HNO_3$ , respectively, and RH 30% (from Seinfeld and Pandis, 2006)

Since the activity of a pure solid equals 1 and the activities of gases (under the assumption of perfect gases) are equal to their partial pressures ( $p_i$ ) with respect to the total

pressure ( $P_i$ ); knowing that the ratio between  $p_i$  and  $p_t$  for a given gas equals its molar fraction ( $\chi_i$ ), the equilibrium constant can be rewritten as:

$$K_d = \frac{p_{NH_3}}{P_t} \cdot \frac{p_{HNO_3}}{P_t} = \chi_{NH_3} \cdot \chi_{HNO_3} \quad \text{Eq. 1.4}$$

In the case of trace atmospheric gases the molar fractions are very small and they are rather expressed in parts per billion (ppb) by multiplying them by  $10^9$ , leading to a new molar fraction ( $p_i^*$ ) (Eq. 1.4). Then, a new  $K_d$  in  $\text{ppb}^2$  ( $K_d^*$ ) is calculated (Eq. 1.5), which is dependent on temperature, as shown in Table 1.5. Different values of  $K_d^*$  are obtained depending on which equation is used: 29 (Stelson and Seinfeld, 1982) and 43  $\text{ppb}^2$  (Mozurkewich, 1983) (both at 25°C and 1 atm).

$$p_i^* (\text{ppb}) = \left( \frac{p_i}{P_t} \right) \cdot 10^9 = \chi_i \cdot 10^9 \quad \text{Eq. 1.5}$$

$$K_d^* (\text{ppb}^2) = p_{NH_3}^* \cdot p_{HNO_3}^* = K_d \cdot 10^{18} \quad \text{Eq. 1.6}$$

Table 1.5 Dependence of the dissociation coefficient on temperature (T, in K)

Equation	Reference
$\ln(K_d^*) = 118.87 - \frac{24084}{T} - 6.025 \ln(T)$	Mozurkewich (1983)
$\ln(K_d^*) = 84.6 - \frac{24220}{T} - 6.1 \ln\left(\frac{T}{298}\right)$	Stelson and Seinfeld (1982)

The equilibrium of ammonium nitrate at a given moment ( $Q^*$ ), defined as  $Q^* = p_{NH_3}^* \cdot p_{HNO_3}^*$ , might be compared with  $K_d^*$ , giving place to three distinct cases, summarized in the table below.

Table 1.6 Thermodynamic cases for ammonium nitrate dissociation

$Q^* < K_d^*$	The dissociation of ammonium nitrate is favored (the reaction is spontaneous in the direction of the dissociation)
$Q^* = K_d^*$	The system is in equilibrium, the gases and the solid coexist
$Q^* > K_d^*$	The formation of ammonium nitrate is favored

The equations proposed above only take into account the effect of temperature on the equilibrium of ammonium nitrate. However, field observations have shown that its thermodynamic partitioning is also dependent on relative humidity (Mozurkewich, 1993). The particles of ammonium nitrate are hygroscopic and therefore can absorb water and become deliquescent (deliquescence is the process by which substances having a strong affinity for moisture will absorb large quantities of water from the air when they are exposed to it, forming an aqueous solution). This process is reversible: the solution might lose water as RH decreases until the phenomenon of efflorescence occurs (i.e. the spontaneous loss of water by a hydrated salt) given by the efflorescence relative humidity (ERH). However, a hysteresis phenomenon might be present, meaning that the absorption and loss of water by the particles is not symmetrical with the change of RH.

The deliquescence point is given by the deliquescence relative humidity (DRH), the RH at a specific temperature for which the hygroscopic solid particle is transformed into a droplet of saturated liquid. When the ambient RH is higher than DRH,  $K_d$  depends both on temperature and RH (and now is named  $K_{db}$  as opposed to the previous, now called  $K_{da}$ , which only depends on the temperature) and is calculated as follows:

$$K_{db} = K_{da} \cdot (p_1 - p_2 RH_1 + p_3 RH_1^2) RH_1^{1.75} \quad \text{Eq. 1.7}$$

where  $RH_1$  is defined as  $(1 - RH/100)$  and  $p_1$ ,  $p_2$ , and  $p_3$  are given by:

$$p_1 = \exp\left[-135.94 + \frac{8763}{T} + 19.12 \ln(T)\right] \quad \text{Eq. 1.8}$$

$$p_2 = \exp\left[-122.65 + \frac{9969}{T} + 16.22 \ln(T)\right] \quad \text{Eq. 1.9}$$

$$p_3 = \exp\left[-182.61 + \frac{13875}{T} + 24.46 \ln(T)\right] \quad \text{Eq. 1.10}$$

The deliquescence-efflorescence phenomenon affects not only ammonium nitrate but also many other atmospheric inorganic salts. As an example, in Figure 1.13 (Hidy, 1984), the deliquescence and efflorescence curves (upward and downward arrows, respectively) are shown for KCl, NaCl and  $MgCl_2 \cdot 6 H_2O$ , by representing the evolution of the wet to dry mass ratio of each salt ( $m_A/m_B$ ) with respect to RH. For instance, a dry particle of NaCl adsorbs water on the surface along with increasing RH values until DRH is reached (75.7% at 20°C for NaCl), where it is transformed into an aqueous saturated droplet of a mass twice that of

the dry particle. If RH increases more, the droplet grows by absorbing water and keeps in equilibrium with ambient RH. When RH decreases, the NaCl droplet decreases its size continuously, retaining the absorbed water for a longer time, and the solid state (efflorescence) does not appear until the RH is less than 50%. In Table 1.7 values of DRH and solubility for some hygroscopic inorganic salts are given.

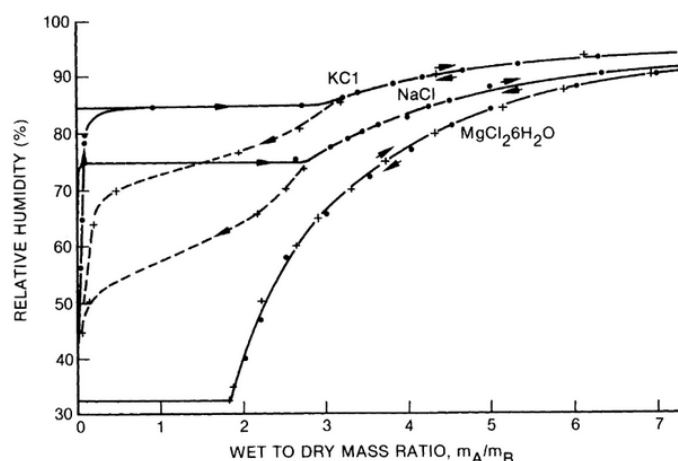


Figure 1.13 Deliquescence and efflorescence curves for some hygroscopic salts in relation to RH at 20 °C (Hidy, 1984)

Table 1.7 DRH and concentration for saturated solutions at 25°C (Hidy, 1984)

Salt	DRH (%)	Solubility (g/100 g H <sub>2</sub> O)
(NH <sub>4</sub> ) <sub>2</sub> SO <sub>4</sub>	81	75.4
NaCl	75.7	36
NH <sub>4</sub> NO <sub>3</sub>	62	192
CaCl <sub>2</sub> · 6 H <sub>2</sub> O	32	74.5

In the specific case of ammonium nitrate, at 25°C the particles will be in the solid phase for RH < 62% and in the aqueous phase for RH > 62%. This process is represented by R 1.34. The enthalpy of reaction ( $\Delta H^\circ$ ) is  $-25.7 \text{ kJ mol}^{-1}$ , which implies that it is exothermic and favored at low temperatures, while the change of entropy  $\Delta S^\circ$  is  $-0.1087 \text{ kJ mol}^{-1} \text{ K}^{-1}$ , implying that the disorder decreases.



If we consider  $\Delta G^\circ = \Delta H^\circ + T\Delta S^\circ$  it follows that R1.34 is at equilibrium ( $\Delta G^\circ = 0$ ) for a temperature of  $-36.72^\circ\text{C}$ , and that above this temperature the reaction will be favored.

In summary, depending on the ambient temperature and RH a total of four cases can be distinguished, all presented in Table 1.8.

Table 1.8 Equilibrium state of ammonium nitrate and its precursor gases with relation to temperature and RH

Temperature	RH	Formation of ammonium nitrate
Low	<DRH	Favored as a particle. Low concentrations of precursor gases at the equilibrium.
Low	≥DRH	Favored as an aqueous solution. Low concentrations of precursor gases at the equilibrium.
High	<DRH	Not favored. High concentrations of precursor gases at the equilibrium.
High	≥DRH	Favored as an aqueous solution, but low since the concentrations of precursor gases are high.

All these phenomena are taken into account in thermodynamic modules integrated in chemical transport models (CTM), such as ISORROPIA II (Fountoukis and Nenes, 2007) which is used in CTM such as CHIMERE (Mailler et al., 2017), or LOTOS-EUROS (Schaap et al. 2008).

### 1.3 Techniques for the measurement of aerosols and gaseous precursors in the ambient air

Up to date, a large number of techniques have been developed for the sampling and analysis of the chemical composition of aerosols and their precursor gases. They can be classified between offline and online methodologies. The former consist of sampling the ambient air on site followed by an analysis in the laboratory, while the latter deals with simultaneous *in situ* sampling and analysis.

#### 1.3.1 Offline measurements

These types of techniques were firstly developed and have been used widely for the sampling of aerosols and precursor gases in the last decades due to their relative simplicity and low cost, but despite of their possible artifacts.

The most common method for the measurement of the composition of aerosols is sampling on filters during a relatively long period (commonly 24 hours) followed by the chemical analysis in the laboratory by different techniques, usually ion chromatography (IC) for SIA. Filters are typically made of cellulose, Teflon, nylon or quartz depending on the purpose of the analysis. Multiple filters are commonly used and named as filter packs. The



filters can be impregnated with different chemical solutions for the sampling of different particulate and gaseous species. For example, cellulose filters impregnated with an alkaline solution are used to sample acidic gases (e.g.  $\text{SO}_2$ ,  $\text{HNO}_3$ ,  $\text{HCl}$ ), whereas filters impregnated with an acid solution are used to sample ammonia.

However, the use of filters suffers from a number of disadvantages. Different positive (retention in the filter material) and negative (volatilization and chemical reaction of some compounds) artifacts have been observed (Dong et al., 2012). For instance, the volatilization of  $\text{NH}_4\text{NO}_3$  has been reported, particularly under high temperatures and dry conditions (Appel et al., 1988; Schaap et al., 2002). In addition, this method presents a low time resolution due to the large collection time, typically from a few hours to days, hampering the study of atmospheric processes which tend to be very fast.

Gas denuders are often coupled to filter packs, resulting in denuder-filter packs, in order to remove interfering gases such as nitric acid before sampling aerosols. For instance the adsorption of nitric acid on filters and particles may cause an overestimation of particulate nitrate (Acker et al., 2005). Figure 1.14 shows an example of a schematic of a denuder-filter pack. Nowadays the use of open-face denuder-filter packs, where the first filter is used to collect aerosols and the second to measure gases, is worldwide common and official in several air quality monitoring networks such as the European Monitoring and Evaluation Program (EMEP).

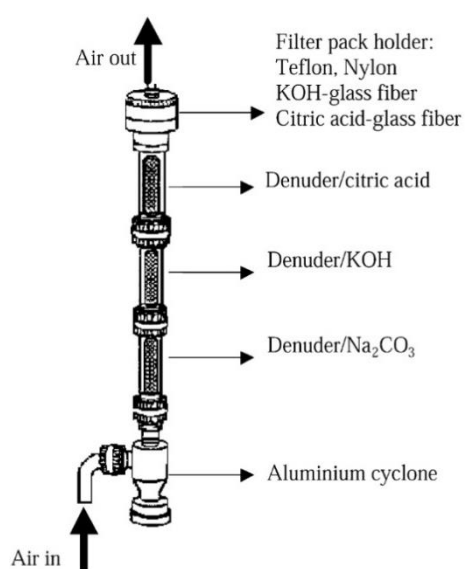


Figure 1.14 Schematic of a denuder-filter pack (Limón-Sánchez et al., 2002)

### **1.3.2 Online measurements**

The wish to find a reliable method for the measurement of aerosols and precursor gases with high time resolution, good gas/aerosol separation, low detection limits and minimal artifacts has led to the development of online techniques. For SIA, these techniques are generally based on the combination of a Wet Rotating Denuder for online water-solubilization of precursor gases (Keuken et al., 1988; Wyers et al., 1993), a Steam Jet Aerosol Collector (SJAC) for online water-solubilization of particulate salts (Khlystov et al., 1995; Slanina et al., 2001) and analysis by IC of solubilized ions.

Commercial examples are the Particle-Into-Liquid Sampler (PILS) (Weber *et al.*, 2001) coupled to an IC, the Gas and Aerosol Collector (GAC) (Dong *et al.*, 2012), the Ambient Ion Monitor-Ion Chromatograph (AIM-IC) (Wu and Wang 2007; Nie et al. 2010; Beccaceci et al., 2015), the Gas Particle Ion Chromatography (GPIC) (Godri et al., 2009) and the Monitor for AeRosols and Gases and ambient air (MARGA) (ten Brink et al., 2007).

The performance of simultaneous measurements of aerosols and precursor gases at high time resolution has proven valuable for the evaluation of secondary inorganic aerosol formation (Schaap et al., 2011) as well as for the partitioning of ammonium nitrate (Aan de Brugh et al., 2012).

On the other hand, different methodologies based on mass spectrometry have been widely used for an exhaustive analysis of the composition of the aerosol phase. For instance, the High Resolution – Time of Flight - Aerosol Mass Spectrometer (HR-ToF-AMS) presents a really high resolution (in the order of a few minutes) and measures the size-resolved composition of the major inorganic aerosol constituents (nitrate, sulfate and ammonium) and of the particulate organic compounds (DeCarlo et al., 2006). However, it does not detect some important inorganic ions including calcium, magnesium, sodium and potassium, due to the nature of the technique, does not allow the speciation of the organic fraction and is limited to PM<sub>1</sub>.

The MARGA, the main instrument of work of this thesis, and the HR-ToF-AMS are described in more detail in the second chapter.

## **1.4 Source apportionment**

### **1.4.1 Source receptor models**

In order to identify and estimate the contribution or apportionment of different pollution sources at a specific site, source receptor models (RMs) have been developed in the last decades. RMs are commonly used in different areas of science in order to reduce very

large datasets into a new one of fewer dimensions with the goal of deriving new meaningful information and to explain the variability of different variables of the dataset. RMs require an input of information given by a set of samples analyzed at the monitoring site, also called the receptor site. These models rely on a series of assumptions that need to be kept in mind when interpreting the data. Firstly, the composition of the source profiles is constant over the whole period, which might not always be realistic, particularly for secondary sources. Secondly, the number of source profiles has to be determined by the user, and this might render the comparison between different studies difficult, depending on the choices of each modeler (Hopke, 2016). In general, they are classified between chemical mass balance (CMB) models and multivariate models.

**CMB models** are used when a large part of the information about the pollution sources is known and the mass contribution of each source wants to be determined. However, in most of the cases the main sources are not well known, hindering the application of this type of models. For such cases, the application of multivariate models is more adequate.

**Multivariate models** have been developed in order to obtain information about the type number of sources, their typology and their contribution, starting from a set of observations at the receptor site. Common examples include Principal Component Analysis (PCA), UNMIX, Positive Matrix Factorization (PMF) and Multilinear Engine (ME) (Viana et al., 2008 and references therein). In Figure 1.15 the main RMs are presented according to the required amount of information about the pollution sources. In this work, the PMF model has been used.

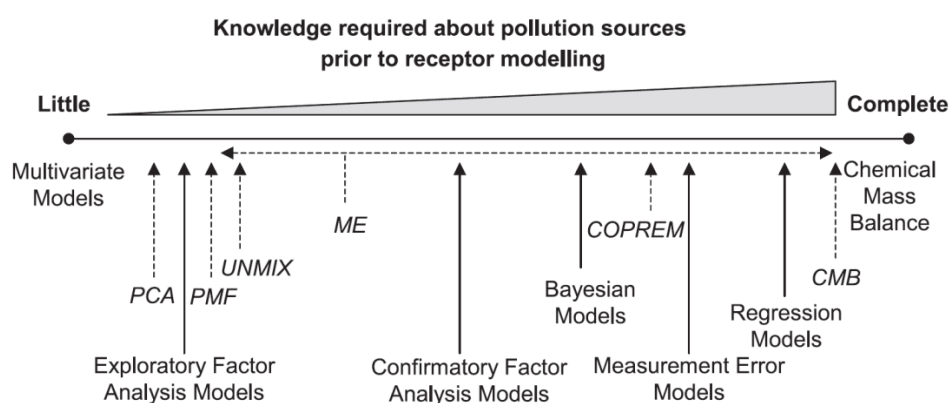


Figure 1.15 Synthesis of the different receptor models used for estimating pollution source contributions (from Viana et al., 2008)

#### 1.4.2 Positive matrix factorization (PMF)

Positive Matrix Factorization (PMF) is a multivariate source-receptor statistical analysis tool based on factor analysis of the data. It was created in an attempt to resolve some limitations of previous receptor models such as the Principal Component Analysis (PCA) (Paatero and Tapper, 1994).

In the present thesis, PMF has been chosen because of its many advantages: (i) no need of prior knowledge of the sources, (ii) possibility to identify unknown or missing sources, (iii) ability to work with missing data and with measurements below the DL, (iv) and application of individual data scaling with an uncertainty matrix assigning a higher weight to data with high precision.

The foundation of the PMF model is the principle of mass conservation and is summarized in the following equation:

$$X = G \cdot F + E \quad \text{Eq. 1.11}$$

or

$$x_{ij} = \sum_{k=1}^p g_{ik} \cdot f_{kj} + e_{ij} \quad \text{Eq. 1.12}$$

where  $X$  or  $x_{ij}$  expresses the concentration of a chemical species  $j$  at time  $i$ ;  $G$  or  $g_{ik}$  the contribution of the factor or source  $k$  at time  $i$ ;  $F$  or  $f_{kj}$  the fraction of the factor or source  $k$  from the chemical species  $j$ ;  $E$  or  $e_{ij}$  the fraction of the species  $j$  at time  $i$  unexplained by the model, or simply the residual (i.e. the difference between the measured value and the predicted value of the concentration of the species  $j$  at each time  $i$ ); and  $p$  is the user-chosen number of factors.

In this model the values of  $G$  and  $F$  are constrained to be zero or positive. For a specific number of factors, the goal is to determine  $G$  and  $F$  by minimizing a new function  $Q(E)$ , defined as:

$$Q(E) = \sum_{i=1}^n \sum_{j=1}^m \frac{e_{ij}^2}{s_{ij}^2} \quad \text{Eq. 1.13}$$

where  $s_{ij}$  is the uncertainty of the species  $j$  at time  $i$ .

The resolution of the previous equation is performed iteratively until a solution converges by the use of the least-squares method. In the minimization of  $Q(E)$ , the model will preferably represent data points with a low uncertainty, or high signal-to-noise ratio, than points with a higher uncertainty, or low signal-to-noise ratio. Different functions of  $Q$  can be defined:  $Q_{\text{true}}$  calculated taking into account all the data;  $Q_{\text{robust}}$  obtained by excluding all the values classified as outliers (i.e. their normalized residual is higher than 4); and  $Q_{\text{theoretical}}$  which is approximated by multiplying  $n$  (the total number of samples) by  $m$  (the total number of species).

The choice of the best number of factors for a specific solution is often the critical step for the interpretation of the results. The observation of the variation of the ratio  $Q_{\text{true}}/Q_{\text{exp}}$  in relation to the number of factors is one of the principal ways to help in choosing the number of factors. A strong decrease of  $Q_{\text{true}}/Q_{\text{exp}}$  with an increase of the number of factors suggests that the additional factor explains a significant part of the residual variability. The correct number of factors generally corresponds to a marked decrease of  $Q$ , followed by a change of slope. The expected value of  $Q$  should not exceed the number of degrees of freedom of the model. Therefore, a proper solution with weak errors should present a value of  $Q_{\text{true}}/Q_{\text{exp}}$  close to 1 (Ulbrich et al., 2009). When the number of factors has been chosen, one needs to verify that each obtained factor has a physical meaning. This can be done by comparing their variability with that of external tracers and analyzing their daily profiles (if possible) and their relationship with meteorological variables.

In order to help evaluate the quality of the obtained solution, the residuals are also analyzed. The residuals of a good solution should resemble a Gaussian distribution with values comprised between  $\pm 3$  and centered on 0. A value higher or lower than 0, suggests that the residuals have been overestimated or underestimated, respectively.

In addition, it is possible to obtain different minimums of  $Q_{\text{true}}/Q_{\text{exp}}$ . To address this, the  $f_{\text{peak}}$  parameter is used, which allows to alter the function  $Q(E)$  by applying a positive or negative rotation which will change the solution of the model. In general, the solutions found in the literature present a  $f_{\text{peak}}$  value between  $\pm 1$  (Reff et al., 2007).

More details on how PMF was used in this work are given in the second chapter.

### **1.4.3 PM<sub>2.5</sub> source apportionment with PMF in North-Western Europe**

To the best of our knowledge, in North-Western Europe, only a limited number of PMF studies have focused on the PM<sub>2.5</sub> fraction. It is worth noting two studies: one conducted in Paris, France (Bressi et al., 2014) and one in the Netherlands (Mooibroek et al., 2011),

which were applied to datasets of at least one year in duration with a daily resolution. Other studies have been conducted only for either a small period of time (e.g. Ledoux et al., 2017) or have been applied to PM<sub>10</sub> (Waked et al., 2014; Maenhaut et al., 2016, Oliveira, 2017).

In the study of Bressi et al. (2014), carried out at an urban background site in Paris during one year in 2009-2010, seven factors were determined: ammonium sulfate-rich (with an average annual contribution to the total PM<sub>2.5</sub> mass of 27%), ammonium nitrate-rich (24%), heavy oil combustion (17%), road traffic (14%), biomass burning (12%), marine aerosol (6%) and metal industry (1%). SIA were clearly the major contributors to PM<sub>2.5</sub>, and were associated to mid- or long-range transport from continental Europe.

Mooibroek et al. (2011) performed a PMF analysis to pooled data from 5 different sites in the Netherlands, consisting of three rural background sites (Cabauw, Hellendoorn and Vredepeel), one urban background site (Schiedam) and one curbside site (Rotterdam), with a duration of one year from 2007 to 2008. Again seven factors were identified, including nitrate-rich secondary aerosol (with an average contribution for all the sites to PM<sub>2.5</sub> mass of 44%), sulfate-rich secondary aerosol (25%), traffic and re-suspended road dust (10%), industrial activities/incineration (10%), sea spray (7%), crustal material (3%) and residual oil combustion (1%). In this study, the nitrate- and sulfate-rich secondary aerosols also appeared to be major contributors to PM<sub>2.5</sub> (69% on average) and their long-range origin was concluded from their limited spatial variability among the five sites.

Both studies highlighted the important contribution of SIA factors in North-Western Europe, as well as their regional origin given by the mid-to-long range transport from continental Europe.

## **1.5 Work motivation**

### **1.5.1 Pollution in Northern France**

The “Hauts-de-France” region is located in northern France (Figure 1.16) and demonstrates a long record of atmospheric pollution events. With a population of 5,987,883 inhabitants and an area of 31,813 km<sup>2</sup>, it presents a high population density of 188 inhabitants per km<sup>2</sup>. The region is the 3<sup>rd</sup> most populated one in France and the 2<sup>nd</sup> most densely populated of Metropolitan France only after the “Île-de-France” region. It is bordered by Belgium to the north-east, by the North Sea to the north and west, by the “Île-de-France” region to the south, by the “Normandie” region to the west and by the “Grand-Est” region to

the east. A total of five departments (Aisne, Nord, Oise, Pas-de-Calais, and Somme) form this region, which until recently was separated in two regions: Nord-Pas-de-Calais (Nord and Pas-de-Calais departments) and Picardie (Aisne, Oise, and Somme).

The capital of the region, Lille (233,897 inhabitants within the city limits in 2014), was part of the APHEKOM project (Improving Knowledge and Communication for Decision Making on Air Pollution and Health in Europe), which compares the impact of atmospheric pollution between cities (Declercq et al., 2012).



Figure 1.16 Maps of France (left, in red the Hauts-de-France) and of the Hauts-de-France region (right).

The climate of the region is temperate oceanic. It is represented by small thermal amplitudes, mild winters and cool summers. The annual average of the temperatures is around 11°C. The inner part of the region is more influenced by the continental climate. Figure 1.17 summarizes the meteorological trends (maximum and minimum temperatures, precipitation and solar radiation) for the weather station of Lille-Lesquin (data from Météo-France weather service). The low average solar radiation characteristic of the region is also clearly seen, which might play a significant role in the photochemical activity of the atmosphere (i.e. resulting to a low production of ozone, or in a low photochemical oxidation of sulfate aerosols precursors). In addition, the topography of the region is relatively flat (e.g. minimum and maximum heights in the northern city of Douai are 16 and 38 m), which should favor the dispersion of pollutants.

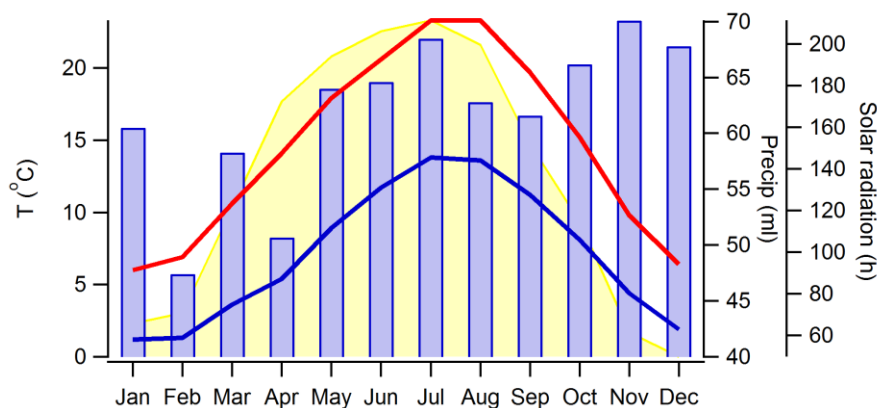


Figure 1.17 Monthly averaged meteorological trends from 1981 to 2010 (blue and red curves: minimum and maximum temperatures; blue bars: cumulative precipitations; shaded yellow area: solar radiation)

The annual limit and target values for  $PM_{2.5}$  ( $25$  and  $20 \mu g m^{-3}$ , respectively) are often exceeded in the region, especially in winter and spring. The main possible reasons include the location (affected by nearby highly populated and industrial areas such as Belgium and western Germany in the west and the metropolis of Paris in the south) and several local activities (road traffic, industrial activity, agriculture, domestic biomass burning, etc.). In Figure 1.18 the seasonal averages of  $PM_{2.5}$  from 2010 to 2016 measured at the station of Douai Theuriet (Atmo-Hauts de France air quality monitoring network) are shown in relation with the limit, target, and recommended annual average values. As can be seen, the WHO recommended value is doubled during most of the period, whereas the EU target and limit values are often exceeded.

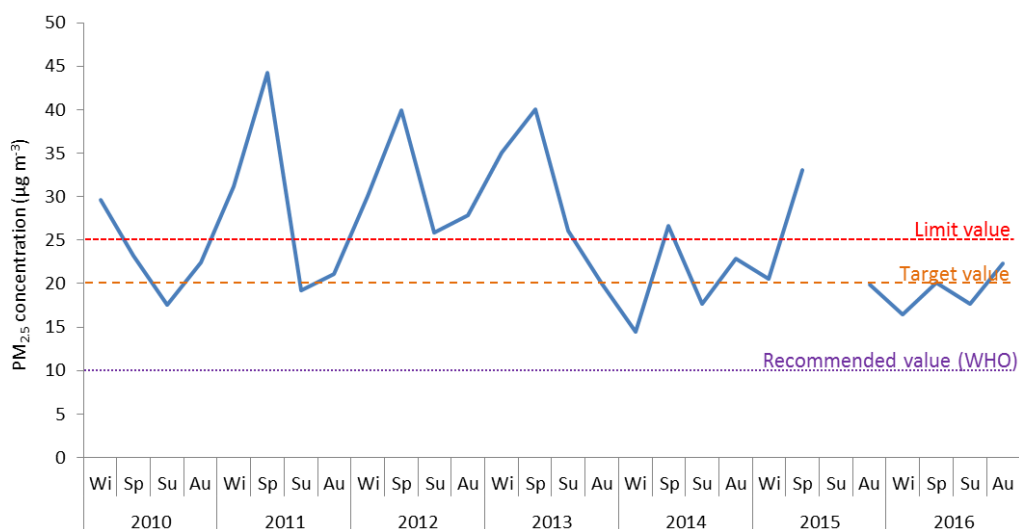


Figure 1.18  $PM_{2.5}$  seasonal averages (Wi: winter, Sp: spring; Su: Summer; Au: Autumn) measured in the station of Douai Theuriet between 2010 and 2016



We can also observe that road transport is the major contributor to the emissions of NO<sub>x</sub> (58%), and that other sectors such as the manufacturing industry, the energy transformation and the residential and tertiary sectors play less important but still significant roles to these emissions NO<sub>x</sub>, which is in agreement with the emission share of NO<sub>x</sub> observed in France (CITEPA, 2017).

On the other hand, the primary emission of particles is distributed more evenly among the different sectors. In the case of PM<sub>2.5</sub>, the residential and tertiary sector is the main responsible for their emissions (47%), which is attributed mainly to household heating. Other sectors also contribute significantly, including road transport (22%), and the manufacturing industry, waste treatment and construction sector (18%).

Table 1.9 Distribution of estimated regional emissions in the Nord-Pas-de-Calais region for 2008 (emission inventory from Atmo Nord- Pas-de-Calais)

	Agriculture/ Forestry	Biogenic sources	Other transport	Manufacturing industry, waste treatment, construction	Residential/ tertiary	Energy transformation	Road transport
SO <sub>2</sub>	0.90%	0.00%	0.02%	31.18%	5.76%	57.18%	4.96%
NO <sub>x</sub>	4.91%	0.02%	1.14%	13.23%	8.35%	14.61%	57.74%
PM <sub>10</sub>	15.51%	0.00%	1.30%	21.42%	34.06%	6.84%	20.88%
PM <sub>2.5</sub>	6.18%	0.00%	1.07%	18.41%	47.19%	5.31%	21.85%
Pb	0.09%	0.00%	2.24%	36.71%	10.11%	50.85%	0.00%
Cd	0.21%	0.00%	0.26%	52.06%	9.62%	31.88%	5.97%
As	0.02%	0.00%	0.00%	89.00%	4.66%	6.31%	0.00%
Ni	2.64%	0.00%	0.14%	15.44%	1.97%	76.58%	3.23%

### 1.5.2 Previous studies in the region of Northern France

Some studies on the measurement of aerosols have already been conducted in the region of Northern France. A majority of them have focused on the study of metallic elements (Mbengue et al., 2014) and the identification of their sources (Alleman et al., 2010; Ledoux et al., 2017), or the source identification of PM<sub>10</sub> (Oliveira, 2017; Waked et al., 2014). A few studies focused on the characterization and source apportionment of non-refractory fine particles (nr-PM<sub>1</sub>), one of them based on two 1-month intensive campaigns conducted in summer and winter (Crenn et al., 2017, 2018), and another one based on a 1-year long campaign (Zhang, 2016) and were carried out by our group.

Most of these studies were performed in the coastal and heavily industrialized area of Dunkirk (90 km NW from Douai) (Alleman et al., 2010; Crenn et al., 2017, 2018; Ledoux et al., 2017; Mbengue et al., 2014). The study of Waked et al. (2014) was conducted at an urban site in the city of Lens (20 km NNW of Douai), and that of Oliveira (2017) in five locations

spread over the north of France: Lens (urban) and Roubaix (curbside) (40 km NNE of Douai), Revin (rural; 120 km SE), Rouen (urban; 175 km SW) and Nogent-sur-Oise (urban; 130 km SSW). Part of the study of Crenn et al. (2017, 2018) was carried out in Douai itself (1.5 km SW from the sampling site of this work).

This latter study used a High Resolution-Time-of-Flight-Aerosol Mass Spectrometer (HR-ToF-AMS) in order to determine the composition of nr-PM<sub>1</sub>. Two intensive campaigns were carried out, one in winter 2010 (November 18 – December 10) and another one in summer 2011 (July 6 – August 6). The mean concentrations of PM<sub>2.5</sub> were particularly high both during the winter ( $32.6 \pm 16.8 \mu\text{g m}^{-3}$ ), and summer campaigns ( $20.5 \pm 9.8 \mu\text{g m}^{-3}$ ). The contribution to nr-PM<sub>1</sub> was similar in both, with major inorganic ions (i.e. the sum of NO<sub>3</sub><sup>-</sup>, SO<sub>4</sub><sup>2-</sup>, and NH<sub>4</sub><sup>+</sup>) making for most of the nr-PM<sub>1</sub> mass (75% and 74%), with a predominance of NO<sub>3</sub><sup>-</sup> (35% and 28% of the total nr-PM<sub>1</sub>), and the rest being attributed to OM (34% and 33%), chloride being negligible (only 1% in both campaigns), for winter and summer, respectively. In addition, BC was measured only in summer with an aethalometer (average of  $0.32 \pm 0.28 \mu\text{g m}^{-3}$ ). In both campaigns, NH<sub>4</sub><sup>+</sup> was found to correlate really well with NO<sub>3</sub><sup>-</sup> ( $r^2 = 0.91$  and  $0.89$ ), and to a lesser degree with SO<sub>4</sub><sup>2-</sup> ( $r^2 = 0.75$  and  $0.46$ ), for winter and summer, respectively. The aerosol was found to be neutral by comparing the measured and predicted NH<sub>4</sub><sup>+</sup> (i.e. amount required for the full neutralization of inorganic ions) with  $r^2$  of 0.98-0.99 and slopes close to 1. The authors attributed the seasonal difference of concentrations due to a variety of factors including the influence of emissions sources at a local scale, regional transport depending on the origin of the air masses, as well as multiple processes related to meteorological conditions.

Additionally, Zhang (2016) monitored the composition of the nr-PM<sub>1</sub> during one year from July 2013 to September 2014 using an Aerosol Chemical Speciation Monitor (ACSM) in Dunkirk, at an urban background site largely influenced by industrial and harbor activities. The mean nr-PM<sub>1</sub> mass for the whole period was  $9.7 \pm 9.0 \mu\text{g m}^{-3}$ , with an average contribution from the major aerosol constituents of 32.5% for OM, 26.4% nitrate, 26.0% sulfate, 14.4% ammonium and 1% chloride. In addition, the conversion of SO<sub>2</sub>-to-SO<sub>4</sub> was studied and found to be enhanced at high RH (>70%), low vertical turbulence and low wind speed ( $0\text{--}2 \text{ m s}^{-1}$ ). A source apportionment study of the organic fraction of the aerosol evidenced three primary sources, related to traffic, biomass combustion and domestic cooking, and one secondary source.

The studies of Waked et al. (2014) and Oliveira (2017) were focused on the PM<sub>10</sub> fraction, but were conducted over longer periods of time. In the work of Waked et al. (2014) the PM<sub>10</sub> composition was measured from March 2011 to March 2012, with a mean concentration of 21  $\mu\text{g m}^{-3}$ , and OM, NO<sub>3</sub><sup>-</sup>, and SO<sub>4</sub><sup>2-</sup> contributed to most of the mass with average concentrations of 5.8, 4.5 and 2.3  $\mu\text{g m}^{-3}$ , respectively. A source apportionment analysis showed that the main emission sources were SIA (28% of total PM<sub>10</sub> mass; divided in nitrate-rich and sulfate-rich with equal contributions of 14%), aged marine emissions (19%), biomass burning (13%), mineral dust (13%), primary biogenic emissions (9%), fresh sea salts (8%), primary traffic emissions (6%) and heavy oil combustion (4%). Some factors were found to present significant seasonal variations, such as biomass burning, which presented higher contribution in winter, and primary biogenic emissions, which were much higher in summer. The contribution of SIA was found to increase to more than 50% of the total PM<sub>10</sub> during exceedance episodes.

The work conducted by Oliveira (2017) at five sites in northern France showed a similar mass composition to that observed by Waked et al. (2014), with the predominance of SIA (particularly NO<sub>3</sub><sup>-</sup>) and OM. A source apportionment analysis showed common sources among the different sites, including nitrate-rich (12-23%), sulfate-rich (7-15%), traffic (10-26%), biomass burning (8-15%), oxalate-rich (4-19%), fresh marine (4-11%), land biogenic (2-9%), and marine biogenic (3-12%). Other sources were identified only at some sites, including an aged marine factor identified at all sites except in Rouen (9-11%) and a road dust/crustal factor identified in Revin (15%) and Roubaix (26%). Similarly to the study of Waked et al., a higher contribution of SIA was observed during high concentration episodes.

All these studies paint an initial picture of the composition of nr-PM<sub>1</sub> and PM<sub>10</sub> in the north of France, as well as the main sources to expect. In addition, they highlight the importance of SIA in the north of France and allow comparing the results with those of this study.

### **1.5.3 Issues in air quality modelling**

The utilization of offline techniques such as filter pack or denuder-filter pack for the measurement of aerosols and their precursor gases, described in section 1.3.1, has been the European reference measurement method and therefore largely employed in several air monitoring networks, such as EMEP, for the speciation of PM<sub>2.5</sub>. The collected data are mainly used to assess the ambient concentrations and the trends of airborne components. In

addition, they are also used for evaluation purposes of the regional modelling work (Schaap et al., 2011 and references therein). Specifically, in the modelling of SIA, observations on the gas-aerosol partitioning of nitrogen species are required, given the non-linear nature of the formation of  $\text{NH}_4\text{NO}_3$  (see section 1.2.4). However, very few sites are able to supply this information with a high temporal resolution, with only large daily datasets available, thus hindering the evaluation of regional models and, consequently, the development of cost effective mitigation strategies in Europe (Schaap et al., 2011).

The use of online high-resolution measurement techniques such as the MARGA has already been proven valuable for regional model evaluation (Schaap et al., 2011). In this work, the measurements of a MARGA 1S were compared with the predictions of the Chemistry Transport Model (CTM) Long Term Ozone Simulation (LOTOS) European Operational Smog (EUROS) version 1.3 in a one year campaign (from 1 Aug. 2007 to 1 Aug. 2008) held at the rural site of Cabauw (The Netherlands). The LOTOS-EUROS model is a combination of two individually-developed models: LOTOS (The Netherlands Organisation for Applied Scientific Research) and EUROS (National Institute for Public Health and the Environment). Both these operational models contain all relevant atmospheric processes and are able to model the concentrations of a wide range of atmospheric compounds, such as oxidants, SIA, SOA, primary aerosols, heavy metals and persistent organic pollutants (POPs) for a large number of scenarios at an hourly time resolution and over large periods of time (Schaap et al., 2008). The 1.3 version of LOTOS-EUROS used in their study was created based on data from filter sampling methods, which present low time resolution and took into account the associated artifacts that could lead to a poor performance of the model.

Indeed, the comparison between the MARGA observations and the predictions by LOTOS-EUROS showed a disagreement between the observed and predicted concentrations of SIA. At the monthly time scale, the variabilities for  $\text{SO}_4^{2-}$  and  $\text{NH}_4^+$  were generally well predicted, even though an underestimation at peak concentrations was observed (Figure 1.19b and c). For  $\text{NO}_3^-$ , there was a general underestimation of the monthly values (Figure 1.19a). However, there was a strong discrepancy between the observed and predicted concentrations of  $\text{HNO}_3$  and  $\text{NH}_3$  (Figure 1.19d and e). The disagreement for  $\text{NH}_3$  was partially attributed to the influence of local emissions not accounted for by the model, since the campaign was carried out in an agricultural area. The authors attributed the disagreements for  $\text{HNO}_3$  to defects in the equilibrium, the meteorological parameters (such as boundary layer height and

stability), the spatial and temporal emission patterns, cloud or multi-phase chemistry, dry deposition, ammonia compensation point and the effective emission height of sources.

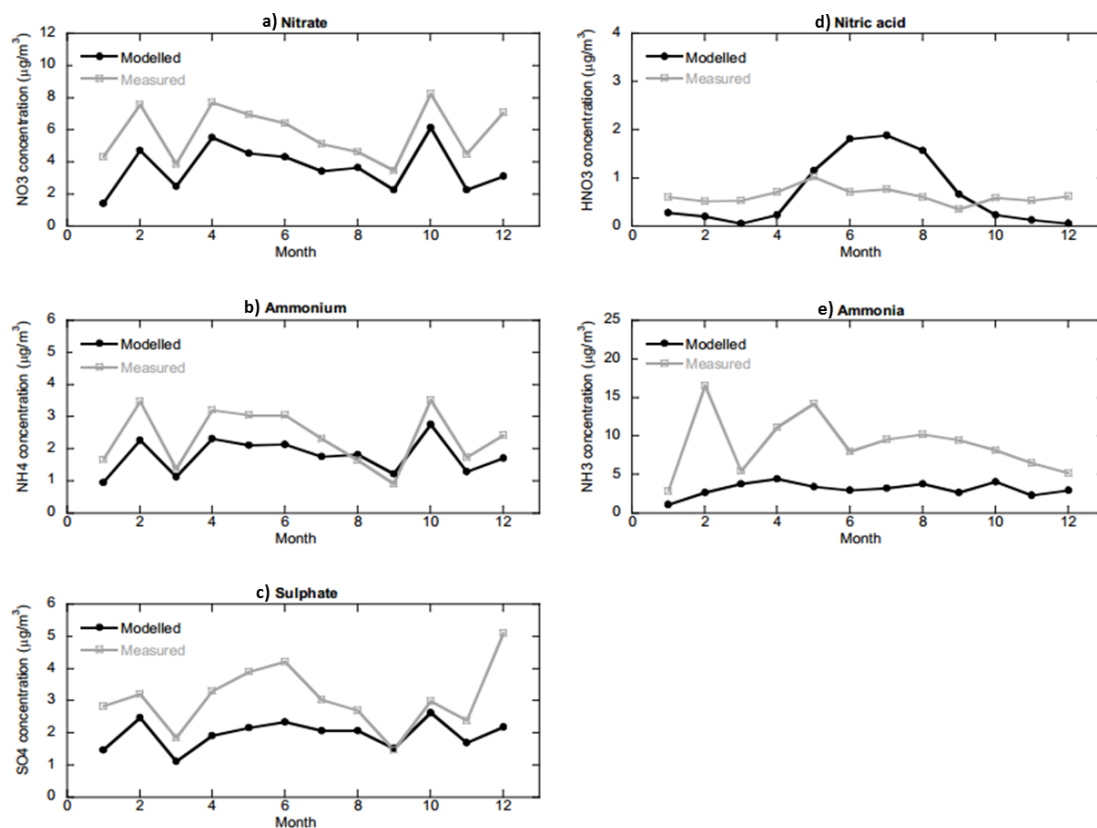


Figure 1.19 Measured and modelled monthly concentrations for  $\text{NO}_3^-$  (a),  $\text{NH}_4^+$  (b),  $\text{SO}_4^{2-}$  (c),  $\text{HNO}_3$  (d) and  $\text{NH}_3$  (e) (Schaap et al., 2011)

On a daily basis, LOTOS-EUROS was also able to model correctly a large part of the day-to-day variability for most species. The concentrations and variabilities for  $\text{SO}_4^{2-}$  and  $\text{NH}_4^+$  were well estimated except when high concentrations occurred, which the model could not predict correctly (Figure 1.20b and c). For  $\text{NO}_3^-$ , the high concentrations were well estimated, although there was a general underestimation (Figure 1.20a).

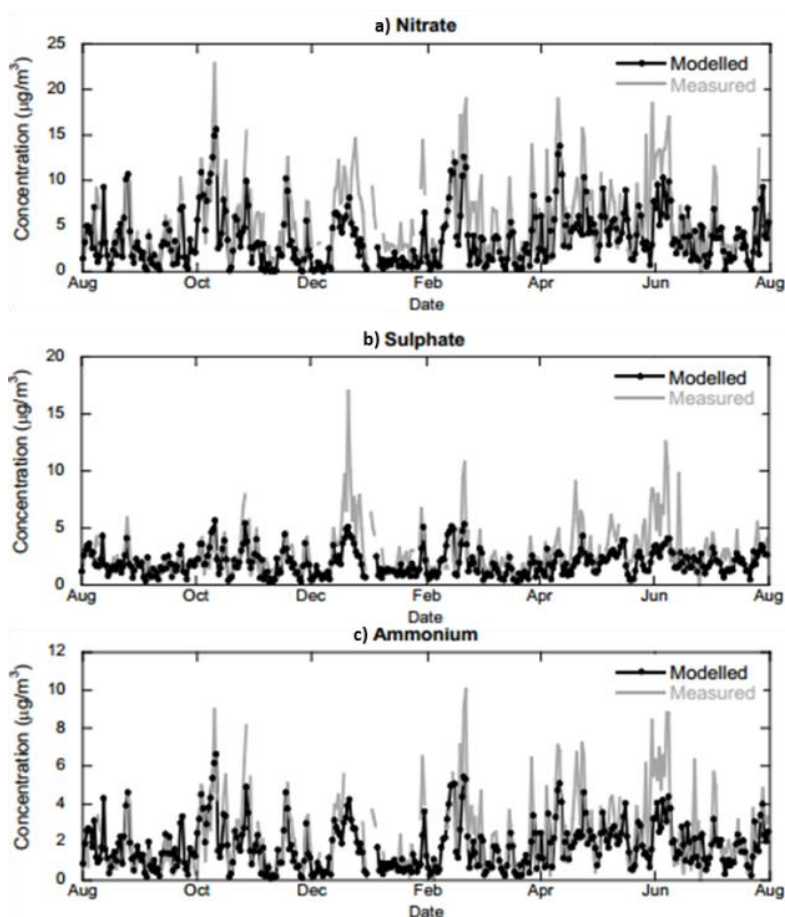


Figure 1.20 Measured and modelled daily concentrations for  $\text{NO}_3^-$  (a),  $\text{SO}_4^{2-}$  (b) and  $\text{NH}_4^+$  (c) (Schaap et al., 2011)

At the hourly time-scale the daily profiles were compared and similar conclusions to the comparisons with lower time resolution were reached. In the cases of  $\text{NO}_3^-$ ,  $\text{NH}_4^+$ ,  $\text{SO}_4^{2-}$  and  $\text{NH}_3$  (Figure 1.21a, b, c and e), the hourly variations were similar between the model and the observations but with a general underestimation, particularly pronounced for  $\text{NH}_3$  and  $\text{NO}_3^-$ . For  $\text{HNO}_3$ , there was a large difference between the model and the observation in the central hours of the day (from 12:00 to 18:00).

Out of all the compared species, the largest discrepancies were always found for  $\text{HNO}_3$  (overestimated by the model) and  $\text{NH}_3$  (underestimated by the model) at all time scales. In general, non-satisfactory modeling might result from several factors, including measurement errors such as artifacts related to volatilization or adsorption of certain species during sampling, miscounting of emission processes and time variability of precursor gases and assumptions done by the model. Particularly for the modelling of  $\text{NH}_4\text{NO}_3$  and its gaseous precursors, it was suggested that the thermodynamic equilibrium module used in the model produced a too stable  $\text{NH}_4\text{NO}_3$  in winter and during summer nights, and too unstable

during summer daytime. The observations of the MARGA were in agreement with previous studies at high-time resolution, which also found out an underestimation of the particulate nitrate concentrations during summer daytime (Fisseha et al., 2006; Morino et al., 2006). Nonetheless, other studies had shown that the modelled equilibrium was in accordance with observations (Takahama et al., 2004; Yu et al., 2005), although sometimes presenting significant inconsistencies between the measured and predicted partitioning.

Overall, the conflicting results between modelling and observations illustrate the need of further work on the thermodynamic gas-aerosol partitioning modules with the use of high-resolution experimental data for different climatic and pollution conditions.

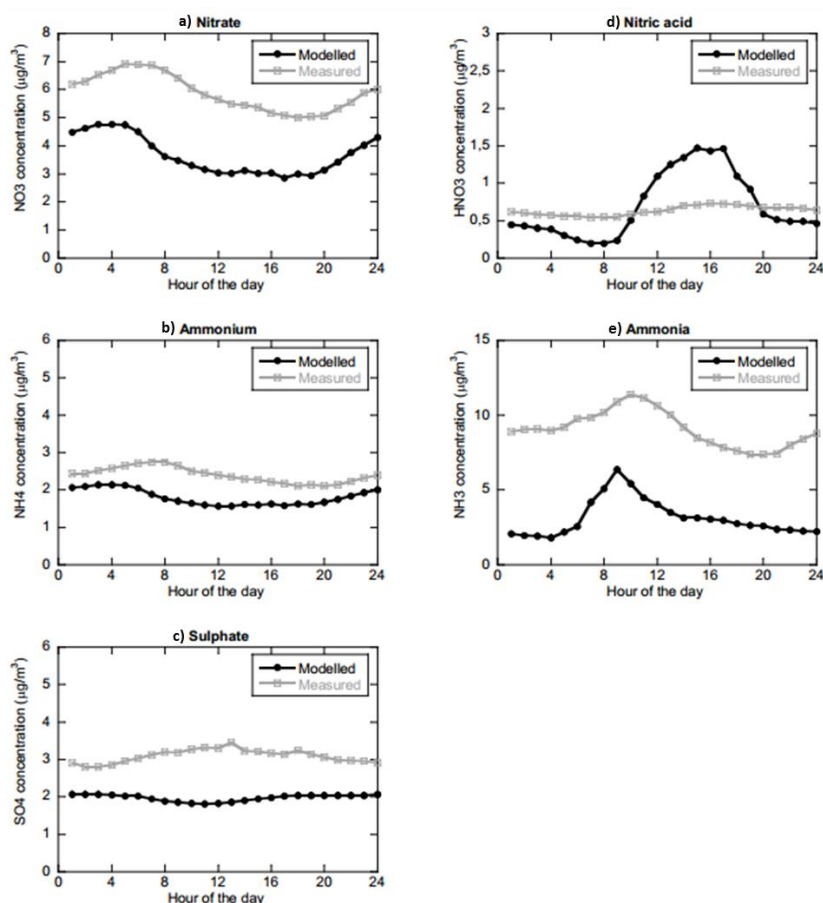


Figure 1.21 Measured and modelled hourly concentrations for  $\text{NO}_3^-$  (a),  $\text{NH}_4^+$  (b),  $\text{SO}_4^{2-}$  (c),  $\text{HNO}_3$  (d) and  $\text{NH}_3$  (e) (Schaap et al., 2011)

## 1.6 Objectives and scientific strategy

In the context of the above motivations, including the air quality issue in north-western Europe and northern France, as well as the topic of correctly modelling SIA concentrations, the main objectives of this work are therefore to:

1. **Improve the scientific knowledge on SIA and their precursor gases in northern France** in order to better understand their origin, formation and improve current modelling.
2. **Get a better knowledge on the main drivers of SIA at the local and regional levels** in order to improve the air quality in the north of France.

High particulate pollution by SIA has been observed to impact the north-west of Europe. However, until now it has been poorly studied in the region of northern France despite the evidence of high PM<sub>2.5</sub> concentrations and their proven health impact (APHEKOM, 2011). Douai was chosen for this study as a typical medium-size city of the former Coal Basin of the north of France, particularly impacted by particulate pollution.

In order to achieve the objectives above mentioned, the work strategy followed in this thesis is summarized as follows:

1. Determine the performance of the MARGA by comparison with other gas analyzers (SO<sub>2</sub>, NH<sub>3</sub>) and HR-ToF-AMS for aerosol components.
2. Constitute a long-term database by continuous observation at the hourly time scale at a fixed site over a period of 1 year, consisting of:
  - Water-soluble inorganic ions (WSII) and precursor gases
  - Source tracers, including heavy metals, nitrogen oxides and black carbon.
  - Total PM<sub>10</sub> and PM<sub>2.5</sub>
3. Implement additional instruments during the cold season, including an HR-ToF-AMS for the apportionment of the organic fraction and a SMPS for the study of the formation of new particles.
4. Perform a source apportionment study for the whole year dataset, based on the hourly (water soluble ions from the MARGA and BC from the Aethalometer) and daily-averaged data (adding heavy metals).
5. Perform a source apportionment study focusing on the high-concentration period (winter-spring), based on the data of the HR-ToF-AMS.
6. Study the influence of local and regional sources with the use of various methods for the geographical determination of sources, including non-parametric wind regression (NWR) to distinguish between local and regional sources and potential source contribution function (PSCF) for distant sources.



7. Compare observations and modelling (using the thermodynamic module ISORROPIA II) in order to verify the consistency of ammonium nitrate thermodynamic partitioning at an hourly resolution.

## 1.7 References

- Aan de Brugh, J. M. J., Henzing, J. S., Schaap, M., Morgan, W. T., van Heerwaarden, C. C., Weijers, E. P., Coe, H. and Krol, M. C.: Modelling the partitioning of ammonium nitrate in the convective boundary layer, *Atmos. Chem. Phys.*, 12(6), 3005–3023, doi:10.5194/acp-12-3005-2012, 2012.
- Acker, K., Möller, D., Auel, R., Wieprecht, W. and Kalaß, D.: Concentrations of nitrous acid, nitric acid, nitrite and nitrate in the gas and aerosol phase at a site in the emission zone during ESCOMPTE 2001 experiment, *Atmos. Res.*, 74(1), 507–524, doi:10.1016/j.atmosres.2004.04.009, 2005.
- Alleman, L. Y., Lamaison, L., Perdrix, E., Robache, A. and Galloo, J.-C.: PM10 metal concentrations and source identification using positive matrix factorization and wind sectoring in a French industrial zone, *Atmos. Res.*, 96(4), 612–625, doi:10.1016/j.atmosres.2010.02.008, 2010.
- Appel, B. R., Povard, V. and Kothny, E. L.: Loss of nitric acid within inlet devices intended to exclude coarse particles during atmospheric sampling, *Atmos. Environ.*, 22(11), 2535–2540, doi:10.1016/0004-6981(88)90485-4, 1988.
- Ayers, G. P., Gillett, R. W. and Gras, J. L.: On the vapor pressure of sulfuric acid, *Geophys. Res. Lett.*, 7(6), 433–436, doi:10.1029/GL007i006p00433, 1980.
- Badarinath, K. V. S., Latha, K. M., Chand, T. R. K. and Gupta, P. K.: Impact of biomass burning on aerosol properties over tropical wet evergreen forests of Arunachal Pradesh, India, *Atmos. Res.*, 91(1), 87–93, doi:10.1016/j.atmosres.2008.03.023, 2009.
- Beccaceci, S., McGhee, E. A., Brown, R. J. C. and Green, D. C.: A Comparison Between a Semi-Continuous Analyzer and Filter-Based Method for Measuring Anion and Cation Concentrations in PM10 at an Urban Background Site in London, *Aerosol Sci. Technol.*, 49(9), 793–801, doi:10.1080/02786826.2015.1073848, 2015.
- Borrás, E., Tortajada-Genaro, L. A. and Muñoz, A.: Determination of reduced sulfur compounds in air samples for the monitoring of malodor caused by landfills, *Talanta*, 148, 472–477, doi:10.1016/j.talanta.2015.11.021, 2016.
- Bressi, M., Sciare, J., Gherzi, V., Mihalopoulos, N., Petit, J.-E., Nicolas, J. B., Moukhtar, S., Rosso, A., Féron, A., Bonnaire, N., Poulakis, E. and Theodosi, C.: Sources and geographical origins of fine aerosols in Paris (France), *Atmos. Chem. Phys.*, 14(16), 8813–8839, doi:10.5194/acp-14-8813-2014, 2014.
- ten Brink, H., Otjes, R., Jongejan, P. and Slanina, S.: An instrument for semi-continuous monitoring of the size-distribution of nitrate, ammonium, sulphate and chloride in aerosol, *Atmos. Environ.*, 41(13), 2768–2779, doi:10.1016/j.atmosenv.2006.11.041, 2007.
- C. Declerq, H. Sarter, M. Pascal, M. Corso, A. Ung, G. Falq, O. Chanel, S. Medina: Aphekom Local city report - Lille. [online] Available from: [http://aphekom.org/c/document\\_library/get\\_file?uuid=ff072a23-f3ba-4a3d-840a-9683484a5e19&groupId=10347](http://aphekom.org/c/document_library/get_file?uuid=ff072a23-f3ba-4a3d-840a-9683484a5e19&groupId=10347) (Accessed 20 September 2017), 2012.

Cakmur, R. V., Modini, R. L., Perlwitz, J., Geogdzhayev, I. V., Ginoux, Koch, D., Kohfeld, K. E., Tegen, I. and Zender, C. S.: Constraining the magnitude of the global dust cycle by minimizing the difference between a model and observations, *J. Geophys. Res. Atmospheres*, 111(D6), doi:10.1029/2005JD005791, 2006.

Calvo, A. I., Alves, C., Castro, A., Pont, V., Vicente, A. M. and Fraile, R.: Research on aerosol sources and chemical composition: Past, current and emerging issues, *Atmos. Res.*, 120–121, 1–28, doi:10.1016/j.atmosres.2012.09.021, 2013.

Christian, T. J., Yokelson, R. J., Cárdenas, B., Molina, L. T., Engling, G. and Hsu, S.-C.: Trace gas and particle emissions from domestic and industrial biofuel use and garbage burning in central Mexico, *Atmos Chem Phys*, 10(2), 565–584, doi:10.5194/acp-10-565-2010, 2010.

CITEPA: SO<sub>2</sub> - CITEPA, [Httpswwwcitepaorgfrair--Clim.-Itemdioxyde--Soufre](https://www.citepa.org/fr/air-et-climat/polluants/aep-item/dioxyde-de-soufre) [online] Available from: <https://www.citepa.org/fr/air-et-climat/polluants/aep-item/dioxyde-de-soufre> (Accessed 31 August 2017), n.d.

Colbeck, I.: *Environmental Chemistry of Aerosols*, 1st ed., Wiley-Blackwell, Oxford., 2008.

Corbett, J. J. and Fischbeck, P.: Emissions from Ships, *Science*, 278(5339), 823–824, doi:10.1126/science.278.5339.823, 1997.

Crenn, V., Fronval, I., Petitprez, D. and Riffault, V.: Fine particles sampled at an urban background site and an industrialized coastal site in Northern France - Part 1: Seasonal variations and chemical characterization, *Sci. Total Environ.*, 578, 203–218, doi:10.1016/j.scitotenv.2015.11.165, 2017.

Crenn, V., Chakraborty, A., Fronval, I., Petitprez, D. and Riffault, V.: Fine particles sampled at an urban background site and an industrialized coastal site in Northern France—Part 2: Comparison of offline and online analyses for carbonaceous aerosols, *Aerosol Sci. Technol.*, 52(3), 287–299, doi:10.1080/02786826.2017.1403008, 2018.

DeCarlo, P. F., Kimmel, J. R., Trimborn, A., Northway, M. J., Jayne, J. T., Aiken, A. C., Gonin, M., Fuhrer, K., Horvath, T., Docherty, K. S., Worsnop, D. R. and Jimenez, J. L.: Field-Deployable, High-Resolution, Time-of-Flight Aerosol Mass Spectrometer, *Anal. Chem.*, 78(24), 8281–8289, doi:10.1021/ac061249n, 2006.

Delmas, R., Mégie, G., Peuch, V. and Brasseur, G.: *Physique et chimie de l’atmosphère*, Belin, Paris., 2005.

Dong, H.-B., Zeng, L.-M., Hu, M., Wu, Y.-S., Zhang, Y.-H., Slanina, J., Zheng, M., Wang, Z.-F. and Jansen, R.: Technical Note: The application of an improved gas and aerosol collector for ambient air pollutants in China, *Atmos Chem Phys*, 12(21), 10519–10533, doi:10.5194/acp-12-10519-2012, 2012.

Finlayson-Pitts, B. J. and Jr, J. N. P.: *Chemistry of the Upper and Lower Atmosphere: Theory, Experiments, and Applications*, Academic Press, San Diego., 1999.

Fisseha, R., Dommen, J., Gutzwiller, L., Weingartner, E., Gysel, M., Emmenegger, C., Kalberer, M. and Baltensperger, U.: Seasonal and diurnal characteristics of water soluble

inorganic compounds in the gas and aerosol phase in the Zurich area, *Atmos Chem Phys*, 6(7), 1895–1904, doi:10.5194/acp-6-1895-2006, 2006.

Fountoukis, C. and Nenes, A.: ISORROPIA II: a computationally efficient thermodynamic equilibrium model for  $K^+-Ca^{2+}-Mg^{2+}-NH_4^+-Na^+-SO_4^{2-}-NO_3^- -Cl^- -H_2O$  aerosols, *Atmos. Chem. Phys.*, 7(17), 4639–4659, doi:10.5194/acp-7-4639-2007, 2007.

Godri, K. J., Evans, G. J., Slowik, J., Knox, A., Abbatt, J., Brook, J., Dann, T. and Dabek-Zlotorzynska, E.: Evaluation and application of a semi-continuous chemical characterization system for water soluble inorganic PM<sub>2.5</sub> and associated precursor gases, *Atmos. Meas. Tech.*, 2(1), 65–80, doi:10.5194/amt-2-65-2009, 2009.

Grice, S., Stedman, J., Kent, A., Hobson, M., Norris, J., Abbott, J. and Cooke, S.: Recent trends and projections of primary NO<sub>2</sub> emissions in Europe, *Atmos. Environ.*, 43(13), 2154–2167, doi:10.1016/j.atmosenv.2009.01.019, 2009.

Hidy, G. M.: *Aerosols, an industrial and environmental science*, Academic Press., 1984.

Hinds, W. C.: *Aerosol Technology: Properties, Behavior, and Measurement of Airborne Particles: Properties, Behaviour and Measurement of Airborne Particles*, 2nd edition, John Wiley & Sons Inc, New York., 1999.

Hopke, P. K.: Review of receptor modeling methods for source apportionment, *J. Air Waste Manag. Assoc.* 1995, 66(3), 237–259, doi:10.1080/10962247.2016.1140693, 2016.

Hutchinson, G. E.: *Marginalia: Eutrophication: The scientific background of a contemporary practical problem*, *Am. Sci.*, 61(3), 269–279, 1973.

Iida, K., Stolzenburg, M., McMurry, P., Dunn, M. J., Smith, J. N., Eisele, F. and Keady, P.: Contribution of ion-induced nucleation to new particle formation: Methodology and its application to atmospheric observations in Boulder, Colorado, *J. Geophys. Res. Atmospheres*, 111(D23), D23201, doi:10.1029/2006JD007167, 2006.

J. -P. Putaud, R. V. D.: Putaud J-P, Van Dingenen R, Alastuey A, et al. A European aerosol phenomenology—3: Physical and chemical characteristics of particulate matter from 60 rural, urban, and kerbside sites across Europe, *Atmos. Environ.*, 44(10), 1308–1320, doi:10.1016/j.atmosenv.2009.12.011, 2010.

Jacob, D.: *Introduction to Atmospheric Chemistry*, Princeton University Press, Princeton, N.J., 1999.

Jang, H.-N., Seo, Y.-C., Lee, J.-H., Hwang, K.-W., Yoo, J.-I., Sok, C.-H. and Kim, S.-H.: Formation of fine particles enriched by V and Ni from heavy oil combustion: Anthropogenic sources and drop-tube furnace experiments, *Atmos. Environ.*, 41(5), 1053–1063, doi:10.1016/j.atmosenv.2006.09.011, 2007.

Jimenez, J. L., Jayne, J. T., Shi, Q., Kolb, C. E., Worsnop, D. R., Yourshaw, I., Seinfeld, J. H., Flagan, R. C., Zhang, X., Smith, K. A., Morris, J. W. and Davidovits, P.: Ambient aerosol sampling using the Aerodyne Aerosol Mass Spectrometer, *J. Geophys. Res. Atmospheres*, 108(D7), 8425, doi:10.1029/2001JD001213, 2003.

Kelly, F. J. and Fussell, J. C.: Size, source and chemical composition as determinants of toxicity attributable to ambient particulate matter, *Atmos. Environ.*, 60(Supplement C), 504–526, doi:10.1016/j.atmosenv.2012.06.039, 2012.

Keuken, M. P., Schoonebeek, C. A. M., van Wensveen-Louter, A. and Slanina, J.: Simultaneous sampling of NH<sub>3</sub>, HNO<sub>3</sub>, HCl, SO<sub>2</sub> and H<sub>2</sub>O<sub>2</sub> in ambient air by a wet annular denuder system, *Atmos. Environ.*, 22(11), 2541–2548, doi:10.1016/0004-6981(88)90486-6, 1988.

Khlystov, A., Wyers, G. P. and Slanina, J.: The steam-jet aerosol collector, *Atmos. Environ.*, 29(17), 2229–2234, doi:10.1016/1352-2310(95)00180-7, 1995.

Kim, K.-H., Kabir, E. and Kabir, S.: A review on the human health impact of airborne particulate matter, *Environ. Int.*, 74, 136–143, doi:10.1016/j.envint.2014.10.005, 2015.

Kulmala, M., Pirjola, L. and Mäkelä, J. M.: Stable sulphate clusters as a source of new atmospheric particles, *Nature*, 404(6773), 66–69, doi:10.1038/35003550, 2000.

Ledoux, F., Kfoury, A., Delmaire, G., Roussel, G., El Zein, A. and Courcot, D.: Contributions of local and regional anthropogenic sources of metals in PM<sub>2.5</sub> at an urban site in northern France, *Chemosphere*, 181, 713–724, doi:10.1016/j.chemosphere.2017.04.128, 2017.

Lemieux, P. M., Lutes, C. C. and Santoianni, D. A.: Emissions of organic air toxics from open burning: a comprehensive review, *Prog. Energy Combust. Sci.*, 30(1), 1–32, doi:10.1016/j.pecs.2003.08.001, 2004.

Li, R., Warneke, C., Graus, M., Field, R., Geiger, F., Veres, P. R., Soltis, J., Li, S.-M., Murphy, S. M., Sweeney, C., Pétron, G., Roberts, J. M. and de Gouw, J.: Measurements of hydrogen sulfide (H<sub>2</sub>S) using PTR-MS: calibration, humidity dependence, inter-comparison and results from field studies in an oil and gas production region, *Atmos. Meas. Tech.*, 7, 3597–3610, doi:10.5194/amt-7-3597-2014, 2014.

Limón-Sánchez, M. T., Arriaga-Colina, J. L., Escalona-Segura, S. and Ruíz-Suárez, L. G.: Observations of formic and acetic acids at three sites of Mexico City, *Sci. Total Environ.*, 287(3), 203–212, doi:10.1016/S0048-9697(01)00985-8, 2002.

Linak, W. P., Yoo, J.-I., Wasson, S. J., Zhu, W., Wendt, J. O. L., Huggins, F. E., Chen, Y., Shah, N., Huffman, G. P. and Gilmour, M. I.: Ultrafine ash aerosols from coal combustion: Characterization and health effects, *Proc. Combust. Inst.*, 31(2), 1929–1937, doi:10.1016/j.proci.2006.08.086, 2007.

Lorenzo, R., Kaegi, R., Gehrig, R. and Grobéty, B.: Particle emissions of a railway line determined by detailed single particle analysis, *Atmos. Environ.*, 40(40), 7831–7841, doi:10.1016/j.atmosenv.2006.07.026, 2006.

Maenhaut, W., Vermeylen, R., Claeys, M., Vercauteren, J. and Roekens, E.: Sources of the PM<sub>10</sub> aerosol in Flanders, Belgium, and re-assessment of the contribution from wood burning, *Sci. Total Environ.*, 562, 550–560, doi:10.1016/j.scitotenv.2016.04.074, 2016.

Mahowald, N. M., Scanza, R., Brahney, J., Goodale, C. L., Hess, P. G., Moore, J. K. and Neff, J.: Aerosol Deposition Impacts on Land and Ocean Carbon Cycles, *Curr. Clim. Change Rep.*, 3(1), 16–31, doi:10.1007/s40641-017-0056-z, 2017.

- Mailler, S., Menut, L., Khvorostyanov, D., Valari, M., Couvidat, F., Siour, G., Turquety, S., Briant, R., Tuccella, P., Bessagnet, B., Colette, A., Létinois, L., Markakis, K. and Meleux, F.: CHIMERE-2017: from urban to hemispheric chemistry-transport modeling, *Geosci Model Dev*, 10(6), 2397–2423, doi:10.5194/gmd-10-2397-2017, 2017.
- Marticorena, B., Bergametti, G., Gillette, D. and Belnap, J.: Factors controlling threshold friction velocity in semiarid and arid areas of the United States, *J. Geophys. Res. Atmospheres*, 102(D19), 23277–23287, doi:10.1029/97JD01303, 1997.
- Maxey, M. R.: The gravitational settling of aerosol particles in homogeneous turbulence and random flow fields, *J. Fluid Mech.*, 174, 441–465, doi:10.1017/S0022112087000193, 1987.
- Mbengue, S., Alleman, L. Y. and Flament, P.: Size-distributed metallic elements in submicronic and ultrafine atmospheric particles from urban and industrial areas in northern France, *Atmospheric Res.*, 135–136, 35–47, doi:10.1016/j.atmosres.2013.08.010, 2014.
- McDonald, J. D., Zielinska, B., Fujita, E. M., Sagebiel, J. C., Chow, J. C. and Watson, J. G.: Emissions from Charbroiling and Grilling of Chicken and Beef, *J. Air Waste Manag. Assoc.*, 53(2), 185–194, doi:10.1080/10473289.2003.10466141, 2003.
- Medeiros, P. M., Conte, M. H., Weber, J. C. and Simoneit, B. R. T.: Sugars as source indicators of biogenic organic carbon in aerosols collected above the Howland Experimental Forest, Maine, *Atmos. Environ.*, 40(9), 1694–1705, doi:10.1016/j.atmosenv.2005.11.001, 2006.
- Meszaros, E.: *Fundamentals of Atmospheric Aerosol Chemistry*, Akademiai Kiado, Budapest., 1999.
- Mooibroek, D., Schaap, M., Weijers, E. P. and Hoogerbrugge, R.: Source apportionment and spatial variability of PM<sub>2.5</sub> using measurements at five sites in the Netherlands, *Atmos. Environ.*, 45(25), 4180–4191, doi:10.1016/j.atmosenv.2011.05.017, 2011.
- Morino, Y., Kondo, Y., Takegawa, N., Miyazaki, Y., Kita, K., Komazaki, Y., Fukuda, M., Miyakawa, T., Moteki, N. and Worsnop, D. R.: Partitioning of HNO<sub>3</sub> and particulate nitrate over Tokyo: Effect of vertical mixing, *J. Geophys. Res. Atmospheres*, 111(D15), D15215, doi:10.1029/2005JD006887, 2006.
- Mozurkewich, M.: The dissociation constant of ammonium nitrate and its dependence on temperature, relative humidity, and particle size, [online] Available from: <https://yorkspace.library.yorku.ca/xmlui/handle/10315/4258> (Accessed 21 September 2017), 1993.
- Nie, W., Wang, T., Gao, X., Pathak, R. K., Wang, X., Gao, R., Zhang, Q., Yang, L. and Wang, W.: Comparison among filter-based, impactor-based and continuous techniques for measuring atmospheric fine sulfate and nitrate, *Atmos. Environ.*, 44(35), 4396–4403, doi:10.1016/j.atmosenv.2010.07.047, 2010.
- O’Dowd, C. D., Facchini, M. C., Cavalli, F., Ceburnis, D., Mircea, M., Decesari, S., Fuzzi, S., Yoon, Y. J. and Putaud, J.-P.: Biogenically driven organic contribution to marine aerosol, *Nature*, 431(7009), 676–680, doi:10.1038/nature02959, 2004.

Oliveira, D.: Identification of the main sources and geographical origins of PM<sub>10</sub> in the northern part of France, [online] Available from: <http://ori.univ-lille1.fr/notice/view/univ-lille1-ori-450821>, 2017.

Paatero, P. and Tapper, U.: Positive matrix factorization: A non-negative factor model with optimal utilization of error estimates of data values, *Environmetrics*, 5(2), 111–126, doi:10.1002/env.3170050203, 1994.

Pierce, J.: Atmospheric chemistry: Particulars of particle formation, *Nat. Geosci.*, 4(10), 665–666, doi:10.1038/ngeo1267, 2011.

Putaud, J.-P., Raes, F., Van Dingenen, R., Brüggemann, E., Facchini, M.-C., Decesari, S., Fuzzi, S., Gehrig, R., Hüglin, C., Laj, P., Lorbeer, G., Maenhaut, W., Mihalopoulos, N., Müller, K., Querol, X., Rodriguez, S., Schneider, J., Spindler, G., Brink, H. ten, Tørseth, K. and Wiedensohler, A.: A European aerosol phenomenology—2: chemical characteristics of particulate matter at kerbside, urban, rural and background sites in Europe, *Atmos. Environ.*, 38(16), 2579–2595, doi:10.1016/j.atmosenv.2004.01.041, 2004.

Querol, X., Alastuey, A., Ruiz, C. R., Artiñano, B., Hansson, H. C., Harrison, R. M., Buringh, E., ten Brink, H. M., Lutz, M., Bruckmann, P., Straehl, P. and Schneider, J.: Speciation and origin of PM<sub>10</sub> and PM<sub>2.5</sub> in selected European cities, *Atmos. Environ.*, 38(38), 6547–6555, doi:10.1016/j.atmosenv.2004.08.037, 2004.

Qureshi, A., MacLeod, M. and Hungerbühler, K.: Modeling aerosol suspension from soils and oceans as sources of micropollutants to air, *Chemosphere*, 77(4), 495–500, doi:10.1016/j.chemosphere.2009.07.051, 2009.

Reff, A., Eberly, S. I. and Bhawe, P. V.: Receptor Modeling of Ambient Particulate Matter Data Using Positive Matrix Factorization: Review of Existing Methods, *J. Air Waste Manag. Assoc.*, 57(2), 146–154, doi:10.1080/10473289.2007.10465319, 2007.

Renoux, A. and Boulaud, D.: Les aérosols : Physique et métrologie, Tec & Doc Lavoisier, Paris., 1998.

Riffault, V., Arndt, J., Marris, H., Mbengue, S., Setyan, A., Alleman, L. Y., Deboudt, K., Flament, P., Augustin, P., Delbarre, H. and Wenger, J.: Fine and Ultrafine Particles in the Vicinity of Industrial Activities: A Review, *Crit. Rev. Environ. Sci. Technol.*, 45(21), 2305–2356, doi:10.1080/10643389.2015.1025636, 2015.

Rivellini, L.-H., Chiapello, I., Tison, E., Fourmentin, M., Féron, A., Diallo, A., N'Diaye, T., Goloub, P., Canonaco, F., Prévôt, A. S. H. and Riffault, V.: Chemical characterization and source apportionment of submicron aerosols measured in Senegal during the 2015 SHADOW campaign, *Atmos. Chem. Phys.*, 17(17), 10291–10314, doi:10.5194/acp-17-10291-2017, 2017.

Santé publique France: Impacts de l'exposition chronique aux particules fines sur la mortalité en France continentale et analyse des gains en santé de plusieurs scénarios de réduction de la pollution atmosphérique, [online] Available from: <http://invs.santepubliquefrance.fr/Publications-et-outils/Rapports-et-syntheses/Environnement-et-sante/2016/Impacts-de-l-exposition-chronique-aux-particules-fines-sur-la-mortalite-en-France-continentale-et-analyse-des-gains-en-sante-de-plusieurs-scenarios-de-reduction-de-la-pollution-atmospherique> (Accessed 31 August 2017), 2016.

Schaap, M., Müller, K. and ten Brink, H. M.: Constructing the European aerosol nitrate concentration field from quality analysed data, *Atmos. Environ.*, 36(8), 1323–1335, doi:10.1016/S1352-2310(01)00556-8, 2002.

Schaap, M., Timmermans, R. M. A., Roemer, M., Boersen, G. A. C., Builtjes, P. J. H., Sauter, F. J., Velders, G. J. M. and Beck, J. P.: The LOTOS EUROS model: description, validation and latest developments, *Int. J. Environ. Pollut.*, 32(2), 270, doi:10.1504/IJEP.2008.017106, 2008.

Schaap, M., Otjes, R. P. and Weijers, E. P.: Illustrating the benefit of using hourly monitoring data on secondary inorganic aerosol and its precursors for model evaluation, *Atmos. Chem. Phys.*, 11(21), 11041–11053, doi:10.5194/acp-11-11041-2011, 2011.

Schauer, J. J., Rogge, W. F., Hildemann, L. M., Mazurek, M. A., Cass, G. R. and Simoneit, B. R. T.: Source apportionment of airborne particulate matter using organic compounds as tracers, *Atmos. Environ.*, 30(22), 3837–3855, doi:10.1016/1352-2310(96)00085-4, 1996.

Schult, I., Feichter, J. and Cooke, W. F.: Effect of black carbon and sulfate aerosols on the Global Radiation Budget, *J. Geophys. Res. Atmospheres*, 102(D25), 30107–30117, doi:10.1029/97JD01863, 1997.

See, S. W. and Balasubramanian, R.: Chemical characteristics of fine particles emitted from different gas cooking methods, *Atmos. Environ.*, 42(39), 8852–8862, doi:10.1016/j.atmosenv.2008.09.011, 2008.

Seinfeld, J. H. and Pandis, S. N.: *Atmospheric Chemistry and Physics: From Air Pollution to Climate Change*, 2nd Revised edition., John Wiley & Sons Inc, Hoboken, N.J., 2006.

Shao, Y.: *Physics and Modelling of Wind Erosion*, Springer Science & Business Media., 2008.

Sharma, M., Kishore, S., Tripathi, S. N. and Behera, S. N.: Role of atmospheric ammonia in the formation of inorganic secondary particulate matter: A study at Kanpur, India, *J. Atmos. Chem.*, 58(1), 1–17, doi:10.1007/s10874-007-9074-x, 2007.

Slanina, J., ten Brink, H. M., Otjes, R. P., Even, A., Jongejan, P., Khlystov, A., Waijers-Ijpelaar, A., Hu, M. and Lu, Y.: The continuous analysis of nitrate and ammonium in aerosols by the steam jet aerosol collector (SJAC): extension and validation of the methodology, *Atmos. Environ.*, 35(13), 2319–2330, doi:10.1016/S1352-2310(00)00556-2, 2001.

Stockwell, W. R. and Calvert, J. G.: The mechanism of the HO-SO<sub>2</sub> reaction, *Atmospheric Environ.* 1967, 17(11), 2231–2235, doi:10.1016/0004-6981(83)90220-2, 1983.

Su, H., Cheng, Y., Oswald, R., Behrendt, T., Trebs, I., Meixner, F. X., Andreae, M. O., Cheng, P., Zhang, Y. and Pöschl, U.: Soil Nitrite as a Source of Atmospheric HONO and OH Radicals, *Science*, 333(6049), 1616–1618, doi:10.1126/science.1207687, 2011.

Suarez-Bertoa, R., Zardini, A. A. and Astorga, C.: Ammonia exhaust emissions from spark ignition vehicles over the New European Driving Cycle, *Atmos. Environ.*, 97, 43–53, doi:10.1016/j.atmosenv.2014.07.050, 2014.



Takahama, S., Wittig, A. E., Vayenas, D. V., Davidson, C. I. and Pandis, S. N.: Modeling the diurnal variation of nitrate during the Pittsburgh Air Quality Study, *J. Geophys. Res. Atmospheres*, 109(D16), D16S06, doi:10.1029/2003JD004149, 2004.

Takenaka, N., Ueda, A., Daimon, T., Bandow, H., Dohmaru, T. and Maeda, Y.: Acceleration Mechanism of Chemical Reaction by Freezing: The Reaction of Nitrous Acid with Dissolved Oxygen, *J. Phys. Chem.*, 100(32), 13874–13884, doi:10.1021/jp9525806, 1996.

Toda, K., Obata, T., Obolkin, V. A., Potemkin, V. L., Hirota, K., Takeuchi, M., Arita, S., Khodzher, T. V. and Grachev, M. A.: Atmospheric methanethiol emitted from a pulp and paper plant on the shore of Lake Baikal, *Atmos. Environ.*, 44(20), 2427–2433, doi:10.1016/j.atmosenv.2010.03.037, 2010.

Ulbrich, I. M., Canagaratna, M. R., Zhang, Q., Worsnop, D. R. and Jimenez, J. L.: Interpretation of organic components from Positive Matrix Factorization of aerosol mass spectrometric data, *Atmos. Chem. Phys.*, 9(9), 2891–2918, doi:10.5194/acp-9-2891-2009, 2009.

Vestreng, V., Myhre, G., Fagerli, H., Reis, S. and Tarrasón, L.: Twenty-five years of continuous sulphur dioxide emission reduction in Europe, *Atmos. Chem. Phys.*, 7(13), 3663–3681, doi:10.5194/acp-7-3663-2007, 2007.

Viana, M., Kuhlbusch, T. A. J., Querol, X., Alastuey, A., Harrison, R. M., Hopke, P. K., Winiwarter, W., Vallius, M., Szidat, S., Prévôt, A. S. H., Hueglin, C., Bloemen, H., Wählin, P., Vecchi, R., Miranda, A. I., Kasper-Giebl, A., Maenhaut, W. and Hitzenberger, R.: Source apportionment of particulate matter in Europe: A review of methods and results, *J. Aerosol Sci.*, 39(10), 827–849, doi:10.1016/j.jaerosci.2008.05.007, 2008.

Waked, A., Favez, O., Alleman, L. Y., Piot, C., Petit, J.-E., Delaunay, T., Verlinden, E., Golly, B., Besombes, J.-L., Jaffrezo, J.-L. and Leoz-Garziandia, E.: Source apportionment of PM<sub>10</sub> in a north-western Europe regional urban background site (Lens, France) using positive matrix factorization and including primary biogenic emissions, *Atmos. Chem. Phys.*, 14(7), 3325–3346, doi:10.5194/acp-14-3325-2014, 2014.

Wang, S., Maltrud, M., Elliott, S., Cameron-Smith, P. and Jonko, A.: Influence of dimethyl sulfide on the carbon cycle and biological production, *Biogeochemistry*, 138(1), 49–68, doi:10.1007/s10533-018-0430-5, 2018.

Weber, R. J., Orsini, D., Daun, Y., Lee, Y.-N., Klotz, P. J. and Brechtel, F.: A Particle-into-Liquid Collector for Rapid Measurement of Aerosol Bulk Chemical Composition, *Aerosol Sci. Technol.*, 35(3), 718–727, doi:10.1080/02786820152546761, 2001.

Wilson, W. E. and Suh, H. H.: Fine Particles and Coarse Particles: Concentration Relationships Relevant to Epidemiologic Studies, *J. Air Waste Manag. Assoc.*, 47(12), 1238–1249, doi:10.1080/10473289.1997.10464074, 1997.

Wingen, L. M., Barney, W. S., Lakin, M. J., Brauers, T. and Finlayson-Pitts, B. J.: A Unique Method for Laboratory Quantification of Gaseous Nitrous Acid (HONO) Using the Reaction  $\text{HONO} + \text{HCl} \rightarrow \text{ClNO} + \text{H}_2\text{O}$ , *J. Phys. Chem. A*, 104(2), 329–335, doi:10.1021/jp992890e, 2000.

Wu, W. S. and Wang, T.: On the performance of a semi-continuous PM<sub>2.5</sub> sulphate and nitrate instrument under high loadings of particulate and sulphur dioxide, *Atmos. Environ.*, 41(26), 5442–5451, doi:10.1016/j.atmosenv.2007.02.025, 2007.

Wyers, G. P., Otjes, R. P. and Slanina, J.: A continuous-flow denuder for the measurement of ambient concentrations and surface-exchange fluxes of ammonia, *Atmos. Environ.*, 27(13), 2085–2090, doi:10.1016/0960-1686(93)90280-C, 1993.

Yu, J. Z., Huang, X.-F., Xu, J. and Hu, M.: When Aerosol Sulfate Goes Up, So Does Oxalate: Implication for the Formation Mechanisms of Oxalate, *Environ. Sci. Technol.*, 39(1), 128–133, doi:10.1021/es049559f, 2005.

Zhang, S.: Analyse dynamique, en champ proche et à résolution temporelle fine, de l'aérosol submicronique en situation urbaine sous influence industrielle, Université du Littoral Côte d'Opale, 14 October. [online] Available from: <https://tel.archives-ouvertes.fr/tel-01548124/document>, 2016.

---

## **CHAPTER 2**

### **Materials and methods**

---



## **CHAPTER 2. Materials and methods**

### **2.1 Location of the campaign and summary of the instrumentation used**

#### **2.1.1 Site description**

The measurement campaign was carried out in the city of Douai, northern France (50°23'03''N, 3°05'08''E, and 20 m above sea level), for a duration of 1 year from 1 August 2015 to 31 July 2016.

The city of Douai has 40,736 inhabitants (INSEE, 2014) and a high population density of 2,366 inhabitants per km<sup>2</sup>. It belongs administratively to the “Hauts de France” region and to the “Nord” French department.

Douai is situated in a flat terrain surrounded by low hills in the southwest (“collines de l’Artois”, maximum height of 200 m) and by the Ardennes massif at the southeast (maximum height of 700 m). It is located around 100 km east from the North Sea and the Strait of Dover and therefore under little influence of air masses from the North Sea (coming from the north and northwest) and the Atlantic Ocean (from the southwest).

The climate of Douai is oceanic and is characterized by mild and rainy winters and cool summers. The mean temperature is 10.5 °C, and differences of temperatures between seasons are not very large. The precipitations are very frequent and spread throughout the whole year. In section 1.5.1 of Chapter 1 the meteorological trends from 1981 to 2010 are given for the weather station of Lille Lesquin, located 25 km north of Douai.

At the European level, Douai is located between three major European capitals: Brussels (~100 km northeast), Paris (~180 km south) and London (~260 km northwest) (Figure 2.1, left). At the regional level, Douai is 30 km south from the city of Lille and other nearby towns (Figure 2.1, right), which form together the “European Metropolis of Lille (MEL)”, with about 1.14 million inhabitants in 2014 and a population density of 1,760 inhabitants per km<sup>2</sup>, being the second most densely populated metropolis in France, only after that of Paris. The city of Douai is also located at the center of the urban area of Douai-Lens (504,796 inhabitants in 2014), which is one of the “agglomerations of more than 250,000 inhabitants” considered in the French decree 2010-1250 transposing the European directive 2008/50/CE on air quality. Besides the MEL conurbation and the city of Lens, Douai is surrounded by several similar cities corresponding for the most part of the former industrialized coal basin of the north of France: 30 km southeast the city of Valenciennes (43,787 inhabitants, 2014), 23 km southwest Arras (40,970 inhabitants, 2014), 36 km

northwest Béthune (25,982 inhabitants, 2014) and 24 km south Cambrai (33,609 inhabitants, 2014). Since the shutdown of the last coal mines in 1990, an industrial conversion has taken place towards the mechanical (automobile, railway) and food processing industries.

The sampling site was set at a suburban location outside the city center of Douai (Figure 2.2), and is considered to be representative of the background pollution of the region.



Figure 2.1 Maps of France (left) and “Hauts-de-France” (right)

### 2.1.2 Air quality in Douai

Douai appears as one of the most polluted cities in France as regards air quality with  $PM_{2.5}$  values often close or over the limit of  $25 \mu g m^{-3}$  (Atmo Hauts-de-France). The  $PM_{2.5}$  seasonal averages of the Atmo Hauts-de-France station in Douai-Theuriet have been given in the first chapter of this manuscript (section 1.5.1), showing that they often exceed the target and limit values established by the European Directive 2008/50/CE. Similarly to what has been previously discussed, the main reasons for the high pollution levels in Douai include its location close to highly-populated and industrial areas and the local activities. The map in Figure 2.2 summarizes the main pollution sources and industrial activities in the city and its close surroundings. In addition, Table 2.1. presents the main industrial activities according to their direction and distance from the sampling site.

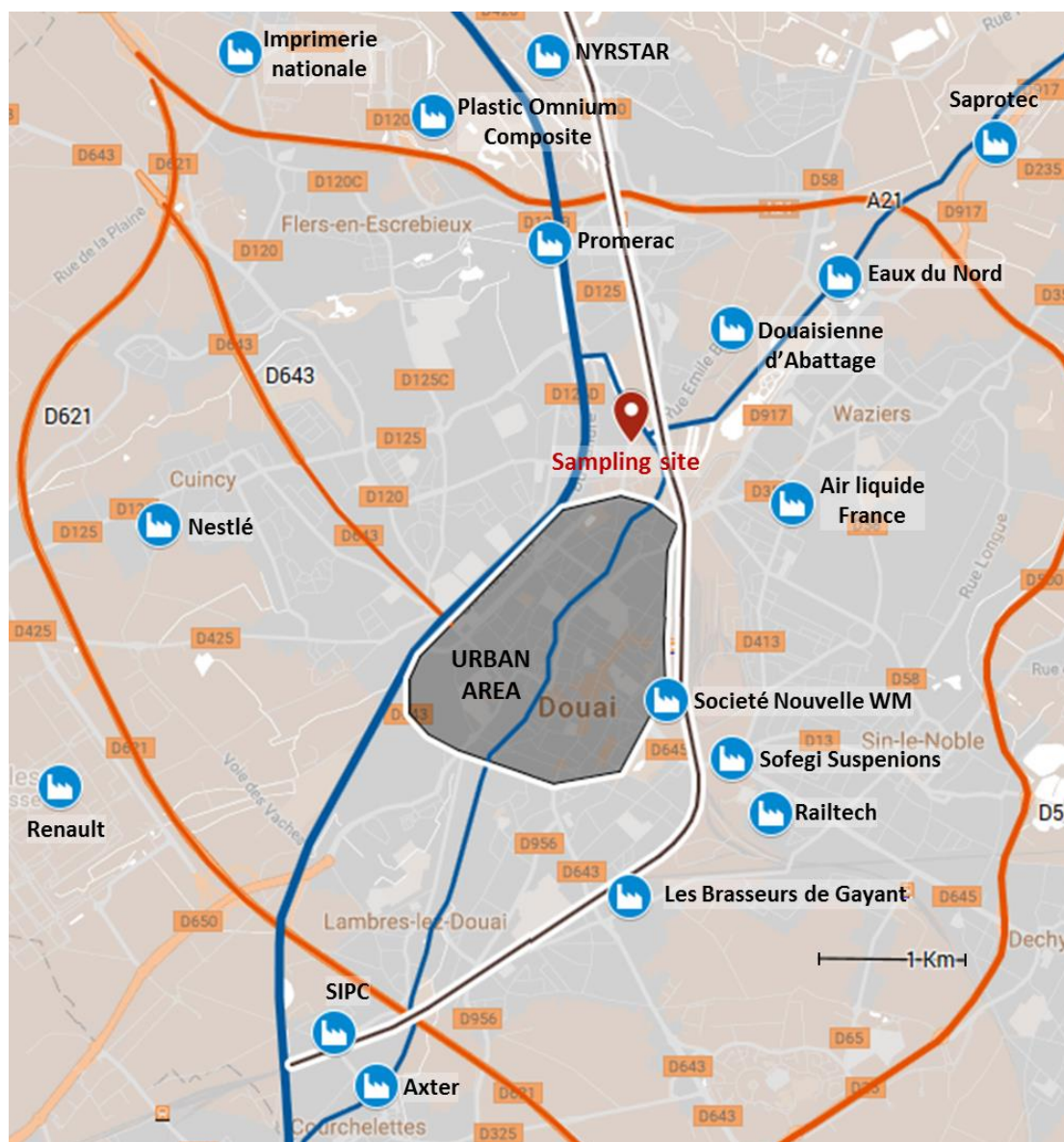


Figure 2.2 Map of Douai showing the urban area (shaded grey area), main roads (orange lines), rivers (blue lines), railroad track (black line), industrial activities (blue symbols) and sampling site (red symbol).

Table 2.1 Summary of main industrial activities in Douai and its surroundings by wind sector

NW			NE		
Industry (distance)	Activities	Expected emissions	Industry (distance)	Activities	Expected emissions
Promerac (1.4 km)	Production of metallic pieces by powder painting	Heavy metals	Douaisienne d'abattage (1 km)	Animal slaughter (cows)	NH <sub>3</sub> , others
Nyrstar (2 km)	Zinc production	Heavy metals, SO <sub>2</sub> , NO <sub>x</sub>	Eaux du Nord (1.7 km)	Waste water treatment	NH <sub>3</sub>
Plastic Omnium Composite (2.6 km)	Manufacturing of parts and accessories for motor vehicles	VOCs	Saprotec (3.2 km)	Surface treatment and coating of metals	Heavy metals
Imprimerie nationale (3.3 km)	Printing	VOCs			
SW			SE		
Industry (distance)	Activities	Expected emissions	Industry (distance)	Activities	Expected emissions
Lactalis Nestlé (3.3 km)	Fabrication of dairy products	VOCs	Air liquide France (1.2 km)	Manufacturing of industrial gases and other chemical products	N <sub>2</sub> O, HFC, HCFC
SIPC (4.7 km)	Manufacturing of pesticides and agrochemical products	VOCs	Société Nouvelle WM (1.9 km)	Assembly of car body parts	Heavy metals
Axter (4.8 km)	Production of bituminous (asphalt) membranes	VOCs	Sofegi suspensions (2.4 km)	Manufacturing of stabilizer bars for vehicles	Heavy metals
Renault (4.9 km)	Manufacturing of cars (surface treatment with organic solvents)	VOCs, NO <sub>x</sub>	Railtech (2.6 km)	Thermit-Welding Techniques, Flash-Butt Welding Systems, Track Equipment and Electrification Systems	Heavy metals
			Les Brasseurs du Gayant (3.2 km)	Beer production	VOCs

Apart from its dense population and industrial areas, transportation is one of the main sources of pollution in the Douai area in the form of roadway, railway and fluvial traffic. Roadway traffic is responsible for the emissions of particulate matter and NO<sub>x</sub>. Douai is 7 km east from the A1 highway connecting Paris with Lille (69,300 vehicles/day at the level of Douai, of which 13,000 are heavy goods vehicles). Much closer, the A21 highway, located 3 km north of the city center of Douai, and two national roadways (D621 and D643, located south and east of the city, respectively) are important contributors to air pollution. The railway crossing the city which bears the high-speed train line (TGV) from Paris to Valenciennes is as well a potential source of pollution, mainly of particles and metals. In addition, the fluvial traffic in the navigation canal of the Scarpe river that crosses the city and the fluvial port could contribute to the emissions of NO<sub>x</sub> and SO<sub>2</sub>.

The urban area of Douai (represented by the shaded grey area in Figure 2.2) is a source of domestic emissions, including residential wood burning (ATMO Nord-Pas de Calais, 2009).



Besides, several industrial activities are carried out in the city and its close surroundings (Table 2.1). Some of these activities are expected to be important sources of pollutants: a slaughterhouse (*Douaisienne d'Abattage*) and a wastewater treatment plant (*Eaux du Nord*) located north-east of the city might emit  $\text{NH}_3$  and sulfur-containing compounds, while a zinc smelter (*Nyrstar*) located north of Douai could emit nitrogen oxides, sulfur dioxide, sulfates and metals. A car manufacturing plant (*Renault*), which in Douai is specialized in surface treatment with organic solvents, could also emit important quantities of  $\text{NO}_x$  and VOCs.

Thereby, the region of northern France – and particularly the city of Douai – appears as an interesting focus point for the study and characterization of atmospheric particulate pollution, with the ultimate goal of finding the most effective ways to prevent and reduce atmospheric pollution and improve the quality of life of its inhabitants.

### **2.1.3 Instrumentation**

A summary of the instruments used in the field campaign, including the time interval of use and the operating rate is reported in Table 2.2. Part of the instrumentation was on site during all the campaign: the Monitor for Gases and AeRosols in ambient Air (MARGA 1S, Metrohm Applikon), a Beta Attenuation Monitor (BAM-1020, Met One), a double wavelength Aethalometer (AE42, Magee Scientific), a low-volume filter sampler (Partisol 2300, Thermo Fisher Scientific), and a  $\text{NO}_x$  monitor (2000G, Seres Environnement). In general, these presented high operation rates and only the  $\text{NO}_x$  analyzer showed missing data in January, June and July due to malfunctioning.

Firstly, the permanent instrumentation is going to be presented, with particular detail in the case of the MARGA. Secondly, a description of the instruments deployed in the intensive campaign will also be given, with particular emphasis on the HR-ToF-AMS.

Table 2.2 Summary of the used instrumentation in the field campaign

Instrument (manufacturer)	Measured species	Time resolution	Start	End	Operating rate
MARGA 1S (Metrohm- Applikon)	Gaseous precursors (HCl, HONO, HNO <sub>3</sub> , SO <sub>2</sub> , NH <sub>3</sub> )	1 h	Aug. 2015	Jul. 2016	88%
	PM <sub>2.5</sub> water-soluble aerosols (NO <sub>3</sub> <sup>-</sup> , SO <sub>4</sub> <sup>2-</sup> , Cl <sup>-</sup> , C <sub>2</sub> O <sub>4</sub> <sup>2-</sup> , NH <sub>4</sub> <sup>+</sup> , Na <sup>+</sup> , K <sup>+</sup> , Mg <sup>2+</sup> , Ca <sup>2+</sup> )				
BAM-1020 (Met One Instruments)	PM <sub>2.5</sub> mass concentration	1 h			94%
Aethalometer AE42 (Magee Scientific)	PM <sub>2.5</sub> absorbing at 370 nm (aromatic species) and 880 nm (black carbon)	5 min			85%
Partisol 2300 (Thermo Fisher Scientific)	Particulate heavy metals in PM <sub>2.5</sub> collected on filters	24 h			92%
NOx 2000G (Seres Environnement)	NO and NO <sub>2</sub>	15 min		May 2016	70%
SO <sub>2</sub> AF22M (Environnement SA)	SO <sub>2</sub>	15 min		Dec. 2015	95%
HR-ToF-AMS (Aerodyne Research)	Non-refractory PM <sub>1</sub> (NO <sub>3</sub> <sup>-</sup> , SO <sub>4</sub> <sup>2-</sup> , Cl <sup>-</sup> , NH <sub>4</sub> <sup>+</sup> and organics)	5 min	Feb. 2016	Mar. 2016	70%
SMPS+C (Grimm)	Particle number size distribution (11.1-1083.3 nm)	5 min	Feb. 2016	May 2016	95%



Figure 2.3 View of the Portakabin where the permanent instrumentation was located (left) and MARGA 1S setup (right)



Figure 2.4 OMEGA trailer (left) where the HR-ToF-AMS (right) was installed

## 2.2 MARGA

### 2.2.1 Description

The Monitor for AeRosols and Gases in ambient Air (MARGA) is a semi-continuous measurement system for the simultaneous analysis of aerosols and gases (Metrohm-Applikon). The MARGA has been deployed with an impactor sampling head with a size cut-off of  $2.5\ \mu\text{m}$  (*Leckel*) coated with Teflon in order to prevent the absorption of acidic gases, as previously recommended in the literature (Rumsey et al., 2014). The sampling head has been connected to the MARGA by a 2.5 m long polyethylene tube of  $\frac{1}{2}$ " O.D.

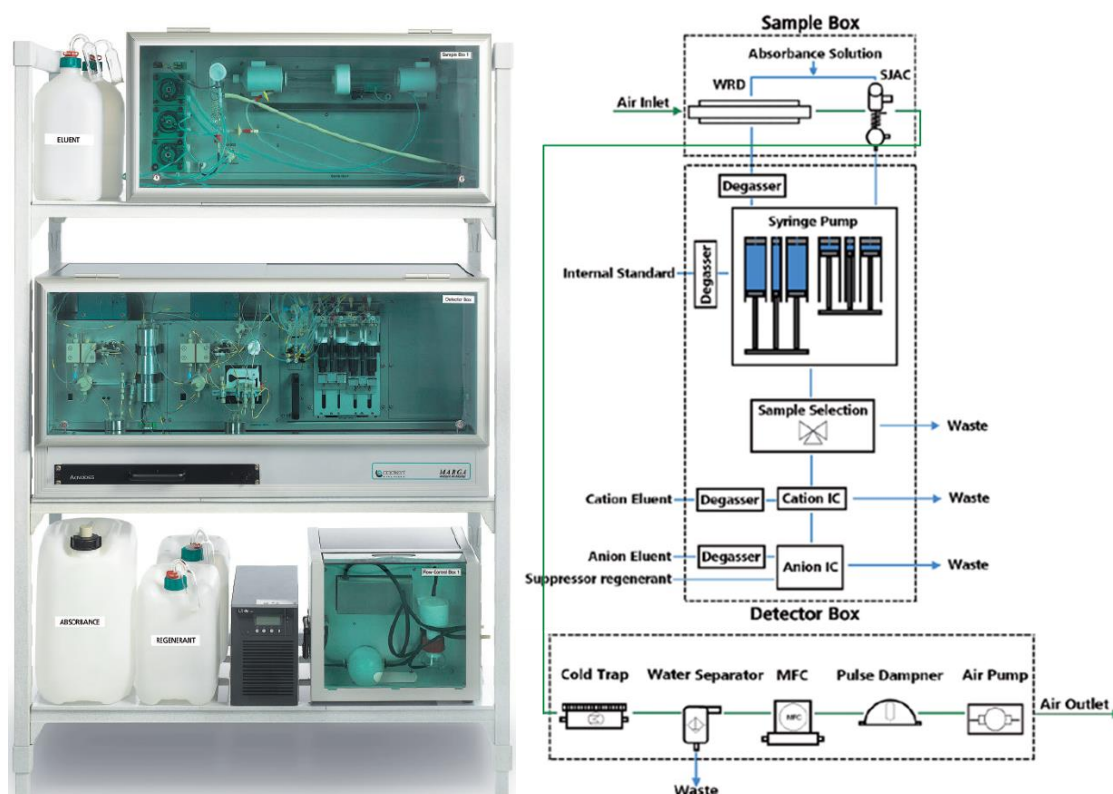


Figure 2.5 MARGA front view (left) and flow diagram (right)

The MARGA system mainly consists of a wet rotating denuder (WRD) which samples five water-soluble gases ( $\text{HCl}$ ,  $\text{HONO}$ ,  $\text{HNO}_3$ ,  $\text{SO}_2$ ,  $\text{NH}_3$ ) and a Steam-Jet Aerosol Collector (SJAC) that samples 8 water-soluble inorganic ions ( $\text{NO}_3^-$ ,  $\text{SO}_4^{2-}$ ,  $\text{Cl}^-$ ,  $\text{NH}_4^+$ ,  $\text{Na}^+$ ,  $\text{K}^+$ ,  $\text{Mg}^{2+}$ , and  $\text{Ca}^{2+}$ ) and 1 water-soluble organic anion ( $\text{C}_2\text{O}_4^{2-}$ ). The hourly resolution of the MARGA measurements allows the study of the relationship between aerosols and their gaseous precursors as well as the (trans)formation processes which cannot be observed with other offline methods such as sampling with denuder-filter packs.

The MARGA is divided in three compartments or boxes: the sample box, containing the WRD and the SJAC; the detector box, which includes two sets of three syringe pumps and

two ion chromatographs and their associated conductivity detector (one chromatograph for cations, the other for anions); and the flow control box, mainly composed of a mass flow controller (MFC) and a 24V diaphragm pump.

In the sample box (Figure 2.6a), the WRD (Figure 2.6b) performs a selective separation of the gases from the aerosols based on the differences of diffusion speed between the gases and aerosols (Keuken et al., 1988; Wyers et al., 1993). It consists of two concentric glass cylindrical tubes forming an annulus constantly fed with a liquid absorbance solution, composed of a dilute  $\text{H}_2\text{O}_2$  solution ( $10 \text{ mg L}^{-1}$ ) in ultrapure water ( $18 \text{ M}\Omega$ ). By rotating at 30 rpm, a continuous liquid film is formed in the space between the two cylinders. When the ambient air is drawn inside the denuder, the gaseous species are collected in the solution mainly due to the diffusion into the air-liquid interface and the absorption of the water-soluble gaseous species into the liquid film. Both phenomena being dependent on temperature, this one is kept constant in order to ensure a good reproducibility. The resulting solution containing the sampled gases is continuously filtered through a PTFE filter ( $0.45 \text{ }\mu\text{m}$  of porosity) and sampled by a syringe pump. After the WRD the sample enters the SJAC (Figure 2.6c), which carries out the collection of aerosol particles (Khlystov et al., 1995; Slanina et al., 2001). Generally, it is composed of a glass mixing chamber and a glass cyclone with a  $2.5 \text{ }\mu\text{m}$  cut-off. In principle, the absorbance solution ( $10 \text{ mg L}^{-1} \text{ H}_2\text{O}_2$ ) is directed into a steam generator (at  $135 \text{ }^\circ\text{C} \pm 5 \text{ }^\circ\text{C}$ ). The obtained supersaturated steam enters the mixing chamber causing the aerosols to grow into larger and heavier droplets due to the deliquescence phenomenon. Further on the air continues through a glass spiral tube which separates the generated particles from the air stream. The particles are finally collected in the absorbance solution at the bottom of the SJAC, and subsequently filtered through a PTFE filter ( $0.45 \text{ }\mu\text{m}$ ) and sampled by the syringe pump. An additional supply of absorbance solution at the bottom of the SJAC ensures a stable level of absorbance solution.

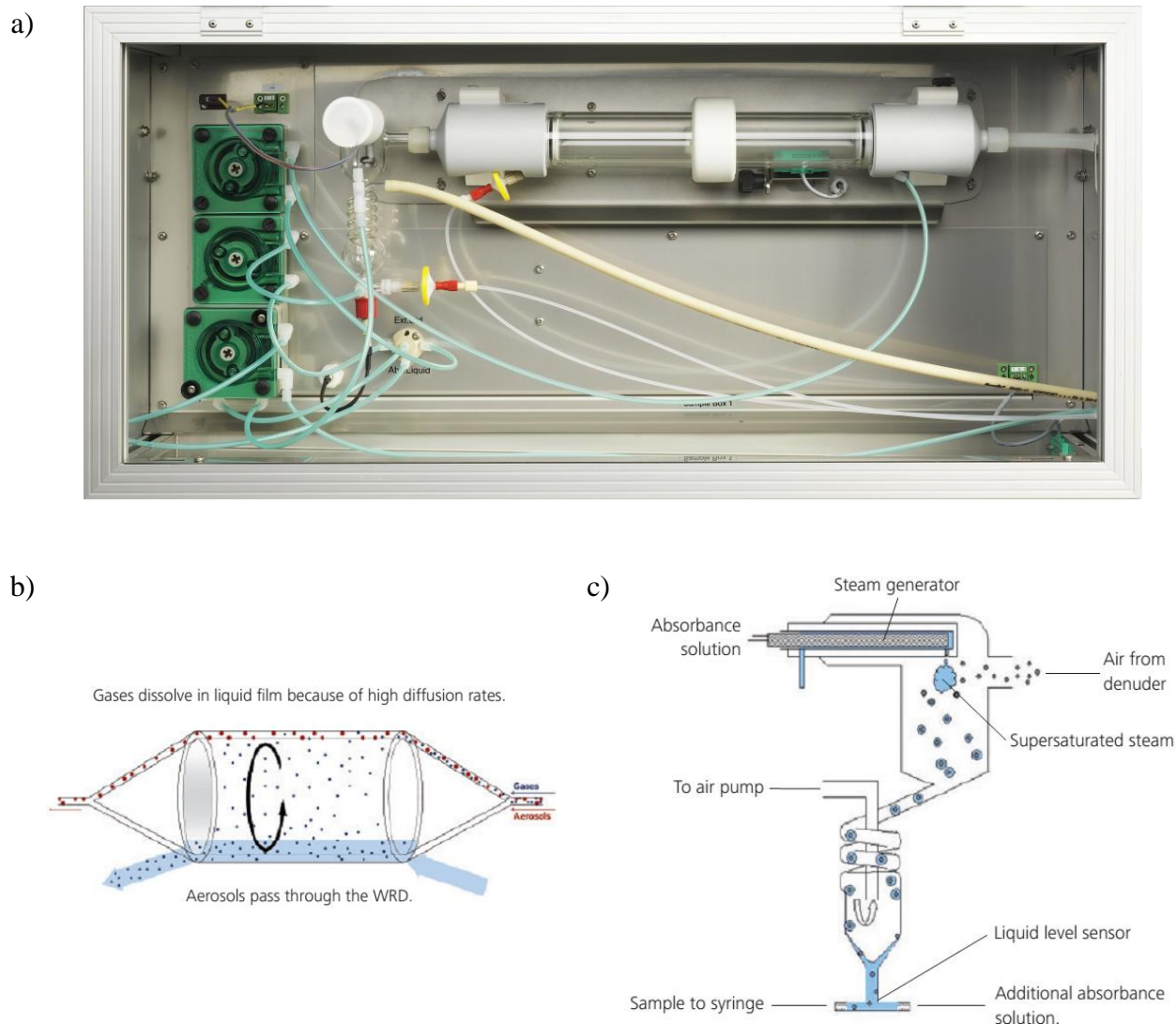


Figure 2.6 (a) Sample box front view; (b) WRD and (c) SJAC schematics

The sample box also includes four peristaltic pumps: (i) the denuder fill pump supplies the absorbance solution to the WRD and is controlled by the denuder level sensor in order to maintain a constant level of liquid; (ii) the SJAC fill pump supplies additional absorbance liquid to the SJAC and is controlled by the SJAC level sensor; (iii) the SJAC supply pump provides the steam generator with absorbance solution; and (iv) the cold trap drain drains the condensed water formed in the cold trap in the flow control box.

In the detector box (Figure 2.7a) the collected solutions of gases and aerosols are continuously drawn by two sets of alternating syringe pumps (Figure 2.7b). Every hour, one set of syringes collects 26 mL of the gases solution to the WRD syringe and 26 mL of the aerosol solution to the SJAC syringe. Simultaneously, 2.6 mL of a lithium bromide (LiBr) internal standard (IS) ( $320 \mu\text{g L}^{-1} \text{Li}^{+}$  and  $3680 \mu\text{g L}^{-1} \text{Br}^{-}$ ) are collected by a third syringe. When the syringes are full, each one contains a sample representative of 1 hour of continuous



sampling. While one of the syringe sets is being filled with the collected sample, the other set injects the previously collected sample and the LiBr standard into the sampling valve (Figure 2.7c). When a cycle has finished (i.e. one syringe set is full of sample solution and the other empty), the direction of each syringe set is reversed in order to continuously draw and inject new samples.

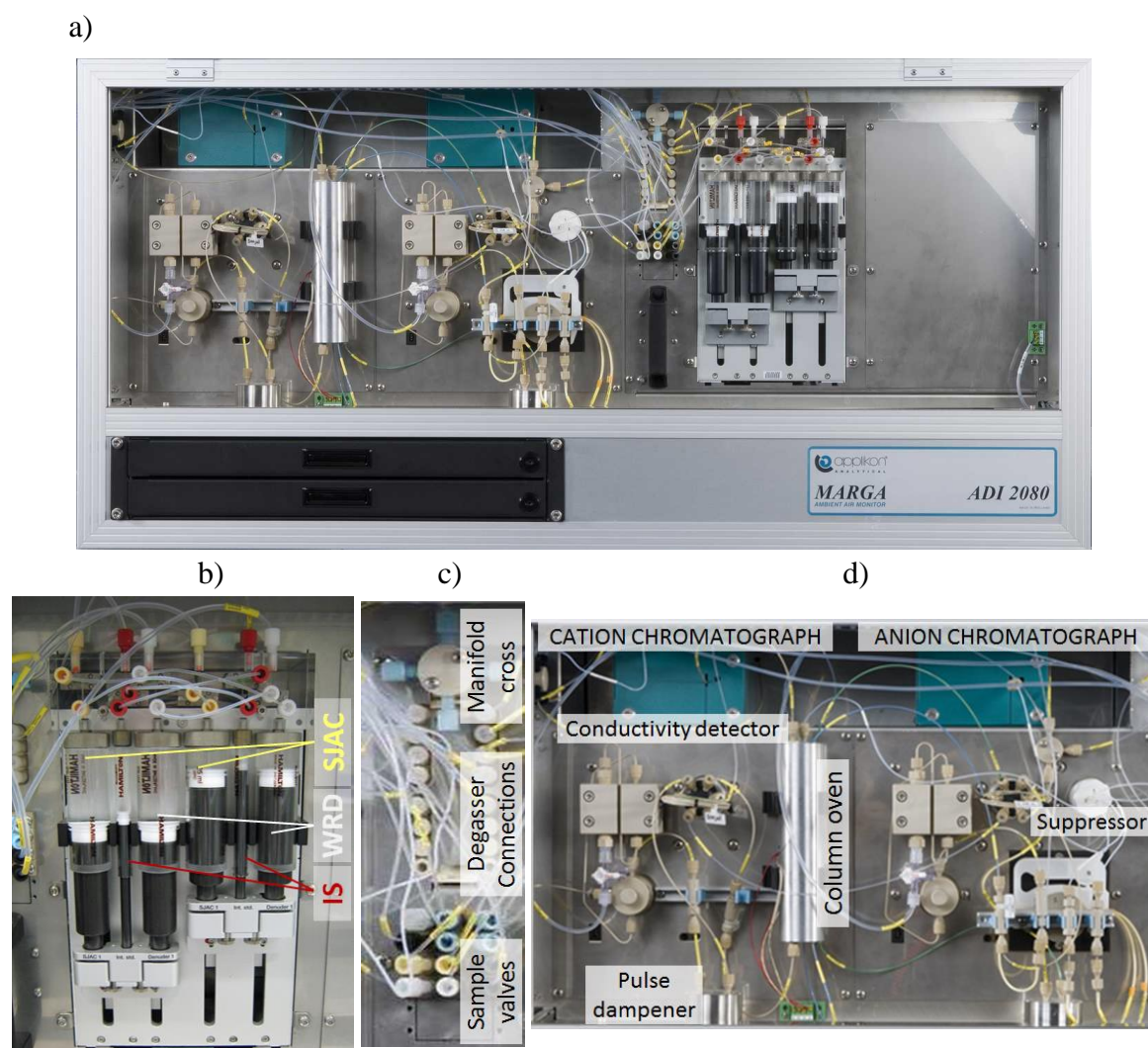


Figure 2.7 (a) Detector box front view; (b) syringe pumps; (c) sampling valves; (d) ion chromatographs

The liquid samples and internal standards are then directed through the sample valve to the manifold cross (Figure 2.7c) for the sample to be mixed with the internal standard. Moreover, a degasser located behind the detector box is responsible to remove any gases from the internal standard, anion and cation eluents and regenerant solution.

Once mixed with the internal standard, the liquid samples enter the ion chromatograph (model 761 Compact IC, Metrohm) through the cation loop ( $V = 500 \mu\text{L}$ ). A pre-column is

placed between the loop and the cation chromatography column in order to prevent any particles from damaging the column (Metrosep C 4 – 100x4.0 mm). At the same time, part of the sample is conducted to the anion loop (250 µL) and similarly, passes through a pre-column in order to protect the anion column (Metrosep A Supp 10 – 75x4.0 mm for anions). Both columns are contained in a column oven ( $40 \pm 5$  °C). Finally, the sample from the cation chromatographic column reaches the conductivity detector while the sample from the anion chromatographic column reaches first the eluent suppressor before the conductivity detector.

The addition of an internal standard to the WRD and SJAC samples makes anion and cation IC data validation possible. It also allows for the retention times to be kept stable over long periods by comparing the relative retention times of  $\text{Br}^-$  and  $\text{SO}_4^{2-}$  and adjusting the column temperature appropriately, by automatically increasing or reducing it 0.1 °C per hour according to the separation between the peaks. To achieve this, the MARGA software uses a retention time factor (RT factor) which determines the retention time relative to the internal standard (lithium or bromide). For Li and Br the RT factor is always 1, from which the rest of the retention times are calculated (e.g. in Figure 2.8), according to Equation 2.1:

$$RT \text{ factor} = \frac{\text{Retention time ion}}{\text{Retention time IS}} \quad \text{Eq. 2.1}$$



Ion	Ret time	RT factor
Cl	3.40	0.405
NO2	4.20	0.501
HSO3	7.25	0.865
Br	8.39	1.000
NO3	10.23	1.220
SO4	11.86	1.413

Figure 2.8 Example of calculated retention times for the anions

The last main part of the MARGA is the flow control box (FCB), which is in charge of controlling the airflow entering the MARGA (Figure 2.9). In the FCB the flow coming from the SJAC, previously filtered to prevent any particles from damaging the pump, enters the cold trap. The cold trap is a Peltier-type cooler (12 °C) which condenses water in the air stream to avoid water droplets in the mass flow controller (MFC). The airflow is then conducted to the water separator, where the condensed water is removed from the cold air. Just above the cold trap, an inline HEPA filter is responsible to remove any remaining



particles and to heat up the cold air in order to prevent condensation in the MFC. After that, the airstream arrives to the MFC (not visible in the figure), which allows a mass-based flow measurement.

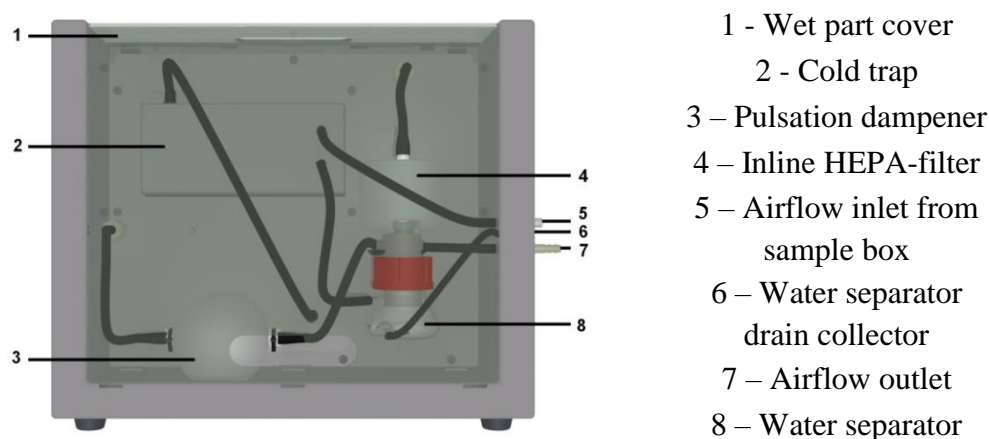


Figure 2.9 Air flow control box

The MFC sends the flow data to the Sample Box with a signal of 4-20 mA and receives back a signal of 4-20 mA, which represents the set point of the Sample Box. According to this signal, the MFC directly controls the speed of the air pump. Later, the air flow goes to the pulse dampener which smooths and stabilizes the airflow, preventing flow measurement failures in the MFC. Finally, the air flow is sucked up by the air pump and exits the system. The air pump is a 24V diaphragm pump and its speed is set by the MFC (0.5-2.6 V). Overall, the flow of the MARGA is set at  $1.0 \pm 0.02 \text{ m}^3 \text{ h}^{-1}$ .

## 2.2.2 Literature review

### 2.2.2.1 Detection limits

The detection limits (DL) for every species analyzed by the MARGA are generally low, in the range of  $0.01$  to  $0.10 \text{ } \mu\text{g m}^{-3}$ . A number of authors working with the MARGA have calculated and reported detection limits for each compound, which are within the same range of concentrations but show some differences. These differences might be attributed to different factors. First of all, the procedures for obtaining the DLs are generally not reported and therefore could lead to different results. In addition, the DLs could be obtained for the whole MARGA system (by sampling zero air or filtering ambient air). Lastly, minor differences could also be attributed to different anion and cation loop volumes or different

types of eluents. The DLs obtained by various studies as well as by the manufacturer (Metrohm-Applikon) are summarized in Table 2.3.

Only the DL provided by Makkonen *et al.* (2012), Rumsey *et al.* (2014) and Schaap *et al.*, (2011) are obtained from the commercially available MARGA. The DL reported by Trebs *et al.* (2004) are from an initial version of the MARGA, whereas those from Dong *et al.* (2012) are from a similar instrument (GAC-IC) and only given as an indication. The DLs presented by the manufacturer are similar to those reported by the different publications. The use of a pre-concentration column permits to lower the DLs by a factor of 10, and is recommended where really low concentrations are expected, in particular for minor ions such as  $\text{Cl}^-$ ,  $\text{Na}^+$ ,  $\text{K}^+$ ,  $\text{Mg}^{2+}$ , and  $\text{Ca}^{2+}$ .

#### 2.2.2.2 Measurement artifacts

Although the use of MARGA prevents some artifacts associated with other techniques such as the evaporation/condensation of  $\text{NH}_4\text{NO}_3$  in denuder-filter packs, other artifacts, mainly related to the measurement of  $\text{HNO}_3$ , have been reported in the literature.

##### i. Detection of nocturnal $\text{N}_2\text{O}_5$ as $\text{HNO}_3$ (overestimation of $\text{HNO}_3$ )

A comparison between the MARGA and a two-channel off-axis cavity ring-down absorption spectrometer (OA-CRDS) system for the measurement of dinitrogen pentoxide ( $\text{N}_2\text{O}_5$ ) showed that the MARGA detection of  $\text{HNO}_3$  is sensitive to this other gas-phase component of oxidized nitrogen (Phillips *et al.*, 2013), and more generally that alkali and aqueous-denuder techniques are sensitive to the sum of  $\text{HNO}_3$  and  $\text{N}_2\text{O}_5$ , especially at nighttime when  $\text{N}_2\text{O}_5$  forms from the reaction between the nocturnal radical  $\text{NO}_3$  and  $\text{NO}_2$ .

The contribution of  $\text{N}_2\text{O}_5$  is an error that depends on various ambient conditions (sunlight,  $[\text{NO}_x]$ ,  $[\text{O}_3]$ ,  $[\text{VOCs}]$ , T, RH...), and therefore nocturnal data of  $\text{HNO}_3$  should be at best handled with care. The formation path of  $\text{N}_2\text{O}_5$  starts with the reaction of  $\text{NO}_2$  with  $\text{O}_3$ :



Table 2.3 Experimental detection limits of the MARGA

Reference		Makkonen <i>et al.</i> , 2012	Rumsey <i>et al.</i> , 2014	Schaap <i>et al.</i> , 2011	Trebs <i>et al.</i> , 2004	Dong <i>et al.</i> , 2012	Manufacturer (Metrohm- Applikon)	
Country		Finland	USA	The Netherlands	Brazil (Amazon basin)	China	The Netherlands	
Site typology		urban background	urban	rural	rural	Rural	-	
Campaign duration (months)		7	1	12	2	1	-	
Type		IC	IC	IC	HPLC	IC (Dionex)	-	
Cation eluent		HNO <sub>3</sub>	HNO <sub>3</sub>	-	-	CH <sub>4</sub> SO <sub>3</sub>	-	
Anion eluent		Na <sub>2</sub> CO <sub>3</sub> NaHCO <sub>3</sub>	Na <sub>2</sub> CO <sub>3</sub> NaHCO <sub>3</sub>	-	Na <sub>2</sub> CO <sub>3</sub> NaHCO <sub>3</sub>	CO <sub>3</sub> <sup>2-</sup> HCO <sub>3</sub> <sup>-</sup>	-	
Cation loop volume (μL)		500	500	-	-	20	500	Preconc. Col. (5000 μm)
Anion loop volume (μL)		250	130	-	199	20	250	Preconc. Col. (2500 μm)
Detection limits (in μg m <sup>-3</sup> )								
GASES	HCl	0.02	-	0.05	0.018*	0.131*	0.01	0.001
	HNO <sub>2</sub>	0.03	-	0.05	0.044*	0.125*	0.02	0.002
	SO <sub>2</sub>	0.04	0.05	0.05	0.026*	0.411*	0.03	0.005
	HNO <sub>3</sub>	0.05	0.10	0.05	0.072*	0.433*	0.05	0.005
	NH <sub>3</sub>	0.05	0.05	0.05	0.049*	0.015*	0.05	0.005
AEROSOLS	Cl <sup>-</sup>	0.02	-	0.05	0.017*	0.043	0.01	0.001
	NO <sub>3</sub> <sup>-</sup>	0.04	0.10	0.05	0.096*	0.034	0.05	0.005
	SO <sub>4</sub> <sup>2-</sup>	0.03	0.08	0.05	0.063*	0.159	0.04	0.004
	Na <sup>+</sup>	0.02	-	0.05	-	-	0.05	0.005
	NH <sub>4</sub> <sup>+</sup>	0.03	0.05	0.05	0.064*	0.030	0.05	0.005
	K <sup>+</sup>	0.01	-	0.05	-	-	0.09	0.009
	Mg <sup>2+</sup>	0.01	-	0.05	-	-	0.06	0.006
	Ca <sup>2+</sup>	0.01	-	0.05	-	-	0.09	0.009

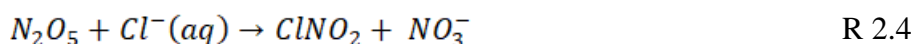
\* Converted from ppb to μg m<sup>-3</sup> assuming atmospheric pressure of 1 atm and ambient temperature of 25°C

In the daytime, NO<sub>3</sub> is rapidly photolyzed by light, leading to the formation of NO and NO<sub>2</sub>. However, at nighttime the photolysis is negligible and NO<sub>3</sub> reacts with NO<sub>2</sub> to form N<sub>2</sub>O<sub>5</sub>, in equilibrium with its precursors, as shown by reaction 2.2. The equilibrium constant K<sub>eq</sub> is strongly dependent on temperature, with cold conditions favoring the formation of N<sub>2</sub>O<sub>5</sub> (Eq. 2.2).



$$[N_2O_5] = K_{eq}[NO_3][NO_2] \quad Eq.\ 2.2$$

On the other hand,  $N_2O_5$  might be lost by heterogeneous hydrolysis on wet particles and other surfaces, and through its reaction with aqueous  $Cl^-$  (e.g. with wet particulate chloride-based salts such as NaCl):



Finally, any process leading to the loss of  $NO_3$ , such as the reaction of  $NO_3$  with biogenic VOCs or with NO, might also influence the formation of  $N_2O_5$ .

These loss processes drive the equilibrium reaction R 2.2 to the right. Therefore, low ambient temperatures and low concentrations of BVOCs, NO and  $Cl^-$  will favor the formation of  $N_2O_5$ . In Europe this phenomenon might be relevant in northern countries, where low temperatures are usual. The study of Phillips et al., (2013) was conducted during summer in Frankfurt (Germany), with high nocturnal temperatures (15-25 °C) and high BVOC concentrations which hinder the formation of  $N_2O_5$ . Yet, the average contribution of  $N_2O_5$  to the nocturnal  $HNO_3$  signal was found to be 17%. Hence, this contribution could be much different in winter, with longer nights, colder temperatures, lower  $NO_3$  formation because of less ozone and lower BVOC production due to lower solar radiation.

## ii. $HNO_3$ adsorption (underestimation of $HNO_3$ )

The adsorption of  $HNO_3$  in sampling heads and inlet tubings used in air monitoring equipment has been reported by several authors (Appel et al., 1988; Appel et al., 1993; Neuman et al., 1999; Li-Jones et al., 2001). This phenomenon is explained by the “sticky” nature of  $HNO_3$ , which adsorbs mainly onto active sites of the inlet and tubing, and accounts for an underestimation of the real  $HNO_3$  concentration. A number of factors may have an influence on this, such as the  $HNO_3$  concentration, the inlet and tubing material, geometry and temperature, as well as the relative humidity of the sample airstream ( $HNO_3$  being extremely soluble in water).

Neuman *et al.* (1999) performed a comparison study between different inlet materials and found that less than 5% of available  $\text{HNO}_3$  was adsorbed on Teflon fluoropolymer tubing after 1 min of exposure to  $\text{HNO}_3$ , while more than 70% was lost when other materials, such as stainless steel, glass, fused silica, aluminum, silica-steel and silane-coated glass, were used. These results recommend the use of Teflon materials for inlet surfaces in air sampling for  $\text{HNO}_3$  measurements.

In another study where the MARGA was tested, Rumsey *et al.* (2014) used a white acrylic separator inlet followed by polyethylene tubing. The MARGA  $\text{HNO}_3$  was compared against that of a denuder-filter pack and noticeable differences between both methods were observed. The MARGA measured concentrations lower than the denuder during daytime (i.e. when  $\text{HNO}_3$  presents the highest concentrations) and lower concentrations during nighttime (i.e. where lower  $\text{HNO}_3$  concentrations are expected). The study concluded that the use of a Teflon-coated inlet and a more inert tubing material, such as perfluoroalkoxy (PFA) Teflon, was strongly recommended for future studies. It was also recommended that the tubing length was as short as possible in order to minimize losses of  $\text{HNO}_3$ . However, PFA exhibits high electrostatic forces that eventually could retain aerosol particles and its use is not as clearly recommended.

In conclusion, the measurement of  $\text{HNO}_3$  appears complicated due to the abovementioned negative and positive artifacts. In this thesis, a Teflon-coated sampling head and PE tubing were used in order to limit the artifacts of  $\text{HNO}_3$  adsorption. However, this does not fully guarantee the correct measurement of this gas. A comparison with the thermodynamic module ISORROPIA II has been performed in order to verify this (Chapter 3).

#### 2.2.2.3 MARGA validation by comparison with other instruments

The commercially available version of the MARGA has been compared to a number of air measurement instrumentation in order to evaluate its performance and reliability. A few authors have reported comparisons between the MARGA and filters, filter-packs, denuder/filter-packs, several gas monitors, an Aerosol Mass Spectrometer (AMS), a Tapered Element Oscillation Monitor – Filter Dynamics Measurement System (TEOM-FDMS) and a Differential Mobility Particle Sizer (DMPS). A comparison between two MARGAs was also performed. Overall, most of the comparisons have shown satisfying results and support the use of the MARGA in ambient air monitoring.

i. Filter and denuder-filter pack

The MARGA has been compared against measurements done with filters (Schaap et al., 2011; Makkonen et al., 2012; Huang et al., 2014), filter-pack (Makkonen et al., 2014) and denuder/filter-pack (Rumsey et al., 2014). The characteristics and results of the comparisons are summarized in Table 2.4.

A study carried out in the Netherlands (Schaap et al., 2011) compared the MARGA with sampling on Quartz filters for  $\text{NO}_3^-$ ,  $\text{NH}_4^+$ , and  $\text{SO}_4^{2-}$ . The authors did not specify the comparison for individual species (and hence it is not shown in Table 2.4) but the results between both methods were satisfying, with slopes of 0.9-1.1, offsets less than  $1 \mu\text{g m}^{-3}$  and correlation coefficients between 0.8 and 0.9.

In Finland, two separate comparisons were performed at an urban background site near Helsinki (Makkonen et al., 2012) and at a rural site in the boreal forest of Hyytiälä (Makkonen et al., 2014). In the first comparison (Makkonen et al., 2012), the 24h-averaged MARGA data were compared to daily measurements carried out by standard sampling on Teflon filters. The regression coefficients were satisfying, with values around 0.9 for ions typically found in high concentrations ( $\text{NO}_3^-$ ,  $\text{SO}_4^{2-}$ ,  $\text{NH}_4^+$ ), and less good for minor cations, which were usually close to the DL ( $\text{Na}^+$ ,  $\text{Mg}^{2+}$  and, particularly,  $\text{K}^+$ ). The slopes were lower than 1, which suggests that the MARGA could be underestimating the concentrations. Higher slopes (ca. 3) were found for  $\text{Mg}^{2+}$  and  $\text{Ca}^{2+}$ . The overestimation of these two cations was found to be caused either by a dirty cation loop, low sensitivity or bad integration of the small peaks by the MARGA software, and was later solved with the replacement of the cation loop with a pre-concentration column. Additionally, the smaller  $r^2$  and slope reported for  $\text{Na}^+$  were justified by a poor integration of the peaks in the chromatogram by the MARGA software, which sometimes did not recognize small peaks of  $\text{Na}^+$  that eluted very close to the  $\text{NH}_4^+$  peaks.

Table 2.4 Characteristics and results of the comparisons between MARGA and filter-based measurements published in recent studies

Reference	Makkonen et al., 2012 (filter, PM <sub>10</sub> )		Makkonen et al., 2014 (filter-pack, PM <sub>10</sub> )		Rumsey et al., 2014 (MARGA, PM <sub>26</sub> / filter-pack, PM <sub>2.5</sub> )				Huang et al., 2014 (filter PM <sub>2.5</sub> )	
					MARGA Unit 1		MARGA Unit 2			
Sampling site	Helsinki, Finland		Hyytiälä, Finland		North Carolina, United States				Hong Kong, China	
Site typology	Urban background		Rural		Urban				Suburban	
Measurement period	1 November 2009 - 24 May 2010		21 June 2010 - 30 April 2011		8 September 2010 - 8 October 2010				1 March 2011-29 February 2012	
Compared species										
	slope	r <sup>2</sup>	slope	r <sup>2</sup>	slope	r <sup>2</sup>	slope	r <sup>2</sup>	slope	r <sup>2</sup>
Cl <sup>-</sup>	0.72/0.77 <sup>A</sup>	0.83/0.82 <sub>A</sub>	-	-	-		-	-	1.08	0.80
NO <sub>3</sub> <sup>-</sup>	0.90/1.00 <sup>A</sup>	0.93/0.90 <sub>A</sub>	1.31	0.93	2.36/1.28 <sub>C</sub>	0.80 <sup>C</sup>	1.73/0.82 <sub>C</sub>	0.81 <sup>C</sup>	0.76	0.77
SO <sub>4</sub> <sup>2-</sup>	0.85/0.93 <sup>A</sup>	0.98/0.97 <sub>A</sub>	1.08	0.90	0.97	0.99	0.98	0.99	0.99	0.70
Na <sup>+</sup>	0.49/0.44 <sup>A</sup>	0.55/0.54 <sub>A</sub>	1.50/0.88 <sub>B</sub>	0.70/0.95 <sub>B</sub>			-	-	0.86	0.61
NH <sub>4</sub> <sup>+</sup>	0.91/0.73 <sup>A</sup>	0.83/0.77 <sub>A</sub>	1.23/1.19 <sub>B</sub>	0.61/0.83 <sub>B</sub>	1.02	0.97	0.97	0.96	0.80	0.94
K <sup>+</sup>	-0.26/0.38 <sub>A</sub>	0.19/-1.0 <sub>A</sub>	1.51/1.00 <sub>B</sub>	0.75/0.90 <sub>B</sub>			-	-	0.58	0.79
Mg <sup>2+</sup>	3.03/2.64 <sup>A</sup>	0.69/0.68 <sub>A</sub>	3.39/0.73 <sub>B</sub>	0.86/0.85 <sub>B</sub>			-	-	-	-
Ca <sup>2+</sup>	3.03/3.43 <sup>A</sup>	0.86/0.83 <sub>A</sub>	2.95/0.89 <sub>B</sub>	0.97/0.62 <sub>B</sub>			-	-	-	-
HNO <sub>3</sub>	-	-	0.50	0.70	0.73/0.90 <sub>D</sub>	0.88/0.91 <sub>D</sub>	0.57/0.69 <sub>D</sub>	0.88/0.90 <sub>D</sub>	-	-
SO <sub>2</sub>	-	-	0.98	0.89	1.11	0.99	1.05	0.99	-	-
NH <sub>3</sub>	-	-	1.00	0.79	0.65	0.78	0.72	0.84	-	-

<sup>A</sup>After forcing the offset to zero

<sup>B</sup>Results after installing a pre-concentration column for the cations

<sup>C</sup>Offset correction due to inlet cutoff size

<sup>D</sup>Averaged HNO<sub>3</sub> concentrations to 24 hours

In the second comparison (Makkonen et al., 2014) the MARGA results were compared to those of the conventional EMEP denuder-filter pack, delivering good results for major ions and better for minor ions when a pre-concentration column for the cations was used. However,  $\text{Ca}^{2+}$  presented worse results, which was attributed to its really low concentrations during the period where the pre-concentration was used.  $\text{SO}_2$  and  $\text{NH}_3$  compared well between both methods, with slopes close to 1 and good correlation coefficients. However,  $\text{HNO}_3$  concentrations were lower in the MARGA (slope = 0.5). This was attributed to the sticky nature of this gas, which could get attached to the walls of the polypropylene inlet tubing.

In the United States, Rumsey et al. (2014) compared two MARGA units (MUs) against the EMEP denuder-filter pack. The results were good for  $\text{SO}_4^{2-}$  and  $\text{SO}_2$ . For  $\text{NO}_3^-$  the initial results were worse with high slopes and lower correlation coefficients, later found to be the consequence of different sampling conditions between the MARGA units and the filter pack (a customized inlet with a cutoff diameter of 26  $\mu\text{m}$  was used with the MUs, while the denuder-filter pack inlet cutoff was 2.5  $\mu\text{m}$ ). Similarly to other comparisons the MARGA measured lower  $\text{HNO}_3$  compared to the denuder-filter pack, which was again associated to the sticky nature of the gas. Since the adsorption was affected by the  $\text{HNO}_3$  concentration, the temperature in the inlet and tubing and the moisture content of the sample stream (all factors varying through a daily cycle), when averaging the  $\text{HNO}_3$  concentrations over 24h, the adsorption effect was reduced and the comparison results improved significantly. For  $\text{NH}_4^+$  and  $\text{NH}_3$ , the main results were not good, later found to be linked to bacterial contamination in the MARGA. It was suggested that  $\text{NH}_4^+$  could be incorporated to the bacterial biomass leading to an underestimation of its concentration. The big cutoff size (26  $\mu\text{m}$ ) could have helped the entry of coarse aerosols, usually more rich in bacteria, especially those of marine origin. A correction for this offset due to bacterial contamination was done and better results were obtained. Although  $\text{NH}_3$  was also suspected to be affected by bacterial consumption, other effects such as adsorption to the inlet tubing and a high variable blank of the denuder could also account for the differences between the MARGA and the denuder-filter pack. The application of an offset to account for the bacterial consumption also resulted in closer  $\text{NH}_3$  values between both methods.

In the study of Huang et al., (2014) concentrations between the MARGA and the filters were generally in agreement and were less good for  $\text{Na}^+$  and  $\text{K}^+$ . It was suggested that a possible contamination of the filter materials by  $\text{Na}^+$  could have affected the comparison results.



## ii. Gas monitors

Two authors have compared the MARGA SO<sub>2</sub> against two conventional SO<sub>2</sub> monitors (Makkonen et al., 2012; Rumsey et al., 2014). The results of the comparisons (Table 2.5) were satisfactory, with high correlation coefficients. However, the slopes indicate that the MARGA was underestimating the concentrations of SO<sub>2</sub>.

Table 2.5 Comparison results of the MARGA SO<sub>2</sub> against two SO<sub>2</sub> monitors

Reference	Makkonen et al., 2012	Rumsey et al., 2014	
SO <sub>2</sub> monitor	TEI 43iTL monitor	TEI 43S PFA	
		MARGA Unit 1	MARGA Unit 2
slope	0.90 0.88 <sup>A</sup>	0.96	0.89
r <sup>2</sup>	0.89 0.89 <sup>A</sup>	0.99	0.99

<sup>A</sup>After forcing the offset to zero

## iii. AMS

Some authors have compared the MARGA with the HR-ToF-AMS (Mensah et al., 2012; Lee et al., 2013) and the Compact-Time of Flight-Aerosol Mass Spectrometer (C-ToF-AMS) (Makkonen et al., 2014). The characteristics and results of each comparison are summarized in Table 2.6.

Table 2.6 Characteristics and results of the comparison between the MARGA and the AMS

Reference	Mensah et al., 2012		Lee et al., 2013		Makkonen et al., 2014	
Sampling site	Cabauw, The Netherlands		Hong Kong		Hyytiälä, Finland	
Site typology	Rural		Suburban		Rural	
Sampling period	May 2008		26 April 2011 – 1 June 2011		21 June 2010 – 30 April 2011	
AMS type	HR-ToF-AMS		HR-ToF-AMS		C-ToF-AMS	
MARGA cutoff size	1 µm (MARGA sizer)		2.5 µm		2.5 µm	
Compared species						
	slope	r <sup>2</sup>	slope	r <sup>2</sup>	slope	r <sup>2</sup>
NO <sub>3</sub> <sup>-</sup>	1.91	0.82	0.33	0.79	0.29	0.07
SO <sub>4</sub> <sup>2-</sup>	1.81	0.69	0.60	0.88	1.01	0.92
NH <sub>4</sub> <sup>+</sup>	1.32	0.72	0.50	0.80	0.66	0.83
Cl <sup>-</sup>	1.30	0.68	-	-	-	-

In the first study, Mensah et al. (2012) compared a MARGA-sizer to a HR-ToF-AMS and obtained satisfying results. The MARGA-sizer (ten Brink et al., 2007) differs from the default MARGA in that it includes a pre-separator of parallel mounted impactors in order to classify the particles by different cutoff sizes (in the study of Mensah et al.: 0.18  $\mu\text{m}$ , 0.32  $\mu\text{m}$ , 0.56  $\mu\text{m}$ , 1 and 2  $\mu\text{m}$ ). When the fraction below 1  $\mu\text{m}$  was compared with the measurements of the AMS (cutoff of 1  $\mu\text{m}$ ) high coefficients of determination were obtained but the concentrations were on average a factor of 1.6 higher than those of the AMS. This was attributed to the different sampling height of both instruments (4 m for the MARGA sizer and 60 m for the AMS), as well as to possible losses along the 60-m sampling line of the AMS.

Lee et al. (2013) observed similar variations between both instruments but a strong underestimation in mass concentrations by the AMS, which was mainly justified by the difference in inlet cut-off sizes.

The study of Makkonen et al. (2014) showed good agreement for  $\text{SO}_4^{2-}$  and  $\text{NH}_4^+$ , and worse for  $\text{NO}_3^-$ . Contrarily to previous comparisons,  $\text{NO}_3^-$  measured by the AMS was often higher than that of the MARGA. However, the MARGA was also compared to filter measurements over the same period and the obtained values were in agreement between both methods. The authors concluded that the differences between the MARGA and the AMS in  $\text{NO}_3^-$  were partly attributed to the low observed concentrations (DL for  $\text{NO}_3^-$  are one order of magnitude lower with the C-ToF-AMS compared to the MARGA), the lower response to organic nitrates by the MARGA and filters (part of the inorganic anion  $\text{NO}_3^-$  measured by the AMS could have a contribution of organic nitrates, although this should be very small) and a constant  $\text{NO}_3^-$  blank subtracted from all the MARGA results which could have varied throughout the campaign and be a source of inaccuracy.

#### iv. Total mass

The sum of water-soluble inorganic ions from the MARGA has also been compared against the total PM mass measured by instruments such as the DMPS or TEOM-FDMS.

Makkonen et al. (2012) compared the sum of the MARGA water-soluble ions ( $\text{PM}_{10}$ ) and the mass concentration measured by a DMPS ( $\text{PM}_1$ ). Both instruments measured the variations in concentrations well. Nevertheless, the DMPS measured higher mass concentrations than the MARGA sum of ions in spite of the lower cut-off of the DMPS. This was attributed to the MARGA only analyzing the water-soluble inorganic fraction of the aerosol instead of the total mass.

In another study, the MARGA water-soluble ions (PM<sub>2.5</sub> and PM<sub>10</sub>) were measured next to a TEOM-FDMS (PM<sub>2.5</sub> and PM<sub>10</sub>) for a period of 6 years (January 2007 to December 2012) at a background site in Auchencorth, United Kingdom (Twigg et al. 2015). On average, the sum of water-soluble inorganic ions measured by the MARGA in the PM<sub>10</sub> size fraction accounted for 78% of the PM<sub>10</sub> mass measured by the TEOM-FDMS, demonstrating their role as major contributors of the aerosol mass. However, a discrepancy was found between both instruments when PM<sub>2.5</sub> was compared. The PM<sub>2.5</sub> concentrations at the site were generally low and often close to the DLs of the TEOM-FDMS, with around 20 % of negative values during all the sampling period, which justified the lack of agreement.

v. Intercomparison of two MARGA units

A comparison between two MARGA units (MU) operated in parallel was performed by Rumsey et al. (2014). The results are summarized in Table 2.7, where the median absolute relative percent difference (MARPD) is calculated taking the paired hourly air concentrations at the time  $i$  for each MU as shown in the next equation:

$$MARPD = \frac{|c(MU_1)_i - c(MU_2)_i|}{[c(MU_1)_i + c(MU_2)_i]/2} \times 100 \quad \text{Eq. 2.3}$$

In the study a precision goal was set to be  $\leq 25\%$ . This was met for most compounds, with particularly good results for SO<sub>4</sub><sup>2-</sup> and NH<sub>4</sub><sup>+</sup>, except for NO<sub>3</sub><sup>-</sup>. The authors explained that the difference of sampling (which included coarse NO<sub>3</sub><sup>-</sup> due to the 26 µm cutoff) – attributed to the fans controlling the bypass flow rate through the inlets of each MU which were operating at different speeds – could create different particle size cutoffs.

Table 2.7 Summary of the performance of the MARGA based on the comparison between two MARGA units performed by Rumsey et al. (2014)

Species	Precision
	MARPD (%)
SO <sub>2</sub>	11.5
SO <sub>4</sub> <sup>2-</sup>	3.2
NO <sub>3</sub> <sup>-</sup>	30.8
HNO <sub>3</sub>	22.7
NH <sub>4</sub> <sup>+</sup>	5.3
NH <sub>3</sub>	22.8

The results of the different comparisons with the MARGA and other instruments as well as between two MARGA units are enough to conclude that the MARGA is suitable for the measurement of inorganic gases and aerosols in ambient air. However, care must be taken when low concentrations of cations are expected (when the use of a pre-concentration column is recommended) and with the data of nitric acid.

### 2.2.3 Data validation

#### 2.2.3.1 Preliminary validation

The data obtained with the MARGA was validated according to the LiBr internal standard concentration which was injected together with the sample every single hour. The concentration of  $\text{Li}^+$  and  $\text{Br}^-$  ought to be within  $320 \pm 10$  and  $3680 \pm 100 \mu\text{g L}^{-1}$ , respectively. When the concentrations of Li and Br were outside of this range, the concentrations for that specific chromatogram were automatically classified as invalid data. Additionally, when the MARGA was not working properly, the data was also marked as invalid.

##### i. Manual validation

All chromatograms were manually checked to see if any errors had been committed by the MARGA automatic integration software. Occasionally, when concentrations of some ions were close to the detection limit, the automatic software did not recognize the small peaks and therefore their integration was omitted, particularly for  $\text{Na}^+$ ,  $\text{Mg}^{2+}$  and  $\text{Ca}^{2+}$ . This was corrected by the modification of the peak search smoothing parameter in the MargaTool v.2.1 post-integration software (Metrohm).

##### ii. Case of data inferior to the limits of detection

The minor ions measured by the MARGA often presented values below the limit of detection (DL). This was particularly frequent for  $\text{Cl}^-$ ,  $\text{C}_2\text{O}_4^{2-}$ ,  $\text{K}^+$ ,  $\text{Mg}^{2+}$  and  $\text{Ca}^{2+}$ . These values below the DL were replaced by half the limit of detection ( $\frac{1}{2} \text{DL}$ ). There were different reasons for the ions under the DL:

- The cations  $\text{K}^+$ ,  $\text{Mg}^{2+}$  and  $\text{Ca}^{2+}$  presented very small concentrations: for  $\text{Mg}^{2+}$  this was general over the entire year; for  $\text{K}^+$  this was less important in winter and for  $\text{Ca}^{2+}$  in summer and autumn.
- The determination of  $\text{Na}^+$  showed an occasional problem: its peak was located really close in between the peaks of  $\text{Li}^+$  and  $\text{NH}_4^+$ , and when concentrations of  $\text{Na}^+$  were close to the DL, its peak could merge with the  $\text{NH}_4^+$  peak and be easily confused.

However, this occurred rarely (mostly during summer) and  $\text{Na}^+$  concentrations were usually above the detection limit.

- For  $\text{Cl}^-$ , a negative peak at its expected position in the chromatogram was observed, instead of a flat line, when the concentrations were close to the detection limit or non-existent. Therefore it was suspected that some chloride could be contained in some of the solutions used with the MARGA, which could originate from the used ultrapure water, the chemical products, and the laboratory material used for the preparation of every solution. Additionally, the  $\text{Cl}^-$  peak was the first to appear in the anion chromatogram (at around 3.5 minutes when the anion column was new), and its retention time shifted to the left with column aging. When the anion column was aged, the chloride peak appeared too close to the injection peak and was easily confused, impeding its determination. Therefore, chloride concentrations were not determined for an important period of time (~2 weeks on average before a new column was installed every 2 months).
- Lastly, the determination of  $\text{C}_2\text{O}_4^{2-}$  was also problematic: when the anion column was new, its elution time (~17 min) was outside the analysis time (15 min) and therefore could not be seen until the anion column was used for 2 or 3 weeks and the oxalate anion could elute within the analysis time. Therefore, no oxalate data was available during periods of around 2 or 3 weeks each time that the anion column was changed.

#### **2.2.4 Detection limit calculations**

The detection limits of every species analyzed by the MARGA have been calculated from the repeated analyses of an analytical blank (ultrapure water of 18 M $\Omega$ ), which was injected into the ion chromatographs. The DL for each species was determined by multiplying the standard deviation of the repeated analyses by 3 ( $3\sigma$ ). It is important to mention that the detection limit obtained with this methodology just concerns the analytical part and not the entire instrument, and hence should be handled with care when making comparisons with the manufacturer DL or those reported in other studies which used different methods for DL determination.

A comparison between the DLs obtained in this work and those presented by the manufacturer of the MARGA (Metrohm-Applikon) is presented in Table 2.8. In the specific case of oxalate, to the best of our knowledge, it has not been reported by the manufacturer.

All detection limits are close to those presented by Metrohm, and well within the range of the DLs reported in previous publications (see Table 2.3).

Table 2.8 This study and manufacturer DLs for every species analyzed by the MARGA (in  $\mu\text{g m}^{-3}$ )

	$\text{NO}_3^-$	$\text{NO}_2^-$	$\text{SO}_4^{2-}$	$\text{C}_2\text{O}_4^{2-}$	$\text{Cl}^-$	$\text{NH}_4^+$	$\text{K}^+$	$\text{Na}^+$	$\text{Mg}^{2+}$	$\text{Ca}^{2+}$
This study	0.06	0.05	0.11	0.08	0.02	0.03	0.03	0.03	0.02	0.05
Manufacturer	0.05	0.02	0.04	-	0.01	0.05	0.09	0.05	0.06	0.09

### 2.3 Aethalometer

The aethalometer is an instrument that measures the absorption coefficients of light-absorbing particulate compounds at one or more wavelengths in near real time (Hansen *et al.*, 1984). In this work, a dual-wavelength aethalometer (Magee Scientific, Model AE-42) was deployed with an impactor-type sampling head with a cutoff size of  $2.5 \mu\text{m}$  and at a volumetric flow rate  $Q$  of  $5 \text{ L min}^{-1}$  in order to determine the carbonaceous compounds absorbing in the near infrared (880 nm), corresponding to black carbon (BC), and to evaluate the compounds absorbing in the UV (370 nm) known as UV-absorbing carbon (UV-C, mostly aromatics) with a time resolution of 5 minutes. Both BC and UV-C are expressed in mass concentration of black carbon. The principle of the instrument is based on light attenuation (ATN):

$$ATN = \ln\left(\frac{I_o}{I}\right) \quad \text{Eq. 2.4}$$

with  $I_o$  the intensity of the incoming light and  $I$  the remaining light intensity passing through a quartz-fiber filter tape spot (area  $A$ ), onto which particles are deposited.

The intensities are related by the Beer-Lambert's law as follows:

$$I = I_o e^{-b_{abs} x} \quad \text{Eq. 2.5}$$

where  $b_{abs}$  is the absorption coefficient ( $\text{m}^{-1}$ ) and  $x$  the total thickness of the particle-loaded filter. The accumulation of particles during a specific time interval ( $\Delta t$ ) modifies the raw attenuation coefficient ( $b_{ATN}$ ):

$$b_{ATN} = \frac{(ATN_t - ATN_{t-1})}{\Delta t} \frac{A}{Q} \quad \text{Eq. 2.6}$$

The filter-based methodology used in the aethalometer presents artifacts including multiple scattering by the filter fibers which increases the optical path, scattering due to particles already collected on the filter, and a shadowing effect due to the accumulation of particles (Weingartner *et al.*, 2003). In order to account for these effects, the measurements of the aethalometer need to be corrected. In this work, the measurements were corrected following the methodology proposed by Weingartner *et al.* (2003), who introduced a filter loading correction factor (f) giving place to the following equation with  $ATN_t$  expressed in %:

$$\begin{aligned} b_{abs,t} &= \frac{b_{ATN,t}}{C_{ref} \cdot R(ATN)_t} = \frac{b_{ATN,t}}{C_{ref} \cdot \left[ \left( \frac{1}{f} - 1 \right) \cdot \frac{\ln(ATN_t) - \ln(10\%)}{\ln(50\%) - \ln(10\%)} + 1 \right]} \\ &= \frac{b_{ATN,t}}{C_{ref} \cdot \left[ \left( \frac{1}{m \cdot (1 - \omega_0) + 1} - 1 \right) \cdot \frac{\ln(ATN_t) - \ln(10\%)}{\ln(50\%) - \ln(10\%)} + 1 \right]} \end{aligned} \quad \text{Eq. 2.7}$$

where  $C_{ref}$  is a constant value (2.14) taking into account the scattering of the light beam by the filter fibers, and  $R(ATN)$  is an empirical function describing all other effects. The parameter  $f$  is the filter loading correction factor calculated as the slope of  $b_{ATN}$  vs  $ATN$ , where  $m$  (the mass concentration of particles expressed in  $\text{g m}^{-3}$ ) is constant and  $\omega_0$  is the single scattering albedo (adimensional), which was obtained from the PHOTON/AERONET network (Lille site) and averaged for each season. The averages of  $\omega_0$  for each season were  $0.876 \pm 0.083$  for summer 2015,  $0.847 \pm 0.075$  for autumn 2015,  $0.882 \pm 0.088$  for winter 2015/2016,  $0.923 \pm 0.066$  for spring 2016 and  $0.949 \pm 0.063$  for summer 2016. The corrected concentrations  $m_{corr}$  ( $\text{g m}^{-3}$ ) were then obtained as follows:

$$m_{corr,t} = \frac{b_{abs,t}}{SG_\lambda} = \frac{b_{abs,t}}{\frac{14625}{\lambda}} \quad \text{Eq. 2.8}$$

where  $SG_\lambda$  ( $\text{m}^2 \text{g}^{-1}$ ) is the spectral mass specific attenuation cross-section for a specific  $\lambda$  (nm).

Additionally, a semi-quantitative variable “Delta-C”, which is representative of organic components of wood-smoke particles, was determined by the difference of light absorption between 370 and 880 nm, i.e. UV-C minus BC (Allen *et al.*, 2004). Delta-C has

previously been found to be correlated with wood-burning markers such as levoglucosan and  $K^+$  and therefore might be used as a tracer of wood combustion (Wang et al., 2012).

#### **2.4 Partisol 2300 – filter sampling and ICP-MS analysis of trace and major elements**

A Partisol 2300 Speciation Sampler (Rupprecht & Patashnick Co., Inc) was used in order to collect daily samples of heavy metals in  $PM_{2.5}$ . This instrument consists of 12 channels which might be used for simultaneous (several channels at the same time) or sequential sampling (one at a time). A ChemComb speciation cartridge (Rupprecht & Patashnick Co., Inc) consisting of an impactor with a cutoff size of  $2.5\ \mu m$  and a collection Teflon filter of 47 mm of diameter and  $2\ \mu m$  of porosity (Zefluor) was placed in each of the 12 sampling slots. Thus, the system allowed for 12 days of unattended sequential sampling, with a 24-h duration for each of the filters. All 12 channels were operated at  $10\ L\ min^{-1}$ , adding up to a total volume of  $14.4\ m^3$  after 24 hours of sampling. The loaded filters were collected on a weekly basis and replaced by new filters. After collection, filters were stored in closed plastic Petri dishes then in closed plastic bags. Every week, the same collection procedure was applied to one blank filter (which was put in a cartridge, stored on site during one week, removed from the cartridge and put in a plastic box inside a plastic bag) in order to account for any possible contamination in the manipulation procedure. The samples and blanks were stored in a fridge at  $4\ ^\circ C$  until further analysis. Additionally, the Partisol recorded every 30 minutes the temperature, atmospheric pressure, and sampling flows.

The filters were analyzed by Inductively Coupled Plasma-Mass Spectrometry (ICP-MS) (Baranov and Tanner, 1999). This technique allows for a simultaneous quantification of a large number of elements. In this work the major elements that were analyzed included Al, Ca, Fe, K, Mg, and Na, and the minor elements included Ag, As, Ba, Be, Bi, Cd, Ce, Co, Cr, Cs, Cu, Fe, Ge, Hg, In, La, Li, Mn, Mo, Ni, Pb, Pd, Pt, Rb, Sb, Se, Sn, Sr, Th, Ti, Tl, U, V, and Zn. Most of these were analyzed by Dynamic Reaction Cell (ICP-MS DRC) (Tanner *et al.*, 2002) and some major ( $^{27}Al$ ,  $^{57}Fe$ ,  $^{39}K$ ,  $^{24}Mg$ ,  $^{23}Na$ , and  $^{28}Si$ ) and minor elements ( $^{52}Cr$ ,  $^{45}Sc$ , and  $^{51}V$ ) were also analyzed by Kinetic Energy Discrimination (ICP-MS KED) (Yamada *et al.*, 2015).

Before the analysis, the filters were submitted to an acid digestion within a solution of 2 mL of  $HNO_3$ , 1 mL of  $H_2O_2$  and 0.3 mL of HF by the use of a microwave oven (Milestone ETHOS) at  $220\ ^\circ C$  during 25 minutes. Each acid-digested sample was then adjusted to a final volume of 50 mL by adding ultrapure water.



The samples were then analyzed by ICP-MS (NeXion 300x, Perkin Elmer). Briefly, the prepared liquid sample was nebulized and transported under an argon flow to the argon plasma at  $\sim 6000\text{ }^{\circ}\text{C}$ , where the elements were atomized and partly ionized. The formed ions in the plasma were captured in an electrostatic field and canalized to a quadrupole mass spectrometer. The instrument was used as a mass filter and performed a selective transmission of the ions according to their mass-to-charge ratio. The ions were caught and amplified by an electron multiplier and finally quantified. The methodology for the quality control of the measurements has been previously described by Mbengue et al. (2014) and Leclercq et al. (2017). Repeated measurement of blanks and quality control (QC) were carried out during each analytical run. An internal standard composed of  $^{69}\text{Ga}$  and  $^{103}\text{Rh}$  was added at a concentration of  $1\text{ }\mu\text{g L}^{-1}$  to all the analyzed solutions in order to correct for the drift of the ICP-MS signal. In addition, samples of 1 mg of the NIST certified standards 2584 (indoor dust) and 1648 (urban particulate matter) were tested to validate the extraction procedure.

The filter samples were analyzed by batches of approximately 60 filters each. For each of the batches the DL of each species was calculated as 3 times the standard deviation of repeated laboratory blank analyses. The analyses of field blanks allowed the calculation of field DL for each species and assessing any possible introduced contamination due to filter handling. The laboratory and field blank DLs for each species and batch are reported in Tables A1 and A2 (Annex 1) for major and trace elements, respectively. The recovery rate of the elements was calculated taking into account the NIST analyses, such as that if NIST recovery was inferior to 85%, the element concentration was divided by the recovery rate.

## **2.5 BAM-1020**

The BAM-1020 (Met One Instruments) is a continuous particle monitor designed for long-term unattended monitoring of ambient particulate concentrations (an inlet with a cutoff of  $2.5\text{ }\mu\text{m}$  was used in this work) based on beta ray attenuation (Jaklevic *et al.*, 1981), offering an hourly time resolution. At the beginning of each sampling hour, a  $^{14}\text{C}$  source emits a constant beam of high energy electrons (i.e. beta rays) through a spot of fresh filter tape (fiber glass) for 8 minutes. An integrated sensitive scintillation detector detects and counts the electrons in order to determine a zero-reading. The instrument then advances this spot of tape to the sample nozzle, where a vacuum pump pulls the sampled air (at a flow rate of  $16.7\text{ L min}^{-1}$ ) through the filter tape, loading it with particulate matter during 42 minutes. At the end of the sampling hour, the spot is disposed again between the beta source and the detector during 8 minutes causing a decrease in the beta ray signal, which is used to determine the PM

mass on the filter tape, and hence to calculate the real concentration of PM in the ambient air. The instrument includes temperature and RH sensors which were integrated in the meteorological database. The hourly detection limit of the BAM-1020 is  $4.8 \mu\text{g m}^{-3}$ .

The BAM-1020 has obtained the United States Environmental Protection Agency (EPA) and European Environment Agency (EEA) certifications for continuous  $\text{PM}_{2.5}$  monitoring and is therefore a common instrument in  $\text{PM}_{2.5}$  mass measurement.

## 2.6 Gas monitors

### 2.6.1 $\text{NO}_x$

In this work, a  $\text{NO}_x$  2000G continuous gas analyzer (Seres Environnement) was used in order to determine the hourly gas concentrations of NO and  $\text{NO}_x$ , from which  $\text{NO}_2$  is calculated by subtracting NO to  $\text{NO}_x$ . Its operating principle is based on UV chemiluminescence following the reaction:



where the reaction of NO with  $\text{O}_3$  leads to the formation of excited  $\text{NO}_2^*$ , which goes back to its stable state ( $\text{NO}_2$ ) by emitting a radiation ( $h\nu$ ), the intensity of which depends on the NO concentration. The instrument operates two ways sequentially: one enables to measure NO only, the other measures the sum of  $\text{NO} + \text{NO}_2$  ( $\text{NO}_x$ ) by previously converting  $\text{NO}_2$  through a molybdenum catalytic converter. The sample is alternatively derived in order to obtain the NO-only signal. The time resolution of the instrument is 15 minutes, with a detection limit of 1 ppb. In this thesis, the  $\text{NO}_x$  2000G monitor was deployed at a flow rate of  $30 \text{ L min}^{-1}$ . The instrument was calibrated by using a certified calibration bottle of NO and  $\text{NO}_x$  (n° 20524 and 20926).

HONO might be measured by the  $\text{NO}_x$  2000G in the conversion of NO into  $\text{NO}_2$ . However, the contribution of HONO to the concentration of  $\text{NO}_2$  is generally very low and can be neglected. In this work, the average contribution of HONO to the  $\text{NO}_x$  concentration was calculated to be around 4%.

### 2.6.2 $\text{SO}_2$

A sulfur dioxide continuous analyzer AF22M (Environnement SA) was used from August to December 2015 for comparison purposes. Its operating principle is based on UV Fluorescence. Under the influence of UV radiation,  $\text{SO}_2$  molecules are temporarily excited by

absorbing this radiation and go back to their original state by releasing a characteristic fluorescence radiation. This emitted radiation is measured by a photomultiplier tube and then converted to SO<sub>2</sub> concentration taking into account the temperature and pressure. The addition of an optical shutter and an enhanced aromatic hydrocarbon scrubber compensates the photomultiplier drift and guarantees the removal of any interference, respectively.

The instrument was calibrated by using a certified calibration bottle of SO<sub>2</sub> (n° 77692). The time resolution of the AF22 analyzer is 15 minutes, with a detection limit of 0.4 ppb. A sample flow rate of 0.3 L min<sup>-1</sup> was used in this work.

## **2.7 HR-ToF-AMS**

### **2.7.1 Description and operating principle**

The high-resolution time-of-flight aerosol mass spectrometer (HR-ToF-AMS) (Aerodyne Research), hereafter named AMS, is designed to measure in real-time the chemical composition and size distribution of the non-refractory PM<sub>1</sub> (nr-PM<sub>1</sub>) (DeCarlo et al., 2006). Non-refractory aerosols are volatilized at temperatures lower than 600 °C: NO<sub>3</sub><sup>-</sup>, NH<sub>4</sub><sup>+</sup>, SO<sub>4</sub><sup>2-</sup>, Cl<sup>-</sup> and organic carbon (Docherty et al., 2015). Other species including elemental carbon, mineral dust and sea salt volatilize at higher temperatures and therefore cannot be detected. The AMS presents a time resolution of a few minutes and DLs in the order of ng m<sup>-3</sup>.

The AMS consists of four main parts (Figure 2.10): an injection system composed of aerodynamic lenses that concentrate the particle beam, a flight chamber that allows the determination of the size distribution, a vaporization and ionization system where the particles are volatilized and transformed into ions, and a detection system (the mass spectrometer) to analyze the chemical composition of particles.

The ambient air is sampled through a critical orifice of 100 μm and focused into a narrow beam through an aerodynamic lens system (where the pressure decreases down to 2 Torr). Due to the limitations of the aerodynamic lens, only particles between ~50 nm and ~1 μm enter the system. At the exit of the lens system, a supersonic expansion accelerates the particles into the flight chamber (at ~10<sup>-5</sup> Torr), where the particle size is determined by measuring the flight time across a fixed distance. The time zero of the particle flight is defined by a mechanical disc, or chopper, which rotates at ~140 Hz and modulates the particle beam letting it through or blocking it, while the end of the particle flight is determined by the mass spectrometric detection. At the end of the flight chamber the particle are vaporized by impaction on a resistively heated surface (~ 600 °C) and ionized by electron ionization at 70 eV.

In addition, the AMS presents two operation modes according to the trajectory of the ions: the low resolution or V-mode and the high resolution or W-mode. The V-mode is the standard mode in which ions follow a trajectory from the extraction into the reflectron and back to the multichannel plate (MCP) detector, with a path length of 1.3 m. In the W-mode the ions are directed from the reflectron to a hard mirror, which focuses them back a second time to the reflectron, before being reflected again, reaching the MCP after a path length of 2.9 m. The mass resolving power increases as the flight path is extended. On the other hand, the lateral broadening of the ions increases over a longer flight path and reduces the total signal as a result of fewer ions impacting the detector. Therefore, the V-mode presents a higher sensitivity but a lower resolution, whereas the W-mode is less sensitive but has a higher mass resolution. The mass spectra obtained from the V-mode allow the speciation of the main inorganic and organic constituents (Allan et al., 2004). The higher mass resolution of the W-mode allows a more in-detail analysis of the mass spectra, allowing to identify the different fragments and to classify them into several chemical families. For a more in-depth description the reader is referred to DeCarlo et al. (2006).

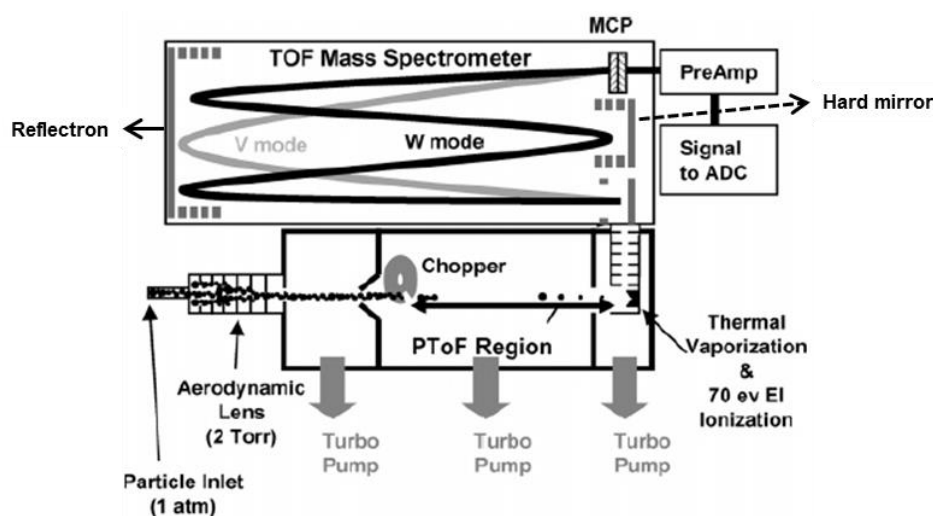


Figure 2.10 HR-ToF-AMS diagram (DeCarlo et al., 2006)

### 2.7.2 Data collection

The collection of the AMS data differs depending on the selected operation mode (V or W). In the W-mode, the data are only collected in the “mass spectrometry” (MS) mode, while in the V-mode the data are collected in the MS mode and “particle time of flight” (PToF) mode (only used in the V-mode due to its higher sensitivity). The difference between the MS and PToF modes is established by the position of the chopper. When the chopper is in

open position the particle beam is transmitted continuously, in closed position the particle beam is completely blocked, and in chopped position, the transmission of the particle beam is modulated. In the PToF mode, the chopped mode is used in order to measure the time of flight of the particles and thus their sizes. In the MS mode, the chopper alternates between the open and closed position every 5 seconds. When it is open, the mass spectrum of the sample (containing the particles and main gases of the ambient air) ranging from 3 to 440 u is recorded. Right after, the chopper closes in order to subtract the background signal of the instrument.

In the intensive campaign carried out in Douai, the time resolution of the AMS was set to 5 minutes, with 3 minutes for the V-mode and 2 minutes for the W-mode, as shown in Figure 2.11. Therefore, with this setting, 6 low-resolution mass spectra for nr-PM<sub>1</sub> aerosols, 6 size distributions and 12 high-resolution mass spectra are averaged every 5 minutes.

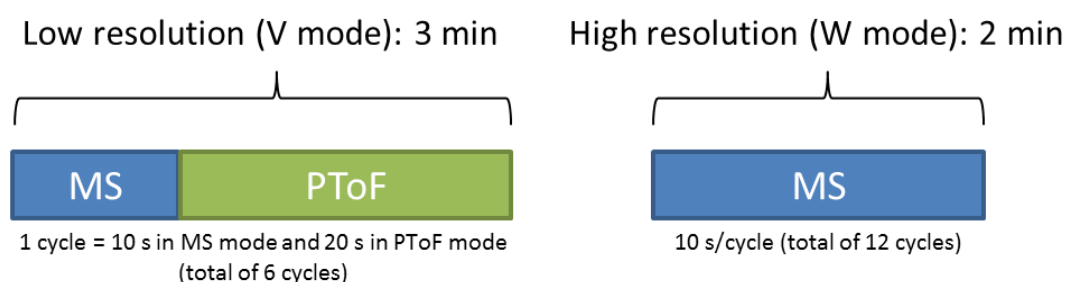


Figure 2.11 Data collection configuration for the campaign carried out in Douai

### 2.7.3 Data analysis

The data collected throughout the different modes of the AMS provide similar or complementary information. The treatment of low resolution data has been done through the IGOR-integrated module SQUIRREL (SeQUential Igor data RetRiEvaL, version 1.60E), while the high resolution data have been treated through another IGOR module known as PIKA (Peak Integration by Key Analysis, version 1.20E).

With the analysis of the MS data obtained in the V-mode, we obtain the mass concentration of major species such as the speciated inorganic ions and the organic compounds. In order to convert the obtained ion signals of a given species  $s$  ( $I_s$ , in counts per second or Hz) detected at specific  $m/z$  ratios into a concentration ( $C_s$  in  $\mu\text{g m}^{-3}$ ) the following formula, developed by Jimenez et al. (2003), is used:

$$C_s = 10^{12} \cdot \frac{MW_s}{IE_s \cdot Q \cdot N_A} \cdot I_s \quad \text{Eq. 2.9}$$

where MW is the molecular weight of the species in g mol<sup>-1</sup>, N<sub>A</sub> the Avogadro number, Q the sampling volumetric flow rate (in cm<sup>3</sup> s<sup>-1</sup>), IE the ionization efficiency, and the 10<sup>12</sup> a factor to convert from g cm<sup>-3</sup> to µg m<sup>-3</sup>. The IE of NO<sub>3</sub><sup>-</sup> (IE<sub>NO3</sub>) is usually experimentally determined through calibrations. For other species, the relative ionization efficiencies (RIE) with respect to NO<sub>3</sub><sup>-</sup> (Eq. 2.10) are used (Canagaratna et al., 2007), allowing the previous equation to be written as shown in Eq. 2.11:

$$\frac{IE_s}{MW_s} = RIE_s \frac{IE_{NO3}}{MW_{NO3}} \quad \text{Eq. 2.10}$$

$$C_s = 10^{12} \cdot \frac{MW_{NO3}}{IE_{NO3} \cdot RIE_s \cdot Q \cdot N_A} \cdot \sum_i I_{s,i} \quad \text{Eq. 2.11}$$

The use of NO<sub>3</sub><sup>-</sup> as the reference compound is justified given that it is a common component of aerosols and produces most of the signal (90%) at only two *m/z* values: *m/z* 30, NO<sup>+</sup>; *m/z* 46, NO<sub>2</sub><sup>+</sup>; it is moreover semi-volatile and hence it is very easily volatilized by the AMS, and it does not leave a significant residue in the background noise of the mass spectrometer (Jayne et al., 2000). However, there is an added difficulty resulting from the process of ionization, where all the species undergo fragmentation, implying that the relative contribution of one species to each fragment needs to be added up in order to get the total concentration of the species. In order to do this, a method for the extraction of mass spectra was developed by Allan et al. (2004). In this method, the contribution of each species to each *m/z* value is given taking into account known isotopic ratios determined in the laboratory for pure species within the use of a so-called “fragmentation table”. Hence, the names of the different non-refractory species analyzed by the AMS (i.e. OM, SO<sub>4</sub>, NO<sub>3</sub>, NH<sub>4</sub>, Cl) correspond to the sum of all the *m/z* fragments related to one given species in the fragmentation table (Allan et al., 2004) and should not be confused with the names of inorganic ions used elsewhere in this manuscript (i.e. SO<sub>4</sub><sup>2-</sup>, NO<sub>3</sub><sup>-</sup>, NH<sub>4</sub><sup>+</sup>, Cl<sup>-</sup>). The fragments used to identify the major chemical species analyzed by the low resolution mode of the AMS are presented in table 2.9. This fragmentation table should be adjusted in each campaign, in order to take into account the exact interferences associated to major gases of the ambient air,

as recommended by the Field Data Analysis Guide edited by the research group of José Jiménez at the University of Colorado in Boulder, USA:

[http://cires1.colorado.edu/jimenez-group/wiki/index.php/Field\\_Data\\_Analysis\\_Guide](http://cires1.colorado.edu/jimenez-group/wiki/index.php/Field_Data_Analysis_Guide)

Table 2.9 Fragments ( $m/z$ ) used for the determination of major chemical species in low resolution mode (from Canagaratna et al., 2007)

Group	Molecule/species	Ion fragments	Fragments ( $m/z$ )
Water	H <sub>2</sub> O $\xrightarrow{e^-}$	<b>H<sub>2</sub>O<sup>+</sup></b> , HO <sup>+</sup> , O <sup>+</sup>	<b>18</b> , 17, 16
Ammonium	NH <sub>3</sub> $\xrightarrow{e^-}$	NH <sub>3</sub> <sup>+</sup> , <b>NH<sub>2</sub><sup>+</sup></b> , NH <sup>+</sup>	17, <b>16</b> , 15
Nitrate	NO <sub>3</sub> $\xrightarrow{e^-}$	HNO <sub>3</sub> <sup>+</sup> , <b>NO<sub>2</sub><sup>+</sup></b> , <b>NO<sup>+</sup></b>	63, <b>46</b> , 30
Sulfate	H <sub>2</sub> SO <sub>4</sub> $\xrightarrow{e^-}$	H <sub>2</sub> SO <sub>4</sub> <sup>+</sup> , HSO <sub>3</sub> <sup>+</sup> , SO <sub>3</sub> <sup>+</sup> , <b>SO<sub>2</sub><sup>+</sup></b> , <b>SO<sup>+</sup></b>	98, 81, 80, <b>64</b> , <b>48</b>
Organic (oxygenated)	C <sub>n</sub> H <sub>m</sub> O <sub>y</sub> $\xrightarrow{e^-}$	H <sub>2</sub> O <sup>+</sup> , CO <sup>+</sup> , <b>CO<sub>2</sub><sup>+</sup></b> , <b>H<sub>3</sub>C<sub>2</sub>O<sup>+</sup></b> , HCO <sub>2</sub> <sup>+</sup> , C <sub>n</sub> H <sub>m</sub> <sup>+</sup>	18, 28, <b>44</b> , <b>43</b> , 45...
Organic (hydrocarbon)	C <sub>n</sub> H <sub>m</sub> $\xrightarrow{e^-}$	C <sub>n</sub> H <sub>m</sub> <sup>+</sup>	27, 29, <b>41</b> , <b>43</b> , <b>55</b> , <b>57</b> , 69, 71...

\* The most abundant fragments are highlighted in bold

In addition, the comparison of the AMS with other co-located instruments has shown that the collection efficiency (CE) of the AMS is inferior to 100%. The CE is defined as the ratio between the mass or the number of particles detected by the AMS and the mass or number of particles that enter the AMS. CE considers the effects of incomplete focusing of the particle beam and bouncing of some particles from the vaporizer (Drewnick et al., 2005). Typically, a default CE value of 0.5 is used (Middlebrook et al., 2012). However, it has been shown that CE is dependent on particle phase, which is influenced by the relative humidity in the sampling line, the acidity/neutralization of the sulfate, ammonium nitrate and organic content (Middlebrook et al., 2012). In this work a Nafion dryer was used in order to reduce the relative humidity in the sampling line. In addition, a composition-dependent CE (CDCE), which recalculates the concentrations of all the chemical species by taking into account the NO<sub>3</sub> fraction of the aerosol, was applied to the AMS data as proposed previously by (Middlebrook et al. 2012). Equation 2.11 presented above is thus further modified in order to include CE (Alfarra et al., 2004):

$$C_s = 10^{12} \cdot \frac{MW_{NO_3}}{CE_s \cdot IE_{NO_3} \cdot RIE_s \cdot Q \cdot N_A} \cdot \sum_i I_{S,i} \quad \text{Eq. 2.12}$$

#### 2.7.4 Calibrations of the AMS

Different types of calibrations need to be performed in order to ensure the proper functioning of the instrument as well as to be able to convert the measured signals in aerosol mass concentrations. A summary of the different calibrations and their frequency performed during the campaign in Douai is presented in Table 2.10.

In the ***m/z* calibration** the goal is to establish a relationship between the time of flight of the ions and their *m/z*. This calibration is based on three peaks of known *m/z* ratios and always present in the instrument ( $\text{N}_2^+$ ,  $\text{O}_2^+$ , and  $\text{W}^+$ ) which comes from the ambient air and the tungsten filament. The identification of the position of the three peaks allows the software to adjust a power fit relating the time of flight and the *m/z* values.

Table 2.10 Summary of the different calibrations and their frequency during the campaign in Douai

Type of calibration	Frequency
<i>m/z</i> calibration	Checked every day in both V and W modes
Flow calibration	At the beginning and at the end of the campaign
Baseline and Single Ion (SI) values	Checked every day
Blank calibration	30 min of filtered air sampled every 3 days in both modes
Ionization efficiency	Once every two weeks
Particle size	At the beginning and at the end of the campaign

The **flow calibration** is required to know the real volume of air entering the system and to be able to correctly calculate the concentration of particles. In order to perform this calibration, a flowmeter is placed in front of an HEPA filter and a critical orifice in order to measure the volume of air that enters the instrument. A valve connected between the flowmeter and the AMS allows adjusting different flows which are measured under standard ambient pressure and temperature conditions (typically 1 atm and 20 °C) and related to the pressure measured inside the aerodynamic lens. The results of the flow calibrations carried out in the campaign of Douai are shown in Figure 2.12. Even though the calibration at the end of the campaign presents less points, both calibrations deliver similar results and a correlation coefficient very close to 1 (0.998) is obtained.



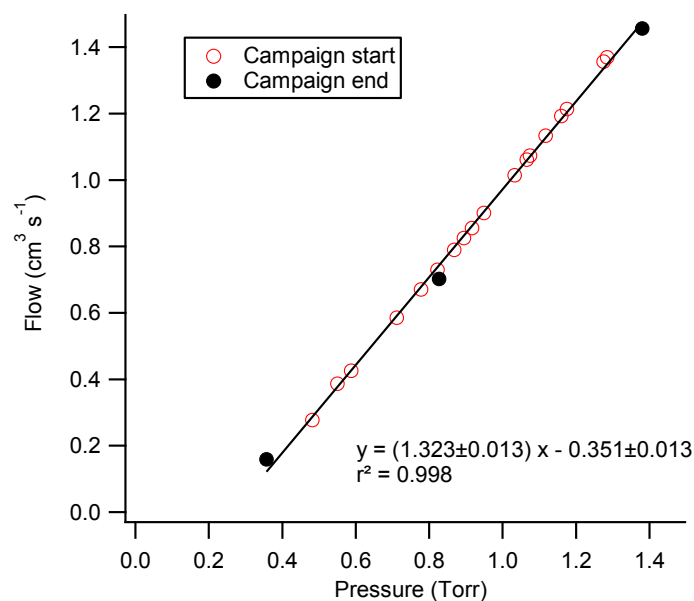


Figure 2.12 Flow calibration curve for the campaign carried out in Douai

The **values of the baseline and the SI** need to be regularly monitored throughout the whole duration of the campaign. The baseline value is defined as the voltage from which all the signals are generated. According to this, a threshold is chosen in order to distinguish the signal of the ions from the background noise. If this threshold is too low, the electronic noise is considered as peaks of ions. On the contrary, if the threshold is too high, the intensity of the real peaks will be underestimated. The value of the SI is generally stable and therefore an average value is usually considered for the duration of a campaign.

The **blank calibration** is done by filtering ambient air during 30 minutes every three days. This allows checking the absence of internal contamination in the AMS.

Different calibrations of the **ionization efficiency** were performed along the field campaign. An aqueous solution of 0.01M  $\text{NH}_4\text{NO}_3$  (Sigma Aldrich, 99.0%) in ultrapure water is used as an aerosol source. The  $\text{NH}_4\text{NO}_3$  particles are generated by an atomizer (TSI 3076) and then dried by passing through a silica gel drier (TSI 3062) in order to eliminate water. A dilution system composed of a system of valves and a HEPA filter is used in order to vary the concentration of particles. An electrostatic classifier (TSI 3080) containing a radioactive source of Kr-85 (TSI 3077A) and a Differential Mobility Analyzer (DMA, TSI 3081) are used to select particles with an electrical mobility diameter of 300 nm. The radioactive source is creates a bipolar and stable distribution of the number of particle charges therefore minimizing multiply-charged particles. The particles enter simultaneously the Condensation Particle Counter (CPC, TSI 3788) and the AMS. The size of the particles (set by the

classifier) and their number concentration (measured by the CPC) allows to derive their mass concentration:

$$[NO_3]_{CPC} = N_{CPC} S V_{part} \rho \frac{MW_{NO_3}}{MW_{NH_4NO_3}} \quad \text{Eq. 2.13}$$

where  $[NO_3]_{CPC}$  is the mass concentration of particles in  $\mu\text{g m}^{-3}$ ,  $S$  the shape factor (0.8 for  $NH_4NO_3$ ),  $V_{part}$  the volume of the particle in  $\text{cm}^3$ ,  $\rho$  the volumetric mass of the particles ( $1.72 \text{ g cm}^{-3}$  for  $NH_4NO_3$ ) and  $MW_i$  the molar mass of the species  $i$ .

The value of  $IE_{NO_3}$  can then be calculated from these calibrations by using the next equation:

$$IE_{NO_3} = \frac{[NO_3]_{AMS}}{[NO_3]_{CPC}} \cdot \frac{AB_{acq,i}}{AB_{meas,i}} \cdot IE_{default} \quad \text{Eq. 2.14}$$

where  $IE_{default}$  is the IE default value used in the acquisition software ( $10^{-7}$  in V-mode and  $5 \times 10^{-8}$  in W-mode),  $AB_{acq}$  and  $AB_{meas}$  are the intensities of the air beam at  $m/z$  28 ( $N_2^+$  signal) during the calibration and the sampling of ambient air, respectively, which allows to normalize the IE value. Several parameters might vary through the duration of a field campaign, such as the filament and the tuning of the voltages, altering the sensitivity of the instrument. This can be corrected by the use of the IE value under the assumption that the quantity of  $N_2$  in every sample is constant.

The relative efficiency of other species can also be calculated, either through the  $NH_4NO_3$  solution in the case of  $NH_4$  or through the use of ammonium sulfate and ammonium chloride solutions for the determination of  $RIE_{SO_4}$  and  $RIE_{Cl}$ , respectively. During the campaign, we performed these additional calibrations using solutions of 0.01 M  $(NH_4)_2SO_4$  (Sigma Aldrich, 99%) and 0.01 M  $NH_4Cl$  (Sigma Aldrich, 99.5%).

Finally, the calibration of the **particle size** was done to be able to convert the velocity of particles of a given size, obtained by the PToF measurements, to aerodynamic diameters ( $D_{va}$ ). The next equation relates the speed of the particles and their size:

$$v = \frac{l}{t} = v_{lens} + \frac{v_{gas} - v_{lens}}{1 + \left(\frac{D_{va}}{D^*}\right)^b} \quad \text{Eq. 2.15}$$

where  $l$  is the length of flight (0.295 m),  $t$  the time of flight in  $\mu\text{s}$ ,  $V_{\text{lens}}$  the speed of gas in the lens in  $\text{m s}^{-1}$ ,  $D_{\text{va}}$  the aerodynamic diameter of the  $\text{NH}_4\text{NO}_3$  particles in nm,  $D^*$  an empirical parameter in nm, and  $b$  an adimensional empirical parameter.

In the particle size calibration, particles of  $\text{NH}_4\text{NO}_3$  (same solution as for the IE calibration) with different  $D_{\text{va}}$  ranging approximately from 70 to 600 nm are generated with the same procedure as followed in the IE calibration. In this case, the signal of  $\text{NO}_2^+$  ( $m/z$  46) is followed in order to determinate the time of flight in the instrument. In Figure 2.13, the velocity of the  $\text{NH}_4\text{NO}_3$  particles relative to their aerodynamic diameter is plotted and fitted in order to obtain the parameters needed in Eq. 2.15.

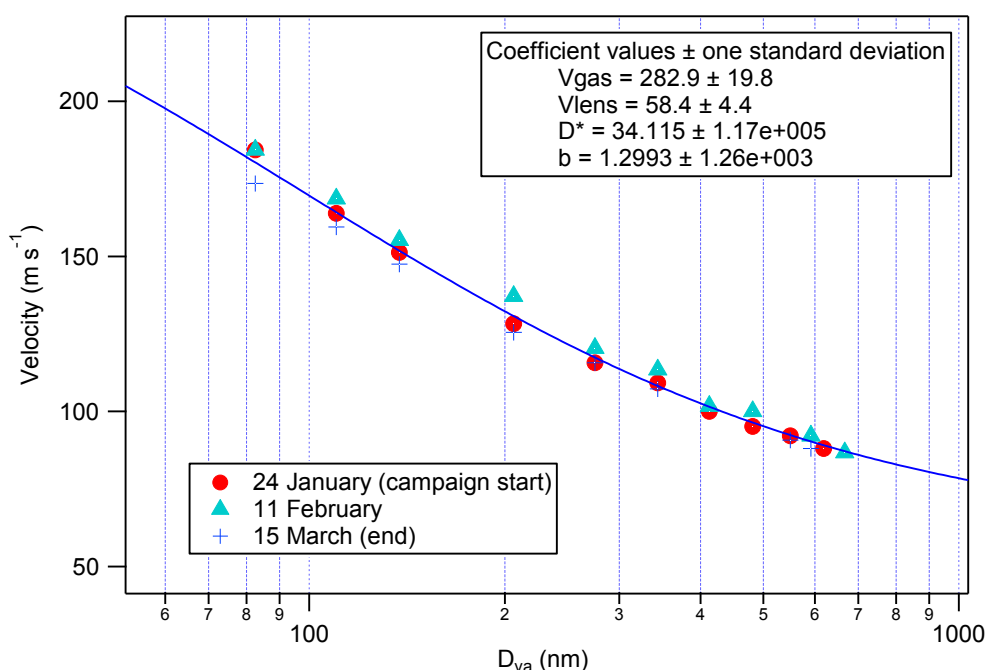


Figure 2.13 Velocity of the particle relative to the aerodynamic diameter

## 2.8 Scanning Mobility Particle Sizer (SMPS)

A SMPS+C (Grimm) was set up to study the size distribution of submicron aerosols as well as their number concentration. It consists of a Condensation Particle Counter (CPC model 5.403) coupled to a Differential Mobility Analyzer (DMA “Vienna type”), also known as a particle classifier (Figure 2.14).

The DMA classifies a poly-disperse aerosol into multiple mono-dispersed size-bins. The air sample first passes through a pre-impactor, to determine the particle cut-off diameter, and a radioactive charger in order to charge the particles with a defined charge distribution. Then the particles are separated according to their mobility in an electric field. Thereby, only

particles with appropriate size and charge will exit the DMA column in order to enter the CPC as mono-dispersed aerosol. In the Vienna-type column, particles are separated into 44 size bins from 11.1 to 1083.3 nm.

In the CPC, the monodispersed particles are counted by passing through a laser beam. However, if the particles are smaller than the laser beam wavelength, the particle counter does not detect them. Therefore, the size of the particles is increased to several microns by a condensation process in order to become observable. In the CPC 5.403, the particles first enter a chamber at 35 °C saturated with butanol vapor and then travel together with the alcohol vapors to a condensation chamber (at 10 °C), where butanol condensates around the particulate matter increasing their size up to 10 µm. The number concentration in particles counted by the CPC goes up to  $10^7$  particles L<sup>-1</sup>, with particle concentration accuracy of 5%.

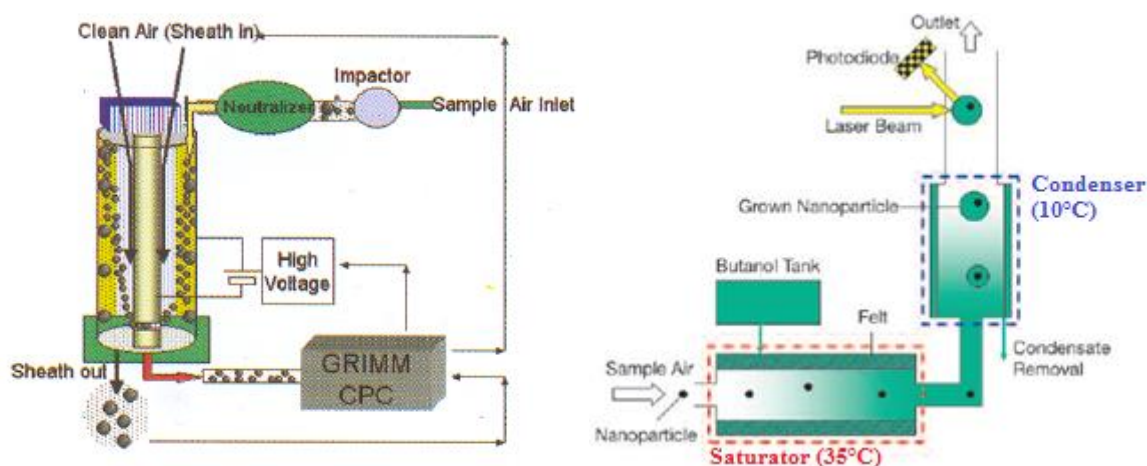


Figure 2.14 Schematics of the DMA (left) and the CPC (right)

The output of the SPMS+C is a data set of different matrices accounting for different parameters: 1) raw particle counts, 2) number size distribution, 3) mass distribution, 4) surface area distribution and 5) volume distribution, with a time resolution of 6 minutes. The data have been processed with IGOR Pro v.6.37 for the creation of particle number size distributions (PNSD) in order to identify new particle formation events (NPFs) typically associated to a pronounced “banana pattern” (Heintzenberg et al., 2007).

## 2.9 Calculation of uncertainties

### 2.9.1 MARGA

The analysis of aerosols and gases by the MARGA is subject to different types of uncertainties. These are summarized in the fishbone diagram presented in Figure 2.15, and are mainly associated to the loss along the sampling line, the sampling volume, the accuracy and precision of the IC analysis and the contamination.

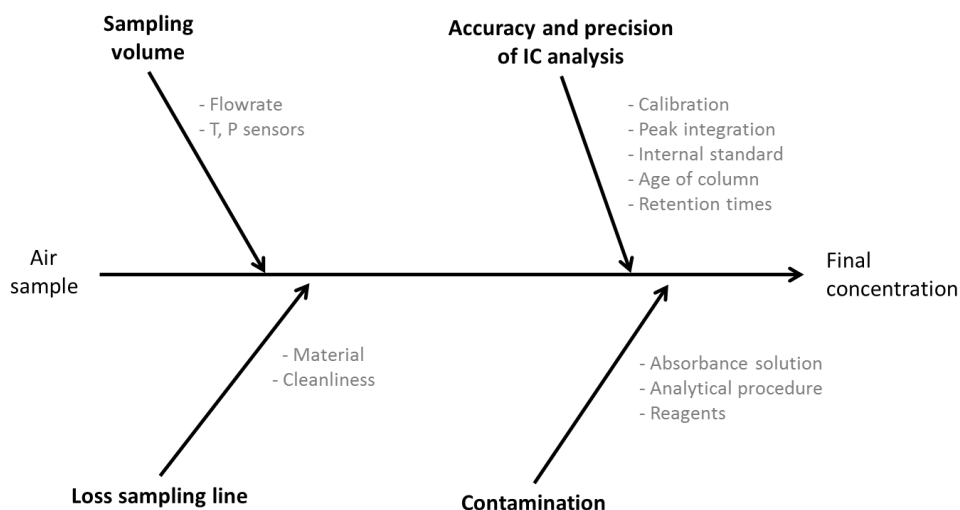


Figure 2.15 Fishbone diagram of the main sources of uncertainty in the analysis of aerosols and gases by the MARGA

Different methodologies can be found in the literature for the calculation of uncertainties of IC-based analytical procedures. Among them, the methodology proposed by Gianini *et al.* (2012) has been widely used for the calculation of uncertainties of filter sampling and subsequent analysis by IC, by explicitly taking into account the systematic contamination (through the DL) and the repeatability (through the coefficient of variation, CV), as is shown in equation 2.16:

$$u_{ij} = \sqrt{(DL)^2 + (CV_j x_{ij})^2 + (ax_{ij})^2} \quad \text{Eq. 2.16}$$

where DL is the detection limit of the compound  $j$  (in  $\mu\text{g m}^{-3}$ ), calculated as three times the standard deviation of the blanks;  $x$  is the concentration of the compound  $i$  at the time  $j$ ;  $CV_{ij}$  is the coefficient of variation of the compound  $j$  (relative uncertainty), calculated as the standard deviation of repeated analyses divided by the average value of the repeated

analyses; and  $a$  is a factor that equals 0.03 (relative uncertainty) and is applied to account for additional sources of uncertainties. The coefficient of variation was calculated from the repeated analysis of the Anion (respectively Cation) Calibration Standard for MARGA (Sigma Aldrich) with 0.25 mg L<sup>-1</sup> of Br<sup>-</sup>, Cl<sup>-</sup>, SO<sub>4</sub><sup>2-</sup>, NO<sub>3</sub><sup>-</sup>, and NO<sub>2</sub><sup>-</sup> (respectively Li<sup>+</sup>, K<sup>+</sup>, Mg<sup>2+</sup>, Ca<sup>2+</sup>, Na<sup>+</sup> and NH<sub>4</sub><sup>+</sup>).

In our work the methodology proposed by Gianini *et al.* (2012) was slightly modified in order to include two additional sources of relative uncertainty: the volume and the loss in the sampling line, resulting in equation 2.17:

$$u_{ij} = \sqrt{\underbrace{(DL_j)^2}_{\text{Detection limit}} + \underbrace{(CV_j x_{ij})^2}_{\text{Repeatability}} + \underbrace{(u_{r,vol} x_{ij})^2}_{\text{Volume}} + \underbrace{(u_{r,loss} x_{ij})^2}_{\text{Loss}} + \underbrace{(a x_{ij})^2}_{\text{Additional unc.}}} \quad \text{Eq.2.17}$$

where  $u_{vol}$  is the uncertainty related to the variation of the volume and  $u_{loss}$  is the uncertainty related to the loss along the sampling line.

The loss in the sampling line was calculated with the Particle Loss Calculator extension for Igor Pro (von der Weiden *et al.*, 2009), considering a tube length of 2.5 m, a tube diameter of 1/2 inch and a flow rate of 1 m<sup>3</sup> h<sup>-1</sup>. It was found to be less than 5% whatever the particle diameter between 10 nm and 5 µm, and therefore was set to be 5%. The uncertainty of the sampling volume was determined to be 2% from the allowed deviation of the sampling flow of the MARGA (1.00 ± 0.02 m<sup>3</sup> h<sup>-1</sup>).

### 2.9.2 Filter sampling and ICP-MS analysis of trace and major elements

The uncertainties associated to the elements analyzed by the ICP-MS instrument are calculated following the methodology of Alleman *et al.* (2010), developed in the PhD thesis of Lamaison (2006). The diagram of Figure 2.16 presents the main uncertainties in the procedure of sampling and analysis of metals in ambient air:

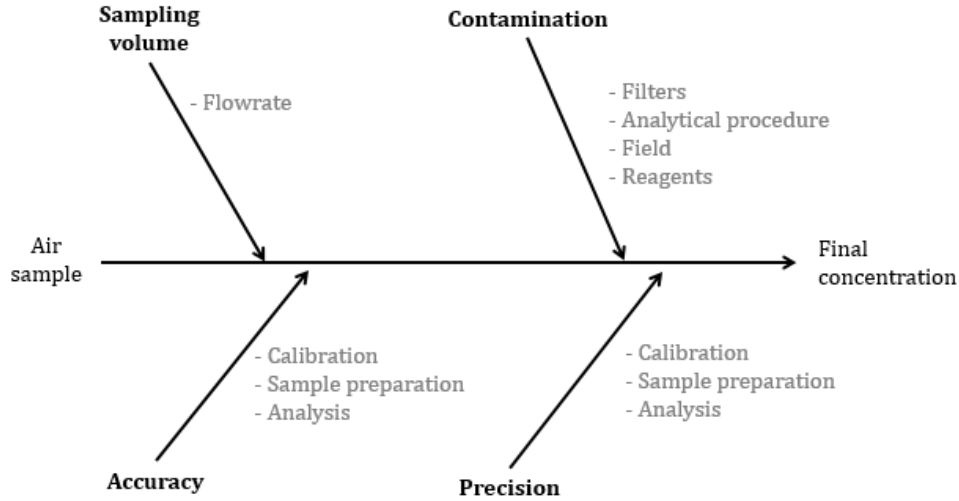


Figure 2.16 Fishbone diagram of sources of uncertainty for metals  
(adapted from Lamaison, 2006)

Following the diagram, the final uncertainty has been calculated according to the next equation:

$$u(C_j) = C_j \sqrt{\underbrace{\left(u_{r,SRM}^2 + \frac{s_{r,bias}^2}{n_{bias}}\right)}_{\text{Accuracy}} + \underbrace{\frac{s_{r,rep(QC)}^2}{n_{rep(QC)}}}_{\text{Repeatability}} + \underbrace{u_r^2(V)}_{\text{Volume}} + \underbrace{\frac{u_{r,cont}^2}{C_j^2}}_{\text{Contamination}}} \quad \text{Eq.2.18}$$

In the calculation, a total of four sources of uncertainty are taken into account:

- (1) The uncertainty related to the **accuracy** of the analysis has been estimated from: (a) the analysis of standard reference materials (SRM): NIST 1648 (urban particulate matter) which contains Al, As, Br, Ca, Ce, Cl, Co, Cr, Cu, Fe, K, Mg, Mn, Na, Ni, Pb, Rb, S, Sb, Sr, Ti, V and Zn, and NIST 2584 (trace elements in indoor dust) which contains Al, As, Ca, Cd, Cr, Fe, Hg, K, La, Mg, Na, P, Pb, Ti, Zn; (b) the bias obtained from the analysis of a number of  $n$  replicates.
- (2) The **repeatability** of the analysis has been calculated through the internal standard analysis ( $^{69}\text{Ga}$  and  $^{107}\text{Rh}$ ) and analysis of QC (Quality control) SCP33MS (PlasmaCal) composed of 33 elements, on a number of  $n$  replicates.
- (3) The uncertainty associated to the **volume of sampling** has been calculated from the allowed drift (5%) relative to the flowrate of the PARTISOL airpump ( $10 \text{ L min}^{-1}$ ).
- (4) The uncertainty related to a **possible contamination** has been calculated from the analysis of several field blanks.

## 2.10 Ratios for the analysis of the aerosol acidity and the oxidation of nitrogen and sulfur

The acidity of the aerosol has been studied in the literature through the use of the ionic balance (IB) and/or the neutralization ratio (NR) ratios (Bencs et al., 2008; Makkonen et al., 2012; Squizzato et al., 2013; Twigg et al., 2015; Stieger et al., 2017). Similarly, many studies have also applied the nitrogen oxidation ratio (NOR) and sulfur oxidation ratio (SOR) in order to characterize the degree of ageing of the aerosol (e.g. Khoder, 2002; Bencs et al., 2008; Behera and Sharma, 2010; Shon et al., 2013; Masiol et al., 2015).

IB is here defined as the sum of anions minus the sums of cations in molar concentrations according to equation 2.19:

$$IB = \left( \frac{[NO_3^-]}{62} + \frac{2[SO_4^{2-}]}{96} + \frac{[Cl^-]}{35.5} \right) - \left( \frac{[NH_4^+]}{18} + \frac{[Na^+]}{23} + \frac{[K^+]}{39} + \frac{2[Ca^{2+}]}{40} + \frac{2[Mg^{2+}]}{24.3} \right)$$

Eq. 2.19

where each species concentration is expressed in  $\mu\text{g m}^{-3}$  and the numbers refer to the molar mass in  $\text{g mol}^{-1}$ . A positive IB means that there is an excess of analyzed anions compared to the analyzed cations, which may be related to an acidic aerosol containing a significant amount of  $\text{H}^+$ ; an IB close to zero indicates that the aerosol is neutral, whereas a negative IB points out a lack of analyzed anions compared to the analyzed cations. This may be due to a significant contribution of organic anions, such as oxalate ( $\text{C}_2\text{O}_4^{2-}$ ).

The IB is also useful to check the quality of the MARGA measurements because a too high value of IB may originate from an error in the IC measurements (due to an error in the retention time, an error in the peak integration, etc.).

The neutralization ratio (NR) was used to assess the neutralization degree of the aerosol. It is calculated as follows:

$$NR = \frac{[NH_4^+]}{[nss-SO_4^{2-}] + [NO_3^-]}$$

Eq. 2.20

where concentrations are given in  $\text{mol m}^{-3}$ .

The NR is based on the assumption that most particulate nitrate and non-sea salt-sulfate in the fine particles ( $\text{PM}_{2.5}$ ) are neutralized by particulate ammonium in the form of  $\text{NH}_4\text{NO}_3$  and  $(\text{NH}_4)_2\text{SO}_4$ . Therefore  $\text{NR} > 1$  means that there is an excess of particulate



ammonium which may indicate the presence of other ammonium-based salts involving different anions (e.g.  $\text{NH}_4\text{Cl}$ ). NR close to 1 means that the neutralization assumption is confirmed. And  $\text{NR} < 1$  means that there is a lack of ammonium; other cations might be involved in the neutralization of the nitrate and sulfate anions, such as protons  $\text{H}^+$  (forming  $\text{NH}_4\text{HSO}_4$ ) or sodium  $\text{Na}^+$  (forming  $\text{NaNO}_3$ ).

The nitrogen oxidation ratio (NOR) has been calculated in order to assess the degree of conversion of  $\text{NO}_2$  (reduced nitrogen +IV) to  $\text{NO}_3^-$  (oxidized nitrogen +V) in the ambient air, as shown in Eq. 2.21:

$$\text{NOR} = \frac{[\text{NO}_3^-]}{[\text{NO}_3^-] + [\text{NO}_2]} \quad \text{Eq. 2.21}$$

where concentrations are expressed in  $\text{mol m}^{-3}$

High NOR values usually suggest a high conversion of  $\text{NO}_2$  to particulate  $\text{NO}_3^-$ . This may indicate either that the  $\text{NO}_x$  precursors originate from distant sources and that the nitrogen conversion has taken place during the transport of the air mass to the measurement site and/or that the rate of nitrogen oxidation is high.

A wide range of NOR values has been reported in the literature. Low values, ranging from 0.01 to 0.10 have been associated to a low conversion of  $\text{NO}_2$  to particulate  $\text{NO}_3^-$  (Wang et al., 2005; Bencs et al., 2008; Squizzato et al., 2013; Percorari et al., 2014; Masiol et al., 2015). On the contrary, high values, ranging from 0.1 to 0.8 have also been reported and were associated to an intense formation of particulate  $\text{NO}_3^-$  (Du et al., 2011, Khezri et al., 2013; Percorari et al., 2014).

The sulfur oxidation ratio (SOR) is another frequently used ratio used to quantify the oxidation of  $\text{SO}_2$  (reduced sulfur +IV) to  $\text{SO}_4^{2-}$  (oxidized sulfur +VI) in ambient air, and is obtained through Eq. 2.22:

$$\text{SOR} = \frac{[\text{nss-SO}_4^{2-}]}{[\text{nss-SO}_4^{2-}] + [\text{SO}_2]} \quad \text{Eq. 2.22}$$

where concentrations are expressed in  $\text{mol m}^{-3}$  and  $\text{nss-SO}_4^{2-}$  stands for non-sea salt sulfate. Some studies have reported SOR values below 0.10 under the predominance of

primary emissions (Pierson *et al.*, 1979; Truex *et al.*, 1980), while values above 0.10 have been suggested to take place under high sulfate formation conditions. (Ohta and Okita, 1990).

## 2.11 Source apportionment

### 2.11.1 Application of PMF to hourly to daily-resolved data of inorganic compounds

To apportion the dataset composed of inorganic ions, metals and black carbon collected with the MARGA, the PARTISOL and the Aethalometer, respectively, we used the stand-alone version of PMF v.5.1 developed by the United States Environmental Protection Agency (US EPA). The PMF model has been explained in detail in Chapter 1 of this manuscript. The EPA PMF software requires two input matrices: (i) the concentrations of each species for each sample and (ii) the uncertainties associated with each concentration. These input matrices were obtained following the general guidelines by Polissar *et al.* (1998). The data points below the detection limit (DL) were replaced by DL/2, and an uncertainty corresponding to 5/6 DL was associated to these values. In addition multiple imputation was used in order to estimate some missing values. This methodology gives estimations for missing values based on statistical relationships (such as linear correlations) between different chemical species and has already been used in previous studies (Mooibroek *et al.* 2011 and references therein). In this work, the uncertainties were multiplied by a factor of 4. For the rest of the data, the calculation of the uncertainties is addressed in section 2.9.

An additional uncertainty can be attributed directly in the software to each species, depending on its signal-to-noise ratio (SNR). According to the SNR, the different chemical species are classified as strong ( $\text{SNR} > 2$ ), weak ( $2 \geq \text{SNR} \geq 0.2$ ) or bad variables ( $\text{SNR} < 0.2$ ). The uncertainty of a strong variable does not change and that of a weak variable is multiplied by 3, while the variables classified as bad are not considered anymore. In addition, the total PM mass is generally defined as the “total variable” of the dataset (i.e. the sum of all the analyzed species), and is automatically categorized as a weak variable in order to decrease its influence.

The quality and robustness of the PMF solution might be evaluated by different methods including the analysis of the  $Q_{\text{true}}/Q_{\text{exp}}$  ratio, the residuals, the comparison of the measured and modelled concentrations, the rotation of the Q function with  $f_{\text{peak}}$ , and the comparison of the results with external variables, as explained in section 1.4.2 of Chapter 1.

In addition, the EPA PMF software presents an additional valuable tool for this purpose known as the bootstrap methodology.

The bootstrap method was developed by Efron (1979) in order to estimate the sampling distribution of a pre-specified random variable on the basis of the observed data. The general idea behind this methodology is to re-distribute the data in order to create replicates of the initial dataset, the variability of which will be evaluated. When applied to the PMF analysis, the bootstrap allows estimating the stability and the uncertainties of the obtained results, and also helps in the determination of the final number of factors. In this work, an approach combining all the precedent methodologies for the evaluation of the PMF solution was taken.

The PMF analysis was applied to two databases composed of different sets of variables with different time resolutions, giving place to two types of PMF which will be considered differently from this point.

- An **hourly-resolved PMF (PMF<sub>h</sub>)** composed of the data of the MARGA and the Aethalometer was studied in order to: (i) explore the possibilities of associating a MARGA and a 2-wavelength Aethalometer as a sufficient tool for source identification; (ii) take advantage of the high time resolution of the MARGA and the Aethalometer to observe the daily evolution of source contributions.
- A **daily-resolved PMF (PMF<sub>d</sub>)** including the 24-h averaged data of the MARGA and Aethalometer and the elemental data from ICP-MS analyses was carried out in order to see if additional sources could be identified by the addition of supplementary information about trace and major elements, with the drawback of degrading the time resolution.

In the application of the PMF analysis for both datasets, the following technical parameters were taken into account:

- 100 simulations were run in order to ensure the quality and robustness of the final solution;
- The start of each run was determined arbitrarily (random seed);
- Different numbers of factors have been tried, ranging from 3 to 7 factors for the PMF<sub>h</sub> and from 3 to 12 factors for the PMF<sub>d</sub>;
- The final solution has been validated by the application of the bootstrap method with a total of 100 simulations with a minimum correlation coefficient of  $r = 0.6$ .

### 2.11.2 Application of PMF to mass spectrometry data of organic compounds

For the source apportionment of the mass spectra obtained with the AMS, the PMF Evaluation Tool (PET v. 2.08) integrated in IGOR Pro was used (Ulbrich et al., 2009). Both datasets obtained from SQUIRREL (unit mass resolution) and PIKA (high resolution) were tried in the source apportionment analysis. It is important to note that only the organic fraction of the analyzed aerosol is apportioned in this methodology, while the inorganic ions might be used as external variables to evaluate the validity of the obtained solution.

The matrix  $X$  or  $x_{ij}$  is composed of the time series of the organic mass spectra, where  $i$  is the time and  $j$  the  $m/z$  ratios (in V-mode) or the observed fragments (in W-mode). The matrices  $G$  or  $g_{ij}$  and  $F$  or  $f_{ij}$  represent the time series of the concentrations ( $ts_i$ ) and the mass spectra ( $ms_i$ ) of each factor  $k$ , respectively, and the matrix  $E$  the residues. A scheme of the deconvolution of the organic matrix  $X$  is shown in Figure 2.17.

PET requires as inputs two 2-D matrices of the same exact dimensions: one corresponds to the concentrations of the organic  $m/z$  values or fragments for the different times, while the other matrix corresponds to the uncertainties of the measurements (for each  $m/z$  value or fragment).

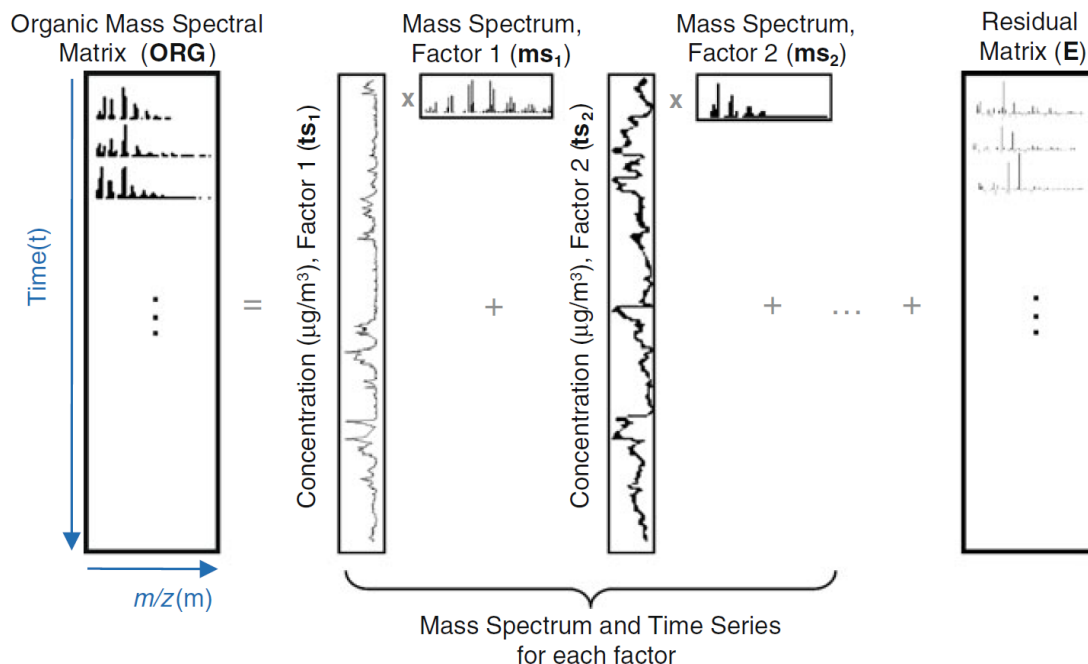


Figure 2.17 Scheme of the deconvolution of the organic matrix  $X$  into two different factors and a residual matrix (Zhang et al., 2011)

Some important steps need to be performed before running the PMF analysis. These include the elimination of missing or zero values, the calculation of a signal-to-noise ratio

(SNR), the down-weighting or elimination of weak and bad  $m/z$  or fragments, as well as  $m/z$  or fragments related to the  $m/z$  16,17,18, 28, 44 for UMR data or O, HO, H<sub>2</sub>O, CO, CO<sub>2</sub> for HR data. Weak fragments (SNR < 2) are down-weighted by a factor of 2, while bad fragments (SNR < 0.2) are not considered.

Similarly to what has been explained in section 2.11.1, the choice of the optimal number of source factors and the quality and robustness of this choice is assessed by several parameters. These include the variation of the  $Q_{\text{true}}/Q_{\text{exp}}$  ratio, the analysis of the residuals, the rotation of the  $Q$  function with  $f_{\text{peak}}$ , the meaningfulness of each source factor by comparing them with similar factors found in the literature and with specific tracers and external variables, as well as the analysis of the temporality of each source factor.

## 2.12 Geographical determination of sources

The possible geographical origin of the pollution sources found in Douai has been assessed through the application of different complementary methodologies including the non-parametric wind regression (NWR) for the distinction between local and regional sources, and the potential source contribution function (PSCF) for the identification of distant source areas. Both methodologies have been applied to individual particulate and gaseous pollutants, as well as to the source factors obtained in the final solutions of the PMF analyses.

### 2.12.1 Local sources

The non-parametric wind regression (NWR) is a hybrid source-receptor model which locates and quantifies sources of a pollutant based on local wind speed ( $u$ ) and direction ( $\theta$ ) (Henry *et al.*, 2009):

$$E(C|\theta, u) = \frac{\sum_{i=1}^N K_1\left(\frac{\theta - W_i}{\sigma}\right) \cdot K_2\left(\frac{u - U_i}{h}\right) \cdot C_i}{\sum_{i=1}^N K_1\left(\frac{\theta - W_i}{\sigma}\right) \cdot K_2\left(\frac{u - U_i}{h}\right)} \quad \text{Eq. 2.23}$$

where  $E$  is the concentration estimate at a wind direction  $\theta$  and wind speed  $u$ ;  $W_i$ ,  $U_i$  and  $C_i$  the wind direction and speed, and atmospheric concentrations, respectively, measured at  $t_i$ ;  $\sigma$  and  $h$  smoothing factors (which were suggested for each species by the software used); and  $K_1$  and  $K_2$  two kernel functions, defined as follows:

$$K_1(x) = \frac{1}{\sqrt{2\pi}} \cdot e^{-0.5 \cdot x^2}, -\infty < x < \infty \quad \text{Eq. 2.24}$$

$$K_2(x) = 0.75 \cdot (1 - x^2), -1 < x < 1 = 0 \quad \text{Eq. 2.25}$$

In order to apportion the weighted concentrations obtained from Eq. 2.23 to source areas, these results have to be weighted by the frequency of the winds. Hence, an empirical joint probability density of wind speed and direction is calculated using the kernel density estimate, as shown in Eq. 2.26:

$$f(\theta, u) = \frac{1}{N\sigma h} \cdot \sum_{i=1}^N K_1\left(\frac{\theta - W_i}{\sigma}\right) K_2\left(\frac{u - U_i}{h}\right) \quad \text{Eq. 2.26}$$

where  $N$  is the total number of points.

Finally, an estimation of the fraction of the weighted pollutant concentration  $E$  associated with wind speed  $u$  in the closed interval  $U = [u_1; u_2]$  and wind direction  $\theta$  in the interval  $\Theta = [\theta_1; \theta_2]$  is obtained by multiplying  $f(\theta, u)$  and  $E(C|\theta, u)$  and integrating over the belonging ranges of wind speed  $u$  and direction  $\theta$  as is shown in Eq. 2.27.:

$$S(\Theta, U) = \int_{u_1}^{u_2} \int_{\theta_1}^{\theta_2} f(\theta, u) E(C|\theta, u) d\theta du \quad \text{Eq. 2.27}$$

where  $S(\Theta, U)$  is the average value of a specific pollutant concentration associated with winds from the sector defined by the intervals  $U$  and  $\Theta$ .

NWR has already been successfully applied in a number of studies to different atmospheric pollutants and pollution sources (Yu et al. 2004; Pancras et al. 2011; Olson et al. 2012; Petit et al. 2017). In this thesis NWR was calculated using the Zefir v3.31 IGOR tool (Petit et al., 2017).

## 2.12.2 Distant sources

### 2.12.2.1 Calculation of back-trajectories

Back-trajectories were calculated with HYSPLIT 4 (HYbrid Single-Particle Lagrangian Integrated Trajectory) (Stein et al., 2015) for an arrival height of half the mixing layer, at a 3-h interval (8 trajectories per day at 0, 3, 6, 9, 12, 15, 18, 21 UTC), 72 h back in time. Therefore each trajectory has  $72/3 = 24$  endpoints. The obtained back-trajectories were

used for the determination of distant sources by using the PSCF method. In addition, a cluster study of the back-trajectories was also performed, in order to obtain further information on the potential geographical origins of the pollutants. Finally, individual trajectories were also evaluated during specific events such as high pollution episodes to better assess their nature.

#### 2.12.2.2 Positive Source Contribution Function (PSCF)

Potential source contribution function (PSCF) was applied using Zefir v3.31 in order to determine the most probable regions of emissions for the gaseous and particulate species. PSCF is calculated by the following equation:

$$PSCF = \frac{m_{ij}}{n_{ij}} \quad \text{Eq. 2.28}$$

where  $m_{ij}$  is the number of endpoints belonging to trajectories which both cross the  $ij^{\text{th}}$  cell (with latitude  $i$  and longitude  $j$ ) and are associated to concentrations exceeding a specific threshold, and  $n_{ij}$  the total number of endpoints belonging to trajectories falling into the  $ij^{\text{th}}$  cell. High values of PSCF generally indicate high probabilities that the  $ij^{\text{th}}$  cell represents a source location. In this study the 75<sup>th</sup> percentile of the concentrations of a species or of the contributions of a source factor was used as a threshold.

The Zefir tool allows the inclusion of additional thresholds for other parameters such as precipitation and altitude. The precipitation threshold permits accounting for wet deposition, assuming that whenever precipitation has taken place ( $>1 \text{ mm h}^{-1}$ ), the air parcel would be cleaned (i.e.  $PSCF=0$ ) and that each of the preceding cells would also present a zero value. Similarly, the altitude threshold allows setting a limit of height for the planetary boundary layer, above which the air parcel is diluted in the free troposphere ( $PSCF = 0$ ). In this work, thresholds of  $1 \text{ mm h}^{-1}$  for rain and 1500 m for altitude were set for all PSCF calculations.

In addition, in order to reduce the influence of back-trajectories with low  $n_{ij}$  (passing only a few times through the  $ij^{\text{th}}$  cell) a weighting function is applied. Two types of weighting functions can be used: discrete or sigmoidal functions. In discrete functions, the average of  $n$  is used, and fixed user-defined coefficients are set over user-defined ranges of  $n$  (or  $\log(n+1)$ ), as shown in equation 2.29, where the values that can be modified by the user are highlighted in bold:

$$W = \left\{ \begin{array}{l} 1 \text{ for } \log(n+1) \geq 0.85 \cdot \max_{\log(n+1)} \\ 0.725 \text{ for } 0.6 \cdot \max_{\log(n+1)} \leq \log(n+1) < 0.85 \cdot \max_{\log(n+1)} \\ 0.475 \text{ for } 0.35 \cdot \max_{\log(n+1)} \leq \log(n+1) < 0.6 \cdot \max_{\log(n+1)} \\ 0.175 \text{ for } \log(n+1) < 0.35 \cdot \max_{\log(n+1)} \end{array} \right\} \quad \text{Eq. 2.29}$$

On the other hand, the sigmoidal function presents a similar shape to that of the discrete function, but is continuous and has less parameters to be controlled. The sigmoidal function used in Zefir is described in equation 2.30:

$$W = \frac{1}{(1+c) \cdot (1+e^{-a \cdot (x-b)})} + \frac{c}{1+c} \quad \text{Eq. 2.30}$$

In this work, the sigmoidal function was applied in all the PSCF analyses, with  $a = 10$ ,  $b = 0.5$  and  $c = 0$ .

### 2.13 Thermodynamic partitioning analysis: ISORROPIA II

The predicted thermodynamics of the  $\text{K}^+$ - $\text{Ca}^{2+}$ - $\text{Mg}^{2+}$ - $\text{NH}_4^+$ - $\text{SO}_4^{2-}$ - $\text{NO}_3^-$ - $\text{Cl}^-$ - $\text{H}_2\text{O}$  aerosol system have been calculated by the use of the thermodynamic equilibrium model ISORROPIA II (Fountoukis and Nenes, 2007). ISORROPIA II performs the calculation of the composition and phase state of the inorganic aerosol system in thermodynamic equilibrium with the gas phase precursors. ISORROPIA II can be applied in two different ways:

- A forward or “closed system” in which the input consists of the temperature, relative humidity and the total (gas+aerosol) concentrations of  $\text{NH}_3$ ,  $\text{H}_2\text{SO}_4$ ,  $\text{Na}^+$ ,  $\text{Ca}^{2+}$ ,  $\text{K}^+$ ,  $\text{Mg}^{2+}$ ,  $\text{HCl}$ , and  $\text{HNO}_3$ .
- A reverse or “open system” in which the input consists of the temperature, relative humidity and the aerosol phase concentrations of eq- $\text{NH}_3$ , eq- $\text{H}_2\text{SO}_4$ ,  $\text{Na}^+$ ,  $\text{Ca}^{2+}$ ,  $\text{K}^+$ ,  $\text{Mg}^{2+}$ , eq- $\text{HCl}$ , and eq- $\text{HNO}_3$  (where “eq-” stands for equivalent concentrations).

In addition, in both cases the aerosol can be either in a thermodynamically stable state, where salts precipitate once the aqueous phase becomes saturated, or in a metastable state, where the aerosol is only composed of a supersaturated aqueous phase. The mutual deliquescence relative humidity (MDRH) is the characteristic RH for which all salts are simultaneously saturated with respect to the other components (Wexler and Seinfeld, 1991). In general, when the RH of an aerosol mixture is below the MDRH, the particles will be solid given that the aerosol follows the deliquescence branch. However, when the RH of a wet aerosol mixture is



decreasing, the wet aerosol might not crystallize below the MDRH and instead it can remain solid, in a so-called metastable state.

In this work, due to the wide range of relative humidities encountered throughout the campaign, the thermodynamically stable state, where both solid and liquid particles are allowed to exist, was chosen. In addition the forward mode was selected since the input provided more information to the module. Furthermore, when the reverse mode was attempted, the solution did not always mathematically converge.

The output results of ISORROPIA II have been used in order to preliminarily assess the validity of  $\text{HNO}_3$  measurements and then to evaluate the gas-aerosol partitioning of  $\text{NH}_4\text{NO}_3$ .

## 2.14 References

- Alfarra, M. R., Coe, H., Allan, J. D., Bower, K. N., Boudries, H., Canagaratna, M. R., Jimenez, J. L., Jayne, J. T., Garforth, A. A., Li, S.-M. and Worsnop, D. R.: Characterization of urban and rural organic particulate in the Lower Fraser Valley using two Aerodyne Aerosol Mass Spectrometers, *Atmos. Environ.*, 38(34), 5745–5758, doi:10.1016/j.atmosenv.2004.01.054, 2004.
- Allan, J. D., Delia, A. E., Coe, H., Bower, K. N., Alfarra, M. R., Jimenez, J. L., Middlebrook, A. M., Drewnick, F., Onasch, T. B., Canagaratna, M. R., Jayne, J. T. and Worsnop, D. R.: A generalised method for the extraction of chemically resolved mass spectra from Aerodyne aerosol mass spectrometer data, *J. Aerosol Sci.*, 35(7), 909–922, doi:10.1016/j.jaerosci.2004.02.007, 2004.
- Alleman, L. Y., Lamaison, L., Perdrix, E., Robache, A. and Galloo, J.-C.: PM10 metal concentrations and source identification using positive matrix factorization and wind sectoring in a French industrial zone, *Atmos. Res.*, 96(4), 612–625, doi:10.1016/j.atmosres.2010.02.008, 2010.
- Appel, B. R.: Sampling of Selected Labile Atmospheric Pollutants, in *Measurement Challenges in Atmospheric Chemistry*, vol. 232, pp. 1–40, American Chemical Society. [online] Available from: <http://dx.doi.org/10.1021/ba-1993-0232.ch001> (Accessed 2 December 2016), 1993.
- Appel, B. R., Povard, V. and Kothny, E. L.: Loss of nitric acid within inlet devices intended to exclude coarse particles during atmospheric sampling, *Atmos. Environ.*, 22(11), 2535–2540, doi:10.1016/0004-6981(88)90485-4, 1988.
- Baranov, V. I. and Tanner, S. D.: A dynamic reaction cell for inductively coupled plasma mass spectrometry (ICP-DRC-MS). Part 1. The rf-field energy contribution in thermodynamics of ion-molecule reactions, *J. Anal. At. Spectrom.*, 14(8), 1133–1142, doi:10.1039/A809889A, 1999.
- Canagaratna, M. r., Jayne, J. t., Jimenez, J. l., Allan, J. d., Alfarra, M. r., Zhang, Q., Onasch, T. b., Drewnick, F., Coe, H., Middlebrook, A., Delia, A., Williams, L. r., Trimborn, A. m., Northway, M. j., DeCarlo, P. f., Kolb, C. e., Davidovits, P. and Worsnop, D. r.: Chemical and microphysical characterization of ambient aerosols with the aerodyne aerosol mass spectrometer, *Mass Spectrom. Rev.*, 26(2), 185–222, doi:10.1002/mas.20115, 2007.
- DeCarlo, P. F., Kimmel, J. R., Trimborn, A., Northway, M. J., Jayne, J. T., Aiken, A. C., Gonin, M., Fuhrer, K., Horvath, T., Docherty, K. S., Worsnop, D. R. and Jimenez, J. L.: Field-Deployable, High-Resolution, Time-of-Flight Aerosol Mass Spectrometer, *Anal. Chem.*, 78(24), 8281–8289, doi:10.1021/ac061249n, 2006.
- Docherty, K. S., Lewandowski, M. and Jimenez, J. L.: Effect of Vaporizer Temperature on Ambient Non-Refractory Submicron Aerosol Composition and Mass Spectra Measured by the Aerosol Mass Spectrometer, *Aerosol Sci. Technol.*, 49(7), 485–494, doi:10.1080/02786826.2015.1042100, 2015.
- Dong, H.-B., Zeng, L.-M., Hu, M., Wu, Y.-S., Zhang, Y.-H., Slanina, J., Zheng, M., Wang, Z.-F. and Jansen, R.: Technical Note: The application of an improved gas and aerosol

collector for ambient air pollutants in China, *Atmos. Chem. Phys.*, 12(21), 10519–10533, doi:10.5194/acp-12-10519-2012, 2012.

Drewnick, F., Hings, S. S., DeCarlo, P., Jayne, J. T., Gonin, M., Fuhrer, K., Weimer, S., Jimenez, J. L., Demerjian, K. L., Borrmann, S. and Worsnop, D. R.: A New Time-of-Flight Aerosol Mass Spectrometer (TOF-AMS)—Instrument Description and First Field Deployment, *Aerosol Sci. Technol.*, 39(7), 637–658, doi:10.1080/02786820500182040, 2005.

Efron, B.: Bootstrap Methods: Another Look at the Jackknife, *Ann. Stat.*, 7(1), 1–26, doi:10.1214/aos/1176344552, 1979.

Fountoukis, C. and Nenes, A.: ISORROPIA II: a computationally efficient thermodynamic equilibrium model for  $\text{K}^+$ – $\text{Ca}^{2+}$ – $\text{Mg}^{2+}$ – $\text{NH}_4^+$ – $\text{Na}^+$ – $\text{SO}_4^{2-}$ – $\text{NO}_3^-$ – $\text{Cl}^-$ – $\text{H}_2\text{O}$  aerosols, *Atmos. Chem. Phys.*, 7(17), 4639–4659, doi:10.5194/acp-7-4639-2007, 2007.

G J Phillips, U. M.: The detection of nocturnal  $\text{N}_2\text{O}_5$  as  $\text{HNO}_3$  by alkali-and aqueous-denuder techniques, *Atmos. Meas. Tech.*, 6(2), 231–237, doi:10.5194/amt-6-231-2013, 2013.

Gianini, M. F. D., Fischer, A., Gehrig, R., Ulrich, A., Wichser, A., Piot, C., Besombes, J.-L. and Hueglin, C.: Comparative source apportionment of  $\text{PM}_{10}$  in Switzerland for 2008/2009 and 1998/1999 by Positive Matrix Factorisation, *Atmos. Environ.*, 54, 149–158, doi:10.1016/j.atmosenv.2012.02.036, 2012.

Hansen, A. D. A., Rosen, H. and Novakov, T.: The aethalometer — An instrument for the real-time measurement of optical absorption by aerosol particles, *Sci. Total Environ.*, 36, 191–196, doi:10.1016/0048-9697(84)90265-1, 1984.

Heintzenberg, J., Wehner, B. and Birmili, W.: ‘How to find bananas in the atmospheric aerosol’: new approach for analyzing atmospheric nucleation and growth events, *Tellus B*, 59(2), 273–282, doi:10.1111/j.1600-0889.2007.00249.x, 2007.

Henry, R., Norris, G. A., Vedantham, R. and Turner, J. R.: Source Region Identification Using Kernel Smoothing, *Environ. Sci. Technol.*, 43(11), 4090–4097, doi:10.1021/es8011723, 2009.

Huang, X. H. H.: Characterization of  $\text{PM}_{2.5}$  Major Components and Source Investigation in Suburban Hong Kong: A One Year Monitoring Study, *Aerosol Air Qual. Res.*, doi:10.4209/aaqr.2013.01.0020, 2014.

Jaklevic, J. M., Gatti, R. C., Goulding, F. S. and Loo, B. W.: A .beta.-gauge method applied to aerosol samples, *Environ. Sci. Technol.*, 15(6), 680–686, doi:10.1021/es00088a006, 1981.

Jayne, J. T., Leard, D. C., Zhang, X., Davidovits, P., Smith, K. A., Kolb, C. E. and Worsnop, D. R.: Development of an Aerosol Mass Spectrometer for Size and Composition Analysis of Submicron Particles, *Aerosol Sci. Technol.*, 33(1–2), 49–70, doi:10.1080/027868200410840, 2000.

Jimenez, J. L., Jayne, J. T., Shi, Q., Kolb, C. E., Worsnop, D. R., Yourshaw, I., Seinfeld, J. H., Flagan, R. C., Zhang, X., Smith, K. A., Morris, J. W. and Davidovits, P.: Ambient aerosol sampling using the Aerodyne Aerosol Mass Spectrometer, *J. Geophys. Res. Atmospheres*, 108(D7), 8425, doi:10.1029/2001JD001213, 2003.

- Keuken, M. P., Schoonebeek, C. A. M., van Wensveen-Louter, A. and Slanina, J.: Simultaneous sampling of NH<sub>3</sub>, HNO<sub>3</sub>, HCl, SO<sub>2</sub> and H<sub>2</sub>O<sub>2</sub> in ambient air by a wet annular denuder system, *Atmos. Environ.*, 22(11), 2541–2548, doi:10.1016/0004-6981(88)90486-6, 1988.
- Khlystov, A., Wyers, G. P. and Slanina, J.: The steam-jet aerosol collector, *Atmos. Environ.*, 29(17), 2229–2234, doi:10.1016/1352-2310(95)00180-7, 1995.
- Leclercq, B., Alleman, L. Y., Perdrix, E., Riffault, V., Happillon, M., Strecker, A., Lo-Guidice, J.-M., Garçon, G. and Coddeville, P.: Particulate metal bioaccessibility in physiological fluids and cell culture media: Toxicological perspectives, *Environ. Res.*, 156, 148–157, doi:10.1016/j.envres.2017.03.029, 2017.
- Lee, B. P., Li, Y. J., Yu, J. Z., Louie, P. K. K. and Chan, C. K.: Physical and chemical characterization of ambient aerosol by HR-ToF-AMS at a suburban site in Hong Kong during springtime 2011, *J. Geophys. Res. Atmospheres*, 118(15), 8625–8639, doi:10.1002/jgrd.50658, 2013.
- Li-Jones, X., Savoie, D. L. and Prospero, J. M.: HNO<sub>3</sub> losses within the cyclone inlet of a diffusion-denuder system under simulated marine environments, *Atmos. Environ.*, 35(5), 985–993, doi:10.1016/S1352-2310(00)00333-2, 2001.
- Makkonen, U.: Semi-continuous gas and inorganic aerosol measurements at a boreal forest site: seasonal and diurnal cycles of NH<sub>3</sub>, HONO and HNO<sub>3</sub>, *Boreal Environ. Res.*, 19 (suppl. B), 311–328, 2014.
- Makkonen, U., Virkkula, A., Mäntykenttä, J., Hakola, H., Keronen, P., Vakkari, V. and Aalto, P. P.: Semi-continuous gas and inorganic aerosol measurements at a Finnish urban site: comparisons with filters, nitrogen in aerosol and gas phases, and aerosol acidity, *Atmos. Chem. Phys.*, 12(12), 5617–5631, doi:10.5194/acp-12-5617-2012, 2012.
- Mbengue, S., Alleman, L. Y. and Flament, P.: Size-distributed metallic elements in submicronic and ultrafine atmospheric particles from urban and industrial areas in northern France, *Atmos. Res.*, 135–136, 35–47, doi:10.1016/j.atmosres.2013.08.010, 2014.
- Mensah, A. A., Holzinger, R., Otjes, R., Trimborn, A., Mentel, T. F., ten Brink, H., Henzing, B. and Kiendler-Scharr, A.: Aerosol chemical composition at Cabauw, The Netherlands as observed in two intensive periods in May 2008 and March 2009, *Atmos. Chem. Phys.*, 12(10), 4723–4742, doi:10.5194/acp-12-4723-2012, 2012.
- Middlebrook, A. M., Bahreini, R., Jimenez, J. L. and Canagaratna, M. R.: Evaluation of Composition-Dependent Collection Efficiencies for the Aerodyne Aerosol Mass Spectrometer using Field Data, *Aerosol Sci. Technol.*, 46(3), 258–271, doi:10.1080/02786826.2011.620041, 2012.
- Mooibroek, D., Schaap, M., Weijers, E. P. and Hoogerbrugge, R.: Source apportionment and spatial variability of PM<sub>2.5</sub> using measurements at five sites in the Netherlands, *Atmos. Environ.*, 45(25), 4180–4191, doi:10.1016/j.atmosenv.2011.05.017, 2011.
- Neuman, J. A., Huey, L. G., Ryerson, T. B. and Fahey, D. W.: Study of Inlet Materials for Sampling Atmospheric Nitric Acid, *Environ. Sci. Technol.*, 33(7), 1133–1136, doi:10.1021/es980767f, 1999.

Ohta, S. and Okita, T.: A chemical characterization of atmospheric aerosol in Sapporo, *Atmos. Environ. Part Gen. Top.*, 24(4), 815–822, doi:10.1016/0960-1686(90)90282-R, 1990.

Olson, D. A., Vedantham, R., Norris, G. A., Brown, S. G. and Roberts, P.: Determining source impacts near roadways using wind regression and organic source markers, *Atmos. Environ.*, 47, 261–268, doi:10.1016/j.atmosenv.2011.11.003, 2012.

Pancras, J. P., Vedantham, R., Landis, M. S., Norris, G. A. and Ondov, J. M.: Application of EPA unmix and nonparametric wind regression on high time resolution trace elements and speciated mercury in Tampa, Florida aerosol, *Environ. Sci. Technol.*, 45(8), 3511–3518, doi:10.1021/es103400h, 2011.

Petit, J.-E., Favez, O., Albinet, A. and Canonaco, F.: A user-friendly tool for comprehensive evaluation of the geographical origins of atmospheric pollution: Wind and trajectory analyses, *Environ. Model. Softw.*, 88, 183–187, doi:10.1016/j.envsoft.2016.11.022, 2017.

Pierson, W. R., Brachaczek, W. W. and McKee, D. E.: Sulfate Emissions from Catalyst-Equipped Automobiles on the Highway, *J. Air Pollut. Control Assoc.*, 29(3), 255–257, doi:10.1080/00022470.1979.10470790, 1979.

Polissar, A. V., Hopke, P. K., Paatero, P., Malm, W. C. and Sisler, J. F.: Atmospheric aerosol over Alaska: 2. Elemental composition and sources, *J. Geophys. Res. Atmospheres*, 103(D15), 19045–19057, doi:10.1029/98JD01212, 1998.

Rumsey, I. C., Cowen, K. A., Walker, J. T., Kelly, T. J., Hanft, E. A., Mishoe, K., Rogers, C., Proost, R., Beachley, G. M., Lear, G., Frelink, T. and Otjes, R. P.: An assessment of the performance of the Monitor for AeRosols and GAses in ambient air (MARGA): a semi-continuous method for soluble compounds, *Atmos. Chem. Phys.*, 14(11), 5639–5658, doi:10.5194/acp-14-5639-2014, 2014.

Schaap, M., Otjes, R. P. and Weijers, E. P.: Illustrating the benefit of using hourly monitoring data on secondary inorganic aerosol and its precursors for model evaluation, *Atmos. Chem. Phys.*, 11(21), 11041–11053, doi:10.5194/acp-11-11041-2011, 2011.

Slanina, J., ten Brink, H. M., Otjes, R. P., Even, A., Jongejan, P., Khlystov, A., Waijers-Ijpelaan, A., Hu, M. and Lu, Y.: The continuous analysis of nitrate and ammonium in aerosols by the steam jet aerosol collector (SJAC): extension and validation of the methodology, *Atmos. Environ.*, 35(13), 2319–2330, doi:10.1016/S1352-2310(00)00556-2, 2001.

Stein, A. F., Draxler, R. R., Rolph, G. D., Stunder, B. J. B., Cohen, M. D. and Ngan, F.: NOAA's HYSPLIT Atmospheric Transport and Dispersion Modeling System, *Bull. Am. Meteorol. Soc.*, 96(12), 2059–2077, doi:10.1175/BAMS-D-14-00110.1, 2015.

Tanner, S. D., Baranov, V. I. and Bandura, D. R.: Reaction cells and collision cells for ICP-MS: a tutorial review, *Spectrochim. Acta Part B At. Spectrosc.*, 57(9), 1361–1452, doi:10.1016/S0584-8547(02)00069-1, 2002.

Trebs, I., Meixner, F. X., Slanina, J., Otjes, R., Jongejan, P. and Andreae, M. O.: Real-time measurements of ammonia, acidic trace gases and water-soluble inorganic aerosol species at a rural site in the Amazon Basin, *Atmos. Chem. Phys.*, 4(4), 967–987, doi:10.5194/acp-4-967-2004, 2004.

Truex, T. J., Pierson, W. R., McKee, D. E., Shelef, M. and Baker, R. E.: Effects of barium fuel additive and fuel sulfur level on diesel particulate emissions, *Environ. Sci. Technol.*, 14(9), 1121–1124, doi:10.1021/es60169a018, 1980.

Twigg, M. M., Di Marco, C. F., Leeson, S., van Dijk, N., Jones, M. R., Leith, I. D., Morrison, E., Coyle, M., Proost, R., Peeters, A. N. M., Lemon, E., Frelink, T., Braban, C. F., Nemitz, E. and Cape, J. N.: Water soluble aerosols and gases at a UK background site – Part 1: Controls of PM<sub>2.5</sub> and PM<sub>10</sub> aerosol composition, *Atmos Chem Phys*, 15(14), 8131–8145, doi:10.5194/acp-15-8131-2015, 2015.

Ulbrich, I. M., Canagaratna, M. R., Zhang, Q., Worsnop, D. R. and Jimenez, J. L.: Interpretation of organic components from Positive Matrix Factorization of aerosol mass spectrometric data, *Atmos. Chem. Phys.*, 9(9), 2891–2918, doi:10.5194/acp-9-2891-2009, 2009.

Wang, Y., Hopke, P. K., Rattigan, O. V., Chalupa, D. C. and Utell, M. J.: Multiple-year black carbon measurements and source apportionment using delta-C in Rochester, New York, *J. Air Waste Manag. Assoc.*, 62(8), 880–887, 2012.

von der Weiden, S.-L., Drewnick, F. and Borrmann, S.: Particle Loss Calculator – a new software tool for the assessment of the performance of aerosol inlet systems, *Atmos. Meas. Tech.*, 2(2), 479–494, doi:10.5194/amt-2-479-2009, 2009.

Weingartner, E., Saathoff, H., Schnaiter, M., Streit, N., Bitnar, B. and Baltensperger, U.: Absorption of light by soot particles: determination of the absorption coefficient by means of aethalometers, *J. Aerosol Sci.*, 34(10), 1445–1463, doi:10.1016/S0021-8502(03)00359-8, 2003.

Wyers, G. P., Otjes, R. P. and Slanina, J.: A continuous-flow denuder for the measurement of ambient concentrations and surface-exchange fluxes of ammonia, *Atmos. Environ.*, 27(13), 2085–2090, doi:10.1016/0960-1686(93)90280-C, 1993.

Yamada, N.: Kinetic energy discrimination in collision/reaction cell ICP-MS: Theoretical review of principles and limitations, *Spectrochim. Acta Part B At. Spectrosc.*, 110, 31–44, doi:10.1016/j.sab.2015.05.008, 2015.

Yu, K. N., Cheung, Y. P., Cheung, T. and Henry, R. C.: Identifying the impact of large urban airports on local air quality by nonparametric regression, *Atmos. Environ.*, 38(27), 4501–4507, doi:10.1016/j.atmosenv.2004.05.034, 2004.

Zhang, Q., Jimenez, J. L., Canagaratna, M. R., Ulbrich, I. M., Ng, N. L., Worsnop, D. R. and Sun, Y.: Understanding atmospheric organic aerosols via factor analysis of aerosol mass spectrometry: a review, *Anal. Bioanal. Chem.*, 401(10), 3045–3067, doi:10.1007/s00216-011-5355-y, 2011.

---

**CHAPTER 3:**  
**Characterization and variability of**  
**inorganic aerosols and their gaseous**  
**precursors at a suburban site in**  
**northern France over one year**  
**(2015-2016)**

---





### **CHAPTER 3. Characterization and variability of inorganic aerosols and their gaseous precursors at a suburban site in northern France over one year (2015-2016) (ARTICLE 1)**

This chapter is based on the measurements obtained with the MARGA from the long-term measurement campaign and is presented under the form of an article which has been submitted to Atmospheric Environment in March 2018. This is the second revised version. The main characteristics and the variability of secondary inorganic aerosols and their gaseous precursors throughout one year will be presented. In addition, a first approach on the possible sources of aerosol and their geographical origins will also be given. The study is complemented by the analysis of the characteristics of high pollution episodes.

The article is complemented with supplementary material which can be found in Annex 2 in the end of the manuscript. This includes a section on the quality assurance and quality control of the presented data, particularly focused on the MARGA measurements. The rest of the supplementary material consists of several figures and tables complementary to the main text.



# Characterization and variability of inorganic aerosols and their gaseous precursors at a suburban site in northern France over one year (2015-2016)

Roger Roig Rodelas<sup>1</sup>, Esperanza Perdrix<sup>1</sup>, Benoît Herbin<sup>1</sup>, Véronique Riffault<sup>1</sup>

<sup>1</sup> IMT Lille Douai, Univ. Lille, SAGE – Département Sciences de l'Atmosphère et Génie de l'Environnement, F-59000 Lille, France

*Correspondence to:* Esperanza Perdrix (esperanza.perdrix@imt-lille-douai.fr)

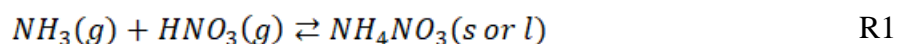
**Abstract.** Measurements of inorganic precursor gases (NO, NO<sub>2</sub>, HONO, NH<sub>3</sub>, SO<sub>2</sub> and HCl) and PM<sub>2.5</sub> inorganic water-soluble ions (NO<sub>3</sub><sup>-</sup>, SO<sub>4</sub><sup>2-</sup>, NH<sub>4</sub><sup>+</sup>, Cl<sup>-</sup>, Na<sup>+</sup>, Mg<sup>2+</sup>, Ca<sup>2+</sup>, K<sup>+</sup>) were performed at a suburban site in northern France for the first time using a MARGA 1S with an hourly time-resolution from August 2015 to July 2016. The observations were compared with other independent methods: HR-ToF-AMS, BAM-1020, SO<sub>2</sub> and NH<sub>3</sub> gas monitors over shorter time periods. The dominant particulate species were NO<sub>3</sub><sup>-</sup>, SO<sub>4</sub><sup>2-</sup> and NH<sub>4</sub><sup>+</sup>, with average annual mass contributions to PM<sub>2.5</sub> of 28.0%, 13.1% and 9.9%, respectively. The highest concentrations of SIA were found in spring likely due to increased agricultural emissions of precursor gases. A strong formation of ammonium nitrate (NH<sub>4</sub>NO<sub>3</sub>) over nighttime was observed for every season and attributed to the condensation of its gaseous precursors NH<sub>3</sub> and HNO<sub>3</sub>. The partitioning of NH<sub>4</sub>NO<sub>3</sub> between the gas and particulate phases was compared with that obtained with the thermodynamic module ISORROPIA II and generally found to agree well except for HNO<sub>3</sub>. The local or distant origin of each species was determined by means of Non parametric Wind Regression (NWR) polar plots and Potential Source Contribution Function (PSCF) maps. SIA main origins were regional with significant contributions from Belgium, The Netherlands and western Germany. Additionally, several high PM<sub>2.5</sub> episodes that lasted more than 2 days were analyzed, showing some common features.

**Keywords:** MARGA, SIA, ammonium nitrate, partitioning, ISORROPIA

## 1. Introduction

Fine particulate matter with an aerodynamic diameter below 2.5  $\mu\text{m}$  ( $\text{PM}_{2.5}$ ) has been shown to cause human health and environmental concerns (Kelly and Fussell, 2012). In Europe, its concentration in ambient air is regulated by the 2008/50/EC Directive, which sets an annual limit value (LV) of 25  $\mu\text{g m}^{-3}$ . This limit is above the air quality guideline value (GV) annual mean of 10  $\mu\text{g m}^{-3}$  for  $\text{PM}_{2.5}$  recommended by the World Health Organization (WHO, 2006). In northwestern European countries, current  $\text{PM}_{2.5}$  annual mean concentrations are above the GV and even exceed the LV at some locations.

A large contributor to  $\text{PM}_{2.5}$  in northwestern Europe is secondary inorganic aerosol (SIA), which includes nitrate ( $\text{NO}_3^-$ ), sulfate ( $\text{SO}_4^{2-}$ ) and ammonium ( $\text{NH}_4^+$ ). SIA might contribute to more than half of the  $\text{PM}_{2.5}$  mass, with ammonium nitrate ( $\text{NH}_4\text{NO}_3$ ) alone as high as 30% (Putaud et al., 2004).  $\text{NH}_4\text{NO}_3$  is formed by the neutralization of gaseous nitric acid ( $\text{HNO}_3$ ) by ammonia ( $\text{NH}_3$ ), as shown by reaction 1 (R1):



Its equilibrium between the gaseous and aerosol phases is reversible, and depends on the temperature, the relative humidity (RH) and the deliquescence state (Stelson and Seinfeld, 1982; Mozurkewich, 1993).

A good knowledge of the concentrations and temporal variability of both gaseous precursors and particulate ions appears essential in order to understand the processes that govern the ambient concentrations of  $\text{PM}_{2.5}$  and to help establish effective policies to reduce their ambient concentrations. Various instruments have been developed over the last decades in order to measure the chemical composition of atmospheric aerosols and their precursor gases. Measurements by filter packs, consisting of a front filter used to sample particles and a second one to collect gases, with subsequent analysis by ion chromatography (IC), have been extensively used in monitoring networks such as the European Monitoring and Evaluating Programme (EMEP) (EMEP, 2014). However, this methodology presents possible negative and positive artifacts (Slanina et al., 2001) and a low time-resolution which does not allow observing phenomena occurring rapidly in the atmosphere. Semi-continuous measurement techniques with higher time-resolution and less subject to artifacts have been developed, many of which are based on wet sampling of airborne compounds in liquid solutions and subsequent IC analysis. Such instruments include the Particle-Into-Liquid Sampler (PILS)

(Weber et al., 2001), the Ambient Ion Monitor (AIM) (Wu and Wang, 2007) and the Monitor for Gases and AeRosols in ambient Air (MARGA) (ten Brink et al., 2007). While the PILS is limited to the analysis of the particle phase, the AIM and MARGA are able to measure simultaneously the precursor gases of inorganic aerosols, which has proven useful for model evaluation (Schaap et al., 2011) and for the study of gas-aerosol partitioning of  $\text{NH}_4\text{NO}_3$  (Aan de Brugh et al., 2012).

In Europe, most of the research efforts on the simultaneous analysis of precursor gases and inorganic aerosols have been focused in rural areas, leaving a few number of studies conducted at urban or suburban sites. Table S1.1 in the supplementary material (SM) summarizes all published studies having used a MARGA from 2007 to 2017. Whereas most of them have been conducted at urban sites in China, only Makkonen et al. (2012) worked at an urban site in Europe. Improving on the knowledge of the composition and variability of precursor gases and inorganic particulate ions at more urban and suburban European sites appears therefore necessary.

Northern France is especially concerned by high levels of  $\text{PM}_{2.5}$ , often exceeding the established annual limit during several days. Main reasons accounting for this include its location amidst various emission source areas including an extensive road network, an elevated urban density, and the proximity to European capitals (London, Paris, and Brussels) as well as the existence of a significant influence of industry and agriculture. However, there is a limited number of studies describing the chemical composition of fine particles in this region, which were either carried over short periods of time (Crenn et al., 2017, 2018), or with a low time-resolution (Waked et al., 2014). These do not bring information about the temporal evolution of  $\text{PM}_{2.5}$ , SIA and their precursor gases with high time-resolution during a long period. Therefore there is still poor knowledge in this region on the chemical processes governing SIA formation, their contribution to  $\text{PM}_{2.5}$  mass and to the pollution episodes, as well as on their local or distant origins.

The present paper presents and discusses the first long-term and highly time-resolved dataset obtained with a MARGA in the north of France, with the aim to explain the time variability of SIA in  $\text{PM}_{2.5}$  at a typical suburban site over different time scales (monthly, daily and hourly), as well as to determine its main drivers.

## 2. Materials and methods

### 2.1. Campaign description

Observations of the chemical composition of atmospheric aerosols have been carried out from August 2015 to July 2016 in Douai, northern France (50°23'03''N, 3°05'08''E, and 20 m above sea level). The city of Douai is located in a fairly flat land and is part of the European Metropolis of Lille, with about 1.2 million inhabitants and a population density of 1,832

inhab. km<sup>-2</sup>, being the second most densely populated metropolis in France, after that of Paris. The climate in northern France is classified as temperate oceanic, characterized by low seasonal thermal amplitudes, and regular precipitations along the year, with the absence of a dry season. The winters are mild and the summers cool.

The sampling site is located at a suburban location outside the city center of Douai (Figure P1.1), and is considered to be representative of the background pollution of the region.

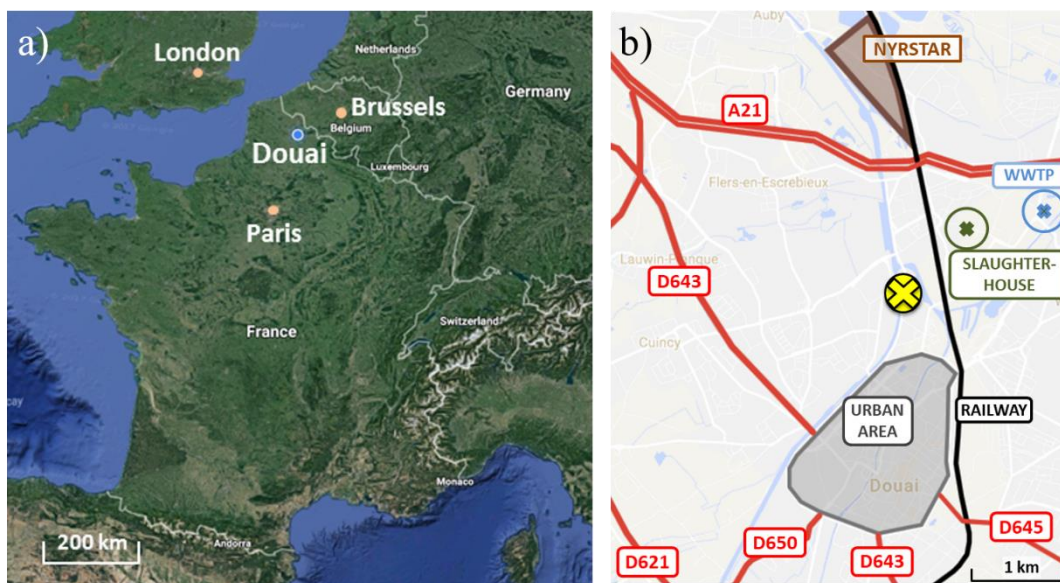


Figure P1.1 Maps of France (left) and Douai (right) with the sampling site (yellow cross), the main roads (red lines), railroad (black line), city center (grey area), non-ferrous metal industry (brown area), slaughterhouse (green cross) and waste water treatment plant (WWTP, blue cross).

## 2.2. Instrumentation

The commercially available MARGA 1S – ADI 2080 (Metrohm Applikon B.V) (ten Brink et al., 2007) has been deployed over the entire period in order to determine the chemical composition of 8 water-soluble inorganic ions ( $\text{NO}_3^-$ ,  $\text{SO}_4^{2-}$ ,  $\text{NH}_4^+$ ,  $\text{Na}^+$ ,  $\text{K}^+$ ,  $\text{Ca}^{2+}$ ,  $\text{Mg}^{2+}$ ,  $\text{Cl}^-$ ), 1 water-soluble organic ion (oxalate) and 5 precursor gases ( $\text{NH}_3$ ,  $\text{SO}_2$ , HONO,  $\text{HNO}_3$  and HCl) with an hourly time-resolution. The MARGA has already been used in a number of studies over Europe, Asia and North America and has been compared to other reference methods (e.g. denuder/filter pack,  $\text{SO}_2$  gas monitors, AMS) generally delivering satisfying results (Huang, 2014; Makkonen et al., 2012, 2014; Mensah et al., 2012; Rumsey et al., 2014). Briefly, ambient air is drawn at a constant flow rate of  $1 \text{ m}^3 \text{ h}^{-1}$  through a Teflon-coated  $\text{PM}_{2.5}$ -inlet (Leckel) followed by a 2.5 m long polyethylene tube of 1/2" outer diameter. Then the air enters the Wet Rotating Denuder (WRD), where water-soluble gases diffuse to the absorption solution (10 ppm hydrogen peroxide in ultrapure water). Subsequently the aerosol particles are collected in a Steam Jet Aerosol Collector (SJAC). The non-soluble compounds are then separated by  $0.45 \mu\text{m}$  PTFE filters. The sampled aerosol and gas compounds are continuously collected in 25-mL syringes and alternatively injected to the ion chromatograph (IC) after addition of LiBr as internal standard. The cation (respectively, anion) loop volume was 500  $\mu\text{L}$  (resp. 250). Metrosep C4 (100 x 4.0 mm; Metrohm) and Metrosep A Supp-10 (75 x 4.0 mm, Metrohm). The cation eluent was composed of 3.2 mmol  $\text{L}^{-1}$   $\text{HNO}_3$ , while the anion eluent consisted of 7.0 mmol  $\text{L}^{-1}$   $\text{Na}_2\text{CO}_3$  and 8 mmol  $\text{L}^{-1}$   $\text{NaHCO}_3$ . In addition, since the anion chromatography worked with chemical suppression, a regenerant solution was used for the chemical suppressor which consisted of 0.35 mol  $\text{L}^{-1}$   $\text{H}_3\text{PO}_4$ . A section on the quality assurance and quality control of the data is presented in the SM, including a comparison of the MARGA with collocated independent instruments.

An AE42 aethalometer (Magee Scientific) has been operated at 2 wavelengths (370 and 880 nm) along with the MARGA for the analysis of aromatic particulate carbon absorbing in the UV and particulate carbon absorbing in the near infrared, respectively, with a time-resolution of 5 minutes. Measurements were corrected using the algorithm from Weingartner et al. (2003). Black carbon (BC) concentrations were calculated from the absorption coefficient at 880 nm. Additionally, a Delta-C variable was determined by the difference of light absorption between 370 and 880 nm (Allen et al., 2004). Delta-C has previously been found to be correlated with wood-burning markers such as levoglucosan and  $\text{K}^+$  and therefore might be used as a tracer of wood combustion (Wang et al., 2012).

Nitrogen oxides have been analyzed every 15 minutes with a chemiluminescence analyzer NOx 2000G (Seres environment). The PM<sub>2.5</sub> total mass has been measured by a Beta Attenuation Monitor BAM-1020 (Met One Instruments) every hour. Meteorological parameters including temperature, relative humidity (RH), pressure, wind speed and direction and precipitation were also monitored on site. Their temporal variability over the campaign is reported in Figure S1.1 and their seasonal daily profiles in Figure S1.2.

All presented measurements are given in Coordinated Universal Time (UTC), and seasons are differentiated as follows: winter (December, January, February), spring (March, April, May), summer (June, July, August) and autumn (September, October, November).

### 2.3. Ratios (NR and GR)

Based on the MARGA data, the neutralization ratio (NR) was calculated (Eq. 1), in order to evaluate the degree of neutralization of the SIA. In addition, the gas ratio (GR) is used in order to assess the limiting species between HNO<sub>3</sub> and NH<sub>3</sub> for the formation of NH<sub>4</sub>NO<sub>3</sub> (Eq. 2).

$$NR = \frac{[NH_4^+]}{2[SO_4^{2-}] + [NO_3^-]} \quad \text{Eq. 1}$$

$$GR = \frac{[TNH_3] - [TS]}{[TNO_3]} \quad \text{Eq. 2}$$

where  $[TNH_3] = [NH_3] + [NH_4^+]$ ,  $[TS] = [SO_2] + [SO_4^{2-}]$  and  $[TNO_3] = [HNO_3] + [NO_3^-]$ , and all concentrations are expressed in  $\mu\text{mol m}^{-3}$ .

### 2.4. Weather and trajectory models

#### 2.4.1. Non-parametric wind regression

The non-parametric wind regression (NWR) is a hybrid source-receptor model which locates and quantifies local sources of hourly averaged atmospheric concentrations of a pollutant based on wind speed ( $u$ ) and direction ( $\theta$ ) (Henry et al., 2009):

$$E(C|\theta, u) = \frac{\sum_{i=1}^N K_1\left(\frac{\theta - W_i}{\sigma}\right) \cdot K_2\left(\frac{u - U_i}{h}\right) \cdot C_i}{\sum_{i=1}^N K_1\left(\frac{\theta - W_i}{\sigma}\right) \cdot K_2\left(\frac{u - U_i}{h}\right)} \quad \text{Eq. 3}$$



where  $E$  is the concentration estimate at a wind direction  $\theta$  and wind speed  $u$ ;  $W_i$ ,  $U_i$  and  $C_i$  the wind direction, speed and atmospheric concentrations, respectively, measured at  $t_i$ ;  $\sigma$  and  $h$  the smoothing factors (which were suggested for each species by the software); and  $K_1$  and  $K_2$  are a Gaussian kernel function for wind direction  $\theta$  and an Epanechnikov kernel function for wind speed  $u$ , respectively (Henry et al., 2009).

In order to apportion the weighed concentrations obtained from Eq. 3 to source areas, these results have to be weighed by the frequency of the winds. Hence, an empirical joint probability density of wind speed and direction is calculated using the kernel density estimate, as shown in Eq. 4:

$$f(\theta, u) = \frac{1}{N\sigma h} \cdot \sum_{i=1}^N K_1\left(\frac{\theta - W_i}{\sigma}\right) K_2\left(\frac{u - U_i}{h}\right) \quad \text{Eq. 4}$$

where  $N$  is the total number of points.

NWR for every season and species were calculated using the Zefir v3.31 IGOR tool (Petit et al., 2017) and results are presented in section 3.4.1.

#### 2.4.2. Back-trajectory calculations

Back-trajectories were calculated with HYSPLIT 4 (HYbrid Single-Particle Lagrangian Integrated Trajectory) (Stein et al., 2015) for an arrival height of half the planetary boundary layer (PBL) at 3-hour intervals (8 trajectories per day at 0, 3, 6, 9, 12, 15, 18, 21 UTC), 72 hours back in time. All obtained back-trajectories were used to perform trajectory-based analyses.

#### 2.4.3. Potential source contribution function

The Potential Source Contribution Function (PSCF) method (Hopke, 1985) was applied using Zefir v3.31 in order to determine the most probable regions of emissions for the gaseous and particulate species. PSCF is calculated through the following equation:

$$PSCF = \frac{m_{ij}}{n_{ij}} \quad \text{Eq. 5}$$

where  $m_{ij}$  is the number of times that the measured concentration exceeds a specific threshold (in this case the 75<sup>th</sup> percentile was used) and  $n_{ij}$  the number of times a trajectory

falls into the  $ij^{\text{th}}$  cell with latitude  $i$  and longitude  $j$ . High values of PSCF indicate high probabilities that the  $ij^{\text{th}}$  cell represents a source location.

## 2.5. Thermodynamic module

The thermodynamics of the  $\text{K}^+ - \text{Ca}^{2+} - \text{Mg}^{2+} - \text{Na}^+ - \text{NH}_4^+ - \text{SO}_4^{2-} - \text{NO}_3^- - \text{Cl}^- - \text{H}_2\text{O}$  aerosol system has been evaluated with the use of the ISORROPIA II thermodynamic equilibrium model (Fountoukis and Nenes, 2007). ISORROPIA II performs the calculation of the composition and phase state of the inorganic aerosol system in thermodynamic equilibrium with the gas-phase precursors.

The results presented in this work correspond to the forward mode, where input data consist of the temperature, RH and the total (gas + aerosol) concentrations of  $\text{NH}_3$ ,  $\text{H}_2\text{SO}_4$ ,  $\text{Na}^+$ ,  $\text{Ca}^{2+}$ ,  $\text{K}^+$ ,  $\text{Mg}^{2+}$ ,  $\text{HCl}$ , and  $\text{HNO}_3$ . The aerosol is considered in a thermodynamically stable state, where salts precipitate once the aqueous phase becomes saturated.

## 3. Results

### 3.1. $\text{PM}_{2.5}$ chemical composition and correlations between species

A summary of the meteorological conditions for each season is presented in Table P1.1 and their temporal variability is plotted in Figure S1.1. Briefly, precipitations were abundant and constant throughout the whole year, with no clear dry or wet season. The autumn and winter were mild, with higher temperatures compared to previous years. In spring and summer the temperatures were more representative of the seasonal average values. The winds were rather calm and with predominant directions from the S and SW, particularly in winter. Monthly statistics are given in Table S1.2.

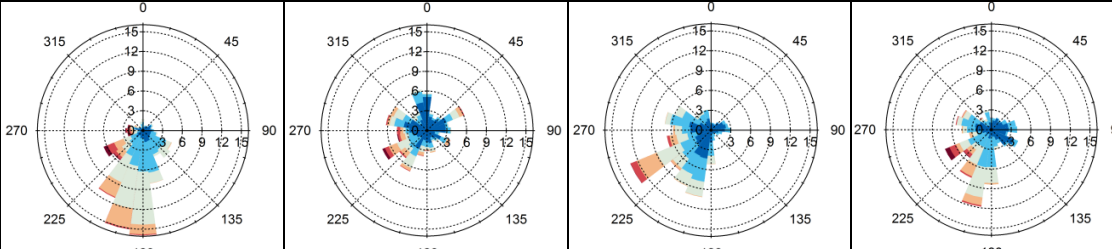
Table P1.2 summarizes the average concentrations, together with the standard deviations, the percentiles 2.5, 50 and 97.5. The data coverage above the detection limit has been calculated for  $\text{PM}_{2.5}$  and every particulate and gaseous species for each season. Most species presented a high percentage of valid data above the DL, particularly gaseous species and water-soluble anions, except  $\text{Cl}^-$ . On the other hand, cations such as  $\text{Mg}^+$ ,  $\text{Ca}^{2+}$  and  $\text{K}^+$  often presented values below the DL of the instrument, and their results should be interpreted with caution.

A high percentage of  $\text{PM}_{2.5}$  is composed of SIA, with  $\text{NO}_3^-$ ,  $\text{SO}_4^{2-}$  and  $\text{NH}_4^+$  being the main inorganic ions (contributions of 28%, 13% and 10%, respectively). The sum of the other

minor ions as well as BC both presented an average contribution of 3%. The remaining PM<sub>2.5</sub> could not be determined by our measurement techniques, and most likely represented organic matter (OM).

The correlations between all gaseous and particulate species for each season are given in Table S1.3. The strongest correlation was found between NO<sub>3</sub><sup>-</sup> and NH<sub>4</sub><sup>+</sup>, with seasonal Pearson coefficients (*r*) higher than 0.9. A lesser but still strong correlation was obtained between NH<sub>4</sub><sup>+</sup> and SO<sub>4</sub><sup>2-</sup> with seasonal *r* values close or higher than 0.8. These significant correlations suggest that both ammonium nitrate and ammonium sulfate species are likely to be formed. These results are in line with what has been found at other sites in north-western Europe (Putaud et al., 2004, 2010) and in a previous study of the non-refractory PM<sub>1</sub> in Douai, where NH<sub>4</sub><sup>+</sup> was highly correlated with NO<sub>3</sub><sup>-</sup> (*r*<sup>2</sup> = 0.91 and 0.89 for winter and summer, respectively) and slightly less with SO<sub>4</sub><sup>2-</sup> (*r*<sup>2</sup> = 0.75 and 0.46) (Crenn et al., 2017). While the presence of (NH<sub>4</sub>)<sub>2</sub>SO<sub>4</sub> and NH<sub>4</sub>HSO<sub>4</sub> was also important, other sulfate compounds might also exist. High *r* values (around 0.6) were observed between C<sub>2</sub>O<sub>4</sub><sup>2-</sup> and SO<sub>4</sub><sup>2-</sup>, suggesting both species may partly originate from similar sources or processes. Significant correlations between gaseous HONO, NO and NO<sub>2</sub>, and BC were found, suggesting combustion sources as the main origins for all of them. These findings are consistent with the variability of the seasonal mean values of these species presented in Table P1.2.

Table P1.1 Statistical summary (mean ± one standard deviation) of meteorological parameters for each season

	Winter	Spring	Summer	Autumn
T (°C)	7.6 ± 3.8	10.8 ± 5.3	19.0 ± 4.7	12.1 ± 4.3
RH (%)	86.0 ± 8.2	76.6 ± 15.2	77.3 ± 15.5	85.8 ± 10.3
P <sub>atm</sub> (mbar)	1012.1 ± 12.0	1010.3 ± 8.6	1015.3 ± 6.5	1016.0 ± 8.0
PBL <sub>max</sub> <sup>a</sup> (m)	861 ± 352	1284 ± 371	1243 ± 387	1003 ± 363
Acc. rain <sup>b</sup> (mm)	157	196	174	173
WS (m s <sup>-1</sup> )	1.9 ± 1.1	1.3 ± 1.1	1.3 ± 0.9	1.5 ± 1.1
Wind speed (WS) (m s <sup>-1</sup> )				

<sup>a</sup> The PBL height was obtained from meteorological data from GDAS; <sup>b</sup> Accumulated rain

Table P1.2 Statistical summary of all measured parameters at the site of Douai for each season: average, standard deviation (SD) and percentiles (P<sub>i</sub>) are concentrations in µg m<sup>-3</sup>; n<sub>v>D</sub>: percentage of valid data, i.e. above the detection limit (DL) for each compound

	WINTER						SPRING						SUMMER						AUTUMN						
	AVG	± SD	P <sub>2.5</sub>	P <sub>50</sub>	P <sub>97.5</sub>	n <sub>v&gt;D</sub>	AVG	± SD	P <sub>2.5</sub>	P <sub>50</sub>	P <sub>97.5</sub>	n <sub>v&gt;D</sub>	AVG	± SD	P <sub>2.5</sub>	P <sub>50</sub>	P <sub>97.5</sub>	n <sub>v&gt;D</sub>	AVG	± SD	P <sub>2.5</sub>	P <sub>50</sub>	P <sub>97.5</sub>	n <sub>v&gt;D</sub>	DL
NO	4.87	11.8	<DL	0.5	36.84	36	2.87	7.52	<DL	0.25	19.8	53	1.57	2.68	<DL	0.25	9.25	20	6.22	12.4	<DL	1.25	37.5	65	0.25
NO <sub>2</sub>	9.72	7.83	<DL	8.25	27.87	59	8.71	6.74	1	7	26	97	7.93	4.15	1.25	7.71	17	34	10	6.54	0.75	9.25	24	92	0.4
O <sub>3</sub> *	37.6	18.1	2.4	39.4	66.2	100	50.1	23.7	4.1	51.9	100	88	46.5	21.4	12.2	44.2	99.2	66	33.1	20.4	1.2	33.5	71.2	97	1
HONO	1.01	0.81	0.27	0.79	3.18	97	1.02	0.79	0.27	0.76	2.95	78	0.72	0.47	0.19	0.59	1.97	91	1.06	0.87	0.29	0.84	3.19	87	0.08
SO <sub>2</sub>	0.63	0.82	0.17	0.36	2.67	97	0.98	1.99	0.2	0.58	3.68	78	1.19	2.62	0.18	0.4	8.01	91	0.87	1.42	0.16	0.37	4.74	87	0.16
NH <sub>3</sub>	1.39	0.68	0.41	1.32	3.04	97	4.28	2.86	0.56	3.71	10.8	79	4.03	2.78	0.84	3.21	11.2	96	2.24	1.82	0.07	1.91	6.74	83	0.04
NO <sub>3</sub> <sup>-</sup>	3.34	3.69	0.52	1.88	14.82	97	5.21	5.81	0.49	2.84	22.7	84	2.69	3.78	0.58	1.27	14.7	90	3.88	3.83	0.58	2.28	14.9	84	0.22
SO <sub>4</sub> <sup>2-</sup>	1.3	0.82	0.33	1.09	3.26	97	2.05	1.65	0.42	1.49	6.97	84	2.02	1.28	0.55	1.7	5.6	90	1.67	1.24	0.39	1.32	5.16	84	0.24
NH <sub>4</sub> <sup>+</sup>	1.14	1.33	<DL	0.67	5.12	94	1.95	2.24	0.11	1.03	8.48	84	1.21	1.54	0.11	0.66	6.03	94	1.01	1.17	<DL	0.59	4.36	80	0.04
Oxal	0.13	0.09	<DL	0.12	0.34	60	0.19	0.12	<DL	0.18	0.45	58	0.19	0.15	<DL	0.16	0.53	64	0.13	0.1	<DL	0.11	0.37	49	0.08
Cl <sup>-</sup>	0.13	0.34	<DL	<DL	1.05	30	0.06	0.16	<DL	<DL	0.57	19	0.03	0.07	<DL	<DL	0.21	9	0.06	0.25	<DL	<DL	0.52	14	0.06
Na <sup>+</sup>	0.13	0.16	<DL	0.07	0.55	79	0.07	0.09	<DL	0.04	0.3	47	0.06	0.07	<DL	0.03	0.25	50	0.12	0.17	<DL	0.09	0.57	63	0.03
K <sup>+</sup>	0.05	0.07	<DL	<DL	0.22	27	0.02	0.02	<DL	<DL	0.11	5	0.02	0.02	<DL	<DL	0.06	4	0.03	0.04	<DL	<DL	0.16	9	0.06
Mg <sup>2+</sup>	0.02	0.03	<DL	<DL	0.09	22	0.02	0.02	<DL	<DL	0.08	9	0.02	0.02	<DL	<DL	0.06	12	0.02	0.03	<DL	<DL	0.12	16	0.04
Ca <sup>2+</sup>	0.04	0.05	<DL	<DL	0.18	13	0.06	0.08	<DL	<DL	0.29	23	0.08	0.09	<DL	<DL	0.32	37	0.08	0.15	<DL	<DL	0.38	31	0.18
BC	0.45	0.46	<DL	0.32	1.69	96	0.4	0.4	<DL	0.29	1.31	93	0.32	0.28	0.05	0.24	1	95	0.52	0.54	<DL	0.35	1.89	61	0.05
PM <sub>2.5</sub>	12.5	7.4	4	10	32.02	93	14.9	10.7	4	11	46	97	12.9	8.1	5	10	36	89	13	7.5	4	11	31	94	4
NR	0.6	0.3	-	-	-	-	0.7	0.2	-	-	-	-	0.7	0.2	-	-	-	-	0.5	0.2	-	-	-	-	-
GR	3.0	1.7	-	-	-	-	6.8	8.9	-	-	-	-	6.8	5.0	-	-	-	-	4.2	4.0	-	-	-	-	-

\*Measured at the Atmo-HdF site of Douai-Theuriet (1.5 km from the sampling site)

The  $\text{NO}_3^-$  and  $\text{NH}_4^+$  ions both show a maximum seasonal average in spring, a season during which nitrogen fertilizers are usually added to agricultural soils. Also  $\text{C}_2\text{O}_4^{2-}$  and  $\text{SO}_4^{2-}$  along with  $\text{O}_3$  have their maximum seasonal average in summer.  $\text{C}_2\text{O}_4^{2-}$  is a final product of the oxidation of organic matter,  $\text{SO}_4^{2-}$  is mainly a product of the oxidation of  $\text{SO}_2$ , while  $\text{O}_3$  is an indicator of the oxidative capacity of the atmosphere. Therefore, all these compounds are typically expected in processed and possibly aged air masses where the oxidation processes have had enough time to occur. HONO, NO,  $\text{NO}_2$ , and BC are higher during the cold seasons, in agreement with the higher occurrence of possible common combustion sources such as road traffic or residential heating. Other species also exhibit marked seasonal averages, including  $\text{NH}_3$ , with higher averages in spring and summer, associated to the increase of agricultural activities and  $\text{NH}_3$  emissions from soils with temperature, and  $\text{Na}^+$  and  $\text{Cl}^-$  with higher averages in winter, when marine storms occur more frequently.

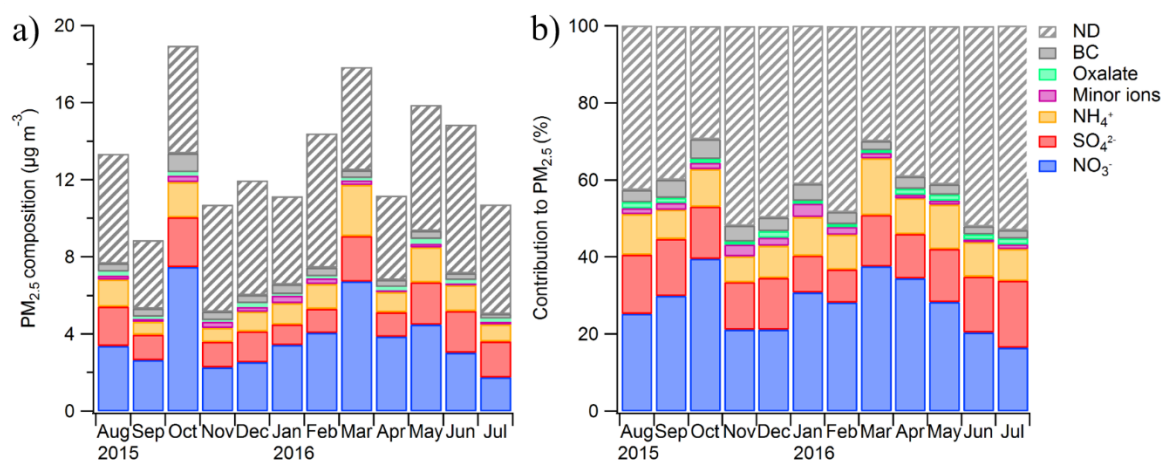


Figure P1.2  $\text{PM}_{2.5}$  average monthly (a) mass concentration and (b) relative contribution for the major chemical species, ND: not determined, BC: Black carbon.

The average monthly composition of  $\text{PM}_{2.5}$  and relative contribution of every particulate species are shown in Figure P1.2. The  $\text{PM}_{2.5}$  concentration varies significantly throughout the year, with particularly higher concentrations in October 2015 and March 2016. Even though the composition of  $\text{PM}_{2.5}$  does not differ a lot over the different months, higher contributions of SIA (70% on average) were observed for months with high  $\text{PM}_{2.5}$  concentrations such as October and March. These higher contributions of SIA will be discussed further on in section 3.5.

Moreover, the speciation of secondary inorganic salts was calculated similarly to Alastuey et al. (2005). The average seasonal contribution of each inorganic salt to the sum of

the main inorganic compounds is shown in Figure S1.3. The following assumptions were taken into account:

- All  $\text{Cl}^-$  is considered to be associated to  $\text{Na}^+$ .
- $\text{NH}_4^+$  is preferentially associated with  $\text{SO}_4^{2-}$  in order to form  $(\text{NH}_4)_2\text{SO}_4$ .
- The excess  $\text{NH}_4^+$  is associated to  $\text{NO}_3^-$  for the formation of  $\text{NH}_4\text{NO}_3$ .
- The excess  $\text{SO}_4^{2-}$  and  $\text{NO}_3^-$  are associated to the remaining  $\text{Na}^+$ , and then to the rest of cations,  $\text{Ca}^{2+}$ ,  $\text{Mg}^{2+}$  and  $\text{K}^+$ .

The species that dominate the inorganic aerosol composition are  $\text{NH}_4\text{NO}_3$  (35-47%) and  $(\text{NH}_4)_2\text{SO}_4$  (36-48%) (with respect to the total mass of measured ions). The contribution of  $\text{NH}_4\text{NO}_3$  was highest in winter and spring, when the condensation of the precursor gases is favored, and lowest in autumn. The lower contribution in autumn was due to a high part of the anions (mostly  $\text{NO}_3^-$ ) not being neutralized. This could be due to different impacts of marine air masses able to carry sea salt and microorganisms. On the other hand, the contribution of  $(\text{NH}_4)_2\text{SO}_4$  was most important in summer, which might be justified by an enhanced conversion of sulfate aerosol precursors due to a higher solar radiation and hence higher concentrations of radicals promoting their oxidation.

The contribution of the marine salts, both fresh ( $\text{NaCl}$ ) and aged ( $\text{NaNO}_3$ ), is low during the whole year (<5% each one). The lowest contributions are observed in spring and summer, whereas the highest are reported in autumn and winter. The enhanced presence of marine salts in the cold seasons might be justified by a higher frequency of air masses coming from the Atlantic Ocean or the North Sea, as will be discussed later (section 3.4.2).

### **3.2. Seasonal daily variability of precursor gases and inorganic aerosol species**

#### **3.2.1. Precursor gases**

The daily variability of the gases is shown by season in Figure P1.3. Both  $\text{NO}$  and  $\text{NO}_2$  concentrations showed daily profiles with morning and afternoon maxima during the rush hours and a minimum during the afternoon (Figure P1.3a-b). These daily profiles are typical of a suburban site under traffic influence (Kendrick et al., 2015). This is supported by the weekly trends (Figure S1.4) which show significantly lower contributions during the weekend, particularly on Sundays, when traffic is the least intense. This conclusion is also consistent with the French emission inventory for  $\text{NO}_x$ , which attributes a large fraction to road transport at the national level (>50%), while other sources such as other types of transport, energy transformation, manufacturing industry, agriculture/forestry, and residential

or tertiary activities contribute similarly to the remaining NO<sub>x</sub> emissions (CITEPA, 2017). The highest concentrations were observed in autumn and winter, and the lowest in summer. Noticeably in spring and summer the NO afternoon maximum disappeared. This suggests the likely contribution in these cold seasons of a source of NO other than traffic, most probably related to residential heating. The seasonal variability for NO<sub>2</sub> was less marked in comparison to that of NO. The higher concentrations observed in autumn and winter may be explained by lower wind speeds (the lowest average wind speed was observed in October) which could hinder the dispersion of gaseous and particulate pollutants, and increased emissions from traffic and household combustion.

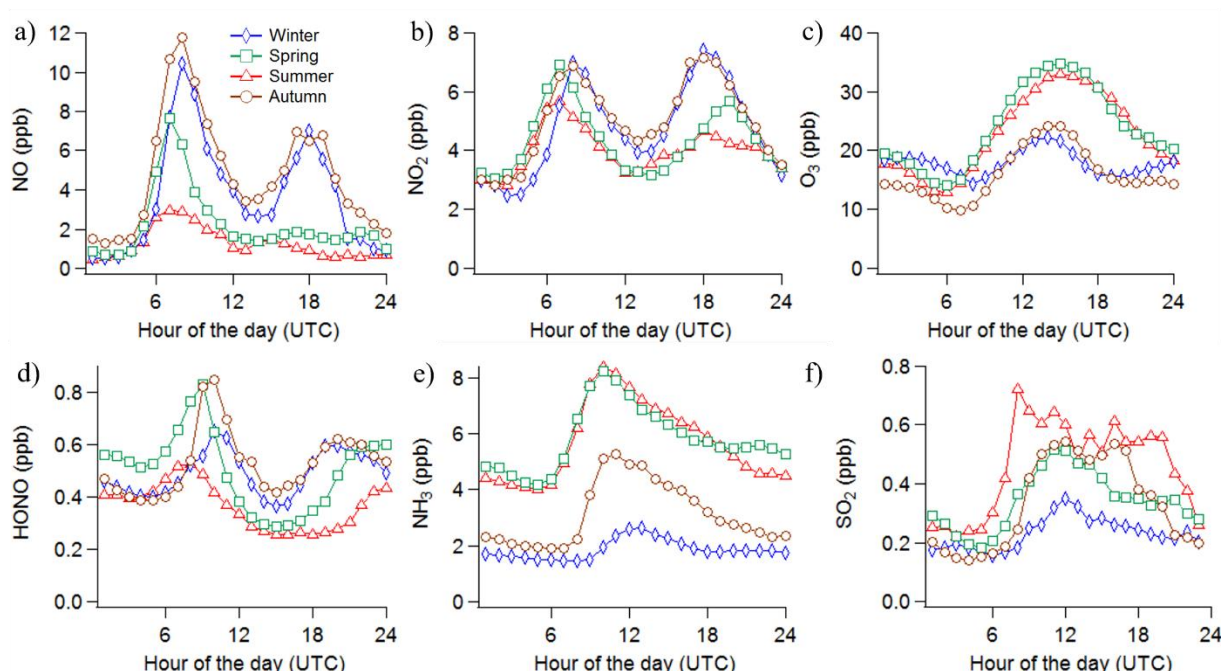


Figure P1.3 Average daily profiles of (a) NO, (b) NO<sub>2</sub>, (c) O<sub>3</sub>, (d) HONO, (e) NH<sub>3</sub>, (f) SO<sub>2</sub> for each season (winter: blue; spring: green, summer: red, autumn: brown). \* O<sub>3</sub> was obtained from the Atmo-HdF station in Douai Theuriet.

Ozone (O<sub>3</sub>) presented higher concentrations during daytime (Figure P1.3c), peaking at around 15:00 coinciding with minima for NO and NO<sub>2</sub>, particularly in summer and spring. Lower concentrations of O<sub>3</sub> were observed in autumn and winter, when the photochemical activity was the lowest and emissions of NO at their highest, the latter favoring the depletion of tropospheric O<sub>3</sub>.

Nitrous acid (HONO) showed clear daily patterns for each season (Figure P1.3d), with a maximum peak in the morning and a smaller one at the end of the day, similar to those observed at other sites in Europe (Fisseha et al., 2006; Makkonen et al., 2012, 2014). Its

concentrations reached a daily minimum in the afternoon, between 14:00 and 18:00, mainly due to HONO daytime photolysis. Similar to  $\text{NO}_x$ , the lowest concentrations were observed on Sundays. The observed concentrations were higher in autumn and spring, while the lowest values were observed in summer. The possible sources of HONO are numerous and still not well known (Gall et al., 2016). Therefore, in order to assess the possible influence of traffic as a source of daytime HONO, the hourly concentrations of HONO were plotted against those of  $\text{NO}_x$  (Figure P1.4 and Table P1.3). In previous studies an average slope of  $0.8 \pm 0.1\%$  was found inside a road traffic tunnel during daytime (6:00-14:00) by Kurtenbach et al. (2001). Another study reported a slope of  $1.6 \pm 0.1\%$  at a highway junction during the rush hours (4:00- 8:00) of weekdays (Rappenglück et al 2013), which is currently recommended for modelling purposes (Czader et al., 2015). More recently, a ratio of  $1.24 \pm 0.35\%$  was measured in a road tunnel (Liang et al., 2017).

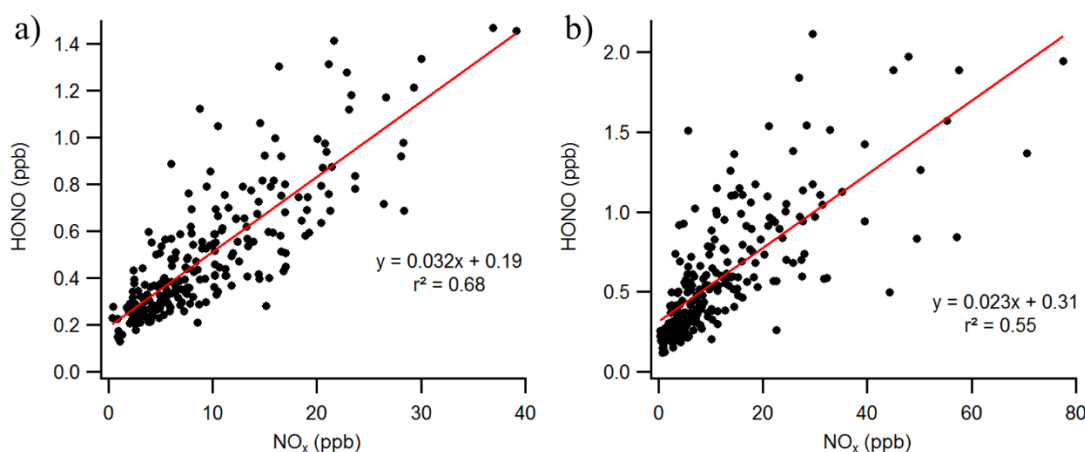


Figure P1.4 HONO vs.  $\text{NO}_x$  concentrations for (a) all daytime-averaged points and (b) data averaged over rush hours (6:00-10:00 am).

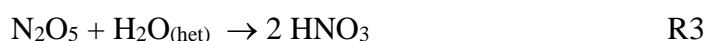
In this study, a moderate correlation ( $r^2 = 0.68$ ) and a slope of  $3.2 \pm 0.1\%$  ppb of HONO per ppb of  $\text{NO}_x$  was obtained for the averaged daytime hours ( $n = 240$ ), which is slightly higher than the values reported in the literature. But when only the morning rush hours were considered ( $n = 234$ ) a lower slope was obtained ( $r^2 = 0.55$ ; slope =  $2.3 \pm 0.1\%$ ). Both ratios are slightly higher than the values reported in the literature, the rush hours ratio being close to the value reported by Rappenglück et al. (2013) but could be explained by the different types of traffic, atmospheric reactivity and/or dispersion conditions at each site.

Therefore, these values suggest that traffic is a possible source of HONO in our site, as has also been suggested from its characteristic daily pattern. However, other sources could contribute as well to the observed concentrations, including emissions from soils (Sörgel et



al., 2015). Recently, it has indeed been suggested that HONO might react with carbonated soils at night, accumulating as nitrite ( $\text{NO}_2^-$ ) which is displaced during the day in the presence of HCl and  $\text{HNO}_3$  (VandenBoer et al., 2015). Since our site is surrounded by grassland on carbonated subsoil, it cannot be excluded that soils contributed as an additional source of HONO.

Secondary processes of HONO formation are also likely to occur, such as the heterogeneous formation of HONO from  $\text{NO}_2$  or the recently proposed homogeneous oxidation of  $\text{NO}_x$  by  $\text{HO}_x$  (Li et al., 2014). In fact in the late evening and the following hours of the night, when the photolysis of both HONO and  $\text{NO}_2$  was hindered, the average concentrations of  $\text{NO}_2$  decreased rather rapidly (about  $-0.7 \text{ ppb h}^{-1}$ ) while those of HONO tended to stay stable or decreased several times slower ( $< -0.1 \text{ ppb h}^{-1}$ ). According to Sörgel et al. (2015) this may be explained by the fact that, except for deposition or uptake by aerosol surfaces, no considerable gas-phase HONO sinks exist in the absence of light, contrary to  $\text{NO}_2$  which may be consumed by several chemical reactions. One of them is the reaction of  $\text{NO}_2$  with ozone to form the nighttime radical  $\text{NO}_3$  (R2). This reaction is the first step leading to the nocturnal formation of  $\text{HNO}_3$ , a known sink for  $\text{NO}_2$ . In fact  $\text{NO}_2$  and  $\text{NO}_3$  are in equilibrium with dinitrogen pentoxide ( $\text{N}_2\text{O}_5$ ), whose heterogeneous hydrolysis leads to nitric acid or nitrate (Phillips et al., 2013) (R3).



Both HONO and  $\text{NO}_2$  correlated better during the night ( $r^2 = 0.55$ ) and less during the day ( $r^2 = 0.23$ ), as expected due to their increased lifetimes in the absence of light. Interestingly the correlation was not so good between HONO and NO (Table S1.4), suggesting that HONO was rather behaving as a secondary species like  $\text{NO}_2$ . Hence as observed at other urbanized sites (Finlayson-Pitts et al., 2003; Acker et al., 2004) it may be assumed that nocturnal HONO builds up through the heterogeneous hydrolysis of  $\text{NO}_2$  on humid surfaces (R4):



This assumption is supported by the positive trend between the  $(\text{HONO})/(\text{NO}_2)$  ratio versus relative humidity (Figure S1.5), suggesting that the conversion of HONO from  $\text{NO}_2$  is more efficient for higher humidity levels, consistent with the role of water in reaction (R4).

Table P1.3 Summary of ambient HONO/NO<sub>x</sub> ratios reported in this work and other studies

HONO/NO <sub>x</sub> (% ppb/ppb)	Dates	Data frequency	Periods of observation	Site location	Country	Reference
2.5 ± 0.1	Aug. 2015 – Jul. 2016	hourly	Daytime, all days	10 m from a 2-lane road	Douai (France)	This study
1.7 ± 0.1	Aug. 2015 – July 2016	hourly	6:00-10:00, all days	10 m from a 2-lane road	Douai (France)	This study
1.6 ± 0.1	July 15 – Oct. 15, 2009	10-min	4:00-8:00, weekdays	Highway junction	Houston, TX (USA)	Rappenglück et al. (2013)
0.8 ± 0.1	1997 – 1998	min	6:00–14:00, all days	tunnel	Wuppertal (Germany)	Kurtenbach et al. (2001)
1.2 ± 0.35	11 – 21Mar. 2015	-	All days	tunnel	Hong Kong	Liang et al. (2017)

NH<sub>3</sub> showed very clear daily patterns for every season, with higher concentrations during daytime and a maximum in the morning around 10:00 in summer and spring, 11:00 in autumn and 12:00 in winter (Figure P1.3e). These higher daytime concentrations can be partly attributed to the volatilization of NH<sub>4</sub>NO<sub>3</sub> but also to the emission of NH<sub>3</sub> from soils with increased temperature (He et al., 1999). The delay in the peak time of NH<sub>3</sub> concentrations for the coldest season (winter) compared to the hottest one (summer) has been observed in previous studies (Wang et al., 2015). It is due to the dependence of NH<sub>3</sub> concentrations on temperature and to the difference in sunrise time with season (around 08:00-9:00 UTC in winter comparatively to around 05:00-6:00 in summer, Figure S1.2). In winter, sunrise occurs later which implies that temperatures also start to increase later, which favors the persistence of particulate ammonium nitrate over that of NH<sub>3</sub> and HNO<sub>3</sub> gases. This is also observed in the daily profiles of NO<sub>3</sub><sup>-</sup> and NH<sub>4</sub><sup>+</sup>, which show that their concentrations start to decrease later in the morning in winter when compared to other seasons (Figure P1.5b-c). Similarly, the dependence on temperature also affects the volatilization of NH<sub>3</sub> from soils and vegetation (Makkonen et al., 2014), which will occur later in winter when compared to other seasons. All these reasons justify why NH<sub>3</sub> concentrations peak later in winter. In France the vast majority of NH<sub>3</sub> (>95%) is emitted by agricultural and forestry activities, and just a minor share results from road transport and manufacturing industry (CITEPA, 2017). Accordingly, higher concentrations of NH<sub>3</sub> were observed in spring and summer, when the agricultural activities are more intense and the temperatures higher. Additional NH<sub>3</sub> emissions might come from traffic due to the use of selective catalytic reduction to reduce NO<sub>x</sub> emissions in heavy duty

diesel vehicles (Sutton et al., 2000) issued from the last European legislation. However no temporal correlation was observed between the morning peak of NO, characteristic of traffic, and the NH<sub>3</sub> morning peak observed several hours later. Therefore the contribution of traffic to NH<sub>3</sub> concentrations may be considered as negligible for this site.

Sulfur dioxide (SO<sub>2</sub>) showed clear daily cycles for every season (Figure P1.3f), with higher concentrations observed during daytime. In France, the emissions of SO<sub>2</sub> are mainly attributed to energy transformation, manufacturing industry and residential or tertiary emissions (CITEPA, 2017). Therefore the emissions can be highly variable at a given site, depending on the presence of local emitters. In Douai, the highest levels were recorded in summer and the lowest ones in winter. This is a peculiar feature since higher concentrations of SO<sub>2</sub> are usually observed in winter due to combustion emissions by domestic heating and power plants (Makkonen et al., 2012; Stieger et al., 2017). In addition, lower levels of OH radicals in winter due to reduced solar radiation lead to less oxidation of SO<sub>2</sub> and thus its concentration is expected to be higher than in summer. However, this was not observed at our site and, surprisingly, winter presented the lowest concentrations. This could be explained by the presence of an industrial zinc smelter 2 km north-east of our sampling site which emits SO<sub>2</sub>, as will be discussed later. An exceptionally low frequency of winds from this sector in winter may partly explain its lower concentrations.

### 3.2.2. Aerosols

Figure P1.5 presents the daily profiles of PM<sub>2.5</sub> and each particulate species according to the season. For PM<sub>2.5</sub> (Figure P1.5a) two peaks can be observed, one in the early morning and another one in the late evening/night. The morning peak is most likely driven by SIA (i.e. NO<sub>3</sub><sup>-</sup>, NH<sub>4</sub><sup>+</sup>, and SO<sub>4</sub><sup>2-</sup>) and traffic-related emissions (mainly BC). The evening peak is probably related to ammonium nitrate, which builds up during the night as discussed below, and to biomass burning emissions, particularly in the cold seasons. The peaks are particularly clear in spring, whereas they are less evident in the other seasons.

Nitrate (Figure P1.5b) presents clear daily patterns in every season, although less obvious in winter. As previously introduced, its concentrations are governed by the thermodynamic equilibrium between NH<sub>4</sub>NO<sub>3</sub> and the gaseous HNO<sub>3</sub> and NH<sub>3</sub>. Accordingly, the highest daily concentrations are observed in the early morning due to the nighttime accumulation of NH<sub>4</sub>NO<sub>3</sub> formed from the condensation of the precursor gases favored by low temperatures and high RH. The decrease after the morning maximum is then explained by

the volatilization of the nighttime-formed  $\text{NH}_4\text{NO}_3$ , but can also be partly attributed to the increase of the PBL height due to the development of the thermal turbulence. After reaching a minimum in the afternoon,  $\text{NO}_3^-$  starts to increase again at the end of the day. Lower  $\text{NO}_3^-$  concentrations are expected in periods with reduced traffic and less work activity (i.e. holiday periods), which are the main sources of  $\text{NO}_x$  emissions in urban sites. This is in agreement with our observations, with lowest  $\text{NO}_3^-$  concentrations in summer, a season for which two thirds of the days corresponded to school holidays. The highest average concentrations of  $\text{NO}_3^-$  were observed in spring. However, a higher frequency of air masses arriving from neighboring northeastern and central European countries associated to high mass loadings, was observed at our site during this season (as discussed further in section 3.4.2). Additionally, the heterogeneous hydrolysis of  $\text{N}_2\text{O}_5$  (R3) might also play an important role in  $\text{NO}_3^-$  production, particularly in spring, where  $\text{N}_2\text{O}_5$  production rate might be increased by higher  $\text{O}_3$  levels.

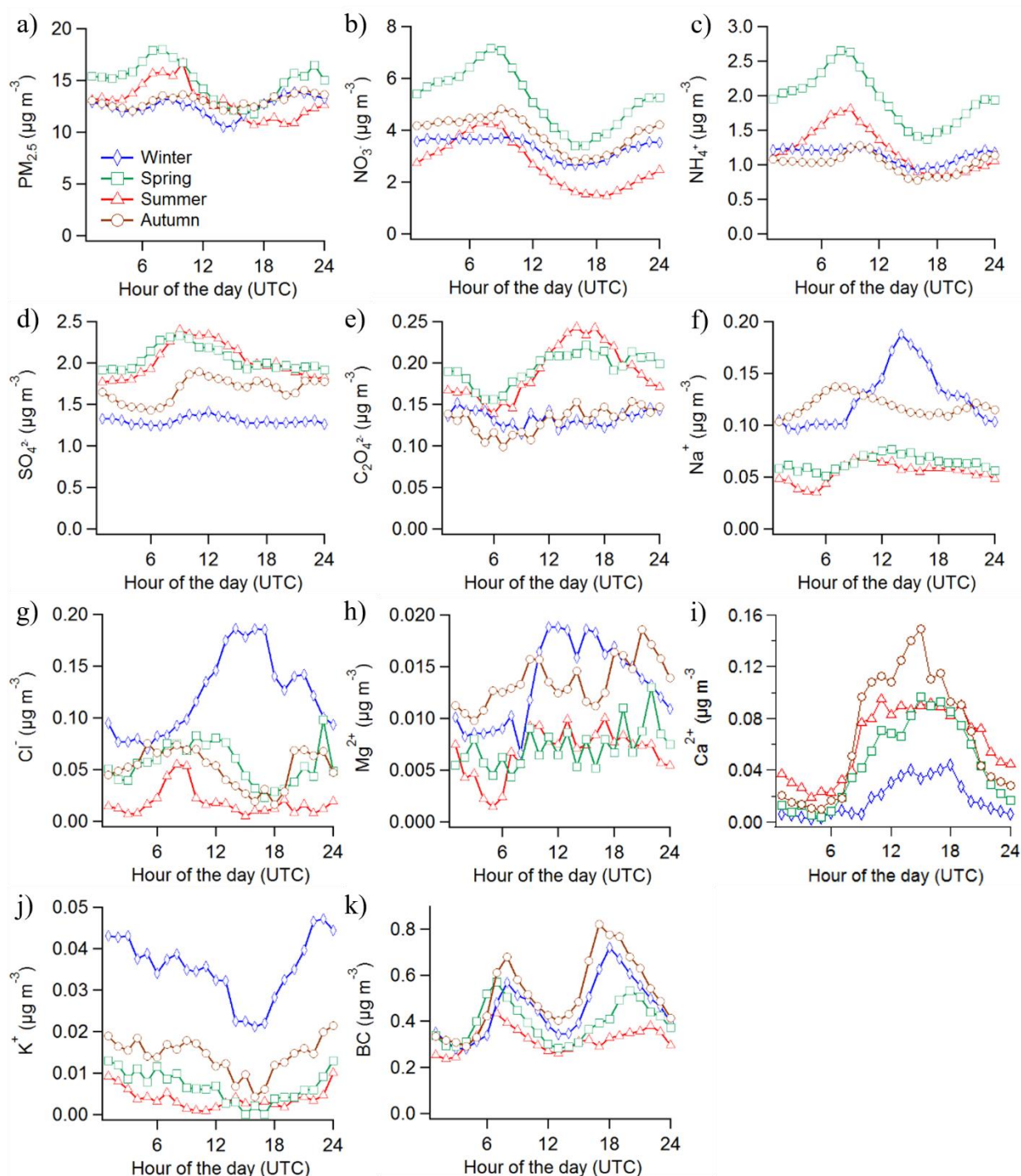


Figure P1.5 Daily profiles of (a)  $\text{PM}_{2.5}$ , (b)  $\text{NO}_3^-$ , (c)  $\text{NH}_4^+$ , (d)  $\text{SO}_4^{2-}$ , (e)  $\text{C}_2\text{O}_4^{2-}$ , (f)  $\text{Na}^+$ , (g)  $\text{Cl}^-$ , (h)  $\text{Mg}^{2+}$ , (i)  $\text{Ca}^{2+}$ , (j)  $\text{K}^+$ , and (k)  $\text{BC}$  for each season (winter: blue; spring: green, summer: red, autumn: brown).

The daily profile of  $\text{NH}_4^+$  (Figure P1.5c) was almost identical to that of  $\text{NO}_3^-$ , with concentrations peaking in the early morning and decreasing steadily until the afternoon, where they started to increase again overnight. As for  $\text{NO}_3^-$ , its concentrations were also dominated by the gas-aerosol equilibrium of  $\text{NH}_4\text{NO}_3$ . Its decrease in the afternoon is not as

strong as that of  $\text{NO}_3^-$ , which might be justified by higher concentrations of  $\text{SO}_4^{2-}$  during daytime supporting the existence of ammonium sulfate salts. The highest  $\text{NH}_4^+$  concentrations were observed in spring and summer, in agreement with the highest concentrations of  $\text{NH}_3$  observed in these seasons originating from agricultural activities. As with  $\text{NO}_3^-$ , transported air masses could cause higher concentrations of  $\text{NH}_4^+$  in spring.

$\text{SO}_4^{2-}$  (Figure P1.5d) only showed clear daily variations in spring and summer, with higher concentrations during daytime, peaking in the late morning or early afternoon. The formation of ammonium sulfate salts is generally a two-step process starting with the conversion (mostly heterogeneous) of  $\text{SO}_2$  to  $\text{H}_2\text{SO}_4$ , and subsequent neutralization with  $\text{NH}_3$ . Hence, the higher daytime concentrations of sulfate could be attributed to the oxidation of its gaseous precursor  $\text{SO}_2$ . However, no apparent relationship was observed between  $\text{SO}_2$  and  $\text{SO}_4^{2-}$ . To further assess if the local conversion of  $\text{SO}_2$  into  $\text{SO}_4^{2-}$  was significant at our site, the particulate sulfur fraction, defined as the ratio of particulate sulfur to total sulfur was also calculated, and the influence of meteorological parameters (mainly RH and T) assessed. Yet no significant correlation was obtained. In addition, it is interesting to note that the daily maximum of  $\text{SO}_4^{2-}$  appears before that of  $\text{SO}_2$ , which confirms that  $\text{SO}_2$  is not a significant local source of inorganic  $\text{SO}_4^{2-}$  at our site, and that it is likely that it has a rather regional origin. The highest  $\text{SO}_4^{2-}$  concentrations were observed in summer and spring, which could be partly attributed to a higher photochemical activity, i.e. highest concentrations of reactive species such as OH,  $\text{HO}_2$ ,  $\text{RO}_2$  and  $\text{O}_3$  (Dudkin et al., 2002) in the atmosphere, leading to a higher rate of conversion from  $\text{SO}_2$  to  $\text{SO}_4^{2-}$  in aged air masses (Lee and Kang, 2001). Similarly to  $\text{NO}_3^-$  and  $\text{NH}_4^+$ , a high frequency of air masses from northeastern and central Europe contributed to the high observed concentrations of  $\text{SO}_4^{2-}$  in spring. We compared these results with a study performed in Lens (20 km NW of Douai) in the  $\text{PM}_{10}$  fraction, which showed also a significant higher contribution of  $\text{SO}_4^{2-}$  in summer (Waked et al., 2014), which may be related in that case either to photochemical oxidation of sulfur or to soil dust resuspension.

Similarly to  $\text{SO}_4^{2-}$ , oxalate  $\text{C}_2\text{O}_4^{2-}$  (Figure P1.5e) presented higher concentrations in summer and spring, and during daytime.  $\text{C}_2\text{O}_4^{2-}$  correlated slightly with  $\text{SO}_4^{2-}$  and  $\text{NH}_4^+$ , suggesting that these compounds could partly originate from similar processes. Oxalic acid is a dicarboxylic acid which is usually an end-product of photochemical oxidation for several hydrocarbons (Martinelango et al., 2007). Positive correlations with temperature and  $\text{O}_3$  were only observed in spring and summer, indicating that photochemical production could be a

predominant formation process in these seasons, and partly explaining the higher concentrations of  $\text{C}_2\text{O}_4^{2-}$  observed during daytime. In winter slightly positive correlations were observed with  $\text{K}^+$ , meaning that part of wintertime  $\text{C}_2\text{O}_4^{2-}$  could originate from biomass combustion processes. On the other hand, small correlations with  $\text{Ca}^{2+}$  were observed in some months and could imply that soil dust would be a minor source of oxalate in certain periods. The concentrations found in this study ( $0.16 \pm 0.12 \mu\text{g m}^{-3}$  on average) are higher than those measured at an urban background site in Zurich, Switzerland for the months of August and September of 2002 and March of 2003 (Fisseha et al., 2006) (monthly averages of 0.03-0.06  $\mu\text{g m}^{-3}$ ), but inferior to those observed at a suburban site in Florida, USA in May 2002 (Martinelango et al., 2007) ( $0.29 \mu\text{g m}^{-3}$ ) and at a suburban site in Hong Kong from April 2012 to February 2013 ( $0.34 \pm 0.18 \mu\text{g m}^{-3}$ ). For spring and summer, the daily profiles are similar to those presented in the abovementioned studies, with higher concentrations in the afternoon and lower during the night, suggesting that photochemical production during daytime was also a predominant process.

The other minor ions ( $\text{Cl}^-$ ,  $\text{Na}^+$ ,  $\text{K}^+$ ,  $\text{Mg}^{2+}$ ,  $\text{Ca}^{2+}$ ) presented often many data points below or close to the detection limits with the exception of some periods of the year.  $\text{Na}^+$  and  $\text{Cl}^-$  showed the highest concentrations in winter (Figure P1.5f-g). This was likely attributed to a higher frequency of air masses enriched in sea salt from the ocean and the North Sea. In this season, the daily profile of  $\text{Na}^+$  and  $\text{Cl}^-$  is very clear, with highest concentrations during daytime and a maximum observed in the afternoon, mainly attributed to strongest winds. An additional peak of chloride is seen in the evening, which could be related to emissions of KCl from biomass burning.  $\text{Cl}^-$  correlated slightly with  $\text{K}^+$  in January, when the lowest temperatures were reached. The daily profiles of  $\text{Na}^+$  in the other seasons are not as clear, and might be more representative of aged marine air masses where  $\text{Cl}^-$  has been depleted and  $\text{NaNO}_3$  has been formed. For  $\text{Cl}^-$ , the concentrations in the other seasons were even lower and robust conclusions cannot be drawn due to the uncertainty of the data. Similarly to  $\text{Na}^+$  and  $\text{Cl}^-$ ,  $\text{Mg}^{2+}$  presented higher concentrations in winter and also during daytime (Figure P1.5h). The concentrations in the other seasons were almost all the time below the detection limit.  $\text{Mg}^{2+}$  correlated very weakly with  $\text{Ca}^{2+}$  suggesting that crustal dust did not contribute to its concentrations and that it mainly had a marine origin.

$\text{Ca}^{2+}$  (Figure P1.5i) showed similar concentrations throughout the year except in winter, when the lowest concentrations were observed. The daily profiles were similar in all seasons, with highest concentrations during daytime and a maximum in the afternoon, which

was mainly attributed to higher wind speed causing soil erosion and dust resuspension. The weekly trends for  $\text{Ca}^{2+}$  show significantly higher concentrations during the weekdays (Figure S1.4). This might be attributed to road traffic causing dust resuspension. Additionally,  $\text{Ca}^{2+}$  was positively correlated with temperature and anti-correlated with relative humidity. A number of studies has demonstrated the influence of higher wind speeds and temperature and low relative humidity on dust generation (Csavina et al. (2014) and references therein).

$\text{K}^+$  is considered a trace marker for biomass combustion (Urban et al., 2012), and therefore it is expected in cold days due to an increase in domestic wood burning. Accordingly, it only presented concentrations above the detection limit in winter and later autumn and early spring (Figure P1.5j). The daily profile for winter is very clear, with highest concentrations in the evening and decreasing thereafter, in accordance with domestic wood combustion which usually occurs after working hours in the evening.

Finally, BC (Figure P1.5k) presented a very clear profile similar to that of NO and  $\text{NO}_2$ , with a maximum in the morning and in the afternoon resulting from traffic emissions and household combustion. While in summer and spring the morning peak was more important than that of the afternoon, in autumn and winter the contrary was observed, suggesting the importance of biomass combustion in these last seasons. The afternoon peak was almost not seen in summer, which reflects the reduced occurrence of traffic and biomass combustion in this season. Overall, and similarly to  $\text{NO}_x$ , the highest concentrations were observed in autumn and winter, highlighting an increase of traffic and biomass combustion during these periods.

### **3.3. Study of ratios and SIA partitioning**

#### **3.3.1. Ammonium neutralization ratio (NR) and gas ratio (GR)**

The neutralization state of the aerosol in each season was evaluated using NR, as defined in section 2.3. The observed  $\text{NH}_4^+$  was plotted against the predicted  $\text{NH}_4^+$ , *i.e.* the required  $\text{NH}_4^+$  to fully neutralize  $\text{NO}_3^-$  and  $\text{SO}_4^{2-}$ . The seasonal averages and daily profiles of NR are shown in Figure P1.6.



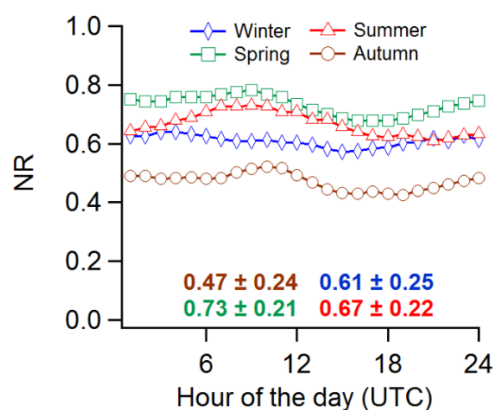


Figure P1.6 Neutralization ratio (NR) daily profiles for each season, with the corresponding seasonal averages.

We observed that SIA was more acidic in autumn (average NR:  $0.47 \pm 0.24$ ) in comparison with the rest of the year (average NR:  $0.62 \pm 0.25$ ), which leads to different hypotheses. On the one hand, the lowest levels of  $\text{NH}_3$  and  $\text{NH}_4^+$  and highest ones of  $\text{NO}$  and  $\text{NO}_2$ , precursors of  $\text{NO}_3^-$  secondary aerosols, were observed in autumn. Therefore, it is possible that the low NR in autumn is a result of both a decrease of reduced nitrogen and an increase in nitrate- and/or sulfate-based acidic species emitted by combustion sources such as traffic. However, the daily profile of NR does not reveal a decrease at traffic hours, suggesting that traffic emissions do not have a major effect on the aerosol NR at our site. On the other hand, high concentrations of  $\text{Na}^+$  were observed in periods of low NR (Figure P1.7a), mainly in autumn as explained previously. These high  $\text{Na}^+$  concentrations probably originated from the Atlantic Ocean in accordance with the SW origin of predominant winds in autumn. However, as the ocean is a few hundred kilometers away from our site, it is likely that  $\text{NaCl}$  could have reacted with gaseous  $\text{HNO}_3$  during its transport to our site that crosses dense urban areas (e.g. Le Havre-Rouen harbour and the Paris area) to give place to particulate  $\text{NaNO}_3$  and gaseous  $\text{HCl}$ . (Dasgupta et al., 2007). Therefore the neutralization ratio is inferior to 1 because the total  $\text{NO}_3^-$  molar concentration may correspond to the sum of  $\text{NH}_4\text{NO}_3$  and  $\text{NaNO}_3$  molar concentrations. When the autumn NR is calculated taking into account  $\text{NaCl}$ , a higher value ( $0.61 \pm 0.25$ ) is obtained, in the range of the other seasonal NR confirming the influence of marine aerosols. Another potential effect related to marine air masses is a measurement artefact related to the consumption of  $\text{NH}_4^+$  and  $\text{NH}_3$  by microorganisms transported in marine air masses (rich in  $\text{Na}^+$ ) into the MARGA system. This negative artefact has been previously reported in other studies (Rumsey et al., 2014). The NWR plot of NR (Figure P1.7b) reveals that the lowest NR values are observed for high wind speeds from the SW sector, which are related to air masses under marine influence (Atlantic

Ocean). On the contrary, continental air masses from the NW are linked with more neutralized aerosols ( $NR \approx 1$ ). In summary, the impact of marine air on the observed low NR in autumn might be a combination of all the above-mentioned factors.

Other studies attributed the apparent particle acidity mainly to the non-inclusion in the NR calculation of species linked to road dust emissions (Makkonen et al., 2012; Stieger et al., 2017). However, this should not play a major role in the present work given their small concentrations. Indeed, when the aerosol NR was calculated taking into account all the water-soluble inorganic ions analyzed by the MARGA (to see the effect of dust and other ions like the marine ones), slightly higher values were obtained (average NR:  $0.73 \pm 0.22$ ) but a fraction of the aerosol phase still remained acidic. The influence of the bisulfate ion was assessed with the use of ISORROPIA II. The module predicted significant concentrations of the bisulfate ion during periods of increased acidity (i.e. autumn). However, the concentrations were rather low and did not totally justify the observed acidity. The causes of the observed acidity are not straightforward at all. While models such as ISORROPIA may suggest the existence of bisulfate, there are other possible explanations such as the influence of organic matter through organic acids or organic coatings preventing inorganic species to reach thermodynamic equilibrium (Silvern et al., 2017).

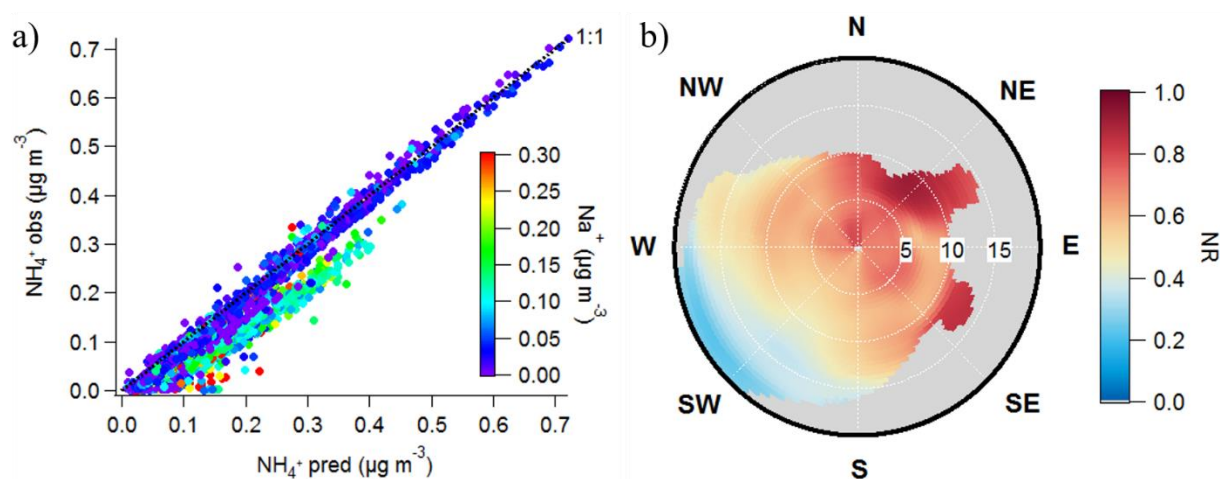


Figure P1.7 (a) Observed vs. predicted  $NH_4^+$  colored by  $Na^+$  concentration; and (b) NWR annual plot for the neutralization ratio (NR).

The values presented here are notably lower than those at different sites in Belgium, where NR ratios higher than 1 were associated with an excess of  $NH_4^+$  (Bencs et al., 2008), but close to those found at a rural site in Germany (Stieger et al., 2017), where fluctuations of the NR between 0.5 and 1 were also observed, with lower values during autumn and winter

which were attributed to more intense anthropogenic emissions. Other studies have also reported measurements of acidic aerosols, for instance in the USA (Kim et al., 2015) or in China (Shi et al., 2017).

In addition GR was also calculated in order to evaluate which species between  $\text{HNO}_3$  and  $\text{NH}_3$  limits the formation of  $\text{NH}_4\text{NO}_3$  (Ansari and Pandis, 1998). The annual average of  $5.7 \pm 6.6$  is close to that reported previously in the city in Paris of 7.3 (Petetin et al., 2016). GR was greater than 1 during most of the campaign, indicating that the formation of  $\text{NH}_4\text{NO}_3$  was limited by nitric acid, as already reported in continental Europe (Pay et al., 2012).

### 3.3.2. Hourly gas-aerosol partitioning of SIA

The thermodynamics of the  $\text{K}^+\text{-Ca}^{2+}\text{-Mg}^{2+}\text{-NH}_4^+\text{-SO}_4^{2-}\text{-NO}_3^-\text{-Cl}^-\text{-H}_2\text{O}$  aerosol system has been evaluated with the use of the thermodynamic equilibrium model ISORROPIA II. The results presented here are those obtained by using the forward mode and the total (sum of gas and aerosol) hourly concentrations of observed  $\text{NH}_3$ ,  $\text{HCl}$ ,  $\text{HNO}_3$ ,  $\text{H}_2\text{SO}_4$ ,  $\text{Na}^+$ ,  $\text{Ca}^{2+}$ ,  $\text{K}^+$  and  $\text{Mg}^{2+}$ , as well as the temperature and RH. Additionally, the stable solution, in which salts precipitate once the aqueous phase becomes saturated, was chosen. Although very important differences were observed when the reverse (only aerosol phase as an input) mode was used, we did not observe remarkable differences between the stable and metastable solutions. The results for  $\text{NH}_3$ ,  $\text{HNO}_3$ ,  $\text{NH}_4^+$  and  $\text{NO}_3^-$  are summarized in Figure P1.8.

For  $\text{NH}_3$  and  $\text{NH}_4^+$ , the model generally predicted very well the concentrations, with  $r^2$  values of 0.99 and 0.96, respectively, and slopes very close to 1.  $\text{NO}_3^-$  was generally observed to be in the particulate phase, and the model showed an overall excellent agreement with the observations ( $r^2 = 0.97$ , slope: 1.03). There was however a disagreement with some of the  $\text{NO}_3^-$  observed concentrations, which were much lower in the model predictions, suggesting it should be in the gas phase. The modelled  $\text{HNO}_3$  was completely different to the observed concentrations. This is clearly reflected in the time series of the observed and modelled  $\text{HNO}_3$  (Figure S1.6a): the modelled  $\text{HNO}_3$  presents lower concentrations in winter and higher in summer when compared to the observed  $\text{HNO}_3$ . This is in accordance with the dependence of  $\text{HNO}_3$  on the gas-aerosol equilibrium of ammonium nitrate with temperature and RH, namely a lower  $\text{HNO}_3$  concentration under low temperature and high humidity as in winter conditions (conversely a higher  $\text{HNO}_3$  concentration under high temperature and low humidity typical of summer conditions). The daily profile of the predicted and modelled  $\text{HNO}_3$  (Figure S1.6b) confirms this, with the expected afternoon maximum in agreement with a higher temperature

and lower relative humidity clearly seen for the modelled  $\text{HNO}_3$ . The discrepancy of the measured  $\text{HNO}_3$  is likely due to the adsorption of this gas in the sampling line (particularly along the PE tubing) and to a possible high nitrate blank in the chromatographic system caused by the use of nitric acid as eluent for cations (Makkonen et al., 2012). In summer, the measured  $\text{HNO}_3$  concentration was lower than expected by the model (Figure S1.6a). This implies that the adsorption effect had been important, even if the temperature and relative humidity were rather unfavorable, because the effect of the high pressure of nitric acid predominated.

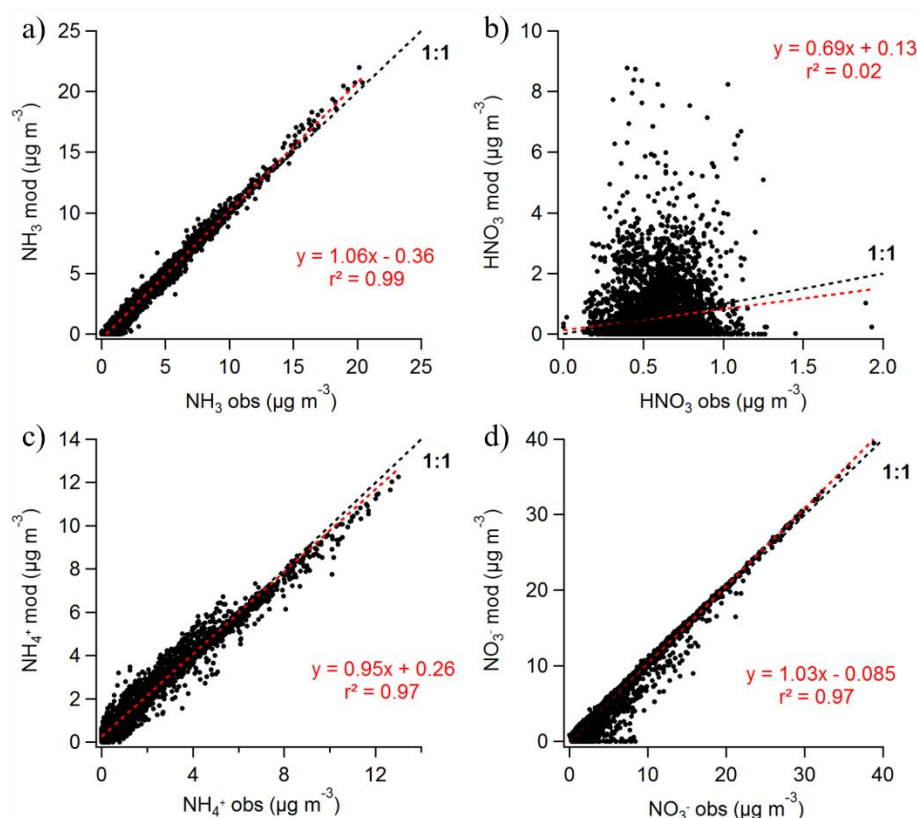


Figure P1.8 Comparison between ISORROPIA II predicted values and MARGA measurements for (a)  $\text{NH}_3$ , (b)  $\text{HNO}_3$ , (c)  $\text{NH}_4^+$ , and (d)  $\text{NO}_3^-$

In winter, the apparent observed effect was a measured concentration of  $\text{HNO}_3$  higher than expected by the model, consistent with a negligible adsorption effect, even if the temperature and relative humidity were rather favorable, because the effect of a low pressure of nitric acid was predominant. In this case, the higher observed concentration of  $\text{HNO}_3$  compared to the thermodynamic prediction may be linked to interference from the cation eluent in the nitrate and nitric acid signals (Makkonen et al., 2012), which was evaluated to be up to a maximum of  $0.5 \mu\text{g m}^{-3}$  in our conditions. In addition Phillips et al. (2013) evidenced the existence of an interference from  $\text{N}_2\text{O}_5$  to the nocturnal  $\text{HNO}_3$  causing an overestimation

of nitric acid. No corrections were applied to the total concentrations of these species however, given the magnitude of the concentrations for particulate nitrate, and the fact that  $\text{HNO}_3$  was anyway not measured correctly by the instrument (as explained in the Supplementary Material sections 1.1. and 1.2) and therefore not considered further in the article.

### **3.4. Source identification**

#### **3.4.1. Local sources**

The NWR approach was used over the 1-year long dataset to identify potential local emission sources for precursor gases and particulate species. The corresponding polar plots are shown in Figure P1.9 for the main precursor gases and particulate species, whereas those for other measured gaseous and particulate species at the seasonal scale are available in the SM (Figure S1.7).

$\text{SO}_2$  presented high concentrations in the NNW sector (Figure 1.9a) when medium wind speeds occurred (5 to 10  $\text{km h}^{-1}$ ). As previously presented, a zinc smelter located 2 km NNW of our sampling site might contribute to these high concentrations, particularly its fluidized bed roasting unit where sulfur dioxide (as well as nitrogen oxides) is produced during the high-temperature oxidation of the sulfidic zinc ore under air conditions. This highlights the fact that most of the  $\text{SO}_2$  presents a local origin while the contribution from regional emissions is much less important.

$\text{NH}_3$  showed higher concentrations when winds came from the NE sector (Figure 1.9b). For weak winds (around 5  $\text{km h}^{-1}$ ), possible local sources of  $\text{NH}_3$  may be a slaughterhouse and a waste water treatment plant located NE to our sampling site in the nearby industrial area. For stronger winds ( $> 10 \text{ km h}^{-1}$ ) from the ENE direction, there is also an important regional contribution which might be associated to agricultural emissions. This is clearly seen in the seasonal plots in Figure S1.7.

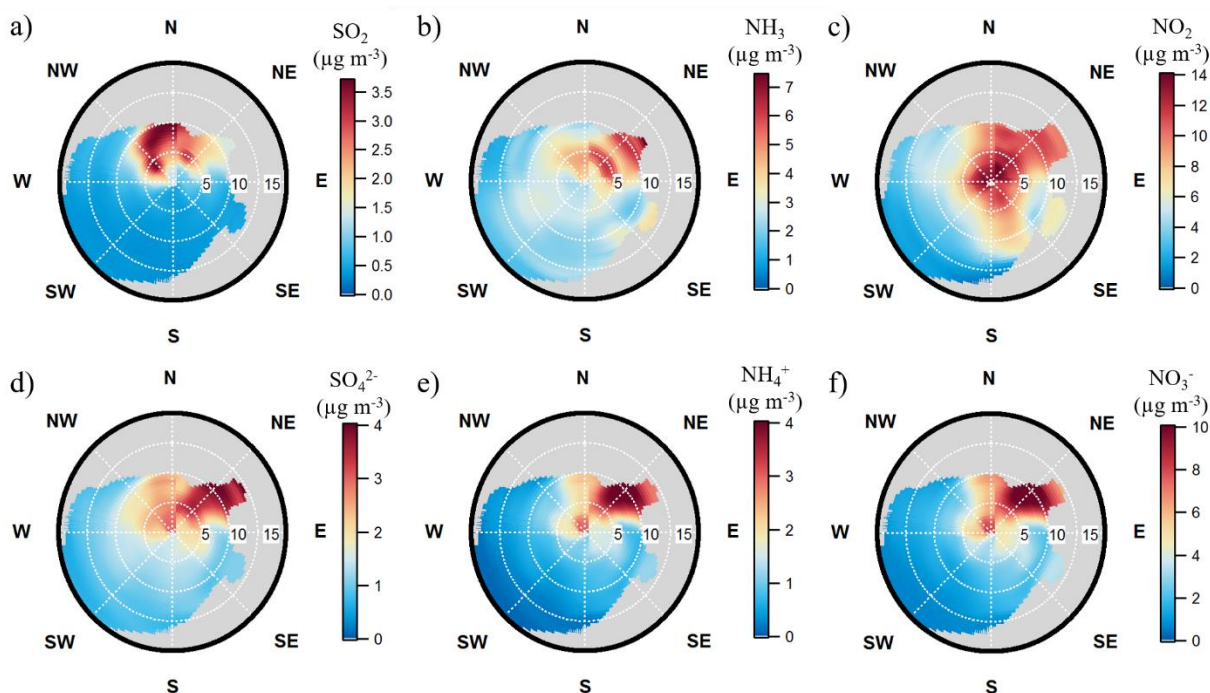


Figure P1.9 NWR plots for the main precursor gases and particulate ions (concentrations in  $\mu\text{g m}^{-3}$ ) over the whole field campaign. The radial and tangential axes represent the wind direction and speed in  $\text{km h}^{-1}$ , respectively.

There was a clear local contribution to the observed concentrations of HONO, NO and  $\text{NO}_2$ , which showed high concentrations at low wind speeds ( $< 5 \text{ km h}^{-1}$ ), likely due to vehicle emissions. The local contribution is particularly clear for NO, which presents highest concentrations in the NE quadrant, where a 2-lane roadway adjacent to our sampling site leads to the nearby industrial area through a narrow 1-lane tunnel, causing frequent stops and restarts of vehicles and transient congestions. However, for the more oxidized species HONO and particularly  $\text{NO}_2$ , there is an important distant contribution from the ENE direction not seen for NO.

$\text{NO}_3^-$ ,  $\text{NH}_4^+$  and  $\text{SO}_4^{2-}$  presented very similar NWR plots (Figure P1.9d-f), with highest concentrations associated with medium and high wind speeds from the NNE sector. This suggests that there is a significant contribution from long-range transport (LRT) in the form of  $\text{NH}_4\text{NO}_3$  and  $(\text{NH}_4)_2\text{SO}_4$ . The long-range contribution seems to be particularly important for  $\text{SO}_4^{2-}$ . Long-range contribution of SIA has been observed in other studies in the regions of Paris (Petit et al., 2015) and northern France in Lens (Waked et al., 2014). In addition to LRT, high concentrations are also observed with low wind speeds ( $< 5 \text{ km h}^{-1}$ ) in the NNW direction. Specifically in autumn (Figure S1.7), high concentrations were observed with medium wind speeds from the NNW sector, suggesting an important possible impact

from the industrial zinc smelter. This is consistent with the fact that this industry emits noticeable amounts of  $\text{NO}_x$  and  $\text{SO}_2$  and that the autumn weather conditions seemed favorable to SIA formation. The NWR plot of  $\text{SO}_4^{2-}$  shows that highest concentrations are observed for strong winds in the NE sector. This suggests that the local  $\text{SO}_2$  does not explain all the  $\text{SO}_4^{2-}$  observed at our site, and that an important part of  $\text{SO}_4^{2-}$  is due to other causes such as LRT.

The NWR plot for  $\text{C}_2\text{O}_4^{2-}$  does not show a preferential region for high contributions and suggests this compound has rather a regional contribution, which is also in accordance with the wide variety of its volatile organic precursors and formation processes. However, slightly high concentrations observed at low wind speeds might also indicate significant contributions from local sources such as traffic, local biomass combustion or industrial activities.

$\text{Na}^+$ ,  $\text{Cl}^-$  and  $\text{Mg}^{2+}$  present highest concentrations associated to strong SW winds, suggesting a pure long-range contribution related to air masses from the Atlantic Ocean rich in sea salt. In winter there is an enhancement of  $\text{Na}^+$  and  $\text{Cl}^-$  observed with calm winds which is likely caused by road salting in order to prevent icing. Moreover,  $\text{Na}^+$  and  $\text{Mg}^{2+}$  also present high concentrations from the N sector (as seen in the seasonal NWR plots) suggesting a contribution from the North Sea.

The highest concentrations of  $\text{Ca}^{2+}$  are observed with low-to-medium wind speeds from the NE, which is probably related to road dust resuspension. This is particularly important in autumn, in accordance with the highest observed  $\text{NO}_x$  emissions. In addition, particularly high concentrations of  $\text{Ca}^{2+}$  are observed in spring for high wind speeds from the ENE sector, suggesting an important long-range contribution of this compound, similarly to  $\text{NO}_3^-$ ,  $\text{NH}_4^+$  and  $\text{SO}_4^{2-}$ .

Finally, BC clearly reflects a local origin, very similar to that of NO, and likely associated to vehicle emissions and household combustion. The same conclusion is reached for  $\text{K}^+$  and Delta C, mainly associated to biomass combustion from the nearby suburban residential area, as highlighted by their winter plots (Figure S1.7).

### **3.4.2. Distant sources**

To further analyze the contribution of distant sources, PSCF was applied to each particulate species which had shown, at least for one season, a regional origin (this excluded  $\text{K}^+$ , BC and Delta-C). In this study, the threshold concentration was set at the 75<sup>th</sup> percentile.



In addition, all back-trajectories were weighted according to their frequency by the use of a sigmoidal function. The PSCF maps for the main particulate species are shown in Figure P1.10, where the color scale indicates the probability for a specific emission region as origin of the measured species. For other particulate species, PSCF graphs are available in the SM (Figure S1.8).

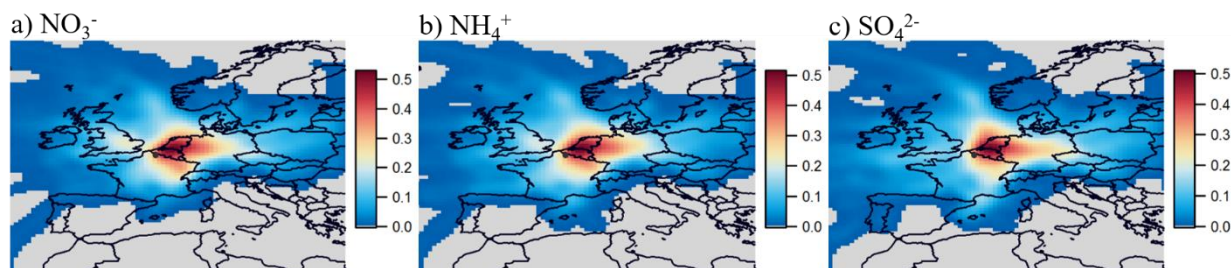


Figure P1.10 PSCF analysis for the three main particulate ions. The selected threshold is set at the 75<sup>th</sup> percentile. All used back-trajectories were weighted using a sigmoidal function.

Highest probabilities for  $\text{NO}_3^-$ ,  $\text{NH}_4^+$  and  $\text{SO}_4^{2-}$  are observed when air masses arrive from Belgium, The Netherlands and western Germany. These neighboring regions are known to present rather high SIA concentrations as shown in the EMEP maps of concentrations for the “fine+coarse  $\text{NO}_3^-$ ” and “fine  $\text{NH}_4^+$ ” modelled for the year 2015 based on emissions from 2014 (Figure S1.9). The PSCF map of  $\text{Ca}^{2+}$  presents some similar source areas, centered over Belgium and southern Netherlands, which correspond to the densest road network in Europe. Therefore this  $\text{Ca}^{2+}$  source might be attributed to intense traffic in this region leading to dust resuspension. Similar results were observed by Waked et al. (2014) at the site of Lens, located 20 km east of Douai, for PSCF applied to PMF factors in the  $\text{PM}_{10}$  size fraction. Particularly the PSCF maps for the “nitrate-rich”, “sulfate-rich” and “dust” factors match well with our PSCF maps for  $\text{NO}_3^-$ ,  $\text{SO}_4^{2-}$  and  $\text{Ca}^{2+}$ , respectively. In a previous campaign carried out in Douai (Chakraborty et al., in prep.), similar results were also observed for the  $\text{NR-PM}_{10}$ .

The source area of  $\text{C}_2\text{O}_4^{2-}$  is less clear and different regions seem to contribute to high concentrations of this organic ion, as suggested by the NWR plot in the previous section. However, it is clear that most  $\text{C}_2\text{O}_4^{2-}$  presents a continental origin, with high probabilities when air masses came from Belgium and eastern France.

For  $\text{Cl}^-$ ,  $\text{Na}^+$  and  $\text{Mg}^{2+}$ , as expected, higher probabilities are observed when air masses come from the North Sea and the English Channel.



### 3.5. Characteristics of high daily PM<sub>2.5</sub> concentrations

High daily PM<sub>2.5</sub> concentrations were further investigated to determine the factors driving their occurrence. Such a study becomes relevant in the application of mitigation policies, which are generally implemented at the local scale. In the European Union, only the annual average of PM<sub>2.5</sub> is limited to 25  $\mu\text{g m}^{-3}$ , and no limitations or recommendations are given for daily values. Nevertheless, the WHO sets a daily guideline value of 25  $\mu\text{g m}^{-3}$ , which is taken here as a criterion to discern days of high daily PM<sub>2.5</sub> concentrations from days of lower ones. The time series of daily averaged PM<sub>2.5</sub> concentrations during the whole campaign together with the meteorological parameters is shown in Figure S1.1. Days with high concentrations were observed throughout the whole year, with significant episodes (defined as continuous periods lasting more than 48 hours) in October 2015, January-March 2016 and end of May 2016. On an hourly basis, spring is the season with the more elevated number of hourly concentrations exceeding 25  $\mu\text{g m}^{-3}$  with an hourly maximum of 72  $\mu\text{g m}^{-3}$ , followed by winter and autumn (Figure P1.11a). No episode was recorded in summer.

In general, low PBL heights ( $333 \pm 308$  m) and wind speeds ( $0.8 \pm 0.6$  m s<sup>-1</sup>) were observed for high daily concentrations (PM<sub>2.5</sub>  $\geq 25$   $\mu\text{g m}^{-3}$ ) when compared to lower ones (for PM<sub>2.5</sub>  $< 25$   $\mu\text{g m}^{-3}$ , average PBL height and wind speed were  $549 \pm 432$  m and  $1.6 \pm 1.1$  m s<sup>-1</sup>, respectively). Most episodes were observed during dry and anticyclonic conditions except for late May 2016. The average composition of PM<sub>2.5</sub> for hourly concentrations higher than 25  $\mu\text{g m}^{-3}$  was significantly different compared to the one for concentrations lower than 25  $\mu\text{g m}^{-3}$  (Figure P1.11b and c), with a significant higher contribution of SIA (67% instead of 49%). The speciation of SIA was also changed with a nitrate-to-sulfate ratio of 3.25 for exceedance days and 1.70 for non-exceedance days, indicating an increase of ammonium nitrate during the pollution episodes.

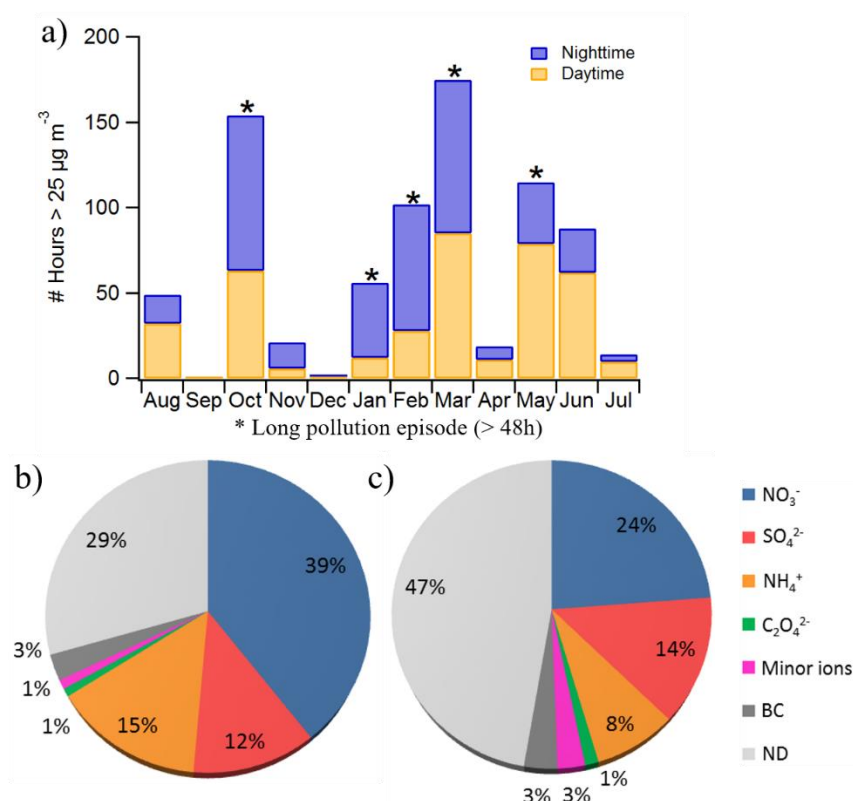


Figure P1.11 (a) Number of hours when hourly PM<sub>2.5</sub> is above 25 µg m<sup>-3</sup>. (b) Average chemical composition for PM<sub>2.5</sub> hourly mass concentrations above 25 µg m<sup>-3</sup> and (c) below 25 µg m<sup>-3</sup>

Four exceedance episodes lasting more than 48 hours which occurred during the months of January, February, March and May 2016 were further analyzed in detail in order to study and identify the formation of secondary particulate species and the potential contributions of primary local emissions versus LRT. The October 2015 episode was excluded due to the lack of half of the chemical composition data. The main characteristics for each episode are summarized in Table S1.4 while maps of 72-h back trajectories and time profiles of RH, temperature, wind direction and speed, precursor gases (NO<sub>x</sub>, HONO, NH<sub>3</sub> and SO<sub>2</sub>), total PM<sub>2.5</sub> and major particulate pollutants (NO<sub>3</sub><sup>-</sup>, NH<sub>4</sub><sup>+</sup>, SO<sub>4</sub><sup>2-</sup>, oxalate, BC, and the sum of minor ions), can be found in Figure S1.10. Each exceedance episode has been described with detail in the supplementary material, while only the general characteristics are given in the next paragraph.

Table P1.4 Summary of PM<sub>2.5</sub> chemical composition for each high concentration episode (concentrations in  $\mu\text{g m}^{-3}$ )

Dates (2016)	Duration (h)	Mean hourly PM <sub>2.5</sub>	Max hourly PM <sub>2.5</sub>	Mean NO <sub>3</sub> <sup>-</sup>	Mean SO <sub>4</sub> <sup>2-</sup>	Mean NH <sub>4</sub> <sup>+</sup>	Mean BC	Mean OM*	Mean SIA/PM <sub>2.5</sub> (%)
19-21 Jan	67	30.4	49.0	14.4	2.7	5.2	1.7	4.8	73
16-18 Feb	66	27.0	38.0	8.7	2.0	3.0	1.1	11.5	51
10-18 Mar	189	32.6	72.0	14.3	4.8	5.7	0.6	6.3	76
26-29 May	63	32.0	57.0	12.6	4.2	5.0	0.5	9.2	68

\* Value calculated assuming OM represents the difference between PM<sub>2.5</sub> mass with the mass of all other particulate species.

Generally all pollution episodes were dominated by SIA, particularly NO<sub>3</sub><sup>-</sup>, which in some cases reached contributions of more than 50% of the total PM<sub>2.5</sub> mass. A high contribution of SIA to total PM for high PM values has already been reported in the region. For instance Waked et al. (2014) reported a contribution to PM<sub>10</sub> of sulfate-rich and nitrate-rich factors of 29% and 54% for PM<sub>10</sub> lower and higher than 42.5  $\mu\text{g m}^{-3}$ , respectively. Oliveira (2017) also showed an increased contribution of SIA to PM<sub>10</sub> in several sites of Northern France (up to 78% depending on the site). In Paris, SIA was also found to be a major contributor during pollution episodes, particularly when back-trajectories originated in Belgium, The Netherlands and Germany (Petit et al., 2015). The difference between the total PM<sub>2.5</sub> mass and the sum of all measured compounds was used as an indicator of the concentration of OM, which appeared quite low in every episode except in February, where the estimated OM was higher than 50% in the first half of the pollution episode.

All of these four episodes have in common unfavorable dispersion conditions (low wind speeds) resulting in the accumulation of PM<sub>2.5</sub> from local sources. In addition, regional contributions always originated from the N to E sectors pointing at the Netherlands, Belgium and Germany. The particulate chemical composition in all the episodes was clearly dominated by SIA, mainly NH<sub>4</sub>NO<sub>3</sub>. This partitioning of NH<sub>4</sub>NO<sub>3</sub> towards the aerosol phase was favored by local weather conditions with relatively high RH (75.1 to 84.5%) and low temperature (-0.4 to 6.3°C), except for the episode of late May (17.4°C). The winter episodes had rather significant contributions from combustion sources (residential biomass burning and road traffic) as indicated by the high mean concentrations of BC (Table P1.4), while the spring

episodes were significantly influenced by agricultural emissions as shown by the high concentrations of  $\text{NH}_3$  (Figure S1.10).

#### 4. Conclusions

The combination of a MARGA and a 2-wavelength Aethalometer has enabled to build up for the first time in the north of France a one-year long database of hourly concentrations of precursor gases and inorganic aerosols at a suburban site, and has allowed us to explain the main drivers of SIA in these conditions, their time variability and their geographical origins. The major conclusions are summarized below:

- The main species forming SIA in the  $\text{PM}_{2.5}$  observed at our site are  $\text{NH}_4\text{NO}_3$  and  $(\text{NH}_4)_2\text{SO}_4$ , with a predominance of ammonium nitrate during most of the year except in summer.
- Long-range transport (LRT) of secondary aerosols and precursor gases from Belgium, The Netherlands and Germany are the main contributors to SIA in the north of France.
- Local emissions are not as determining as LRT but might also play an important role, particularly during the cold months, where local traffic and biomass burning contribute significantly to  $\text{NO}_x$  emissions and  $\text{PM}_{2.5}$  concentrations.
- Several high concentration episodes have been highlighted in winter and spring, in which SIA have contributed to most of the  $\text{PM}_{2.5}$  mass. Almost all episodes have been linked to LRT combined with meteorological conditions unfavorable to dispersion.
- The thermodynamic conditions have also influenced the SIA observed at our site, especially regarding the formation of  $\text{NH}_4\text{NO}_3$ .

In view of these results, mitigation policies in the north of France should focus on reducing emissions of precursor gases such as  $\text{SO}_2$ ,  $\text{NO}_x$  and  $\text{NH}_3$ . A substantial reduction of the first two has already been achieved in the last years, but the emissions of  $\text{NH}_3$  have not decreased and are still the same than 30 years ago (CITEPA, 2017). However, given the importance of LRT contribution at our site, it is also a priority to put an emphasis on European policies to reduce emissions of precursor gases in north-eastern countries in the vicinity of the north of France.

## 5. Data availability

Data from all instruments are available upon request to the corresponding author, E. Perdrix (esperanza.perdrix@imt-lille-douai.fr).

## 6. Acknowledgements

IMT Lille Douai acknowledges financial support from the CaPPA project, which is funded by the French National Research Agency (ANR) through the PIA (Programme d'Investissement d'Avenir) under contract ANR-11-LABX-0005-01, the CLIMIBIO project, both financed by the Regional Council "Hauts-de-France" and the European Regional Development Fund (ERDF); and the Central Laboratory of Air Quality Monitoring (LCSQA). This field campaign was carried out within the framework of the ISARD project funded by the AACT-AIR (ADEME) program (grant 1562C0011) with the support of the city of Douai, the urban community of Douai area (CAD), the mixed syndicate for public transport of Douai area (SMTD), the territorial coherence scheme in charge of the Douai area (SCoT Grand Douaisis) and atmo Hauts-de-France. R. Roig Rodelas thanks ARMINES for his PhD fellowship. The authors thank atmo Hauts-de-France and Météo-France for providing air monitoring and meteorological data, respectively.

## 7. References

- Aan de Brugh, J. M. J., Henzing, J. S., Schaap, M., Morgan, W. T., van Heerwaarden, C. C., Weijers, E. P., Coe, H. and Krol, M. C.: Modelling the partitioning of ammonium nitrate in the convective boundary layer, *Atmos. Chem. Phys.*, 12(6), 3005–3023, doi:10.5194/acp-12-3005-2012, 2012.
- Acker, K., Spindler, G. and Brüggemann, E.: Nitrous and nitric acid measurements during the INTERCOMP2000 campaign in Melpitz, *Atmos. Environ.*, 38(38), 6497–6505, doi:10.1016/j.atmosenv.2004.08.030, 2004.
- Alastuey, A., Querol, X., Castillo, S., Escudero, M., Avila, A., Cuevas, E., Torres, C., Romero, P.-M., Exposito, F., García, O., Pedro Diaz, J., Dingenen, R. V. and Putaud, J. P.: Characterisation of TSP and PM<sub>2.5</sub> at Izaña and Sta. Cruz de Tenerife (Canary Islands, Spain) during a Saharan Dust Episode (July 2002), *Atmos. Environ.*, 39(26), 4715–4728, doi:10.1016/j.atmosenv.2005.04.018, 2005.
- Allen, G. A., Babich, P. and Poirot, R. L.: Evaluation of a New Approach for Real Time Assessment of Wood Smoke PM, in *Proceedings of the Regional and Global Perspectives on Haze: Causes, Consequences, and Controversies*, NC: Air and Waste Management Association Visibility Specialty Conference, paper 16., 2004.
- Ansari, A. S. and Pandis, S. N.: Response of Inorganic PM to Precursor Concentrations, *Environ. Sci. Technol.*, 32(18), 2706–2714, doi:10.1021/es971130j, 1998.

Bencs, L., Ravindra, K., de Hoog, J., Rasoazanany, E. O., Deutsch, F., Bleux, N., Berghmans, P., Roekens, E., Krata, A. and Van Grieken, R.: Mass and ionic composition of atmospheric fine particles over Belgium and their relation with gaseous air pollutants, *J. Environ. Monit.*, 10(10), 1148–1157, doi:10.1039/b805157g, 2008.

ten Brink, H., Otjes, R., Jongejan, P. and Slanina, S.: An instrument for semi-continuous monitoring of the size-distribution of nitrate, ammonium, sulphate and chloride in aerosol, *Atmos. Environ.*, 41(13), 2768–2779, doi:10.1016/j.atmosenv.2006.11.041, 2007.

Chakraborty, A., Crenn, V., Petitprez, D. and Riffault, V.: Fine particles sampled at an urban background site and an industrialized coastal site in Northern France – Part 3: Sources, composition, and evolution of organic aerosols, in prep.

CITEPA: CITEPA, [online] Available from: <https://www.citepa.org/fr/air-et-climat/polluants/aep-item> (Accessed 28 February 2018), 2017.

Crenn, V., Fronval, I., Petitprez, D. and Riffault, V.: Fine particles sampled at an urban background site and an industrialized coastal site in Northern France - Part 1: Seasonal variations and chemical characterization, *Sci. Total Environ.*, 578, 203–218, doi:10.1016/j.scitotenv.2015.11.165, 2017.

Crenn, V., Chakraborty, A., Fronval, I., Petitprez, D. and Riffault, V.: Fine particles sampled at an urban background site and an industrialized coastal site in Northern France—Part 2: Comparison of offline and online analyses for carbonaceous aerosols, *Aerosol Sci. Technol.*, 52(3), 287–299, doi:10.1080/02786826.2017.1403008, 2018.

Csavina, J., Field, J., Félix, O., Corral-Avitia, A. Y., Sáez, A. E. and Betterton, E. A.: Effect of Wind Speed and Relative Humidity on Atmospheric Dust Concentrations in Semi-Arid Climates, *Sci. Total Environ.*, 487, 82–90, doi:10.1016/j.scitotenv.2014.03.138, 2014.

Czader, B. H., Choi, Y., Li, X., Alvarez, S. and Lefer, B.: Impact of updated traffic emissions on HONO mixing ratios simulated for urban site in Houston, Texas, *Atmos. Chem. Phys.*, 15(3), 1253–1263, doi:10.5194/acp-15-1253-2015, 2015.

Dasgupta, P. K., Campbell, S. W., Al-Horr, R. S., Ullah, S. M. R., Li, J., Amalfitano, C. and Poor, N. D.: Conversion of sea salt aerosol to NaNO<sub>3</sub> and the production of HCl: Analysis of temporal behavior of aerosol chloride/nitrate and gaseous HCl/HNO<sub>3</sub> concentrations with AIM, *Atmos. Environ.*, 41(20), 4242–4257, doi:10.1016/j.atmosenv.2006.09.054, 2007.

Dudkin, V. A., Rukhin, V. B. and Chizhov, Y. L.: Photochemical Oxidation of Sulfur Dioxide in Air in the Presence of Ozone, *Theor. Found. Chem. Eng.*, 36(2), 172–175, doi:10.1023/A:1014951416267, 2002.

Fisseha, R., Dommen, J., Gutzwiller, L., Weingartner, E., Gysel, M., Emmenegger, C., Kalberer, M. and Baltensperger, U.: Seasonal and diurnal characteristics of water soluble inorganic compounds in the gas and aerosol phase in the Zurich area, *Atmos Chem Phys*, 6(7), 1895–1904, doi:10.5194/acp-6-1895-2006, 2006.

Fountoukis, C. and Nenes, A.: ISORROPIA II: a computationally efficient thermodynamic equilibrium model for K<sup>+</sup>–Ca<sup>2+</sup>–Mg<sup>2+</sup>–NH<sub>4</sub><sup>+</sup>–Na<sup>+</sup>–SO<sub>4</sub><sup>2-</sup>–NO<sub>3</sub><sup>-</sup>–Cl<sup>-</sup>–H<sub>2</sub>O aerosols, *Atmos. Chem. Phys.*, 7(17), 4639–4659, doi:10.5194/acp-7-4639-2007, 2007.

Gall, E. T., Griffin, R. J., Steiner, A. L., Dibb, J., Scheuer, E., Gong, L., Rutter, A. P., Cevik, B. K., Kim, S., Lefer, B. and Flynn, J.: Evaluation of nitrous acid sources and sinks in urban outflow, *Atmos. Environ.*, 127, 272–282, doi:10.1016/j.atmosenv.2015.12.044, 2016.

He, Z. L., Alva, A. K., Calvert, D. V. and Banks, D. J.: Ammonia volatilization from different fertilizer sources and effects of temperature and soil pH, *Soil Sci.*, 164(10), 750–758, 1999.

Henry, R., Norris, G. A., Vedantham, R. and Turner, J. R.: Source Region Identification Using Kernel Smoothing, *Environ. Sci. Technol.*, 43(11), 4090–4097, doi:10.1021/es8011723, 2009.

Huang, X. H. H.: Characterization of PM<sub>2.5</sub> Major Components and Source Investigation in Suburban Hong Kong: A One Year Monitoring Study, *Aerosol Air Qual. Res.*, doi:10.4209/aaqr.2013.01.0020, 2014.

Kelly, F. J. and Fussell, J. C.: Size, source and chemical composition as determinants of toxicity attributable to ambient particulate matter, *Atmos. Environ.*, 60(Supplement C), 504–526, doi:10.1016/j.atmosenv.2012.06.039, 2012.

Kendrick, C. M., Koonce, P. and George, L. A.: Diurnal and seasonal variations of NO, NO<sub>2</sub> and PM<sub>2.5</sub> mass as a function of traffic volumes alongside an urban arterial, *Atmos. Environ.*, 122(Supplement C), 133–141, doi:10.1016/j.atmosenv.2015.09.019, 2015.

Kim, P. S., Jacob, D. J., Fisher, J. A., Travis, K., Yu, K., Zhu, L., Yantosca, R. M., Sulprizio, M. P., Jimenez, J. L., Campuzano-Jost, P., Froyd, K. D., Liao, J., Hair, J. W., Fenn, M. A., Butler, C. F., Wagner, N. L., Gordon, T. D., Welti, A., Wennberg, P. O., Crounse, J. D., Clair, J. M. S., Teng, A. P., Millet, D. B., Schwarz, J. P., Markovic, M. Z. and Perring, A. E.: Sources, seasonality, and trends of southeast US aerosol: an integrated analysis of surface, aircraft, and satellite observations with the GEOS-Chem chemical transport model, *Atmospheric Chem. Phys.*, 15(18), 10411–10433, doi:https://doi.org/10.5194/acp-15-10411-2015, 2015.

Kurtenbach, R., Becker, K. H., Gomes, J. A. G., Kleffmann, J., Lörzer, J. C., Spittler, M., Wiesen, P., Ackermann, R., Geyer, A. and Platt, U.: Investigations of emissions and heterogeneous formation of HONO in a road traffic tunnel, *Atmos. Environ.*, 35(20), 3385–3394, doi:10.1016/S1352-2310(01)00138-8, 2001.

Lee, H. S. and Kang, B.-W.: Chemical characteristics of principal PM<sub>2.5</sub> species in Chongju, South Korea, *Atmos. Environ.*, 35(4), 739–746, doi:10.1016/S1352-2310(00)00267-3, 2001.

Li, X., Rohrer, F., Hofzumahaus, A., Brauers, T., Häseler, R., Bohn, B., Broch, S., Fuchs, H., Gomm, S., Holland, F., Jäger, J., Kaiser, J., Keutsch, F. N., Lohse, I., Lu, K., Tillmann, R., Wegener, R., Wolfe, G. M., Mentel, T. F., Kiendler-Scharr, A. and Wahner, A.: Missing Gas-Phase Source of HONO Inferred from Zeppelin Measurements in the Troposphere, *Science*, 344(6181), 292–296, doi:10.1126/science.1248999, 2014.

Liang, Y., Zha, Q., Wang, W., Cui, L., Lui, K. H., Ho, K. F., Wang, Z., Lee, S.-C. and Wang, T.: Revisiting nitrous acid (HONO) emission from on-road vehicles: A tunnel study with a mixed fleet, *J. Air Waste Manag. Assoc.* 1995, 67(7), 797–805, doi:10.1080/10962247.2017.1293573, 2017.

Makkonen, U., Virkkula, A., Mäntykenttä, J., Hakola, H., Keronen, P., Vakkari, V. and Aalto, P. P.: Semi-continuous gas and inorganic aerosol measurements at a Finnish urban site: comparisons with filters, nitrogen in aerosol and gas phases, and aerosol acidity, *Atmos. Chem. Phys.*, 12(12), 5617–5631, doi:10.5194/acp-12-5617-2012, 2012.

Makkonen, U., Virkkula, A., Hellén, H., Hemmila, M., Sund, J., Aijala, M., Ehn, M., Junninen, H., Keronen, P., Petaja, T., Worsnop, D. R., Kulmala, M. and Hakola, H.: Semi-continuous gas and inorganic aerosol measurements at a boreal forest site, *Boreal Environ. Res.*, 19 (suppl. B), 311–328, 2014.

Martinelango, P. K., Dasgupta, P. K. and Al-Horr, R. S.: Atmospheric production of oxalic acid/oxalate and nitric acid/nitrate in the Tampa Bay airshed: Parallel pathways, *Atmos. Environ.*, 41(20), 4258–4269, doi:10.1016/j.atmosenv.2006.05.085, 2007.

Mensah, A. A., Holzinger, R., Otjes, R., Trimborn, A., Mentel, T. F., ten Brink, H., Henzing, B. and Kiendler-Scharr, A.: Aerosol chemical composition at Cabauw, The Netherlands as observed in two intensive periods in May 2008 and March 2009, *Atmos. Chem. Phys.*, 12(10), 4723–4742, doi:10.5194/acp-12-4723-2012, 2012.

Pay, M. T., Jiménez-Guerrero, P. and Baldasano, J. M.: Assessing sensitivity regimes of secondary inorganic aerosol formation in Europe with the CALIOPE-EU modeling system, *Atmos. Environ.*, 51, 146–164, doi:10.1016/j.atmosenv.2012.01.027, 2012.

Petetin, H., Sciare, J., Bressi, M., Gros, V., Rosso, A., Sanchez, O., Sarda-Estève, R., Petit, J.-E. and Beekmann, M.: Assessing the ammonium nitrate formation regime in the Paris megacity and its representation in the CHIMERE model, *Atmos. Chem. Phys.*, 16(16), 10419–10440, doi:10.5194/acp-16-10419-2016, 2016.

Petit, J.-E., Favez, O., Sciare, J., Crenn, V., Sarda-Estève, R., Bonnaire, N., Močnik, G., Dupont, J.-C., Haeffelin, M. and Leoz-Garziandia, E.: Two years of near real-time chemical composition of submicron aerosols in the region of Paris using an Aerosol Chemical Speciation Monitor (ACSM) and a multi-wavelength Aethalometer, *Atmos. Chem. Phys.*, 15(6), 2985–3005, doi:10.5194/acp-15-2985-2015, 2015.

Petit, J.-E., Favez, O., Albinet, A. and Canonaco, F.: A user-friendly tool for comprehensive evaluation of the geographical origins of atmospheric pollution: Wind and trajectory analyses, *Environ. Model. Softw.*, 88, 183–187, doi:10.1016/j.envsoft.2016.11.022, 2017.

Putaud, J.-P., Raes, F., Van Dingenen, R., Brüggemann, E., Facchini, M.-C., Decesari, S., Fuzzi, S., Gehrig, R., Hüglin, C., Laj, P., Lorbeer, G., Maenhaut, W., Mihalopoulos, N., Müller, K., Querol, X., Rodriguez, S., Schneider, J., Spindler, G., Brink, H. ten, Tørseth, K. and Wiedensohler, A.: A European aerosol phenomenology—2: chemical characteristics of particulate matter at kerbside, urban, rural and background sites in Europe, *Atmos. Environ.*, 38(16), 2579–2595, doi:10.1016/j.atmosenv.2004.01.041, 2004.

Putaud, J.-P., Van Dingenen, R., Alastuey, A., Bauer, H., Birmili, W., Cyrus, J., Flentje, H., Fuzzi, S., Gehrig, R., Hansson, H. C., Harrison, R. M., Herrmann, H., Hitznerberger, R., Hüglin, C., Jones, A. M., Kasper-Giebl, A., Kiss, G., Koussa, A., Kuhlbusch, T. A. J., Löschau, G., Maenhaut, W., Molnar, A., Moreno, T., Pekkanen, J., Perrino, C., Pitz, M., Puxbaum, H., Querol, X., Rodriguez, S., Salma, I., Schwarz, J., Smolik, J., Schneider, J., Spindler, G., ten Brink, H., Tursic, J., Viana, M., Wiedensohler, A. and Raes, F.: A European



aerosol phenomenology – 3: Physical and chemical characteristics of particulate matter from 60 rural, urban, and kerbside sites across Europe, *Atmos. Environ.*, 44(10), 1308–1320, doi:10.1016/j.atmosenv.2009.12.011, 2010.

Rappenglück, B., Lubertino, G., Alvarez, S., Golovko, J., Czader, B. and Ackermann, L.: Radical precursors and related species from traffic as observed and modeled at an urban highway junction, *J. Air Waste Manag. Assoc.*, 63(11), 1270–1286, 2013.

Rumsey, I. C., Cowen, K. A., Walker, J. T., Kelly, T. J., Hanft, E. A., Mishoe, K., Rogers, C., Proost, R., Beachley, G. M., Lear, G., Frelink, T. and Otjes, R. P.: An assessment of the performance of the Monitor for AeRosols and GAses in ambient air (MARGA): a semi-continuous method for soluble compounds, *Atmos. Chem. Phys.*, 14(11), 5639–5658, doi:10.5194/acp-14-5639-2014, 2014.

Schaap, M., Otjes, R. P. and Weijers, E. P.: Illustrating the benefit of using hourly monitoring data on secondary inorganic aerosol and its precursors for model evaluation, *Atmos. Chem. Phys.*, 11(21), 11041–11053, doi:10.5194/acp-11-11041-2011, 2011.

Shi, G., Xu, J., Peng, X., Xiao, Z., Chen, K., Tian, Y., Guan, X., Feng, Y., Yu, H., Nenes, A. and Russell, A. G.: pH of Aerosols in a Polluted Atmosphere: Source Contributions to Highly Acidic Aerosol, *Environ. Sci. Technol.*, 51(8), 4289–4296, doi:10.1021/acs.est.6b05736, 2017.

Silvern, R. F., Jacob, D. J., Kim, P. S., Marais, E. A., Turner, J. R., Campuzano-Jost, P. and Jimenez, J. L.: Inconsistency of ammonium–sulfate aerosol ratios with thermodynamic models in the eastern US: a possible role of organic aerosol, *Atmos. Chem. Phys.*, 17(8), 5107–5118, doi:https://doi.org/10.5194/acp-17-5107-2017, 2017.

Slanina, J., ten Brink, H. M., Otjes, R. P., Even, A., Jongejan, P., Khlystov, A., Waijers-Ijpelaan, A., Hu, M. and Lu, Y.: The continuous analysis of nitrate and ammonium in aerosols by the steam jet aerosol collector (SJAC): extension and validation of the methodology, *Atmos. Environ.*, 35(13), 2319–2330, doi:10.1016/S1352-2310(00)00556-2, 2001.

Sörgel, M., Trebs, I., Wu, D. and Held, A.: A comparison of measured HONO uptake and release with calculated source strengths in a heterogeneous forest environment, *Atmos. Chem. Phys.*, 15(16), 9237–9251, doi:10.5194/acp-15-9237-2015, 2015.

Stein, A. F., Draxler, R. R., Rolph, G. D., Stunder, B. J. B., Cohen, M. D. and Ngan, F.: NOAA's HYSPLIT Atmospheric Transport and Dispersion Modeling System, *Bull. Am. Meteorol. Soc.*, 96(12), 2059–2077, doi:10.1175/BAMS-D-14-00110.1, 2015.

Stieger, B., Spindler, G., Fahlbusch, B., Müller, K., Grüner, A., Poulain, L., Thöni, L., Seitler, E., Wallasch, M. and Herrmann, H.: Measurements of PM<sub>10</sub> ions and trace gases with the online system MARGA at the research station Melpitz in Germany – A five-year study, *J. Atmos. Chem.*, 1–38, doi:10.1007/s10874-017-9361-0, 2017.

Sutton, M. A., Dragosits, U., Tang, Y. S. and Fowler, D.: Ammonia emissions from non-agricultural sources in the UK, *Atmos. Environ.*, 34(6), 855–869, doi:10.1016/S1352-2310(99)00362-3, 2000.

Urban, R. C., Lima-Souza, M., Caetano-Silva, L., Queiroz, M. E. C., Nogueira, R. F. P., Allen, A. G., Cardoso, A. A., Held, G. and Campos, M. L. A. M.: Use of levoglucosan,

potassium, and water-soluble organic carbon to characterize the origins of biomass-burning aerosols, *Atmos. Environ.*, 61, 562–569, doi:10.1016/j.atmosenv.2012.07.082, 2012.

VandenBoer, T. C., Young, C. J., Talukdar, R. K., Markovic, M. Z., Brown, S. S., Roberts, J. M. and Murphy, J. G.: Nocturnal loss and daytime source of nitrous acid through reactive uptake and displacement, *Nat. Geosci.*, 8(1), 55–60, doi:10.1038/ngeo2298, 2015.

Waked, A., Favez, O., Alleman, L. Y., Piot, C., Petit, J.-E., Delaunay, T., Verlinden, E., Golly, B., Besombes, J.-L., Jaffrezo, J.-L. and Leoz-Garziandia, E.: Source apportionment of PM<sub>10</sub> in a north-western Europe regional urban background site (Lens, France) using positive matrix factorization and including primary biogenic emissions, *Atmos. Chem. Phys.*, 14(7), 3325–3346, doi:10.5194/acp-14-3325-2014, 2014.

Wang, Y., Hopke, P. K., Rattigan, O. V., Chalupa, D. C. and Utell, M. J.: Multiple-year black carbon measurements and source apportionment using delta-C in Rochester, New York, *J. Air Waste Manag. Assoc.*, 62(8), 880–887, 2012.

Weber, R. J., Orsini, D., Daun, Y., Lee, Y.-N., Klotz, P. J. and Brechtel, F.: A Particle-into-Liquid Collector for Rapid Measurement of Aerosol Bulk Chemical Composition, *Aerosol Sci. Technol.*, 35(3), 718–727, doi:10.1080/02786820152546761, 2001.

Weingartner, E., Saathoff, H., Schnaiter, M., Streit, N., Bitnar, B. and Baltensperger, U.: Absorption of light by soot particles: determination of the absorption coefficient by means of aethalometers, *J. Aerosol Sci.*, 34(10), 1445–1463, doi:10.1016/S0021-8502(03)00359-8, 2003.

WHO: WHO | Air quality guidelines - global update 2005, WHO [online] Available from: [http://www.who.int/phe/health\\_topics/outdoorair/outdoorair\\_aqg/en/](http://www.who.int/phe/health_topics/outdoorair/outdoorair_aqg/en/) (Accessed 7 August 2017), n.d.

Wu, W. S. and Wang, T.: On the performance of a semi-continuous PM<sub>2.5</sub> sulphate and nitrate instrument under high loadings of particulate and sulphur dioxide, *Atmos. Environ.*, 41(26), 5442–5451, doi:10.1016/j.atmosenv.2007.02.025, 2007.

---

**CHAPTER 4:**  
**Real-time assessment of wintertime  
organic aerosol characteristics and  
sources at a suburban site in northern  
France**

---



## **CHAPTER 4. Real-time assessment of wintertime organic aerosol characteristics and sources at a suburban site in northern France**

The fourth chapter is centered on the results of the intensive measurement campaign and focuses on the assessment of winter organic aerosol characteristics and sources in Douai with a high-time resolution. It is also presented as an article which has been submitted to Atmospheric Environment in June 2018. This is the first version. The article describes the main characteristics of the organic aerosol during winter and presents the results obtained from a typical source apportionment study applied to the organic fraction of the aerosol. In addition, the impact of meteorological parameters and long-range transport on NR-PM<sub>1</sub> characteristics is also evaluated and discussed.

Similarly to the previous chapter, this article is complemented by supplementary information which can be found in Annex 3 of this manuscript.



## Real-time assessment of wintertime organic aerosol characteristics and sources at a suburban site in northern France

Roger Roig<sup>1</sup>, Abhishek Chakraborty<sup>1</sup>, Esperanza Perdrix<sup>1</sup>, Emmanuel Tison<sup>1</sup>, Véronique Riffault<sup>1,\*</sup>

IMT Lille Douai, Univ. Lille, SAGE – Département Sciences de l'Atmosphère et  
Génie de l'Environnement, F-59000 Lille, France

\* Corresponding author: Véronique Riffault ([veronique.riffault@imt-lille-douai.fr](mailto:veronique.riffault@imt-lille-douai.fr))

**Abstract.** A high-resolution time-of-flight aerosol mass spectrometer (HR-ToF-AMS) was deployed during wintertime (5 February to 15 March 2016) at a suburban site in Douai, northern France, in order to investigate the characteristics and sources of the organic matter (OM). The campaign average concentration of non-refractory submicron particulate matter (NR-PM<sub>1</sub>) was  $11.1 \pm 9.3 \mu\text{g m}^{-3}$ , and composed of 38% OM, 36% NO<sub>3</sub>, 16% NH<sub>4</sub> and 9% SO<sub>4</sub>. The average values for the OM:OC, O:C, H:C and N:C ratios were  $1.60 \pm 0.15$ ,  $0.32 \pm 0.11$ ,  $1.55 \pm 0.14$  and  $0.04 \pm 0.02$ , respectively, indicating a moderate level of aerosol oxidation. The positive matrix factorization (PMF) source apportionment method was applied to the high-resolution organic aerosol (OA) mass spectra, resulting in five factors: two primary OA factors – hydrocarbon-like (HOA) and cooking-like (COA); one factor associated with oxidized biomass burning (oBBOA); and two oxygenated factors (OOA) denoted as less oxidized (LO-OOA) and more oxidized (MO-OOA), with average contributions to OA of 15%, 11%, 25%, 16% and 33%, respectively. The oBBOA factor was found to be mainly local as shown by non-parametric wind regression (NWR) analysis, and to correlate well with relative humidity (RH), indicating possible aqueous processing of locally emitted primary biomass burning emissions. During most part of the campaign, the sampling site was affected by different air masses. However, during the last period of the campaign (5-16 March 2016) the site was heavily impacted by air masses from Eastern Europe which were rich in secondary inorganic and organic aerosols. The H:C versus O:C (Van Krevelen, VK) diagram highlighted that the aerosol followed an oxidation process throughout the whole campaign,

with an average slope of -1.05. The impact of continental air masses towards the end of the campaign confined the aerosol towards a narrower space in the VK diagram, suggesting a homogenization of the different aerosol sources due to OA ageing during transport.

**Keywords:** AMS, organic aerosols, source apportionment, aqueous processing

## 1. Introduction

Atmospheric aerosols have gained attention worldwide due to their various impacts on human health (Kelly and Fussell, 2012), climate, visibility and ecosystems (Hallquist et al., 2009; IPCC, 2013; Watson, 2002). In the year 2012 only, ambient air pollution was responsible for 3.7 million deaths worldwide (WHO, 2014), mostly due to inhalation of fine particulate matter (PM<sub>2.5</sub>). In Europe, the premature mortality associated to ambient air pollution is also alarmingly high, with the estimations for the year 2012 ranging from 203,000 to 280,000 for low- to middle-income and high-income countries, respectively (WHO, 2014). The region of northern France is also affected by high levels of PM<sub>2.5</sub>, particularly during winter and spring (Atmo Nord-Pas-de-Calais, 2014). These high levels are mainly attributed to its location amidst various emission source areas including an extensive highway network, a high urban density, and the proximity to several European capitals (London, Paris, and Brussels) as well as a significant influence of industry and agriculture.

While the elemental and inorganic fractions of ambient aerosols are rather well understood, the characterization of the organic matter (OM) still remains a challenge due to their complex nature, associated to numerous emission sources and atmospheric transformations (Hallquist et al., 2009; Jimenez et al., 2009). OM can represent from 20 to 90% of the total submicron aerosol (PM<sub>1</sub>) mass (Jimenez et al., 2009), and hence understanding its sources and transformation processes is essential in order to develop effective mitigation policies. OM, also called organic aerosol (OA), is typically divided into primary (POA) and secondary organic aerosols (SOA). POA are directly emitted to the atmosphere by a variety of sources comprising anthropogenic ones such as traffic, industrial activities, and residential biomass combustion; and natural ones like sea spray, volcanic emissions, forest fires, etc. (Hallquist et al., 2009; Mohr et al., 2009). SOA are formed in the atmosphere through several physicochemical processes of gas phase VOCs (volatile organic compounds) or POA (Kanakidou et al., 2005).

Different techniques have been developed in the past decades to analyze the nature and composition of OA. Most of these techniques work in offline mode; post analysis of the collected samples. These techniques can provide more exhaustive information on the nature



and characteristics of individual organic species, but they require large amounts of samples which generally result in a low time resolution (of several hours). Since most of the atmospheric reactions occur at a timescale of few tens of minutes, these offline techniques often fail to elucidate the underlying atmospheric processes (Hallquist et al., 2009). On the contrary, online techniques provide less exhaustive information on individual chemical species but can characterize bulk OA with a very high time resolution (of seconds to minutes). Among the available online techniques, aerosol mass spectrometry (AMS) has become quite popular, since it allows the measurement of the chemical composition and mass loading as a function of the particle size in the submicron range (Canagaratna et al., 2007).

Besides, the combination of AMS data with source apportionment techniques, mainly positive matrix factorization (PMF) and multi-linear engine (ME-2), has allowed for the study of the OA sources and characteristics (Ulbrich et al., 2009). Several AMS-PMF studies have shown that OA can typically be separated into secondary or oxygenated OA (OOA), and several primary OA types like hydrocarbon-like OA (HOA), biomass burning OA (BBOA) and cooking OA (COA), depending on the site location and sampling season (Bozzetti et al., 2017; Crippa et al., 2014; Florou et al., 2017; Lanz et al., 2010; Mohr et al., 2012; Poulain et al., 2011; Saarikoski et al., 2012; Timonen et al., 2013). In France, a few studies have focused on the OA sources and characteristics using real-time measurements in Paris (Crippa et al., 2013), Marseille (Bozzetti et al., 2017), and in the north of France in Douai and Dunkirk which showed that winter OA was moderately oxidized and mostly composed of OOA, while significant contributions of BBOA, HOA and sulfur-containing OA (SCOA) were also found (Crenn et al., 2017, 2018; Chakraborty et al., in prep.).

In this context, this intensive campaign using a high-resolution time-of-flight aerosol mass spectrometer (HR-ToF-AMS) and carried out in winter 2016 at a suburban site in Douai was deployed with the aim of complementing ongoing long-term measurements with a Monitor for Gases and AeRosols in ambient Air (MARGA) and other collocated instrumentation which focused on the source apportionment of the PM<sub>2.5</sub> inorganic aerosol with an hourly resolution (Roig et al., submitted; in prep.). This work focuses on the characterization of the chemical composition of NR-PM<sub>1</sub> and of the sources of OA obtained by PMF analysis during winter in Douai. In addition, the influence of meteorological characteristics and long-range transport on the characteristics of NR-PM<sub>1</sub> is also evaluated.

## **2. Materials and methods**

### **2.1. Measurement site**

Observations of the chemical composition of atmospheric aerosols were carried out from 5 February to 16 March 2016 in Douai, northern France, at a suburban location outside the city center (Figure S2.1) which is considered as representative of the background pollution of the area (50°23'03''N, 3°05'08''E, and 20 m above sea level). The city of Douai is located in a fairly flat land and is close (about 25-30 km south) of the European Metropolis of Lille which, with about 1.2 million inhabitants and a population density of 1,832 inhab. km<sup>-2</sup>, is the second most densely populated metropolis in France, after that of Paris. The climate in northern France is classified as temperate oceanic, characterized by low seasonal thermal amplitudes, and regular precipitations along the year, with no dry season.

### **2.2. Instrumentation**

The high resolution-time of flight-aerosol mass spectrometer (HR-ToF-AMS) (Aerodyne Research, USA), hereafter named AMS, was deployed in order to measure in real-time the chemical composition and concentrations of the non-refractory PM<sub>1</sub> (NR-PM<sub>1</sub>) (DeCarlo et al., 2006). The major species composing NR-PM<sub>1</sub> include NO<sub>3</sub>, NH<sub>4</sub>, SO<sub>4</sub>, Cl and organic aerosols/matter (OA). The AMS operates in two modes according to the trajectory of the ions: the low resolution but highly sensitive V mode and the high resolution but less sensitive W mode. In this study, the time resolution of the AMS was set to 5 minutes, with 3 minutes for mode V and 2 minutes for mode W. Only the results for the V mode are shown, since the lower sensitivity of the W mode delivered a too low signal-to-noise ratio during most of the campaign.

The mass concentration measurement accuracy of AMS depends on collection efficiency (CE) and ionization efficiency (IE) values. The CE considers the effects of incomplete focusing of the particle beam and bouncing of some particles from the vaporizer (Drewnick et al., 2005). Typically, a default CE value of 0.5 is used (Middlebrook et al., 2012). However, it has been shown that the CE is dependent on particle phase, which is influenced by the relative humidity in the sampling line above 80%, the acidity/neutralization of the sulfate, ammonium nitrate, and organic content (Middlebrook et al., 2012). In this work a Nafion dryer was used in order to reduce the relative humidity in the sampling line. In addition, a composition dependent CE (CDCE), which recalculates the concentrations of all

the chemical species by taking into account the NO<sub>3</sub> fraction of the aerosol, was applied to the AMS data as proposed previously by Middlebrook et al. (2012).

The IE is defined as the ratio between the number of ions detected and the molecules of the parent species (Jimenez et al., 2003), and is species specific. Its value is determined through calibrations. However, since it is not practical to perform individual calibrations for all compounds in ambient aerosol, a reference calibration is typically performed for nitrate, and the relative IE (RIE) of every species is obtained relative to that of nitrate (Alfarra et al., 2004). We carried out calibrations every two weeks in order to determine IE(NO<sub>3</sub>) and RIE(NH<sub>4</sub>) using aqueous solutions of 10<sup>-2</sup> mol L<sup>-1</sup> NH<sub>4</sub>NO<sub>3</sub> (Sigma Aldrich, 99.0%). NH<sub>4</sub>NO<sub>3</sub> particles were generated by an atomizer (TSI 3076) and then dried by passing through a silica gel drier (TSI 3062). A dilution system composed of a set of valves and a HEPA (High Efficiency Particle Arrestance) filter was used in order to vary the particle concentration. In addition, an electrostatic classifier (TSI 3080) and a differential mobility analyzer (TSI 3081) allowed selecting the particles with an electrical mobility diameter of 300 nm. Finally, the particles entered simultaneously a condensation particle counter (TSI, 3788) and the AMS. Additional calibrations were carried out using aqueous solutions of 10<sup>-2</sup> mol L<sup>-1</sup> of (NH<sub>4</sub>)<sub>2</sub>SO<sub>4</sub> (Sigma Aldrich, 99.0%) and NH<sub>4</sub>Cl (Sigma Aldrich, 99.5%) in order to determine the RIE for SO<sub>4</sub> and Cl, respectively. The RIE values were determined to be 4.0, 1.1 and 1.6 for NH<sub>4</sub>, SO<sub>4</sub> and Cl, respectively.

The processing of the AMS unit mass resolution (UMR) and high resolution (HR) data has been carried out by using the modules SQUIRREL (SeQUential Igor data RetRiEvaL, version 1.60E) and PIKA (Peak Integration by Key Analysis, version 1.20E), respectively (D. Sueper, University of Colorado-Boulder, Boulder, CO, USA) for Igor Pro v. 6.37 (Wavemetrics, Inc. Portland, OR, USA).

Additionally, several other instruments were used as part of a longer campaign (Roig et al., submitted), whose data are used for comparison purposes and as external tracers to validate the PMF identified factors. These included a MARGA 1S (Metrohm Applikon B.V, Netherlands) (ten Brink et al., 2007) for the measurement of water-soluble ions (NO<sub>3</sub><sup>-</sup>, SO<sub>4</sub><sup>2-</sup>, NH<sub>4</sub><sup>+</sup>, K<sup>+</sup>) and precursor gases (HONO) with an hourly resolution, a double-wavelength aethalometer AE42 (Magee Scientific, USA) for black carbon (BC) and Delta-C with a 5-min time resolution, a chemiluminescence analyzer NOx 2000G (Seres environment, France) for nitrogen oxides every 15 minutes and a BAM-1020 (Met One Instruments, USA) for the PM<sub>2.5</sub> total mass concentration every hour. The Delta-C variable was determined as the

difference of light absorption between 370 and 880 nm, and represents the enhanced optical absorption of some specific OA compounds (Allen et al., 2004). It has previously been found to correlate with wood-burning markers such as levoglucosan and  $K^+$  and therefore might be used as a tracer of wood combustion (Allen et al., 2004; Wang et al., 2012). Meteorological parameters including temperature, relative humidity (RH), and pressure were acquired from a BAM-1020 and a TEOM-FDMS. The wind speed and direction, and precipitation were monitored on site with an anemometer. The mixing layer height (MLH) was obtained from the GDAS meteorological data (1 degree) on the NOAA website.

### 2.3. Source apportionment of OA

The Positive Matrix Factorization (PMF) method (Paatero and Tapper, 1994) was applied to the V mode HR OA mass spectra ( $m/z = 12$  to  $m/z = 150$ ) in order to investigate the different sources of OA using the PMF Evaluation Tool (PET) v. 3.00 integrated into Igor Pro (Paatero and Tapper, 1994; Ulbrich et al., 2009). PMF analysis was carried out as per the guidelines of Paatero and Tapper (1994) and Ulbrich et al. (2009). Weak species, with a signal-to-noise ratio (SNR) below 2 were down-weighted by a factor of 2. In addition, the errors of the ions associated with the  $CO_2^+$  signal (O, HO,  $H_2O$ , CO, and  $CO_2$ ) were also down-weighted by a factor of 2 in order to prevent excessive weighting of the signal at  $m/z$  44 (Allan et al., 2004; Ulbrich et al., 2009). No fragments ( $SNR < 0.2$ ) were removed from the database. We examined PMF solutions between 2 and 8 factors. The selection of the most appropriate solution was made by taking into account several criteria such as the variation of the  $Q/Q_{exp}$  ratio, the physical meaningfulness of the mass spectra representing each factor, the time series and daily cycles, and the relationship with external variables.

### 2.4. Geographical determination of sources

In order to get insight into the geographical origins of the sources of OA, we combined the data obtained by the PMF analysis with the wind speed and direction and the back-trajectories. The wind speed and wind direction were used by applying the non-parametric wind regression (NWR), a hybrid source-receptor model which locates and quantifies local sources of hourly averaged atmospheric concentrations of a pollutant based on wind speed ( $u$ ) and direction ( $\theta$ ) (Henry et al., 2009) following equation 1:

$$E(C|\theta, u) = \frac{\sum_{i=1}^N K_1\left(\frac{\theta - \theta_i}{\sigma}\right) \cdot K_2\left(\frac{u - u_i}{h}\right) \cdot C_i}{\sum_{i=1}^N K_1\left(\frac{\theta - \theta_i}{\sigma}\right) \cdot K_2\left(\frac{u - u_i}{h}\right)} \quad \text{Eq. 1}$$

where  $E$  is the concentration estimate at a wind direction  $\theta$  and wind speed  $u$ ;  $W_i$ ,  $U_i$  and  $C_i$  the wind direction, speed and atmospheric concentrations, respectively, measured at  $t_i$ ;  $\sigma$  and  $h$  the smoothing factors (suggested by the software); and  $K_1$  and  $K_2$  are a Gaussian kernel function for wind direction  $\theta$  and an Epanechnikov kernel function for wind speed  $u$ , respectively, used to get the smoothing (Henry et al., 2009).

The weighed concentrations obtained from Eq. 1 are then weighted by the wind frequency. Hence, an empirical joint probability density of wind speed and direction is calculated using the kernel density estimate, as shown in equation 2:

$$f(\theta, u) = \frac{1}{N\sigma h} \cdot \sum_{i=1}^N K_1\left(\frac{\theta - W_i}{\sigma}\right) K_2\left(\frac{u - U_i}{h}\right) \quad \text{Eq. 2}$$

where  $N$  is the total number of points.

The Potential Source Contribution Function (PSCF) is a statistical source-receptor model aiming at determining the geographical origins of high concentrations of air pollutants. It is based on the analysis of the residence times of air masses using air mass trajectories back in time. The main idea is that the longer an air mass stays over a pollution source, the higher the pollution brought by the air mass to the receptor site. Generally, the domain covered by the backtrajectories is meshed according to a regular grid. The PSCF model calculates the probability of having a pollutant source located inside each grid cell of the domain and responsible for pollutant concentrations measured at the receptor site above a given threshold, following equation 3:

$$PSCF = \frac{m_{ij}}{n_{ij}} \quad \text{Eq. 3}$$

where  $m_{ij}$  is the number of backtrajectory endpoints passing over the  $ij^{\text{th}}$  grid cell at latitude  $i$  and longitude  $j$  and associated to concentrations measured at the receptor site exceeding a specific threshold (in this case the 75<sup>th</sup> percentile was used); and  $n_{ij}$  the total number of trajectory endpoints passing over the  $ij^{\text{th}}$  gridcell. A high value of the PSCF probability for the  $ij^{\text{th}}$  grid cell indicates a high probability that this grid cell corresponds to a source location. The backtrajectories used for PSCF analysis were calculated with HYSPLIT 4 (HYbrid Single-Particle Lagrangian Integrated Trajectory) for an arrival height of half of the planetary boundary layer, at 3-h intervals (8 trajectories per day at 0, 3, 6, 9, 12, 15, 18, 21 UTC), and 72 hours back in time. Due to spatial resolution, PSCF was applied only to OA sources identified as regional by the NWR approach.

The calculation of both NWR and PSCF was carried out using the Zefir v3.31 IGOR tool (Petit et al., 2017).

## **2.5. Ventilation coefficient**

Additionally, we calculated the ventilation coefficient (i.e. the product of the mixing layer height and the wind speed; in  $\text{m}^2 \text{s}^{-1}$ ) in order to evaluate whether the atmospheric conditions favor dispersion or accumulation of the pollutants at the sampling location (Goyal and Chalapati Rao, 2007). The dispersion conditions at the site are considered as bad, moderate, good and excellent for ventilation coefficients between 0 and 2,000, 2,001 and 4,000, 4,001 and 6,000 and  $>6,000 \text{ m}^2 \text{s}^{-1}$  respectively, according to the criteria of Eagleman (1991).

## **3. Results and discussion**

### **3.1. Overview of NR-PM<sub>1</sub>**

The time series of the meteorological parameters, concentrations of the main components of NR-PM<sub>1</sub> and OA elemental ratios are shown in Figure P2.1. The weather conditions during the campaign were mostly humid and cold, with average values for RH and T of  $82 \pm 12\%$  and  $5.7 \pm 3.3^\circ\text{C}$ , respectively. Relatively low wind speeds were observed during the campaign, with an average of  $1.6 \pm 1.2 \text{ m s}^{-1}$ , with calm winds from north and northeast alternating with strong winds from the southwest.

Moderate to high levels of NR-PM<sub>1</sub> were observed during the measurement campaign, with concentrations ranging from 0.23 to  $50.9 \mu\text{g m}^{-3}$  and a campaign average concentration of  $11.1 \pm 9.3 \mu\text{g m}^{-3}$ . The NR-PM<sub>1</sub> composition was dominated by OA (38.4%;  $4.2 \pm 3.1 \mu\text{g m}^{-3}$ ) and NO<sub>3</sub> (35.9%;  $4.0 \pm 4.3 \mu\text{g m}^{-3}$ ) followed by NH<sub>4</sub> (15.9%;  $1.8 \pm 1.8 \mu\text{g m}^{-3}$ ) and SO<sub>4</sub> (8.8%;  $1.0 \pm 0.9 \mu\text{g m}^{-3}$ ). The contribution of Cl was particularly low (1.0%,  $0.23 \mu\text{g m}^{-3}$ ) throughout the campaign, and hence will not be further discussed. Previous studies in northern France carried out in winter also observed similar compositions for NR-PM<sub>1</sub> (Crenn et al., 2017, 2018; Zhang et al., in prep.). In addition, the major inorganic species in NR-PM<sub>1</sub> measured by the AMS (NO<sub>3</sub>, NH<sub>4</sub> and SO<sub>4</sub>) are well correlated ( $r > 0.95$ ) to those measured in PM<sub>2.5</sub> by a MARGA 1S (Roig et al., submitted). Some interesting changes were observed between the first part (5 February – 4 March 2016) and the second part (5-16 March 2016) of the campaign. During the second period, particularly high concentrations of NR-PM<sub>1</sub> (up to  $50 \mu\text{g m}^{-3}$ ) were observed. This was attributed to an impact of air masses originating from continental Europe and rich in secondary aerosols, as will be discussed in detail in section 3.4.

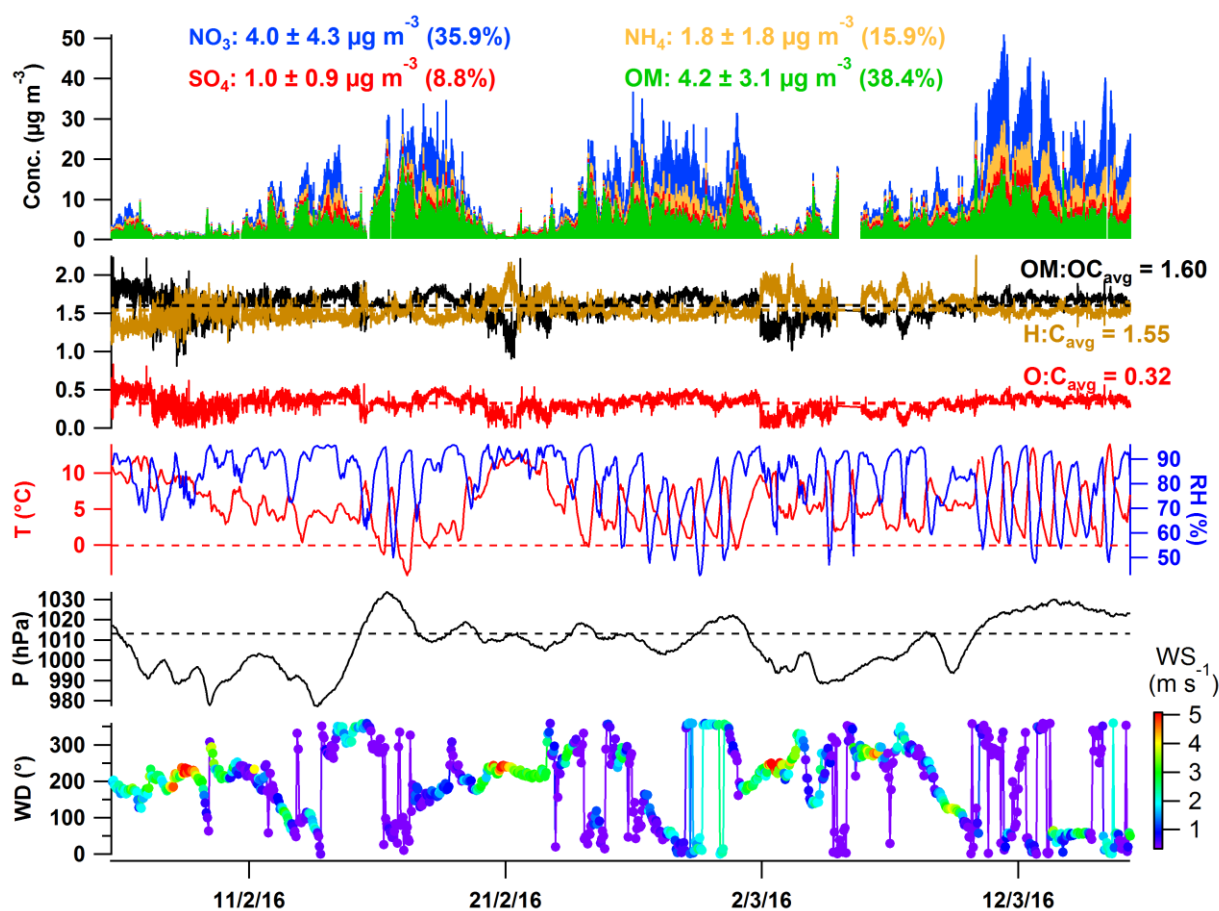


Figure P2.1 Time series of NR-PM<sub>1</sub>, elemental ratios (OM:OC, H:C and O:C) and of the main meteorological parameters (T: temperature, RH: relative humidity, P: atmospheric pressure, WD: wind direction and WS: wind speed)

The daily profiles of the average concentrations and fractional contributions for the main species of NR-PM<sub>1</sub> are shown in Figure S2.2. Concentrations of NO<sub>3</sub> and NH<sub>4</sub> are higher during the nighttime, in accordance with the lower temperatures and higher RH favoring the partitioning of ammonium nitrate to the aerosol phase. On the other hand, the concentrations of sulfate do not show noticeable differences throughout the day, suggesting that it might be a result of transformation of regionally emitted SO<sub>2</sub>. In addition, the daytime production of SO<sub>4</sub> might have been masked by the expansion of the boundary layer, and the nighttime lower boundary layer values might have caused higher SO<sub>4</sub> thus the similar levels between daytime and nighttime. The daily cycle of OA shows two maxima, one in the early morning which could be linked to the vehicular emissions during the traffic rush hours, and one in the evening, which could be attributed to emissions from biomass burning, as will be

further discussed in section 3.3. The difference in composition of the NR-PM<sub>1</sub> between daytime and nighttime was small, although the contribution of OA was higher through the night (41% compared to 35% during daytime; Figure S2.2b), which could be attributed to a higher contribution of OA sources such as biomass burning during the nighttime, as will be discussed later.

The origin of the main components of NR-PM<sub>1</sub> was assessed with the use of polar plots, shown in Figure S2.3. We observed higher concentrations of NO<sub>3</sub> and NH<sub>4</sub> for low and moderate wind speeds from the NE sector, suggesting that a combination of local and regional sources could have contributed to the observed concentrations. High levels of SO<sub>4</sub> are observed for low and moderate wind speeds in the NE sector. However, high concentrations of SO<sub>4</sub> are also observed for other directions, implying that its origin could be rather regional, in agreement with its daily cycle. The polar plot for OA shows highest concentrations for very calm winds (<1 m s<sup>-1</sup>), pointing out significant local contributions. However, high concentrations of OA are also observed for moderate wind speeds from the NE and SE sectors, suggesting that regional sources are also important.

The acidity of the NR-PM<sub>1</sub> aerosol was evaluated by using the neutralization ratio (NR) (Figure S2.4). This is defined as the ratio between the observed ammonium and that required for the full neutralization of nitrate and sulfate. NR was close to 1 during most of the campaign, implying that there was always enough NH<sub>4</sub> to neutralize NO<sub>3</sub> and SO<sub>4</sub>.

### **3.2. OA characteristics**

Calculation of OA elemental ratios indicates that OA was moderately oxidized during the campaign. The average values for the OM:OC, O:C, H:C and N:C ratios were  $1.60 \pm 0.15$ ,  $0.32 \pm 0.11$ ,  $1.55 \pm 0.14$  and  $0.04 \pm 0.02$ , respectively. These values are consistent with previous wintertime observations at urban sites in France (Chakraborty et al., in prep.; Crenn et al., 2018; Crippa et al., 2013).

The daily profiles of the elemental ratios are shown in Figure P2.2. The OM:OC and O:C ratios are found to be slightly higher during nighttime than daytime hours, which could be attributed to aqueous processing during nighttime due to very high RH levels and occurrence of some fog events. Higher or comparable nighttime OM:OC and O:C values have also been observed in previous studies (Brown et al., 2013; Florou et al., 2017; Hayes et al., 2013). High humidity and fog events can create a suitable environment for aqueous oxidation leading to higher O:C ratios. Stagnant conditions during winter nights, suggested by



ventilation coefficient values lower than  $1000 \text{ m}^2 \text{ s}^{-1}$  (Eagleman, 1991; Figure S2.5b), may have also allowed more time for the processing of local air masses. For instance, aqueous oxidation of primary biomass burning aerosols has already been reported (Gilardoni et al., 2016) and this will be discussed further in section 3.3. Relatively lower solar radiation (and thus less photochemical activity) may have led to the observed lower OA oxidation levels during daytime. The minima for OM:OC and O:C are found in the early morning (7-8 am UTC, that is to say 8-9 am local time) and afternoon (5-6 pm UTC), during the traffic rush hours. On the contrary, the H:C ratio presents higher values during daytime, with maximum values during the traffic rush hours. In the literature, H:C usually shows a sharp decrease after reaching its maximum in the morning (Crippa et al., 2013; Docherty et al., 2011; Florou et al., 2017; Saarikoski et al., 2012). However, in this study H:C shows only a minor dip after its morning maximum, and remains steady until the afternoon traffic rush hours. This could be linked to the substantial contribution from some primary sources such as traffic outside rush hours (the road next to the sampling site is situated between an industrial zone and a commercial zone, implying that there is always some traffic of cars, trucks and buses) or even cooking with high H:C values during daytime as will be discussed in section 3.3. The N:C ratio showed higher values during the night and early morning, during the traffic rush hours.

The Van Krevelen plot (H:C vs O:C) can reveal some important information on the aging of the atmospheric OA (Heald et al., 2010). In Figure P2.3, OA elemental ratios are observed to move towards the lower right (higher O:C and lower H:C) as the campaign proceeds. Some inferences can be drawn on OA aging based on the slope of this change of OA elemental ratios. In the same plot, reactions involving the addition/subtraction of several functional groups are illustrated with straight lines of different slope values. For instance, a slope of -2 is obtained when an aliphatic carbon group ( $-\text{CH}_2-$ ) is replaced by a carbonyl group ( $-\text{C}(=\text{O})-$ ), representing the loss of 2 hydrogens and the gain of 1 oxygen. The replacement of one hydrogen atom with an alcohol group ( $-\text{OH}-$ ) results in a slope value of 0. Lastly, a slope of -1 is obtained by the simultaneous addition of the carbonyl and alcohol groups (Heald et al., 2010). The data plotted in Figure P2.3 presented an average slope of -1.05, which is in the range of values reported for other field campaigns (-0.8 to -1.1) (Hayes et al., 2013; Heald et al., 2010; Timonen et al., 2013). It is also observed that the elemental ratios of OA tend to be confined within a narrow area towards the end of the campaign, when aged air masses were arriving from continental Europe, as will be discussed in detail in section 3.4. This observed tendency implies that with the atmospheric aging due to transport,

the chemical characteristics of bulk OA tend to be homogenized, as reported in several previous studies (Pan, 2015; Williams et al., 2007).

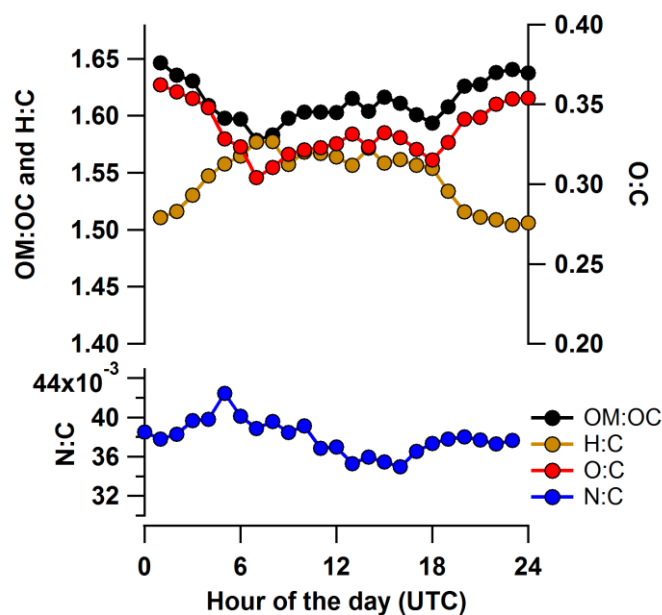


Figure P2.2 Median daily profiles for OM:OC, O:C, H:C and N:C

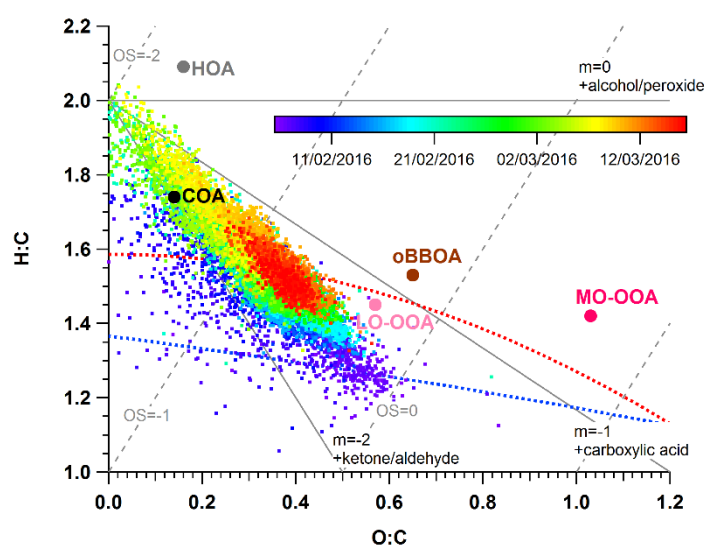


Figure P2.3 Van Krevelen diagram for all the data colored by time, with identified PMF factors (HOA: Hydrogen-like OA, COA: cooking-like OA; oBBOA: oxidized biomass burning OA, MO-OOA: more oxidized – oxygenated OA, LO-OOA: less oxidized – oxygenated OA).

### 3.3. Source apportionment of OA

The PMF analysis was applied to the high resolution mass spectra of OA by varying the number of factors from two to eight. The five factor solution was chosen based on the  $Q/Q_{\text{exp}}$

ratio, the chemical signatures of the different mass spectra, the time series and daily cycles, and the correlation with tracers and external variables. Reasoning behind this choice is presented in Table S2.1. The PMF diagnostics for the chosen solution are shown in Figure S2.6. The five factors were identified as hydrocarbon-like OA (HOA), cooking-like OA (COA), oxidized biomass burning OA (oBBOA), more oxygenated oxidized OA (MO-OOA) and less oxygenated oxidized OA (LO-OOA).

The mass spectra profiles and time series for each factor are shown in Figure P2.4a and b, respectively. The higher contributions are observed for MO-OOA (33%) and oBBOA (25%), while LO-OOA (16%), HOA (15%) and COA (11%) constituted the remaining OA mass. The time series of each PMF factor and their correlation with tracer(s) are shown in Figure S2.7. In addition, in Table S2.2 the correlations between the PMF factors and the additionally available external variables are also presented.

As mentioned in section 2.4, linking the wind speed and direction data to the PMF factors can bring about additional information on the sources of OA. Hence, in Figure P2.6 the NWR plots for each PMF factor are shown.

### 3.3.1. HOA

The HOA mass spectrum is dominated by the  $C_nH_{2n-1}^+$  and  $C_nH_{2n+1}^+$  ion series (Figure P2.4a), which are characteristic of OA mass spectra from diesel exhaust emissions (Canagaratna et al., 2004). Accordingly, the HOA factor has the highest H:C ratio (2.09), and lowest OM:OC (1.41) and O:C (0.16) ratios among all the factors. The daily profile of HOA (Figure P2.5a) shows two prominent peaks in the morning and evening hours corresponding to higher traffic activities during the rush hours. HOA is observed to be strongly correlated with  $m/z$  57 ( $r = 0.94$ ; Figure S2.7a), which is typically used as an internal tracer for HOA. Good correlations are also observed with external traffic tracers like BC ( $r = 0.83$ ) and  $NO_x$  ( $r = 0.85$ ) (Figure S2.7a and Table S2.2). The obtained HOA mass spectrum is also compared to reference ambient spectra (Crippa et al., 2013; Docherty et al., 2011; Mohr et al., 2012; Struckmeier et al., 2016) obtained from the High Resolution AMS Spectral Database (<http://cires1.colorado.edu/jimenez-group/HRAMSsd/>) and excellent correlations are obtained ( $r = 0.94-0.99$ ) (Figure S2.8). As shown in the NWR plot for HOA in Figure P2.6a, the highest concentrations are observed for very low wind speeds, particularly from the NE and E directions, suggesting that most of the HOA was locally formed or emitted. In fact, a 2-lane road is located adjacent to the sampling site and likely contributed notably to the observed HOA.

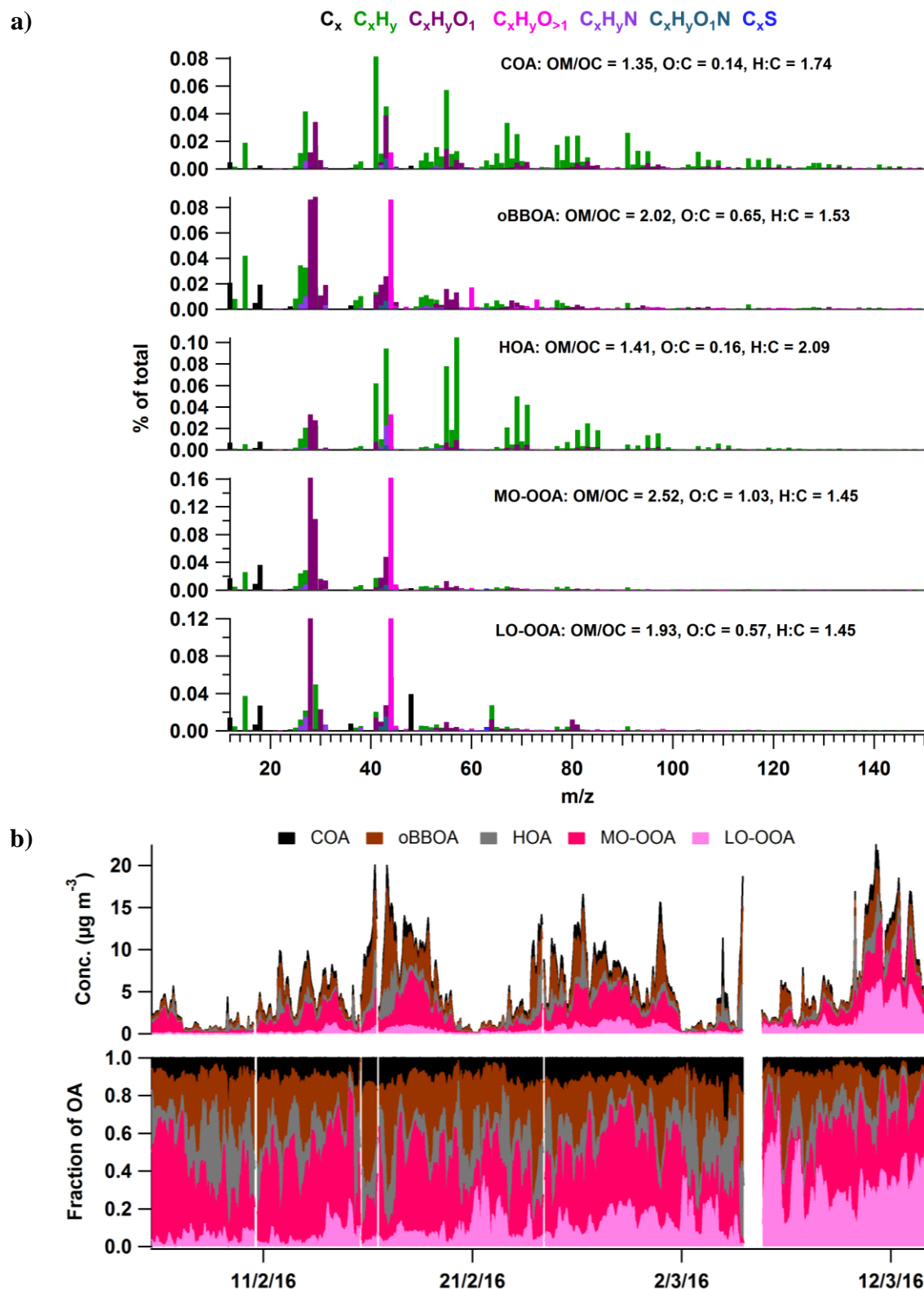


Figure P2.4 (a) Factor profiles with fragments colored by chemical families, and (b) time series of the concentrations and mass fractions of the PMF factors (HOA: Hydrogen-like OA, COA: cooking-like OA; oBBOA: oxidized biomass burning OA, MO-OOA: more oxidized – oxygenated OA, LO-OOA: less oxidized – oxygenated OA).

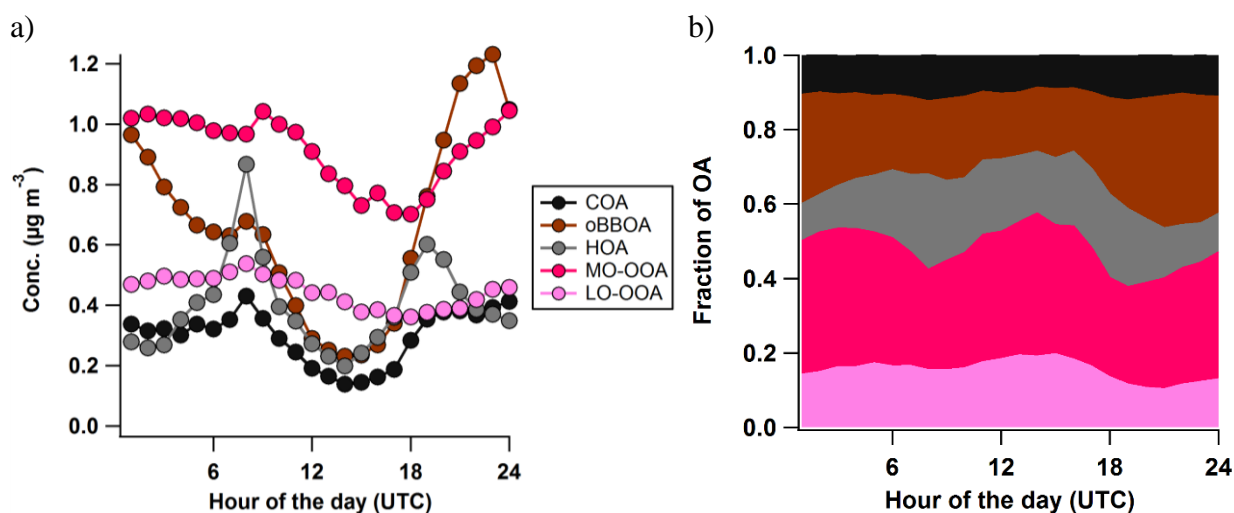


Figure P2.5 Daily profiles of PMF factors by (a) concentration and (b) contribution to OA (HOA: Hydrogen-like OA, COA: cooking-like OA; oBBOA: oxidized biomass burning OA, MO-OOA: more oxidized – oxygenated OA, LO-OOA: less oxidized – oxygenated OA).

### 3.3.2. COA

The mass spectrum of COA is similar to that of HOA (Figure P2.4a), but differs in that it contains more highly oxygenated fragments at the same nominal masses (Crippa et al., 2013; Mohr et al., 2012), particularly in  $m/z$  43 ( $\text{C}_2\text{H}_3\text{O}^+$ ) and 55 ( $\text{C}_3\text{H}_3\text{O}^+$ ) than HOA, in agreement with the higher degree of oxygenation of fatty acids that compose COA (Mohr et al., 2009). The daily profile of COA (Figure P2.5a) also resembles that of HOA, with maxima in the morning and the night, the latter appearing after that of HOA, in accordance with the dinner time. However, the characteristic lunch peak of COA was not observed. The absence of high COA during lunchtime could be attributed to a dilution effect of the mixing layer, which showed maximum values between 12 pm and 3 pm UTC (Figure S2.5a) and the absence of nearby local sources. The COA factor was nonetheless well correlated with its main tracer,  $m/z$  55 ( $r = 0.86$ ) (Figure S2.7b). Good correlations were also obtained when COA was compared to BC ( $r = 0.70$ ) and  $\text{NO}_x$  ( $r = 0.68$ ) (Table S2.2). Additionally, the COA mass spectrum was compared to reference spectra of previous studies (Crippa et al., 2013; Mohr et al., 2012; Struckmeier et al., 2016) and good correlations were obtained ( $r = 0.94$ – $0.95$ ) (Figure S2.9). The NWR plot for COA (Figure P2.6b) also shows highest concentrations for low wind speeds from all directions, implying that COA was mostly emitted locally.

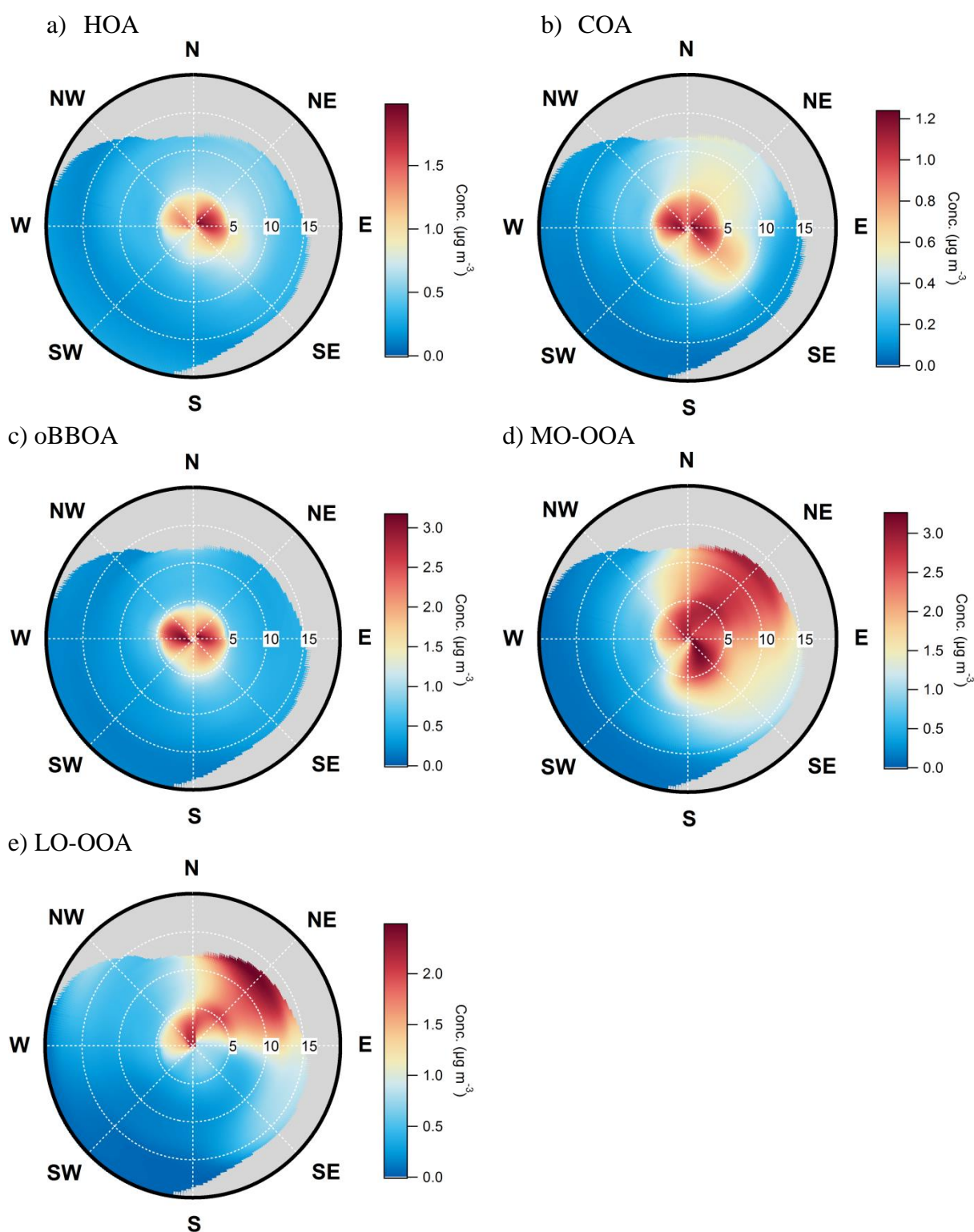


Figure P2.6 NWR plots for AMS PMF factors, colored by mass concentration (radius: wind speed in  $\text{km h}^{-1}$ ). HOA: Hydrogen-like OA, COA: cooking-like OA; oBBOA: oxidized biomass burning OA, MO-OOA: more oxidized – oxygenated OA, LO-OOA: less oxidized – oxygenated OA.

### 3.3.3. oBBOA

An oxidized BBOA factor was also retrieved by the PMF analysis. This factor is characterized by the presence of characteristic fragments of biomass burning at  $m/z$  60 and 73, associated to  $C_2H_4O_2^+$  and  $C_3H_5O_2^+$ , respectively (Figure P2.4a; Alfarrar et al., 2007). Accordingly, oBBOA is well correlated with its main tracer  $m/z$  60 ( $r = 0.90$ ; Figure S2.7c). In addition, good correlations are observed between oBBOA and Delta-C ( $r = 0.72$ ; Figure S2.7c and Table S2.2) and water-soluble  $K^+$  from MARGA measurements ( $r = 0.60$ ) (Table S2.2). As explained in section 2.2, Delta-C can be used as a tracer of wood combustion. oBBOA has a high degree of oxidation ( $OM:OC = 2.02$  and  $O:C = 0.65$ ), with notable peaks in its mass spectrum at  $m/z$  28 ( $CO^+$ ), 29 ( $CHO^+$ ) and 44 ( $CO_2^+$ ). The observation of a unique oxidized BBOA factor in OA PMF analysis is not common. Instead, most studies typically report a primary BBOA factor or two separate primary and oxidized BBOA factors. However, a recent study conducted in Houston, USA (Wallace et al., 2018), also reported the presence of a single oxidized BBOA factor ( $OM:OC$  and  $O:C$  of 2.03 and 0.65, respectively).

One previous field study has provided evidence of aqueous processing of primary BBOA (Gilardoni et al., 2016), mainly through its correlation with RH. RH values during the present measurement campaign were particularly high, with an average of  $82 \pm 12\%$ , which could promote aqueous processing of the OA. Indeed, when the correlation between the PMF factors and the RH (by bins) is evaluated, the concentration (and relative contribution) of oBBOA increases from  $0.7 \mu g m^{-3}$  (13% of OA) for  $RH < 60\%$  to  $2.24 \mu g m^{-3}$  (28%) for  $RH > 95\%$ . This positive trend is observed between oBBOA and RH, while it is not observed for the other PMF factors. This, together with the NWR graph for oBBOA (Figure P2.6c) where higher concentrations are associated with low wind speeds, suggests that aqueous processing possibly led to the rapid oxidation of locally emitted biomass burning emissions forming oBBOA.

The aqSOA (aqueous SOA) factor reported by Gilardoni et al. (2016), which was attributed to aqueous processing of primary BBOA, presented a similar oxidation degree to that of our oBBOA as shown by its  $O:C$  ratio (0.57). Elevated values for  $O:C$  ratios were also observed for laboratory-generated SOA from the photo-oxidation of organic precursors in the aqueous phase (Lee et al., 2011, 2012). Similarly to the oBBOA factor, the mass spectrum of the aqSOA factor presented characteristic signals at  $m/z$  29 ( $CHO^+$ ),  $m/z$  44 ( $CO_2^+$ ), but also in  $m/z$  43 ( $C_2H_3O^+$ ). As in this work, the moderate peak observed at  $m/z$  60 ( $C_2H_4O_2^+$ ) is

justified by the occurrence of degradation and oxidation reactions during atmospheric processing of fresh biomass-burning emissions.

The daily profile of oBBOA (Figure P2.5) shows an increase of the concentration in the late afternoon and a maximum before midnight, after which the concentrations show a sharp decrease. This profile is in agreement with the time of biomass burning activities (in the evening), then lower MLH and higher RH values during the night, promoting the aqueous processing of fresh BBOA emissions.

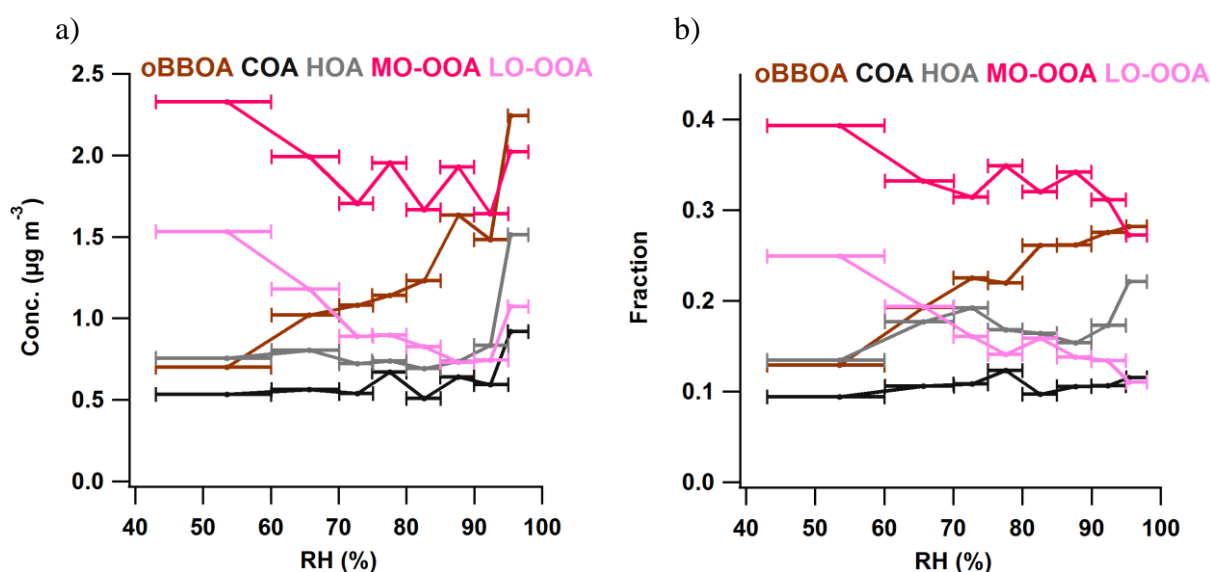


Figure P2.7 Averaged mass concentrations and relative contributions of PMF factors as a function of RH bins (the width of the bins, represented by the horizontal bars, was chosen to increase the representativeness of each interval, with  $n \geq 40$ ). HOA: Hydrogen-like OA, COA: cooking-like OA; oBBOA: oxidized biomass burning OA, MO-OOA: more oxidized – oxygenated OA, LO-OOA: less oxidized – oxygenated OA.

### 3.3.4. LO-OOA and MO-OOA

Two OOA factors were obtained and denoted as LO-OOA and MO-OOA (Figure P2.4a). Even though their mass spectra are similar ( $r = 0.82$ ), they are being considered as two separate factors since their degree of oxidation and time series are different ( $r = 0.64$ ; Figure P2.4b). The mass spectra of both factors are characterized by major peaks at  $m/z$  28 and 44, attributed to  $\text{CO}^+$  and  $\text{CO}_2^+$ , respectively. However, the MO-OOA also includes a peak at  $m/z$  29 associated to  $\text{CHO}^+$ , whereas the LO-OOA does not and instead presents small contributions from alkyl fragments at  $m/z$  29 and 64, attributed to  $\text{C}_2\text{H}_5^+$  and  $\text{C}_5\text{H}_4^+$ , respectively. Therefore, the MO-OOA factor presents higher OM:OC and O:C ratios (2.52 and 1.03, respectively) in comparison to the LO-OOA factor (1.93 and 0.57). However, both



factors have very similar H:C values (around 1.4) suggesting there was no evolution of the LO-OOA towards the MO-OOA, but rather that each OOA factor has a different origin and/or has been processed over a different timescale. While both factors showed a high correlation with  $\text{NO}_3^-$  ( $r = 0.88$  and  $0.89$  for MO-OOA and LO-OOA, respectively), the LO-OOA factor correlated better with  $\text{SO}_4^{2-}$  ( $r = 0.85$ ) than MO-OOA ( $r = 0.62$ ). This suggests that the LO-OOA could have a more regional origin.

The time series of the MO-OOA factor shows similar concentrations throughout the whole campaign (Figure P2.4b). However, the LO-OOA factor presented low concentrations during most of the time except in the last period, where its contribution showed a remarkable increase (Figure P2.4b) due to the impact of air masses from continental Europe, as will be further discussed in section 3.4. The daily profiles of both factors showed a similar cycle, with smaller concentrations in the daytime (Figure P2.5a). For MO-OOA, the concentrations are observed to be steady during the night and early morning, but showed a decrease until the evening, and then started to increase again. For LO-OOA, the observed daily profile showed a similar but less pronounced trend. Concentrations of oxygenated factors are expected to be usually observed in the daytime, particularly in the afternoon, due to higher solar radiation which promotes photochemistry leading to the formation of secondary organic aerosols. However, in this study, the concentrations of OOA factors have decreased over the day (Figure P2.5a). This could be attributed to the strong dilution effect of the mixing layer, the values of which are higher in the afternoon (Figure S2.5a). Besides, although their concentrations are going down, their contributions to total OA are increasing (Figure P2.5b) indicating that OOA is produced but somewhat masked by the enhanced ML heights.

The NWR plots for the MO-OOA and LO-OOA factors show higher concentrations for moderate wind speeds from the NE sector (Figure P2.6d-e). In addition high concentrations of the MO-OOA factor are also observed for low and moderate wind speeds from the SE sector (Figure P2.6d). This suggests that the origin of both factors is rather regional, particularly for the LO-OOA factor. The PSCF plots show that higher probabilities are observed for air masses from Belgium and Germany (Figure S2.10).

### **3.4. Impact of meteorological parameters and long range transport on NR-PM<sub>1</sub> characteristics**

The entire campaign was further divided into two different periods based on mass loadings and meteorological conditions to gain further insights about the impact of

meteorology and long range transport on aerosol characteristics. Period I (5 February to 4 March 2016) was characterized by moderate NR-PM<sub>1</sub> (average of  $8.8 \pm 7.3 \mu\text{g m}^{-3}$ ), ranging from 0.4 to  $31.5 \mu\text{g m}^{-3}$ . On the other hand, period II (5 to 16 March 2016) showed high concentrations of NR-PM<sub>1</sub> (average of  $17.2 \pm 10.9 \mu\text{g m}^{-3}$ ) with values up to  $50 \mu\text{g m}^{-3}$ . The average temperatures and RH values were similar between both periods. However, period II was associated with anticyclonic conditions, with atmospheric pressure values higher than 1020 hPa, no precipitation (4 mm in comparison to 73 mm for period I) and calm winds from the N and NE. In addition, during period II significantly lower values were observed for the mixing layer height during the nighttime (Figure S2.5a), which could favor the accumulation of pollutants. The ventilation coefficient (Figure S2.5b) also shows a similar trend, with lower nighttime values in period II ( $< 500 \text{ m}^2 \text{ s}^{-1}$ ) which indicate adverse conditions for the dispersion of pollutants (Eagleman, 1991). The backtrajectory density maps for each period (Figure S2.11) show that during period I higher probabilities of occurrence are observed for air masses from the north of France, suggesting that there is a higher influence from local areas. On the contrary, in period II high probabilities are observed for Belgium, Germany and Western Poland. Overall, this combination of factors contributed to the long-range transport of NR-PM<sub>1</sub> and its accumulation over the region of northern France.

The composition of the NR-PM<sub>1</sub> was also significantly different between both periods (Figure P2.8). In period I, the NR-PM<sub>1</sub> was dominated by OA, with an average of 43%, while the inorganic ions constituted the rest of the mass, with 33% NO<sub>3</sub>, 15% NH<sub>4</sub>, 8% SO<sub>4</sub> and 1% Cl. In period II the OA contribution decreased to 32%, and the percentage of the inorganic ions increases notably, particularly of NO<sub>3</sub> to 39%, but also of NH<sub>4</sub> (18%) and SO<sub>4</sub> (10%). This suggests that during period I, local sources contributed more significantly to OA, while during period II the long-range transported air masses led to an increase of the levels of the inorganic aerosols.

While the total OA mass in period II was not significantly higher in comparison to period I (as opposed to the inorganic part of the aerosol), we observed significant differences in its composition (Figure P2.8). On the one hand, period I the OA was dominated by local sources (59%) with average contributions of 30% for oBBOA, 17% for HOA and 12% for COA. Among the rather regional OA factors, MO-OOA clearly dominates (33%) over LO-OOA (8%) (Figure P2.8). This confirms that period I was mainly influenced by local sources.

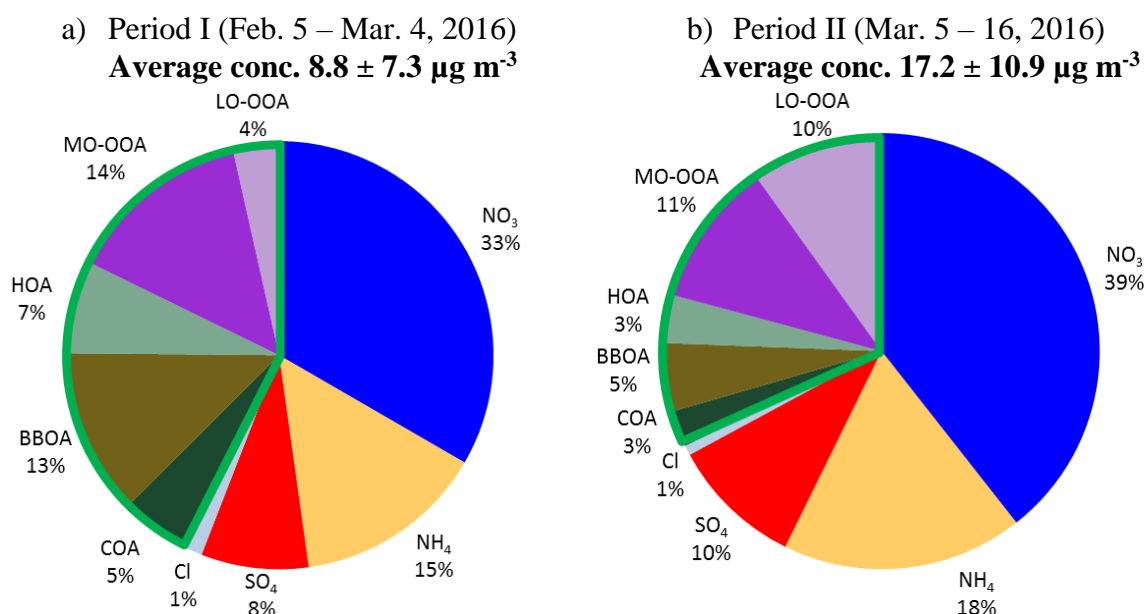


Figure P2.8 Average chemical composition of NR-PM<sub>1</sub> for (a) period I and (b) period II. The OA fraction (highlighted in light green) is subdivided into its PMF factors.

In addition, a nocturnal new particle formation (NPF) event was distinguished in period I from 15 to 16 February 2016, which has already been described in a previous article (Roig et al., submitted) and here is briefly presented in relation with the composition of the OA. A NPF event corresponds to the formation of nanometer-sized particles in the nucleation mode, mainly through gas-to-particle conversion. In Figure S2.12, the time series of the particle number size distribution (PNSD) and the geometric mean diameter of PM<sub>1</sub> obtained with a scanning mobility particle sizer (SMPS) is shown together with the time series of the PMF factors. The event took place under anticyclonic conditions, with clear sky, calm winds, low temperatures and high RH values. Additionally, the ambient concentrations of PM<sub>2.5</sub> in the previous hours of the NPF event were particularly low due to the occurrence of precipitation and marine air masses with little anthropogenic influence impacting the site (Roig et al., submitted). The NPF started at 6 pm and finished at 4 am (local time), with an average growth rate of  $5.1 \text{ nm h}^{-1}$  reaching a geometric mean diameter of 70 nm. At the same time, the concentrations of OA increased simultaneously up to  $14 \mu\text{g m}^{-3}$ , with oBBOA clearly dominating with a contribution higher than 50% during most of the event. The concentrations of soluble K<sup>+</sup> measured with a MARGA also showed the same increasing trend (Roig et al., submitted). This suggests that fast processing of organic matter from biomass burning emissions was strongly involved in this NPF event.

On the other hand, in period II the total contribution from local OA decreased significantly to 35%, with average contributions of 16% for oBBOA, 11% for HOA and 8 % for COA. The lower contribution of oBBOA during period II (i.e. under the influence of transported air masses from continental Europe) proves that primary biomass burning emissions are locally processed. The contribution of the regional factors increased up to 65% during period II. However, though the contribution of the MO-OOA factor is similar to that of period I (34%), the contribution of LO-OOA sharply increased to 31%. Therefore, it seems that the increase in LO-OOA in period II could be attributed to the impact of aged air masses transported from continental Europe.

Despite a significantly different composition of OA between both periods, the elemental ratios were rather similar. This could be attributed to a compensation of these ratios between the different OA factors (i.e. lower oBBOA and higher LO-OOA during period II).

#### **4. Conclusions**

In this study, the characteristics and sources of submicron OA were investigated during an intensive winter (5 February to 16 March 2016) in northern France. Moderate concentrations of NR-PM<sub>1</sub> ( $11.1 \pm 9.3 \mu\text{g m}^{-3}$ ) were observed, generally dominated by inorganic ions (62%). Nitrate was the dominant inorganic ion (35.9%), followed by NH<sub>4</sub> (15.9%) and SO<sub>4</sub> (8.8%). In addition, the NR (neutralization ratio) of the aerosol was close to 1 during most of the campaign, implying that there was always enough NH<sub>4</sub> to neutralize NO<sub>3</sub> and SO<sub>4</sub>.

OA was found to be moderately oxidized (O/C = 0.32) and evolving along a slope of -1 in the Van Krevelen plot (H:C vs O:C) indicating that the simultaneous addition of carbonyl and alcohol groups could be predominant in the oxidation of OA. Application of the PMF analysis to the OA mass spectra revealed the presence of several types of OA at the sampling location. Identified OA were denoted as hydrocarbon-like (HOA), cooking-like (COA), oxidized biomass burning (oBBOA), and two oxygenated factors classified into less oxidized (LO-OOA) and more oxidized (MO-OOA). The concentrations of the oBBOA factor were positively correlated with relative humidity, suggesting aqueous processing of primary biomass burning emissions took place. This was supported by high values of OM:OC and O:C during nighttime and by the NWR analysis which showed higher oBBOA concentrations for calm winds indicating local origins. On average, OA was dominated by MO-OOA (33%) and oBBOA (25%). In addition, oBBOA was shown to be involved in a nighttime NPF event

during period I suggesting a fast processing of organic species under high humidity conditions. However, during the last part of the campaign (5 to 16 March 2016) the contribution of the LO-OOA factor increased up to 31%. During the first period of the campaign (5 February to 4 March 2016) the origin of the air masses alternated from oceanic and continental, which led to low to moderate concentrations of NR-PM<sub>1</sub>. However, during the second period of the campaign (5 to 16 March 2016) the sampling site was heavily impacted by air masses from Eastern Europe rich in aged aerosols, evidenced by the high contributions from secondary inorganic and organic aerosols. In combination with an anticyclonic situation and low ventilation coefficient values, this favored the presence of high NR-PM<sub>1</sub> concentrations in the north of France. Lastly, the OA confined into a narrower space in the VK diagram during the last period of the campaign, suggesting a homogenization of the different aerosol sources due to ageing of OA during transportation.

These results indicate that during winter, aqueous processing of primary biomass burning emissions in North-Western Europe could be more important than what was previously thought. In addition, air masses arriving from Eastern Europe have a considerable impact in the region of northern France, with higher concentrations of secondary inorganic and organic aerosols. Hence, the improvement of the mitigation policies in neighboring countries of France, mainly Belgium, Germany and Poland, should exert a significant impact on the air quality.

## **5. Acknowledgements**

IMT Lille Douai acknowledges financial support from the CaPPA project, which is funded by the French National Research Agency (ANR) through the PIA (Programme d'Investissement d'Avenir) under contract ANR-11-LABX-0005-01, the CLIMIBIO project, both financed by the Regional Council "Hauts-de-France" and the European Regional Development Fund (ERDF). This field campaign was carried out within the framework of the ISARD project funded by the AACT-AIR (ADEME) program (grant 1562C0011). R. Roig Rodelas thanks ARMINES for his PhD fellowship. The authors thank Atmo Hauts-de-France and Météo-France for providing air monitoring and meteorological data, respectively.

## 6. References

- Alfarra, M. R., Coe, H., Allan, J. D., Bower, K. N., Boudries, H., Canagaratna, M. R., Jimenez, J. L., Jayne, J. T., Garforth, A. A., Li, S.-M. and Worsnop, D. R.: Characterization of urban and rural organic particulate in the Lower Fraser Valley using two Aerodyne Aerosol Mass Spectrometers, *Atmos. Environ.*, 38(34), 5745–5758, doi:10.1016/j.atmosenv.2004.01.054, 2004.
- Alfarra, M. R., Prevot, A. S. H., Szidat, S., Sandradewi, J., Weimer, S., Lanz, V. A., Schreiber, D., Mohr, M. and Baltensperger, U.: Identification of the Mass Spectral Signature of Organic Aerosols from Wood Burning Emissions, *Environ. Sci. Technol.*, 41(16), 5770–5777, doi:10.1021/es062289b, 2007.
- Allan, J. D., Delia, A. E., Coe, H., Bower, K. N., Alfarra, M. R., Jimenez, J. L., Middlebrook, A. M., Drewnick, F., Onasch, T. B., Canagaratna, M. R., Jayne, J. T. and Worsnop, D. R.: A generalised method for the extraction of chemically resolved mass spectra from Aerodyne aerosol mass spectrometer data, *J. Aerosol Sci.*, 35(7), 909–922, doi:10.1016/j.jaerosci.2004.02.007, 2004.
- Allen, G. A., Babich, P. and Poirot, R. L.: Evaluation of a New Approach for Real Time Assessment of Wood Smoke PM, in *Proceedings of the Regional and Global Perspectives on Haze: Causes, Consequences, and Controversies*, NC: Air and Waste Management Association Visibility Specialty Conference, paper 16., 2004.
- Atmo Nord-Pas-de-Calais: Bilan Annuel 2013 - Rapport Integral., 2014.
- Bozzetti, C., El Haddad, I., Salameh, D., Daellenbach, K. R., Fermo, P., Gonzalez, R., Minguillón, M. C., Iinuma, Y., Poulain, L., Elser, M., Müller, E., Slowik, J. G., Jaffrezo, J.-L., Baltensperger, U., Marchand, N. and Prévôt, A. S. H.: Organic aerosol source apportionment by offline-AMS over a full year in Marseille, *Atmos. Chem. Phys.*, 17(13), 8247–8268, doi:10.5194/acp-17-8247-2017, 2017.
- ten Brink, H., Otjes, R., Jongejan, P. and Slanina, S.: An instrument for semi-continuous monitoring of the size-distribution of nitrate, ammonium, sulphate and chloride in aerosol, *Atmos. Environ.*, 41(13), 2768–2779, doi:10.1016/j.atmosenv.2006.11.041, 2007.
- Brown, S. G., Lee, T., Roberts, P. T. and Jr, J. L. C.: Variations in the OM/OC ratio of urban organic aerosol next to a major roadway, *Journal of the Air & Waste Management Association*, 63(12), 1422–1433, doi:10.1080/10962247.2013.826602, 2013.
- Canagaratna, M. R., Jayne, J. T., Ghertner, D. A., Herndon, S., Shi, Q., Jimenez, J. L., Silva, P. J., Williams, P., Lanni, T., Drewnick, F., Demerjian, K. L., Kolb, C. E. and Worsnop, D. R.: Chase Studies of Particulate Emissions from in-use New York City Vehicles, *Aerosol Sci. Technol.*, 38(6), 555–573, doi:10.1080/02786820490465504, 2004.
- Canagaratna, M. R., Jayne, J. T., Jimenez, J. L., Allan, J. D., Alfarra, M. R., Zhang, Q., Onasch, T. B., Drewnick, F., Coe, H., Middlebrook, A., Delia, A., Williams, L. R., Trimborn, A. M., Northway, M. J., DeCarlo, P. F., Kolb, C. E., Davidovits, P. and Worsnop, D. R.: Chemical and microphysical characterization of ambient aerosols with the aerodyne aerosol mass spectrometer, *Mass Spectrom. Rev.*, 26(2), 185–222, doi:10.1002/mas.20115, 2007.

Chakraborty, A., Crenn, V., Petitprez, D. and Riffault, V.: Fine particles sampled at an urban background site and an industrialized coastal site in Northern France – Part 3: Sources, composition, and evolution of organic aerosols, in prep.

Crenn, V., Fronval, I., Petitprez, D. and Riffault, V.: Fine particles sampled at an urban background site and an industrialized coastal site in Northern France - Part 1: Seasonal variations and chemical characterization, *Sci. Total Environ.*, 578, 203–218, doi:10.1016/j.scitotenv.2015.11.165, 2017.

Crenn, V., Chakraborty, A., Fronval, I., Petitprez, D. and Riffault, V.: Fine particles sampled at an urban background site and an industrialized coastal site in Northern France—Part 2: Comparison of offline and online analyses for carbonaceous aerosols, *Aerosol Science and Technology*, 52(3), 287–299, doi:10.1080/02786826.2017.1403008, 2018.

Crippa, M., DeCarlo, P. F., Slowik, J. G., Mohr, C., Heringa, M. F., Chirico, R., Poulain, L., Freutel, F., Sciare, J., Cozic, J., Di Marco, C. F., Elsasser, M., Nicolas, J. B., Marchand, N., Abidi, E., Wiedensohler, A., Drewnick, F., Schneider, J., Borrmann, S., Nemitz, E., Zimmermann, R., Jaffrezo, J.-L., Prévôt, A. S. H. and Baltensperger, U.: Wintertime aerosol chemical composition and source apportionment of the organic fraction in the metropolitan area of Paris, *Atmos. Chem. Phys.*, 13(2), 961–981, doi:10.5194/acp-13-961-2013, 2013.

Crippa, M., Canonaco, F., Lanz, V. A., Äijälä, M., Allan, J. D., Carbone, S., Capes, G., Ceburnis, D., Dall'Osto, M., Day, D. A., DeCarlo, P. F., Ehn, M., Eriksson, A., Freney, E., Hildebrandt Ruiz, L., Hillamo, R., Jimenez, J. L., Junninen, H., Kiendler-Scharr, A., Kortelainen, A.-M., Kulmala, M., Laaksonen, A., Mensah, A. A., Mohr, C., Nemitz, E., O'Dowd, C., Ovadnevaite, J., Pandis, S. N., Petäjä, T., Poulain, L., Saarikoski, S., Sellegri, K., Swietlicki, E., Tiitta, P., Worsnop, D. R., Baltensperger, U. and Prévôt, A. S. H.: Organic aerosol components derived from 25 AMS data sets across Europe using a consistent ME-2 based source apportionment approach, *Atmos. Chem. Phys.*, 14(12), 6159–6176, doi:10.5194/acp-14-6159-2014, 2014.

DeCarlo, P. F., Kimmel, J. R., Trimborn, A., Northway, M. J., Jayne, J. T., Aiken, A. C., Gonin, M., Fuhrer, K., Horvath, T., Docherty, K. S., Worsnop, D. R. and Jimenez, J. L.: Field-Deployable, High-Resolution, Time-of-Flight Aerosol Mass Spectrometer, *Anal. Chem.*, 78(24), 8281–8289, doi:10.1021/ac061249n, 2006.

Docherty, K. S., Aiken, A. C., Huffman, J. A., Ulbrich, I. M., DeCarlo, P. F., Sueper, D., Worsnop, D. R., Snyder, D. C., Peltier, R. E., Weber, R. J., Grover, B. D., Eatough, D. J., Williams, B. J., Goldstein, A. H., Ziemann, P. J. and Jimenez, J. L.: The 2005 Study of Organic Aerosols at Riverside (SOAR-1): instrumental intercomparisons and fine particle composition, *Atmos. Chem. Phys.*, 11(23), 12387–12420, doi:10.5194/acp-11-12387-2011, 2011.

Drewnick, F., Hings, S. S., DeCarlo, P., Jayne, J. T., Gonin, M., Fuhrer, K., Weimer, S., Jimenez, J. L., Demerjian, K. L., Borrmann, S. and Worsnop, D. R.: A New Time-of-Flight Aerosol Mass Spectrometer (TOF-AMS)—Instrument Description and First Field Deployment, *Aerosol Sci. Technol.*, 39(7), 637–658, doi:10.1080/02786820500182040, 2005.

Eagleman, J. R.: Air pollution meteorology, Kansas: Trimedia., 1991.

Florou, K., Papanastasiou, D. K., Pikridas, M., Kaltsonoudis, C., Louvaris, E., Gkatzelis, G. I., Patoulas, D., Mihalopoulos, N. and Pandis, S. N.: The contribution of wood burning and other pollution sources to wintertime organic aerosol levels in two Greek cities, *Atmos. Chem. Phys.*, 17(4), 3145–3163, doi:10.5194/acp-17-3145-2017, 2017.

Gilardoni, S., Massoli, P., Paglione, M., Giulianelli, L., Carbone, C., Rinaldi, M., Decesari, S., Sandrini, S., Costabile, F., Gobbi, G. P., Pietrogrande, M. C., Visentin, M., Scotto, F., Fuzzi, S. and Facchini, M. C.: Direct observation of aqueous secondary organic aerosol from biomass-burning emissions, *PNAS*, 113(36), 10013–10018, doi:10.1073/pnas.1602212113, 2016.

Goyal, S. K. and Chalapati Rao, C. V.: Assessment of atmospheric assimilation potential for industrial development in an urban environment: Kochi (India), *Sci. Total Environ.*, 376(1), 27–39, doi:10.1016/j.scitotenv.2007.01.067, 2007.

Hallquist, M., Wenger, J. C., Baltensperger, U., Rudich, Y., Simpson, D., Claeys, M., Dommen, J., Donahue, N. M., George, C., Goldstein, A. H., Hamilton, J. F., Herrmann, H., Hoffmann, T., Iinuma, Y., Jang, M., Jenkin, M. E., Jimenez, J. L., Kiendler-Scharr, A., Maenhaut, W., McFiggans, G., Mentel, T. F., Monod, A., Prévôt, A. S. H., Seinfeld, J. H., Surratt, J. D., Szmigielski, R. and Wildt, J.: The formation, properties and impact of secondary organic aerosol: current and emerging issues, *Atmos. Chem. Phys.*, 9(14), 5155–5236, doi:10.5194/acp-9-5155-2009, 2009.

Hayes, P. L., Ortega, A. M., Cubison, M. J., Froyd, K. D., Zhao, Y., Cliff, S. S., Hu, W. W., Toohey, D. W., Flynn, J. H., Lefer, B. L., Grossberg, N., Alvarez, S., Rappenglück, B., Taylor, J. W., Allan, J. D., Holloway, J. S., Gilman, J. B., Kuster, W. C., de Gouw, J. A., Massoli, P., Zhang, X., Liu, J., Weber, R. J., Corrigan, A. L., Russell, L. M., Isaacman, G., Worton, D. R., Kreisberg, N. M., Goldstein, A. H., Thalman, R., Waxman, E. M., Volkamer, R., Lin, Y. H., Surratt, J. D., Kleindienst, T. E., Offenberg, J. H., Dusanter, S., Griffith, S., Stevens, P. S., Brioude, J., Angevine, W. M. and Jimenez, J. L.: Organic aerosol composition and sources in Pasadena, California, during the 2010 CalNex campaign, *J. Geophys. Res. Atmos.*, 118(16), 9233–9257, doi:10.1002/jgrd.50530, 2013.

Heald, C. L., Kroll, J. H., Jimenez, J. L., Docherty, K. S., DeCarlo, P. F., Aiken, A. C., Chen, Q., Martin, S. T., Farmer, D. K. and Artaxo, P.: A simplified description of the evolution of organic aerosol composition in the atmosphere, *Geophys. Res. Lett.*, 37(8), L08803, doi:10.1029/2010GL042737, 2010.

Henry, R., Norris, G. A., Vedantham, R. and Turner, J. R.: Source Region Identification Using Kernel Smoothing, *Environ. Sci. Technol.*, 43(11), 4090–4097, doi:10.1021/es8011723, 2009.

IPCC: Climate Change 2013: The Physical Science Basis. Contribution of Working Group I to the Fifth Assessment Report of the Intergovernmental Panel on Climate Change, Cambridge, United Kingdom and New York, NY, USA. [online] Available from: <http://www.ipcc.ch/report/ar5/wg1/>, 2013.

Jimenez, J. L., Jayne, J. T., Shi, Q., Kolb, C. E., Worsnop, D. R., Yourshaw, I., Seinfeld, J. H., Flagan, R. C., Zhang, X., Smith, K. A., Morris, J. W. and Davidovits, P.: Ambient aerosol sampling using the Aerodyne Aerosol Mass Spectrometer, *J. Geophys. Res. Atmos.*, 108(D7), 8425, doi:10.1029/2001JD001213, 2003.



Jimenez, J. L., Canagaratna, M. R., Donahue, N. M., Prevot, A. S. H., Zhang, Q., Kroll, J. H., DeCarlo, P. F., Allan, J. D., Coe, H., Ng, N. L., Aiken, A. C., Docherty, K. S., Ulbrich, I. M., Grieshop, A. P., Robinson, A. L., Duplissy, J., Smith, J. D., Wilson, K. R., Lanz, V. A., Hueglin, C., Sun, Y. L., Tian, J., Laaksonen, A., Raatikainen, T., Rautiainen, J., Vaattovaara, P., Ehn, M., Kulmala, M., Tomlinson, J. M., Collins, D. R., Cubison, M. J., Dunlea, J., Huffman, J. A., Onasch, T. B., Alfarra, M. R., Williams, P. I., Bower, K., Kondo, Y., Schneider, J., Drewnick, F., Borrmann, S., Weimer, S., Demerjian, K., Salcedo, D., Cottrell, L., Griffin, R., Takami, A., Miyoshi, T., Hatakeyama, S., Shimono, A., Sun, J. Y., Zhang, Y. M., Dzepina, K., Kimmel, J. R., Sueper, D., Jayne, J. T., Herndon, S. C., Trimborn, A. M., Williams, L. R., Wood, E. C., Middlebrook, A. M., Kolb, C. E., Baltensperger, U. and Worsnop, D. R.: Evolution of Organic Aerosols in the Atmosphere, *Science*, 326(5959), 1525, doi:10.1126/science.1180353, 2009.

Kanakidou, M., Seinfeld, J. H., Pandis, S. N., Barnes, I., Dentener, F. J., Facchini, M. C., Van Dingenen, R., Ervens, B., Nenes, A., Nielsen, C. J., Swietlicki, E., Putaud, J. P., Balkanski, Y., Fuzzi, S., Horth, J., Moortgat, G. K., Winterhalter, R., Myhre, C. E. L., Tsigaridis, K., Vignati, E., Stephanou, E. G. and Wilson, J.: Organic aerosol and global climate modelling: a review, *Atmos. Chem. Phys.*, 5(4), 1053–1123, doi:10.5194/acp-5-1053-2005, 2005.

Kelly, F. J. and Fussell, J. C.: Size, source and chemical composition as determinants of toxicity attributable to ambient particulate matter, *Atmos. Environ.*, 60(Supplement C), 504–526, doi:10.1016/j.atmosenv.2012.06.039, 2012.

Lanz, V. A., Prévôt, A. S. H., Alfarra, M. R., Weimer, S., Mohr, C., DeCarlo, P. F., Gianini, M. F. D., Hueglin, C., Schneider, J., Favez, O., D'Anna, B., George, C. and Baltensperger, U.: Characterization of aerosol chemical composition with aerosol mass spectrometry in Central Europe: an overview, *Atmos. Chem. Phys.*, 10(21), 10453–10471, doi:10.5194/acp-10-10453-2010, 2010.

Lee, A. K. Y., Herckes, P., Leaitch, W. R., Macdonald, A. M. and Abbatt, J. P. D.: Aqueous OH oxidation of ambient organic aerosol and cloud water organics: Formation of highly oxidized products, *Geophys. Res. Lett.*, 38(11), doi:10.1029/2011GL047439, 2011.

Lee, A. K. Y., Hayden, K. L., Herckes, P., Leaitch, W. R., Liggio, J., Macdonald, A. M. and Abbatt, J. P. D.: Characterization of aerosol and cloud water at a mountain site during WACS 2010: secondary organic aerosol formation through oxidative cloud processing, *Atmos. Chem. Phys.*, 12(15), 7103–7116, doi:10.5194/acp-12-7103-2012, 2012.

Middlebrook, A. M., Bahreini, R., Jimenez, J. L. and Canagaratna, M. R.: Evaluation of Composition-Dependent Collection Efficiencies for the Aerodyne Aerosol Mass Spectrometer using Field Data, *Aerosol Sci. Technol.*, 46(3), 258–271, doi:10.1080/02786826.2011.620041, 2012.

Mohr, C., Huffman, J. A., Cubison, M. J., Aiken, A. C., Docherty, K. S., Kimmel, J. R., Ulbrich, I. M., Hannigan, M. and Jimenez, J. L.: Characterization of Primary Organic Aerosol Emissions from Meat Cooking, Trash Burning, and Motor Vehicles with High-Resolution Aerosol Mass Spectrometry and Comparison with Ambient and Chamber Observations, *Environ. Sci. Technol.*, 43(7), 2443–2449, doi:10.1021/es8011518, 2009.

Mohr, C., DeCarlo, P. F., Heringa, M. F., Chirico, R., Slowik, J. G., Richter, R., Reche, C., Alastuey, A., Querol, X., Seco, R., Peñuelas, J., Jiménez, J. L., Crippa, M., Zimmermann, R.,

Baltensperger, U. and Prévôt, A. S. H.: Identification and quantification of organic aerosol from cooking and other sources in Barcelona using aerosol mass spectrometer data, *Atmos. Chem. Phys.*, 12(4), 1649–1665, doi:10.5194/acp-12-1649-2012, 2012.

Paatero, P. and Tapper, U.: Positive matrix factorization: A non-negative factor model with optimal utilization of error estimates of data values, *Environmetrics*, 5(2), 111–126, doi:10.1002/env.3170050203, 1994.

Pan, Y.-L.: Detection and characterization of biological and other organic-carbon aerosol particles in atmosphere using fluorescence, *Journal of Quantitative Spectroscopy and Radiative Transfer*, 150, 12–35, doi:10.1016/j.jqsrt.2014.06.007, 2015.

Petit, J.-E., Favez, O., Albinet, A. and Canonaco, F.: A user-friendly tool for comprehensive evaluation of the geographical origins of atmospheric pollution: Wind and trajectory analyses, *Environ. Mod. Soft.*, 88, 183–187, doi:10.1016/j.envsoft.2016.11.022, 2017.

Poulain, L., Inuma, Y., Müller, K., Birmili, W., Weinhold, K., Brüggemann, E., Gnauk, T., Hausmann, A., Löschau, G., Wiedensohler, A. and Herrmann, H.: Diurnal variations of ambient particulate wood burning emissions and their contribution to the concentration of Polycyclic Aromatic Hydrocarbons (PAHs) in Seiffen, Germany, *Atmos. Chem. Phys.*, 11(24), 12697–12713, doi:10.5194/acp-11-12697-2011, 2011.

Roig, R., Perdrix, E., Herbin, B. and Riffault, V.: Characterization and variability of inorganic aerosols and their gaseous precursors at a suburban site in northern France over one year (2015-2016), submitted.

Roig, R., Perdrix, E., Alleman, L., Malet, B., Herbin, B. and Riffault, V.: Sensitivity of PM<sub>2.5</sub> source apportionment to temporal resolution in a suburban site of northern France, in prep.

Saarikoski, S., Carbone, S., Decesari, S., Giulianelli, L., Angelini, F., Canagaratna, M., Ng, N. L., Trimborn, A., Facchini, M. C., Fuzzi, S., Hillamo, R. and Worsnop, D.: Chemical characterization of springtime submicrometer aerosol in Po Valley, Italy, *Atmos. Chem. Phys.*, 12(18), 8401–8421, doi:10.5194/acp-12-8401-2012, 2012.

Struckmeier, C., Drewnick, F., Fachinger, F., Gobbi, G. P. and Borrmann, S.: Atmospheric aerosols in Rome, Italy: sources, dynamics and spatial variations during two seasons, *Atmos. Chem. Phys.*, 16(23), 15277–15299, doi:10.5194/acp-16-15277-2016, 2016.

Timonen, H., Carbone, S., Aurela, M., Saarnio, K., Saarikoski, S., Ng, N. L., Canagaratna, M. R., Kulmala, M., Kerminen, V.-M., Worsnop, D. R. and Hillamo, R.: Characteristics, sources and water-solubility of ambient submicron organic aerosol in springtime in Helsinki, Finland, *J. Aerosol Sci.*, 56, 61–77, doi:10.1016/j.jaerosci.2012.06.005, 2013.

Ulbrich, I. M., Canagaratna, M. R., Zhang, Q., Worsnop, D. R. and Jimenez, J. L.: Interpretation of organic components from Positive Matrix Factorization of aerosol mass spectrometric data, *Atmos. Chem. Phys.*, 9(9), 2891–2918, doi:10.5194/acp-9-2891-2009, 2009.

Wallace, H. W., Sanchez, N. P., Flynn, J. H., Erickson, M. H., Lefer, B. L. and Griffin, R. J.: Source apportionment of particulate matter and trace gases near a major refinery near the Houston Ship Channel, *Atmos. Environ.*, 173, 16–29, doi:10.1016/j.atmosenv.2017.10.049, 2018.

Wang, Y., Hopke, P. K., Rattigan, O. V., Chalupa, D. C. and Utell, M. J.: Multiple-year black carbon measurements and source apportionment using delta-C in Rochester, New York, *J. Air Waste Manag. Assoc.*, 62(8), 880–887, 2012.

Watson, J. G.: Visibility: Science and Regulation, *J. Air Waste Manag. Assoc.*, 52(6), 628–713, doi:10.1080/10473289.2002.10470813, 2002.

WHO: Mortality and burden of disease from ambient air pollution, WHO [online] Available from: [http://www.who.int/gho/phe/outdoor\\_air\\_pollution/burden\\_text/en/](http://www.who.int/gho/phe/outdoor_air_pollution/burden_text/en/), 2014.

Williams, B. J., Goldstein, A. H., Millet, D. B., Holzinger, R., Kreisberg, N. M., Hering, S. V., White, A. B., Worsnop, D. R., Allan, J. D. and Jimenez, J. L.: Chemical speciation of organic aerosol during the International Consortium for Atmospheric Research on Transport and Transformation 2004: Results from in situ measurements, *J. Geophys. Res.: Atmospheres*, 112(D10), doi:10.1029/2006JD007601, 2007.



---

## **CHAPTER 5:**

# **Effect of high temporal resolution and database composition on source apportionment of PM<sub>2.5</sub> using positive matrix factorization**

---



## **CHAPTER 5. Effect of high temporal resolution and database composition on source apportionment of PM<sub>2.5</sub> using positive matrix factorization**

The fifth chapter presents a thorough source apportionment study of PM<sub>2.5</sub> based on the hourly database of MARGA and 2- $\lambda$  aethalometer measurements (PMF<sub>h</sub>). Since this approach is not very common, a comparison with other source apportionment approaches is performed with two more typical datasets (different input variables and/or temporal resolutions). The first one consists of a daily database where the hourly MARGA and aethalometer measurements have been averaged to daily values and major and trace elements have been included in order to take advantage of their tracing capabilities and eventually determine additional sources (PMF<sub>d</sub>). The second one is based on the organic mass spectra presented in the previous chapter (PMF<sub>org</sub>). This chapter is also presented as a research article named which is currently under preparation and needs to be sent to some co-authors.

Supplementary information to this article is also available in Annex 4 of this manuscript. This includes complementary figures and tables, as well as a section concerning the calculation of the uncertainties and another on the comparison between PMF<sub>h</sub> and PMF<sub>d</sub> with the same input variables.





## Effect of high temporal resolution and database composition on source apportionment of PM<sub>2.5</sub> using positive matrix factorization

Roger Roig, Esperanza Perdrix\*, Laurent Alleman, Bruno Malet, Benoît Herbin,  
Véronique Riffault

IMT Lille Douai, Univ. Lille, SAGE – Département Sciences de l'Atmosphère et Génie de  
l'Environnement, F-59000 Lille, France

\* Corresponding author: Esperanza Perdrix ([esperanza.perdrix@imt-lille-douai.fr](mailto:esperanza.perdrix@imt-lille-douai.fr))

**Abstract.** The increasing availability of online measurements for the chemical speciation of aerosols enables performing source apportionment studies with high temporal resolution, typically of an hour or less. However online instruments cannot generally analyze as many chemical tracers as offline methodologies manage to do. One question may arise is the extent to which the coupling of a higher measurements frequency with lower chemical information impacts source apportionment. In the present work, two source apportionment studies of fine particulate matter (PM<sub>2.5</sub>) at a suburban site in northern France, a region frequently impacted by particulate pollution episodes, were performed and compared using positive matrix factorization (PMF). The PMF analysis was applied to differently time-resolved datasets of PM<sub>2.5</sub> species concentrations: (i) an hourly dataset with 9 chemical variables consisting of water-soluble ions (WSI) (NO<sub>3</sub><sup>-</sup>, SO<sub>4</sub><sup>2-</sup>, NH<sub>4</sub><sup>+</sup>, Na<sup>+</sup>, K<sup>+</sup>, Mg<sup>2+</sup>, C<sub>2</sub>O<sub>4</sub><sup>2-</sup>) in the aerosol phase obtained with a MARGA system and two types of particulate absorbing carbon (BC and Delta-C) acquired with a double-wavelength aethalometer, leading to an hourly-based PMF (PMF<sub>h</sub>); (ii) a daily-resolved dataset with 29 chemical variables composed of the daily averages of all the variables used in the PMF<sub>h</sub> and of several major (Ca, Fe, K) and trace elements (As, Ba, Bi, Cd, Ce, Co, Cr, Cu, Mn, Mo, Ni, Pb, Rb, Sb, Se, Sr, Zn) obtained through 24-h filter sampling and subsequent ICP-MS analysis, giving a daily-based PMF (PMF<sub>d</sub>). Additionally, PMF was applied to 5-min resolved data of PM<sub>1</sub> organic mass spectra (PMF<sub>org</sub>) collected during wintertime with a HR-ToF-AMS, and hourly averages were compared to the PMF<sub>h</sub> for common sources. Besides, the geographical origins of the source factors was investigated using non-parametric wind regression (NWR) and positive source contribution function (PSCF) applied to the obtained contributions of the source factors coupled with local wind characteristics and air mass back-trajectories, respectively, in order to distinguish between local and regional sources. Five common source factors were found both

in the PMF<sub>h</sub> and PMF<sub>d</sub>, identified as: sulfate-rich, nitrate-rich, marine, road traffic and biomass combustion. The hourly resolution of the database allowed observing aerosol formation processes such as the night-time increase of the nitrate-rich factor as well as the daily variability of certain sources including road traffic and biomass combustion. In addition, the higher number of data points resulting from hourly measurements also led to more robust and precise results for the determination of the geographical origin of sources by means of NWR and PSCF. However, some differences in the contributions to PM<sub>2.5</sub> of the common source factors were found between both approaches, which were attributed to the loss of variability due to averaging of the hourly data and to the splitting into more source factors in the PMF<sub>d</sub>. In fact, the addition of the major and trace elements in PMF<sub>d</sub> allowed the deconvolution of three extra source factors: metal industry background (MIB), local industry and dust, which constitute 10% of the PM<sub>2.5</sub> fraction on average. The NWR and PSCF analyses determined the regional origin of the sulfate-rich, nitrate-rich and marine aerosol, while the remaining source factors were found to have a rather local origin. This work shows that in the north of France the continuous hourly measurement of a few selected variables, namely ionic species and different types of absorbing carbon, is sufficient to perform a consistent source apportionment, although the knowledge of the major and trace elements temporal variability is essential to highlight some industrial sources.

**Keywords:** MARGA, aethalometer, ICP-MS, PMF

## 1. Introduction

In order to apply effective pollution reduction strategies, it is required to have a good knowledge on the sources at both the regional and local levels. One efficient approach for their identification is the use of statistical receptor models. These models can be employed even when there is little or no knowledge about the sources. Based on a mass balance with mass conservation, they apportion different chemical species to a given number of sources in what is commonly known as source apportionment (SA). Positive matrix factorization (PMF) is one of the most used receptor-based techniques, which determines, from a set of observations of different chemical species, the possible sources and their contributions by applying physical constraints (Paatero and Tapper, 1994; Viana et al., 2008). PMF has been widely applied to particulate matter (PM) such as PM<sub>2.5</sub>, i.e. fine particles with an aerodynamic diameter inferior to 2.5 µm (Amato et al., 2009; Bressi et al., 2014; Crilley et al.,

2017; Ledoux et al., 2017; Masiol et al., 2017; Mooibroek et al., 2011; Yli-Tuomi et al., 2015), which is an important contributor to air pollution in Europe (EEA, 2015). Exposure to PM<sub>2.5</sub> has been associated with severe health effects and life expectancy reduction in the long term (Kim et al., 2015). In France alone, a comprehensive study reported an annual average of 48,000 premature deaths related to PM<sub>2.5</sub> exposure (Santé publique France, 2016). In order to reduce the exposure to ambient PM<sub>2.5</sub> in Europe, the 2008/50/EC Directive establishes an annual limit value of 25 µg m<sup>-3</sup>. More strictly, a recommended value of 10 µg m<sup>-3</sup> is set by the World Health Organization (WHO).

To the best of our knowledge, only two long-term studies focusing on the SA of daily PM<sub>2.5</sub> species in North-Western Europe with a minimum duration of one year have been published in recent years. In France, a study was carried out at an urban background site in Paris in 2009-2010 (Bressi et al., 2014). In the Netherlands, a PMF analysis was performed on pooled data from 5 different sites of various typologies in 2007-2008 (Mooibroek et al., 2011). In both studies, factors of secondary aerosol sources including “nitrate-rich” and “sulfate-rich” secondary aerosols were clearly dominating, with average annual contributions of 51% in Paris and 69% in the Netherlands, and in both cases were attributed to mid- to long-range transport from continental Europe.

In addition, most of the SA studies have been applied to daily-resolved data obtained by offline filter sampling. This kind of datasets does not provide information regarding the (trans)formation processes of aerosols or the change of pollution sources at a high time resolution, and are rather a reflection of a long-term equilibrium state. This hinders the understanding of source patterns, which may be critical in the implementation of mitigation policies (Peng et al., 2016). To overcome this limitation, near real-time measurements have been used to determine the composition and sources of aerosols with a high-time resolution (~1 hour or less). Nevertheless, most of these studies either used aerosol mass spectrometers (in PM<sub>1</sub>) and just focused on the apportionment of the organic fraction of the aerosol (Crippa et al., 2014; Fröhlich et al., 2015; Lanz et al., 2010), or were limited to the PM characterization but did not further identify the possible sources and their variability (Makkonen et al., 2012, 2014; Stieger et al., 2017; Twigg et al., 2015).

This study aims at finding out the advantages and limitations of carrying out a SA study of PM<sub>2.5</sub> using near real-time information with a limited number of chemical species, instead of using daily-averaged data with a more detailed chemical speciation. For this purpose, sources of PM<sub>2.5</sub> were investigated by carrying out two SA studies using PMF based on a 1-year long database from a suburban site of northern France. The geographical origins

of the source factors were determined using Non-Parametric Wind Regression (NWR) and Potential Source Contribution Function (PSCF). The influence of the temporal resolution of the data and the extent of the database on the PMF results was assessed by comparing different approaches. A first approach is based on hourly-resolved data (PMF<sub>h</sub>) of water soluble ions (WSI), black carbon (BC), Delta-C and PM<sub>2.5</sub>. This type of database is often obtained with online instruments but in the case of the MARGA, it consists of a limited number of variables and has been rarely tested in order to provide information on sources (Fan et al., 2014; Gao et al., 2016; Peng et al., 2016). The other approach (PMF<sub>d</sub>) uses all of the above variables averaged on a daily basis and adds supplementary daily variables, namely major and trace elements obtained from filter sampling and subsequent ICP-MS analysis. PMF<sub>d</sub> is directed at the detection of additional source factors which could not be deconvolved without considering the major and trace elements, in order to evaluate the possible error on sources associated with the hourly approach. Additionally, the PMF results (PMF<sub>org</sub>) obtained only over the wintertime period with a third dataset acquired with a high resolution-time of flight-aerosol mass spectrometer (HR-ToF-AMS; time resolution of 5 minutes) and whose details can be found elsewhere (Roig et al., in prep.), were used as a consistency check for common sources. The comparison between these approaches and the advantages and limitations of using each one are assessed.

## **2. Materials and methods**

### **2.1. Site description**

Hourly and daily observations were carried out for 1 year from August 2015 to July 2016 in Douai, northern France (50°23'03''N, 3°05'08''E, and 20 m above sea level). Douai is situated in a flat region and is about 25-30 km to the European Metropolis of Lille, which is the second most densely populated metropolis of France with about 1.2 million inhabitants and a population of 1,832 inhab. km<sup>-2</sup>. The climate of the region is characterized by low seasonal thermal amplitudes and regular precipitations throughout the year, with no dry season. The sampling site was located outside the city center and is considered to be representative of the background pollution of the region.

The area of northern France is affected by high ambient concentrations of PM<sub>2.5</sub> which often exceed the recommended and limit values during several day long pollution events. For the year 2016, 15 of those were recorded by the local air quality monitoring network totaling 34 days (Atmo Hauts-de-France, 2017). As the north of France has a rather flat topography and because it is under the predominant influence of marine winds from the Atlantic Ocean

and the North Sea, it may be considered that the relief situation generally favors the dispersion of pollutants. Therefore, these repeated particulate pollution episodes are rather attributed partly to the high population density and intense industrial and agricultural activity in the region, but also to the proximity of major industrialized, agricultural and/or highly populated areas including the Benelux and the Ruhr regions in the east, Paris in the south, and London in the north.

## 2.2. Instrumentation

The commercially available MARGA 1S (Metrohm Applikon B.V, Netherlands) (ten Brink et al., 2007) was used for the hourly determination of 8 water-soluble inorganic ions (WSII) ( $\text{NO}_3^-$ ,  $\text{SO}_4^{2-}$ ,  $\text{NH}_4^+$ ,  $\text{Na}^+$ ,  $\text{Cl}^-$ ,  $\text{K}^+$ ,  $\text{Mg}^{2+}$ ,  $\text{Ca}^{2+}$ ), 1 organic water-soluble ion ( $\text{C}_2\text{O}_4^{2-}$ ) in  $\text{PM}_{2.5}$  and 5 gaseous precursors ( $\text{HCl}$ ,  $\text{HONO}$ ,  $\text{HNO}_3$ ,  $\text{SO}_2$ ,  $\text{NH}_3$ ). Briefly, ambient air was drawn at  $1 \text{ m}^3 \text{ h}^{-1}$  through a Teflon-coated  $\text{PM}_{2.5}$ -inlet (Leckel) followed by a 2-m long polyethylene tube of 1/2" in diameter. The air then entered the Wet Rotating Denuder (WRD), where water-soluble gases diffused to an absorption solution (made of 10 ppm hydrogen peroxide in ultrapure water). Aerosol particles were collected downstream in a Steam Jet Aerosol Collector (SJAC) where the water-soluble fraction of the aerosol was solubilized while the non-soluble compounds were retained by a  $0.45 \mu\text{m}$  porosity PFTE filter. The water-soluble gas phase sampled from the WRD and the aerosol phase from the SJAC were collected in separate 25 mL syringes and successively analyzed in an ion chromatography system with both cation and anion columns. More details on the QA/QC of the measurements can be found in a previous paper from our group (Roig et al., submitted).

An aethalometer AE42 (Magee Scientific, USA) was operated at 2 wavelengths (370 and 880 nm) for the analysis of carbonaceous compounds absorbing in the UV (among which aromatic compounds) and near infrared (mostly black carbon), respectively, with a time resolution of 5 minutes. Black carbon (BC) concentrations were calculated from the absorption coefficient at 880 nm, and corrected for artifacts (Weingartner et al., 2003). In addition, another variable called Delta-C was determined by the difference of light absorption between 370 nm and 880 nm ( $\text{Delta-C} = \text{BC}_{370\text{nm}} - \text{BC}_{880\text{nm}}$ ) (Allen et al., 2004). Delta-C has previously been found to correlate with wood-burning markers such as levoglucosan and  $\text{K}^+$  and might therefore be used as a proxy of wood combustion (Wang et al., 2012).

The  $\text{PM}_{2.5}$  total mass was measured by a Beta Attenuation Monitor (BAM-1020; Met One Instruments, USA) every hour. Metals (Al, Ca, Fe, K, Mg, Na, As, Ba, Bi, Cd, Ce, Co, Cr, Cu, Mn, Mo, Ni, Pb, Rb, Sb, Se, Sn, Sr, Ti, Zn, V) were sampled on Teflon filters on a

daily basis using a PARTISOL 2300 air sampler with PM<sub>2.5</sub> cartridges, then analyzed by acid microwave digestion by inductively coupled plasma and mass-spectrometry (ICP-MS) (Alleman et al., 2010; Mbengue et al., 2014). In addition, nitrogen oxides were analyzed every 15 minutes with a chemiluminescence analyzer (NOx 2000G: Seres environment, France). Meteorological parameters such as temperature, relative humidity, pressure, wind speed and direction, and precipitation were also monitored on site and a summary is presented in Table S3.1 in the supplementary material (SM).

In addition, a high resolution-time of flight-aerosol mass spectrometer (HR-ToF-AMS; Aerodyne Research Inc., USA), hereafter named AMS, was deployed in an intensive campaign from 5 February to 16 March 2016 in order to obtain information about the chemical composition and concentrations of the non-refractory PM<sub>1</sub>, which includes NO<sub>3</sub>, NH<sub>4</sub>, SO<sub>4</sub>, Cl and organic aerosols/matter (OA). Further details on the instrument principle and operation during this campaign can be found elsewhere (DeCarlo et al., 2006; Roig et al., in prep.).

All the presented measurements are given in Coordinated Universal Time (UTC) unless otherwise stated, and seasons are differentiated as follows: winter (December, January, February), spring (March, April, May), summer (June, July, August) and autumn (September, October, November).

### 2.3. Source apportionment

The Positive Matrix Factorization (PMF) multivariate source-receptor statistical analysis model has been applied in this study. PMF is based on factor analysis of the data and on the principle of mass conservation (Paatero and Tapper, 1994). When applied to a dataset of concentrations, the model apportions the input variables to a user-chosen number of factors depending on their temporal covariability. A regression between each of the factors and the measured concentrations allows to estimate the contributions from each source/factor. This is achieved by solving the mass balance equation (Eq.1):

$$x_{ij} = \sum_{k=1}^p g_{ik} \cdot f_{kj} + e_{ij} \quad \text{Eq. 1}$$

where  $x_{ij}$  expresses the concentration of a chemical species  $j$  at time  $i$ ;  $p$  is the number of considered factors;  $g_{ik}$  the contribution of the factor or source  $k$  at time  $i$ ;  $f_{kj}$  the fraction of the species  $j$  in the chemical profile of the factor or source  $k$ ; and  $e_{ij}$  the fraction of the concentration of species  $j$  at time  $i$  not explained by the model (residual concentration, i.e. the

difference between the measured and modelled values of the concentration of every species at each time). To find the solution, a given number of factors ( $p$ ) has to be assumed, then the model minimizes the objective function  $Q$  (Eq.2), in which  $n$  is the number of observations,  $m$  the number of species, and  $\sigma_{ij}$  is the uncertainty associated with the concentration of the  $j^{\text{th}}$  species at time  $i$ :

$$Q = \sum_{i=1}^n \sum_{j=1}^m \left( \frac{e_{ij}}{\sigma_{ij}} \right)^2 \quad \text{Eq. 2}$$

A stand-alone version of PMF developed by the United States Environmental Protection Agency (US EPA PMF 5.0) was used in this work. In order to perform the PMF analysis, two input matrices were prepared following the general guidelines of Polissar et al. (1998): one with the concentrations of each species for each sample and another of the exact same size with the uncertainties associated to each measurement. The data points below the detection limit (DL) were replaced by  $DL/2$ , with an associated uncertainty of  $5/6$  DL. In addition multiple imputation was used in order to estimate some missing values. This methodology gives estimations based on statistical relationships between different chemical species and has already been used in previous studies (Mooibroek et al., 2011). The corresponding uncertainties were multiplied by a factor of 4. The detailed calculation of the uncertainties is presented in section 3 of the supplementary material.

The PMF analysis was applied to both datasets ( $PMF_h$  and  $PMF_d$ ) using the following parameters: (i) 100 simulations were run in order to ensure the quality and robustness of the final solution with an arbitrary start for each run (random seed); (ii) different numbers of factors were tried, ranging from 2 to 7 factors for  $PMF_h$  and from 3 to 12 factors for  $PMF_d$ ; (iii) the final solution was validated by the application of the bootstrap method with a total of 100 simulations and a minimum correlation coefficient ( $r = 0.6$ ). The quality and robustness of the PMF solution was also assessed by the analysis of the  $Q_{\text{true}}/Q_{\text{exp}}$  ratio, the residuals, the comparison of the measured and modelled concentrations and the comparison of the results with external variables according to the recommendations of the European Joint Research Center guides (Belis et al., 2014; Comero et al., 2009).

It should be noted that a second type of  $PMF_d$  where the exact same variables as in  $PMF_h$  were used, was also run in order to evaluate the influence of time resolution alone in the output of the PMF. This comparison is described in more detail in section 3.3 and section 4 of the supplementary material.

In addition, PMF<sub>h</sub> results have been compared to those of the PMF<sub>org</sub> applied to the organic mass spectra obtained by AMS measurements. Five factors were deconvolved from that source apportionment study, including cooking-like organic aerosol (COA), hydrocarbon-like OA (HOA), biomass burning-like OA (BBOA), more and less oxidized oxygenated OA (MO-OOA and LO-OOA). For more details of the PMF<sub>org</sub>, the reader is referred to another article (Roig et al., in prep.).

## 2.4. Geographical determination of sources

### 2.4.1. Non-parametric wind regression (NWR)

The non-parametric wind regression (NWR) is a hybrid source-receptor model which provides smoothed pollution roses, useful to distinguish between local and regional sources of hourly averaged atmospheric concentrations of a pollutant based on wind speed ( $u$ ) and direction ( $\theta$ ) (Henry et al., 2009):

$$E(C|\theta, u) = \frac{\sum_{i=1}^N K_1\left(\frac{\theta - W_i}{\sigma}\right) \cdot K_2\left(\frac{u - U_i}{h}\right) \cdot C_i}{\sum_{i=1}^N K_1\left(\frac{\theta - W_i}{\sigma}\right) \cdot K_2\left(\frac{u - U_i}{h}\right)} \quad \text{Eq.3}$$

where  $E$  is the concentration estimate at a wind direction  $\theta$  and wind speed  $u$ ;  $W_i$ ,  $U_i$  and  $C_i$  the wind direction, speed and atmospheric concentrations, respectively, measured at  $t_i$ ;  $\sigma$  and  $h$  the smoothing factors (which were suggested for each species by the software); and  $K_1$  and  $K_2$  are a Gaussian kernel function for wind direction  $\theta$  and an Epanechnikov kernel function for wind speed  $u$ , respectively, used to smooth the data (Henry et al., 2009). These results are then weighted by the frequency of the winds to apportion the weighted concentrations obtained from Eq.3 to source areas. Hence, an empirical joint probability density of wind speed and direction is calculated using the kernel density estimate:

$$f(\theta, u) = \frac{1}{N\sigma h} \cdot \sum_{i=1}^N K_1\left(\frac{\theta - W_i}{\sigma}\right) K_2\left(\frac{u - U_i}{h}\right) \quad \text{Eq.4}$$

where  $N$  is the total number of points. NWR plots for every PMF factor were calculated using the Zefir v3.31 IGOR tool (Petit et al., 2017).

### 2.4.2. Potential source contribution function (PSCF)

PSCF is a statistical source-receptor model aiming at determining the geographical origins of high concentrations of air pollutants. It is based on the analysis of the residence



times of air masses using air mass trajectories back in time. The main idea is that the longer an air mass stays over a pollution source, the higher the pollution brought by the air mass to the receptor site. Generally, the domain covered by the back-trajectories is meshed according to a regular grid. The PSCF model calculates the probability of having a pollutant source located in a grid cell of the domain and responsible for pollutant concentrations measured at the receptor site above a given threshold, following the equation:

$$PSCF = \frac{m_{ij}}{n_{ij}} \quad \text{Eq.5}$$

where  $m_{ij}$  is the number of endpoints of backtrajectories passing over the  $ij^{\text{th}}$  gridcell at latitude  $i$  and longitude  $j$  and associated to concentrations measured at the receptor site exceeding a specific threshold (in this case the 75<sup>th</sup> percentile was used); and  $n_{ij}$  the total number of endpoints of trajectories passing over the  $ij^{\text{th}}$  gridcell. A high value of the PSCF probability for the  $ij^{\text{th}}$  gridcell indicates a high probability that the  $ij^{\text{th}}$  gridcell corresponds to a source location.

The backtrajectories used for PSCF analysis were calculated with HYSPLIT 4 (HYbrid Single-Particle Lagrangian Integrated Trajectory) (Stein et al., 2015) for an arrival height of half the planetary boundary layer, at a 3-hour interval (8 trajectories per day at 0, 3, 6, 9, 12, 15, 18, 21 UTC), 72 hours back in time. PSCF was applied using the Zefir v3.31 tool for Igor Pro v. 6.37 software (Wavemetrics Inc.), which allows the inclusion of additional constraints for parameters such as precipitation and altitude. The precipitation threshold allows to account for wet deposition, meaning that whenever precipitation has taken place, the air parcel would be cleaned (i.e. PSCF probability = 0) and that each of the preceding cells would also present a zero value. This zero probability is assigned to the preceding endpoints because the information on possible pollution sources is lost when wet deposition occurs. Similarly, the altitude threshold allows to ignore backtrajectory endpoints with an altitude above the planetary boundary layer height (PSCF probability = 0). If a height above the set threshold is found, the air parcel is also cleaned as well as all the preceding cells because the air parcel is considered “diluted” in the free troposphere. In this work, thresholds of 1 mm/hour for the rain and 1500 m for the altitude were set for all PSCF calculations.

In order to reduce the influence of backtrajectories with low  $n_{ij}$  (passing only a few times over the  $ij^{\text{th}}$  grid cell) a weighting function is applied, giving more weight to those with more backtrajectory endpoints and thus being statistically more significant. The sigmoidal function used in Zefir is described in Equation 6:

$$W = \frac{1}{(1+c) \cdot (1+e^{-a \cdot (x-b)})} + \frac{c}{1+c} \quad \text{Eq.6}$$

The fixed coefficients a, b and c are chosen by the user and were kept by default at 10, 0.5 and 0, respectively, in this study.

### 3. Results and discussion

#### 3.1. Dataset presentation

The chemical species used in each of the PMF analyses have been categorized according to their signal-to-noise ratio (S/N). The variables with S/N higher than 1.6 were categorized as strong, those with S/N lower than 1.6 but above 0.2 as weak and their uncertainty was multiplied by 3, other species with S/N lower than 0.2 (i.e.  $\text{Ca}^{2+}$ ) were removed from the analysis. The major components of the aerosol (i.e.  $\text{NO}_3^-$ ,  $\text{SO}_4^{2-}$ ,  $\text{NH}_4^+$ , BC) presented high S/N and were marked as strong. On the other hand, the majority of the minor ions and trace elements were marked as weak. It is worth noting the case of  $\text{Mg}^{2+}$  and  $\text{K}^+$ , which presented very low S/N due to their high number of points below the DL during some periods of the year. However, they were included in the analysis since they are valuable tracers of the sea spray and biomass combustion emissions, respectively. In addition, for the specific case of Delta-C, with S/N of 0.9 due to a lack of points above the DL in the warm months, it was classified as a strong variable due to its relevance in tracing the biomass combustion source. Finally, the  $\text{PM}_{2.5}$  mass was categorized as the total variable with an uncertainty multiplied by 3.

Other variables were not included in the PMF analysis due to various reasons. This was the case of  $\text{Cl}^-$ , which was not correctly measured by the MARGA when the anion chromatographic column was aging, and  $\text{Ca}^{2+}$ , which was excluded as well since too many data points were below the DL. Some elements from the ICP-MS analysis (mainly Al, Sn and Ti) were not well modelled ( $r^2 < 0.1$ ) by PMF and hence were also dismissed to help improving the solution.

The main statistics for the variables used in the  $\text{PMF}_h$  and  $\text{PMF}_d$  are given in Table P3.1. For more information about the composition of the aerosol, the reader is referred to a previous article from Roig et al. (submitted).

### 3.2. Hourly PMF results

The number of factors was varied between 2 and 7 factors and the solution with 5 factors was chosen as the most appropriate, yielding a  $Q_{\text{true}}/Q_{\text{exp}}$  ratio of 2.0, a robust bootstrap (Table S3.2 in the supplementary material), and meaningful chemical profiles. The source factors are shown in Figure P3.1, together with their time series and the main tracer for each factor. The modelled and measured  $\text{PM}_{2.5}$  agreed satisfactorily ( $r^2 = 0.83$ ) with 83% of the variability of  $\text{PM}_{2.5}$  well represented by the model (Figure S3.1), which gives confidence in the solution. In addition, the seasonal contributions of each factor are shown in Figure P3.2, the comparison between the contributions during daytime and nighttime in Figure P3.3. and their daily profiles for the whole year and every season in Figure P3.4. In decreasing order of total  $\text{PM}_{2.5}$  mass contribution, the obtained factors are sulfate-rich (41%), nitrate-rich (26%), road traffic (17%), marine (11%) and biomass combustion (5%) aerosols.

The first source factor consists of high shares of  $\text{SO}_4^{2-}$  (76%),  $\text{C}_2\text{O}_4^{2-}$  (69%) and  $\text{NH}_4^+$  (32%), and lower shares of BC (8%),  $\text{Mg}^{2+}$  (17%) and  $\text{K}^+$  (22%) (Figure P3.1a, left). The molar ratio of  $\text{NH}_4^+$  over  $\text{SO}_4^{2-}$  is equal to 1.6, which is close to the value of 2 for ammonium sulfate, suggesting its presence in this factor along with some  $\text{NH}_4\text{HSO}_4$ . The high contribution of this factor to the  $\text{PM}_{2.5}$  mass is not explained by the contribution of secondary sulfate alone, which totals only 1.6 out of  $4.9 \mu\text{g m}^{-3}$ . Thus about two thirds of the mass concentration due to this source factor (corresponding to ~25% of the  $\text{PM}_{2.5}$  mass) is brought by other constituents than ammonium sulfate salts, probably by a significant (but not measured) contribution of organic matter (OM) which is supported by the highest share of oxalate. As expected, a higher contribution of this source factor is observed in the warmer months (August 2015; end of May, June and July 2016), mainly due to the higher solar radiation which can promote the photochemical activity in the atmosphere leading to (i) a higher oxidation of sulfate precursors and (ii) a higher oxidation of organic compounds (promoting the formation of oxalate) (Figure P3.1a, right). March 2016 also experienced elevated concentrations due to the occurrence of exceedance episodes favored by aged air mass transport from continental Europe (Roig et al., submitted).

Table P3.1 Main statistics for the input data as used in PMF<sub>h</sub> (7862 points) and PMF<sub>d</sub> (298 points) (concentrations are in  $\mu\text{g m}^{-3}$  except for elements analyzed by ICP-MS (from Ca to Zn) which are in  $\text{ng m}^{-3}$ ).

	Variable	S/N	Category	Min	25 <sup>th</sup>	Median	75 <sup>th</sup>	Max	DL
PMF <sub>h</sub>	PM <sub>2.5</sub>	5.0	Weak (T)	0.50	8.0	11.0	16.0	72.0	0.5
	NO <sub>3</sub> <sup>-</sup>	7.2	Strong	0.03	1.01	1.93	4.51	38.8	0.06
	SO <sub>4</sub> <sup>2-</sup>	5.5	Strong	0.06	0.89	1.43	2.19	12.6	0.11
	NH <sub>4</sub> <sup>+</sup>	5.6	Strong	0.02	0.32	0.75	1.63	13.0	0.03
	C <sub>2</sub> O <sub>4</sub> <sup>2-</sup>	0.8	Weak	0.04	0.09	0.15	0.22	1.10	0.08
	Na <sup>+</sup>	1.6	Strong	0.02	0.02	0.05	0.11	0.87	0.03
	Mg <sup>2+</sup>	0.3	Weak	0.01	0.01	0.01	0.01	0.23	0.02
	K <sup>+</sup>	0.3	Weak	0.02	0.02	0.02	0.02	0.45	0.03
	BC	3.5	Strong	0.03	0.16	0.31	0.57	3.45	0.05
	Delta-C	0.9	Strong	0.00	0.00	0.00	0.02	0.80	0.01
	Variable	S/N	Category	Min	25 <sup>th</sup>	Median	75 <sup>th</sup>	Max	DL
PMF <sub>d</sub>	PM <sub>2.5</sub>	5.0	Weak (T)	2.5	8.4	11.0	16.2	46.4	0.5
	NO <sub>3</sub> <sup>-</sup>	7.3	Strong	0.34	1.25	2.37	4.57	20.9	0.06
	SO <sub>4</sub> <sup>2-</sup>	5.6	Strong	0.31	0.98	1.46	2.14	6.09	0.11
	NH <sub>4</sub> <sup>+</sup>	5.8	Strong	0.04	0.37	0.81	1.71	8.12	0.03
	C <sub>2</sub> O <sub>4</sub> <sup>2-</sup>	0.8	Weak	0.04	0.10	0.15	0.21	0.64	0.08
	Na <sup>+</sup>	1.8	Strong	0.02	0.03	0.07	0.13	0.89	0.03
	Mg <sup>2+</sup>	0.2	Weak	0.01	0.01	0.01	0.02	0.13	0.02
	K <sup>+</sup>	0.3	Weak	0.02	0.02	0.02	0.03	0.37	0.03
	BC	3.5	Strong	0.05	0.22	0.36	0.60	2.15	0.05
	Delta-C	0.9	Strong	0.00	0.00	0.01	0.03	0.25	0.01
	Ca	1.7	Strong	15.4	31.5	59.1	119	738	30.8
	Fe	1.6	Strong	10.2	24.4	55.4	123	854	20.5
	K	1.7	Strong	10.1	27.6	52.1	105	463	20.3
	As	0.9	Weak	0.05	0.12	0.31	0.69	4.73	0.10
	Ba	1.4	Weak	0.16	0.43	1.17	2.37	12.4	0.31
	Bi	1.0	Weak	0.01	0.01	0.03	0.08	0.59	0.01
	Cd	1.4	Weak	0.01	0.02	0.08	0.18	1.21	0.01
	Ce	1.2	Weak	0.02	0.03	0.07	0.15	1.89	0.03
	Co	1.4	Weak	0.01	0.02	0.03	0.08	0.43	0.01
	Cr	1.0	Weak	0.25	0.56	1.26	3.00	18.9	0.50
	Cu	1.3	Weak	0.51	1.15	2.49	5.46	25.9	1.00
	Mn	1.8	Strong	0.25	0.82	1.96	4.11	32.1	0.50
	Mo	1.2	Weak	0.05	0.15	0.29	0.66	5.13	0.10
	Ni	1.6	Strong	0.08	0.22	0.55	1.35	11.8	0.16
	Pb	1.5	Weak	0.25	0.92	2.43	5.62	33.1	0.50
	Rb	2.1	Strong	0.02	0.06	0.12	0.25	1.89	0.03
	Sb	1.3	Weak	0.10	0.25	0.54	1.10	8.38	0.20
	Se	1.3	Weak	0.10	0.31	0.70	1.61	8.24	0.21
	Sr	1.2	Weak	0.05	0.16	0.31	0.60	3.10	0.11
	Zn	1.0	Weak	1.51	5.05	13.1	29.9	252	3.0

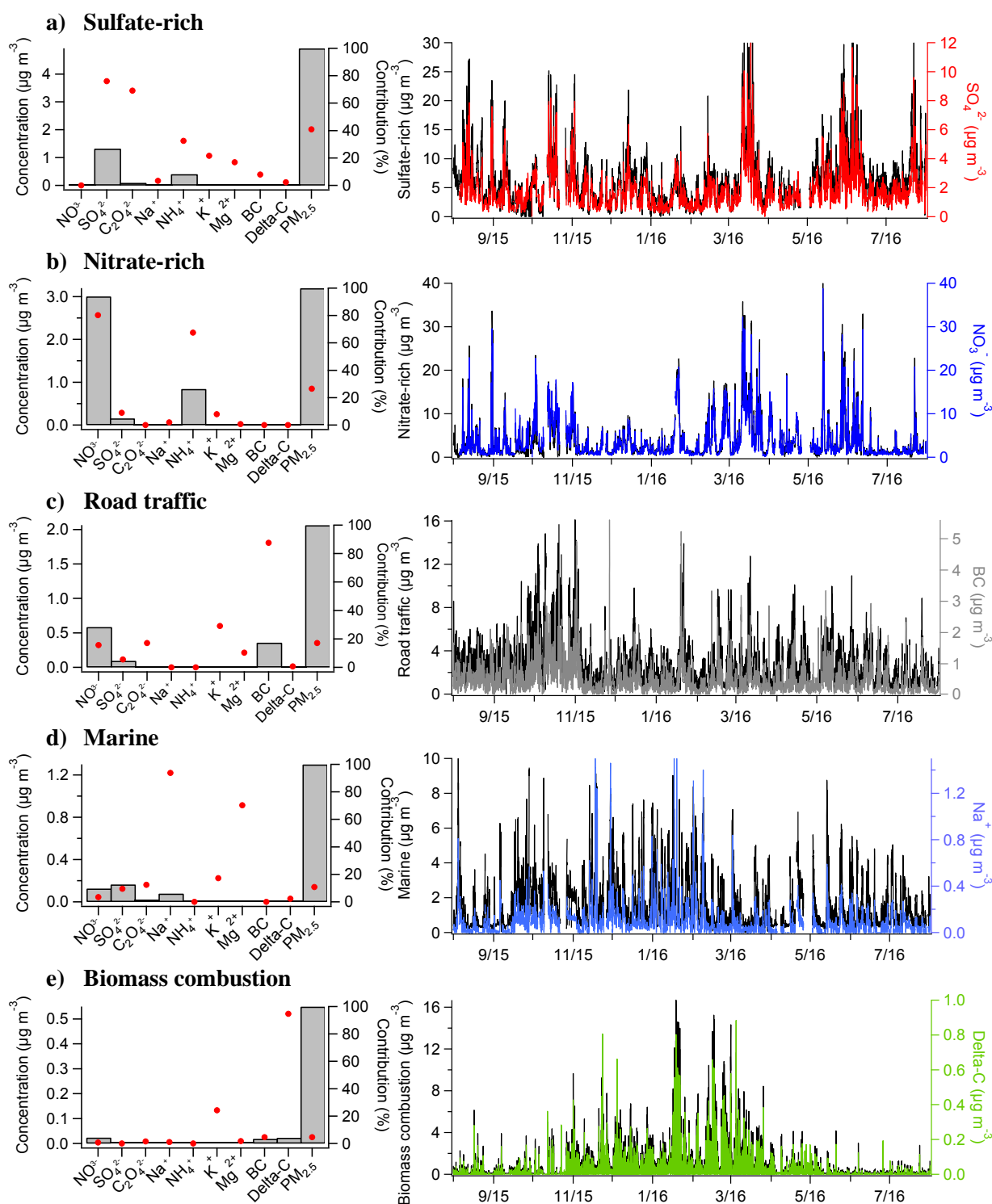


Figure P3.1 (Left) PMF<sub>h</sub> factor profiles with concentrations (shaded grey bars) in  $\mu\text{g m}^{-3}$  and contributions (red dots) in % for every species; (Right) Time series of PMF<sub>h</sub> factors together with the main tracer of each source.

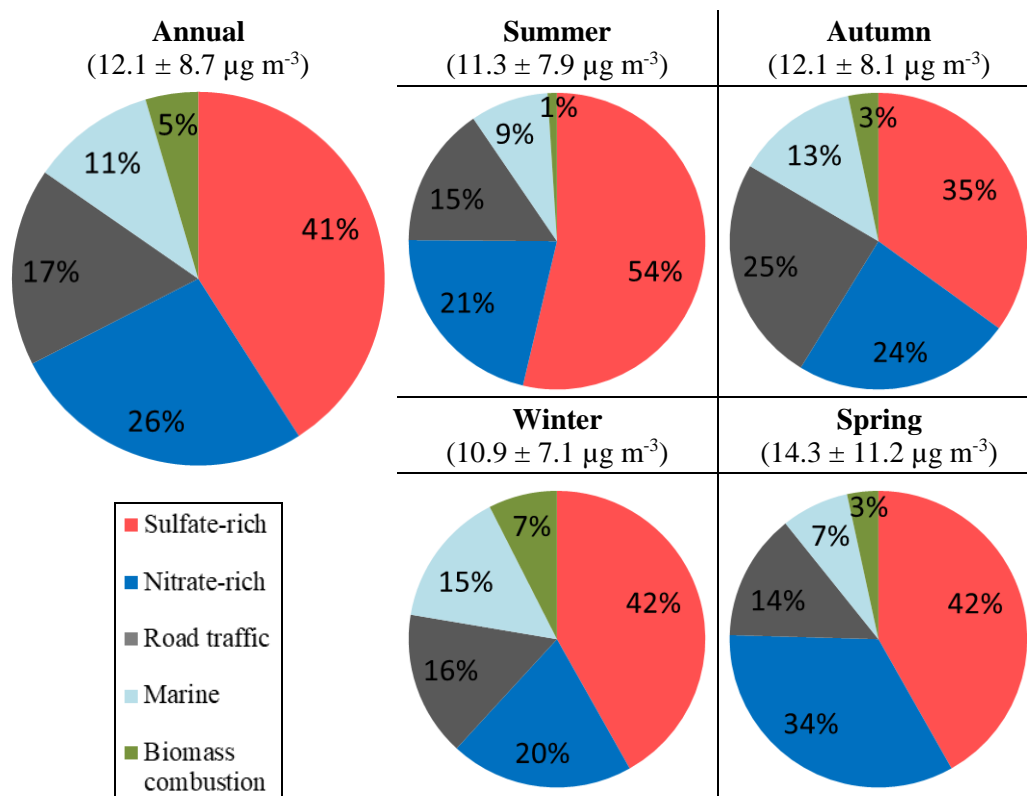


Figure P3.2 (Left) annual and (right) seasonal average contributions (in %) of  $\text{PMF}_h$  source factors to  $\text{PM}_{2.5}$  (modeled concentrations)

The average contributions of the source factors by season show how the sulfate-rich factor accounts for 54% of the  $\text{PM}_{2.5}$  mass in summer, whereas in autumn it is reduced to 35% (Figure P3.2). The contribution during daytime (45%) is also significantly higher than during nighttime (37%) (Figure P3.3) as is also observed in the daily profiles, where the concentrations start to increase in the early morning and decrease in the evening, particularly in summer (Figure P3.4). This confirms the importance of the photochemical activity for the origin of this source factor.

These observations are also consistent with the results of a previous short campaign carried out in July 2011 in Douai, which showed a contribution of OM to  $\text{PM}_{2.5}$  of the same order of magnitude ( $\sim 17\%$ ) (Crenn et al., 2017). Finally, the sulfate-rich factor was compared over the corresponding period to the  $\text{PMF}_{\text{org}}$  source factors obtained by the SA study of the organic mass spectra from AMS measurements, as has been mentioned previously. The comparison of the time series between both approaches is presented in Figure S2.2. A good correlation ( $r = 0.80$ ; Figure S2.2a) was obtained between the sulfate-rich and LO-OOA, which was previously shown to be predominantly a regional factor (Roig et al., in prep.). In order to evaluate preliminarily the influence of local emissions in the formation of ammonium sulfate, the daily profile of the sulfate-rich factor was plotted together with that of  $\text{SO}_2$ , which

according to a previous work is mainly locally emitted in Douai (Roig et al., submitted) (Figure P3.5a). The daily maximum of SO<sub>2</sub> appears after that of the sulfate-rich factor, which suggests that the observed sulfate is rather produced during long-range transport, as will be confirmed in section 3.4 about the geographical determination of sources.

The second “nitrate-rich” factor, characterized by high shares of NO<sub>3</sub><sup>-</sup> (80%) and NH<sub>4</sub><sup>+</sup> (68%), and a minor share of SO<sub>4</sub><sup>2-</sup> (9%) (Figure P3.1b, left) is the second largest contributing factor to PM<sub>2.5</sub> (27%). The molar ratio between NH<sub>4</sub><sup>+</sup> and NO<sub>3</sub><sup>-</sup> is 0.97, which is almost equal to the value of 1 of ammonium nitrate, and strongly suggests its predominant presence in this factor. A seasonal variation is also expected in this factor due to (i) the dependence of ammonium nitrate on the temperature and relative humidity and (ii) the higher emissions of ammonium nitrate precursors (i.e. nitrogen oxides and ammonia) in some periods of the year. The dependence of ammonium nitrate on meteorological parameters will favor its formation in colder months, when the temperatures are lower and RH higher. On the other hand, the emissions of nitrogen oxides will be particularly important in months when road traffic is enhanced (mainly during autumn and spring) whereas ammonia emissions will be higher when agricultural activities are more important (spring and summer). The time series of this factor shows that higher concentrations of this factor are particularly observed in spring (Figure P3.1b, right) and therefore the seasonal contribution of this factor is significantly higher in this season (34%) (Figure P3.2). The contributions in the other seasons are similar (20-24%). Contrary to the previous factor, a slightly higher contribution is observed during nighttime (28%) in comparison to daytime (25%) (Figure P3.3). This is better observed in the daily profiles, where the concentration of nitrate-rich starts to increase in the late afternoon, and to build up during the night until a maximum is reached in the early morning (Figure P3.4b). After that the concentrations decrease and reach a minimum in the middle of the afternoon, probably due to the increase of temperature and decrease of RH favoring the partitioning of ammonium nitrate towards its gaseous precursors (Figure P3.5b). This is particularly well observed in spring and summer, where the concentration in the early morning doubles and triples, respectively, the minimum observed in the afternoon. In addition, the factor correlated very well with NO<sub>3</sub><sup>-</sup> and NH<sub>4</sub><sup>+</sup> (r of 0.99 and 0.97, respectively) and well with PM<sub>2.5</sub> (r = 0.86) and SO<sub>4</sub><sup>2-</sup> (r = 0.68) (Table S3.6). Similarly, very good correlations were obtained between the nitrate-rich factor and the MO-OOA (r = 0.87) and LO-OOA (r = 0.90) factors from PMF<sub>org</sub> (Figure S3.2b).

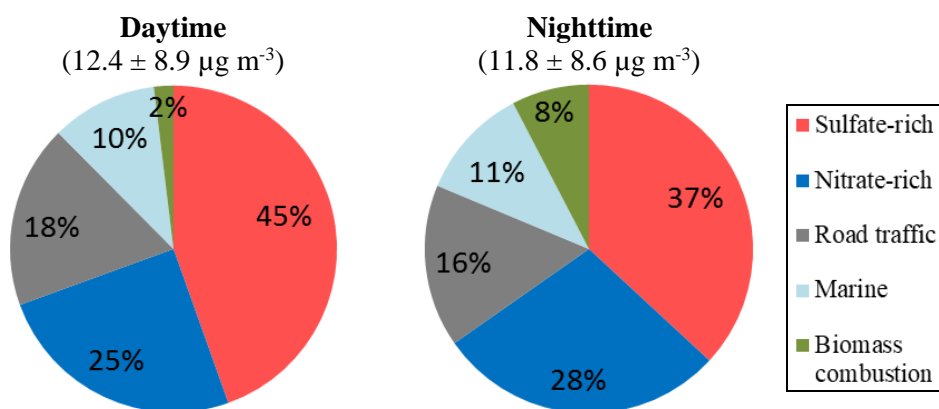


Figure P3.3 Daytime and nighttime averaged contributions (in %) of PMF<sub>h</sub> source factors to PM<sub>2.5</sub> (modeled concentrations)

The third factor is road traffic, which is identified by a high share of BC (88%), moderate shares of NO<sub>3</sub><sup>-</sup> (16%), C<sub>2</sub>O<sub>4</sub><sup>2-</sup> (17%) and K<sup>+</sup> (29%), and a contribution to total PM<sub>2.5</sub> mass of 17% (Figure P3.1c, left). A marked seasonal variation is observed for this factor profile, with particularly higher contributions during autumn (25%), probably attributed to the increased traffic emissions (Figure P3.2). Accordingly, the concentrations of NO and NO<sub>2</sub> were highest in this season, with seasonal averages of  $6.2 \pm 12.4$  and  $10.0 \pm 6.5$  µg m<sup>-3</sup>, respectively. The time series shows a particularly high contribution of this factor in the month of October 2015 (Figure P3.1c, right). This might be attributed to the exceptionally low wind speeds observed during this month (average wind speed of  $0.95 \pm 0.59$  m s<sup>-1</sup>) in comparison to the annual average ( $1.48 \pm 1.08$  m s<sup>-1</sup>), which could prevent atmospheric dispersion and favor the accumulation of local pollutants.

Even though there is not a significant difference in the contribution of road traffic to PM<sub>2.5</sub> between daytime and nighttime (Figure P3.3), a clear trend is observed in the daily profiles, where the factor is found to peak in the morning and late afternoon, when traffic activity is usually the most intense (Figure P3.4c). The morning peak is generally more important than that of the afternoon, although in winter the contrary is observed. This might be attributed to the increased emission of BC by household combustion of solid and liquid fuels. The daily profile of this factor was plotted together with that of the precursor gases NO, NO<sub>2</sub> and HONO (Figure P3.5c), and the morning and afternoon peaks of the factor were found to match those of NO<sub>x</sub>, whereas those of HONO were found a few hours later. A strong weekly trend is also observed for this factor, with higher concentrations during weekdays and lower in the weekend (particularly on Sundays), as expected (Figure S3.3). This factor was well correlated with BC ( $r = 0.91$ ) and slightly less with gases emitted by combustion processes such as HONO, NO and NO<sub>2</sub> ( $r = 0.54$ ,  $0.54$  and  $0.63$ , respectively). In addition, the



anti-correlation of the factor with the wind speed ( $r = -0.41$ ) gives evidence of the local nature of this source. When the road traffic factor was compared to the analogous HOA factor from the PMF<sub>org</sub> analysis, a good correlation was obtained ( $r = 0.81$ ; Figure S3.2c).

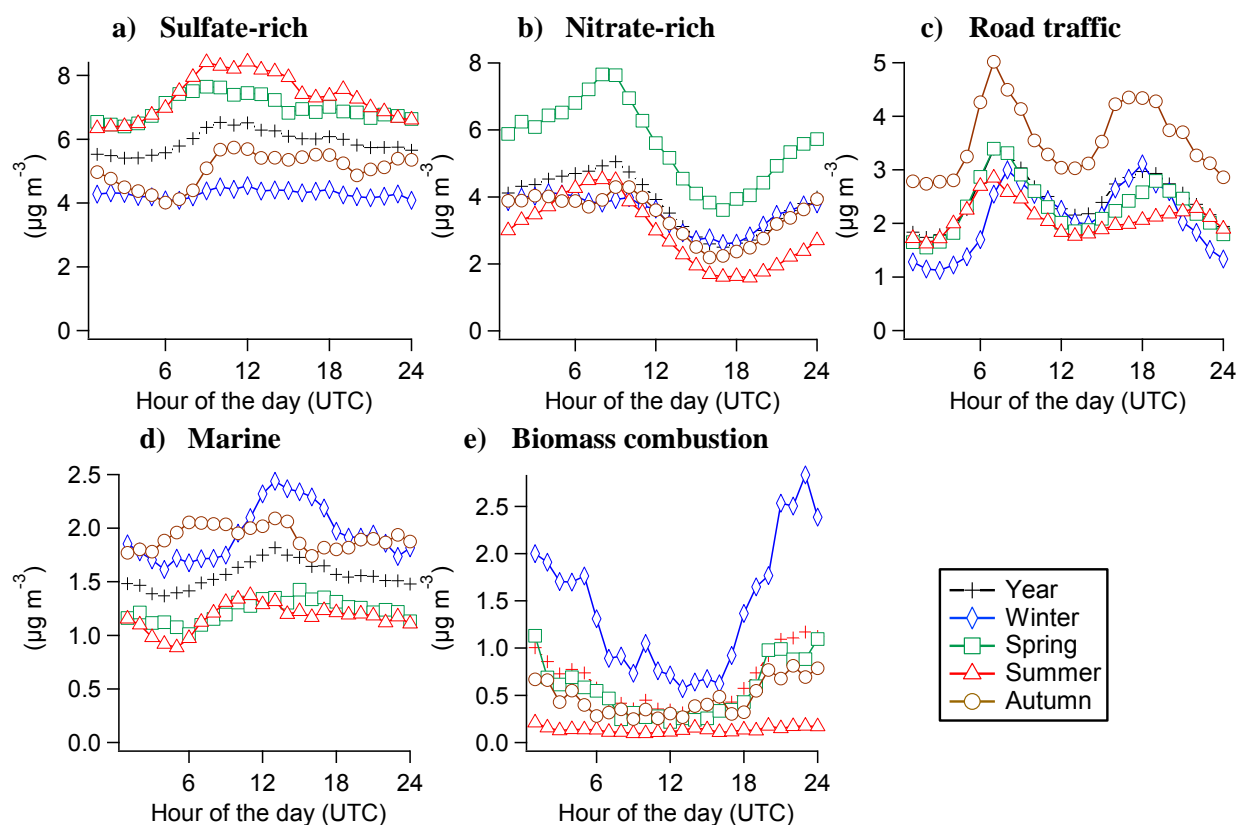


Figure P3.4 Daily variations of PMF<sub>h</sub> factor concentrations (in  $\mu\text{g m}^{-3}$ ) for every season and for the whole year.

The fourth factor is the marine aerosol factor, which presents a very high share of  $\text{Na}^+$  (94%) and  $\text{Mg}^{2+}$  (70%), and small shares of  $\text{SO}_4^{2-}$  (10%),  $\text{NO}_3^-$  (3%),  $\text{C}_2\text{O}_4^{2-}$  (12%) and  $\text{K}^+$  (17%) (Figure P3.1d, left). This factor contributes to 11% of the PM<sub>2.5</sub> mass. The observed  $\text{Mg}^{2+}/\text{Na}^+$  ratio of 0.12 is very close to that of the standard composition of sea water of 0.11 (Tang et al., 1997). The small amounts of  $\text{SO}_4^{2-}$  and  $\text{NO}_3^-$  might be related to the processing of sea salt during its transport to the inner land, giving place to partly aged marine aerosol, such as sodium nitrate salts. Higher contributions of this factor are observed in autumn and winter with 13 and 15%, respectively (Figure P3.2), which is explained by a higher frequency of air masses originating from the North Sea and the Atlantic Ocean and higher wind speeds, particularly from November 2015 to February 2016 (Table S3.1). There is no significant difference daily variation for this factor (Figure P3.3) with only slightly higher concentrations observed during the day, particularly in winter, again due to higher daytime wind speeds promoting the long-range transport of sea spray (Figure P3.4d). The marine factor was well

correlated with  $\text{Na}^+$  and  $\text{Mg}^{2+}$  ( $r$  of 0.96 and 0.63, respectively), and less with  $\text{Cl}^-$  ( $r = 0.40$ ), which was not always correctly measured as previously mentioned, and part of  $\text{Cl}^-$  could also have been depleted over time by photochemical reactions.

The last source factor is attributed to biomass combustion, which is represented by a high share of Delta-C (95%), and a minor share of  $\text{K}^+$  (25%) and BC (5%) (Figure P3.1e, left). Delta-C has been identified in the literature as a biomass burning marker (Wang et al., 2011) and has been used in different source apportionment studies (Wang et al., 2012a, 2012b). This factor is the least important contributor to the  $\text{PM}_{2.5}$  mass, with an average of only 5%. As expected, it presents a strong seasonal variation, with the highest concentrations observed in the cold winter months due to the increased combustion of wood. On average, its contribution is more important in winter (7%) as opposed to summer (1%) (Figure P3.2). The nighttime contribution of the biomass combustion factor is clearly more important than in daytime (8% and 2%, respectively), which is expected as residential biomass combustion mainly takes place in the evening (Figure P3.3) and besides, the boundary layer height decreases at night. This is clearly seen in the winter daily profile, for which the concentration increases from the early afternoon until a maximum is reached before midnight, and decreases thereafter (Figure P3.4e). A similar but much less marked pattern is observed in spring and autumn, whereas no variation is observed in summer. This factor was totally correlated with Delta-C ( $r = 0.99$ ) and slightly less with  $\text{K}^+$  ( $r = 0.45$ ). In addition, it showed an anti-correlation with temperature ( $r = -0.42$ ) (Figure S3.5), which is consistent with its higher concentrations observed for low temperatures. A good correlation was furthermore obtained between the biomass combustion factor and the BBOA factor from the  $\text{PMF}_{\text{org}}$  analysis ( $r = 0.77$ ).

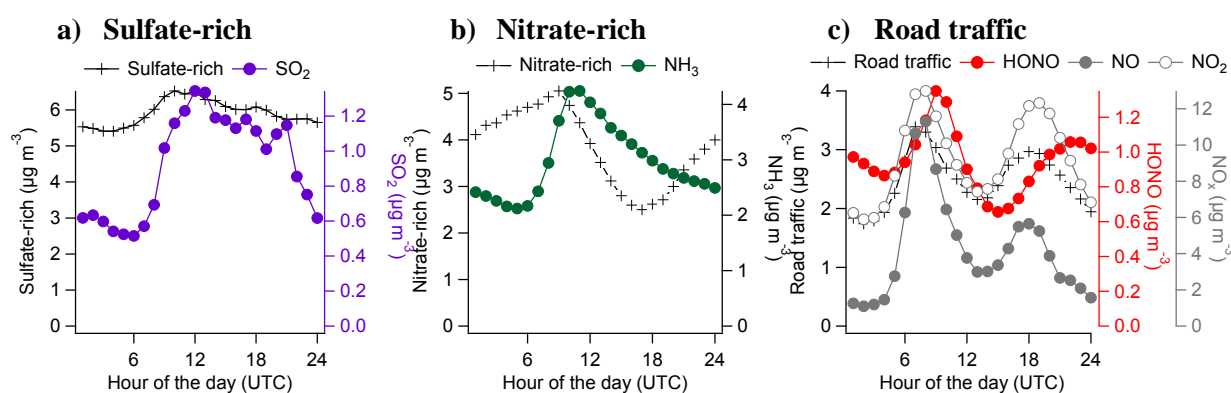


Figure P3.5 Daily variations of (a) sulfate-rich, (b) nitrate-rich and (c) road traffic concentrations (in  $\mu\text{g m}^{-3}$ ) together with the main trace gases for each source

### 3.3. Daily PMF results

The comparison between the PMF<sub>h</sub> and PMF<sub>d</sub> using the same input variables (section 4 in the SM) showed that the same factors were obtained. However, differences in contributions to PM<sub>2.5</sub> were observed, particularly for the nitrate-rich and biomass combustion factors (4% lower and 6% higher in the PMF<sub>d</sub>, respectively). These were mainly attributed to the loss of information caused by the averaging of the data, which could have been responsible for the partial merging of both factors due to their close occurrence in time within a daily cycle.

When the PMF was applied to the extended daily database, a range of 3 to 12 factors was investigated. A solution with 8 factors was determined to be the best, giving a  $Q_{\text{true}}/Q_{\text{exp}}$  ratio of 1.9, a robust bootstrap (Table S3.3) and meaningful source factors. The chemical profiles and time series of the source factors are shown in decreasing order of contribution to PM<sub>2.5</sub> in Figure P3.6 and Figure P3.7, respectively. The annual and seasonal contributions are shown in Figure P3.8. From higher to lower contributions to the PM<sub>2.5</sub> mass the obtained source factors are sulfate-rich (35%), nitrate-rich (31%), biomass combustion (12%), marine (8%), road traffic (6%), a metal industry background (MIB, 6%), dust (3%) and a local metal processing industry (local industry, 1%).

In comparison to PMF<sub>h</sub>, adding the elements analyzed by ICP-MS in the database, as well as downgrading the hourly time resolution to a daily one, has allowed the determination of three additional factors (MIB, dust and local industry), which all together account for approximately 10% of the PM<sub>2.5</sub> mass on average. However, they can reach daily contributions up to 38% of the PM<sub>2.5</sub> mass, particularly on days with low wind speeds, and therefore should not be neglected.

Regarding the 5 common factors between PMF<sub>d</sub> and PMF<sub>h</sub> (i.e. sulfate-rich, nitrate-rich, road traffic, marine and biomass combustion), their contributions are ranked in the same order of importance. However, as will be discussed below, significant differences in the composition of each factor are observed, which might partly explain the different contributions to PM<sub>2.5</sub> observed in comparison with the PMF<sub>h</sub>. Averaging the hourly data into daily values causes the loss of some information, thus resulting in the merging of different processes or sources which were better differentiated with a finer temporal resolution. The comparison between both types of daily- and hourly-resolved PMF using the same variables presented in the supplementary material addresses this issue in more detail. Furthermore, deconvolving three new factors might also cause some variables to partly split (for instance,

15% of the  $\text{SO}_4^{2-}$  variable is observed in the new MIB factor). Altogether, it might partly explain why the contributions of the sulfate-rich, road traffic and marine factors are lower and

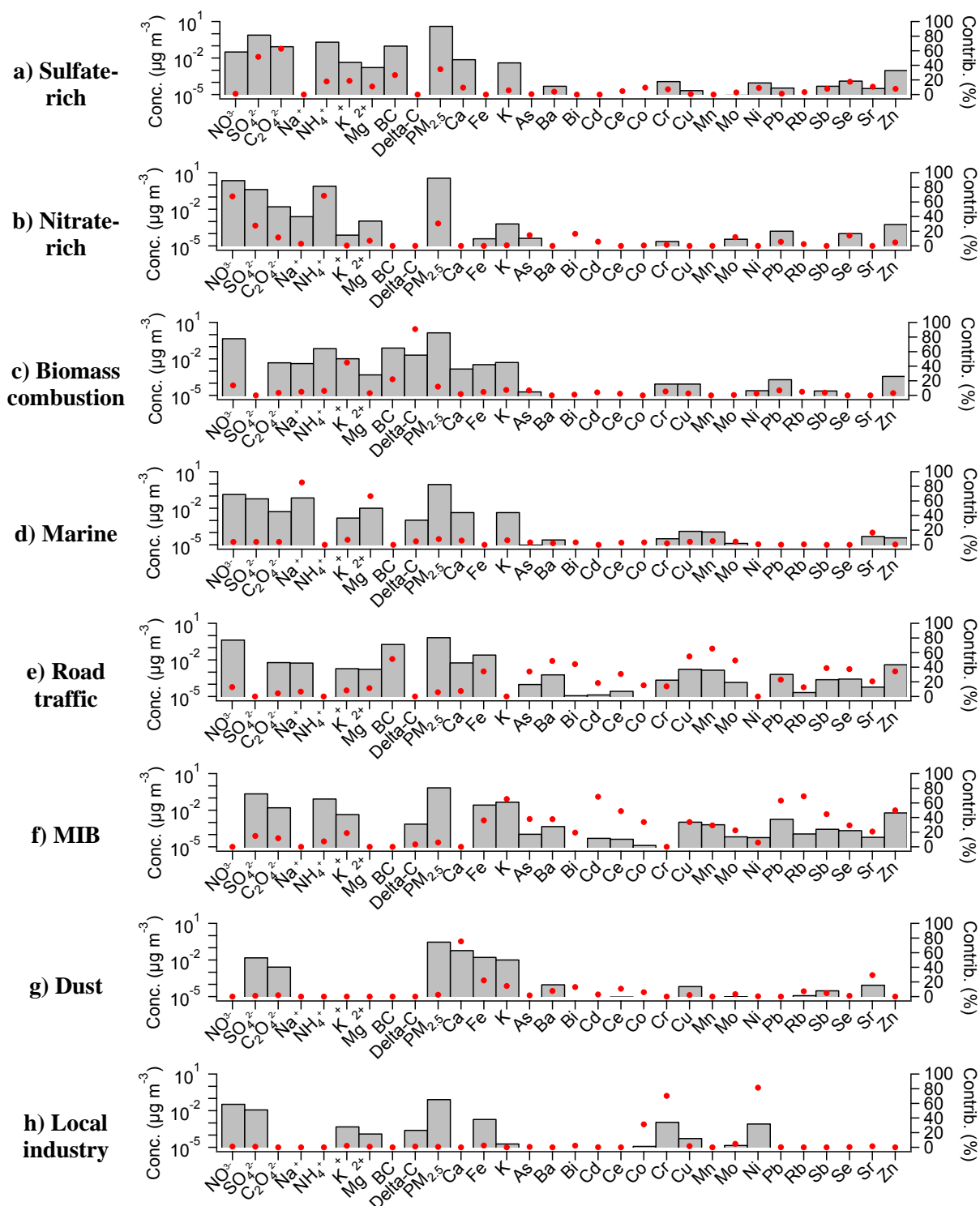


Figure P3.6 PMF<sub>d</sub> source profiles with the concentrations (shaded grey bars) in  $\mu\text{g m}^{-3}$  and contributions (red dots) in % for every species. MIB: Metal Industry Background.

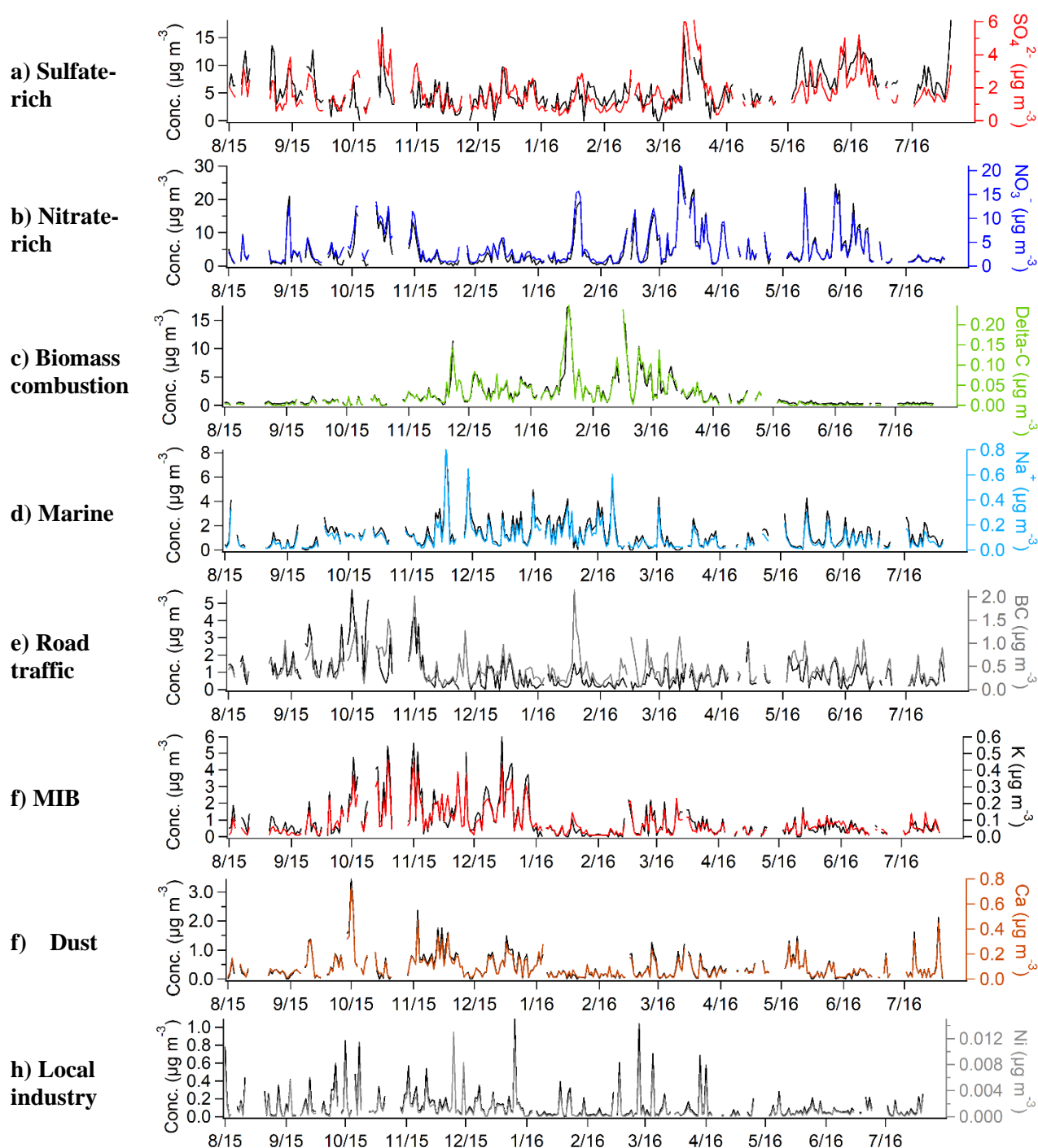


Figure P3.7 Time series of PMF<sub>d</sub> factors together with the main tracer for each source (concentrations in  $\mu\text{g m}^{-3}$ ). MIB: Metal Industry Background.

those of the nitrate-rich and biomass combustion higher, in comparison to the same factors obtained with PMF<sub>h</sub>. A summary of the concentrations and contributions of each variable to the common source factors is presented in P3.9 and in Tables S3.4 and S3.5.

The sulfate-rich factor is characterized by a high share of SO<sub>4</sub><sup>2-</sup> (52%) and C<sub>2</sub>O<sub>4</sub><sup>2-</sup> (63%) and moderate shares of BC (27%), NH<sub>4</sub><sup>+</sup> (18%), K<sup>+</sup> (19%) and Mg<sup>2+</sup> (11%) (Figure P3.6a). Some trace elements are found in small percentages, notably Ca (10%), Co (10%), Cr (7%), Ni (9%), Sb (8%), Se (18%), Sr (11%) and Zn (8%). The enhanced presence of BC and metals together with the lower contributions of SO<sub>4</sub><sup>2-</sup> and NH<sub>4</sub><sup>+</sup> in comparison to the equivalent factor obtained in PMF<sub>h</sub> could imply that sulfate is mixed with other sources such as road traffic or other combustion sources. In addition, a lower contribution to PM<sub>2.5</sub> is found (35% instead of 41%). The seasonal contribution of this factor is similar to that observed in the PMF<sub>h</sub>, with the highest value in summer (57%). The factor also correlates less well with its main tracers SO<sub>4</sub><sup>2-</sup> and C<sub>2</sub>O<sub>4</sub><sup>2-</sup> (r of 0.66 and 0.65, respectively), suggesting a more mixed character in comparison to that of PMF<sub>h</sub>. In addition, a slightly positive correlation (r = 0.43) is observed with temperature, confirming an enhanced contribution of this factor in the warmer months as has been previously discussed.

The second source factor, identified as nitrate-rich, contains high shares of NO<sub>3</sub><sup>-</sup> (68%) and NH<sub>4</sub><sup>+</sup> (68%), and moderate contributions of SO<sub>4</sub><sup>2-</sup> (28%) and C<sub>2</sub>O<sub>4</sub><sup>2-</sup> (12%) (Figure P3.6b). Small contributions of some trace elements are also observed, including As (15%), Bi (17%), Mo (12%) and Se (14%). Although this source factor mainly represents ammonium nitrate, an important presence of ammonium sulfate (in comparison to its equivalent in PMF<sub>h</sub>) is also observed here. In addition, the small share of C<sub>2</sub>O<sub>4</sub><sup>2-</sup> in this factor might suggest that some OM is present. The presence of OM in a nitrate-rich factor has been reported elsewhere (Bressi et al., 2014; Mooibroek et al., 2011; Waked et al., 2014) and is consistent with the semi-volatile nature of part of the organic aerosol. The good correlation obtained between the PMF<sub>h</sub> nitrate-rich factor and OOA factors from PMF<sub>org</sub> presented in the previous section supports this assumption. Hence, similarly to the previous factor, the nitrate-rich factor presents a less “pure” nature than its equivalent in PMF<sub>h</sub>, as confirmed by a higher correlation with SO<sub>4</sub><sup>2-</sup> (r = 0.82). This might also explain why this factor presents a slightly higher contribution to PM<sub>2.5</sub> (30%) than the same factor in PMF<sub>h</sub> (26%).

The third factor obtained with PMF<sub>d</sub> is the biomass combustion, which presents high shares of Delta-C (91%) and K<sup>+</sup> (45%), and small shares of NO<sub>3</sub><sup>-</sup> (14%), NH<sub>4</sub><sup>+</sup> (6%) and BC (22%) (Figure P3.6c). The higher contribution to PM<sub>2.5</sub> (12%) in comparison to PMF<sub>h</sub> (5%) is significant and partly attributed to the larger contributions of NO<sub>3</sub><sup>-</sup>, NH<sub>4</sub><sup>+</sup> and BC. A much

higher contribution is particularly observed in winter (26% of the PM<sub>2.5</sub> mass). As previously mentioned (and also observed when using the exact same set of input variables, see section 4 in SM), the averaging of hourly variables might cause the mixture of different factors which could justify the observed increase. This partly explains why some ammonium nitrate and BC are found in this factor when they may be actually associated to other processes. In addition, the absence of OC might bias the results, as previously mentioned, and makes it difficult to determine the real contribution of the biomass combustion factor. The factor is highly correlated with Delta-C ( $r = 0.97$ ) and  $K^+$  ( $r = 0.70$ ), and anti-correlated with temperature ( $r = -0.65$ ). In addition, significant correlations are observed with gases from combustion processes such as NO, NO<sub>2</sub> and HONO ( $r$  of 0.49, 0.51 and 0.59, respectively), which might be justified by the presence of BC in the factor.

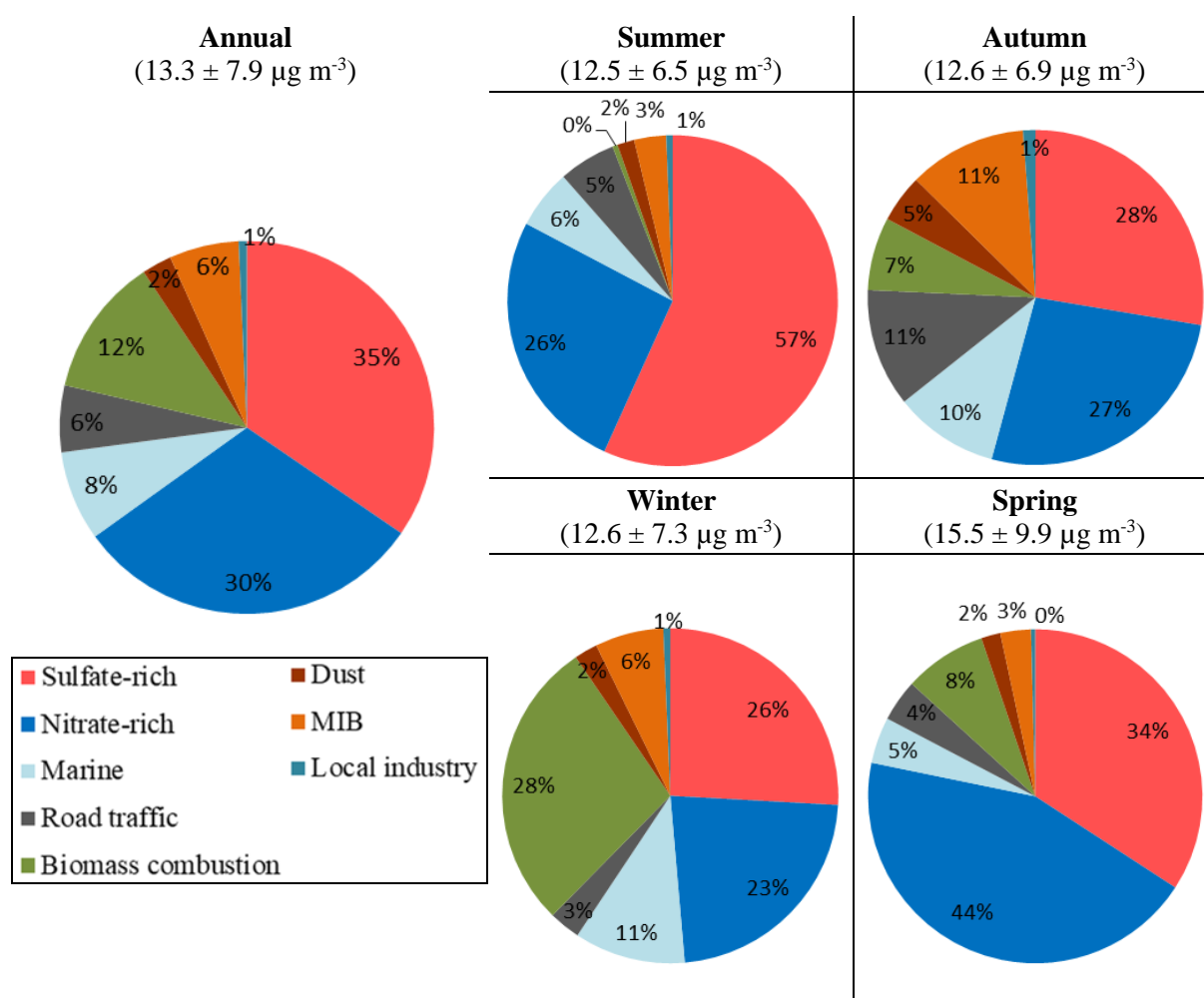


Figure P3.8 Annual (left) and seasonal (right) average contributions (in %) of PMF<sub>d</sub> source factors to PM<sub>2.5</sub> (modeled concentrations). MIB: Metal Industry Background.

The fourth factor is the marine aerosol, which is rich in  $\text{Na}^+$  (85%) and  $\text{Mg}^{2+}$  (67%), and presents small shares of other variables, including  $\text{NO}_3^-$  (4%),  $\text{SO}_4^{2-}$  (4%),  $\text{C}_2\text{O}_4^{2-}$  (4%) and Sr (17%) (Figure P3.6d). The observed  $\text{Mg}^{2+}/\text{Na}^+$  ratio of 0.14 is slightly higher than that of  $\text{PMF}_h$  (0.12) but still similar to that of the standard composition of sea water of 0.11 (Tang et al., 1997). Unlike the other factors, the composition of the marine aerosol factor is very similar to that observed with  $\text{PMF}_h$ , even though its contribution to  $\text{PM}_{2.5}$  is slightly lower (8% instead of 11%). Good correlations between this factor and sea salt components such as  $\text{Na}^+$  and  $\text{Mg}^{2+}$  are obtained ( $r$  of 0.97 and 0.78, respectively). A slightly positive correlation with wind speed ( $r = 0.54$ ) also indicates the long-distance nature of this source.

The last common factor is road traffic, which presents a much smaller contribution (6%) when compared to  $\text{PMF}_h$  (17%). The composition of this factor is also different from that of  $\text{PMF}_h$ , with lower BC (51% instead of 88%), and low shares of  $\text{NO}_3^-$  (13%) and other minor ions. Many metals are added in this factor, notably Fe (34%), As (34%), Ba (49%), Bi (44%), Ce (31%), Cu (55%), Mn (66%), Mo (49%), Sb (39%), Se (38%) and Zn (34%) (Figure P3.6e). Ba, Cu, Fe and Zn have been reported as indicators of vehicular brake abrasion (Johansson et al., 2009). The presence of Zn might be attributed to the mechanical abrasion of tires (Amato et al., 2011). In addition, Mo is known to be used as an additive in lubricants and hence to be emitted by the combustion of fossil fuels (Salminen et al., 2005). The Cu/Sb ratio obtained from the traffic profile is 7.1, similar to the one reported in a SA study of  $\text{PM}_{10}$  carried out in Lens, northern France (Waked et al., 2014) of 8.1, and within the range of  $5.35 \pm 2.9$  found in a road-tunnel study of heavy metal emissions from traffic (Sternbeck et al., 2002). The road traffic factor is less well correlated to BC when compared to  $\text{PMF}_h$  ( $r = 0.64$ ). Similarly, slightly weaker correlations are observed with NO,  $\text{NO}_2$  and HONO issued from combustion processes ( $r$  of 0.46, 0.43 and 0.44, respectively). However, high correlation coefficients are obtained for trace elements, particularly for Fe, Ba, Bi, Co, Cu, Mo, Sb and Se ( $r > 0.6$ ; Table S3.7).

The sixth factor includes small fractions of  $\text{SO}_4^{2-}$  (15%),  $\text{C}_2\text{O}_4^{2-}$  (12%),  $\text{NH}_4^+$  (7%) and  $\text{K}^+$  (19%), and important percentages of several trace elements including Fe (36%), K (65%), As (38%), Ba (38%), Cd (69%), Ce (49%), Co (34%), Cu (34%), Pb (63%), Rb (69%), Sb (45%), and Zn (50%) (Figure P3.6f). The source has been called “metal industry background” (MIB) as it includes many metals emitted by the metal-producing and processing industry as well as other activities carried out in the north of France (see section on the geographical determination of sources). It contributes to 6% of the  $\text{PM}_{2.5}$  mass on average, showing a remarkable increase in autumn where it reaches 11%. The Pb/Cd ratio has been previously



used to differentiate between different sources of heavy metals (Dulac et al., 1987). Small Pb/Cd values between 5 and 15 were attributed to aerosols issuing from the nonferrous metallurgy (i.e. source of Cd), whereas really high values of around 2,300 were linked to the combustion of leaded gasoline (i.e. Pb source) which has been banned since 2000 in the European Union. The mean ratio for the anthropogenic European emissions has been reported to be 46 (Dulac et al., 1987). The Pb/Cd value obtained in our study is 36.7, which is between the ratio for nonferrous metallurgy and the mean ratio for the anthropogenic European emissions. The MIB source is well correlated with most of the metals within the factor:  $r > 0.6$  for Fe, K, Ba, Cd, Ce, Co, Cu, Pb, Rb and Sb (Table S3.7). The high shares of Cd-Pb-Zn suggest a possible contribution to the MIB factor of a zinc smelter located 2 km N-NW of our sampling site.

The seventh factor includes a high percentage of Ca (75%), and minor shares of other trace elements including Fe (22%), K (15%), Bi (13%), Ce (11%) and Sr (29%) (Figure P3.6g) and has been identified as dust. The contribution of this factor is small (3%), which is expected since these elements are mainly found in the coarse fraction of the aerosol (Thorpe et al., 2007). The contribution is higher in autumn (4%) as opposed to the other seasons (2% in each one). The factor correlates well with Ca ( $r = 0.99$ ), Fe ( $r = 0.70$ ), Ba ( $r = 0.61$ ) and Sr ( $r = 0.67$ ).

The last factor is characterized by high fractions of Co (34%), Cr (73%) and Ni (85%) and has been attributed to a “local industry” (Figure P3.6h). As will be discussed in the section on the geographical determination of sources, several local industries working on the surface treatment of metals and the processing of metals (metal sharpening) might emit significant amounts of Co, Cr and Ni. However, the contribution of this factor to  $PM_{2.5}$  is very small ( $<1\%$ ) given the negligible contribution of other species to this source. The seasonal variation is also very small, and only slightly higher concentrations are observed in autumn.

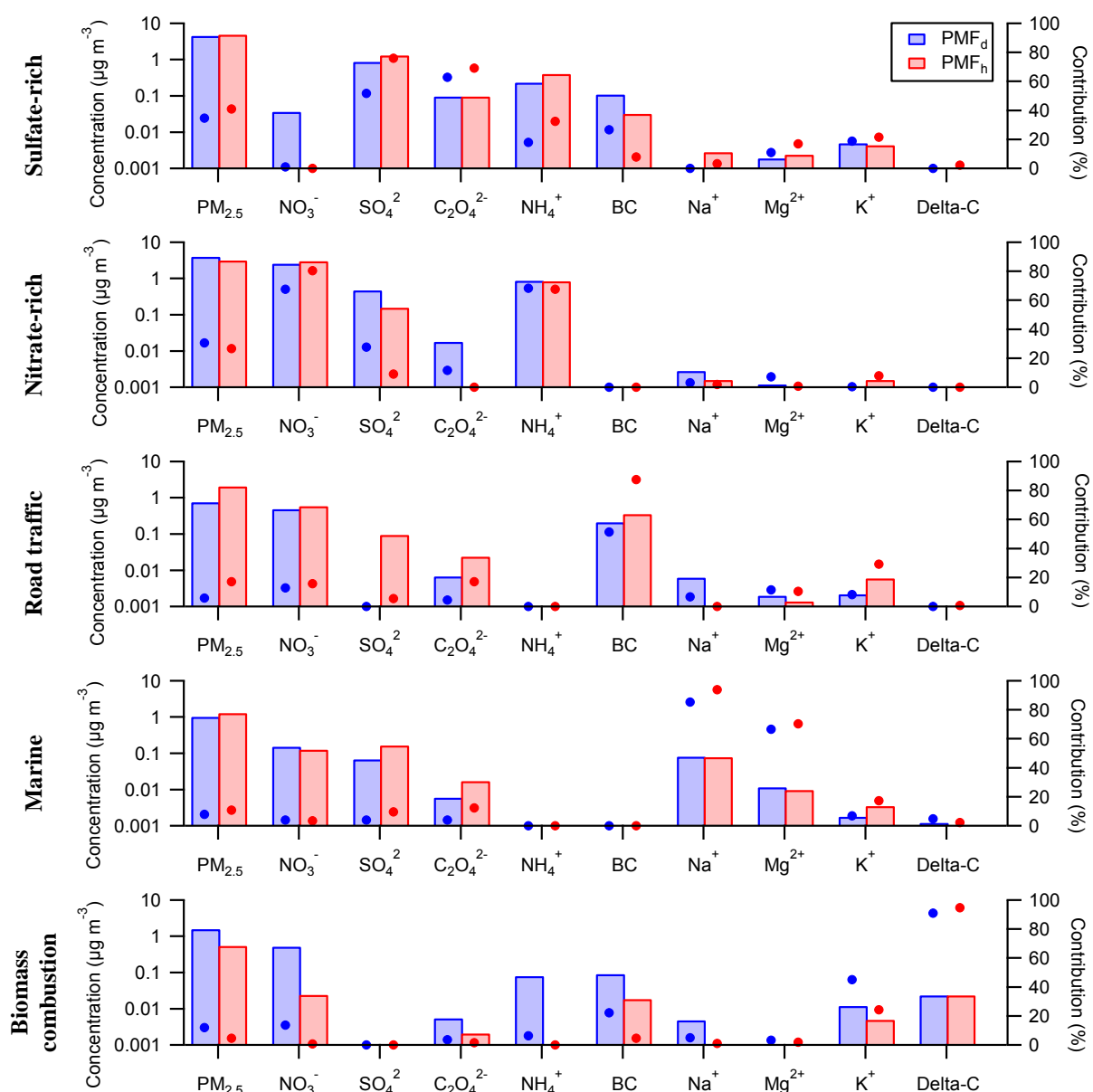


Figure P3.9 Comparison of the species concentrations (shaded bars, in  $\mu\text{g m}^{-3}$ ) and contributions (filled circles, in %) for the common factors between PMF<sub>d</sub> (in blue) and PMF<sub>h</sub> (in red) approaches (only common species are shown).

### 3.4. Geographical determination of source factors

The geographical origins of the source factors identified by the PMF analysis were investigated by means of NWR polar plots and PSCF maps. The results are given in Figure P3.10 and Figure P3.11, respectively. It should be noted that the NWR plots report concentrations in  $\mu\text{g m}^{-3}$ , whereas PSCF maps refer to probabilities. For the five common factors, both the NWR polar plots and PSCF maps are shown for the results obtained with PMF<sub>h</sub>, since they present more data points (close to 8,000 compared to 300) and are therefore more robust; for the three distinct source factors, the results are shown for PMF<sub>d</sub>.

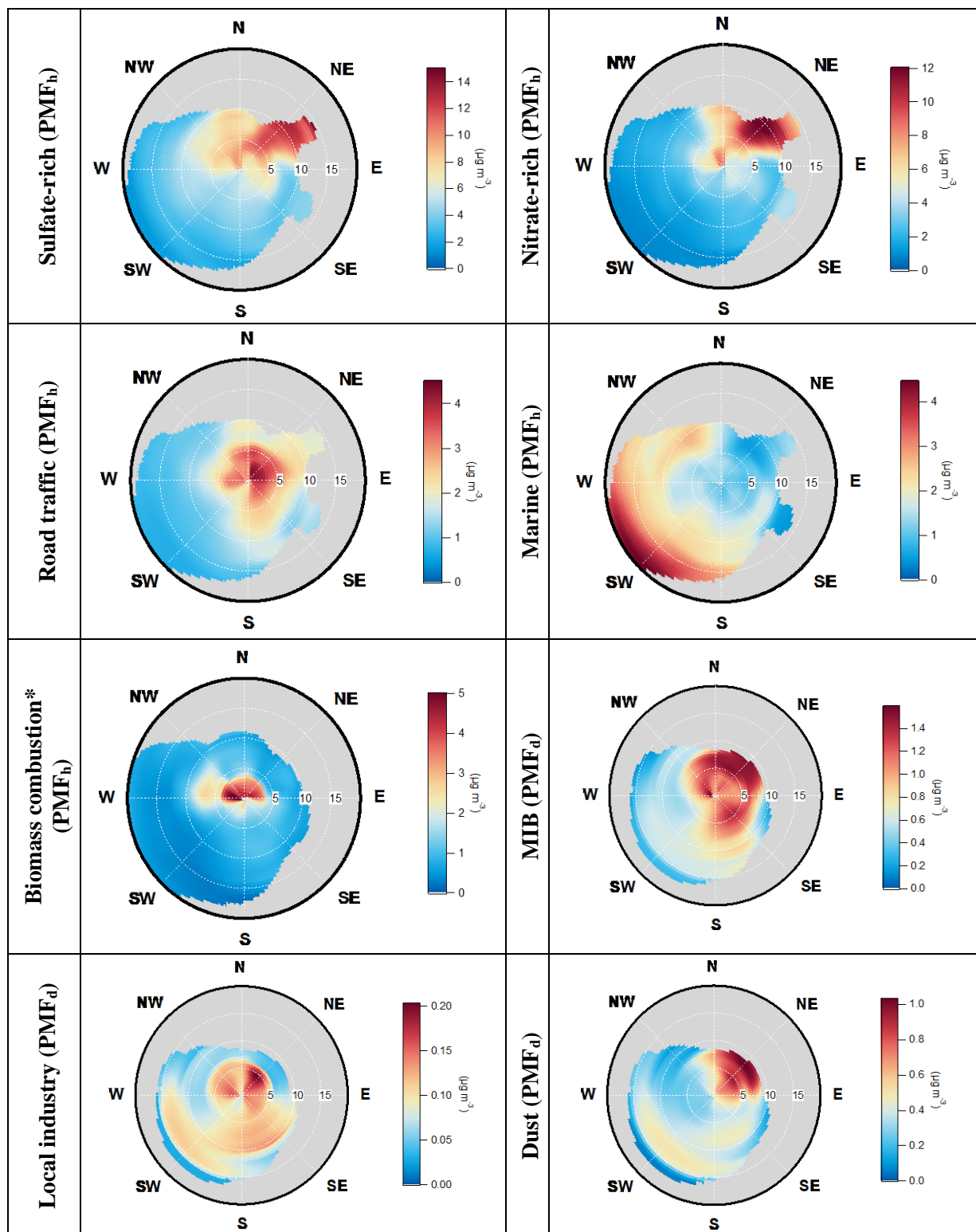


Figure P3.10 Annual NWR plots of PMF<sub>h</sub> and PMF<sub>d</sub> factor concentrations (in  $\mu\text{g m}^{-3}$ ) per wind direction. The radial axis represents the wind speed in  $\text{km h}^{-1}$ .

\* The graph for the biomass combustion factor is shown for winter only.

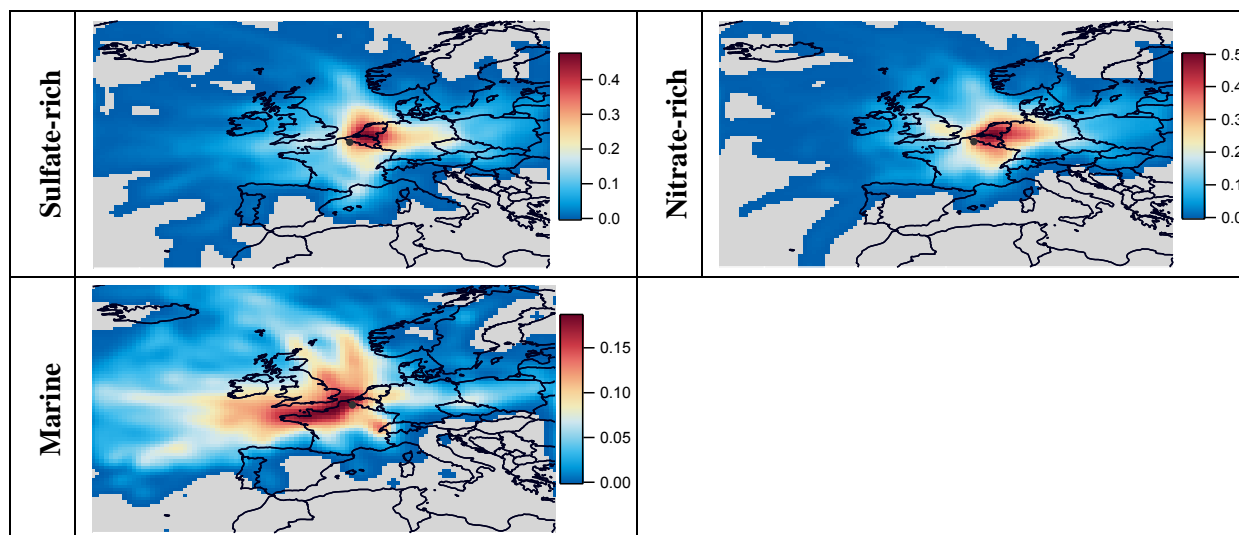


Figure P3.11 Annual PSCF probability maps for  $\text{PMF}_h$  factors identified as regional. The selected threshold is set at the 75<sup>th</sup> percentile. All used backtrajectories were weighted using a sigmoidal function.

For the sulfate-rich factor, high concentrations are observed in the NE direction, particularly for strong winds (up to  $15 \text{ km h}^{-1}$ ). This suggests that a significant part of this source factor is attributed to long-range transport (LRT). This is confirmed by the PSCF map, which shows high probabilities for air masses coming from the NE, where Belgium, The Netherlands and Luxemburg, also known as the Benelux region, are located. It has been previously reported that these regions are one of the main  $\text{SO}_2$  emitters in Europe, which is the main precursor of secondary sulfate (Pay et al., 2012) (see Figure S3.6 for the  $\text{SO}_x$  emission map).

The NWR plot for the nitrate-rich factor is similar to that of the sulfate-rich factor, with high concentrations in the NE sector. However, higher concentrations are observed for lower wind speeds ( $5\text{-}10 \text{ km h}^{-1}$ ). This might be attributed to particularly intense emissions of  $\text{NO}_x$  by road traffic in the A-21 highway, passing by N-NE of Douai, which could enhance the local formation of  $\text{NO}_3^-$  in that sector. In addition, a small hotspot is observed for very calm winds ( $< 5 \text{ m s}^{-1}$ ), which adds up to the hypothesis that a significant part of ammonium nitrate might be produced locally. However, LRT might also contribute significantly to the observed concentrations of this factor, as is reflected in the PSCF analysis, which shows a similar distribution to that of the sulfate-rich factor but with even higher probabilities. Slightly higher probabilities are also observed for western Germany. These results agree with the Benelux region and western Germany being important emitters of  $\text{NO}_x$  and  $\text{NH}_3$  (Fig S6), the main precursors of ammonium nitrate. The road traffic factor presents a clear local origin as

shown by the NWR plot. Concentrations are higher in the NE sector, which might be due to the presence of the highway A21.

As expected, the marine aerosol factor presents very high concentrations at very high wind speeds, mainly from the SW-W sector, implying the contribution of LRT to this factor. The PSCF map supports this, with distinctly higher probabilities in the coastal area of northern France, the North Sea, the English Channel, and the Atlantic Ocean.

The NWR plot for the biomass combustion factor is shown for winter since the other seasons are partly or not representative of the factor. From the NWR plot, it appears to have mainly a local origin, with the highest concentrations observed at very calm winds ( $<5 \text{ m s}^{-1}$ ), which is likely associated to the biomass combustion from the nearby suburban residential area.

The MIB factor presents particularly higher concentrations at moderate wind speeds ( $< 10 \text{ km h}^{-1}$ ) in the N to NE sectors. Important concentrations are also observed in the SE for low-to-moderate wind speeds, while a small hotspot is also seen with calm winds at the NW. This suggests that this factor could be explained by a mixture of rather local but also slightly regional emissions. In fact our study site is surrounded by a zinc smelter at the N-NW, an industrial area at the NE with several metal-processing activities such as metal machining and surface treatment and another area at the SE with several mechanical industry activities, as shown in the Supplementary Material (Figure S3.7). All these activities could contribute notably to the observed concentrations of metals. Other important sources of metals are also present at greater distances. For instance, around 40 km to the north, a Pb-battery manufacturer and a waste incinerator are located in the surroundings of Lille, while approximately 30 km to the east direction a metal refinery is located in the city of Valenciennes (Figure S3.8). Hence, the MIB factor could be explained by this combination of local and semi-regional factors.

The NWR plot for the dust factor shows high concentrations for low ( $< 5 \text{ km h}^{-1}$ ) to moderate (between 5 to  $10 \text{ km h}^{-1}$ ) wind speeds in the NE direction. This suggests that, similarly to the MIB factor, a mix of local and slightly regional sources contribute to the observed concentrations of dust. Possible local sources of dust include the community gardens at approximately 500 m NE from our sampling site. In addition, a brick manufacturer located 10 km NE of Douai could also be a significant dust emitter. Further away, possible sources of dust include the big cement plants located next to the Belgian city of Tournai, 30 km NE of Douai (Figure S3.8). Hence, the combination of these sources could partly explain the high concentrations of dust observed in the NE sector.

The last factor, local industry, presents high concentrations for low wind speeds at the NE sector, where the industrial area is located. However, it is also found at low and moderate wind speeds at the other directions. In Douai several industries, including hot surface treatment of metals, are present at different directions (Figure S3.7). These could be the major contributors to the observed concentrations of this factor.

### **3.5. Comparison with other SA studies**

The source factors obtained with the PMF<sub>d</sub> analysis have been compared to those of other PM<sub>2.5</sub> source apportionment studies of daily data conducted in North-Western Europe with a minimum duration of 1 year. This includes the studies of Bressi et al. (2014) in Paris and Mooibroek et al. (2011) in 5 cities in the Netherlands, presented in the introduction. In addition, a SA study of PM<sub>10</sub> conducted in Lens is also taken into account for certain factors due to the geographical proximity (20 km) despite of the different size fraction (Waked et al., 2014). It needs to be borne in mind that both studies used organic carbon (OC) in the source apportionment exercise in order to account for the organic aerosol (OA), whereas in this study only oxalate is used as tracer of OA. Therefore, this might lead to discrepancies in the composition of the factors as well as on their contribution to PM<sub>2.5</sub>, as will be discussed below. The comparison between the relative contributions of this work and those of other PM<sub>2.5</sub> source apportionment studies of North-Western Europe are presented in Figure P3.12 and Table S3.8.

The sulfate-rich factor (denominated as secondary sulfate or ammonium sulfate factor in other studies) has been reported in the aforementioned SA studies as a dominant source together with that of secondary nitrate. The contribution found in this study (35%) is higher but of the same order of magnitude than that found in the other PM<sub>2.5</sub> SA studies, that is to say 27% in the study of Bressi et al. (2014) and 20 to 30% in that of Mooibroek et al. (2011). This higher contribution might be partly justified by a higher weight of the organic part of the aerosol in the present work (as reported in Table S3.3, around 70% of the mass of the sulfate-rich factor is not attributed to any of the input variables and could be partly due to organic matter). When the absolute concentrations are compared to the one of this study (4.6  $\mu\text{g m}^{-3}$ ), closer values are found (4.0 for Bressi et al. (2014) and 4.6 for Mooibroek et al. (2011)). However, it needs to be borne in mind that absolute concentrations are dependent on many factors which make the comparison less reliable. Regarding its geographical origin, Mooibroek et al. (2011), Bressi et al. (2014) and Waked et al. (2014) also associated this factor to long-range transport.

The nitrate-rich factor (named secondary nitrate or ammonium nitrate factor in the other studies) is also a very important factor in the other PM<sub>2.5</sub> SA studies, particularly at the different sites of the Netherlands where its contributions range from 41 to 48% (Mooibroek et al., 2011). This agrees with the fact that The Netherlands is one of the hotspot regions for nitrate and ammonia emissions (Figure S3.6). Bressi et al. (2014) report a smaller contribution of 24% which is more in accordance with the observed contribution of 31% in this work. Bressi et al. (2014) and Waked et al. (2014) also characterized this factor as rather regional.

The contribution of road traffic presents a much more pronounced variation among the different sites, consistent with its rather local origin. The value observed in this work (6%) is closer to that of the rural sites (5-7%) or urban site (9%) in the Netherlands, but much inferior to the curbside site in Rotterdam (21%) or the regional background site in Paris (14%). This is consistent since even though the sampling site in Douai is located next to a road, this is not very congested, and the nearest large road (highway A21) is located 1.5 km north of the site, and might therefore not exert a very important influence. Bressi et al. (2014) and Mooibroek et al. (2011) also classified this factor as predominantly local.

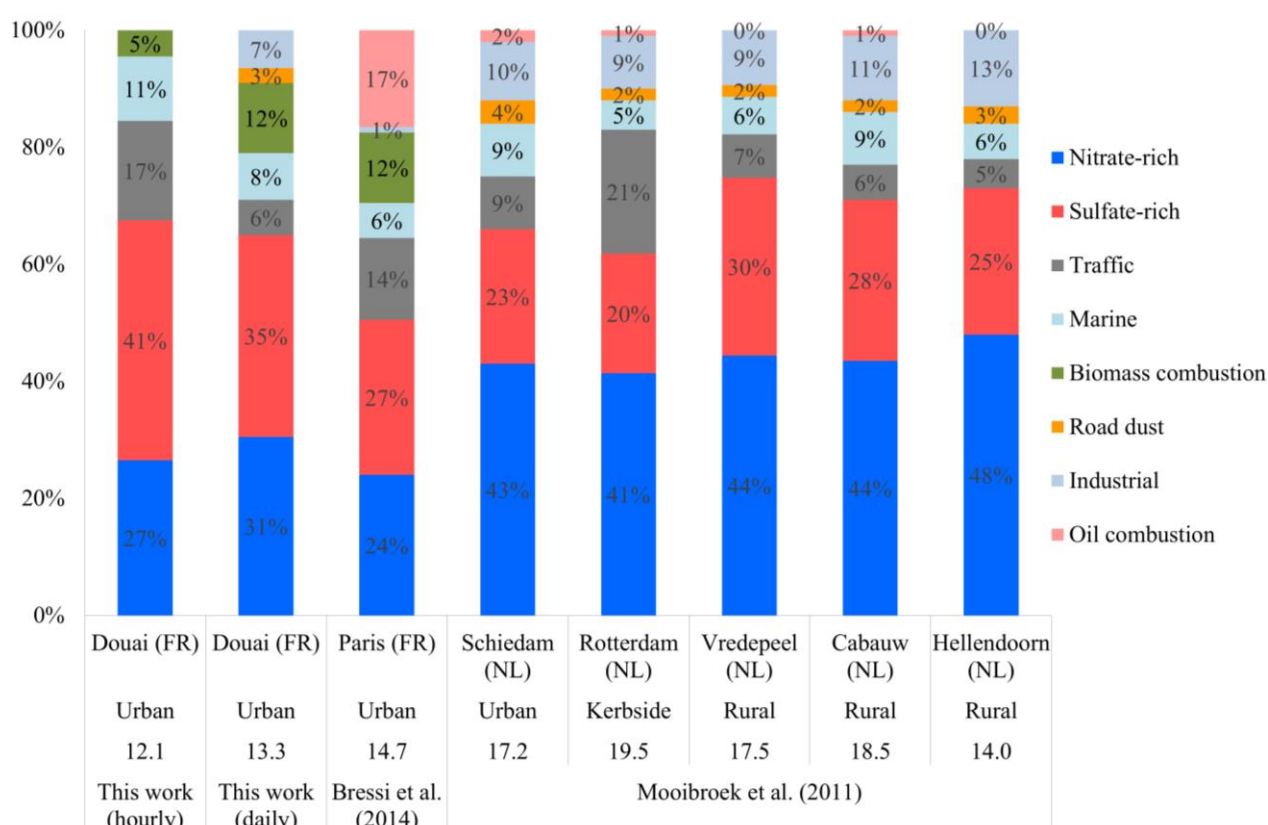


Figure P3.12 Comparison of the relative contributions of sources to PM<sub>2.5</sub> (in %) between various western European sites where the site typology and average PM mass concentration (in μg m<sup>-3</sup>) are indicated below each bar.

The marine factor contribution (8%) is similar to that found in the other studies (8% in Paris and 5-9% in the Netherlands). These low contributions are logical since most of the sea salt mass is located in the coarse mode, as is reflected in the study of Waked et al. (2014) which showed an annual contribution of 27% to PM<sub>10</sub> for the sum of aged and fresh marine aerosols. A regional origin was also found by all of the compared SA studies (Mooibroek et al., 2011; Bressi et al., 2014; Waked et al., 2014).

The biomass combustion factor has only been reported in the study of Paris, where a very close contribution (12%) was found. This value is similar to other PM<sub>10</sub> SA studies, such as the one carried out in Lens (Waked et al., 2014), where 13% was found, and in Belgium (Maenhaut et al., 2016), where a contribution ranging from 7 to 11% was obtained. These last comparisons are feasible since most of the biomass combustion emissions are found in the fine fraction of the aerosol (Karanasiou et al., 2009). Surprisingly, no biomass combustion factor was retrieved from the SA study of Mooibroek et al. (2011), which could have been partly attributed to the lack of specific tracers such as soluble K<sup>+</sup> or Delta-C.

The dust factor of this work, with a contribution of 3%, is in line with the contributions of the crustal factor reported by Mooibroek et al. (2011), ranging from 2% to 4%. Other studies did not separate road traffic and dust and present a combined source profile (Bressi et al., 2014).

The contribution of the remaining factors (MIB and local industry) is reported as a sum (7%) in order to be comparable with the other studies who just report one factor related to industrial emissions. Bressi et al. (2014) found a very low contribution of 1%, and attributed the factor to a large-scale pollution. On the other hand, Mooibroek et al. (2011) found higher contributions ranging from 9 to 13% for a factor named industrial (metal) activities/incineration, and attributed it to a rather regional origin, since only 2 of the sites presented industrial areas nearby and all of them showed similar contributions.

#### **4. Conclusions**

In this work, PMF was applied to two databases of different composition and time-resolution leading to significantly different chemical profiles and contributions. The combination of the MARGA and a 2-wavelength aethalometer at a suburban receptor site mostly under the influence of SIA led to a large dataset (nearly 8,000 data points) consisting of a few variables that was satisfyingly used to identify the main aerosol sources and determine their geographical origins with robustness. A total of five sources were determined



for the hourly-resolved data set ( $\text{PMF}_h$ ), including sulfate-rich, nitrate-rich, road traffic, marine aerosol and biomass combustion, with contributions of 41, 27, 17, 11 and 5%, respectively. The high time resolution has allowed the observation of processes such as the nighttime formation of ammonium nitrate, as well as the variability of anthropogenic-driven sources such as road traffic and biomass combustion. In addition, the analysis of precursor gases by the MARGA has proven valuable for the validation of certain source factors. Finally, a comparison with hourly-averaged PMF factors obtained from a 5-min resolved dataset of  $\text{PM}_{10}$  organic mass spectra ( $\text{PMF}_{\text{org}}$ ) collected during wintertime with a HR-ToF-AMS showed good correlations with common factors and supports the  $\text{PMF}_h$  results. Even though the use of the MARGA for SA has proven valuable, improvements on the detection limit of some minor ions such as  $\text{K}^+$ ,  $\text{Ca}^{2+}$  and  $\text{Mg}^{2+}$  would dramatically increase the number of points above the DL and hence the validity and robustness of the results. Besides, the addition of  $\text{Ca}^{2+}$  in the analysis could eventually lead to extracting a dust source in the  $\text{PMF}_h$ . This could be easily performed by the addition of a pre-concentration column for the cations, as previously suggested by other authors (Makkonen, 2014; Makkonen et al., 2012).

The application of PMF to the daily-resolved database ( $\text{PMF}_d$ ) with the added major and trace elements obtained by ICP-MS analysis allowed the deconvolution of eight source factors, of which five were common with the results of the  $\text{PMF}_h$ , namely sulfate-rich (contribution of 35%), nitrate-rich (30%), biomass combustion (12%), marine aerosol (8%), road traffic (6%), whereas three additional factors were anthropogenic and named as MIB (metal industry background, 6%), dust (3%) and local industry (1%). Differences in contributions between the two PMF analyses were mainly attributed to the loss of information due to the averaging of variables and to their splitting into different factors. These differences were greater for anthropogenic sources, particularly road traffic and biomass combustion. The combination of the MARGA and aethalometer with online techniques for the detection of metals such as X-ray fluorescence (XRF) is highly desirable as it would allow for the detection of additional anthropogenic sources at a higher time resolution, as has already been performed in China (Peng et al., 2016). Another option could be the combination of multiple datasets with different time resolution, as already applied successfully in other studies including Kuo et al. (2014) and Liao et al. (2017), who combined volatile organic compounds and  $\text{PM}_{2.5}$  filter-based data.

The analysis of the geographical origin of source factors by means of NWR and PSCF led to the determination of the rather regional character for the sulfate-rich, nitrate-rich and marine aerosol, a mixed local/regional source origins for the MIB and dust factors, and a

rather local origin for road-traffic, biomass combustion, and local industry. Given the important contribution of the secondary sulfate-rich and nitrate-rich factors (close to 70% as determined in this study) which have a rather regional origin, including hotspots over the Benelux region and western Germany, it is critical to address the reduction of precursor gases emissions (particularly NO<sub>x</sub> and NH<sub>3</sub>) in these areas at the European level in order to eventually decrease the concentrations of fine particulate matter in the north of France and surrounding countries.

## **5. Acknowledgements**

IMT Lille Douai acknowledges financial support from the CaPPA project, which is funded by the French National Research Agency (ANR) through the PIA (Programme d'Investissement d'Avenir) under contract ANR-11-LABX-0005-01, the CLIMIBIO project, both financed by the Regional Council "Hauts-de-France" and the European Regional Development Fund (ERDF); and the Central Laboratory of Air Quality Monitoring (LCSQA). This field campaign was carried out within the framework of the ISARD project funded by the AACT-AIR (ADEME) program (grant 1562C0011). R. Roig Rodelas thanks ARMINES for his PhD fellowship. The authors thank atmo Hauts-de-France and Météo-France for providing air monitoring and meteorological data, respectively.

## **6. References**

Alleman, L. Y., Lamaison, L., Perdrix, E., Robache, A. and Galloo, J.-C.: PM10 metal concentrations and source identification using positive matrix factorization and wind sectoring in a French industrial zone, *Atmos. Res.*, 96(4), 612–625, doi:10.1016/j.atmosres.2010.02.008, 2010.

Allen, G. A., Babich, P. and Poirot, R. L.: Evaluation of a New Approach for Real Time Assessment of Wood Smoke PM, in *Proceedings of the Regional and Global Perspectives on Haze: Causes, Consequences, and Controversies*, NC: Air and Waste Management Association Visibility Specialty Conference, paper 16., 2004.

Amato, F., Pandolfi, M., Escrig, A., Querol, X., Alastuey, A., Pey, J., Perez, N. and Hopke, P. K.: Quantifying road dust resuspension in urban environment by Multilinear Engine: A comparison with PMF2, *Atmos. Environ.*, 43(17), 2770–2780, doi:10.1016/j.atmosenv.2009.02.039, 2009.

Amato, F., Viana, M., Richard, A., Furger, M., Prévôt, A. S. H., Nava, S., Lucarelli, F., Bukowiecki, N., Alastuey, A., Reche, C., Moreno, T., Pandolfi, M., Pey, J. and Querol, X.:

Size and time-resolved roadside enrichment of atmospheric particulate pollutants, *Atmos. Chem. Phys.*, 11(6), 2917–2931, doi:10.5194/acp-11-2917-2011, 2011.

Atmo Hauts-de-France: Bilan de la qualité de l'air en 2016- Hauts-de-France. [online] Available from: [http://www.atmo-hdf.fr/joomlatools-files/docman-files/Bilan\\_annuel/Bilan\\_Qualite\\_Air\\_HdF\\_2016\\_VF-min.pdf](http://www.atmo-hdf.fr/joomlatools-files/docman-files/Bilan_annuel/Bilan_Qualite_Air_HdF_2016_VF-min.pdf), 2017.

Belis, C. A., Larsen, B. R., Amato, F., El Haddad, I., Favez, O., Harrison, R. M., Hopke, P. K., Nava, S., Paatero, P., Prévôt, A. and Quass, U., Vecchi, R., Viana, M.: European guide on air pollution source apportionment with receptor models, Joint Research Centre., 2014.

Bressi, M., Sciare, J., Gherzi, V., Mihalopoulos, N., Petit, J.-E., Nicolas, J. B., Moukhtar, S., Rosso, A., Féron, A., Bonnaire, N., Poulakis, E. and Theodosi, C.: Sources and geographical origins of fine aerosols in Paris (France), *Atmos. Chem. Phys.*, 14(16), 8813–8839, doi:10.5194/acp-14-8813-2014, 2014.

ten Brink, H., Otjes, R., Jongejan, P. and Slanina, S.: An instrument for semi-continuous monitoring of the size-distribution of nitrate, ammonium, sulphate and chloride in aerosol, *Atmos. Environ.*, 41(13), 2768–2779, doi:10.1016/j.atmosenv.2006.11.041, 2007.

Comero, S., Capitani, L. and Gawlik, B.: Positive Matrix Factorisation (PMF) - An Introduction to the Chemometric Evaluation of Environmental Monitoring Data Using PMF, EUR - Scientific and Technical Research Reports, OP., 2009.

Crilley, L. R., Lucarelli, F., Bloss, W. J., Harrison, R. M., Beddows, D. C., Calzolari, G., Nava, S., Valli, G., Bernardoni, V. and Vecchi, R.: Source apportionment of fine and coarse particles at a roadside and urban background site in London during the 2012 summer ClearfLo campaign, *Environ. Pollut.*, 220, 766–778, doi:10.1016/j.envpol.2016.06.002, 2017.

Crippa, M., Canonaco, F., Lanz, V. A., Äijälä, M., Allan, J. D., Carbone, S., Capes, G., Ceburnis, D., Dall'Osto, M., Day, D. A., DeCarlo, P. F., Ehn, M., Eriksson, A., Freney, E., Hildebrandt Ruiz, L., Hillamo, R., Jimenez, J. L., Junninen, H., Kiendler-Scharr, A., Kortelainen, A.-M., Kulmala, M., Laaksonen, A., Mensah, A. A., Mohr, C., Nemitz, E., O'Dowd, C., Ovadnevaite, J., Pandis, S. N., Petäjä, T., Poulain, L., Saarikoski, S., Sellegri, K., Swietlicki, E., Tiitta, P., Worsnop, D. R., Baltensperger, U. and Prévôt, A. S. H.: Organic aerosol components derived from 25 AMS data sets across Europe using a consistent ME-2 based source apportionment approach, *Atmos. Chem. Phys.*, 14(12), 6159–6176, doi:10.5194/acp-14-6159-2014, 2014.

DeCarlo, P. F., Kimmel, J. R., Trimborn, A., Northway, M. J., Jayne, J. T., Aiken, A. C., Gonin, M., Fuhrer, K., Horvath, T., Docherty, K. S., Worsnop, D. R. and Jimenez, J. L.: Field-Deployable, High-Resolution, Time-of-Flight Aerosol Mass Spectrometer, *Anal. Chem.*, 78(24), 8281–8289, doi:10.1021/ac061249n, 2006.

Dulac, F., Buat-Ménard, P., Arnold, M., Ezat, U. and Martin, D.: Atmospheric input of trace metals to the western Mediterranean Sea: 1. Factors controlling the variability of atmospheric concentrations, *J. Geophys. Res. Atmospheres*, 92(D7), 8437–8453, doi:10.1029/JD092iD07p08437, 1987.

Fan, J., Yue, X., Jing, Y., Chen, Q. and Wang, S.: Online monitoring of water-soluble ionic composition of PM<sub>10</sub> during early summer over Lanzhou City, *J. Environ. Sci.*, 26(2), 353–361, doi:10.1016/S1001-0742(13)60431-3, 2014.

Fröhlich, R., Crenn, V., Setyan, A., Belis, C. A., Canonaco, F., Favez, O., Riffault, V., Slowik, J. G., Aas, W., Aijälä, M., Alastuey, A., Artiñano, B., Bonnaire, N., Bozzetti, C., Bressi, M., Carbone, C., Coz, E., Croteau, P. L., Cubison, M. J., Esser-Gietl, J. K., Green, D. C., Gros, V., Heikkinen, L., Herrmann, H., Jayne, J. T., Lunder, C. R., Minguillón, M. C., Močnik, G., O'Dowd, C. D., Ovadnevaite, J., Petralia, E., Poulain, L., Priestman, M., Ripoll, A., Sarda-Estève, R., Wiedensohler, A., Baltensperger, U., Sciare, J. and Prévôt, A. S. H.: ACTRIS ACSM intercomparison – Part 2: Intercomparison of ME-2 organic source apportionment results from 15 individual, co-located aerosol mass spectrometers, *Atmos. Meas. Tech.*, 8(6), 2555–2576, doi:<https://doi.org/10.5194/amt-8-2555-2015>, 2015.

Gao, J., Peng, X., Chen, G., Xu, J., Shi, G.-L., Zhang, Y.-C. and Feng, Y.-C.: Insights into the chemical characterization and sources of PM<sub>2.5</sub> in Beijing at a 1-h time resolution, *Sci. Total Environ.*, 542, Part A, 162–171, doi:[10.1016/j.scitotenv.2015.10.082](https://doi.org/10.1016/j.scitotenv.2015.10.082), 2016.

Henry, R., Norris, G. A., Vedantham, R. and Turner, J. R.: Source Region Identification Using Kernel Smoothing, *Environ. Sci. Technol.*, 43(11), 4090–4097, doi:[10.1021/es8011723](https://doi.org/10.1021/es8011723), 2009.

Johansson, C., Norman, M. and Burman, L.: Road traffic emission factors for heavy metals, *Atmos. Environ.*, 43(31), 4681–4688, doi:[10.1016/j.atmosenv.2008.10.024](https://doi.org/10.1016/j.atmosenv.2008.10.024), 2009.

Karanasiou, A. A., Siskos, P. A. and Eleftheriadis, K.: Assessment of source apportionment by Positive Matrix Factorization analysis on fine and coarse urban aerosol size fractions, *Atmos. Environ.*, 43(21), 3385–3395, doi:[10.1016/j.atmosenv.2009.03.051](https://doi.org/10.1016/j.atmosenv.2009.03.051), 2009.

Kim, K.-H., Kabir, E. and Kabir, S.: A review on the human health impact of airborne particulate matter, *Environ. Int.*, 74, 136–143, doi:[10.1016/j.envint.2014.10.005](https://doi.org/10.1016/j.envint.2014.10.005), 2015.

Kuo, C.-P., Liao, H.-T., Chou, C. C.-K. and Wu, C.-F.: Source apportionment of particulate matter and selected volatile organic compounds with multiple time resolution data, *Sci. Total Environ.*, 472, 880–887, doi:[10.1016/j.scitotenv.2013.11.114](https://doi.org/10.1016/j.scitotenv.2013.11.114), 2014.

Lanz, V. A., Prévôt, A. S. H., Alfarra, M. R., Weimer, S., Mohr, C., DeCarlo, P. F., Gianini, M. F. D., Hueglin, C., Schneider, J., Favez, O., D'Anna, B., George, C. and Baltensperger, U.: Characterization of aerosol chemical composition with aerosol mass spectrometry in Central Europe: an overview, *Atmos. Chem. Phys.*, 10(21), 10453–10471, doi:[10.5194/acp-10-10453-2010](https://doi.org/10.5194/acp-10-10453-2010), 2010.

Ledoux, F., Kfoury, A., Delmaire, G., Roussel, G., El Zein, A. and Courcot, D.: Contributions of local and regional anthropogenic sources of metals in PM<sub>2.5</sub> at an urban site in northern France, *Chemosphere*, 181, 713–724, doi:[10.1016/j.chemosphere.2017.04.128](https://doi.org/10.1016/j.chemosphere.2017.04.128), 2017.

Liao, H.-T., Yau, Y.-C., Huang, C.-S., Chen, N., Chow, J. C., Watson, J. G., Tsai, S.-W., Chou, C. C.-K. and Wu, C.-F.: Source apportionment of urban air pollutants using constrained receptor models with a priori profile information, *Environ. Pollut.*, 227, 323–333, doi:[10.1016/j.envpol.2017.04.071](https://doi.org/10.1016/j.envpol.2017.04.071), 2017.

Maenhaut, W., Vermeylen, R., Claeys, M., Vercauteren, J. and Roekens, E.: Sources of the PM<sub>10</sub> aerosol in Flanders, Belgium, and re-assessment of the contribution from wood burning, *Sci. Total Environ.*, 562, 550–560, doi:[10.1016/j.scitotenv.2016.04.074](https://doi.org/10.1016/j.scitotenv.2016.04.074), 2016.

Makkonen, U.: Semi-continuous gas and inorganic aerosol measurements at a boreal forest site: seasonal and diurnal cycles of NH<sub>3</sub>, HONO and HNO<sub>3</sub>, *Boreal Environ. Res.*, 19 (suppl. B), 311–328, 2014.

Makkonen, U., Virkkula, A., Mäntykenttä, J., Hakola, H., Keronen, P., Vakkari, V. and Aalto, P. P.: Semi-continuous gas and inorganic aerosol measurements at a Finnish urban site: comparisons with filters, nitrogen in aerosol and gas phases, and aerosol acidity, *Atmos. Chem. Phys.*, 12(12), 5617–5631, doi:10.5194/acp-12-5617-2012, 2012.

Makkonen, U., Virkkula, A., Hellén, H., Hemmila, M., Sund, J., Aijala, M., Ehn, M., Junninen, H., Keronen, P., Petaja, T., Worsnop, D. R., Kulmala, M. and Hakola, H.: Semi-continuous gas and inorganic aerosol measurements at a boreal forest site, *Boreal Environ. Res.*, 19 (suppl. B), 311–328, 2014.

Masiol, M., Hopke, P. K., Felton, H. D., Frank, B. P., Rattigan, O. V., Wurth, M. J. and LaDuke, G. H.: Source apportionment of PM<sub>2.5</sub> chemically speciated mass and particle number concentrations in New York City, *Atmos. Environ.*, 148, 215–229, doi:10.1016/j.atmosenv.2016.10.044, 2017.

Mbengue, S., Alleman, L. Y. and Flament, P.: Size-distributed metallic elements in submicronic and ultrafine atmospheric particles from urban and industrial areas in northern France, *Atmos. Res.*, 135–136, 35–47, doi:10.1016/j.atmosres.2013.08.010, 2014.

Mooibroek, D., Schaap, M., Weijers, E. P. and Hoogerbrugge, R.: Source apportionment and spatial variability of PM<sub>2.5</sub> using measurements at five sites in the Netherlands, *Atmos. Environ.*, 45(25), 4180–4191, doi:10.1016/j.atmosenv.2011.05.017, 2011.

Paatero, P. and Tapper, U.: Positive matrix factorization: A non-negative factor model with optimal utilization of error estimates of data values, *Environmetrics*, 5(2), 111–126, doi:10.1002/env.3170050203, 1994.

Pay, M. T., Jiménez-Guerrero, P. and Baldasano, J. M.: Assessing sensitivity regimes of secondary inorganic aerosol formation in Europe with the CALIOPE-EU modeling system, *Atmos. Environ.*, 51, 146–164, doi:10.1016/j.atmosenv.2012.01.027, 2012.

Peng, X., Shi, G.-L., Gao, J., Liu, J.-Y., HuangFu, Y.-Q., Ma, T., Wang, H.-T., Zhang, Y.-C., Wang, H., Li, H., Ivey, C. E. and Feng, Y.-C.: Characteristics and sensitivity analysis of multiple-time-resolved source patterns of PM<sub>2.5</sub> with real time data using Multilinear Engine 2, *Atmos. Environ.*, 139, 113–121, doi:10.1016/j.atmosenv.2016.05.032, 2016.

Petit, J.-E., Favez, O., Albinet, A. and Canonaco, F.: A user-friendly tool for comprehensive evaluation of the geographical origins of atmospheric pollution: Wind and trajectory analyses, *Environ. Model. Softw.*, 88, 183–187, doi:10.1016/j.envsoft.2016.11.022, 2017.

Polissar, A. V., Hopke, P. K., Paatero, P., Malm, W. C. and Sisler, J. F.: Atmospheric aerosol over Alaska: 2. Elemental composition and sources, *J. Geophys. Res. Atmospheres*, 103(D15), 19045–19057, doi:10.1029/98JD01212, 1998.

Roig, R., Perdrix, E., Herbin, B. and Riffault, V.: Characterization and variability of inorganic aerosols and their gaseous precursors at a suburban site in northern France over one year (2015-2016), submitted.

Roig, R., Chakraborty, A., Perdrix, E., Tison, E. and Riffault, V.: Real-time assessment of wintertime organic aerosol characteristics and sources at a suburban site in northern France, in prep.

Salminen, R., Batista, M., M, B., Demetriades, A., De Vivo, B., De Vos, W., Duris, A. G., Gregorauskiene, V., Halamić, J., P, H., Lima, A., G, J., G, K., P, K., J, L., Locutura, J., K, M., A., M. and Tarvainen, T.: FOREGS Geochemical Atlas of Europe, Part 1: Background Information, Methodology and Maps., 2005.

Santé publique France: Impacts de l'exposition chronique aux particules fines sur la mortalité en France continentale et analyse des gains en santé de plusieurs scénarios de réduction de la pollution atmosphérique, [online] Available from: <http://invs.santepubliquefrance.fr/Publications-et-outils/Rapports-et-syntheses/Environnement-et-sante/2016/Impacts-de-l-exposition-chronique-aux-particules-fines-sur-la-mortalite-en-France-continentale-et-analyse-des-gains-en-sante-de-plusieurs-scenarios-de-reduction-de-la-pollution-atmospherique> (Accessed 31 August 2017), 2016.

Stein, A. F., Draxler, R. R., Rolph, G. D., Stunder, B. J. B., Cohen, M. D. and Ngan, F.: NOAA's HYSPLIT Atmospheric Transport and Dispersion Modeling System, Bull. Am. Meteorol. Soc., 96(12), 2059–2077, doi:10.1175/BAMS-D-14-00110.1, 2015.

Sternbeck, J., Sjödin, Å. and Andréasson, K.: Metal emissions from road traffic and the influence of resuspension—results from two tunnel studies, Atmos. Environ., 36(30), 4735–4744, doi:10.1016/S1352-2310(02)00561-7, 2002.

Stieger, B., Spindler, G., Fahlbusch, B., Müller, K., Grüner, A., Poulain, L., Thöni, L., Seitler, E., Wallasch, M. and Herrmann, H.: Measurements of PM<sub>10</sub> ions and trace gases with the online system MARGA at the research station Melpitz in Germany – A five-year study, J. Atmos. Chem., 1–38, doi:10.1007/s10874-017-9361-0, 2017.

Tang, I. N., Tridico, A. C. and Fung, K. H.: Thermodynamic and optical properties of sea salt aerosols, J. Geophys. Res. Atmospheres, 102(D19), 23269–23275, doi:10.1029/97JD01806, 1997.

Thorpe, A. J., Harrison, R. M., Boulter, P. G. and McCrae, I. S.: Estimation of particle resuspension source strength on a major London Road, Atmos. Environ., 41(37), 8007–8020, doi:10.1016/j.atmosenv.2007.07.006, 2007.

Twigg, M. M., Di Marco, C. F., Leeson, S., van Dijk, N., Jones, M. R., Leith, I. D., Morrison, E., Coyle, M., Proost, R., Peeters, A. N. M., Lemon, E., Frelink, T., Braban, C. F., Nemitz, E. and Cape, J. N.: Water soluble aerosols and gases at a UK background site – Part 1: Controls of PM<sub>2.5</sub> and PM<sub>10</sub> aerosol composition, Atmos. Chem. Phys., 15(14), 8131–8145, doi:10.5194/acp-15-8131-2015, 2015.

Viana, M., Kuhlbusch, T. A. J., Querol, X., Alastuey, A., Harrison, R. M., Hopke, P. K., Winiwarter, W., Vallius, M., Szidat, S., Prévôt, A. S. H., Hueglin, C., Bloemen, H., Wählin, P., Vecchi, R., Miranda, A. I., Kasper-Giebl, A., Maenhaut, W. and Hitzengerger, R.: Source apportionment of particulate matter in Europe: A review of methods and results, J. Aerosol Sci., 39(10), 827–849, doi:10.1016/j.jaerosci.2008.05.007, 2008.

Waked, A., Favez, O., Alleman, L. Y., Piot, C., Petit, J.-E., Delaunay, T., Verlinden, E., Golly, B., Besombes, J.-L., Jaffrezo, J.-L. and Leoz-Garziandia, E.: Source apportionment of

PM10 in a north-western Europe regional urban background site (Lens, France) using positive matrix factorization and including primary biogenic emissions, *Atmos. Chem. Phys.*, 14(7), 3325–3346, doi:10.5194/acp-14-3325-2014, 2014.

Wang, Y., Hopke, P. K., Rattigan, O. V., Xia, X., Chalupa, D. C. and Utell, M. J.: Characterization of Residential Wood Combustion Particles Using the Two-Wavelength Aethalometer, *Environ. Sci. Technol.*, 45(17), 7387–7393, doi:10.1021/es2013984, 2011.

Wang, Y., Hopke, P. K., Rattigan, O. V., Chalupa, D. C. and Utell, M. J.: Multiple-year black carbon measurements and source apportionment using delta-C in Rochester, New York, *J. Air Waste Manag. Assoc.*, 62(8), 880–887, 2012a.

Wang, Y., Hopke, P. K., Xia, X., Rattigan, O. V., Chalupa, D. C. and Utell, M. J.: Source apportionment of airborne particulate matter using inorganic and organic species as tracers, *Atmos. Environ.*, 55(Supplement C), 525–532, doi:10.1016/j.atmosenv.2012.03.073, 2012b.

Weingartner, E., Saathoff, H., Schnaiter, M., Streit, N., Bitnar, B. and Baltensperger, U.: Absorption of light by soot particles: determination of the absorption coefficient by means of aethalometers, *J. Aerosol Sci.*, 34(10), 1445–1463, doi:10.1016/S0021-8502(03)00359-8, 2003.

Yli-Tuomi, T., Siponen, T., Taimisto, R. P., Aurela, M., Teinilä, K., Hillamo, R., Pekkanen, J., Salonen, R. O. and Lanki, T.: Impact of Wood Combustion for Secondary Heating and Recreational Purposes on Particulate Air Pollution in a Suburb in Finland, , doi:10.1021/es5053683, 2015.





---

# **CONCLUSIONS AND PERSPECTIVES**

---



## CONCLUSIONS AND PERSPECTIVES

This work has focused on the characterization, origin and variability of secondary inorganic aerosols (SIA) and their gaseous precursors over one year and on an hourly basis for the first time in France. The campaign site was implemented in a middle-size city (Douai) in northern France, a region of northwestern Europe where SIA were expected to be large contributors to PM, with particularly high contributions during pollution episodes. The combination of (i) several high time resolution instruments for monitoring both the inorganic gas and particulate phases during a long term field campaign (from August 2015 to July 2016), as well as (ii) daily filter sampling for heavy metals and trace elements, and (iii) the addition of an intensive field campaign specifically aiming at assessing the influence of organics and possible particle formation events during wintertime pollution episodes, allowed for the constitution of a unique and comprehensive database.

On the methodological level, the main instrument used in this study (MARGA) has proven to be able to monitor correctly in near real-time and over a long period most of the water-soluble inorganic ions and one organic species (oxalate), as well as most of their gaseous precursors. The comparison between these observations and other independent methods has shown a good measurement performance for the major ions ( $\text{NO}_3^-$ ,  $\text{SO}_4^{2-}$  and  $\text{NH}_4^+$ ) and precursor gases ( $\text{SO}_2$ ,  $\text{NH}_3$ ). However, several issues could be highlighted:

(i) the concentrations of minor ions including  $\text{K}^+$ ,  $\text{Mg}^{2+}$  and  $\text{Ca}^{2+}$  were below the detection limit during most of the campaign, which hindered the study of their variability and use as tracers in PMF analysis;

(ii) the measurement of chloride was also difficult as the anion chromatography column aged, since its peak was merged with that of the injection. In addition, when the ions were very close to the detection limit, the software did not automatically integrate them. Although this could be corrected with the MargaTool software provided by Metrohm, this correction was not at all straightforward since the software allowed little freedom to the user and rendered the process very time consuming;

(iii) the measurement of  $\text{HNO}_3$  could not be performed correctly by the instrument, which was attributed to its sticky nature causing the adsorption of the gas along the sampling line as has already been reported in previous studies using the same instrument (Makkonen et al., 2012, 2014; Stieger et al., 2017);

(iv) another more episodic problem was the microbiological contamination of the MARGA which led to the malfunctioning of the system and demanded a thorough manual cleaning, very time-consuming in some cases.

All these issues indicate that there is room for technical improvements, some of which will be specified in the perspectives given in this chapter. It is also recommended that the MARGA is used together with other instrumentation, and to perform additional comparisons for problematic species such as minor ions and  $\text{HNO}_3$ .

On the other hand, the use of ISORROPIA II has proved useful for the study of particle-gas partitioning of the main inorganic aerosol compounds, which has rarely been done over such a long duration, and allowed for the re-calculation of  $\text{HNO}_3$  at the hourly time scale. However, it would be interesting to compare these modelled concentrations to other measurements such as those performed by an online  $\text{HNO}_3$  analyzer. It also needs to be borne in mind that the ISORROPIA module is based on rather simple assumptions, which are useful in order to improve the calculation speed in chemistry-transport models, but cannot completely reflect the complex reality.

The scientific results of this work have been divided in three parts from which major conclusions are summarized below.

In the first part, the characterization and variability of SIA and their precursor gases were presented. In line with other measurements in North-Western Europe, the main components of SIA (i.e.  $\text{NO}_3^-$ ,  $\text{SO}_4^{2-}$  and  $\text{NH}_4^+$ ) were shown to contribute largely to  $\text{PM}_{2.5}$  with annual mean mass contributions of 28.0%, 13.1% and 9.9%, respectively. The highest concentrations of SIA were observed in spring, most likely due to the increased emissions of ammonia, a precursor gas from agricultural activities and one of the main drivers of SIA, combined with temperatures low enough to convert it to the particulate phase in the presence of  $\text{SO}_2$  or  $\text{NO}_x$ . We have indeed shown the importance of ammonium nitrate ( $\text{NH}_4\text{NO}_3$ ) and ammonium sulfate ( $(\text{NH}_4)_2\text{SO}_4$ ) as main SIA species, with a predominance of ammonium nitrate during most of the year except in summer due to higher temperature favoring the presence of the gas phase precursors of  $\text{NH}_4\text{NO}_3$  and higher photochemical activity promoting the oxidation of  $(\text{NH}_4)_2\text{SO}_4$  precursors. The high time resolution of the MARGA has allowed to observe a particularly strong formation of  $\text{NH}_4\text{NO}_3$  during nighttime in every season, attributed to the partitioning to the aerosol phase of its gaseous precursors  $\text{NH}_3$  and  $\text{HNO}_3$ , and to the occurrence of nocturnal formation of  $\text{HNO}_3$  and  $\text{HONO}$  via the heterogeneous

oxidation of  $\text{NO}_2$  by the nitrate radical. Other sources have also been evidenced, including road traffic and biomass combustion, especially during the cold season. Through the modelling of gas and particle partitioning with ISORROPIA II, we have also observed that the thermodynamic conditions have influenced the SIA observed at our site, especially regarding the formation of  $\text{NH}_4\text{NO}_3$ . A first approach for the study of the origin of SIA and their precursor gases by means of non-parametric wind regression (NWR) and positive source contribution function (PSCF) have confirmed that long-range transport (LRT) from Belgium, The Netherlands and Germany is a major contributor for the observed concentrations of SIA, in accordance with European emission inventories of  $\text{SO}_2$ ,  $\text{NH}_3$  and  $\text{NO}_x$  (EMEP, 2016). This has been particularly observed in spring with the occurrence of exceedance episodes in which SIA have contributed to most of the  $\text{PM}_{2.5}$  mass. Besides LRT, local emissions have been shown to play an important role particularly during the cold months, with traffic and biomass combustion contributing significantly to the  $\text{NO}_x$  emissions and observed  $\text{PM}_{2.5}$ .

The second part of this work focused on the composition of OA and its main sources during wintertime. We have shown that the non-refractory submicron particulate matter ( $\text{NR-PM}_1$ ) was again dominated by inorganic aerosols, with contributions of 36%  $\text{NO}_3$ , 16%  $\text{NH}_4$  and 9%  $\text{SO}_4$ , with organic matter (OM) making up for the remaining 38%. The elemental ratios of OA were evaluated and pointed to a moderate level of aerosol oxidation ( $\text{OM/OC} = 1.60 \pm 0.15$ ). The positive matrix factorization (PMF) source-receptor modelling was applied to the high-resolution OA mass spectra and allowed the identification of five factors: two primary (local) OA factors – hydrocarbon-like (HOA) and cooking-like OA (COA); one factor associated with oxidized biomass burning (oBBOA); and two oxygenated factors (OOA) denoted as less oxidized (LO-OOA) and more oxidized (MO-OOA), with average contributions to OA of 15%, 11%, 25%, 16% and 33%, respectively. We observed that the oBBOA factor, which has rarely been observed in other studies, had mainly a local origin and correlated well with relative humidity, indicating possible aqueous processing of locally emitted primary biomass burning emissions. In addition, oBBOA was shown to be involved in one nighttime NPF event suggesting a fast processing of organic species under high humidity conditions. This confirms the relevance of tackling biomass combustion emissions in northern France and also suggests that during winter, aqueous processing of primary biomass burning emissions in North-Western Europe could be more important than what was previously thought. In addition, we demonstrated that the impact of air masses from Eastern

Europe enhances OA concentrations and the contribution of secondary OA factors, which increased from 41% to 65% in the last part of the intensive campaign.

The last section dealt with the application of PMF modelling to yearly datasets from this work: a first hourly dataset taking advantage of the maximum temporal resolution (hourly basis) consisting of the water-soluble inorganic ions and two types of light-absorbing carbon (PMF<sub>h</sub>), and a second one including more tracers (several trace and major elements) but averaged on a daily basis (PMF<sub>d</sub>). Five common sources were obtained with both approaches, identified as sulfate-rich, nitrate-rich, marine, road traffic and biomass combustion. These sources explained most of the PM<sub>2.5</sub> mass in both approaches, suggesting that the combination of the MARGA and a 2-wavelength aethalometer with an hourly temporal resolution (during a 1-year long period) should be enough to estimate the main aerosol sources at a site mostly influenced by SIA. Secondary factors (sulfate-rich and nitrate-rich) have been clearly predominant in Douai throughout the year, adding up to more than 60% of the PM<sub>2.5</sub> mass in both approaches. However, high contributions of anthropogenic factors, particularly biomass combustion and road traffic, have also been observed in the cold months. The hourly resolution of the PMF<sub>h</sub> allowed the observation of processes such as the nighttime increase of the nitrate-rich factor as well as the daily trends of certain sources including road traffic and biomass combustion. However, the addition of several trace and major elements in the PMF<sub>d</sub> brought more information on three additional anthropogenic source factors: metal industry background (MIB), local industry and dust. Even though these sources have been shown to present low contributions in Douai, they should not be neglected since they can contribute up to more than 30% of PM<sub>2.5</sub> on specific days. In addition, slightly different contributions to PM<sub>2.5</sub> were observed between both approaches, which were mainly attributed to the loss of information due to averaging the hourly variables, the asynchronous behavior of some primary and secondary sources which could be separated in PMF<sub>h</sub> but were mixed in PMF<sub>d</sub> (e.g. separation of primary biomass combustion emissions and evidence of secondary processing in the PMF<sub>h</sub>,) and the splitting into more source factors in the PMF<sub>d</sub>. With the application of NWR and PSCF, we determined the regional origin of sulfate-rich, nitrate-rich and marine aerosol, while a rather local origin was associated to the other source factors. In comparison to a typical SA study performed with filters, where typically a few hundreds of data points are usually available over the same period, the high number of data points of the PMF<sub>h</sub> (nearly 8,000) has given great robustness to the geographical determination of the sources. Lastly, the analysis of gases by the MARGA has proven valuable for the validation

of certain source factors, including  $\text{NH}_3$  for the nitrate-rich factor,  $\text{SO}_2$  for sulfate-rich factor and HONO for the road traffic factor.

The results of this work should prove useful to policymakers to devise effective mitigation strategies in order to improve air quality in northern France. In view of the important contribution of secondary factors including sulfate-rich and nitrate-rich (close to 70% as determined in this thesis) which have a rather regional origin, with hotspots over the Benelux region and western Germany, it is important to put emphasis on European policies in order to diminish emissions of precursor gases such as  $\text{SO}_2$ ,  $\text{NO}_x$  and  $\text{NH}_3$ . While a considerable reduction of the first two has already been achieved in the last years, the emissions of  $\text{NH}_3$  have kept the same levels during the last three decades (EEA, 2016; CITEPA, 2017). The reduction of emissions of precursor gases in these areas would eventually lead to a decrease in the concentrations of fine particulate matter in the north of France and surrounding countries. However, local mitigation policies should not be neglected, particularly during the cold months, where road traffic and biomass combustion have been shown to be important contributors to fine particles.

Regarding the perspectives of this work, some ideas in order to improve and continue the research carried out in this thesis are presented below.

Concerning the analyses performed with the MARGA itself, it would be interesting to add a pre-concentration column in order to improve the detection limits of minor cations, especially  $\text{Ca}^{2+}$  as mentioned before (Makkonen et al., 2012, 2014), to reduce the length of the sampling line in order to minimize the absorption phenomenon of acidic gases (Rumsey et al., 2014), and to use a different anion eluent (Makkonen et al., 2014) in order to improve the analysis of nitric acid (although this species concentration can be recalculated using modelling). A collocated analysis with a  $\text{HNO}_3$  online analyzer should also be implemented in order to check the efficiency of these improvements

In addition, it would also be interesting to implement more online instrumentation for:

(i) The continuous analysis of organic carbon, which would allow for chemical mass closure when performing a source-receptor analysis and to study its possible combined effect with SIA, especially in case of high pollution events.

(ii) Trace and major elements which would allow studying the variability of crustal and anthropogenic sources with a high time resolution (Peng et al., 2016).

(iii) Particle size distribution and number over a longer period, to capture other types of new particle formation events such as secondary organic aerosol formation in summertime.

(iv) Nitrate radical to better understand whether nighttime nitrate formation results from thermodynamic condensation or from oxidation reactions.

Additionally investigating the isotopic composition of nitrogen depending on its origin, for both gas and aerosol phases, would help to better distinguish between the local formation and long-range transport of nitrogen-containing secondary aerosols. This approach could also be performed through the use of chemistry-transport models. In relation to the PMF analysis, the combination of the multiple datasets with different time resolution is another interesting possibility (Kuo et al., 2014; Liao et al., 2017). Finally, since this work has been carried out at a suburban location, which is necessarily more affected by anthropogenic sources such as road traffic, biomass combustion and industrial activities, a similar study at a rural site with a similar methodology would enable to evaluate the influence of these and other sources which play a less important role in urban locations. This is currently under progress through the PhD thesis of Pablo Espina-Martin in our group. Chemical processes occurring under significantly different chemical regimes (different  $\text{NO}_x/\text{NH}_3$  ratios, more ozone than in urban locations) will therefore be studied as well and compared to the highly time-resolved observations performed in this thesis. Finally, it is necessary to improve our knowledge on the influence of fog events and relevant meteorological parameters on biomass combustion emissions, SIA and OA chemistry, and to investigate the mechanism and kinetics of the aqueous oxidation of BBOA to o-BBOA.



## References

- CITEPA: CITEPA, [online] Available from: <https://www.citepa.org/fr/air-et-climat/polluants/aep-item> (Accessed 28 February 2018), 2017.
- EMEP: EMEP database, [online] Available from: [http://www.ceip.at/ms/ceip\\_home1/ceip\\_home/webdab\\_emepdatabase/](http://www.ceip.at/ms/ceip_home1/ceip_home/webdab_emepdatabase/), 2016.
- Kuo, C.-P., Liao, H.-T., Chou, C. C.-K. and Wu, C.-F.: Source apportionment of particulate matter and selected volatile organic compounds with multiple time resolution data, *Sci. Total Environ.*, 472, 880–887, doi:10.1016/j.scitotenv.2013.11.114, 2014.
- Liao, H.-T., Yau, Y.-C., Huang, C.-S., Chen, N., Chow, J. C., Watson, J. G., Tsai, S.-W., Chou, C. C.-K. and Wu, C.-F.: Source apportionment of urban air pollutants using constrained receptor models with a priori profile information, *Environ. Pollut.*, 227, 323–333, doi:10.1016/j.envpol.2017.04.071, 2017.
- Makkonen, U., Virkkula, A., Mäntykenttä, J., Hakola, H., Keronen, P., Vakkari, V. and Aalto, P. P.: Semi-continuous gas and inorganic aerosol measurements at a Finnish urban site: comparisons with filters, nitrogen in aerosol and gas phases, and aerosol acidity, *Atmos. Chem. Phys.*, 12(12), 5617–5631, doi:10.5194/acp-12-5617-2012, 2012.
- Makkonen, U., Virkkula, A., Hellén, H., Hemmila, M., Sund, J., Aijala, M., Ehn, M., Junninen, H., Keronen, P., Petaja, T., Worsnop, D. R., Kulmala, M. and Hakola, H.: Semi-continuous gas and inorganic aerosol measurements at a boreal forest site, *Boreal Environ. Res.*, 19 (suppl. B), 311–328, 2014.
- Peng, X., Shi, G.-L., Gao, J., Liu, J.-Y., HuangFu, Y.-Q., Ma, T., Wang, H.-T., Zhang, Y.-C., Wang, H., Li, H., Ivey, C. E. and Feng, Y.-C.: Characteristics and sensitivity analysis of multiple-time-resolved source patterns of PM<sub>2.5</sub> with real time data using Multilinear Engine 2, *Atmos. Environ.*, 139(Supplement C), 113–121, doi:10.1016/j.atmosenv.2016.05.032, 2016.
- Rumsey, I. C., Cowen, K. A., Walker, J. T., Kelly, T. J., Hanft, E. A., Mishoe, K., Rogers, C., Proost, R., Beachley, G. M., Lear, G., Frelink, T. and Otjes, R. P.: An assessment of the performance of the Monitor for AeRosols and GAses in ambient air (MARGA): a semi-continuous method for soluble compounds, *Atmos. Chem. Phys.*, 14(11), 5639–5658, doi:10.5194/acp-14-5639-2014, 2014.
- Stieger, B., Spindler, G., Fahlbusch, B., Müller, K., Grüner, A., Poulain, L., Thöni, L., Seitler, E., Wallasch, M. and Herrmann, H.: Measurements of PM<sub>10</sub> ions and trace gases with the online system MARGA at the research station Melpitz in Germany – A five-year study, *J. Atmos. Chem.*, 1–38, doi:10.1007/s10874-017-9361-0, 2017.



---

# **ANNEXES**

---



## ANNEX 0: Scientific Valorization

### 1) International journals

#### SUBMITTED PUBLICATIONS

- [A1] **R. ROIG RODELAS**, E. PERDRIX, B. HERBIN, V. RIFFAULT, Characterization and variability of inorganic aerosols and their gaseous precursors at a suburban site in northern France over one year (2015-2016), soumis à Atmospheric Environment
- [A2] **R. ROIG RODELAS**, E. PERDRIX, B. MALET, B. HERBIN, L. Y. ALLEMAN, V. RIFFAULT, Sensitivity of PM<sub>2.5</sub> source apportionment to temporal resolution in a suburban site of northern France, soumis à Atmospheric Environment

#### PUBLICATIONS IN PREPARATION

- [A3] **R. ROIG RODELAS**, A. CHAKRABORTY, E. PERDRIX, B. HERBIN, E. TISON, V. RIFFAULT, Real-time assessment of wintertime organic aerosols characteristics and sources at a suburban site in northern France, en preparation

### 2) International conferences

- [B1] **R. ROIG**, E. PERDRIX, L. ALLEMAN, B. MALET, B. HERBIN, V. RIFFAULT, Characterization of secondary inorganic aerosol and their precursor gases at a suburban site in Northern France, **Poster**, European Aerosol Conference, Tours (France), 4-9 septembre 2016.
- [B2] **R. ROIG**, E. PERDRIX, E. TISON, B. MALET, B. HERBIN, V. RIFFAULT, Identification of main sources of PM<sub>2.5</sub> during winter at a suburban site in Douai, Northern France, **Poster**, European Aerosol Conference, Tours (France), 4-9 septembre 2016.
- [B3] **R. ROIG**, E. PERDRIX, B. HERBIN, V. RIFFAULT, Evaluation of the gas-aerosol partitioning of Secondary Inorganic Aerosols at an urban site in Northern France, **Communication orale**, International Conference on Aerosol Cycle, Villeneuve d'Ascq (France), 21-23 mars 2017.
- [B4] **R. ROIG**, E. PERDRIX, B. HERBIN, V. RIFFAULT, *Study of the temporal variability and gas-aerosol partitioning of ammonium nitrate at an urban site in Northern France*, **Communication orale**, RICTA 2017 - 5<sup>th</sup> Iberian Meeting on Aerosol Science and Technology, Barcelone (Espagne), 3-6 juillet 2017.

### 3) National conferences

- [C1] **R. ROIG**, E. PERDRIX, L. ALLEMAN, B. MALET, B. HERBIN, E. TISON, V. RIFFAULT, *Caractérisation et origine des aérosols inorganiques dans un site urbain du nord de la France*, **Communication orale**, 9<sup>èmes</sup> Journées Interdisciplinaires de la Qualité de l'Air, Villeneuve d'Ascq, 2-3 février 2017.

## ANNEX 1: Detection limits for major and trace elements

Table A1 Detection limits for major elements for each batch determined by laboratory and field blank analyses

Method	Element	Laboratory blank DLs (ppb)						Field blank DLs ( $\mu\text{g m}^{-3}$ )					
		Set 1	Set 2	Set 3	Set 4	Set 5	Set 6	Set 1	Set 2	Set 3	Set 4	Set 5	Set 6
DRC	Al 27	0.16	1.01	0.45	0.42	0.22	0.31	0.01	0.05	0.03	0.02	0.11	0.03
	Ca 42	8.26	61.76	26.44	21.35	17.07	27.11	0.12	0.56	0.24	0.19	0.00	0.25
	Ca 44	1.84	17.96	7.66	6.68	3.67	1.70	0.03	0.04	0.08	0.04	0.78	0.02
	Fe 56	0.08	0.74	0.34	0.19	0.19	0.15	0.00	0.04	0.02	0.01	0.06	0.01
	K 39	0.22	1.10	0.14	0.56	0.56	0.91	0.01	0.02	0.00	0.01	0.00	0.01
	Mg 24	0.20	1.34	0.58	0.54	0.26	0.36	0.02	0.10	0.03	0.02	0.17	0.03
	Mg 26	1.10	7.77	3.35	3.84	1.70	2.74	0.00	0.10	0.10	0.08	0.80	0.05
	Na 23	0.19	1.13	0.53	0.35	0.33	0.31	0.01	0.02	0.01	0.00	0.24	0.01
	Si 28	64.70	177.31	24.14	5.22	6.23	11.54	2.62	6.33	1.15	0.10	2.86	0.14
KED	Al-1 27	24.19	13.74	12.57	14.72	6.08	9.16	0.27	0.12	0.23	0.13	0.08	0.08
	Fe-1 57	112.22	59.20	64.40	0.92	0.78	0.82	1.27	0.22	0.99	0.02	0.02	0.01
	K-1 39	16.23	16.93	9.85	10.88	5.44	5.17	0.18	0.06	0.15	0.14	0.09	0.05
	Mg-1 24	10.44	8.12	7.20	7.64	3.29	5.34	0.05	0.05	0.13	0.07	0.05	0.10
	Na-1 23	4.17	3.87	3.60	3.57	1.60	2.61	0.05	0.02	0.07	0.03	0.03	0.02
	Si-1 28	99.78	26.44	37.75	46.64	30.47	20.04	44.82	1.97	1.20	0.71	0.35	0.38

Table A2 Detection limits for trace elements for each batch  
determined by laboratory and field blank analyses

Method	Element	Laboratory blank DLs (ppt)						Field blank DLs (ng m <sup>-3</sup> )					
		Set 1	Set 2	Set 3	Set 4	Set 5	Set 6	Set 1	Set 2	Set 3	Set 4	Set 5	Set 6
DRC	Ag 107	2.11	0.33	0.32	0.89	0.47	0.64	0.03	0.01	0.01	0.01	0.01	0.01
	As 75	2.78	4.58	4.24	3.35	2.46	2.55	0.04	0.12	0.11	0.06	0.15	0.09
	Ba 137	2.61	1.87	3.14	3.75	7.75	4.43	0.16	0.42	0.12	0.03	0.10	0.10
	Be 9	0.51	0.80	0.95	1.49	1.62	0.77	0.01	0.01	0.00	0.01	0.01	0.01
	Bi 209	0.38	1.06	0.64	0.63	1.25	0.85	0.00	0.01	0.01	0.01	0.01	0.01
	Cd 111	0.70	0.59	0.58	1.34	0.71	1.18	0.01	0.03	0.02	0.01	0.01	0.01
	Ce 140	0.07	0.17	0.09	0.27	0.28	0.18	0.01	0.02	0.01	0.01	0.02	0.00
	Co 59	0.22	0.46	0.84	1.24	0.79	1.03	0.03	0.07	0.03	0.01	0.02	0.02
	Cr 52	5.65	3.41	2.71	2.73	1.49	2.54	1.90	3.33	1.16	0.59	0.76	0.40
	Cs 133	0.04	0.07	0.15	0.47	0.41	3.75	0.00	0.00	0.00	0.00	0.00	0.04
	Cu 63	2.66	1.79	2.62	4.74	8.06	7.85	0.70	1.16	0.50	0.37	0.43	0.08
	Fe 56	184.21	45.94	51.35	21.34	25.15	35.96	158.79	45.38	41.23	7.83	7.09	7.55
	Ge 74	0.72	1.07	0.96	2.06	0.60	1.07	0.01	0.01	0.01	0.02	0.00	0.01
	Hg 202	34.06	9.08	8.71	12.05	16.00	19.43	0.44	0.08	0.08	0.10	0.13	0.19
	In 115	0.65	0.56	0.48	0.63	0.65	0.53	0.01	0.01	0.00	0.01	0.01	0.01
	La 139	0.09	0.14	0.07	0.33	0.16	0.17	0.00	0.01	0.01	0.00	0.00	0.00
	Li 7	0.34	0.59	0.88	1.41	1.06	1.34	0.03	0.03	0.01	0.01	0.01	0.01
	Mn 55	1.41	1.33	1.54	1.54	1.05	1.08	3.25	2.38	2.61	0.57	0.58	0.30
	Mo 98	1.90	1.71	1.30	2.52	1.40	2.31	0.49	0.17	0.23	0.17	0.22	0.09
	Ni 60	53.10	2.76	1.91	2.07	2.83	2.12	0.69	1.04	0.86	0.44	0.25	0.25
	Pb 208	3.29	1.59	1.33	3.70	1.04	2.53	0.27	0.40	0.17	0.08	0.05	0.15
	Pd 105	1.05	0.48	0.82	1.78	14.44	3.26	0.02	0.01	0.01	0.02	0.12	0.03
	Pd 106	0.21	1.07	0.39	1.74	13.35	1.42	0.07	0.01	0.01	0.01	0.11	0.01
	Pd 108	0.27	0.71	0.48	1.34	12.47	1.74	0.03	0.01	0.01	0.01	0.10	0.02
	Pt 196	0.65	0.44	0.72	0.68	1.19	1.54	0.01	0.01	0.01	0.01	0.01	0.01
	Pt 195	0.48	0.83	1.18	0.97	0.50	1.16	0.01	0.01	0.01	0.01	0.00	0.01
	Pt 194	1.05	0.71	0.53	1.11	0.47	0.85	0.01	0.01	0.01	0.01	0.01	0.01
	Rb 87	1.36	0.92	1.07	2.09	1.12	1.00	0.03	0.05	0.01	0.02	0.01	0.02
	Rb 85	1.04	0.84	0.72	1.46	0.87	1.14	0.04	0.05	0.02	0.01	0.02	0.02
	Sb 121	20.90	0.99	0.72	1.11	1.99	1.11	0.27	0.07	0.09	0.01	0.08	0.03
	Se 78	11.94	9.43	12.53	13.97	8.26	14.73	0.25	0.13	0.11	0.12	0.14	0.14
	Sn 120	23.29	371.99	255.37	3.72	3.12	1.22	32.24	21.42	21.52	3.21	20.02	12.22
	Sr 88	1.80	0.75	4.34	1.50	1.51	1.01	0.07	0.24	0.25	0.02	0.04	0.09
	Th 232	0.26	3.04	1.75	50.98	8.86	1.19	0.00	0.03	0.02	0.44	0.10	0.01
	Ti 47	57.30	41.61	28.54	19.46	65.61	57.19	27.95	9.54	10.30	3.88	4.76	3.04
	Tl 205	0.31	0.55	0.19	0.92	0.82	0.84	0.00	0.01	0.00	0.01	0.01	0.01
	U 238	0.06	0.25	0.00	0.25	0.30	0.19	0.01	0.00	0.00	0.00	0.00	0.00
	V 51	0.87	1.09	0.65	4.83	1.83	2.84	0.23	0.06	0.10	0.04	0.02	0.07
	Zn 64	186.58	195.69	20.47	47.21	86.05	51.39	5.29	18.99	4.13	2.69	2.89	0.58
	Zn 66	194.44	199.20	23.77	41.57	91.57	56.32	4.45	19.23	4.18	2.63	2.92	0.64
KED	Cr-1 52	11.89	10.88	5.92	22.62	7.24	13.85	3.43	9.42	4.40	0.56	5.32	0.43
	Fe-1 57	269.78	174.16	183.88	168.38	148.42	251.01	13.30	79.02	35.07	6.57	7.34	10.33
	Sc-1 45	1.53	5.82	3.66	18.52	8.71	6.19	0.05	0.00	0.03	0.17	0.26	0.06
	V-1 51	0.76	0.77	1.72	1.51	1.58	1.54	0.14	0.18	0.11	0.08	0.05	0.01

## **ANNEX 2: Supplementary material for Article 1**

Characterization and variability of inorganic aerosols and their gaseous precursors at a suburban site in northern France over one year (2015-2016)

Roig, Roger<sup>1</sup>, Perdrix, Esperanza<sup>1</sup>, Herbin, Benoît<sup>1</sup>, Riffault, Véronique<sup>1</sup>

<sup>1</sup> IMT Lille Douai, Univ. Lille, SAGE - Département Sciences de l'Atmosphère et Génie de l'Environnement, F-59000 Lille, France

Corresponding author: Esperanza Perdrix ([esperanza.perdrix@imt-lille-douai.fr](mailto:esperanza.perdrix@imt-lille-douai.fr))

**Section 1. Quality Assurance/ Quality Control (QA/QC)**

**Section 2. Exceedance episodes**

**Section 3. Supplementary figures (Figures S1.1 – S1.10)**

**Section 4. Supplementary tables (Tables S1.1 – S1.4)**



## 1. Quality Assurance/ Quality Control (QA/QC)

### 1.1. MARGA limits of detection, uncertainties and data validation

The detection limits (DLs) of the species analyzed by the MARGA were calculated based on repeated analyses (n=10) of an analytical blank (ultrapure (UP) water, 18 MΩ), which was manually injected into the ion chromatograph. The DL for every species was determined by multiplying the standard deviation of the repeated analyses by 3 (3σ) and are shown in Table P1.2. They were in the same range as the DLs found in previous studies (Makkonen et al., 2012; Rumsey et al., 2014; Twigg et al., 2015). However it should be borne in mind that this methodology (UP water manual injection) just concerned the analytical part of the MARGA and not the entire instrument. The blank analyses performed by manually injecting UP water into the ion chromatograph of the MARGA, showed low values and were therefore not subtracted from our measurements. Even the blank values for nitric acid were satisfactory (0.1 μg m<sup>-3</sup>) with this method, although the actual blank (resulting from the whole system not only from the chromatograph) was possibly in the range of nitric acid gas concentrations, as discussed in section 3.3.3, and could therefore partly explain the erroneous measurements for HNO<sub>3</sub>.

Regarding the uncertainty calculations, the equation below, derived from Gianini et al. (2012), was slightly modified to include two additional sources of relative uncertainty: the volume and the loss in the sampling line.

$$u_{ij} = \sqrt{\underbrace{(DL_j)^2}_{\text{Detection limit}} + \underbrace{(CV_j x_{ij})^2}_{\text{Repeatability}} + \underbrace{(u_{r,vol} x_{ij})^2}_{\text{Volume}} + \underbrace{(u_{r,loss} x_{ij})^2}_{\text{Loss}} + \underbrace{(a x_{ij})^2}_{\text{Additional unc.}}}$$

The uncertainty  $u_{ij}$  refers to the uncertainty of species  $j$  in sample  $i$ , linked to the concentration  $x_{ij}$  of species  $j$  in sample  $i$ . The  $DL_j$  is the detection limit of the compound  $j$  (in μg m<sup>-3</sup>) and is calculated as previously explained. The  $CV_j$  is the coefficient of variation of the compound  $j$  (relative uncertainty), and has been calculated as the standard deviation of repeated analyses (n=10) of certified multi-ion standards divided by the average value obtained in the analyses. More specifically, we used the Anion (respectively Cation) Calibration Standard for MARGA (Sigma Aldrich) with 0.25 mg L<sup>-1</sup> of Br<sup>-</sup>, Cl<sup>-</sup>, SO<sub>4</sub><sup>2-</sup>, NO<sub>3</sub><sup>-</sup>, and NO<sub>2</sub><sup>-</sup> (respectively Li<sup>+</sup>, K<sup>+</sup>, Mg<sup>2+</sup>, Ca<sup>2+</sup>, Na<sup>+</sup> and NH<sub>4</sub><sup>+</sup>). The relative uncertainty due to

losses in the sampling line ( $u_{r,loss}$ ) was calculated with the Particle Loss Calculator extension for Igor Pro (von der Weiden et al., 2009)\*\*, considering a tube length of 2.5 m, a tube diameter of ½ inch and a flow rate of  $1 \text{ m}^3 \text{ h}^{-1}$ . It was found to be less than 5% whatever the particle diameter between 10 nm and 5  $\mu\text{m}$ , and therefore was set to be 5%. The sampling head was regularly cleaned (once every two weeks), the PE inlet tubing remained the same throughout the whole campaign. The relative uncertainty of the sampling volume ( $u_{r,vol}$ ) was determined to be 2% from the allowed deviation of the sampling flow of the MARGA ( $1.00 \pm 0.02 \text{ m}^3 \text{ h}^{-1}$ ). In addition,  $a$  is a factor that equals 0.03 (relative uncertainty) which accounts for additional sources of uncertainties.”

The data obtained with the MARGA were validated according to a LiBr internal standard which was injected together with the sample every single hour. When the concentrations were outside of the normal range, that is to say  $320 \pm 10 \mu\text{g L}^{-1}$  for  $\text{Li}^+$  and  $3680 \pm 100 \mu\text{g L}^{-1}$  for  $\text{Br}^-$ , the measurements were considered as invalid. In addition, an integrated error code also invalidated any value obtained when the instrument did not work properly. Every single chromatogram ( $n = 15460$  in total) was manually checked for any error of automatic peak integration by the MARGA software. For instance, when concentrations of some ions were close to the detection limit (DL), the software often did not take them into account, particularly for  $\text{Na}^+$ ,  $\text{Mg}^{2+}$  and  $\text{Ca}^{2+}$ . This was corrected by the modification of the peak search smoothing parameter in the MargaTool v.2.1 reprocessing software (Metrohm).

Minor ions, especially  $\text{Cl}^-$ ,  $\text{K}^+$ ,  $\text{Mg}^{2+}$  and  $\text{Ca}^{2+}$ , often presented values below the DL for various reasons. First,  $\text{K}^+$ ,  $\text{Mg}^{2+}$  and  $\text{Ca}^{2+}$  frequently presented low concentrations at our site. For  $\text{Mg}^{2+}$  this was observed over the whole year. For  $\text{K}^+$  concentrations below the DL were less frequent in winter and for  $\text{Ca}^{2+}$  in summer and autumn. Second, the determination of  $\text{Na}^+$  was hindered by the location of its peak close to those of  $\text{Li}^+$  and  $\text{NH}_4^+$ . This sometimes caused very small peaks of  $\text{Na}^+$  to merge with those of  $\text{NH}_4^+$  and to easily be confused by the software, mostly during summer. Finally,  $\text{Cl}^-$  was the first to elute in the anion chromatogram (at around 3.5 minutes when the anion chromatographic column was new), and its retention time constantly shifted to shorter retention times with column aging. Thus when the anion column was getting old, chloride eluted too close to the injection peak and was easily confused, often impeding its determination.

## 1.2. Nitric acid measurement artefact

The measurement of  $\text{HNO}_3$  could not be performed correctly by the instrument as already reported in other studies using a MARGA (Makkonen et al., 2012, 2014; Stieger et al., 2017). This has been attributed to several artefacts of measurement caused by: (i) the sticky nature of this gas, which gets easily adsorbed in the inlet sampling head and/or along the sampling line before the analysis; (ii) the interference from the cation eluent (made of aqueous nitric acid) which increases the nitric acid blanks in the chromatographic analysis; (iii) the overestimation of nocturnal  $\text{HNO}_3$  due to the interference with  $\text{N}_2\text{O}_5$  which has been estimated on average to be 17% by Phillips et al. (2013). Hence the  $\text{HNO}_3$  measurements have not been included in the article (except in Figure 8 where the disagreement with modeled concentrations is reported) and are not discussed further.

## 1.3. Comparison with collocated instruments

The quality of the MARGA data was assessed by comparing it to other collocated instruments for shorter periods of time: a UV fluorescence  $\text{SO}_2$  monitor AF22MF (15-min time resolution) (Environnement SA), one PICARRO G2103  $\text{NH}_3$  monitor (Picarro) based on cavity ring down spectroscopy (15-min time resolution), and a High Resolution Time-of-Flight Aerosol Mass Spectrometer (HR-ToF-AMS) (5-min time resolution) for the non-refractory submicron particulate species  $\text{NO}_3^-$ ,  $\text{NH}_4^+$ ,  $\text{SO}_4^{2-}$ , and  $\text{Cl}^-$ . In particular, chloride cannot be directly compared to the MARGA  $\text{Cl}^-$  which also includes refractory chloride coming from sea salt influence. All measurements were averaged to 1-hour values in order to be compared with the hourly data of the MARGA, except for the  $\text{PM}_{2.5}$  concentrations which were averaged over 2 hours.

The sum of water-soluble ions (WSI) measured by the MARGA was compared against the total  $\text{PM}_{2.5}$  mass measured by the BAM-1020 (Figure Q1a) for the whole database (August 2015 to July 2016) and a good correlation was obtained ( $r^2 = 0.84$ ). The correlation coefficient means that 84% of the variability of the hourly mass concentration of  $\text{PM}_{2.5}$  is statistically linked to the variability of the measured WSI. The slope and intercept (1.12 and  $5.41 \mu\text{g m}^{-3}$ , respectively) indicate that most of the  $\text{PM}_{2.5}$  consisted primarily of WSI, as has also been observed at other sites over northwestern Europe (Putaud et al., 2010). When the comparison was performed using 24-h averages, the correlation improved notably ( $r^2 = 0.90$ ), although the slope and intercept values (1.13 and 5.24) were similar. The improvement of the

correlation might be explained by the reduction of the uncertainty of hourly data and of the influence of outliers.

A comparison between one PICARRO NH<sub>3</sub> monitor and the MARGA NH<sub>3</sub> was performed from 7 to 19 August 2015 (Figure Q1b). The results were satisfactory with  $r^2 = 0.88$ , although the MARGA concentrations were slightly below (slope = 1.11). An underestimation of NH<sub>3</sub> by the MARGA has been reported elsewhere (Rumsey et al., 2014) and was attributed to the sticky nature of NH<sub>3</sub>, which can adsorb onto active sites of the inlet and sampling line.

The MARGA SO<sub>2</sub> measurements were compared to those of a SO<sub>2</sub> AF22MF monitor from August to December 2015 (Figure Q1c). The correlation was good ( $r^2 = 0.79$ ), although the concentrations of the gas monitor were significantly higher than those of the MARGA. A previous study compared the MARGA SO<sub>2</sub> with a TEI43 SO<sub>2</sub> gas monitor and obtained a better correlation ( $r^2 = 0.89$ ) and a lower slope indicating the concentrations between both instruments were much more similar (Makkonen et al., 2012). Therefore, it is possible that the AF22MF monitor overestimated the concentrations of SO<sub>2</sub>.

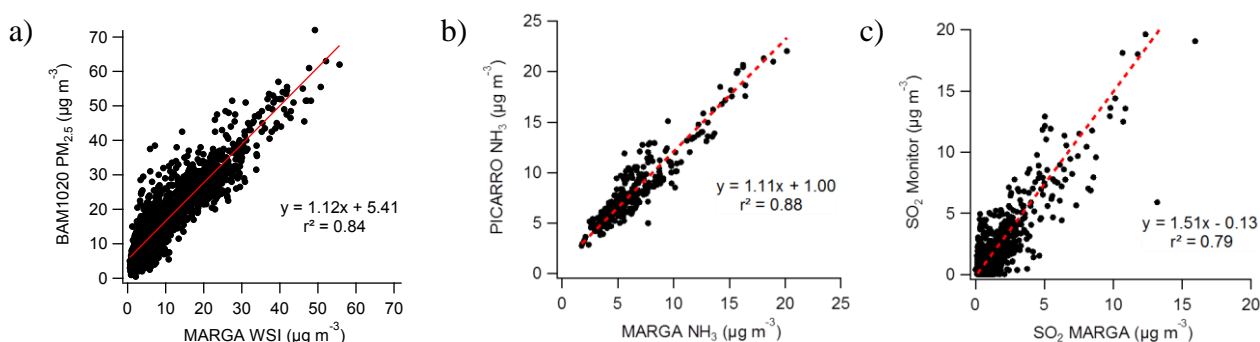


Figure Q1 MARGA comparison with other instrumentation: (a) BAM-1020; (b) PICARRO NH<sub>3</sub> and SO<sub>2</sub> AF22MF

Additionally, a HR-ToF-AMS (DeCarlo et al., 2006) was deployed during one month and a half from February to March 2016. Due to the limitations of its inlet system, the cut-off size of the AMS was 1 µm, and lower values were expected when compared to the MARGA (cutoff of 2.5 µm). Relative ionization efficiency (RIE) values were determined to be 4 and 1.1 for NH<sub>4</sub><sup>+</sup> and SO<sub>4</sub><sup>2-</sup>, respectively, using NH<sub>4</sub>NO<sub>3</sub> and (NH<sub>4</sub>)<sub>2</sub>SO<sub>4</sub> aqueous solutions at 10<sup>-2</sup> mol L<sup>-1</sup>. In addition, all the concentrations of the AMS were corrected by using the algorithm proposed by (Middlebrook et al., 2012) which recalculates the concentrations by taking into account the NO<sub>3</sub><sup>-</sup> fraction of the aerosol. More details can be found in (Crenn et al., 2017). The hourly-averaged AMS measurements were compared to those of the MARGA (Figure Q2

Q2) and very good correlations were found, with  $r^2$  values of 0.96, 0.94 and 0.92 for  $\text{NO}_3^-$ ,  $\text{NH}_4^+$  and  $\text{SO}_4^{2-}$ , respectively. The concentrations of the AMS were lower than those of the MARGA, as shown by the slopes (values of 0.68, 0.72 and 0.53 for  $\text{NO}_3^-$ ,  $\text{NH}_4^+$  and  $\text{SO}_4^{2-}$ , respectively). The agreement was better for lower concentrations but increased during the peaks at the end of the field campaign, as can be seen on the time series. When the last period of the campaign (10-16 March) was excluded, the slopes values were 0.79, 0.86 and 0.74 for  $\text{NO}_3^-$ ,  $\text{NH}_4^+$  and  $\text{SO}_4^{2-}$ , respectively. The difference was higher for sulfate, which could be attributed to its RIE or to a higher fraction of sulfate in the 1-2.5  $\mu\text{m}$  size fraction. The comparison with chloride (not shown here) delivered a very weak correlation as expected, because of the different types of chloride measured by each instrument (the MARGA measuring water-soluble chloride whereas the AMS measures non-refractory chloride).

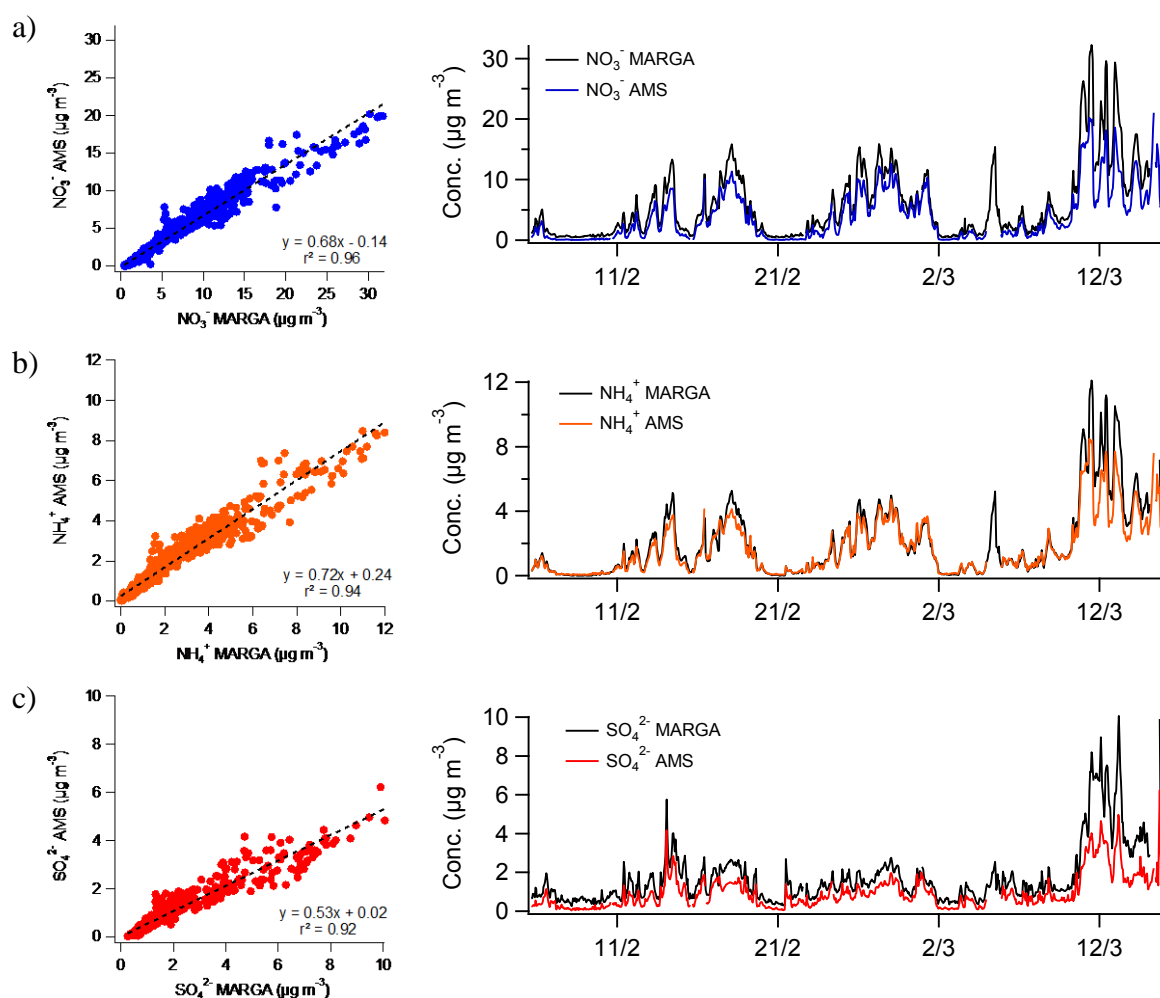


Figure Q2 Correlations and time series of AMS ( $\text{PM}_{1.0}$ ) and MARGA ( $\text{PM}_{2.5}$ ) measurements. The RIE values used for  $\text{NH}_4^+$  and  $\text{SO}_4^{2-}$  were 4 and 1.1, respectively. The AMS concentrations were corrected for the CE using the algorithm of (Middlebrook et al., 2012)

## 2. Exceedance episodes

In the main text of this article, the general characteristics and similarities of the observed exceedance episodes have been given. In this section of the supplementary material we describe each episode with a greater level of detail. At the end of section 3 of this SM, Figure S10 presents the maps of 72-h back trajectories and time profiles of RH, temperature, wind direction and speed, precursor gases ( $\text{NO}_x$ , HONO,  $\text{NH}_3$  and  $\text{SO}_2$ ), total  $\text{PM}_{2.5}$  and major particulate pollutants ( $\text{NO}_3^-$ ,  $\text{NH}_4^+$ ,  $\text{SO}_4^{2-}$ , oxalate, BC, and the sum of minor ions).

The first episode (19-21 January 2016) was characterized by freezing temperatures (average of  $-0.4 \pm 3.0^\circ\text{C}$ ) and relatively high RH (average of  $83.4 \pm 8.3\%$ ) but no precipitations. Winds were slow and from E in the first half of the episode and faster from SSE in the second half, while back-trajectories mainly originated from SE, experiencing a clock-wise recirculation over the north of France (anticyclonic conditions centered over the British Isles and the north of France). In the first part of the episode there was a high contribution of  $\text{Na}^+$  and  $\text{Cl}^-$ , related to the recirculation of the back-trajectories over the North Sea and the English Channel. In addition, high concentrations of  $\text{K}^+$  were observed during the whole episode (mean of  $0.31 \pm 0.16 \mu\text{g m}^{-3}$ ), which, together with high concentrations of BC and weak winds, suggest a significant local contribution of combustion sources, probably biomass burning. Much higher concentrations of  $\text{Cl}^-$  than  $\text{Na}^+$  also suggest that part of  $\text{Cl}^-$  could originate from biomass combustion. In the second half of the episode, lower concentrations of  $\text{K}^+$ , BC and HONO and stronger winds suggest a rather regional contribution.

The second exceedance episode (16-18 February 2016) resembles the first one, presenting low temperatures ( $1.4 \pm 2.8^\circ\text{C}$ ) and high RH ( $84.5 \pm 11.4\%$ ) with no precipitations. In the first day and a half of the episode, calm winds from E were dominating. The back trajectories presented a very clear origin from NE. The concentrations of  $\text{NO}_x$ , HONO and BC were really high during this first period but the concentrations of  $\text{K}^+$  stayed rather low ( $0.05 \pm 0.07 \mu\text{g m}^{-3}$ ), suggesting a strong contribution from local emissions, presumably road transport. The unaccounted  $\text{PM}_{2.5}$  mass was particularly high, suggesting that OM could have contributed notably. During the second day and a half, strong SW winds predominated, whereas back-trajectories originated mainly from the NE and showed some recirculation over central France. Lower concentrations of  $\text{NO}_x$ , HONO and BC and a higher ratio of SIA to  $\text{PM}_{2.5}$  suggest an important regional contribution over that period.

The third episode (10-18 March 2016) showed a greater daily variation in RH ( $75.1 \pm 14.5\%$ ) and temperature ( $6.3 \pm 3.7^\circ\text{C}$ ). Calm NW winds alternated with stronger NE winds, while back-trajectories originated in the E and clearly passed over Belgium and Germany. High concentrations of  $\text{NO}_x$  were observed, with  $\text{NO}_2$  predominating over  $\text{NO}$ , attributed to aged air masses carrying regional combustion emissions. Very high concentrations of  $\text{NH}_3$ , particularly during the second half of the episode, suggest that the contribution from regional agricultural activities (soil amendment) was also very important. A really high contribution of SIA to  $\text{PM}_{2.5}$  mass was observed, with a predominance of ammonium nitrate, suggesting that the contribution of OM was almost insignificant. Similar observations were made in a previous high  $\text{PM}_{2.5}$  episode in March 2015, during which four Aerosol Chemical Speciation Monitors (ACSM) spread over France recorded the same inorganic aerosol chemistry for non-refractory (nr)- $\text{PM}_1$  in all places, highlighting the role of LRT in this episode (Petit et al., 2017b). Hence, this exceedance episode has most likely been caused by regional transport of SIA linked to agricultural fertilization from Belgium, Germany and potentially Central and Eastern Europe. According to the space-based observations of the  $\text{NH}_3$  total column (Fortems-Cheiney et al., 2016) these areas can produce high emissions of ammonia during springtime, which may induce an increase by about 30% in the concentrations of  $\text{PM}_{2.5}$  over Central Europe and in turn impact the north of France through transboundary advection of pollutants.

Finally, the fourth episode (26-29 May 2016) presented higher temperatures ( $17.4 \pm 4.4^\circ\text{C}$ ) and similar RH ( $78.9 \pm 15.5\%$ ). Calm winds fluctuated from NW to NE, although NW winds predominated, whereas back-trajectories were short and originated in Belgium and The Netherlands. The concentrations of  $\text{NO}_x$  were moderately high and decreased in the second half of the episode since it was a weekend. High concentrations of  $\text{NH}_3$  suggest a strong contribution from agricultural activities as for the third episode. The very high SIA-to- $\text{PM}_{2.5}$  ratio with a predominance of ammonium nitrate also points to a low contribution of OM. Similarly to the previous episode, regional transport of SIA seems to be the main responsible.

### 3. Supplementary figures

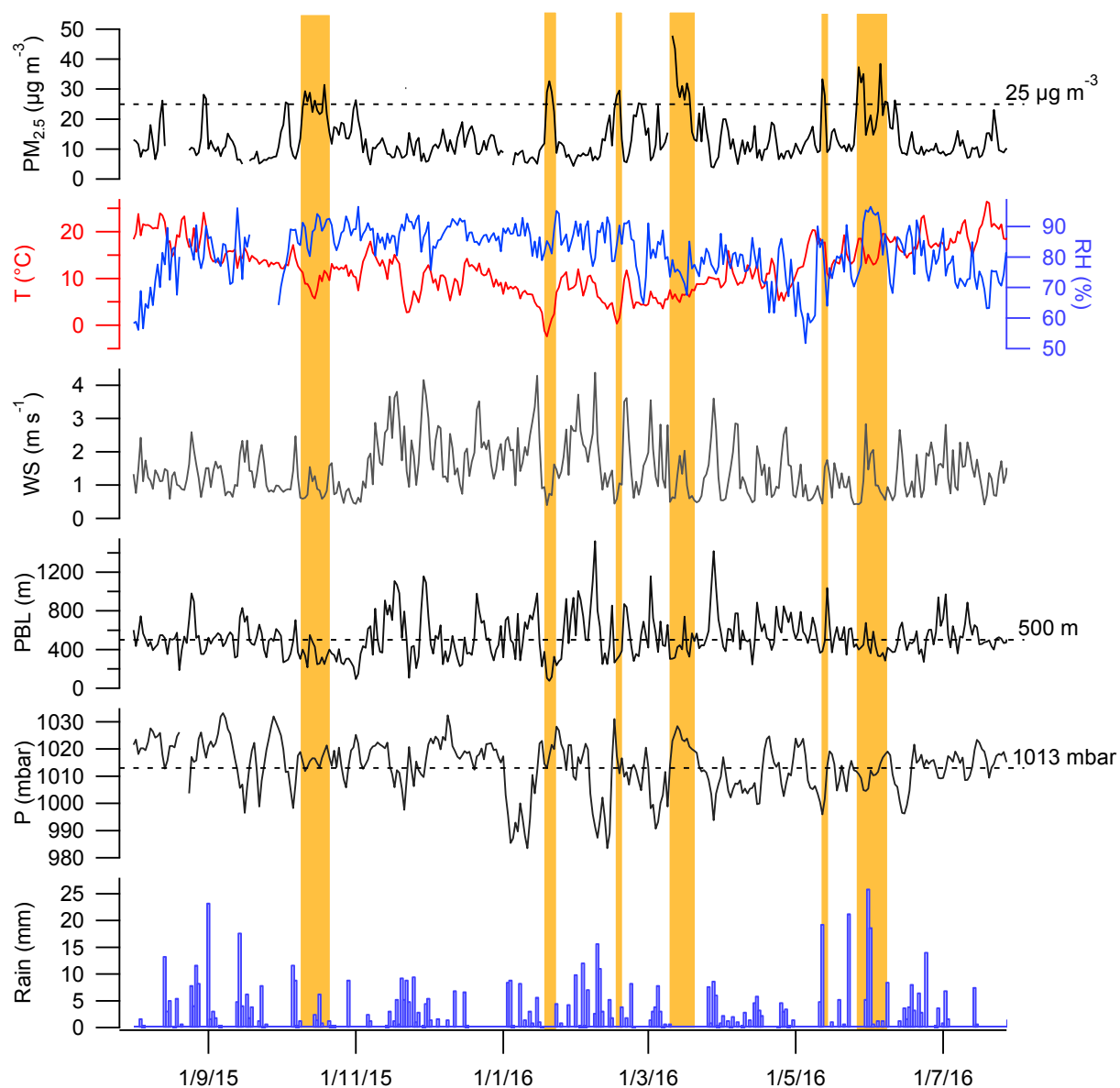


Figure S1.1 Time series of PM<sub>2.5</sub> and the main meteorological parameters with exceedance episodes highlighted in orange



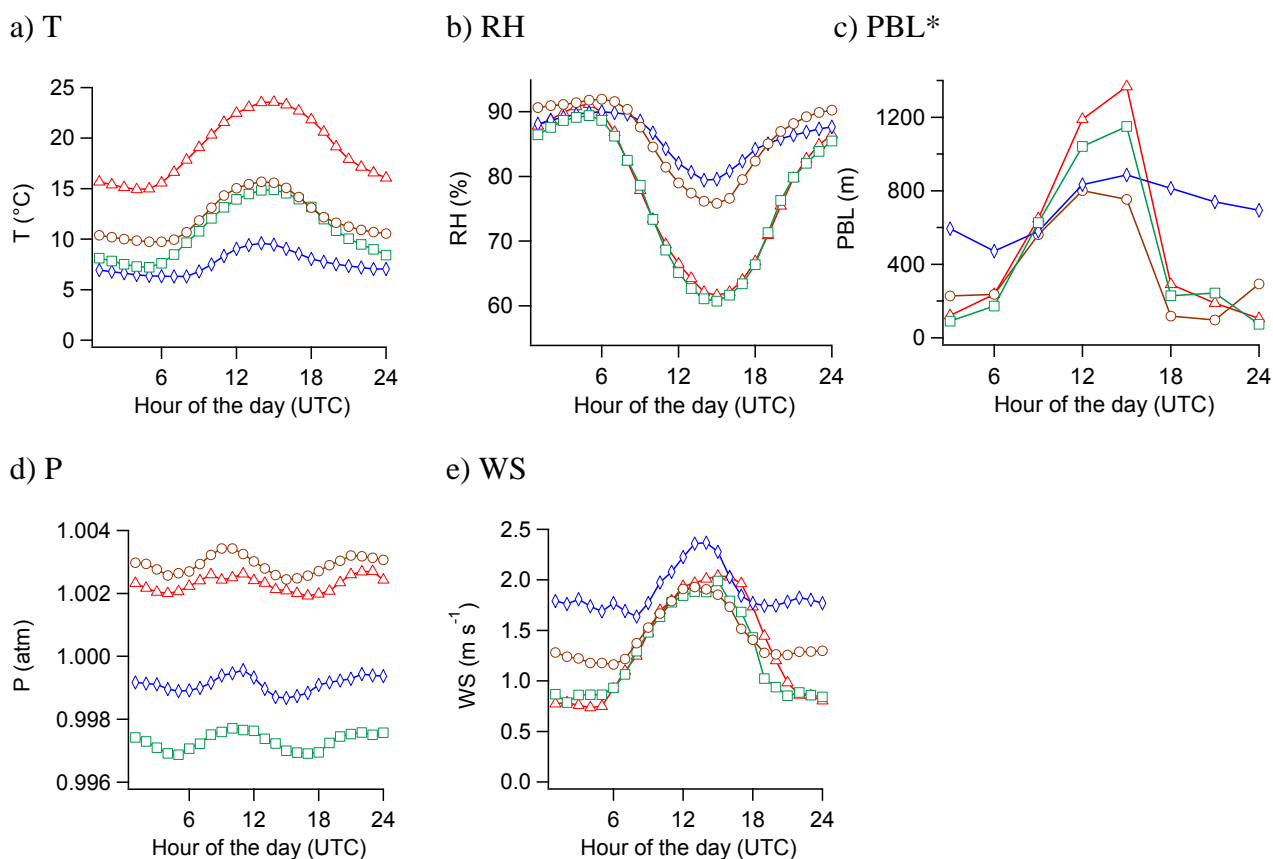


Figure S1.2 Seasonal daily profiles of (a) temperature (T), (b) relative humidity (RH), (c) Planetary Boundary Layer (PBL) height, (d) atmospheric pressure (P) and (e) wind speed (WS).

\* PBL values were obtained from meteorological data from the GDAS (1 deg) archive of the NOAA website.

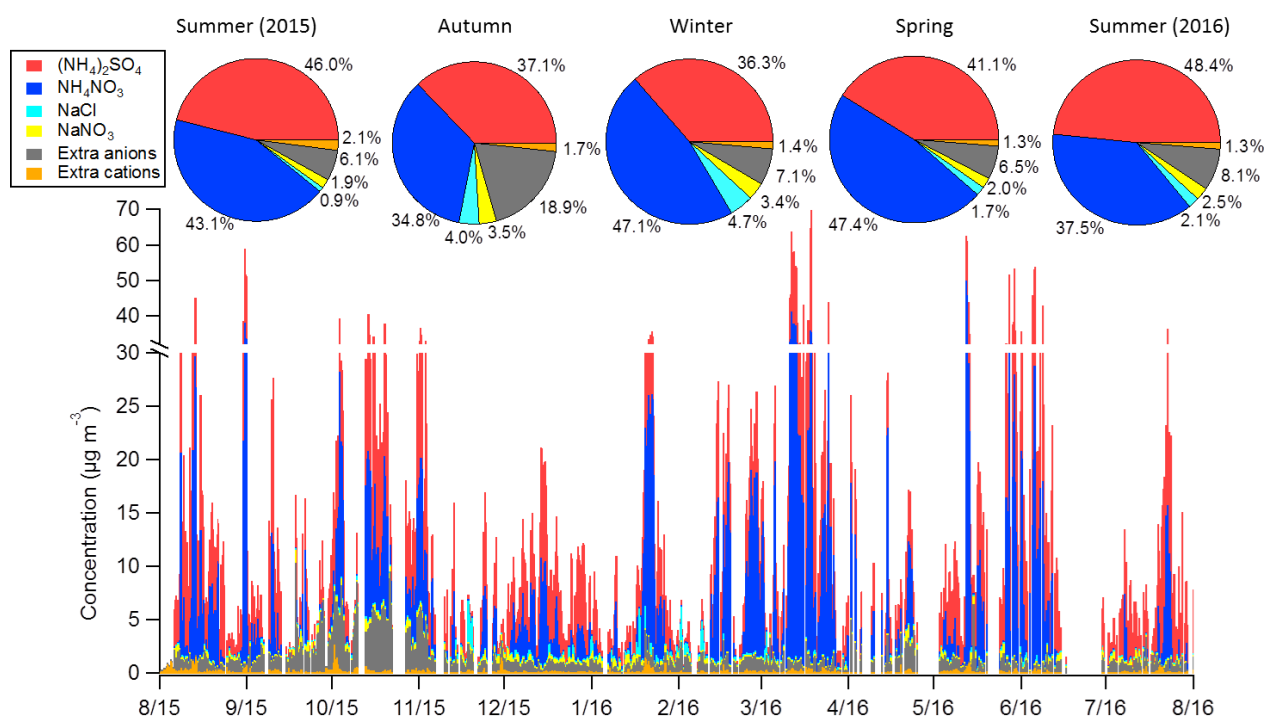
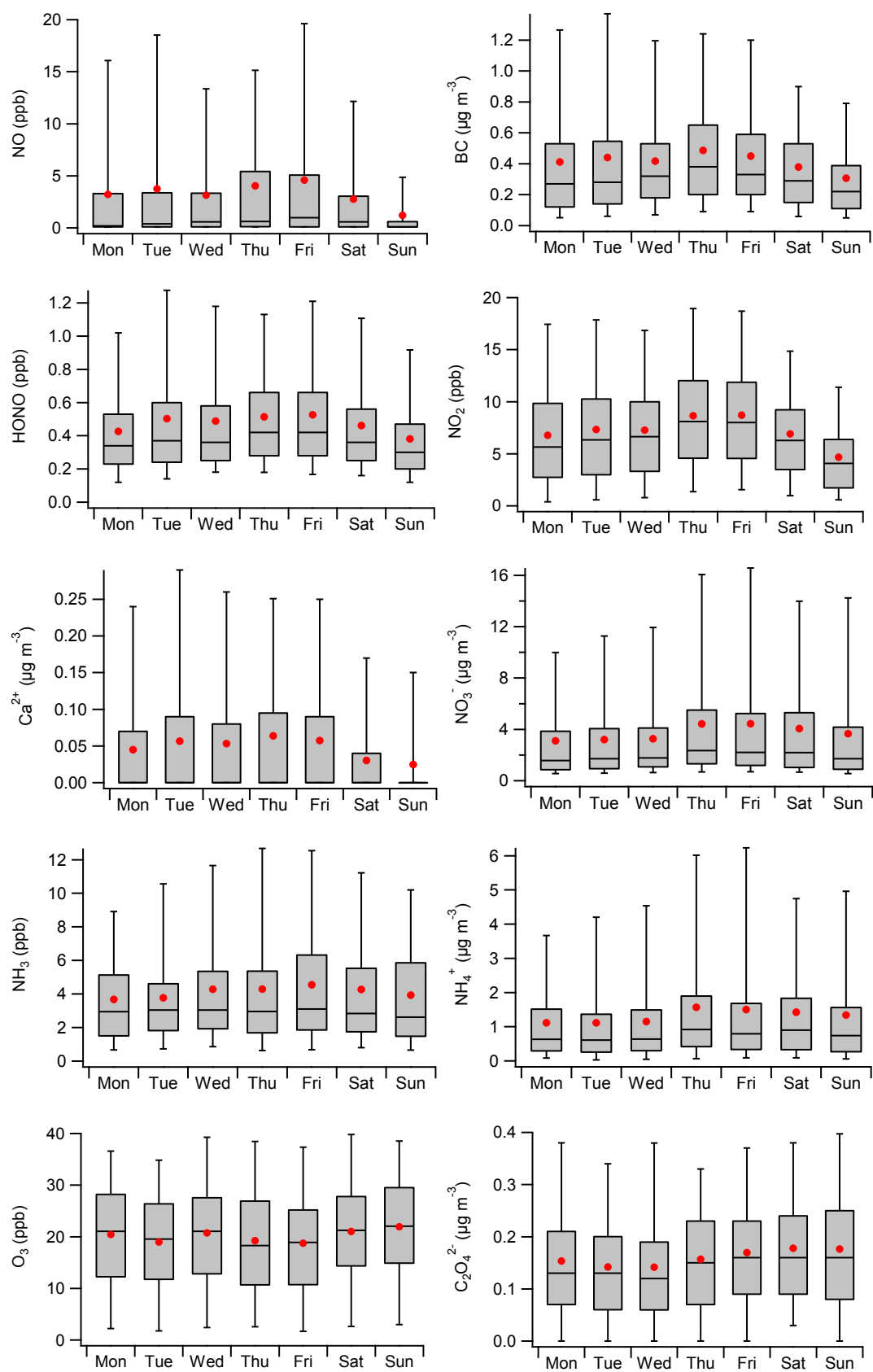


Figure S1.3 Average inorganic speciation for each season (calculated in  $\mu\text{g m}^{-3}$ ). “Extra anions” and “Extra cations” refer to the molar percentages of respectively anions and cations that remain non associated to any of the considered salts.



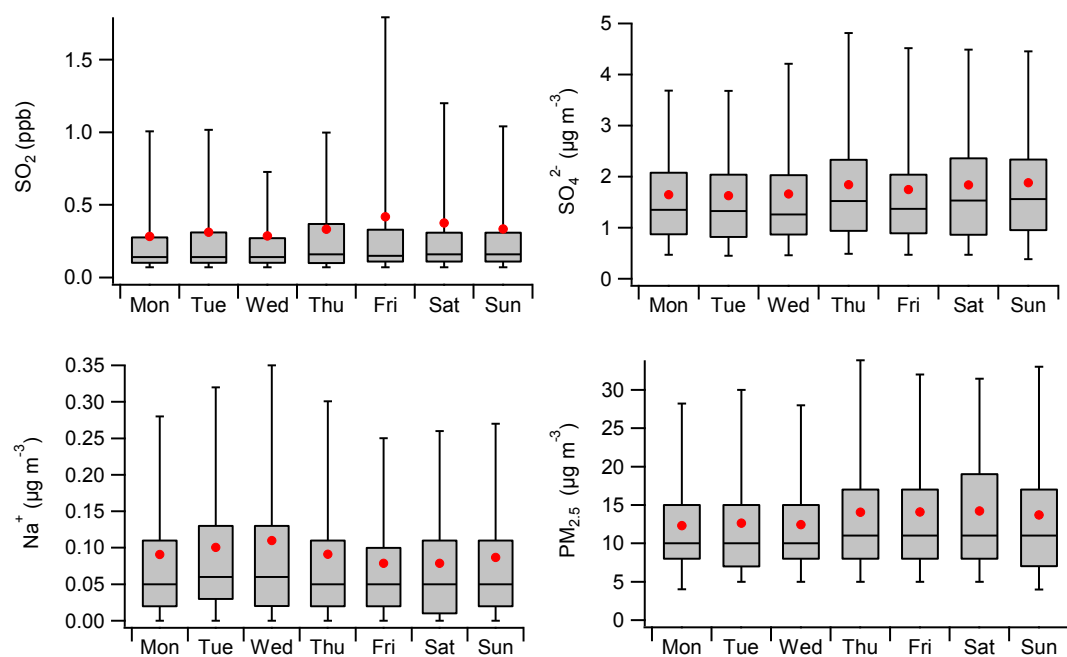


Figure S1.4 Weekly trends for selected gaseous and particulate pollutants. Data bins correspond to the mean (red circle), median (horizontal line), 25<sup>th</sup> and 75<sup>th</sup> percentiles (lower and upper box), and 5<sup>th</sup> and 95<sup>th</sup> percentiles (lower and upper whiskers).

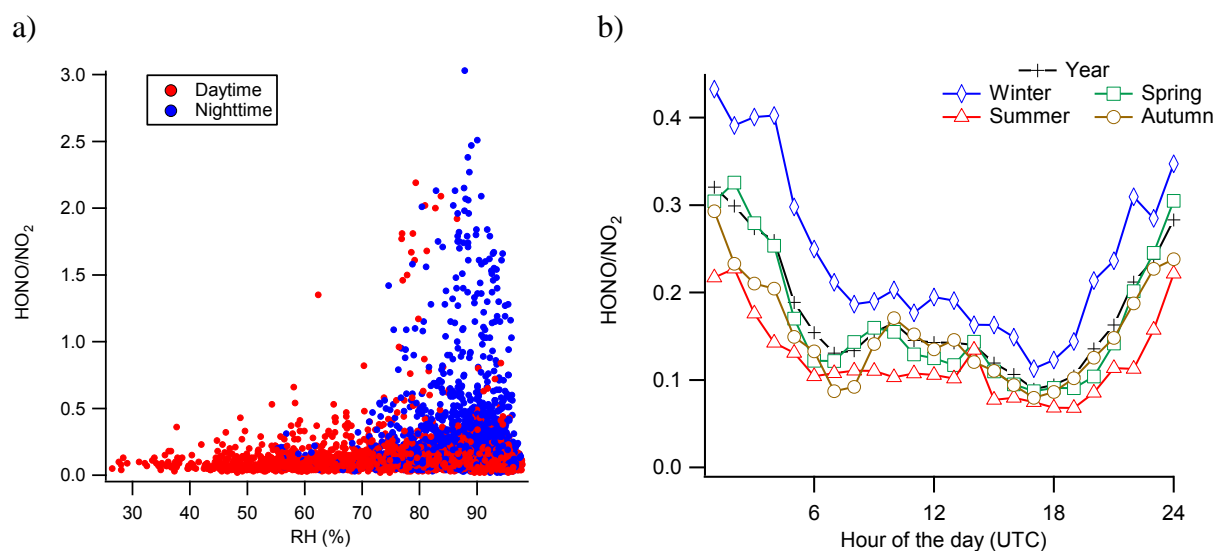


Figure S1.5 (a) Dependence of the  $\text{HONO}/\text{NO}_2$  ratio on RH colored by half-day time step (daytime: red, nighttime: blue) and (b) seasonal daily profiles of the  $\text{HONO}/\text{NO}_2$  ratio

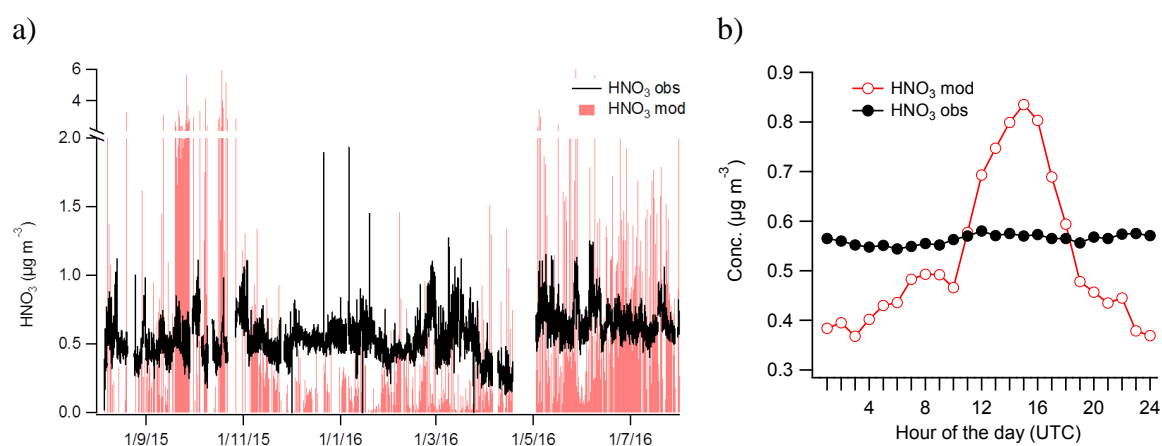
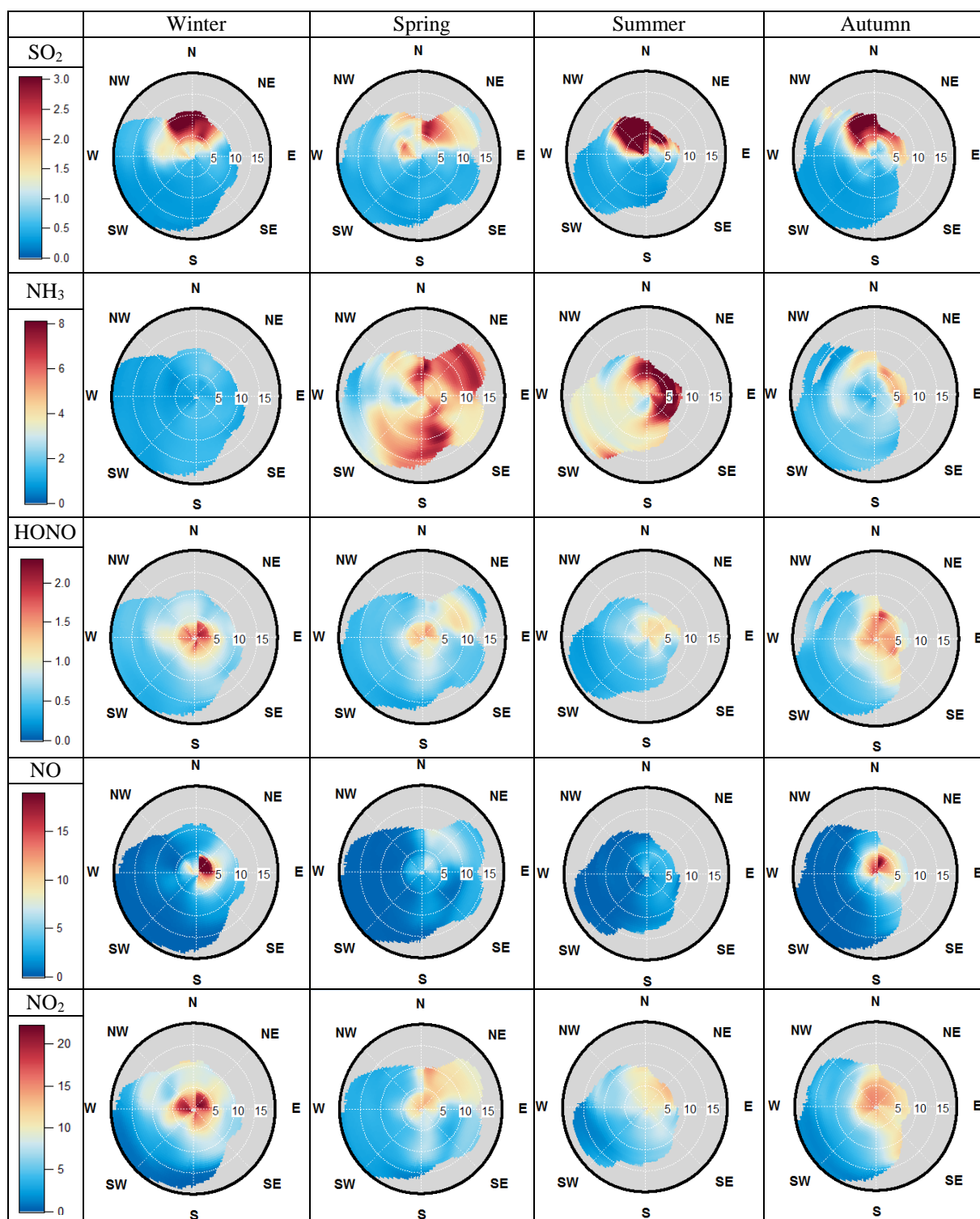
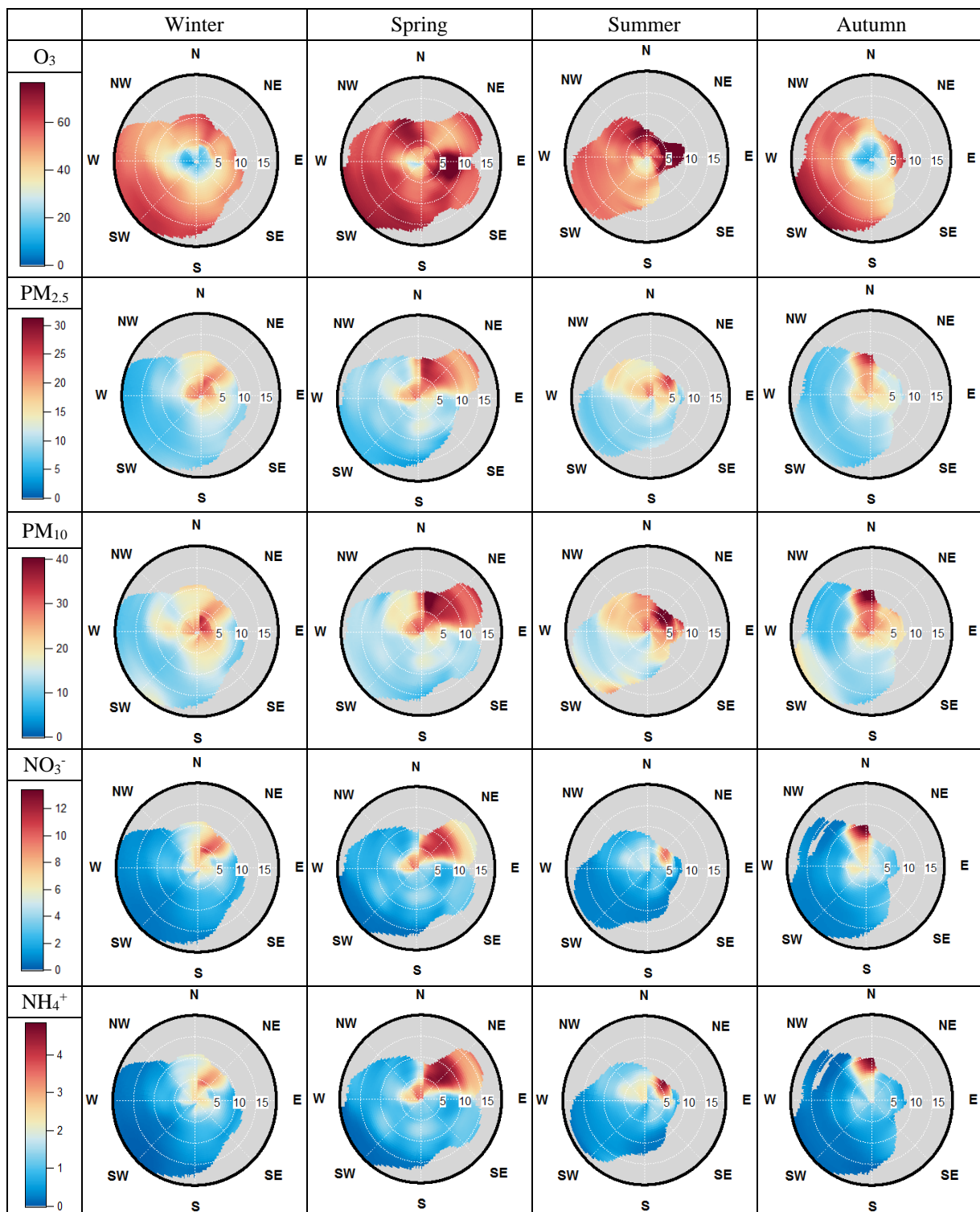
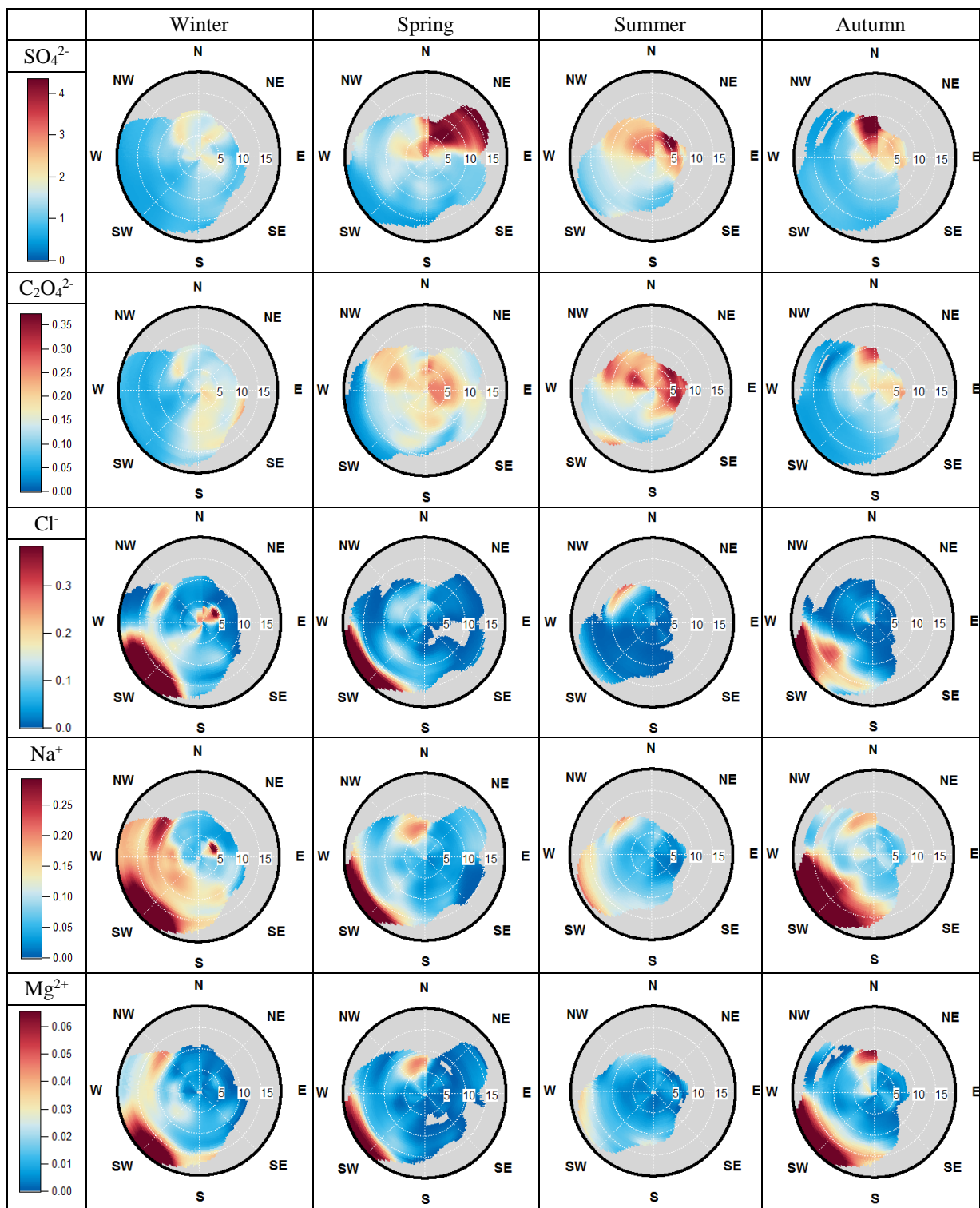


Figure S1.6 (a) Time series and (b) daily profiles of modelled and observed  $\text{HNO}_3$









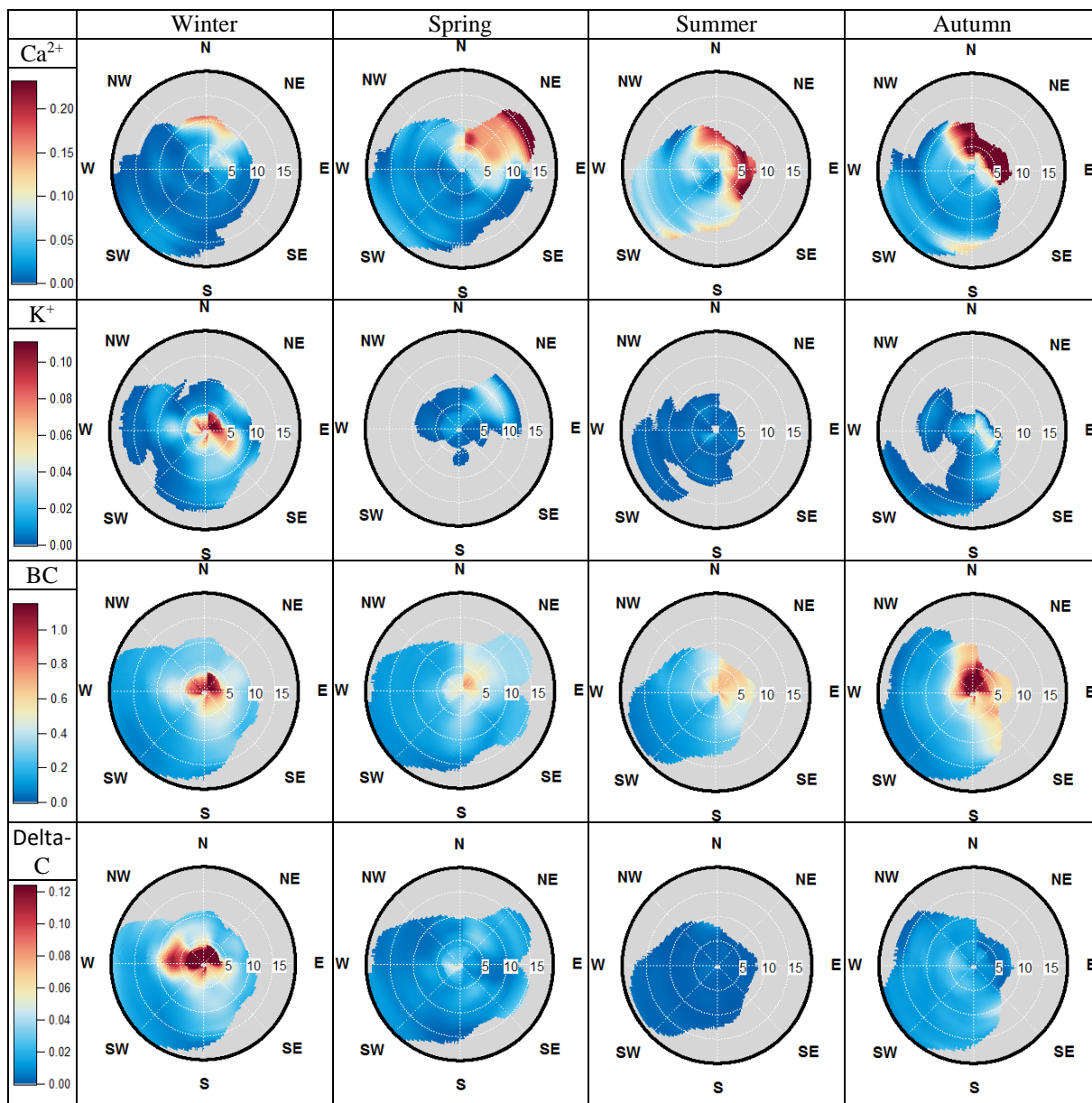


Figure S1.7 Seasonal NWR plots for each gaseous precursor, particulate species and Delta-C (the color scales refer to concentrations in  $\mu\text{g m}^{-3}$ )

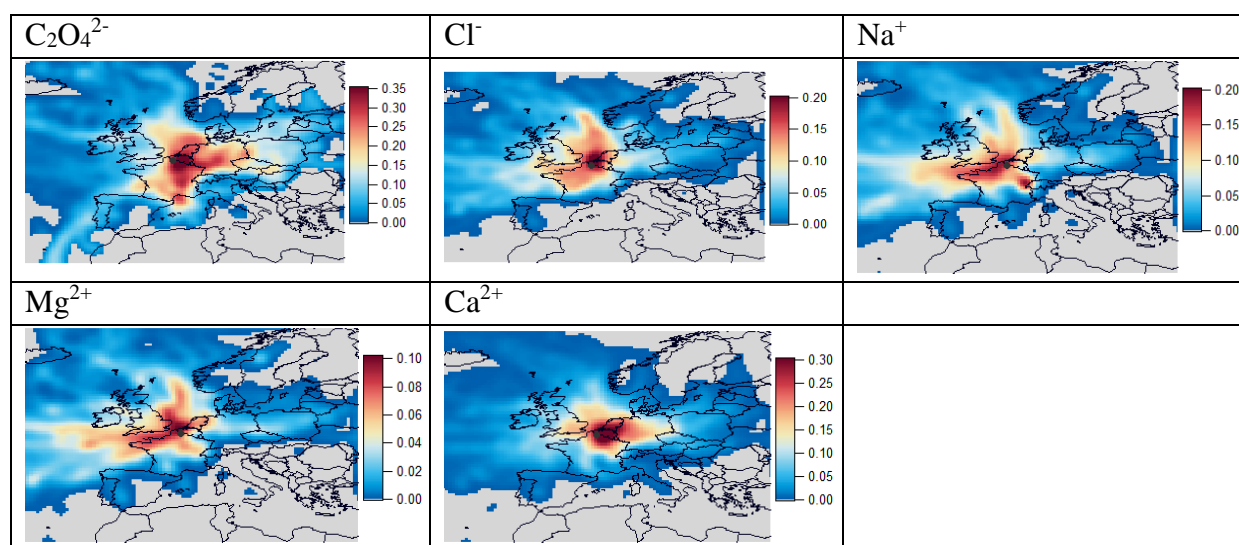


Figure S1.8 PSCF annual maps for selected particulate ions. The selected probability threshold is set at the 75<sup>th</sup> percentile. All used back-trajectories were weighted using a sigmoidal function.

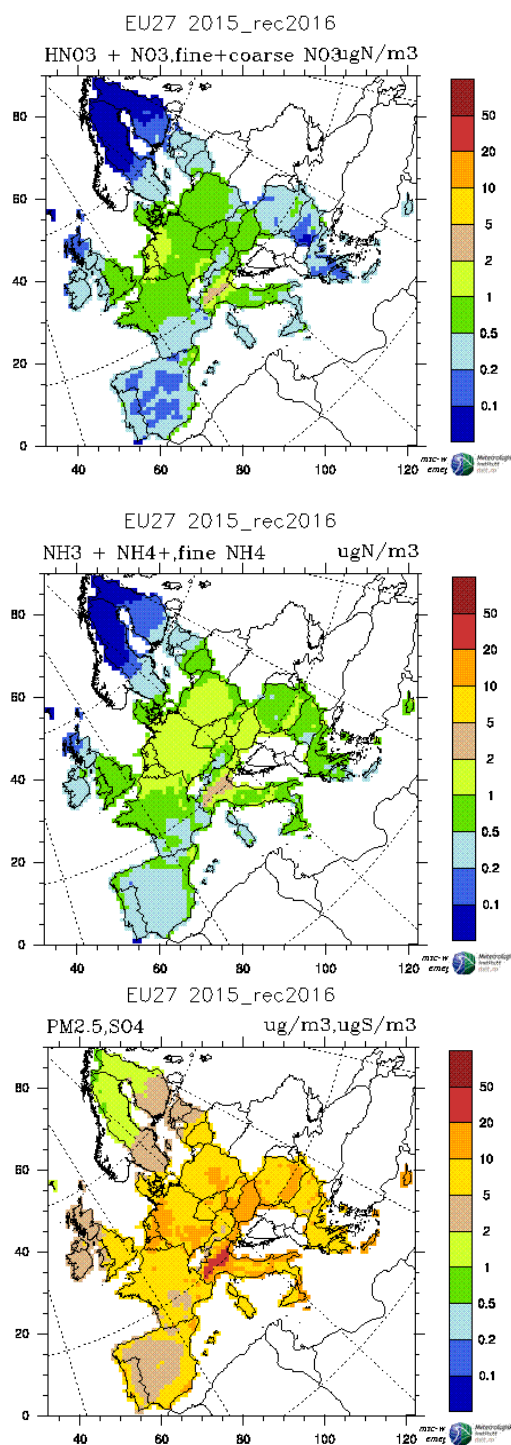
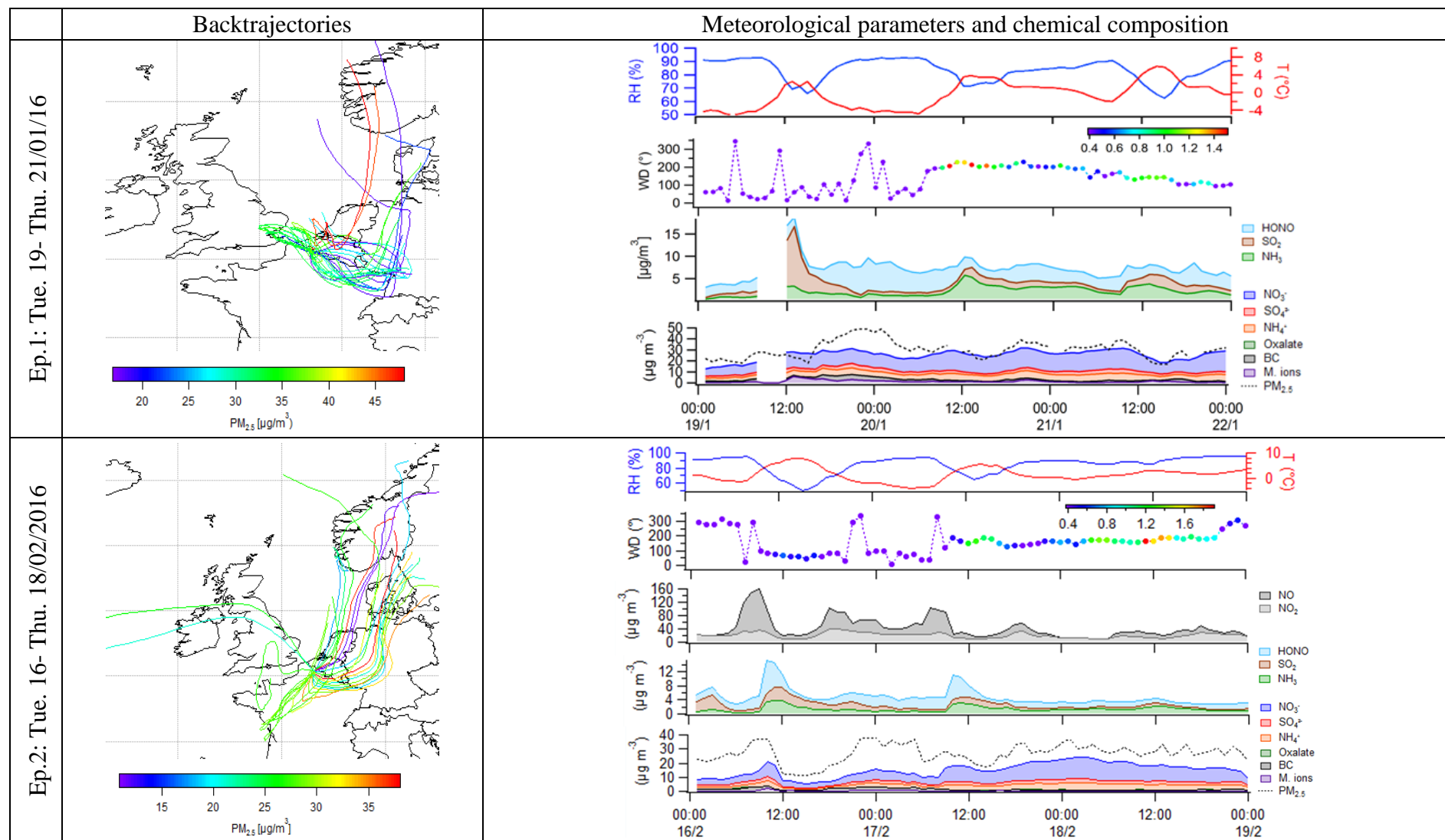


Figure S1.9 Modelled air concentrations for (from top to bottom) fine+coarse total NO<sub>3</sub>, fine total NH<sub>4</sub>, and SO<sub>4</sub><sup>2-</sup> for the year 2015 with emissions of 2014 for the EU-27 (EMEP)



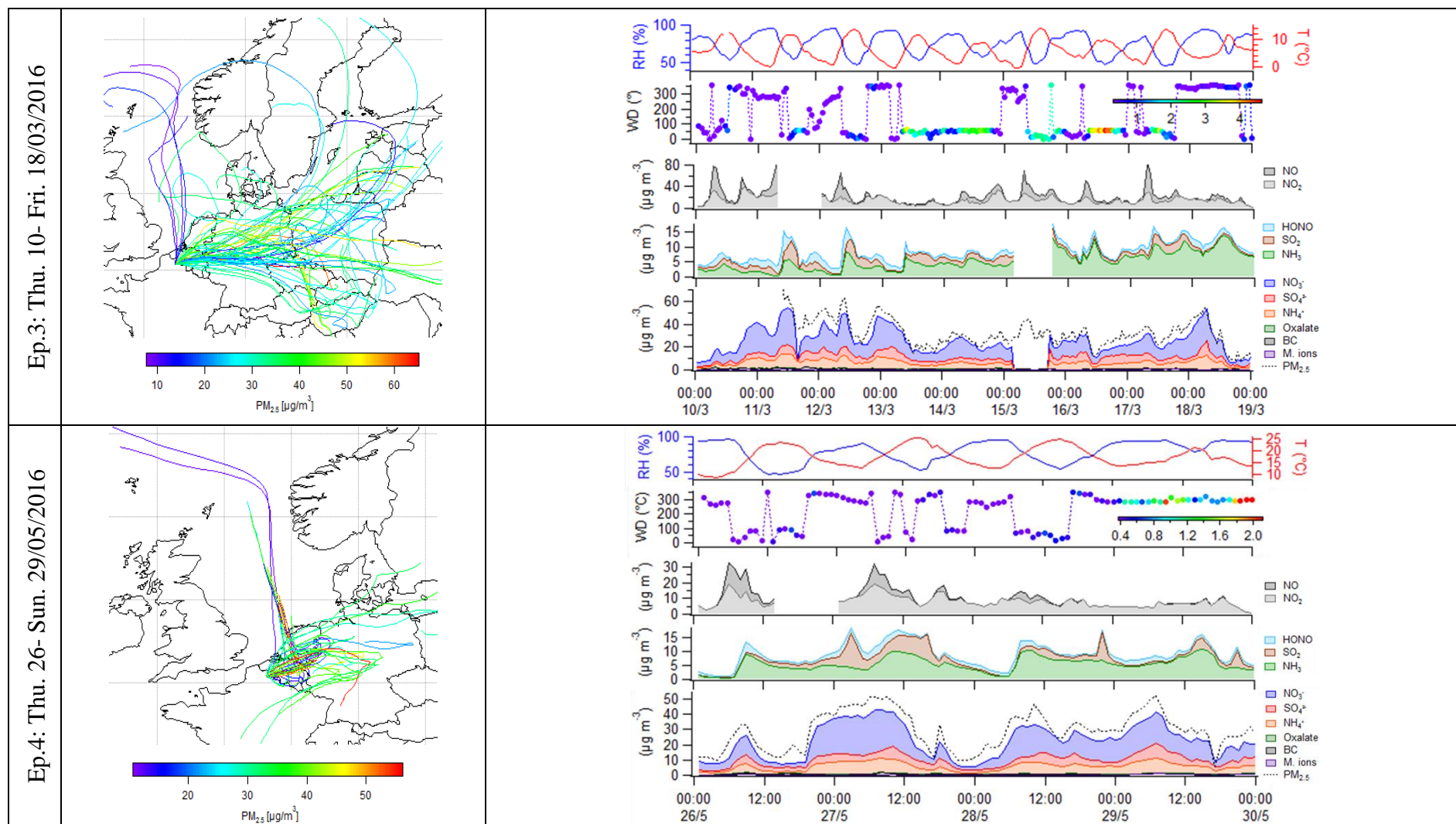


Figure S1.10 (left) 72-hour backtrajectories related to (right, from top to bottom) meteorological parameters (RH, temperature; wind direction colored by wind speed in  $\text{m s}^{-1}$ ), precursor gases,  $\text{PM}_{2.5}$  chemical composition (where “M. ions” is the sum of all the minor ions), and total  $\text{PM}_{2.5}$  for each pollution episode.

## 4. Supplementary tables

Table S1.1 List of studies which have utilized the MARGA from 2007 to 2017

Reference	Location	Site typology	Size fraction	Period
EUROPE				
ten Brink et al. (2007)	Cabauw, NL	Rural	MARGA-Sizer (1, 0.56, 0.32 and 0.18 $\mu\text{m}$ )	Jun.-Aug. '02
Schaap et al. (2011)	Cabauw, NL	Rural	PM <sub>10</sub>	Aug. '07-Aug. '08
Mensah et al. (2012)	Cabauw, NL	Rural	PM <sub>10</sub> & PM <sub>2.5</sub> MARGA-Sizer	Sep. '07-Oct. '08
Schlag et al. (2016)	Cabauw, NL	Rural	PM <sub>10</sub> & PM <sub>2.5</sub>	Jul. '12 –Jun. '13
Phillips et al. (2013)	Kleiner Feldberg, DE	Rural	PM <sub>10</sub>	Aug. '12
Stieger et al. (2017)	Melpitz, DE	Rural	PM <sub>2.5</sub>	Jan. '10-Dec. '14
Makkonen et al. (2012)	Helsinki, FI	Urban	PM <sub>10</sub> & PM <sub>2.5</sub>	Nov. '09-May. '10
Makkonen et al. (2014)	Hyytiälä, FI	Remote	PM <sub>2.5</sub>	Jun. '10-Apr. '11
Twigg et al. (2015)	Auchencorth Moss, UK	Rural	PM <sub>2.5</sub>	Jun. '06-Jan. '13
NORTH AMERICA				
Rumsey et al. (2014)	Research Triangle Park, North Carolina, US	Urban	PM <sub>10</sub>	Sep.-Oct. '10
Allen et al. (2015)	Centreville, Virginia, US	Urban	PM <sub>10</sub>	Jun.-Jul. '13
Rumsey and Walker (2016)	Duke Forest, North Carolina, US	Rural	PM <sub>2.5</sub>	Sep.-Oct. '12
Chen et al. (2017)	Duke Forest, North Carolina, US	Rural	PM <sub>2.5</sub>	Oct.-Nov. '14
ASIA				
Jeon et al. (2011)	Seochogu, KR	Urban	PM <sub>2.5</sub>	May.-Jun. '08
Kim et al. (2012)	Seoul, KR	Urban	PM <sub>2.5</sub>	Jan.-Dec. '10
Shon et al. (2012)				
Shon et al. (2013)				
Song et al. (2017)				
Behera et al. (2013)	Singapore, SG	Urban	PM <sub>2.5</sub>	Sep.-Nov. '11
Khezri et al. (2013)	Singapore, SG	Urban	PM <sub>2.5</sub>	Apr.-Jun. '11
Huang (2014)	Hong Kong, HK	Suburban	PM <sub>2.5</sub>	Mar. '11-Feb. '12
Griffith et al. (2015)	Hong Kong, HK	Suburban	PM <sub>2.5</sub>	Jan. '11-Feb. '13
Zhou et al. (2015)	Hong Kong, HK	Suburban	PM <sub>1</sub>	Apr. '12-Feb. '13
Zhou et al. (2016b)	Hong Kong, HK	Suburban	PM <sub>2.5</sub>	Jan.-Apr. '13
Du et al. (2010)	Shanghai, CN	Urban	PM <sub>2.5</sub>	Jun.-Jul. '09
Li (2010)	Shanghai, CN	Urban	PM <sub>10</sub> & PM <sub>2.5</sub>	May.-Jun. '09
Ye et al. (2011)	Shanghai, CN	Urban	PM <sub>2.5</sub>	Sep. '06
Fu et al. (2012)	Shanghai, CN	Urban	PM <sub>2.5</sub>	Oct.-Nov. '10
Huang et al. (2013)	Shanghai, CN	Urban	PM <sub>2.5</sub>	Oct. '11
Leng et al. (2013)	Shanghai, CN	Urban	PM <sub>2.5</sub>	Sep.10-Aug. '11
Li et al. (2013)	Shanghai, CN	Urban	PM <sub>2.5</sub>	Apr. '10
Wang et al. (2013)	Shanghai, CN	Urban	PM <sub>2.5</sub>	Mar.-May '10
Ye et al. (2013)	Shanghai, CN	Urban	PM <sub>2.5</sub>	Sep. '09
Zhang et al. (2013)	Shanghai, CN	Urban	PM <sub>2.5</sub>	May-Oct. '10
Jansen et al. (2014a)	Shanghai, CN	Urban	PM <sub>1</sub>	Dec. '12
Leng et al. (2014a)	Shanghai, CN	Urban	PM <sub>2.5</sub>	Apr. '12
Leng et al. (2014b)	Shanghai, CN	Urban	PM <sub>2.5</sub>	Nov. '10
Shi et al. (2014)	Shanghai, CN	Urban	PM <sub>1</sub>	Oct.-Nov. '12
Zhou et al. (2014)	Shanghai, CN	Urban	PM <sub>10</sub>	Sep. '09
Han et al. (2015)	Shanghai, CN	Urban	PM <sub>2.5</sub>	Dec. '12
Wang et al. (2015)	Shanghai, CN	Urban	PM <sub>10</sub> & PM <sub>2.5</sub>	Nov. '13-Jan. '14
Yin et al. (2015)	Shanghai, CN	Urban	PM <sub>2.5</sub>	Dec. '12-Jan. '13

Hu et al. (2016)	Shanghai, CN	Urban	PM <sub>2.5</sub>	Dec. '13
Wang et al. (2016b)	Shanghai, CN	Rural	PM <sub>1</sub> & PM <sub>2.5</sub>	Jan.'11-Dec. '13
Zhou et al. (2016a)	Shanghai, CN	Urban	PM <sub>2.5</sub>	Jan.-Dec. '11
Gao et al. (2014)	Beijing, CN	Urban	PM <sub>2.5</sub>	Oct. '11
Gao et al. (2016)	Beijing, CN	Urban	PM <sub>2.5</sub>	Jul.-Aug. '14
Peng et al. (2016)	Beijing, CN	Urban	PM <sub>2.5</sub>	Jul.-Aug. '14
Wen and Chen (2013)	Jinan, CN	Urban	PM <sub>2.5</sub>	Feb. '13
Wang et al. (2014)	Jinan, CN	Urban	PM <sub>1</sub>	Jan. '13
Chen et al. (2016)	Guangzhou, CN	Urban	PM <sub>2.5</sub>	Mar. '12
Tan et al. (2017)	Guangzhou, CN	Suburban	PM <sub>2.5</sub>	Jan.-Mar. '14
Wen et al. (2015)	Yucheng, CN	Urban	PM <sub>2.5</sub>	Jun. '13
Yao et al. (2016)	Yucheng, CN	Urban	PM <sub>2.5</sub>	Jun.-Jul. '13 ; Jun.-Jul. '14
Fan et al. (2014)	Lanzhou, CN	Urban	PM <sub>10</sub>	Apr.-May. '11
Wang et al. (2016a)	Dian Shan Lake, CN	Urban	PM <sub>2.5</sub>	Jul.-Aug. '13
Jansen et al. (2014b)	Hangzhou, CN	Urban	PM <sub>2.5</sub>	Apr.-May. '12
Kong et al. (2014)	Shanghai, CN	Urban	PM <sub>10</sub> & PM <sub>2.5</sub>	May-Jun. '09 Jul.-Oct. '09 Feb.-Oct. '10
	Hangzhou, CN		PM <sub>2.5</sub>	Jul. '11
	Guangzhou, CN		PM <sub>2.5</sub>	Aug. '10

Table S1.2 Monthly statistical summary of the main meteorological parameters between August 2015 and July 2016

Month	Wind speed (m s <sup>-1</sup> )	Temperature (°C)	RH (%)	P (mbar)	PBL* (m)	Rain (mm)
August	1.30 ± 0.74	19.9 ± 5.01	74.0 ± 17.3	1020.6 ± 4.96	1371 ± 374	87.2
September	1.31 ± 0.78	14.3 ± 3.50	81.0 ± 12.8	1019.2 ± 10.1	1283 ± 283	58.0
October	0.95 ± 0.59	11.3 ± 3.84	86.6 ± 10.9	1014.7 ± 5.76	838 ± 254	46.2
November	2.10 ± 1.30	10.9 ± 4.57	88.0 ± 6.22	1014.8 ± 6.74	892 ± 372	69.2
December	1.94 ± 0.88	10.3 ± 2.49	87.1 ± 5.16	1020.3 ± 4.57	699 ± 250	19.6
January	1.93 ± 1.16	6.14 ± 3.71	86.7 ± 6.97	1008.4 ± 13.7	817 ± 368	60.8
February	1.79 ± 1.27	6.26 ± 3.61	83.9 ± 11.1	1008.2 ± 12.1	1082 ± 324	76.4
March	1.45 ± 1.23	7.15 ± 3.28	78.8 ± 12.1	1011.3 ± 10.9	1200 ± 363	50.4
April	1.34 ± 1.13	9.93 ± 4.00	76.6 ± 14.2	1009.7 ± 6.83	1404 ± 302	41.4
May	1.00 ± 0.78	15.3 ± 4.80	74.5 ± 18.3	1010.6 ± 7.27	1251 ± 417	104.6
June	1.27 ± 0.92	17.2 ± 3.84	83.5 ± 12.5	1011.5 ± 6.66	1380 ± 377	64.6
July	1.41 ± 1.11	19.7 ± 4.49	74.3 ± 14.6	1015.2 ± 4.19	984 ± 268	21.8
YEAR	1.48 ± 1.08	12.4 ± 6.16	81.3 ± 13.5	1013.6 ± 9.39	1099 ± 406	700.2

\* PBL height was obtained from meteorological data from the GDAS (1 deg) archive of the NOAA website



Table S1.3 Seasonal correlation matrices ( $r$  values) for (a) summer 2015 and 2016, (b) spring 2016, (c) autumn 2015 and (d) winter 2015-2016. The values in red indicate negative correlations. The correlations  $\geq 0.7$  are highlighted in bold, and those  $\geq 0.8$  and  $0.9$  with simple and double underline, respectively.

a)	<i>HONO</i>	<i>HNO<sub>3</sub></i>	<i>SO<sub>2</sub></i>	<i>NH<sub>3</sub></i>	<i>Cl<sup>-</sup></i>	<i>NO<sub>3</sub><sup>-</sup></i>	<i>SO<sub>4</sub><sup>2-</sup></i>	<i>C<sub>2</sub>O<sub>4</sub><sup>2-</sup></i>	<i>Na<sup>+</sup></i>	<i>NH<sub>4</sub><sup>+</sup></i>	<i>K<sup>+</sup></i>	<i>Mg<sup>2+</sup></i>	<i>Ca<sup>2+</sup></i>	<i>PM<sub>10</sub></i>	<i>PM<sub>2.5</sub></i>	<i>BC</i>	<i>NO</i>	<i>NO<sub>2</sub></i>
<i>HNO<sub>3</sub></i>	0.31																	
<i>SO<sub>2</sub></i>	0.05	0.28																
<i>NH<sub>3</sub></i>	0.34	0.18	0.15															
<i>Cl<sup>-</sup></i>	0.07	0.03	0.14	<b>-0.04</b>														
<i>NO<sub>3</sub><sup>-</sup></i>	0.43	0.34	0.16	0.33	0.18													
<i>SO<sub>4</sub><sup>2-</sup></i>	0.25	0.45	0.31	0.38	0.23	0.67												
<i>C<sub>2</sub>O<sub>4</sub><sup>2-</sup></i>	0.12	0.28	0.13	0.38	0.13	0.36	0.56											
<i>Na<sup>+</sup></i>	<b>-0.19</b>	<b>-0.03</b>	0.08	<b>-0.14</b>	0.37	<b>-0.13</b>	<b>-0.02</b>	<b>-0.05</b>										
<i>NH<sub>4</sub><sup>+</sup></i>	0.41	0.40	0.20	0.42	0.21	<u>0.96</u>	<u>0.83</u>	0.47	<b>-0.14</b>									
<i>K<sup>+</sup></i>	0.07	<b>0.00</b>	<b>0.00</b>	0.02	<b>-0.01</b>	<b>-0.01</b>	0.02	0.03	0.06	<b>-0.02</b>								
<i>Mg<sup>2+</sup></i>	<b>-0.06</b>	<b>-0.04</b>	0.02	<b>-0.01</b>	0.20	<b>-0.07</b>	<b>-0.04</b>	0.03	0.63	<b>-0.10</b>	0.17							
<i>Ca<sup>2+</sup></i>	0.09	0.02	0.07	0.54	<b>-0.04</b>	<b>-0.01</b>	0.15	0.24	0.04	0.04	0.09	0.19						
<i>PM<sub>10</sub></i>	0.33	0.54	0.06	0.50	0.22	0.69	0.75	0.50	<b>-0.10</b>	0.75	0.07	<b>-0.10</b>	0.28					
<i>PM<sub>2.5</sub></i>	0.47	0.46	0.20	0.34	0.25	<u>0.87</u>	0.77	0.52	<b>-0.08</b>	<u>0.90</u>	<b>0.00</b>	<b>-0.06</b>	0.01	<u>0.79</u>				
<i>BC</i>	0.62	0.20	0.10	0.31	0.02	0.24	0.23	0.20	<b>-0.17</b>	0.27	0.03	<b>-0.03</b>	0.26	0.37	0.37			
<i>NO</i>	0.30	<b>-0.06</b>	<b>-0.06</b>	0.08	<b>-0.07</b>	0.07	0.02	<b>-0.12</b>	<b>-0.11</b>	0.07	<b>-0.07</b>	<b>-0.09</b>	0.03	0.24	0.11	0.58		
<i>NO<sub>2</sub></i>	0.45	0.19	0.09	0.17	0.04	0.10	0.17	0.14	<b>-0.15</b>	0.13	0.10	<b>-0.16</b>	0.16	0.32	0.20	0.68	0.48	
<i>O<sub>3</sub></i>	<b>-0.10</b>	0.36	0.26	0.52	0.00	0.01	0.31	0.43	0.10	0.14	<b>-0.09</b>	0.10	0.43	<b>-0.47</b>	0.16	0.13	<b>-0.18</b>	<b>-0.48</b>

b)	<i>HONO</i>	<i>HNO<sub>3</sub></i>	<i>SO<sub>2</sub></i>	<i>NH<sub>3</sub></i>	<i>Cl<sup>-</sup></i>	<i>NO<sub>3</sub><sup>-</sup></i>	<i>SO<sub>4</sub><sup>2-</sup></i>	<i>C<sub>2</sub>O<sub>4</sub><sup>2-</sup></i>	<i>Na<sup>+</sup></i>	<i>NH<sub>4</sub><sup>+</sup></i>	<i>K<sup>+</sup></i>	<i>Mg<sup>2+</sup></i>	<i>Ca<sup>2+</sup></i>	<i>PM<sub>10</sub></i>	<i>PM<sub>2.5</sub></i>	<i>BC</i>	<i>NO</i>	<i>NO<sub>2</sub></i>
<i>HNO<sub>3</sub></i>	0.22																	
<i>SO<sub>2</sub></i>	0.03	0.22																
<i>NH<sub>3</sub></i>	0.17	0.23	0.06															
<i>Cl<sup>-</sup></i>	0.01	0.00	<b>-0.03</b>	0.08														
<i>NO<sub>3</sub><sup>-</sup></i>	0.53	0.40	0.18	0.25	0.04													
<i>SO<sub>4</sub><sup>2-</sup></i>	0.32	0.46	0.20	0.25	0.18	0.74												
<i>C<sub>2</sub>O<sub>4</sub><sup>2-</sup></i>	0.20	0.46	0.15	0.44	<b>-0.03</b>	0.28	0.46											
<i>Na<sup>+</sup></i>	<b>-0.20</b>	<b>0.00</b>	0.09	<b>-0.06</b>	0.49	<b>-0.19</b>	<b>-0.07</b>	<b>-0.21</b>										
<i>NH<sub>4</sub><sup>+</sup></i>	0.49	0.44	0.18	0.29	0.11	<u>0.97</u>	<u>0.86</u>	0.35	<b>-0.18</b>									
<i>K<sup>+</sup></i>	0.41	0.11	0.07	<b>-0.14</b>	<b>-0.01</b>	0.39	0.31	0.05	<b>-0.06</b>	0.39								
<i>Mg<sup>2+</sup></i>	<b>-0.06</b>	<b>-0.02</b>	0.11	<b>-0.03</b>	0.28	<b>-0.10</b>	<b>-0.12</b>	<b>-0.16</b>	0.62	<b>-0.12</b>	<b>-0.07</b>							
<i>Ca<sup>2+</sup></i>	0.05	0.36	0.19	0.29	0.01	0.16	0.26	0.33	0.08	0.20	0.05	0.07						
<i>PM<sub>10</sub></i>	0.58	0.50	0.26	0.28	0.15	<u>0.87</u>	<u>0.80</u>	0.43	<b>-0.02</b>	<u>0.89</u>	0.43	0.00	0.34					
<i>PM<sub>2.5</sub></i>	0.58	0.46	0.19	0.24	0.10	<u>0.92</u>	<u>0.79</u>	0.38	<b>-0.16</b>	<u>0.93</u>	0.40	<b>-0.08</b>	0.21	<u>0.91</u>				
<i>BC</i>	0.58	0.22	0.05	<b>-0.04</b>	<b>-0.04</b>	0.32	0.24	0.24	<b>-0.18</b>	0.31	0.41	<b>-0.07</b>	0.22	0.49	0.48			
<i>NO</i>	0.44	<b>-0.03</b>	0.00	<b>-0.06</b>	0.01	0.20	0.09	<b>-0.03</b>	<b>-0.07</b>	0.16	0.23	<b>0.00</b>	0.10	0.34	0.29	0.69		
<i>NO<sub>2</sub></i>	0.62	0.11	0.04	0.03	<b>-0.02</b>	0.41	0.25	0.07	<b>-0.17</b>	0.36	0.33	<b>-0.02</b>	0.23	0.51	0.48	0.78	0.62	
<i>O<sub>3</sub></i>	<b>-0.52</b>	0.12	0.08	0.18	0.01	<b>-0.42</b>	<b>-0.15</b>	0.27	0.19	<b>-0.36</b>	<b>-0.32</b>	0.10	0.29	<b>-0.27</b>	<b>-0.38</b>	<b>-0.37</b>	<b>-0.33</b>	<b>-0.54</b>



c)	<i>HONO</i>	<i>HNO<sub>3</sub></i>	<i>SO<sub>2</sub></i>	<i>NH<sub>3</sub></i>	<i>Cl<sup>-</sup></i>	<i>NO<sub>3</sub><sup>-</sup></i>	<i>SO<sub>4</sub><sup>2-</sup></i>	<i>C<sub>2</sub>O<sub>4</sub><sup>2-</sup></i>	<i>Na<sup>+</sup></i>	<i>NH<sub>4</sub><sup>+</sup></i>	<i>K<sup>+</sup></i>	<i>Mg<sup>2+</sup></i>	<i>Ca<sup>2+</sup></i>	<i>PM<sub>10</sub></i>	<i>PM<sub>2.5</sub></i>	<i>BC</i>	<i>NO</i>	<i>NO<sub>2</sub></i>
<i>HNO<sub>3</sub></i>	0.30																	
<i>SO<sub>2</sub></i>	0.16	0.19																
<i>NH<sub>3</sub></i>	0.27	0.24	0.28															
<i>Cl<sup>-</sup></i>	0.03	0.00	0.00	-0.05														
<i>NO<sub>3</sub><sup>-</sup></i>	0.50	0.37	0.20	0.02	-0.04													
<i>SO<sub>4</sub><sup>2-</sup></i>	0.38	0.33	0.26	0.16	-0.02	0.74												
<i>C<sub>2</sub>O<sub>4</sub><sup>2-</sup></i>	0.32	0.29	0.17	0.28	-0.08	0.50	0.60											
<i>Na<sup>+</sup></i>	-0.09	-0.04	-0.04	-0.17	0.66	-0.04	-0.05	-0.17										
<i>NH<sub>4</sub><sup>+</sup></i>	0.47	0.37	0.20	0.15	-0.03	<u>0.92</u>	<u>0.85</u>	0.57	-0.07									
<i>K<sup>+</sup></i>	0.31	0.29	-0.02	-0.11	0.00	0.22	0.15	0.10	-0.01	0.24								
<i>Mg<sup>2+</sup></i>	0.01	-0.07	0.14	-0.09	0.48	0.02	0.04	-0.06	0.68	0.00	-0.06							
<i>Ca<sup>2+</sup></i>	0.22	0.28	0.37	0.32	0.03	0.16	0.27	0.30	0.02	0.15	-0.08	0.10						
<i>PM<sub>10</sub></i>	0.55	0.33	0.27	0.10	0.20	0.76	0.70	0.50	0.17	0.76	0.27	0.19	0.34					
<i>PM<sub>2.5</sub></i>	0.50	0.29	0.16	0.00	0.09	<u>0.82</u>	0.75	0.54	0.04	<u>0.81</u>	0.28	0.12	0.16	<u>0.86</u>				
<i>BC</i>	0.59	0.28	0.12	-0.07	-0.07	0.45	0.35	0.29	-0.13	0.42	0.50	-0.09	0.18	0.65	0.64			
<i>NO</i>	0.44	0.11	0.07	-0.05	0.03	0.26	0.21	0.13	-0.02	0.24	0.46	0.00	0.12	0.47	0.38	<u>0.81</u>		
<i>NO<sub>2</sub></i>	0.55	0.17	0.24	0.04	-0.03	0.41	0.39	0.30	-0.15	0.39	0.26	0.00	0.28	0.55	0.47	0.76	0.66	
<i>O<sub>3</sub></i>	-0.46	-0.09	0.05	0.30	0.10	-0.57	-0.36	-0.24	0.20	-0.48	-0.32	0.09	0.08	-0.51	-0.53	-0.63	-0.44	-0.60

d)	<i>HONO</i>	<i>HNO<sub>3</sub></i>	<i>SO<sub>2</sub></i>	<i>NH<sub>3</sub></i>	<i>Cl<sup>-</sup></i>	<i>NO<sub>3</sub><sup>-</sup></i>	<i>SO<sub>4</sub><sup>2-</sup></i>	<i>C<sub>2</sub>O<sub>4</sub><sup>2-</sup></i>	<i>Na<sup>+</sup></i>	<i>NH<sub>4</sub><sup>+</sup></i>	<i>K<sup>+</sup></i>	<i>Mg<sup>2+</sup></i>	<i>Ca<sup>2+</sup></i>	<i>PM<sub>10</sub></i>	<i>PM<sub>2.5</sub></i>	<i>BC</i>	<i>NO</i>	<i>NO<sub>2</sub></i>
<i>HNO<sub>3</sub></i>	0.20																	
<i>SO<sub>2</sub></i>	0.25	0.21																
<i>NH<sub>3</sub></i>	0.31	0.20	0.17															
<i>Cl<sup>-</sup></i>	0.18	-0.10	0.18	0.04														
<i>NO<sub>3</sub><sup>-</sup></i>	0.59	0.34	0.36	0.25	0.11													
<i>SO<sub>4</sub><sup>2-</sup></i>	0.41	0.18	0.29	0.28	0.02	0.64												
<i>C<sub>2</sub>O<sub>4</sub><sup>2-</sup></i>	0.17	0.16	0.06	0.31	-0.20	0.36	0.65											
<i>Na<sup>+</sup></i>	-0.15	-0.08	0.08	-0.02	0.75	-0.23	-0.24	-0.28										
<i>NH<sub>4</sub><sup>+</sup></i>	0.60	0.31	0.36	0.27	0.13	<u>0.98</u>	0.76	0.48	-0.26									
<i>K<sup>+</sup></i>	0.66	0.13	0.18	0.18	0.26	0.55	0.55	0.39	-0.09	0.61								
<i>Mg<sup>2+</sup></i>	-0.10	-0.09	-0.01	-0.03	0.59	-0.15	-0.20	-0.28	0.69	-0.18	-0.06							
<i>Ca<sup>2+</sup></i>	0.25	0.20	0.36	0.27	0.23	0.21	0.13	0.09	0.15	0.19	0.11	0.07						
<i>PM<sub>10</sub></i>	0.76	0.24	0.34	0.29	0.37	0.77	0.63	0.36	0.04	<u>0.79</u>	0.71	0.03	0.32					
<i>PM<sub>2.5</sub></i>	0.68	0.28	0.31	0.20	0.16	<u>0.84</u>	0.69	0.43	-0.20	<u>0.86</u>	0.62	-0.14	0.21	<u>0.84</u>				
<i>BC</i>	0.75	0.14	0.22	0.10	0.20	0.51	0.45	0.22	-0.14	0.55	0.64	-0.10	0.23	0.77	0.71			
<i>NO</i>	0.54	0.05	0.07	-0.04	-0.01	0.25	0.21	0.08	-0.11	0.25	0.32	-0.11	0.22	0.53	0.44	0.76		
<i>NO<sub>2</sub></i>	0.64	0.25	0.21	-0.02	-0.07	0.43	0.28	0.07	-0.16	0.41	0.32	-0.17	0.27	0.62	0.60	<u>0.83</u>	0.64	
<i>O<sub>3</sub></i>	-0.64	-0.17	-0.13	-0.07	0.08	-0.56	-0.48	-0.29	0.30	-0.57	-0.48	0.25	-0.06	-0.64	-0.68	-0.69	-0.45	-0.77

Table S1.4 Correlations between HONO and NO<sub>2</sub> by season for the entire day, nighttime and daytime

	HONO vs NO <sub>2</sub> (Entire day)			HONO vs NO <sub>2</sub> (Nighttime)			HONO vs NO <sub>2</sub> (Daytime)		
	r <sup>2</sup>	Slope	Intercept	r <sup>2</sup>	Slope	Intercept	r <sup>2</sup>	Slope	Intercept
Winter	0.40	0.057	0.19	0.61	0.054	0.22	0.25	0.066	0.13
Spring	0.37	0.065	0.20	0.58	0.067	0.27	0.29	0.066	0.15
Summer	0.20	0.050	0.19	0.36	0.060	0.23	0.19	0.053	0.14
Autumn	0.30	0.074	0.18	0.57	0.077	0.17	0.17	0.070	0.19

## References

- Allen, H. M., Draper, D. C., Ayres, B. R., Ault, A., Bondy, A., Takahama, S., Modini, R. L., Baumann, K., Edgerton, E., Knote, C., Laskin, A., Wang, B. and Fry, J. L.: Influence of crustal dust and sea spray supermicron particle concentrations and acidity on inorganic NO<sub>3</sub>-aerosol during the 2013 Southern Oxidant and Aerosol Study, *Atmos. Chem. Phys.*, 15(18), 10669–10685, doi:10.5194/acp-15-10669-2015, 2015.
- Behera, S. N., Betha, R., Liu, P. and Balasubramanian, R.: A study of diurnal variations of PM<sub>2.5</sub> acidity and related chemical species using a new thermodynamic equilibrium model, *Sci. Total Environ.*, 452–453, 286–295, doi:10.1016/j.scitotenv.2013.02.062, 2013.
- ten Brink, H., Otjes, R., Jongejan, P. and Slanina, S.: An instrument for semi-continuous monitoring of the size-distribution of nitrate, ammonium, sulphate and chloride in aerosol, *Atmos. Environ.*, 41(13), 2768–2779, doi:10.1016/j.atmosenv.2006.11.041, 2007.
- Chen, H., Wu, D. and Yu, J.: Comparison of characteristics of aerosol during rainy weather and cold air-dust weather in Guangzhou in late March 2012, *Theor. Appl. Climatol.*, 124(1–2), 451–459, doi:10.1007/s00704-015-1424-z, 2016.
- Chen, X., Walker, J. T. and Geron, C.: Chromatography related performance of the Monitor for AeRosols and GAses in ambient air (MARGA): laboratory and field-based evaluation, *Atmos Meas Tech*, 10(10), 3893–3908, doi:10.5194/amt-10-3893-2017, 2017.
- Cheung, H. C., Morawska, L. and Ristovski, Z. D.: Observation of new particle formation in subtropical urban environment, *Atmos. Chem. Phys.*, 11(8), 3823–3833, doi:10.5194/acp-11-3823-2011, 2011.
- Crenn, V., Fronval, I., Petitprez, D. and Riffault, V.: Fine particles sampled at an urban background site and an industrialized coastal site in Northern France - Part 1: Seasonal variations and chemical characterization, *Sci. Total Environ.*, 578, 203–218, doi:10.1016/j.scitotenv.2015.11.165, 2017.
- DeCarlo, P. F., Kimmel, J. R., Trimborn, A., Northway, M. J., Jayne, J. T., Aiken, A. C., Gonin, M., Fuhrer, K., Horvath, T., Docherty, K. S., Worsnop, D. R. and Jimenez, J. L.: Field-Deployable, High-Resolution, Time-of-Flight Aerosol Mass Spectrometer, *Anal. Chem.*, 78(24), 8281–8289, doi:10.1021/ac061249n, 2006.
- Du, H., Kong, L., Cheng, T., Chen, J., Yang, X., Zhang, R., Han, Z., Yan, Z. and Ma, Y.: Insights into Ammonium Particle-to-Gas Conversion: Non-sulfate Ammonium Coupling with Nitrate and Chloride, *Aerosol Air Qual. Res.*, 10(6), 589–595, doi:10.4209/aaqr.2010.04.0034, 2010.
- Fan, J., Yue, X., Jing, Y., Chen, Q. and Wang, S.: Online monitoring of water-soluble ionic composition of PM<sub>10</sub> during early summer over Lanzhou City, *J. Environ. Sci.*, 26(2), 353–361, doi:10.1016/S1001-0742(13)60431-3, 2014.
- Fiedler, V., Dal Maso, M., Boy, M., Aufmhoff, H., Hoffmann, J., Schuck, T., Birmili, W., Hanke, M., Uecker, J., Arnold, F. and Kulmala, M.: The contribution of sulphuric acid to atmospheric particle formation and growth: a comparison between boundary layers in

Northern and Central Europe, *Atmos. Chem. Phys.*, 5(7), 1773–1785, doi:10.5194/acp-5-1773-2005, 2005.

Fu, H., Zhang, M., Li, W., Chen, J., Wang, L., Quan, X. and Wang, W.: Morphology, composition and mixing state of individual carbonaceous aerosol in urban Shanghai, *Atmos. Chem. Phys.*, 12(2), 693–707, doi:10.5194/acp-12-693-2012, 2012.

G J Phillips, U. M.: The detection of nocturnal N<sub>2</sub>O<sub>5</sub> as HNO<sub>3</sub> by alkali-and aqueous-denuder techniques, *Atmos. Meas. Tech.*, 6(2), 231–237, doi:10.5194/amt-6-231-2013, 2013.

Gao, J., Zhang, Y., Zhang, M., Zhang, J., Wang, S., Tao, J., Wang, H., Luo, D., Chai, F. and Ren, C.: Photochemical properties and source of pollutants during continuous pollution episodes in Beijing, October, 2011, *J. Environ. Sci.*, 26(1), 44–53, doi:10.1016/S1001-0742(13)60379-4, 2014.

Gao, J., Peng, X., Chen, G., Xu, J., Shi, G.-L., Zhang, Y.-C. and Feng, Y.-C.: Insights into the chemical characterization and sources of PM<sub>2.5</sub> in Beijing at a 1-h time resolution, *Sci. Total Environ.*, 542, Part A, 162–171, doi:10.1016/j.scitotenv.2015.10.082, 2016.

Gianini, M. F. D., Fischer, A., Gehrig, R., Ulrich, A., Wichser, A., Piot, C., Besombes, J.-L. and Hueglin, C.: Comparative source apportionment of PM<sub>10</sub> in Switzerland for 2008/2009 and 1998/1999 by Positive Matrix Factorisation, *Atmos. Environ.*, 54, 149–158, doi:10.1016/j.atmosenv.2012.02.036, 2012.

Griffith, S. M., Huang, X. H. H., Louie, P. K. K. and Yu, J. Z.: Characterizing the thermodynamic and chemical composition factors controlling PM<sub>2.5</sub> nitrate: Insights gained from two years of online measurements in Hong Kong, *Atmos. Environ.*, 122, 864–875, doi:10.1016/j.atmosenv.2015.02.009, 2015.

Hamed, A., Joutsensaari, J., Mikkonen, S., Sogacheva, L., Dal Maso, M., Kulmala, M., Cavalli, F., Fuzzi, S., Facchini, M. C., Decesari, S., Mircea, M., Lehtinen, K. E. J. and Laaksonen, A.: Nucleation and growth of new particles in Po Valley, Italy, *Atmos. Chem. Phys.*, 7(2), 355–376, doi:10.5194/acp-7-355-2007, 2007.

Han, T., Qiao, L., Zhou, M., Qu, Y., Du, J., Liu, X., Lou, S., Chen, C., Wang, H., Zhang, F., Yu, Q. and Wu, Q.: Chemical and optical properties of aerosols and their interrelationship in winter in the megacity Shanghai of China, *J. Environ. Sci.*, 27, 59–69, doi:10.1016/j.jes.2014.04.018, 2015.

Hu, Q., Fu, H., Wang, Z., Kong, L., Chen, M. and Chen, J.: The variation of characteristics of individual particles during the haze evolution in the urban Shanghai atmosphere, *Atmos. Res.*, 181, 95–105, doi:10.1016/j.atmosres.2016.06.016, 2016.

Huang, X. H. H.: Characterization of PM<sub>2.5</sub> Major Components and Source Investigation in Suburban Hong Kong: A One Year Monitoring Study, *Aerosol Air Qual. Res.*, doi:10.4209/aaqr.2013.01.0020, 2014.

Huang, Y., Li, L., Li, J., Wang, X., Chen, H., Chen, J., Yang, X., Gross, D. S., Wang, H., Qiao, L. and Chen, C.: A case study of the highly time-resolved evolution of aerosol chemical and optical properties in urban Shanghai, China, *Atmos. Chem. Phys.*, 13(8), 3931–3944, doi:10.5194/acp-13-3931-2013, 2013.

Iida, K., Stolzenburg, M. R., McMurry, P. H. and Smith, J. N.: Estimating nanoparticle growth rates from size-dependent charged fractions: Analysis of new particle formation events in Mexico City, *J. Geophys. Res. Atmospheres*, 113(D5), D05207, doi:10.1029/2007JD009260, 2008.

Jansen, R. C., Chen, J. and Hu, Y.: The Impact of Nonlocal Ammonia on Submicron Particulate Matter and Visibility Degradation in Urban Shanghai, *Adv. Meteorol.*, 2014, e534675, doi:10.1155/2014/534675, 2014a.

Jansen, R. C., Shi, Y., Chen, J., Hu, Y., Xu, C., Hong, S., Li, J. and Zhang, M.: Using hourly measurements to explore the role of secondary inorganic aerosol in PM<sub>2.5</sub> during haze and fog in Hangzhou, China, *Adv. Atmos. Sci.*, 31(6), 1427–1434, doi:10.1007/s00376-014-4042-2, 2014b.

Jeon, E. M., Kim, H. J., Jung, K., Kim, J. H., Kim, M. Y., Kim, Y. P. and Ka, J.-O.: Impact of Asian dust events on airborne bacterial community assessed by molecular analyses, *Atmos. Environ.*, 45(25), 4313–4321, doi:10.1016/j.atmosenv.2010.11.054, 2011.

Khezri, B., Mo, H., Yan, Z., Chong, S.-L., Heng, A. K. and Webster, R. D.: Simultaneous online monitoring of inorganic compounds in aerosols and gases in an industrialized area, *Atmos. Environ.*, 80, 352–360, doi:10.1016/j.atmosenv.2013.08.008, 2013.

Kim, W., Lee, H., Kim, J., Jeong, U. and Kweon, J.: Estimation of seasonal diurnal variations in primary and secondary organic carbon concentrations in the urban atmosphere: EC tracer and multiple regression approaches, *Atmos. Environ.*, 56, 101–108, doi:10.1016/j.atmosenv.2012.03.076, 2012.

Kong, L., Yang, Y., Zhang, S., Zhao, X., Du, H., Fu, H., Zhang, S., Cheng, T., Yang, X., Chen, J., Wu, D., Shen, J., Hong, S. and Jiao, L.: Observations of linear dependence between sulfate and nitrate in atmospheric particles, *J. Geophys. Res. Atmospheres*, 119(1), 341–361, doi:10.1002/2013JD020222, 2014.

Leng, C., Cheng, T., Chen, J., Zhang, R., Tao, J., Huang, G., Zha, S., Zhang, M., Fang, W., Li, X. and Li, L.: Measurements of surface cloud condensation nuclei and aerosol activity in downtown Shanghai, *Atmos. Environ.*, 69, 354–361, doi:10.1016/j.atmosenv.2012.12.021, 2013.

Leng, C., Zhang, Q., Tao, J., Zhang, H., Zhang, D., Xu, C., Li, X., Kong, L., Cheng, T., Zhang, R., Yang, X., Chen, J., Qiao, L., Lou, S., Wang, H. and Chen, C.: Impacts of new particle formation on aerosol cloud condensation nuclei (CCN) activity in Shanghai: case study, *Atmos. Chem. Phys.*, 14(20), 11353–11365, doi:10.5194/acp-14-11353-2014, 2014a.

Leng, C., Zhang, Q., Zhang, D., Xu, C., Cheng, T., Zhang, R., Tao, J., Chen, J., Zha, S., Zhang, Y., Li, X., Kong, L. and Gao, W.: Variations of cloud condensation nuclei (CCN) and aerosol activity during fog–haze episode: a case study from Shanghai, *Atmos. Chem. Phys.*, 14(22), 12499–12512, doi:10.5194/acp-14-12499-2014, 2014b.

Li, H.: Agricultural Fire Impacts on the Air Quality of Shanghai during Summer Harvesttime, *Aerosol Air Qual. Res.*, doi:10.4209/aaqr.2009.08.0049, 2010.

Li, L., Chen, J., Wang, L., Melluki, W. and Zhou, H.: Aerosol single scattering albedo affected by chemical composition: An investigation using CRDS combined with MARGA, *Atmos. Res.*, 124, 149–157, doi:10.1016/j.atmosres.2012.11.007, 2013.

Makkonen, U., Virkkula, A., Mäntykenttä, J., Hakola, H., Keronen, P., Vakkari, V. and Aalto, P. P.: Semi-continuous gas and inorganic aerosol measurements at a Finnish urban site: comparisons with filters, nitrogen in aerosol and gas phases, and aerosol acidity, *Atmos. Chem. Phys.*, 12(12), 5617–5631, doi:10.5194/acp-12-5617-2012, 2012.

Makkonen, U., Virkkula, A., Hellén, H., Hemmila, M., Sund, J., Aijala, M., Ehn, M., Junninen, H., Keronen, P., Petaja, T., Worsnop, D. R., Kulmala, M. and Hakola, H.: Semi-continuous gas and inorganic aerosol measurements at a boreal forest site, *Boreal Environ. Res.*, 19 (suppl. B), 311–328, 2014.

Man, H., Zhu, Y., Ji, F., Yao, X., Lau, N. T., Li, Y., Lee, B. P. and Chan, C. K.: Comparison of Daytime and Nighttime New Particle Growth at the HKUST Supersite in Hong Kong, *Environ. Sci. Technol.*, 49(12), 7170–7178, doi:10.1021/acs.est.5b02143, 2015.

Mensah, A. A., Holzinger, R., Otjes, R., Trimborn, A., Mentel, T. F., ten Brink, H., Henzing, B. and Kiendler-Scharr, A.: Aerosol chemical composition at Cabauw, The Netherlands as observed in two intensive periods in May 2008 and March 2009, *Atmos. Chem. Phys.*, 12(10), 4723–4742, doi:10.5194/acp-12-4723-2012, 2012.

Middlebrook, A. M., Bahreini, R., Jimenez, J. L. and Canagaratna, M. R.: Evaluation of Composition-Dependent Collection Efficiencies for the Aerodyne Aerosol Mass Spectrometer using Field Data, *Aerosol Sci. Technol.*, 46(3), 258–271, doi:10.1080/02786826.2011.620041, 2012.

Peng, X., Shi, G.-L., Gao, J., Liu, J.-Y., HuangFu, Y.-Q., Ma, T., Wang, H.-T., Zhang, Y.-C., Wang, H., Li, H., Ivey, C. E. and Feng, Y.-C.: Characteristics and sensitivity analysis of multiple-time-resolved source patterns of PM<sub>2.5</sub> with real time data using Multilinear Engine 2, *Atmos. Environ.*, 139, 113–121, doi:10.1016/j.atmosenv.2016.05.032, 2016.

Putaud, J.-P., Van Dingenen, R., Alastuey, A., Bauer, H., Birmili, W., Cyrys, J., Flentje, H., Fuzzi, S., Gehrig, R., Hansson, H. C., Harrison, R. M., Herrmann, H., Hitzenberger, R., Hüglin, C., Jones, A. M., Kasper-Giebl, A., Kiss, G., Koussa, A., Kuhlbusch, T. A. J., Löschau, G., Maenhaut, W., Molnar, A., Moreno, T., Pekkanen, J., Perrino, C., Pitz, M., Puxbaum, H., Querol, X., Rodriguez, S., Salma, I., Schwarz, J., Smolik, J., Schneider, J., Spindler, G., ten Brink, H., Tursic, J., Viana, M., Wiedensohler, A. and Raes, F.: A European aerosol phenomenology – 3: Physical and chemical characteristics of particulate matter from 60 rural, urban, and kerbside sites across Europe, *Atmos. Environ.*, 44(10), 1308–1320, doi:10.1016/j.atmosenv.2009.12.011, 2010.

Rumsey, I. C. and Walker, J. T.: Application of an online ion-chromatography-based instrument for gradient flux measurements of speciated nitrogen and sulfur, *Atmos. Meas. Tech.*, 9(6), 2581–2592, doi:10.5194/amt-9-2581-2016, 2016.

Rumsey, I. C., Cowen, K. A., Walker, J. T., Kelly, T. J., Hanft, E. A., Mishoe, K., Rogers, C., Proost, R., Beachley, G. M., Lear, G., Frelink, T. and Otjes, R. P.: An assessment of the performance of the Monitor for AeRosols and GAses in ambient air (MARGA): a semi-

continuous method for soluble compounds, *Atmos. Chem. Phys.*, 14(11), 5639–5658, doi:10.5194/acp-14-5639-2014, 2014.

Salimi, F., Rahman, M. M., Clifford, S., Ristovski, Z. and Morawska, L.: Nocturnal new particle formation events in urban environments, *Atmos. Chem. Phys.*, 17(1), 521–530, doi:10.5194/acp-17-521-2017, 2017.

Schaap, M., Otjes, R. P. and Weijers, E. P.: Illustrating the benefit of using hourly monitoring data on secondary inorganic aerosol and its precursors for model evaluation, *Atmospheric Chem. Phys.*, 11(21), 11041–11053, doi:10.5194/acp-11-11041-2011, 2011.

Schlag, P., Kiendler-Scharr, A., Blom, M. J., Canonaco, F., Henzing, J. S., Moerman, M., Prévôt, A. S. H. and Holzinger, R.: Aerosol source apportionment from 1-year measurements at the CESAR tower in Cabauw, the Netherlands, *Atmos. Chem. Phys.*, 16(14), 8831–8847, doi:10.5194/acp-16-8831-2016, 2016.

Shi, Y., Chen, J., Hu, D., Wang, L., Yang, X. and Wang, X.: Airborne submicron particulate (PM<sub>1</sub>) pollution in Shanghai, China: Chemical variability, formation/dissociation of associated semi-volatile components and the impacts on visibility, *Sci. Total Environ.*, 473–474, 199–206, doi:10.1016/j.scitotenv.2013.12.024, 2014.

Shon, Z.-H., Kim, K.-H., Song, S.-K., Jung, K., Kim, N.-J. and Lee, J.-B.: Relationship between water-soluble ions in PM<sub>2.5</sub> and their precursor gases in Seoul megacity, *Atmos. Environ.*, 59, 540–550, doi:10.1016/j.atmosenv.2012.04.033, 2012.

Shon, Z.-H., Ghosh, S., Kim, K.-H., Song, S.-K., Jung, K. and Kim, N.-J.: Analysis of water-soluble ions and their precursor gases over diurnal cycle, *Atmos. Res.*, 132–133, 309–321, doi:10.1016/j.atmosres.2013.06.003, 2013.

Song, S.-K., Shon, Z.-H. and Park, Y.-H.: Diurnal and seasonal characteristics of the optical properties and direct radiative forcing of different aerosol components in Seoul megacity, *Sci. Total Environ.*, 599–600, 400–412, doi:10.1016/j.scitotenv.2017.04.195, 2017.

Stieger, B., Spindler, G., Fahlbusch, B., Müller, K., Grüner, A., Poulain, L., Thöni, L., Seidler, E., Wallasch, M. and Herrmann, H.: Measurements of PM<sub>10</sub> ions and trace gases with the online system MARGA at the research station Melpitz in Germany – A five-year study, *J. Atmos. Chem.*, 1–38, doi:10.1007/s10874-017-9361-0, 2017.

Stolzenburg, M. R., McMurry, P. H., Sakurai, H., Smith, J. N., Mauldin, R. L., Eisele, F. L. and Clement, C. F.: Growth rates of freshly nucleated atmospheric particles in Atlanta, *J. Geophys. Res. Atmospheres*, 110(D22), D22S05, doi:10.1029/2005JD005935, 2005.

Tan, H., Cai, M., Fan, Q., Liu, L., Li, F., Chan, P. W., Deng, X. and Wu, D.: An analysis of aerosol liquid water content and related impact factors in Pearl River Delta, *Sci. Total Environ.*, 579, 1822–1830, doi:10.1016/j.scitotenv.2016.11.167, 2017.

Twigg, M. M., Di Marco, C. F., Leeson, S., van Dijk, N., Jones, M. R., Leith, I. D., Morrison, E., Coyle, M., Proost, R., Peeters, A. N. M., Lemon, E., Frelink, T., Braban, C. F., Nemitz, E. and Cape, J. N.: Water soluble aerosols and gases at a UK background site – Part 1: Controls of PM<sub>2.5</sub> and PM<sub>10</sub> aerosol composition, *Atmos. Chem. Phys.*, 15(14), 8131–8145, doi:10.5194/acp-15-8131-2015, 2015.

- Wang, D., Zhou, B., Fu, Q., Zhao, Q., Zhang, Q., Chen, J., Yang, X., Duan, Y. and Li, J.: Intense secondary aerosol formation due to strong atmospheric photochemical reactions in summer: observations at a rural site in eastern Yangtze River Delta of China, *Sci. Total Environ.*, 571, 1454–1466, doi:10.1016/j.scitotenv.2016.06.212, 2016a.
- Wang, H. L., Qiao, L. P., Lou, S. R., Zhou, M., Chen, J. M., Wang, Q., Tao, S. K., Chen, C. H., Huang, H. Y., Li, L. and Huang, C.: PM<sub>2.5</sub> pollution episode and its contributors from 2011 to 2013 in urban Shanghai, China, *Atmos. Environ.*, 123, Part B, 298–305, doi:10.1016/j.atmosenv.2015.08.018, 2015.
- Wang, H. L., Qiao, L. P., Lou, S. R., Zhou, M., Ding, A. J., Huang, H. Y., Chen, J. M., Wang, Q., Tao, S. K., Chen, C. H., Li, L. and Huang, C.: Chemical composition of PM<sub>2.5</sub> and meteorological impact among three years in urban Shanghai, China, *J. Clean. Prod.*, 112, Part 2, 1302–1311, doi:10.1016/j.jclepro.2015.04.099, 2016b.
- Wang, L., Du, H., Chen, J., Zhang, M., Huang, X., Tan, H., Kong, L. and Geng, F.: Consecutive transport of anthropogenic air masses and dust storm plume: Two case events at Shanghai, China, *Atmos. Res.*, 127, 22–33, doi:10.1016/j.atmosres.2013.02.011, 2013.
- Wang, X., Chen, J., Sun, J., Li, W., Yang, L., Wen, L., Wang, W., Wang, X., Collett Jr., J. L., Shi, Y., Zhang, Q., Hu, J., Yao, L., Zhu, Y., Sui, X., Sun, X. and Mellouki, A.: Severe haze episodes and seriously polluted fog water in Ji'nan, China, *Sci. Total Environ.*, 493, 133–137, doi:10.1016/j.scitotenv.2014.05.135, 2014.
- Wen, L. and Chen, J.: Severe Aerosol Pollution Derived from Fireworks: A Case In Jinan, China, *JSM Environ. Sci. Ecol.*, 1(1), 2013.
- Wen, L., Chen, J., Yang, L., Wang, X., Xu, C., Sui, X., Yao, L., Zhu, Y., Zhang, J., Zhu, T. and Wang, W.: Enhanced formation of fine particulate nitrate at a rural site on the North China Plain in summer: The important roles of ammonia and ozone, *Atmos. Environ.*, 101, 294–302, doi:10.1016/j.atmosenv.2014.11.037, 2015.
- Wu, Z., Hu, M., Liu, S., Wehner, B., Bauer, S., Maßling, A., Wiedensohler, A., Petäjä, T., Dal Maso, M. and Kulmala, M.: New particle formation in Beijing, China: Statistical analysis of a 1-year data set, *J. Geophys. Res. Atmospheres*, 112(D9), D09209, doi:10.1029/2006JD007406, 2007.
- Yao, L., Yang, L., Chen, J., Wang, X., Xue, L., Li, W., Sui, X., Wen, L., Chi, J., Zhu, Y., Zhang, J., Xu, C., Zhu, T. and Wang, W.: Characteristics of carbonaceous aerosols: Impact of biomass burning and secondary formation in summertime in a rural area of the North China Plain, *Sci. Total Environ.*, 557–558, 520–530, doi:10.1016/j.scitotenv.2016.03.111, 2016.
- Ye, X., Ma, Z., Zhang, J., Du, H., Chen, J., Chen, H., Yang, X., Gao, W. and Geng, F.: Important role of ammonia on haze formation in Shanghai, *Environ. Res. Lett.*, 6(2), 024019, doi:10.1088/1748-9326/6/2/024019, 2011.
- Ye, X., Tang, C., Yin, Z., Chen, J., Ma, Z., Kong, L., Yang, X., Gao, W. and Geng, F.: Hygroscopic growth of urban aerosol particles during the 2009 Mirage-Shanghai Campaign, *Atmos. Environ.*, 64, 263–269, doi:10.1016/j.atmosenv.2012.09.064, 2013.



Yin, Z., Ye, X., Jiang, S., Tao, Y., Shi, Y., Yang, X. and Chen, J.: Size-resolved effective density of urban aerosols in Shanghai, *Atmos. Environ.*, 100, 133–140, doi:10.1016/j.atmosenv.2014.10.055, 2015.

Zhang, M., Chen, J., Chen, X., Cheng, T., Zhang, Y., Zhang, H., Ding, A., Wang, M. and Mellouki, A.: Urban Aerosol Characteristics during the World Expo 2010 in Shanghai, *Aerosol Air Qual. Res.*, 13(1), 36–48, doi:10.4209/aaqr.2012.02.0024, 2013.

Zhou, G., Yang, F., Geng, F., Xu, J., Yang, X. and Tie, X.: Measuring and Modeling Aerosol: Relationship with Haze Events in Shanghai, China, *Aerosol Air Qual. Res.*, 14(3), 783–792, doi:10.4209/aaqr.2013.01.0019, 2014.

Zhou, M., Qiao, L., Zhu, S., Li, L., Lou, S., Wang, H., Wang, Q., Tao, S., Huang, C. and Chen, C.: Chemical characteristics of fine particles and their impact on visibility impairment in Shanghai based on a 1-year period observation, *J. Environ. Sci.*, 48, 151–160, doi:10.1016/j.jes.2016.01.022, 2016a.

Zhou, Y., Huang, X. H., Bian, Q., Griffith, S. M., Louie, P. K. K. and Yu, J. Z.: Sources and atmospheric processes impacting oxalate at a suburban coastal site in Hong Kong: Insights inferred from 1 year hourly measurements, *J. Geophys. Res. Atmospheres*, 120(18), 2015JD023531, doi:10.1002/2015JD023531, 2015.

Zhou, Y., Huang, X. H. H., Griffith, S. M., Li, M., Li, L., Zhou, Z., Wu, C., Meng, J., Chan, C. K., Louie, P. K. K. and Yu, J. Z.: A field measurement based scaling approach for quantification of major ions, organic carbon, and elemental carbon using a single particle aerosol mass spectrometer, *Atmos. Environ.*, 143, 300–312, doi:10.1016/j.atmosenv.2016.08.054, 2016b.

## **ANNEX 3: Supplementary material for Article 2**

### **Real-time assessment of wintertime organic aerosol characteristics and sources at a suburban site in northern France**

Roger Roig<sup>1</sup>, Abhishek Chakraborty<sup>1</sup>, Esperanza Perdrix<sup>1</sup>, Emmanuel Tison<sup>1</sup>, Véronique Riffault<sup>1,\*</sup>

IMT Lille Douai, Univ. Lille, SAGE – Département Sciences de l'Atmosphère et  
Génie de l'Environnement, F-59000 Lille, France

\* Corresponding author: Véronique Riffault ([veronique.riffault@imt-lille-douai.fr](mailto:veronique.riffault@imt-lille-douai.fr))



Figure S2.1 Maps of France (left) and Douai (right) with the sampling site (yellow cross), the main roads (red lines), railroad (black line), city center (grey area), non-ferrous metal industry (brown area), slaughterhouse (green cross) and waste water treatment plant (WWTP, blue cross)

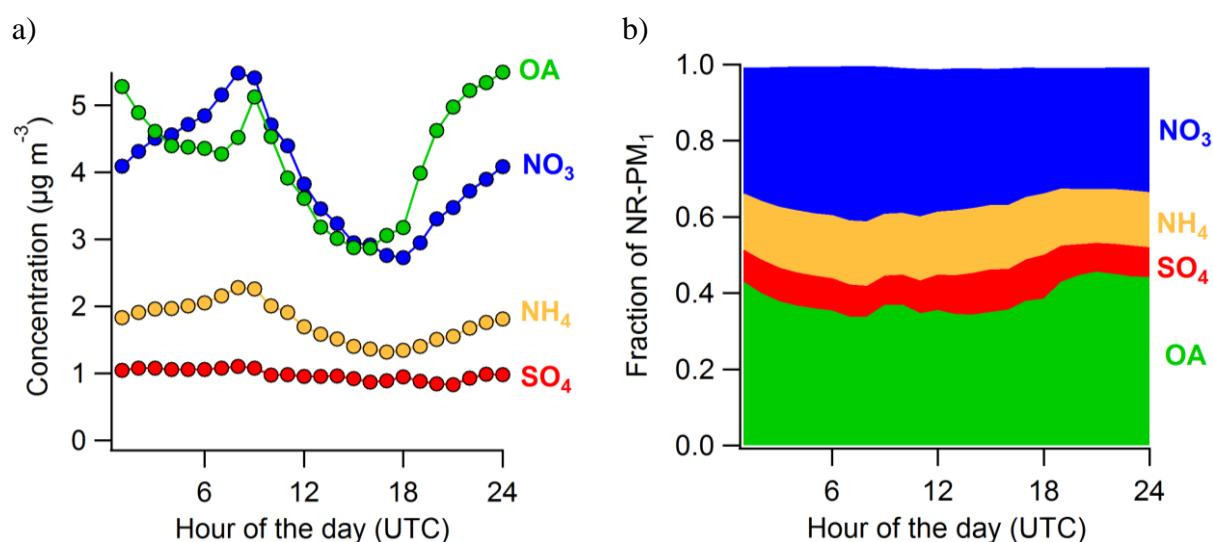


Figure S2.2 Daily profiles of main NR-PM<sub>1</sub> components (OA, NO<sub>3</sub>, NH<sub>4</sub> and SO<sub>4</sub>) by (a) average concentration and (b) relative contribution during the whole campaign

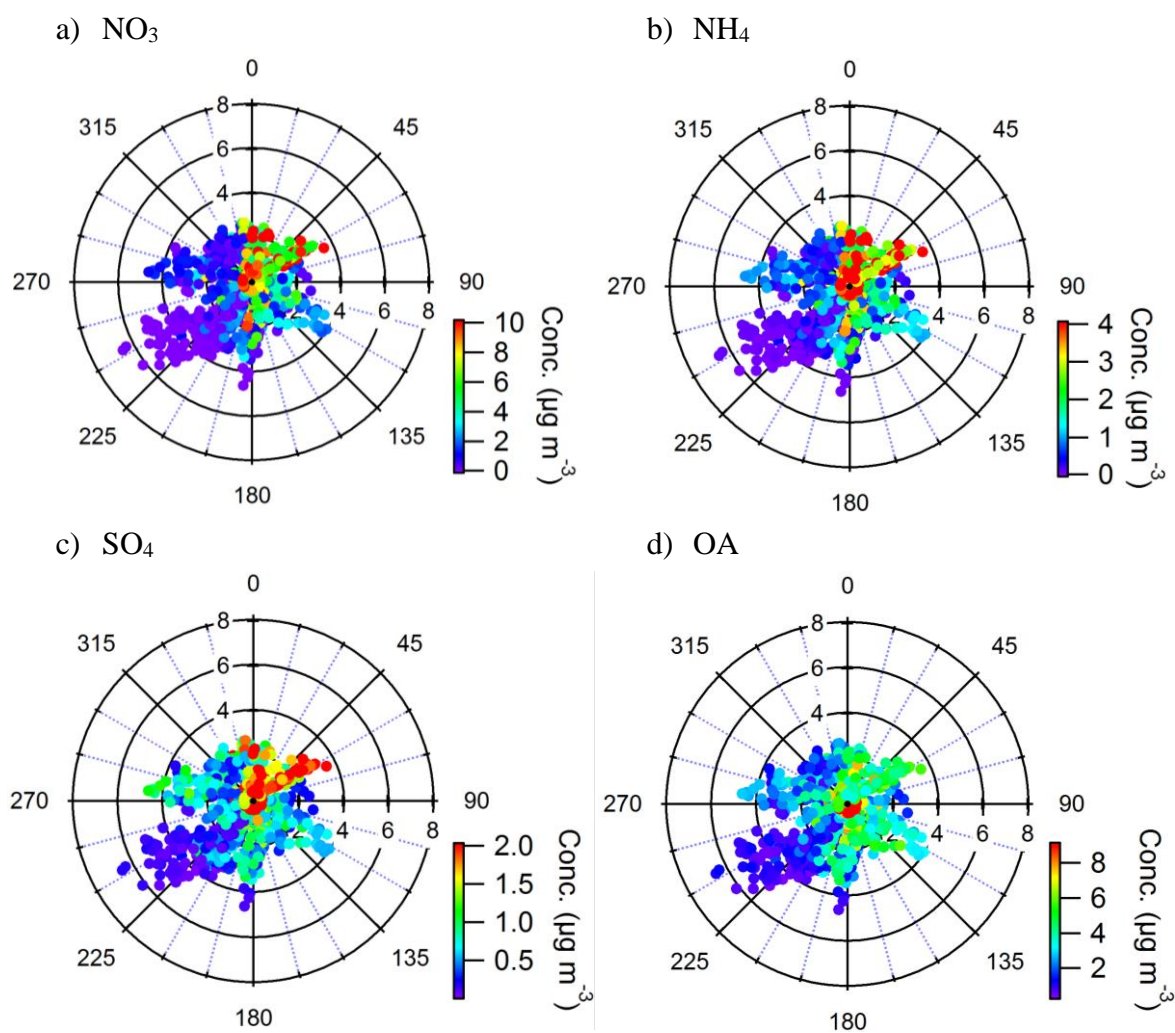


Figure S2.3 Polar graphs of the wind direction (radius: wind speed in  $\text{m s}^{-1}$ ) colored by concentration of (a)  $\text{NO}_3$ , (b)  $\text{NH}_4$ , (c)  $\text{SO}_4$  and (d) OA (organic aerosol) for the whole campaign

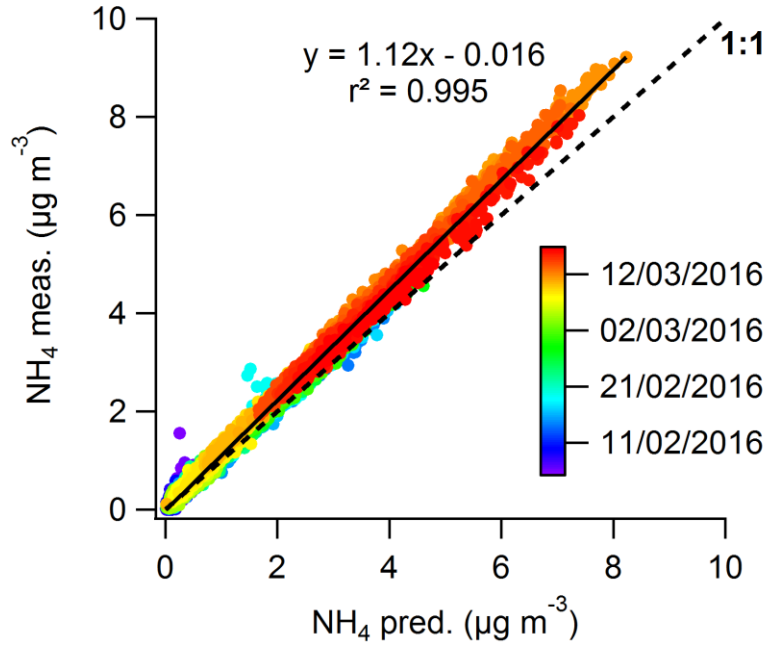


Figure S2.4 Comparison between measured and predicted  $\text{NH}_4$  colored by date. The predicted  $\text{NH}_4$  is calculated as the  $\text{NH}_4$  required to neutralize all  $\text{NO}_3$  and  $\text{SO}_4$ .

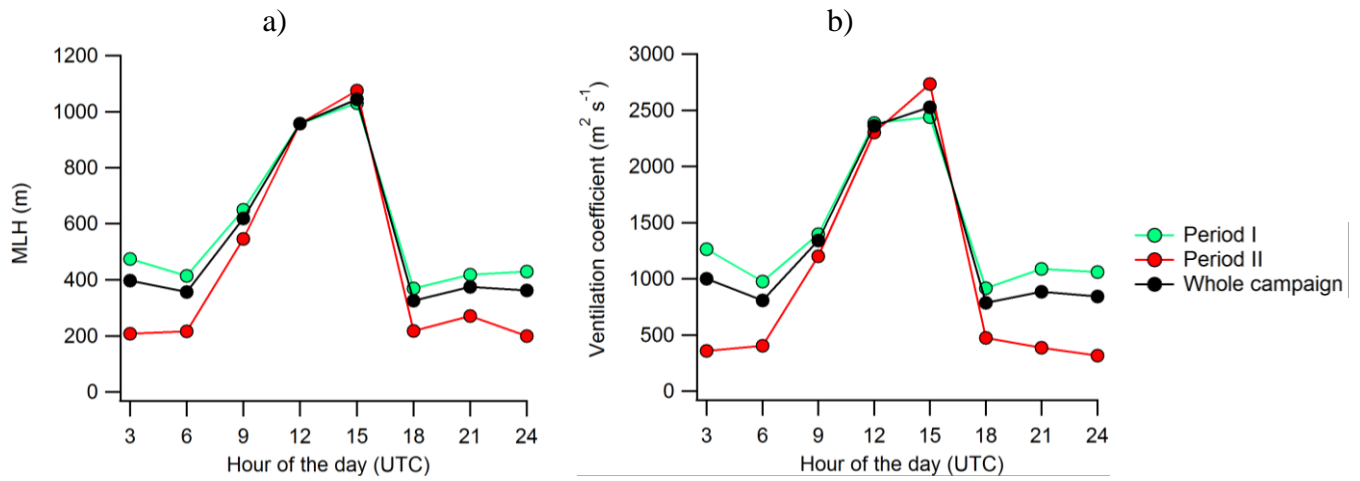


Figure S2.5 Average daily profiles for the (a) MLH (mixing layer height) and (b) ventilation coefficients ( $\text{MLH} \times \text{wind speed}$ ) for the whole campaign, period I and period II

Table S2.1 Justification for the number of selected PMF factors (chosen solution highlighted in bold)

No. of factors	Description of solution
2	Too few factors (mixed mass spectra), no oBBOA or COA were retrieved, large residuals
3	Too few factors (mixed mass spectra), splitting of OOA into two separate factors (MO-OOA and LO-OOA), no oBBOA or COA were retrieved, large residuals at key m/z's
4	HOA, oBBOA, MO-OOA and LO-OOA were identified but key HOA m/z's seem influenced by oxygenated fragments. Residuals reduced but remain fairly high for some m/z's
<b>5</b>	<b>A new COA factor has been identified. Residuals decreased significantly.</b>
6	OOAs now started splitting, but the third OOA factor has similar profile and time series with residuals level remaining the same.
7	HOA started to split without any significant changes of profiles and time series and no changes observed in residuals level.
8	More splitting of OOAs without the emergence of any meaningful new factor or any significant drop in residuals values.

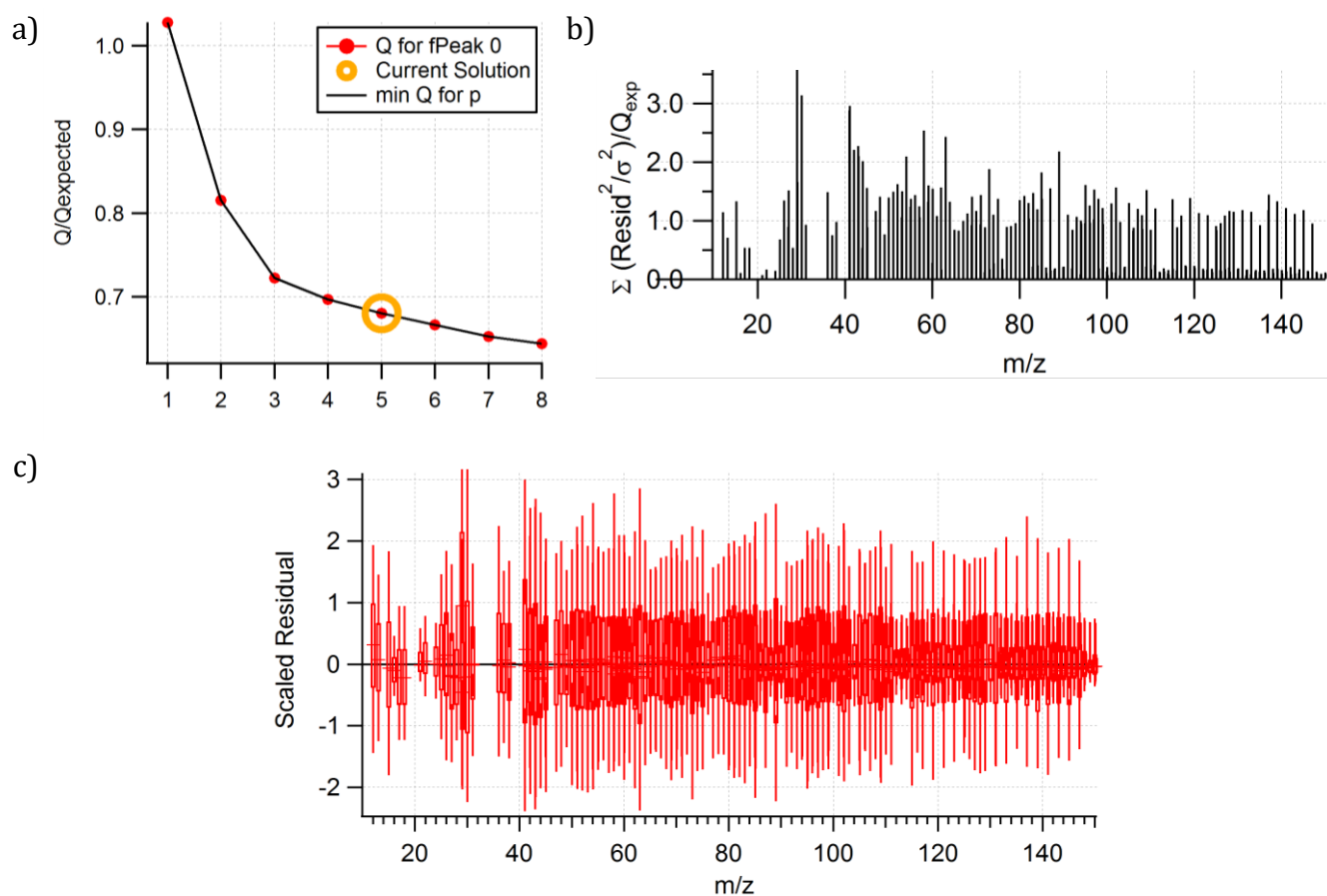


Figure S2.6 PMF diagnostics for the chosen 5-factor solution: (a)  $Q/Q_{\text{expected}}$  variation vs number of factors, (b) Absolute residuals for each  $m/z$ , (c) Scaled residuals for each  $m/z$

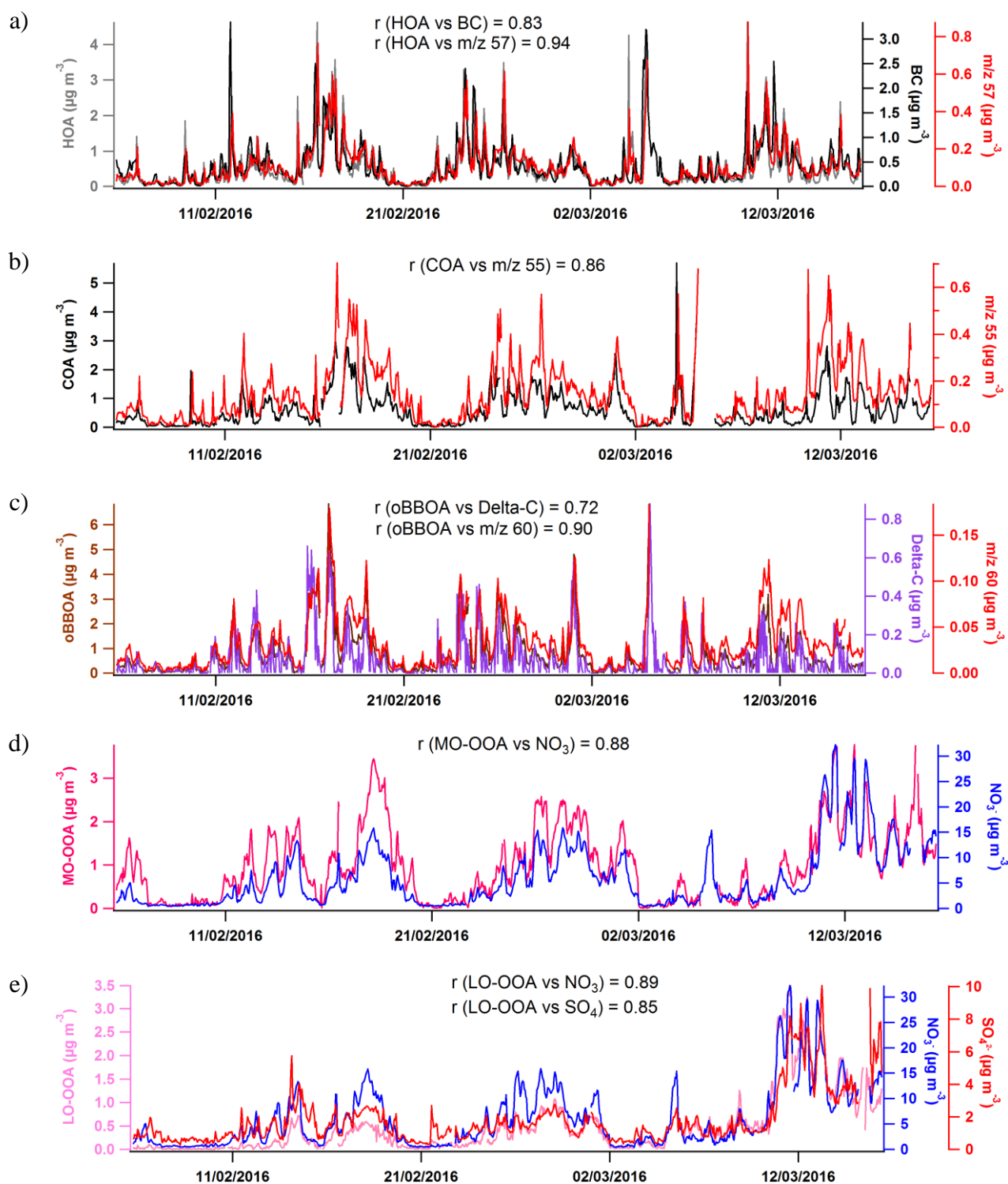


Figure S2.7 Time series of the PMF factors and their respective main inorganic external tracers or specific organic masses from AMS analysis. The determination coefficients ( $r^2$ ) are indicated (see also Table S2).



Table S2.2 Correlation of PMF factors with external variables and meteorological parameters

	NO <sub>3</sub> <sup>-</sup>	SO <sub>4</sub> <sup>2-</sup>	NH <sub>4</sub> <sup>+</sup>	K <sup>+</sup>	PM <sub>2.5</sub>	BC	Delta-C	NO <sub>x</sub>	O <sub>3</sub>	T (°)	RH (%)
COA	0.49	0.31	0.45	0.59	0.65	<b>0.70</b>	0.44	0.68	-0.67	-0.57	0.10
oBBOA	0.32	0.16	0.29	0.60	0.52	0.65	<b>0.72</b>	0.58	-0.72	-0.62	0.24
HOA	0.30	0.18	0.27	0.46	0.49	<b>0.83</b>	0.19	<b>0.85</b>	-0.55	-0.41	0.09
MO-OOA	<b>0.88</b>	0.62	<b>0.84</b>	0.47	<b>0.82</b>	0.35	0.21	0.28	-0.48	-0.35	-0.11
LO-OOA	<b>0.89</b>	<b>0.85</b>	<b>0.92</b>	0.51	<b>0.81</b>	0.28	0.04	0.18	-0.27	-0.14	-0.17

\* Values in red indicate negative correlations. Correlations  $\geq |0.7|$  are highlighted in bold and  $\geq |0.8|$  are underlined. K<sup>+</sup> as measured by MARGA; BC and Delta-C measured by a 2λ-aethalometer; NO<sub>x</sub> measured by NO<sub>x</sub> monitor, O<sub>3</sub> obtained from Atmo Hauts-de-France nearby monitoring station; T (temperature) obtained from a BAM-1020 and RH (relative humidity) from a TEOM-FDMS (Roig et al., submitted).

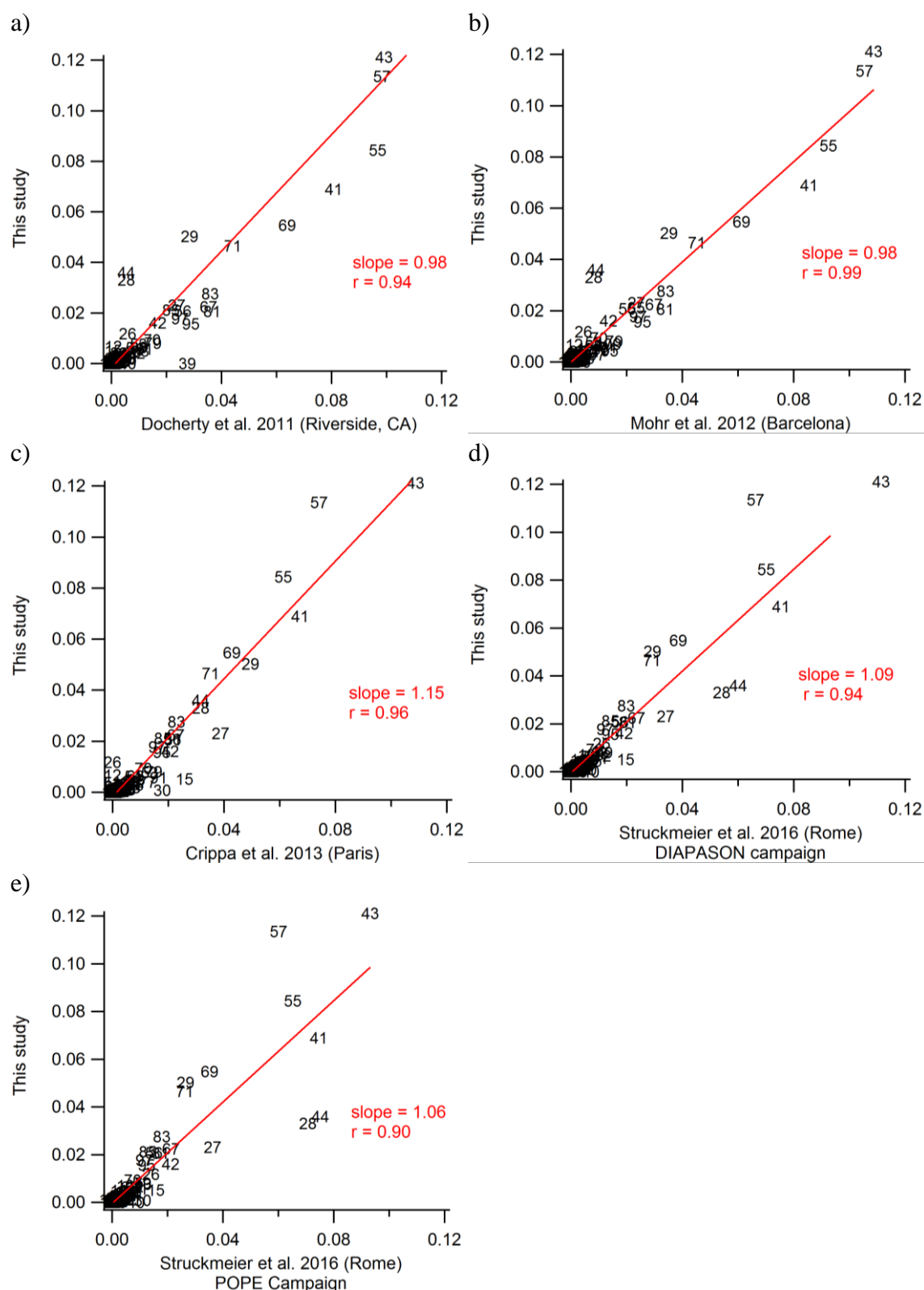


Figure S2.8 Comparison of the HOA mass spectrum obtained in this work with those of other studies (Crippa et al., 2013; Docherty et al., 2011; Mohr et al., 2012; Struckmeier et al., 2016). The numbers indicate the different m/z of the HOA mass spectra. The red line represents the linear fit between both factors, with the slope value and r in red.

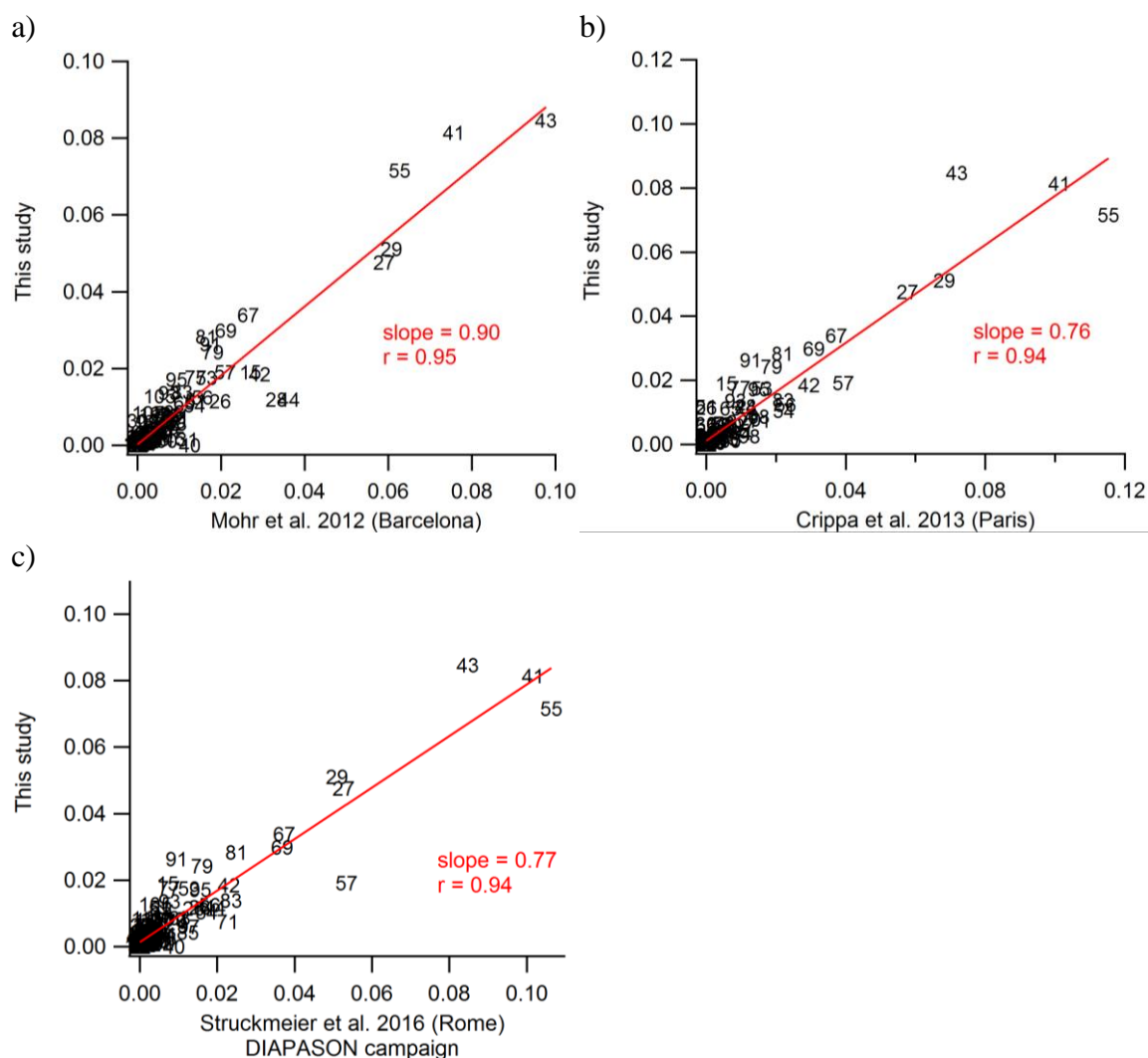


Figure S2.9 Comparison of the COA mass spectrum obtained in this work with those of other studies (Crippa et al., 2013; Mohr et al., 2012; Struckmeier et al., 2016). The numbers indicate the different  $m/z$  of the COA mass spectra. The red line represents the linear fit between both factors, with the slope value and  $r$  in red.

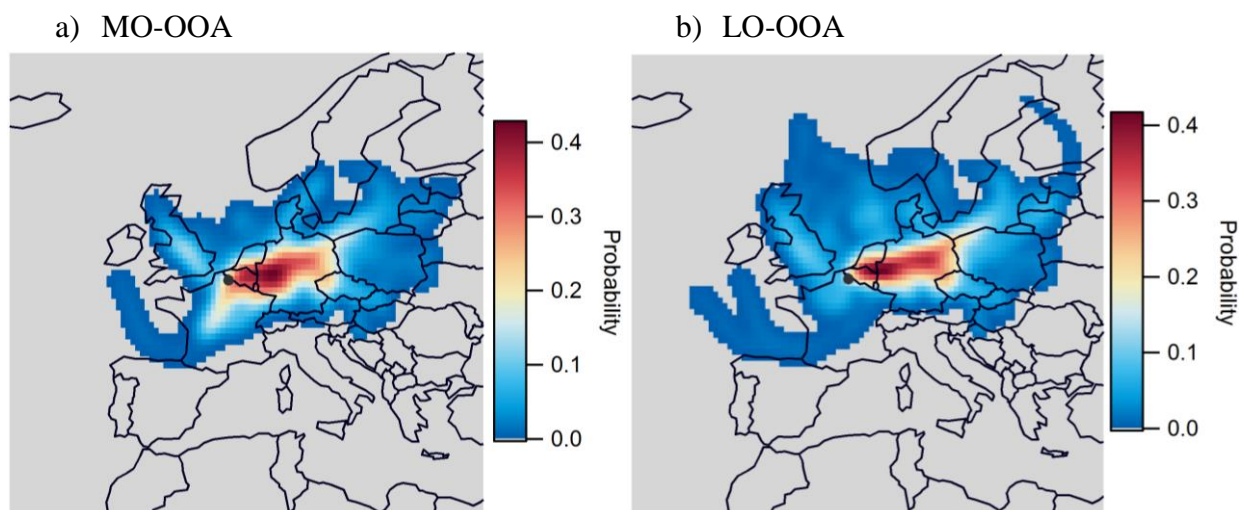


Figure S2.10 PSCF maps for (a) MO-OOA and (b) LO-OOA factors during the whole campaign with a threshold at the 75<sup>th</sup> percentile.

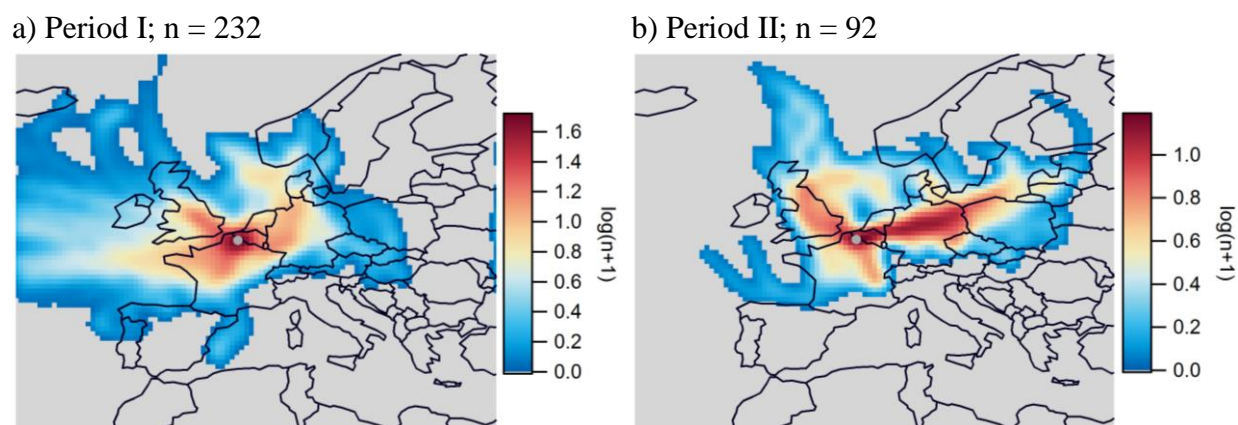


Figure S2.11 Trajectory density map for (a) period I and (b) period II. The color scale is related to the number of trajectories ( $n$ , represented as  $\log(n+1)$ ) which have passed by a specific source area and impacted the sampling site afterwards.

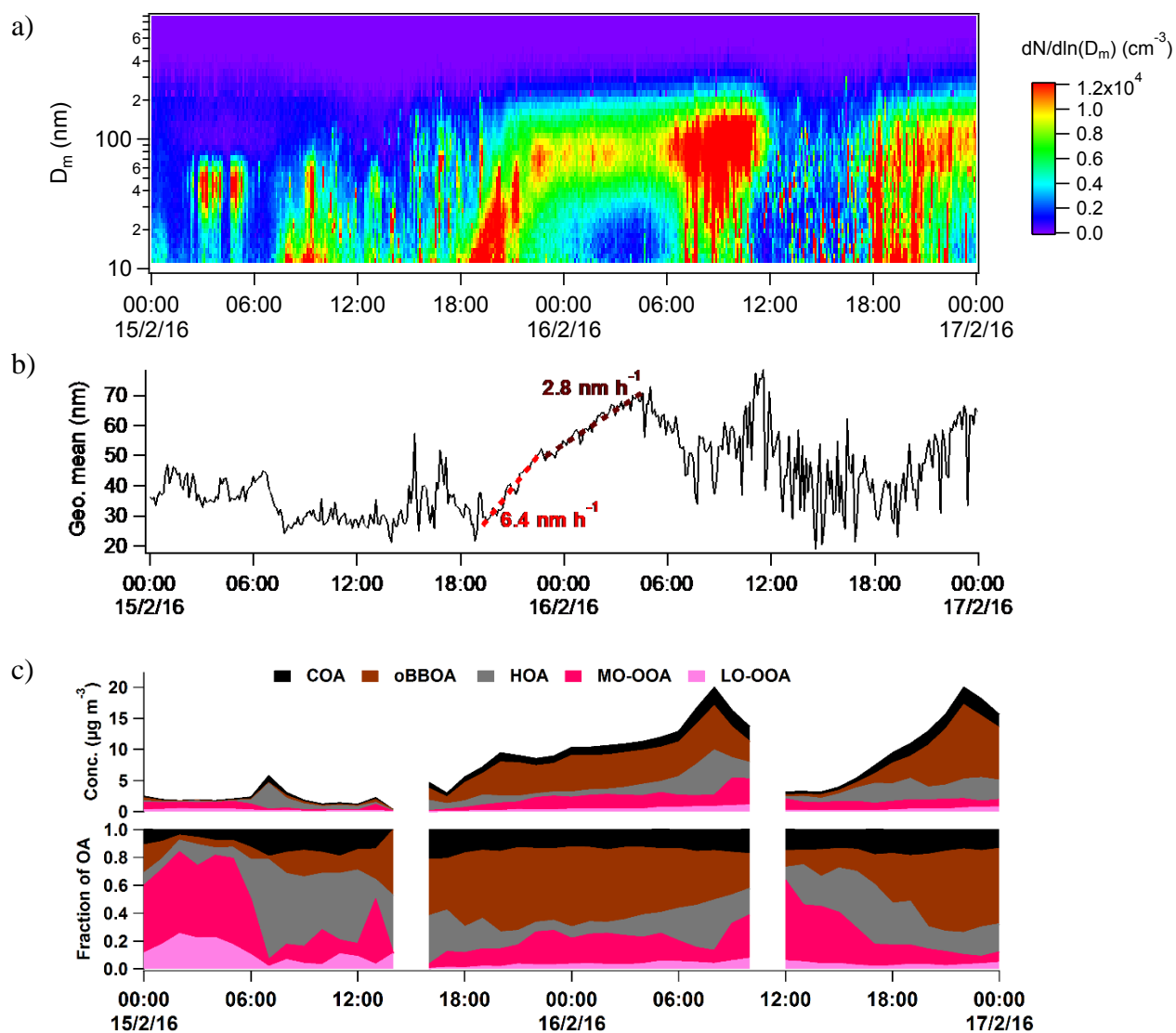


Figure S2.12 (a) Time series of the particle number size distribution (PNSD), (b) geometric mean diameter, (c) PMF factors for the Feb.15-16, 2016 NPF event

## References

- Crippa, M., DeCarlo, P. F., Slowik, J. G., Mohr, C., Heringa, M. F., Chirico, R., Poulain, L., Freutel, F., Sciare, J., Cozic, J., Di Marco, C. F., Elsasser, M., Nicolas, J. B., Marchand, N., Abidi, E., Wiedensohler, A., Drewnick, F., Schneider, J., Borrmann, S., Nemitz, E., Zimmermann, R., Jaffrezo, J.-L., Prévôt, A. S. H. and Baltensperger, U.: Wintertime aerosol chemical composition and source apportionment of the organic fraction in the metropolitan area of Paris, *Atmos. Chem. Phys.*, 13(2), 961–981, doi:10.5194/acp-13-961-2013, 2013.
- Docherty, K. S., Aiken, A. C., Huffman, J. A., Ulbrich, I. M., DeCarlo, P. F., Sueper, D., Worsnop, D. R., Snyder, D. C., Peltier, R. E., Weber, R. J., Grover, B. D., Eatough, D. J., Williams, B. J., Goldstein, A. H., Ziemann, P. J. and Jimenez, J. L.: The 2005 Study of Organic Aerosols at Riverside (SOAR-1): instrumental intercomparisons and fine particle composition, *Atmos. Chem. Phys.*, 11(23), 12387–12420, doi:10.5194/acp-11-12387-2011, 2011.
- Mohr, C., DeCarlo, P. F., Heringa, M. F., Chirico, R., Slowik, J. G., Richter, R., Reche, C., Alastuey, A., Querol, X., Seco, R., Peñuelas, J., Jiménez, J. L., Crippa, M., Zimmermann, R., Baltensperger, U. and Prévôt, A. S. H.: Identification and quantification of organic aerosol from cooking and other sources in Barcelona using aerosol mass spectrometer data, *Atmos. Chem. Phys.*, 12(4), 1649–1665, doi:10.5194/acp-12-1649-2012, 2012.
- Roig, R., Perdrix, E., Herbin, B. and Riffault, V.: Characterization and variability of inorganic aerosols and their gaseous precursors at a suburban site in northern France over one year (2015-2016), submitted.
- Struckmeier, C., Drewnick, F., Fachinger, F., Gobbi, G. P. and Borrmann, S.: Atmospheric aerosols in Rome, Italy: sources, dynamics and spatial variations during two seasons, *Atmos. Chem. Phys.*, 16(23), 15277–15299, doi:10.5194/acp-16-15277-2016, 2016.

## **ANNEX 4: Supplementary material for Article 3**

### **Effect of high temporal resolution and database composition on source apportionment of PM<sub>2.5</sub> using positive matrix factorization**

Roger Roig<sup>1</sup>, Esperanza Perdrix<sup>1</sup>, Laurent Alleman<sup>1</sup>, Bruno Malet<sup>1</sup>, Benoît Herbin<sup>1</sup>,  
Véronique Riffault<sup>1</sup>

<sup>1</sup> IMT Lille Douai, Univ. Lille, SAGE - Département Sciences de l'Atmosphère et Génie de l'Environnement, F-59000 Lille, France

Corresponding author: Esperanza Perdrix (esperanza.perdrix@imt-lille-douai.fr)

#### **Section 1. Supplementary tables**

Table S3.1 Monthly summary of main meteorological parameters  
Table S3.2 Mapping of bootstrap factors to base factors for PMF<sub>h</sub> and PMF<sub>d</sub>  
Table S3.3 Concentration of each variable in the chemical profile for each PMF type  
Table S3.4 Contribution of each variable in the chemical profile for each PMF type  
Table S3.5 Statistics of the comparison between modelled and measured concentrations for each variable for PMF<sub>h</sub> and PMF<sub>d</sub>  
Table S3.6 Correlation of source factors with external variables for PMF<sub>h</sub>.  
Table S3.7 Correlation of source factors with external variables for PMF<sub>d</sub>.  
Table S3.8 Comparison of different SA studies carried out over one year in North Western Europe as discussed in section 3.5

#### **Section 2. Supplementary figures**

Figure S3.1 Correlation between modelled and observed hourly PM<sub>2.5</sub> concentrations  
Figure S3.2 Time series of analogous source factors between PMF<sub>h</sub> and PMF<sub>org</sub>  
Figure S3.3 Contribution of the different PMF<sub>h</sub> source factors in weekdays, Saturdays and Sundays  
Figure S3.4 Contribution of the different PMF<sub>h</sub> source factors during daytime and nighttime for each season  
Figure S3.5 Correlation between biomass factor concentrations and observed temperatures  
Figure S3.6 Gridded NO<sub>x</sub>, SO<sub>x</sub> and NH<sub>3</sub> emissions for 2015 from EMEP  
Figure S3.7 NWR plot for the MIB factor together with the map of northern France

Figure S3.8 NWR plot for the local industry factor together with the map of Douai and its surroundings

### Section 3. Calculation of uncertainties

#### Section 4. Comparison between PMFh and PMFd with the same input variables

Figure S3.9 Contribution of source factors to modelled PM<sub>2.5</sub> mass for PMFh and PMFd with the same input variables

Table S3.9 Concentrations of each variable in the chemical profile of the source factors for the hourly and daily PMF with the same input variables.

Table S3.10 Contributions (%) of each variable in the source chemical profiles for the hourly and daily PMF with the same input variables.

Table S3.11 Statistics comparing the modelled and measured concentrations for each variable used in the hourly and daily PMF with the same input variables.

## SECTION 1. SUPPLEMENTARY TABLES

Table S3.1 Annual and monthly averages and standard deviations of the main meteorological parameters (except for the rain where the value accumulated over each month is given)

Month	Wind speed (m s <sup>-1</sup> )	Temperature (°C)	RH (%)	P (mbar)	Rain (mL)
August	1.3 ± 0.7	20 ± 5	74 ± 17	1021 ± 5	87
September	1.3 ± 0.8	14 ± 4	81 ± 13	1019 ± 10	58
October	1.0 ± 0.6	11 ± 4	86 ± 11	1015 ± 6	46
November	2.1 ± 1.3	11 ± 5	88 ± 6	1015 ± 7	69
December	1.9 ± 0.9	10 ± 3	87 ± 5	1020 ± 5	20
January	1.9 ± 1.2	6 ± 4	87 ± 7	1008 ± 14	61
February	1.8 ± 1.3	6 ± 4	84 ± 11	1008 ± 12	76
March	1.5 ± 1.2	7 ± 3	79 ± 12	1011 ± 11	50
April	1.3 ± 1.1	10 ± 4	77 ± 14	1010 ± 7	41
May	1.0 ± 0.8	15 ± 5	75 ± 18	1011 ± 7	105
June	1.3 ± 0.9	17 ± 4	84 ± 13	1012 ± 7	65
July	1.4 ± 1.1	20 ± 5	74 ± 15	1015 ± 4	22
<b>YEAR</b>	<b>1.5 ± 1.1</b>	<b>12 ± 6</b>	<b>81 ± 14</b>	<b>1014 ± 9</b>	<b>700</b>



Table S3.2 Mapping of bootstrap factors to base factors for PMF<sub>h</sub> and PMF<sub>d</sub> (n = 100)

		Base factors								
		Sulfate-rich	Nitrate-rich	Biomass combustion	Marine	Road traffic	MIB*	Dust	Local industry	Unmapped
PMF <sub>h</sub> boot factors	Sulfate-rich	100	0	0	0	0				0
	Nitrate-rich	0	92	8	0	0				0
	Biomass combustion	0	0	100	0	0				0
	Marine	0	0	0	100	0				0
	Road traffic	0	0	0	0	100				0
PMF <sub>d</sub> boot factors	Sulfate-rich	100	0	0	0	0	0	0	0	0
	Nitrate-rich	0	100	0	0	0	0	0	0	0
	Biomass combustion	0	0	99	0	1	0	0	0	0
	Marine	0	0	0	100	0	0	0	0	0
	Road traffic	1	0	0	0	99	0	0	0	0
	MIB*	1	0	0	0	0	99	0	0	0
	Dust	0	0	0	0	5	0	95	0	0
	Local industry	0	0	0	0	3	0	0	97	0

\* MIB: Metal Industry Background

Table S3.3 Concentrations of each variable in the chemical profile of the source factors for the hourly and daily PMF (PM<sub>2.5</sub>, NO<sub>3</sub><sup>-</sup>, SO<sub>4</sub><sup>2-</sup>, C<sub>2</sub>O<sub>4</sub><sup>2-</sup>, NH<sub>4</sub><sup>+</sup>, BC and Delta-C are in µg m<sup>-3</sup>, the rest in ng m<sup>-3</sup>).

Factor		Sulfate-rich		Nitrate-rich		Road traffic		Biomass combustion		Marine		MIB*	Dust	Local industry
PMF <sub>type</sub>		PMF <sub>d</sub>	PMF <sub>h</sub>	PMF <sub>d</sub>	PMF <sub>h</sub>	PMF <sub>d</sub>	PMF <sub>h</sub>	PMF <sub>d</sub>	PMF <sub>h</sub>	PMF <sub>d</sub>	PMF <sub>h</sub>	PMF <sub>d</sub>	PMF <sub>d</sub>	PMF <sub>d</sub>
Variables	PM <sub>2.5</sub>	4.59	4.92	4.03	3.20	0.76	2.06	1.59	0.55	1.03	1.30	0.79	0.34	0.09
	NO <sub>3</sub> <sup>-</sup>	0.04	0.00	2.58	3.01	0.49	0.59	0.52	0.02	0.15	0.13	0.00	0.00	0.04
	SO <sub>4</sub> <sup>2-</sup>	0.88	1.32	0.47	0.16	0.00	0.10	0.00	0.00	0.07	0.17	0.25	0.02	0.01
	C <sub>2</sub> O <sub>4</sub> <sup>2-</sup>	0.10	0.10	0.02	0.00	0.01	0.02	0.01	0.00	0.01	0.02	0.02	0.00	0.00
	NH <sub>4</sub> <sup>+</sup>	0.23	0.41	0.88	0.84	0.00	0.00	0.08	0.00	0.00	0.00	0.09	0.00	0.00
	BC	0.11	0.03	0.00	0.00	0.21	0.36	0.09	0.02	0.00	0.00	0.00	0.00	0.00
	Na <sup>+</sup>	0.00	2.82	2.82	1.64	6.33	0.00	4.75	0.83	81.31	79.33	0.00	0.00	0.00
	Mg <sup>+</sup>	1.90	2.36	1.24	0.10	1.98	1.45	0.56	0.25	11.56	9.83	0.00	0.00	0.14
	K <sup>+</sup>	5.01	4.42	0.09	1.62	2.20	5.97	12.01	4.98	1.80	3.53	5.01	0.00	0.54
	Delta-C	0.00	0.57	0.00	0.00	0.00	0.16	23.37	23.35	1.21	0.58	0.83	0.00	0.28
	Ca	8.53		0.00		6.54		1.69		5.06		0.00	66.98	0.00
	Fe	0.00		0.04		29.09		3.94		0.00		30.65	18.78	2.17
	K	4.60		0.72		0.00		5.88		4.98		52.08	11.60	0.02
	As	0.00		0.05		0.11		0.02		0.01		0.12	0.01	0.00
	Ba	0.05		0.00		0.68		0.00		0.03		0.53	0.11	0.00
	Bi	0.00		0.01		0.01		0.00		0.00		0.01	0.00	0.00
	Cd	0.00		0.00		0.02		0.00		0.00		0.06	0.00	0.00
	Ce	0.00		0.00		0.03		0.00		0.00		0.05	0.01	0.00
	Co	0.00		0.00		0.01		0.00		0.00		0.01	0.00	0.01
	Cr	0.13		0.03		0.25		0.10		0.04		0.00	0.00	1.28
	Cu	0.02		0.00		1.94		0.10		0.14		1.20	0.08	0.06
	Mn	0.00		0.00		1.68		0.00		0.13		0.75	0.00	0.00
	Mo	0.01		0.04		0.17		0.00		0.01		0.08	0.01	0.02
	Ni	0.10		0.00		0.00		0.03		0.01		0.07	0.00	0.93
	Pb	0.04		0.19		0.75		0.23		0.01		2.07	0.00	0.01
	Rb	0.01		0.00		0.02		0.01		0.00		0.13	0.01	0.00
	Sb	0.06		0.00		0.27		0.03		0.00		0.32	0.03	0.00
	Se	0.15		0.12		0.31		0.00		0.00		0.24	0.01	0.00
	Sr	0.04		0.00		0.07		0.00		0.06		0.07	0.10	0.00
	Zn	1.08		0.65		4.68		0.41		0.04		6.82	0.00	0.00

\* MIB: Metal Industry Background

Table S3.4 Contributions (%) of each variable in the chemical profile of the source factors for the hourly and daily PMF.

Factor		Sulfate-rich		Nitrate-rich		Road traffic		Biomass combustion		Marine		MIB*	Dust	Local industry
PMF <sub>type</sub>		PMF <sub>d</sub>	PMF <sub>h</sub>	PMF <sub>d</sub>	PMF <sub>h</sub>	PMF <sub>d</sub>	PMF <sub>h</sub>	PMF <sub>d</sub>	PMF <sub>h</sub>	PMF <sub>d</sub>	PMF <sub>h</sub>	PMF <sub>d</sub>	PMF <sub>d</sub>	PMF <sub>d</sub>
Variables	PM <sub>2.5</sub>	34.7	40.9	30.5	26.6	5.8	17.1	12.0	4.6	7.8	10.8	5.9	2.6	0.7
	NO <sub>3</sub> <sup>-</sup>	1.0	0.0	67.5	80.3	12.8	15.7	13.7	0.6	4.0	3.4	0.0	0.0	1.0
	SO <sub>4</sub> <sup>2-</sup>	51.7	76.0	27.7	9.0	0.0	5.5	0.0	0.0	4.0	9.5	14.8	1.0	0.8
	C <sub>2</sub> O <sub>4</sub> <sup>2-</sup>	62.8	69.1	11.6	0.0	4.4	17.0	3.6	1.5	3.9	12.3	11.8	1.9	0.0
	NH <sub>4</sub> <sup>+</sup>	18.0	32.4	68.3	67.6	0.0	0.0	6.3	0.0	0.0	0.0	7.4	0.0	0.0
	BC	26.6	7.9	0.0	0.0	51.3	87.6	22.1	4.6	0.0	0.0	0.0	0.0	0.0
	Na <sup>+</sup>	0.0	3.3	3.0	1.9	6.6	0.0	5.0	1.0	85.4	93.8	0.0	0.0	0.0
	Mg <sup>+</sup>	10.9	16.9	7.1	0.7	11.4	10.4	3.2	1.8	66.5	70.3	0.0	0.0	0.8
	K <sup>+</sup>	18.8	21.5	0.3	7.9	8.2	29.1	45.0	24.2	6.8	17.2	18.8	0.0	2.0
	Delta-C	0.0	2.3	0.0	0.0	0.0	0.7	91.0	94.7	4.7	2.3	3.2	0.0	1.1
	Ca	9.6		0.0		7.4		1.9		5.7		0.0	75.4	0.0
	Fe	0.0		0.1		34.4		4.7		0.0		36.2	22.2	2.6
	K	5.8		0.9		0.0		7.4		6.2		65.2	14.5	0.0
	As	0.6		14.8		34.0		6.8		3.4		37.9	1.8	0.7
	Ba	3.9		0.0		48.6		0.0		2.0		37.8	7.7	0.0
	Bi	0.0		16.6		44.3		1.0		3.2		19.5	13.1	2.3
	Cd	0.0		5.8		18.4		4.2		0.0		68.5	2.9	0.2
	Ce	4.7		0.0		30.7		2.2		2.8		48.8	10.8	0.0
	Co	9.5		0.6		15.3		0.0		3.3		34.0	5.9	31.4
	Cr	7.3		1.4		13.8		5.3		2.0		0.0	0.0	70.2
	Cu	0.7		0.0		54.8		2.8		4.1		33.9	2.1	1.7
	Mn	0.0		0.0		65.6		0.0		5.1		29.3	0.0	0.0
	Mo	3.0		12.0		49.2		0.7		4.4		22.6	3.3	4.8
	Ni	9.1		0.0		0.0		2.4		0.9		5.8	0.4	81.4
	Pb	1.2		5.6		22.9		6.9		0.2		63.0	0.0	0.2
	Rb	3.2		2.5		12.5		5.0		0.6		69.0	7.2	0.0
	Sb	7.8		0.0		38.9		3.8		0.0		44.7	4.8	0.0
	Se	17.6		14.0		37.4		0.0		0.0		29.4	1.1	0.5
	Sr	10.8		0.0		20.8		0.0		16.8		20.8	29.3	1.5
	Zn	7.9		4.7		34.2		3.0		0.3		49.8	0.0	0.0

\* MIB: Metal Industry Background

Table S3.5 Statistics comparing the modelled and measured concentrations for each variable used in PMF<sub>d</sub> and PMF<sub>h</sub>. Intercept in  $\mu\text{g m}^{-3}$

	PMF <sub>d</sub>			PMF <sub>h</sub>		
Species	r <sup>2</sup>	Slope	Intercept	r <sup>2</sup>	Slope	Intercept
NO <sub>3</sub> <sup>-</sup>	0.98	1.01	-0.05	0.99	1.04	-0.11
SO <sub>4</sub> <sup>2-</sup>	0.96	0.97	0.04	0.98	1.01	-0.02
C <sub>2</sub> O <sub>4</sub> <sup>2-</sup>	0.58	0.73	0.03	0.38	0.52	0.05
Na <sup>+</sup>	0.96	0.85	0.01	0.92	0.81	0.02
NH <sub>4</sub> <sup>+</sup>	0.99	0.93	0.04	0.99	0.90	0.06
K <sup>+</sup>	0.58	0.41	0.01	0.26	0.20	0.01
Mg <sup>2+</sup>	0.64	0.59	0.01	0.38	0.32	0.01
BC	0.69	0.71	0.09	0.79	0.77	0.08
Delta-C	0.94	0.95	0.00	1.00	1.00	0.00
PM <sub>2.5</sub>	0.90	1.01	-0.44	0.83	0.92	-0.20
Ca	0.99	0.99	0.00			
Fe	0.84	0.63	0.02			
K	0.93	0.90	0.00			
As	0.51	0.31	0.00			
Ba	0.67	0.55	0.00			
Bi	0.60	0.21	0.00			
Cd	0.54	0.35	0.00			
Ce	0.57	0.36	0.00			
Co	0.66	0.49	0.00			
Cr	0.79	0.67	0.00			
Cu	0.80	0.69	0.00			
Mn	0.37	0.33	0.00			
Mo	0.55	0.29	0.00			
Ni	0.98	0.97	0.00			
Pb	0.66	0.53	0.00			
Rb	0.89	0.82	0.00			
Sb	0.61	0.51	0.00			
Se	0.59	0.41	0.00			
Sr	0.48	0.34	0.00			
Zn	0.40	0.28	0.01			

Table S3.6 Correlation coefficients (r) of source factors with external variables for PMF<sub>h</sub>. The values in red indicate negative correlations. The correlations  $\geq 0.7$  are highlighted in bold, and those  $\geq 0.8$  and  $0.9$  with simple and double underline, respectively. (BC: Black carbon, T: Temperature, RH: Relative humidity, P<sub>atm</sub>: atmospheric pressure, WS: wind speed)

	Sulfate-rich	Nitrate-rich	Road traffic	Biomass combustion	Marine
<b>Nitrate-rich</b>	0.57				
<b>Road traffic</b>	0.19	0.26			
<b>Biomass combustion</b>	-0.01	0.18	-0.02		
<b>Marine</b>	-0.32	-0.23	-0.11	-0.08	
<b>Cl<sup>-</sup></b>	0.01	0.06	-0.02	0.07	0.40
<b>NO<sub>3</sub><sup>-</sup></b>	0.56	<u><b>0.99</b></u>	0.38	0.18	-0.21
<b>SO<sub>4</sub><sup>2-</sup></b>	<u><b>0.97</b></u>	0.68	0.26	0.01	-0.21
<b>C<sub>2</sub>O<sub>4</sub><sup>2-</sup></b>	0.62	0.36	0.20	-0.03	-0.27
<b>Na<sup>+</sup></b>	-0.24	-0.16	-0.09	-0.03	<u><b>0.96</b></u>
<b>NH<sub>4</sub><sup>+</sup></b>	<b>0.74</b>	<u><b>0.97</b></u>	0.27	0.16	-0.28
<b>K<sup>+</sup></b>	0.13	0.28	0.21	0.45	-0.04
<b>Mg<sup>2+</sup></b>	-0.15	-0.10	-0.03	-0.04	0.63
<b>Ca<sup>2+</sup></b>	0.21	0.07	0.27	-0.07	-0.01
<b>PM<sub>2.5</sub></b>	0.69	<u><b>0.86</b></u>	0.41	0.20	-0.22
<b>BC</b>	0.26	0.28	<u><b>0.91</b></u>	0.17	-0.19
<b>Delta-C</b>	0.00	0.18	-0.02	<u><b>0.99</b></u>	-0.07
<b>HONO</b>	0.23	0.47	0.54	0.27	-0.14
<b>SO<sub>2</sub></b>	0.25	0.17	0.10	0.00	-0.01
<b>NH<sub>3</sub></b>	0.40	0.24	0.03	-0.17	-0.24
<b>NO</b>	0.07	0.13	0.54	0.07	-0.03
<b>NO<sub>2</sub></b>	0.23	0.30	0.63	0.26	-0.17
<b>O<sub>3</sub></b>	-0.02	-0.31	-0.41	-0.31	0.12
<b>T</b>	0.20	-0.21	-0.04	-0.42	-0.13
<b>RH</b>	-0.13	0.07	0.06	0.13	-0.06
<b>P<sub>atm</sub></b>	0.20	0.11	0.15	0.05	0.04
<b>WS</b>	-0.27	-0.27	-0.41	-0.11	0.30
<b>Rain</b>	-0.06	-0.06	-0.04	-0.03	-0.05

Table S3.7 Correlation coefficients (r) of source factors with external variables for PMF<sub>d</sub>. The values in red indicate negative correlations. The correlations  $\geq 0.7$  are highlighted in bold, and those  $\geq 0.8$  and  $\geq 0.9$  with simple and double underline, respectively. (MIB: Metal industry background, BC: Black carbon, T: Temperature, RH: Relative humidity, Patm: atmospheric pressure, WS: wind speed)

	Sulfate-rich	Nitrate-rich	Road traffic	Biomass combustion	Marine	MIB	Dust	Local industry
Nitrate-rich	0.29							
Road traffic	0.03	0.14						
Biomass	-0.19	0.21	-0.16					
Marine	-0.25	-0.34	-0.24	-0.11				
MIB	-0.15	0.19	0.45	0.14	-0.09			
Dust	-0.11	0.01	0.48	-0.03	0.01	0.44		
Local industry	-0.06	0.00	0.30	0.03	-0.10	0.25	0.27	
Cl <sup>-</sup>	-0.07	0.04	-0.13	0.25	0.55	-0.06	-0.01	-0.08
NO <sub>3</sub> <sup>-</sup>	0.20	<u>0.97</u>	0.25	0.34	-0.33	0.29	0.07	0.07
SO <sub>4</sub> <sup>2-</sup>	0.66	<u>0.82</u>	0.24	0.04	-0.30	0.36	0.11	0.05
C <sub>2</sub> O <sub>4</sub> <sup>2-</sup>	0.65	0.54	0.16	-0.02	-0.37	0.23	0.03	0.00
Na <sup>+</sup>	-0.23	-0.25	-0.15	-0.03	<u>0.97</u>	-0.04	0.06	-0.07
NH <sub>4</sub> <sup>+</sup>	0.38	<u>0.98</u>	0.16	0.32	-0.36	0.24	0.04	0.03
K <sup>+</sup>	-0.05	0.26	0.13	<b>0.70</b>	-0.07	0.34	0.04	0.11
Mg <sup>2+</sup>	-0.17	-0.14	-0.04	-0.09	<b>0.78</b>	-0.03	-0.01	-0.03
Ca <sup>2+</sup>	0.24	0.16	0.57	-0.05	-0.11	0.22	0.55	0.16
BC	0.22	0.41	0.64	0.33	-0.30	0.46	0.22	0.14
Delta-C	-0.22	0.19	-0.16	<u>0.97</u>	-0.08	0.14	-0.03	0.05
PM <sub>2.5</sub>	0.41	<u>0.91</u>	0.22	0.33	-0.34	0.32	0.08	0.06
Ca	-0.07	0.01	0.52	-0.04	0.04	0.43	<u>0.99</u>	0.26
Fe	-0.10	0.15	<b>0.72</b>	0.12	-0.15	<b>0.75</b>	<b>0.70</b>	0.39
K	-0.16	0.18	0.40	0.21	-0.01	<u>0.95</u>	0.52	0.25
Mg	-0.21	-0.13	0.18	-0.16	0.42	0.21	0.44	0.17
Na	-0.23	-0.20	-0.11	-0.05	0.66	0.09	0.29	0.07
As	0.08	0.34	0.58	0.03	-0.11	0.59	0.36	0.17
Ba	-0.04	0.05	<b>0.70</b>	0.00	-0.15	0.66	0.61	0.28
Bi	-0.02	0.25	0.65	-0.01	-0.11	<b>0.71</b>	0.45	0.19
Cd	-0.03	0.18	0.59	0.04	-0.11	0.69	0.34	0.22
Ce	-0.11	0.04	0.48	0.06	-0.10	<b>0.76</b>	0.39	0.24
Co	-0.07	0.11	0.60	-0.03	-0.10	0.61	0.48	0.61
Cr	-0.03	0.05	0.45	0.04	-0.16	0.28	0.29	<u>0.87</u>
Cu	-0.06	0.14	<u>0.80</u>	0.00	-0.16	<b>0.71</b>	0.52	0.31
Mn	-0.10	0.00	0.55	-0.12	-0.06	0.47	0.38	0.31
Mo	0.04	0.22	<b>0.73</b>	-0.02	-0.14	0.45	0.50	0.25
Ni	-0.03	0.02	0.30	0.05	-0.10	0.29	0.27	<u>0.99</u>
Pb	-0.03	0.24	0.56	0.10	-0.16	<b>0.77</b>	0.38	0.27
Rb	-0.08	0.26	0.51	0.15	-0.13	<u>0.94</u>	0.47	0.25
Sb	-0.04	0.10	0.65	0.02	-0.18	0.69	0.38	0.20
Se	0.15	0.39	0.62	0.02	-0.22	0.60	0.32	0.16
Sn	-0.11	0.03	0.19	-0.06	0.04	0.24	0.26	0.10
Sr	-0.07	-0.08	0.35	-0.11	0.18	0.47	0.67	0.19
Zn	0.00	0.17	0.56	-0.03	-0.13	0.54	0.30	0.29
V	0.16	0.06	0.16	0.00	-0.07	0.55	0.24	0.25
HONO	0.10	0.53	0.44	0.59	-0.32	0.38	0.17	0.11
SO <sub>2</sub>	0.35	0.37	0.22	0.02	-0.06	0.15	0.07	0.01
NH <sub>3</sub>	0.40	0.35	0.18	-0.25	-0.34	-0.06	0.04	-0.05
NO	0.03	0.26	0.46	0.49	-0.22	0.43	0.24	0.17
NO <sub>2</sub>	0.12	0.44	0.43	0.51	-0.39	0.37	0.24	0.13
O <sub>3</sub>	0.22	-0.28	-0.31	-0.49	0.22	-0.47	-0.10	-0.19
T	0.43	-0.16	0.19	-0.65	-0.13	-0.11	0.06	0.00
RH	-0.23	-0.04	-0.17	0.17	0.07	0.12	-0.22	-0.02
Patm	0.15	0.11	0.25	0.06	-0.05	0.28	0.22	0.12
WS	-0.37	-0.39	-0.46	-0.12	0.54	-0.18	-0.09	-0.09
Rain	-0.10	-0.09	-0.11	-0.11	0.04	-0.14	-0.17	-0.06

Table S3.8 Comparison of different SA studies carried out over one year in North Western Europe as discussed in section 3.5

Source factor	Reference	Location	Site typology	Receptor model	Year	PM fraction	PM mass $\mu\text{g m}^{-3}$	Source contribution $\mu\text{g m}^{-3}$	%
Sulfate-rich	This study (PMF <sub>a</sub> )	Douai (FR)	Suburb.	EPA PMF 5.0	2015-2016	PM <sub>2.5</sub>	13.3	4.6	35%
	This study (PMF <sub>b</sub> )	Douai (FR)	Suburb.	EPA PMF 5.0	2015-2016	PM <sub>2.5</sub>	12.1	4.9	41%
	Bressi et al. (2014)	Paris (FR)	Urban	EPA PMF 3.0	2009-2010	PM <sub>2.5</sub>	14.7	3.9	27%
	Mooibroek et al. (2011)	Schiedam (NL)	Urban	EPA PMF 3.0	2007-2008	PM <sub>2.5</sub>	13	3.0	23%
	Mooibroek et al. (2011)	Hellendoorn (NL)	Rural	EPA PMF 3.0	2007-2008	PM <sub>2.5</sub>	12.5	3.1	25%
	Mooibroek et al. (2011)	Rotterdam (NL)	Kerbside	EPA PMF 3.0	2007-2008	PM <sub>2.5</sub>	16.4	3.3	20%
	Mooibroek et al. (2011)	Vredepeel (NL)	Rural	EPA PMF 3.0	2007-2008	PM <sub>2.5</sub>	14.5	4.4	30%
	Mooibroek et al. (2011)	Cabauw (NL)	Rural	EPA PMF 3.0	2007-2008	PM <sub>2.5</sub>	17.5	4.9	28%
Nitrate-rich	Waked et al. (2014)	Lens (FR)	Urban	EPA PMF 3.0	2011-2012	PM <sub>10</sub>	20.5	2.8	14%
	This study (PMF <sub>a</sub> )	Douai (FR)	Suburb.	EPA PMF 5.0	2015-2016	PM <sub>2.5</sub>	13.3	4.0	30%
	This study (PMF <sub>b</sub> )	Douai (FR)	Suburb.	EPA PMF 5.0	2015-2016	PM <sub>2.5</sub>	12.1	3.2	26%
	Bressi et al. (2014)	Paris (FR)	Urban	EPA PMF 3.0	2009-2010	PM <sub>2.5</sub>	14.7	3.5	24%
	Mooibroek et al. (2011)	Schiedam (NL)	Urban	EPA PMF 3.0	2007-2008	PM <sub>2.5</sub>	13	5.6	43%
	Mooibroek et al. (2011)	Hellendoorn (NL)	Rural	EPA PMF 3.0	2007-2008	PM <sub>2.5</sub>	12.5	6.0	48%
	Mooibroek et al. (2011)	Rotterdam (NL)	Kerbside	EPA PMF 3.0	2007-2008	PM <sub>2.5</sub>	16.4	6.7	41%
	Mooibroek et al. (2011)	Vredepeel (NL)	Rural	EPA PMF 3.0	2007-2008	PM <sub>2.5</sub>	14.5	6.4	44%
Road traffic	Mooibroek et al. (2011)	Cabauw (NL)	Rural	EPA PMF 3.0	2007-2008	PM <sub>2.5</sub>	17.5	7.7	44%
	Waked et al. (2014)	Lens (FR)	Urban	EPA PMF 3.0	2011-2012	PM <sub>10</sub>	20.5	2.8	14%
	This study (PMF <sub>a</sub> )	Douai (FR)	Suburb.	EPA PMF 5.0	2015-2016	PM <sub>2.5</sub>	13.3	0.8	6%
	This study (PMF <sub>b</sub> )	Douai (FR)	Suburb.	EPA PMF 5.0	2015-2016	PM <sub>2.5</sub>	12.1	2.1	17%
	Bressi et al. (2014)	Paris (FR)	Urban	EPA PMF 3.0	2009-2010	PM <sub>2.5</sub>	14.7	2.1	14%
	Mooibroek et al. (2011)*	Schiedam (NL)	Urban	EPA PMF 3.0	2007-2008	PM <sub>2.5</sub>	13	1.2	9%
	Mooibroek et al. (2011)*	Hellendoorn (NL)	Rural	EPA PMF 3.0	2007-2008	PM <sub>2.5</sub>	12.5	0.6	5%
	Mooibroek et al. (2011)*	Rotterdam (NL)	Kerbside	EPA PMF 3.0	2007-2008	PM <sub>2.5</sub>	16.4	3.4	21%
Biomass combustion	Mooibroek et al. (2011)*	Vredepeel (NL)	Rural	EPA PMF 3.0	2007-2008	PM <sub>2.5</sub>	14.5	1.0	7%
	Mooibroek et al. (2011)*	Cabauw (NL)	Rural	EPA PMF 3.0	2007-2008	PM <sub>2.5</sub>	17.5	1.1	6%
	Waked et al. (2014)	Lens (FR)	Urban	EPA PMF 3.0	2011-2012	PM <sub>10</sub>	20.5	1.2	6%
	This study (PMF <sub>a</sub> )	Douai (FR)	Suburb.	EPA PMF 5.0	2015-2016	PM <sub>2.5</sub>	13.3	1.6	12%
Marine aerosols	This study (PMF <sub>b</sub> )	Douai (FR)	Suburb.	EPA PMF 5.0	2015-2016	PM <sub>2.5</sub>	12.1	0.6	5%
	Bressi et al. (2014)	Paris (FR)	Urban	EPA PMF 3.0	2009-2010	PM <sub>2.5</sub>	14.7	1.8	12%
	Waked et al. (2014)	Lens (FR)	Urban	EPA PMF 3.0	2011-2012	PM <sub>10</sub>	20.5	2.6	13%
	This study (PMF <sub>a</sub> )	Douai (FR)	Suburb.	EPA PMF 5.0	2015-2016	PM <sub>2.5</sub>	13.3	1.0	8%
Industry	This study (PMF <sub>b</sub> )	Douai (FR)	Suburb.	EPA PMF 5.0	2015-2016	PM <sub>2.5</sub>	12.1	1.3	11%
	Bressi et al. (2014)	Paris (FR)	Urban	EPA PMF 3.0	2009-2010	PM <sub>2.5</sub>	14.7	0.8	5%
	Mooibroek et al. (2011)	Schiedam (NL)	Urban	EPA PMF 3.0	2007-2008	PM <sub>2.5</sub>	13	1.2	9%
	Mooibroek et al. (2011)	Hellendoorn (NL)	Rural	EPA PMF 3.0	2007-2008	PM <sub>2.5</sub>	12.5	0.8	6%
	Mooibroek et al. (2011)	Rotterdam (NL)	Kerbside	EPA PMF 3.0	2007-2008	PM <sub>2.5</sub>	16.4	0.8	5%
	Mooibroek et al. (2011)	Vredepeel (NL)	Rural	EPA PMF 3.0	2007-2008	PM <sub>2.5</sub>	14.5	0.9	6%
	Mooibroek et al. (2011)	Cabauw (NL)	Rural	EPA PMF 3.0	2007-2008	PM <sub>2.5</sub>	17.5	1.6	9%
	Waked et al. (2014)	Lens (FR)	Urban	EPA PMF 3.0	2011-2012	PM <sub>10</sub>	20.5	5.4	26%
Dust	This study (PMF <sub>a</sub> )	Douai (FR)	Suburb.	EPA PMF 5.0	2015-2016	PM <sub>2.5</sub>	13.3	0.9	7%
	Bressi et al. (2014)	Paris (FR)	Urban	EPA PMF 3.0	2009-2010	PM <sub>2.5</sub>	14.7	0.1	1%
	Mooibroek et al. (2011)	Schiedam (NL)	Urban	EPA PMF 3.0	2007-2008	PM <sub>2.5</sub>	13	1.3	10%
	Mooibroek et al. (2011)	Hellendoorn (NL)	Rural	EPA PMF 3.0	2007-2008	PM <sub>2.5</sub>	12.5	1.6	13%
	Mooibroek et al. (2011)	Rotterdam (NL)	Kerbside	EPA PMF 3.0	2007-2008	PM <sub>2.5</sub>	16.4	1.5	9%
	Mooibroek et al. (2011)	Vredepeel (NL)	Rural	EPA PMF 3.0	2007-2008	PM <sub>2.5</sub>	14.5	1.3	9%
Dust	Mooibroek et al. (2011)	Cabauw (NL)	Rural	EPA PMF 3.0	2007-2008	PM <sub>2.5</sub>	17.5	1.9	11%
	This study (PMF <sub>a</sub> )	Douai (FR)	Suburb.	EPA PMF 5.0	2015-2016	PM <sub>2.5</sub>	13.3	0.3	3%
	Mooibroek et al. (2011)	Schiedam (NL)	Urban	EPA PMF 3.0	2007-2008	PM <sub>2.5</sub>	13	0.5	4%
	Mooibroek et al. (2011)	Hellendoorn (NL)	Rural	EPA PMF 3.0	2007-2008	PM <sub>2.5</sub>	12.5	0.4	3%
	Mooibroek et al. (2011)	Rotterdam (NL)	Kerbside	EPA PMF 3.0	2007-2008	PM <sub>2.5</sub>	16.4	0.3	2%
	Mooibroek et al. (2011)	Vredepeel (NL)	Rural	EPA PMF 3.0	2007-2008	PM <sub>2.5</sub>	14.5	0.4	3%
Dust	Mooibroek et al. (2011)	Cabauw (NL)	Rural	EPA PMF 3.0	2007-2008	PM <sub>2.5</sub>	17.5	0.4	2%
	Waked et al. (2014)	Lens (FR)	Urban	EPA PMF 3.0	2011-2012	PM <sub>10</sub>	20.5	2.6	13%

\* The road traffic factor of Mooibroek et al. (2011) includes resuspended road dust.

## SECTION 2. SUPPLEMENTARY FIGURES

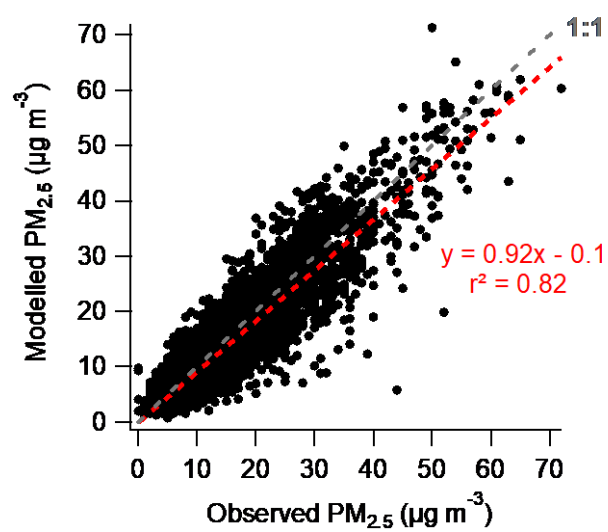


Figure S3.1 Correlation between modelled and observed hourly PM<sub>2.5</sub> concentrations. The dashed red line corresponds to the linear least-squares fit through the data.



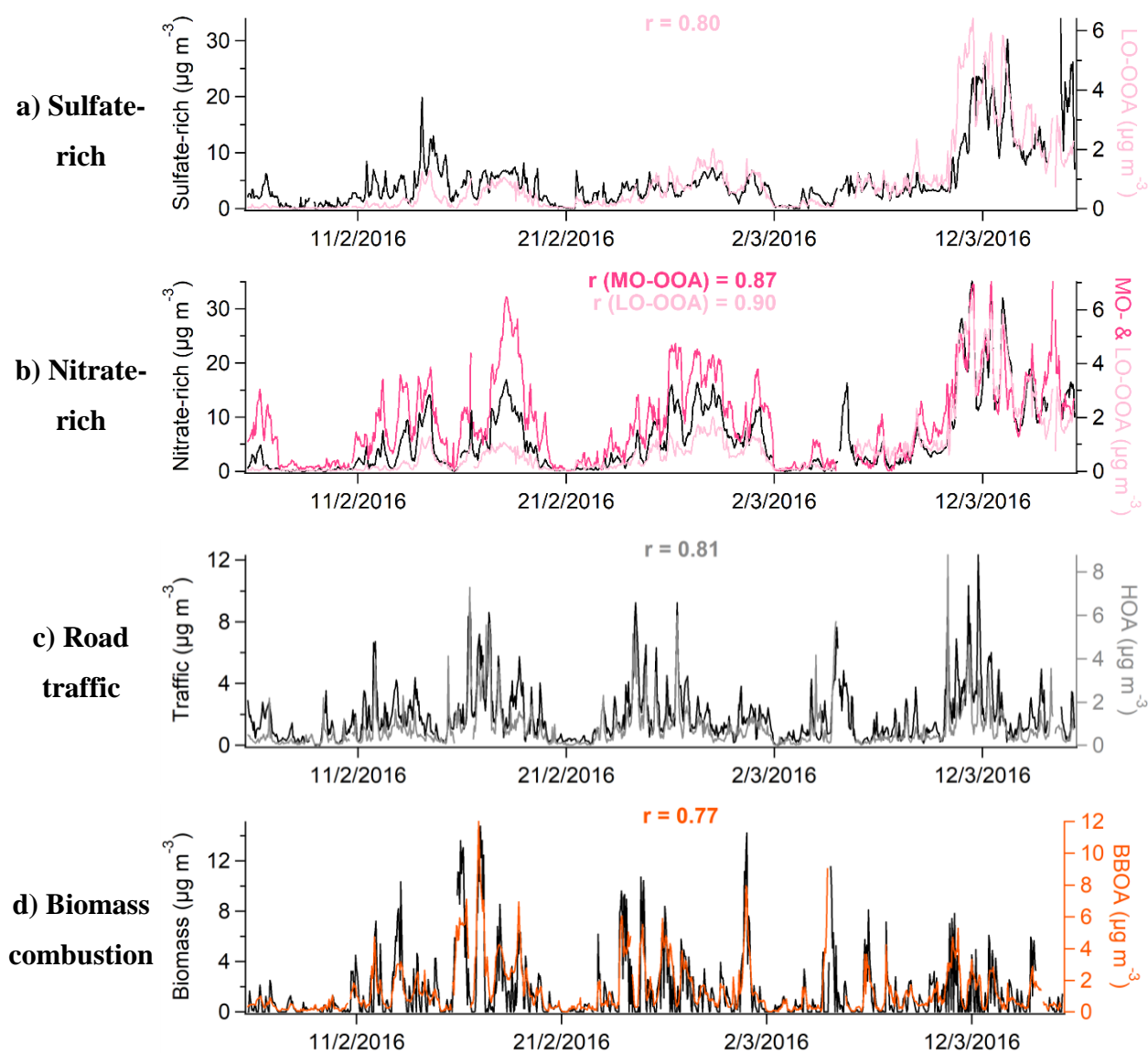


Figure S3.2 Time series of analogous source factors between  $\text{PMF}_h$  (left axis) and  $\text{PMF}_{\text{org}}$  (right axis)

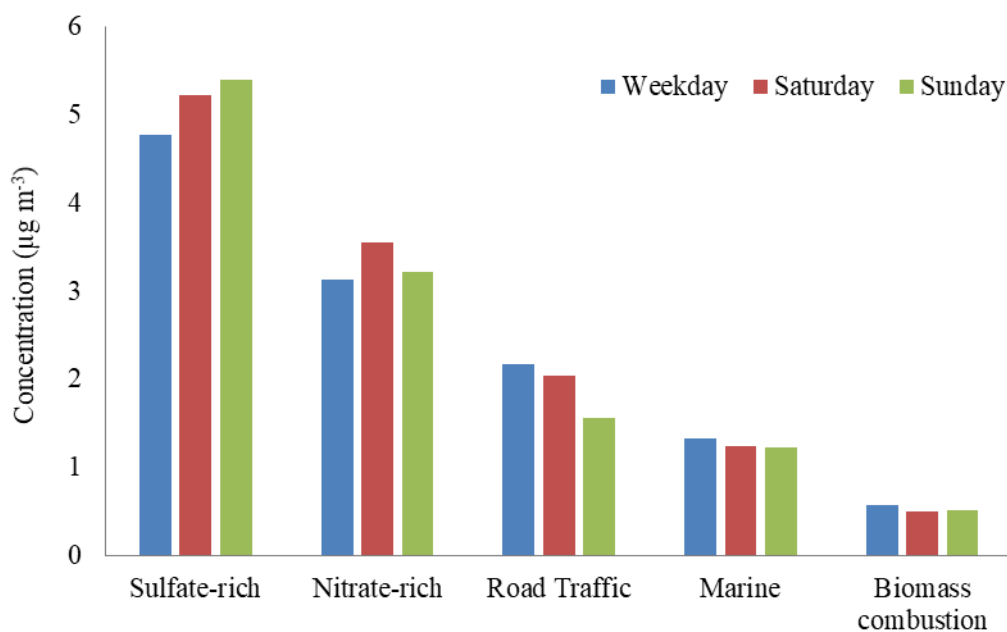


Figure S3.3 Contributions (in  $\mu\text{g m}^{-3}$ ) of the different PMF<sub>h</sub> source factors for weekdays, Saturdays and Sundays

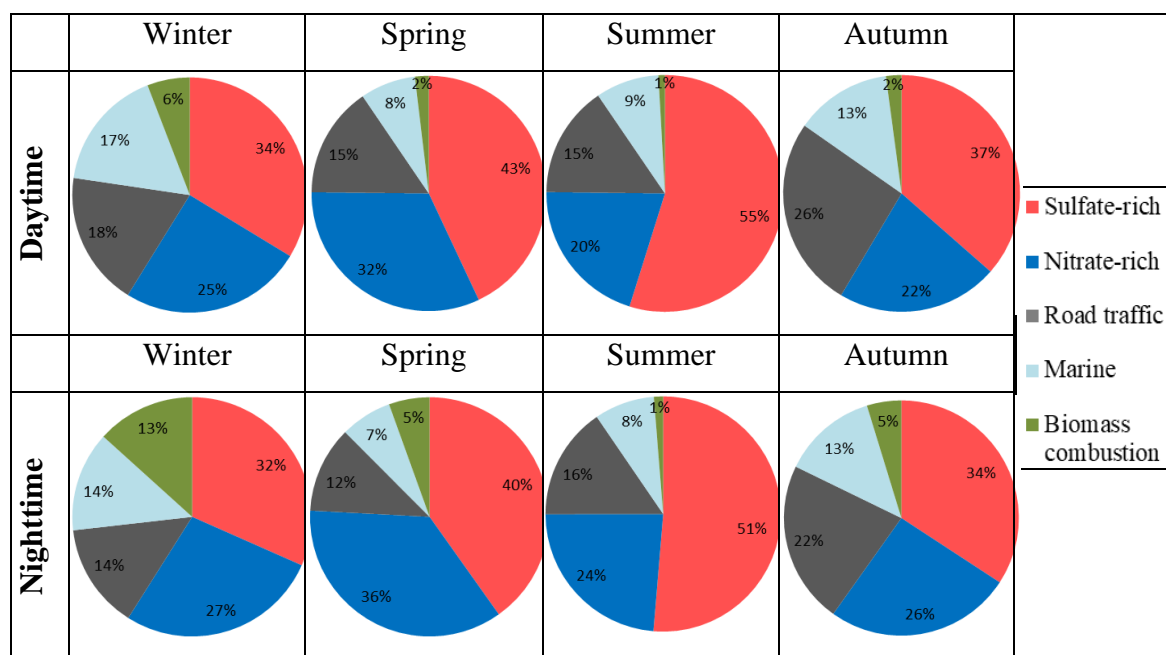


Figure S3.4 Contribution (%) of the different PMF<sub>h</sub> source factors during daytime and nighttime for each season

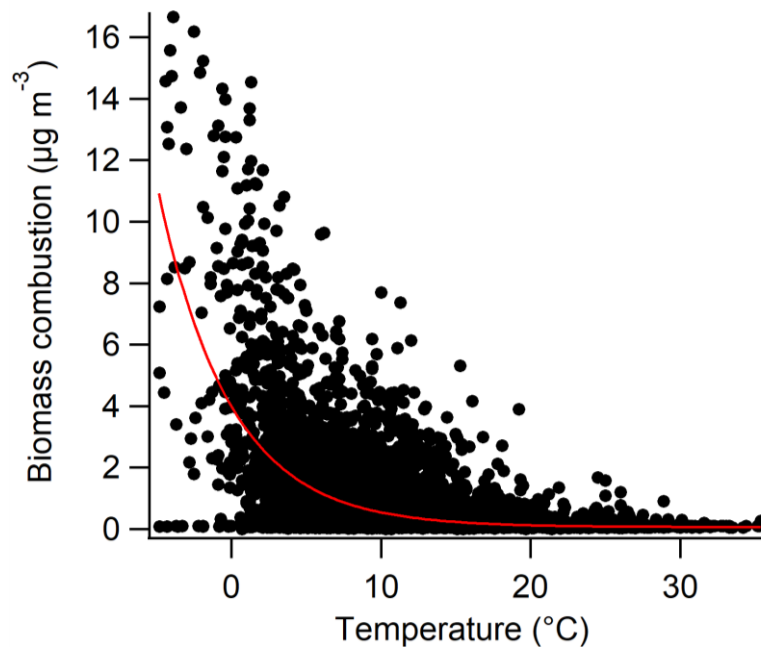
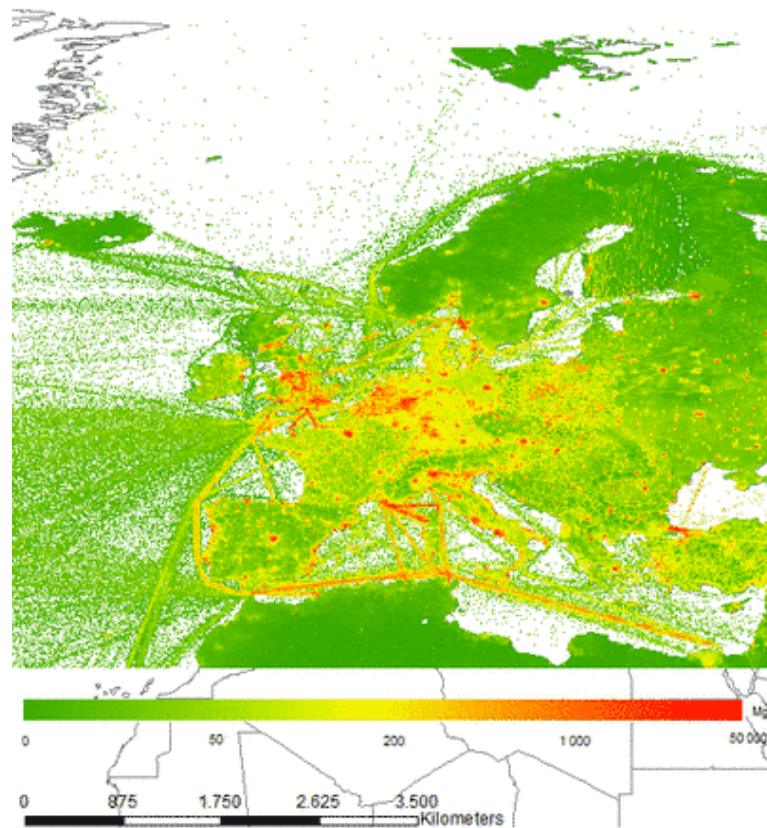
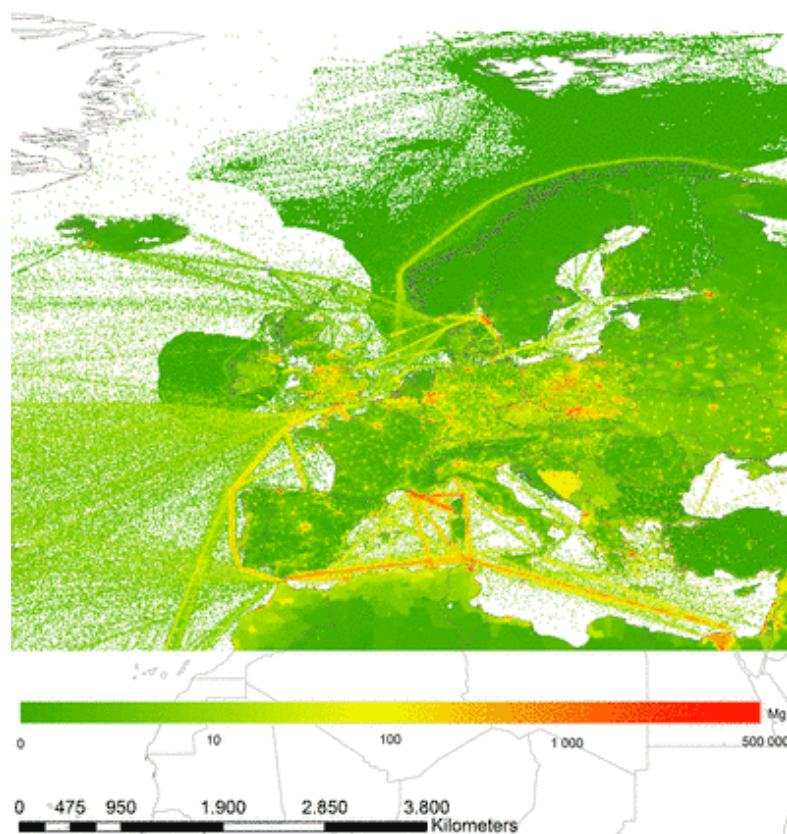


Figure S3.5 Biomass combustion factor concentrations vs. observed temperatures. The solid red line represents the exponential decrease fit which follows best the observed trend of the data and is there just to guide the eye.

a)



b)



c)

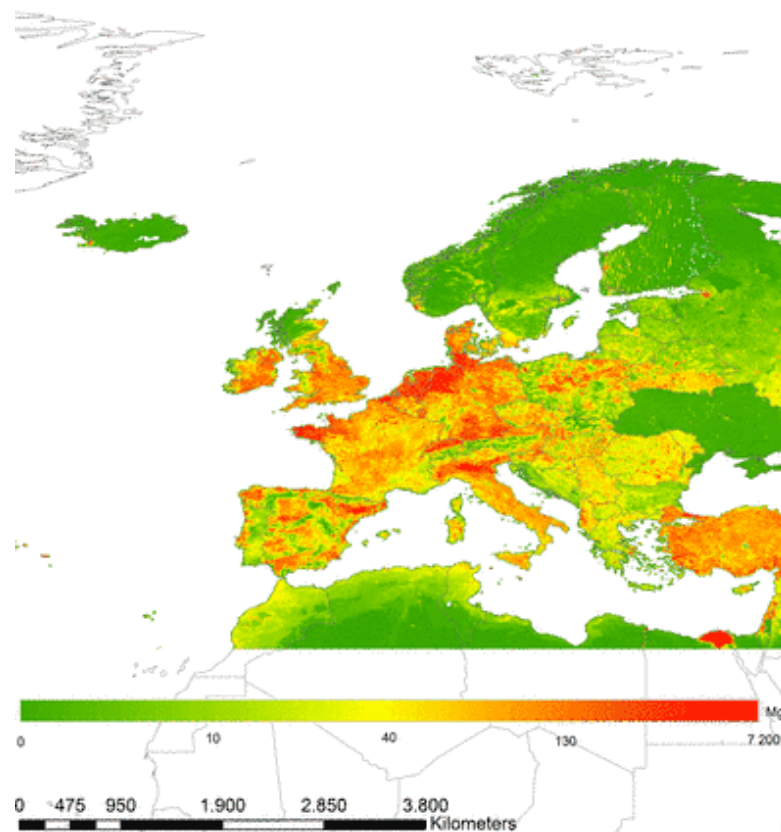


Figure S3.6 Gridded NO<sub>x</sub> (a), SO<sub>x</sub> (b) and NH<sub>3</sub> (c) emissions for 2015 (EMEP, 2016)



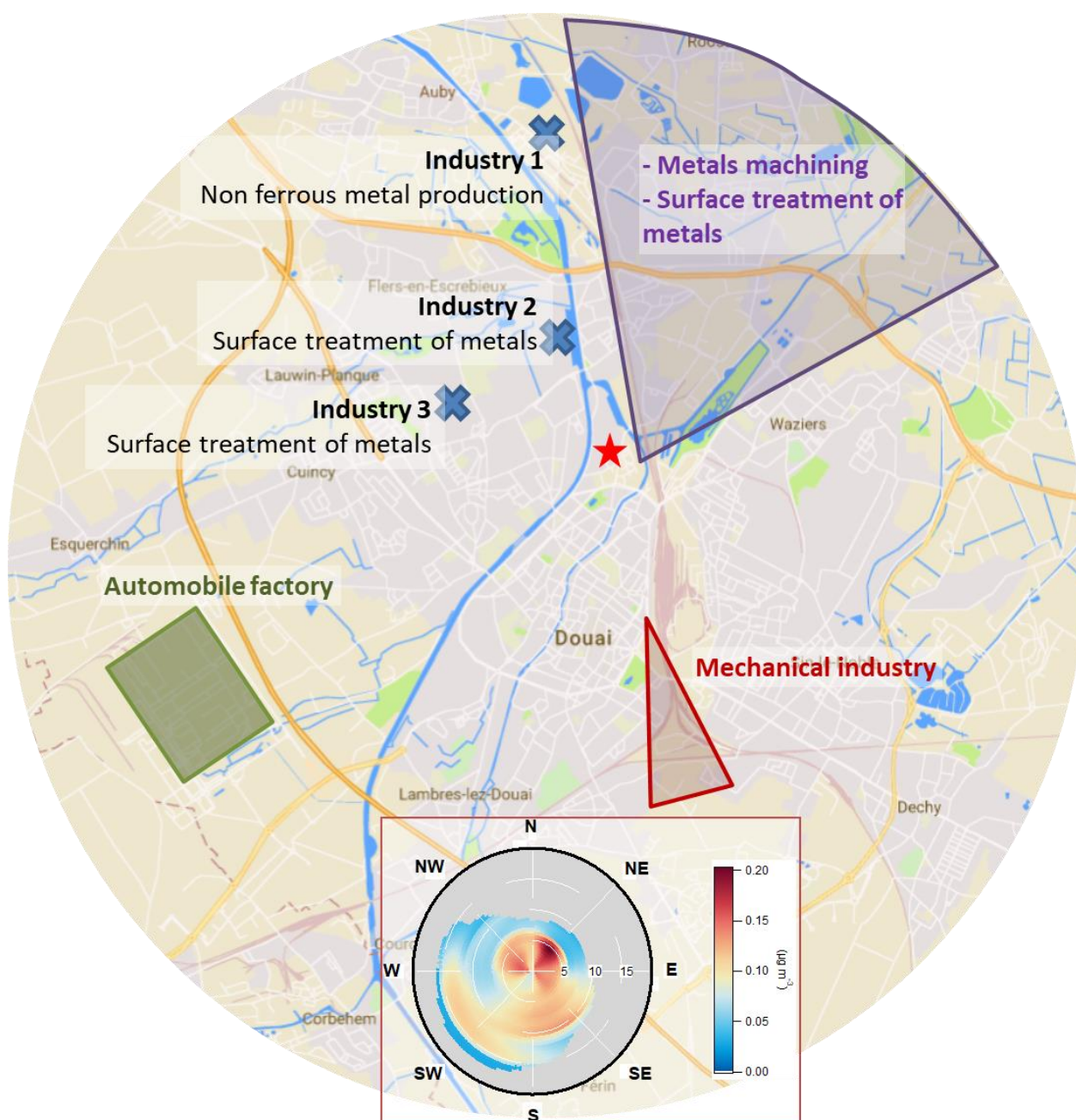


Figure S3.7 NWR plot for the local industry source factor together with the map of Douai and its surroundings, where the sampling site is represented with a red star and possible emitters of Co, Cr and Ni are shown with blue crosses and colored areas.

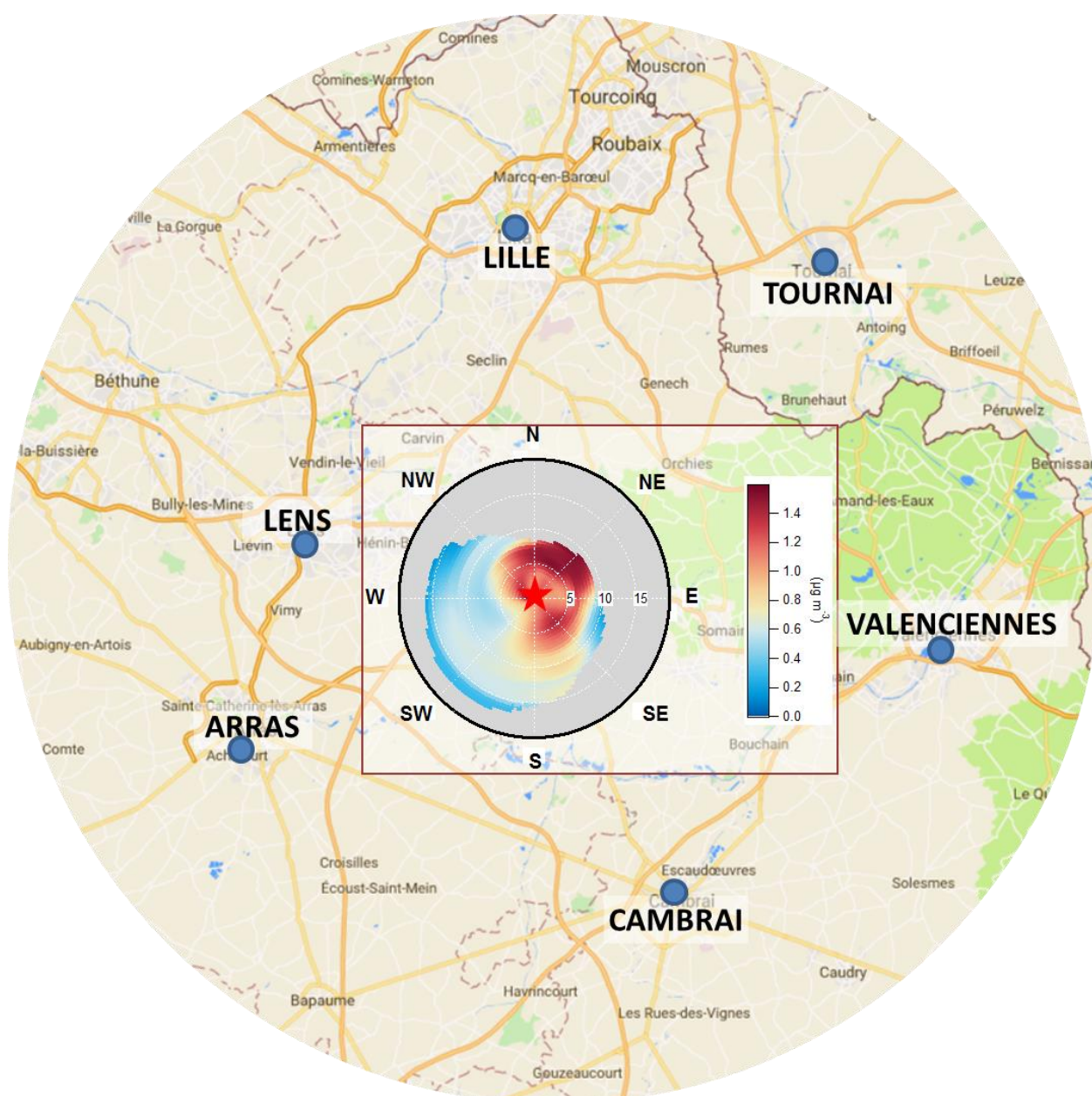


Figure S3.8 NWR plot for the MIB (Metal Industry Background) source factor together with the map of northern France, where the sampling site is represented with a red star and the main cities with blue circles

### Section 3. Calculation of uncertainties

The methodology proposed by Gianini et al. (2012) was used as a basis for the calculation of the uncertainties associated to the ions analyzed by the MARGA, following equation S1:

$$u_{ij} = \sqrt{(DL_j)^2 + (CV_j x_{ij})^2 + (ax_{ij})^2} \quad \text{Eq. S1}$$

where  $u_{ij}$  is the uncertainty associated with the concentration  $x_{ij}$  of compound  $j$  at time  $i$ ,  $DL_j$  is the detection limit of compound  $j$  calculated as three times the standard deviation of the field blanks,  $CV_j$  is the coefficient of variation of compound  $j$ , calculated as the standard deviation of repeated analyses of anion and cation certified standards divided by the average value of the repeated analyses, and  $a$  is a factor that equals 0.03 and is applied to account for additional sources of uncertainties.

The calculation proposed by Gianini et al. (2012) was slightly modified by adding two extra sources of uncertainty: the volume of air sampled and the losses of species in the inlet and sampling line, resulting in equation S2. The relative uncertainty of the sampling volume was determined to be 3%. The relative uncertainty related to the loss in the sampling line was set to 5%, after assessment with the Particle Loss Calculator extension for Igor Pro (von der Weiden et al., 2009). The factor “a” accounting for additional error sources was set to 0.01.

$$u_{ij} = \sqrt{\underbrace{(DL_j)^2}_{\text{Detection limit}} + \underbrace{(CV_j x_{ij})^2}_{\text{Repeatability}} + \underbrace{(u_{r,vol} x_{ij})^2}_{\text{Volume}} + \underbrace{(u_{r,loss} x_{ij})^2}_{\text{Loss}} + \underbrace{(ax_{ij})^2}_{\text{Additional unc.}}} \quad \text{Eq. S2}$$

In a similar way, the overall uncertainty associated with the concentration  $C_j$  of an element  $j$  analyzed by ICP-MS is calculated following equation S3 (Alleman et al., 2010):

$$u(C_j) = C_j \sqrt{\underbrace{\left(u_{r,SRM}^2 + \frac{s_{r,bias}^2}{n_{bias}}\right)}_{\text{Accuracy}} + \underbrace{\frac{s_{r,rep(QC)}^2}{n_{rep(QC)}}}_{\text{Repeatability}} + \underbrace{u_r^2(V)}_{\text{Volume}} + \underbrace{\frac{u_{r,cont}^2}{C_j^2}}_{\text{Contamination}}} \quad \text{Eq. S3}$$

Four sources of uncertainty are taken into account: (1) accuracy, (2) repeatability, (3) air sampling volume, and (4) contamination:

- (1) The uncertainty related to the accuracy of the analysis has been estimated from: (a) the analysis of standard reference materials (SRM): NIST 1648 (urban particulate matter) and NIST 2584 (trace elements in indoor dust); (b) the bias obtained from the analysis of a number of replicates  $n$ .
- (2) The repeatability of the analysis has been calculated through a QC (Quality control) analysis on a number of replicates  $n$ .
- (3) The uncertainty associated to the volume of sampling has been calculated from the allowed drift (5%) relative to the flow rate of the PARTISOL air pump ( $10 \text{ L min}^{-1}$ ).
- (4) The uncertainty related to a possible contamination has been calculated from the analysis of several field blanks.



## Section 4. Comparison between PMF<sub>h</sub> and PMF<sub>d</sub> with the same input variables

A comparison of the results between PMF<sub>h</sub> and PMF<sub>d</sub> with the exact same variables was performed in order to evaluate the influence of time resolution alone. The used variables were the ones obtained with the MARGA and the aethalometer (PM<sub>2.5</sub>, NO<sub>3</sub><sup>-</sup>, SO<sub>4</sub><sup>2-</sup>, C<sub>2</sub>O<sub>4</sub><sup>2-</sup>, NH<sub>4</sub><sup>+</sup>, Na<sup>+</sup>, Mg<sup>2+</sup>, K<sup>+</sup>, BC and Delta-C). In Figure S3.9, the contribution of the source factors to PM<sub>2.5</sub> are given for each PMF type. The concentrations and contributions of each variable in the source chemical profiles are given in Tables S3.9 and S3.10, respectively. The statistics from the comparison between the measured and modelled variables for each PMF type are presented in Table S3.11.

The five source factors obtained were the same for both PMF<sub>h</sub> and PMF<sub>d</sub>: sulfate-rich, nitrate-rich, traffic, marine and biomass combustion. However, there are discrepancies regarding the contributions of the source factors to PM<sub>2.5</sub> between both approaches (Figure S9). While these differences were not large for the sulfate-rich, traffic and marine factors ( $\pm 2\%$  in absolute contributions, corresponding to 13 to 18% of maximum relative variations), they were more important for the nitrate-rich (-4%, from 26 to 22%) and biomass combustion factors (+6%, from 5 to 11%) between PMF<sub>h</sub> and PMF<sub>d</sub> analyses. These two source factors have similar daily profiles, with higher concentrations during the nighttime/early morning due to the nature of the biomass combustion activities (performed mostly during the evening and night) and to the formation of ammonium nitrate which is maximum during nighttime and the early morning when temperatures are lowest. These two processes are clearly distinguished within the hourly timescale (there is a shift of about 6 hours between the maximum concentrations of both source factors as seen in the main manuscript of this article). However, the averaging of variables into 24-h values causes a loss information and the two processes are likely slightly merged in the PMF<sub>d</sub> results. This is partly observed in the composition of the biomass combustion source (Tables S3.9 and S3.10), where the contributions of variables other than K<sup>+</sup> and Delta-C are negligible for PMF<sub>h</sub>, whereas noticeable ones for NO<sub>3</sub><sup>-</sup>, NH<sub>4</sub><sup>+</sup> and SO<sub>4</sub><sup>2-</sup> (>5 % for each variable) are observed for PMF<sub>d</sub>. This mass transfer for these compounds reflects the merging of biomass combustion and nitrate-rich factors.

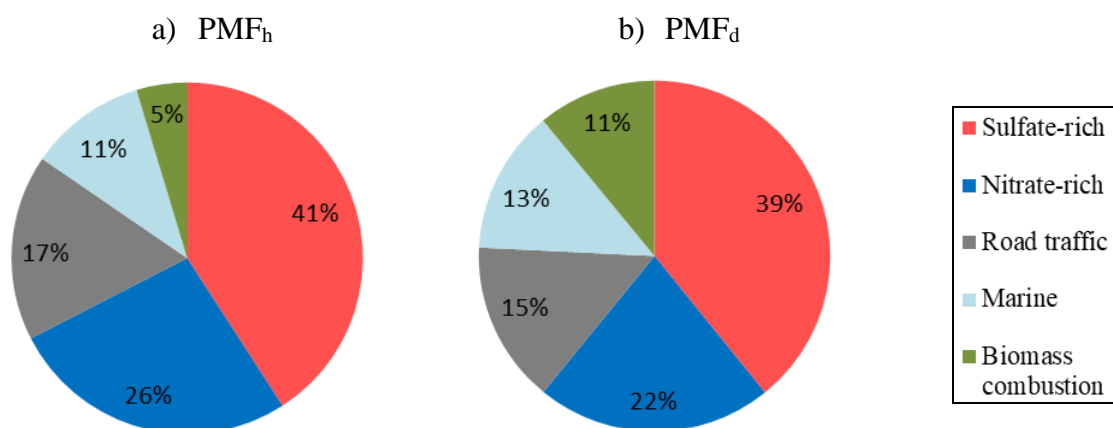


Figure S3.9 Contribution of source factors to modelled PM<sub>2.5</sub> mass for PMF<sub>h</sub> and PMF<sub>d</sub> with the same input variables

Table S3.9 Concentrations of each variable in the chemical profile of the source factors for the hourly and daily PMF with the same input variables ( $\text{PM}_{2.5}$ ,  $\text{NO}_3^-$ ,  $\text{SO}_4^{2-}$ ,  $\text{C}_2\text{O}_4^{2-}$ ,  $\text{NH}_4^+$ , BC and Delta-C are in  $\mu\text{g m}^{-3}$ , the rest in  $\text{ng m}^{-3}$ ).

Source factor		Sulfate-rich		Nitrate-rich		Road traffic		Biomass combustion		Marine	
PMF type		PMF <sub>d</sub>	PMF <sub>h</sub>	PMF <sub>d</sub>	PMF <sub>h</sub>	PMF <sub>d</sub>	PMF <sub>h</sub>	PMF <sub>d</sub>	PMF <sub>h</sub>	PMF <sub>d</sub>	PMF <sub>h</sub>
Variables	$\text{PM}_{2.5}$	5.17	4.92	2.83	3.20	1.96	2.06	1.42	0.55	1.76	1.30
	$\text{NO}_3^-$	0.11	0.00	2.37	3.01	0.84	0.59	0.21	0.02	0.23	0.13
	$\text{SO}_4^{2-}$	1.16	1.32	0.23	0.16	0.07	0.10	0.12	0.00	0.18	0.17
	$\text{C}_2\text{O}_4^{2-}$	0.11	0.10	0.00	0.00	0.02	0.02	0.01	0.00	0.02	0.02
	$\text{NH}_4^+$	0.40	0.41	0.77	0.84	0.00	0.00	0.10	0.00	0.04	0.00
	BC	0.00	0.03	0.06	0.00	0.35	0.36	0.00	0.02	0.02	0.00
	$\text{Na}^+$	0.00	2.82	0.00	1.64	0.00	0.00	0.00	0.83	0.09	79.33
	$\text{Mg}^+$	0.00	2.36	0.00	0.10	0.00	1.45	0.00	0.25	0.01	9.83
	$\text{K}^+$	0.01	4.42	0.00	1.62	0.01	5.97	0.01	4.98	0.00	3.53
	Delta-C	0.00	0.57	0.00	0.00	0.00	0.16	0.02	23.35	0.00	0.58

Table S3.10 Contributions (%) of each variable in the source chemical profiles for the hourly and daily PMF with the same input variables.

Source factor		Sulfate-rich		Nitrate-rich		Road traffic		Biomass combustion		Marine	
PMF type		PMF <sub>d</sub>	PMF <sub>h</sub>	PMF <sub>d</sub>	PMF <sub>h</sub>	PMF <sub>d</sub>	PMF <sub>h</sub>	PMF <sub>d</sub>	PMF <sub>h</sub>	PMF <sub>d</sub>	PMF <sub>h</sub>
Variables	$\text{PM}_{2.5}$	39.4	40.9	21.5	26.6	14.9	17.2	10.8	4.6	13.4	10.8
	$\text{NO}_3^-$	2.8	0.0	63.1	80.3	22.4	15.7	5.6	0.7	6.0	3.4
	$\text{SO}_4^{2-}$	66.0	76.0	13.4	9.0	4.0	5.5	6.6	0.0	10.1	9.5
	$\text{C}_2\text{O}_4^{2-}$	69.1	69.1	0.0	0.0	11.9	17.0	8.3	1.5	10.8	12.4
	$\text{NH}_4^+$	30.7	32.4	58.9	67.6	0.0	0.0	7.5	0.0	2.9	0.0
	BC	0.1	7.9	14.0	0.0	81.1	87.6	0.0	4.6	4.8	0.0
	$\text{Na}^+$	0.0	3.3	0.0	1.9	0.0	0.0	1.6	1.0	98.4	93.8
	$\text{Mg}^+$	10.4	16.9	3.9	0.7	8.0	10.4	0.0	1.8	77.7	70.3
	$\text{K}^+$	23.0	21.6	0.3	7.9	23.3	29.1	42.3	24.3	11.1	17.2
	Delta-C	4.6	2.3	0.0	0.0	1.6	0.7	89.2	94.7	4.6	2.3

Table S3.11 Statistics comparing the modelled and measured concentrations for each variable used in the hourly and daily PMF with the same input variables. Intercept in  $\mu\text{g m}^{-3}$

	<b>PMF<sub>d</sub></b>			<b>PMF<sub>h</sub></b>		
<b>Species</b>	<b>r<sup>2</sup></b>	<b>Slope</b>	<b>Intercept</b>	<b>r<sup>2</sup></b>	<b>Slope</b>	<b>Intercept</b>
NO <sub>3</sub> <sup>-</sup>	0.99	1.01	-0.04	0.99	1.04	-0.11
SO <sub>4</sub> <sup>2-</sup>	0.98	1.00	0.00	0.98	1.01	-0.02
C <sub>2</sub> O <sub>4</sub> <sup>2-</sup>	0.57	0.73	0.04	0.38	0.52	0.05
Na <sup>+</sup>	0.97	0.87	0.01	0.92	0.81	0.02
NH <sub>4</sub> <sup>+</sup>	0.99	0.96	0.02	0.99	0.90	0.06
K <sup>+</sup>	0.55	0.37	0.01	0.26	0.20	0.01
Mg <sup>2+</sup>	0.64	0.61	0.01	0.38	0.32	0.01
BC	0.84	0.95	0.02	0.79	0.77	0.08
Delta-C	0.99	1.00	0.00	0.99	1.00	0.00
PM <sub>2.5</sub>	0.89	1.00	-0.32	0.83	0.92	-0.20

## References

Alleman, L. Y., Lamaison, L., Perdrix, E., Robache, A. and Galloo, J.-C.: PM10 metal concentrations and source identification using positive matrix factorization and wind sectoring in a French industrial zone, *Atmos. Res.*, 96(4), 612–625, doi:10.1016/j.atmosres.2010.02.008, 2010.

Bressi, M., Sciare, J., Gherzi, V., Mihalopoulos, N., Petit, J.-E., Nicolas, J. B., Moukhtar, S., Rosso, A., Féron, A., Bonnaire, N., Poulakis, E. and Theodosi, C.: Sources and geographical origins of fine aerosols in Paris (France), *Atmos. Chem. Phys.*, 14(16), 8813–8839, doi:10.5194/acp-14-8813-2014, 2014.

EMEP: EMEP database, [online] Available from: [http://www.ceip.at/ms/ceip\\_home1/ceip\\_home/webdab\\_emepdatabase/](http://www.ceip.at/ms/ceip_home1/ceip_home/webdab_emepdatabase/), 2016.

Gianini, M. F. D., Fischer, A., Gehrig, R., Ulrich, A., Wichser, A., Piot, C., Besombes, J.-L. and Hueglin, C.: Comparative source apportionment of PM10 in Switzerland for 2008/2009 and 1998/1999 by Positive Matrix Factorisation, *Atmos. Environ.*, 54, 149–158, doi:10.1016/j.atmosenv.2012.02.036, 2012.

Mooibroek, D., Schaap, M., Weijers, E. P. and Hoogerbrugge, R.: Source apportionment and spatial variability of PM2.5 using measurements at five sites in the Netherlands, *Atmos. Environ.*, 45(25), 4180–4191, doi:10.1016/j.atmosenv.2011.05.017, 2011.

Waked, A., Favez, O., Alleman, L. Y., Piot, C., Petit, J.-E., Delaunay, T., Verlinden, E., Golly, B., Besombes, J.-L., Jaffrezo, J.-L. and Leoz-Garziandia, E.: Source apportionment of PM10 in a north-western Europe regional urban background site (Lens, France) using positive matrix factorization and including primary biogenic emissions, *Atmos. Chem. Phys.*, 14(7), 3325–3346, doi:10.5194/acp-14-3325-2014, 2014.

von der Weiden, S.-L., Drewnick, F. and Borrmann, S.: Particle Loss Calculator – a new software tool for the assessment of the performance of aerosol inlet systems, *Atmos. Meas. Tech.*, 2(2), 479–494, doi:10.5194/amt-2-479-2009, 2009.

